AN INVESTIGATION OF THE TUFA DEPOSITS AT GA-MOHANA HILL IN THE NORTHERN CAPE, SOUTH AFRICA: PALAEOENVIRONMENTAL CONTEXT FOR LATE PLEISTOCENE AND HOLOCENE HUMAN OCCUPATION IN THE SOUTHERN KALAHARI

Jessica Johanna von der Meden

ORCID: 0000-0003-3957-5824

Submitted in total fulfilment of
the requirements for the degree of

DOCTOR OF PHILOSOPHY

June 2024

Department of Geological Sciences
Faculty of Science
The University of Cape Town

ABSTRACT

There is a rich record of human occupation in the southern Kalahari, but the palaeoclimatic backdrop to early human activity in this area is poorly understood. Secondary calcium carbonates, including tufa, are common in the Kalahari, yet their palaeoclimate potential remains relatively unexploited. Tufa deposits at Ga-Mohana Hill, an archaeological site in the southern Kalahari, represent past water availability in a presently semi-arid region. Tufa are useful palaeoclimate proxies that form from freshwater springs and streams. They are amenable to radiometric dating, and conditions during their formation can be investigated through geochemical proxies, such as carbon and oxygen isotopes. In this study, I use the tufa deposits at Ga-Mohana Hill, and their association with the archaeological record of Late Pleistocene and Holocene human occupation, to investigate the interplay between environmental changes and human evolution in this previously understudied region.

I show that the Ga-Mohana tufa deposits comprise cascade, barrage, terrace breccia and dome morphologies that formed from a presently inactive perched-springline system, and that these represent past streams, waterfalls, and shallow pools. Based on petrographic observations, bulk X-ray diffraction, and *in situ* laser ablation analysis, calcite is identified as the main crystalline phase, along with variable inclusions of quartz and other non-carbonate phases rich in Mn, Fe and Al. Element distribution maps constructed from laser ablation analysis were used to identify portions of the tufa samples suitable for uranium-thorium dating.

Episodic tufa formation over the last ~114 ka is inferred from thirty-three U-Th ages obtained from twelve tufa samples. These episodes are interpreted to indicate water availability during MIS 5d (~114 - 100 ka), MIS 4 (~73-57 ka), two stages during MIS 3 (~57-48 ka, and ~44-32 ka), and two stages during the Holocene (~15 - 6 ka, and ~4-2 ka). This timing supports the notion that conditions for tufa formation are not restricted to warm and wet interglacial periods.

The tufa carbon (-8.83 to +3 .55‰) and oxygen (-6.14 to -0.05‰) isotope values indicate some kinetic fractionation effects, likely driven by evaporation. The carbon isotopes indicate a combined input of soil-derived CO_2 and heavier bedrock CO2, along with a high proportion of C4 vegetation, except during MIS 4, during which lower $\delta^{13}C$ values indicate a higher input of soil-derived CO_2 and/or a greater proportion of C3 vegetation. Overall, the carbon and oxygen isotope values indicate a gradual increase in aridity over the last ~70 ka, i.e., warmer temperatures, increased evaporation, and a higher proportion of C4 vegetation, albeit wet enough to sustain tufa formation.

Three of the tufa episodes coincide with archaeological units at Ga-Mohana Hill, dated to ~105 ka, ~31 ka, and ~15 ka. I propose that prior to ~70 ka, human occupation in the region coincided with water availability, whereas by ~30 ka, water availability was much reduced, yet human occupation persisted. Following the last glacial maximum (LGM) there is evidence of human occupation despite variable water availability at Ga-Mohana Hill, and in the region. This may point to early human development of arid-adaptive behaviours in the southern Kalahari.

DECLARATION

This is to certify that:

i. the work on which this thesis is based is my original work, except where acknowledgements indicate otherwise

ii. that neither the whole work nor any part of it has been, is being, or is to be submitted for another degree in this or any other university

iii. I authorise the University of Cape Town to reproduce for the purpose of research either the whole or any portion of the contents in any manner whatsoever.

Signed,

Signed by candidate

Jessica Johanna von der Meden

June 2024

PREFACE

Publications arising from this PhD work:

1) von der Meden., J., Pickering, R., Schoville, B. J., Green, H., Weij, R., Hellstrom, J., Greig, A., Woodhead, J., Khumalo, W., Wilkins, J. (2022). Tufas indicate prolonged periods of water availability linked to human occupation in the southern Kalahari. *PLOS ONE*, 17(7). https://doi.org/10.1371/journal.pone.0270104
2) Wilkins, J., Schoville, B. J., Pickering, R., Gliganic, L., Collins, B., Brown, K. S., von der Meden, J., Khumalo, W., Meyer, M.C., Maape, S., Blackwood, A.F., Hatton, A. (2021). Innovative Homo sapiens behaviours 105,000 years ago in a wetter Kalahari. *Nature*, *592*(7853), 248–252. https://doi.org/10.1038/s41586-021-03419-0

I acknowledge the following financial support:

i. South African National Research Foundation (NRF) Postgraduate PhD Scholarship (2022) facilitated by the Competitive Programme for Rated Researchers Grant (120806) to Robyn Pickering
ii. South African NRF Centre of Excellence in Palaeosciences Operations Grants (CoE2017-065, COE2018-05OP, COE2019-OP17 and COE2018-10OP) facilitated by Jayne Wilkins and Robyn Pickering
iii. South African NRF Research Development Grant for Y-rated Researchers facilitated by Jayne Wilkins
iv. Australian Research Council Discovery Early Career Research Award - DE 190100160 facilitated by Jayne Wilkins
v. University of Cape Town Vice Chancellors Future Leaders funding to Rosalie Tostevin
vi. South African NRF Centre of Excellence in Palaeosciences Masters student bursary (2018, 2019)

vii. South African NRF Masters student bursary facilitated by the African Origins Platform Grant (AOP150924142990) to Robyn Pickering (2017, 2018)
viii. National Geographic Society Waitt Grant facilitated by Benjamin J Schoville

The funding agencies had no role in study design, data collection and analysis.

I acknowledge the following for their role in supervision and collaboration:

Dr Robyn Pickering (Department of Geological Sciences, UCT) for the conceptualisation of this project, early supervision of this thesis, and funding contributions for fieldwork, analyses, conference attendance, and a research visit to the University of Melbourne, Australia.

Prof Chris Harris, Dr Rosalie Tostevin (Department of Geological Sciences, UCT), and Dr Jayne Wilkins (Australian Research Centre for Human Evolution, Griffith University, Australia) for their unconditional support and supervision of this thesis to completion.

Benjamin J. Schoville (School of Social Science, University of Queensland, Australia) for assistance with field work, sample collection and map-making.

Dr Julie Luyt (Department of Archaeology, UCT) for assistance with stable isotope analysis and data processing.

In the Department of Geological Sciences at UCT:

Christel Tinguely for solution ICP-MS element analysis and data processing
Rene van der Merwe for thin section preparation
Warwick Joe for isotope analysis of water samples

Prof Jon Woodhead, Dr John Hellstrom, Dr Alan Greig, Dr Roland Maas, Dr Helen Green, and Prof Russel Drysdale for facilitating my research visit to the Isotope Geoscience Group at the University of Melbourne, Australia, and for assistance with LA-ICP-MS, U-Th dating, and stable isotope analysis and data processing.

ACKNOWLEDGMENTS

My PhD journey has been a long and challenging one, but it has also been filled with valuable life lessons and personal growth, incredible learning and travel opportunities, and many wonderful new friendships - for all of this, and for all the people who have supported and encouraged me along the way, I am extremely grateful.

My most sincere thanks and deep gratitude to:

Jayne Wilkins, for believing in me, and for invaluable supervision and mentorship. Thank you, Jayne, for your unconditional and unwavering support, encouragement, advice and guidance whenever I needed it. I couldn't have made it to this point without you.

Rosalie Tostevin, for consistent support and willingness to step in as a co-supervisor on this project. Thank you, Rosalie, for the constructive discussions and feedback, and for all your encouragement.

Chris Harris, for supporting me throughout this journey. Thank you, Chris, for patiently and generously sharing your knowledge and expertise, and for your super speedy feedback on drafts of this thesis. I especially appreciate your support and willingness to supervise the completion of this thesis.

Ben Schoville, for all your assistance and fun company in the field, and for including me in the Tswalu survey team. Thanks especially for the GIS tutorials and your map-making wizardry!

Phil Janney, for tireless support and assistance as HoD, and for encouraging me to see this project to completion.

David Gammon, for listening to me, and for your kindness and support when I didn't know who to turn to.

Jon Woodhead, Roland Maas, John Hellstrom, Alan Greig, Russ Drysdale, Helen Green, Ellen Corrick, **Serene Paul, and Bence Paul**, for generously hosting me in the labs in 2019, and for all the assistance, valuable discussions and guidance.

Thanks too to **Alice**, **Angus**, **Bianca**, **Claire**, **Hayden**, **Jeremy**, **John**, **Jessie**, **Maddy**, **Rob**, **Rien**, **and Schirin**, for including me in the Melb Uni postgrad group, Friday afternoon beers at the Clyde, and for making my time in Melbourne such fun!

Julie Luyt, for accommodating me in the Stable Light Isotope Lab, and for assisting me with data processing and isotope queries.

Kyle Brown, Simangaliso Makalima, Khumo Matlhoko, and Alex Blackwood for help with tufa sampling, and for your great company in the field.

Andrea Borsato and Adam Hartland for valuable input and discussions at the Summer School on Speleothem Science (S4) workshop in Cluj-Napoca, in 2019.

Friends, lecturers and colleagues in the UCT Geology Department. Thanks in particular to **Emese Bordy**, **Alastair Sloan, Petrus Le Roux, and Christel Tinguely** for taking an interest in how I was doing, and for words of encouragement. **John Harrison and Ivan Wilson** for always being willing to assist with technical support. **Nathalie Barends and Elretha Roos** for assisting with administrative processes, and for friendly chats. My fellow postgrad students and office mates over the years for the friendly working environment. In particular, **Fiona, Zoë, Cami, Osvaldo, Rob, Josh, McDonald, Aidan, Bontle, and Ansa**. Special thanks to **Ansa** for fun in the field, help with data processing, and PhD chats.

Sarah, Rebecca, Kat, Nonku, and Aaron, my geo crew, for your friendship and support over the years.

Rosie, Matt, Ana, Diego, Tara and Alex, for your warm and genuine friendship, support, and encouragement. Thank you for always being willing to listen to me, give me hugs, a pep talk, or some perspective.

Rien, my dearest friend, for your warmth, love and beautiful friendship. Thank you for your kind understanding, and for being willing to support me in every way.

My family - Mom, Rolfie, Charlie and Ele, your immeasurable love and support is everything to me. Thank you for always having my back and for being there for me whenever I need you, in big ways and small.

Ginny and Luna, for reminding me to take a break from my desk to go for a walk or throw a ball in the garden.

Geoffrey, for everything.

DEDICATION

This thesis is dedicated to:

My dad, **Eric Alfred von der Meden** (1941-2012), who developed and nurtured my curiosity, instilled in me a love for nature, always trusted and supported my decisions, and ensured my access to quality education and opportunities. I know he would have loved to have been part of my journey, and that he would be very proud.

My childhood friend, **Spencer Stanley Slabber** (1993-2019), the most intelligent and gentle soul who braved life's highest mountain, solo.

TABLE OF CONTENTS

CHAPTER 1 INTRODUCTION

In this chapter, I present the rationale behind this study and highlight the gaps this thesis aims to address. I also articulate the key objectives that guide the research presented herein, along with background information on the project's timeline and context. Finally, I provide an overview of the thesis structure, which will help readers navigate the subsequent chapters.

1.1 Overview

Tufas are secondary calcium-carbonate deposits that form from ambient temperature spring waters, often in association with botanical or microbial organisms (Marker, 1988; Ford and Pedley, 1996; Andrews, 2006). Found in a variety of global settings, tufas record the local water chemistry and environmental conditions during their formation. Their amenability to radiometric dating makes relict tufa deposits valuable archives of past environmental conditions. While speleothems, such as stalagmites and flowstones, are the staple of terrestrial carbonate-based palaeoclimate studies, tufa deposits remain a relatively under-explored alternative, particularly in regions with limited terrestrial palaeoclimate records.

One such region is the southern Kalahari Basin, located in the northernmost part of the Northern Cape, South Africa. Here, the existing understanding of past environmental changes is incomplete (Lukich and Ecker, 2021). Presently, this area is semi-arid, receiving limited seasonal rainfall (~300-400 mm per annum in summer). However, landforms in this region, such as pans, palaeolakes and secondary carbonate deposits, suggest periods of increased precipitation and water availability in the past (e.g. Butzer, 1974; Marker, 1988; Nash and McLaren, 2003; Burrough et al., 2009a; Brook et al., 2010; Doran et al., 2015; Lukich et al., 2020). Despite this potential, these archives have not been fully explored.

Moreover, the southern Kalahari Basin has a rich record of Pleistocene and Holocene human occupation spanning the Earlier, Middle, and Later Stone Ages (Thackeray et al., 1981; Humphreys and Thackeray, 1983; Beaumont and Morris, 1990; Beaumont and Vogel, 2006; Curnoe et al., 2006; Porat et al., 2010; Chazan et al., 2012; Wilkins and Chazan, 2012; Burrough, 2016; McKee and Kuykendall, 2016; Lukich et al., 2019). However, archaeological sites in this interior region of South Africa have been largely overlooked in the current narrative of early modern human evolution (Wilkins et al., 2020; Wilkins et al., 2021). Research has instead predominantly focused on coastal sites in the southern Cape, where the emergence of modern humans during the Middle Stone Age (MSA) has been linked to the availability of marine resources and favourable climatic conditions (Marean, 2010; Parkington, 2010; Marean, 2014; Henshilwood et al., 2018; Smith et al., 2018). The paucity of well-dated MSA sites with robust palaeoclimate records from the South Africa's interior leaves these hypotheses largely unchallenged.

Evidence from Ga-Mohana Hill, situated in the Kuruman hills in the Northern Cape of provides an opportunity to address these gaps. This site features well-stratified MSA deposits that are contemporaneous with those found along the coast (Wilkins et al., 2020; Wilkins et al., 2021). Additionally, abundant tufa deposits on the Ga-Mohana Hillside, present an opportunity to explore the environmental conditions of the southern Kalahari Basin during the Late Pleistocene and Holocene human occupations. This thesis is centred on the tufa deposits at Ga-Mohana Hill and the past environments they represent.

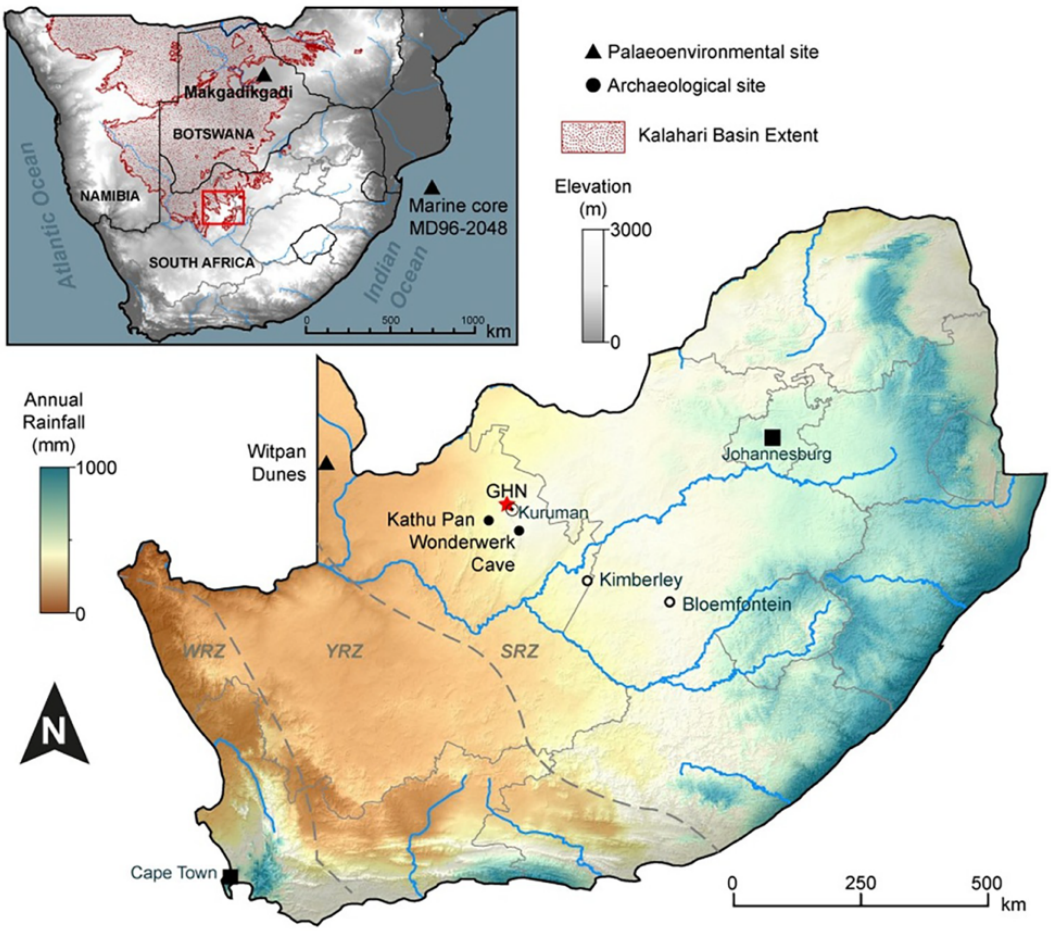

Figure 1.1 Map of South Africa with elevation (Fick and Hijmans, 2017) overlain by annual rainfall (Hijmans et al., 2005) data from WorldClim.org database. The location of Ga-Mohana Hill (GHN, red star) and nearby archaeological and palaeoenvironmental sites are shown. Dashed lines demarcate the summer, winter and year-round rainfall zone boundaries (SRZ, WRZ, YRZ, as defined in Roffe et al., 2021). The inset map shows the approximate extent of the Kalahari Basin in southern Africa (from Mendelsohn et al., 2002) and the location of the region of interest in relation to it (red square).

1.1 Aims and approaches

The overarching goal of this work is to investigate the depositional setting, chronology, and palaeoenvironment that the Ga-Mohana Hill tufa deposits represent, and to relate this to the archaeological record of Late Pleistocene and Holocene human occupation in the region.

To accomplish this, I:

1) Characterise the field expressions and petrography of the tufa deposits at Ga-Mohana Hill to determine their depositional environment.
2) Establish the mineralogy of the Ga-Mohana tufa deposits using X-ray Diffraction (XRD), and evaluate the use of trace elements to constrain processes relating to tufa formation at this site.
3) Date the tufa deposits using the U-Th method, supported by laser ablation pre-screening to guide sample selection, to place temporal constraints on tufa formation at Ga-Mohana Hill.
4) Use oxygen and carbon isotope data to identify patterns preserved in the tufas that may signal shifts in past rainfall, temperature, and vegetation at the site.
5) Relate the inferred climatic and environmental conditions to the archaeological findings, and place them in context with other local, regional, and global records.

My research was conducted over six years and included four field seasons in the Northern Cape. The first field season involved a survey of Ga-Mohana Hill and the surrounding landscape, and tufa sample collection. This was partially informed by a previous pilot study carried out by Dr Robyn Pickering in 2016. The samples collected were catalogued and their macromorphologies were described. Several of these were selected for thin section preparation, and sub-sampled for stable isotope analysis and U-Th dating. The thin sections and stable isotopes were prepared and analysed in the Geological Sciences and Archaeology departments at the University of Cape Town (UCT), respectively, during the first half of 2018. The sub-samples for U-Th dating were couriered to Melbourne University and processed there. The data returned from the U-Th dating was used to inform further targeted sampling of tufa deposits during a field visit in 2018, for which we used a modified hand drill to extract small cores from the tufa deposits. In addition to the tufa sampling, a water sampling campaign was also carried out during two visits to the Northern Cape in January and July 2018. The deuterium and oxygen isotopes in the water samples were analysed in 2018 at UCT.

During the first half of 2019, I was hosted by Prof Jon Woodhead and Dr Roland Maas in the Isotope Group at the Earth Science department at Melbourne University to

conduct U-Th analyses on the additional tufa samples. With assistance from Dr Alan Greig and Dr Helen Green, I first analysed selected tufa samples using a laser ablation inductively coupled mass spectrometer (LA-ICP-MS) to map the U and Th concentrations within the tufa samples. The results from the LA-ICP-MS were used to inform sub-sampling for U-Th dating, conducted by myself with the help of Dr Rieneke Weij, and under the guidance of Dr John Hellstrom. The results from these analyses were processed during 2019 and 2020 by John Hellstrom. A final field visit in early 2021 involved further water sampling and collection of bedrock dolomite samples. These were prepared for solution analysis by myself, under the guidance of Dr Rosalie Tostevin at UCT. Trace element concentrations in these samples were measured on an ICP-MS by Christel Tinguely at UCT in mid-2021.

Some of the results I present here have been peer-reviewed and published. In 2021, I contributed as co-author to a journal article in *Nature* titled 'Innovative *Homo sapiens* behaviours 105,000 years ago in a wetter Kalahari' (Wilkins et al., 2021). Results from my U-Th analyses showed that the 105 ka human occupation at Ga-Mohana Hill occurred during a wet period, represented by the presence of tufa deposits dated to the same time. In 2022, as first-author and with guidance from my supervisor Dr Jayne Wilkins, I published a more comprehensive presentation of my findings in *PLOS ONE* (von der Meden et al., 2022) based on Chapters 4, 6 and 8 of this thesis. We showed that the tufa deposits at Ga-Mohana Hill represent a depositional environment characterised by waterfalls, shallow pools and streams, which were active during several punctuated episodes over the last ~110 ka. Together with archaeological and palaeoenvironmental records from two other nearby sites, Kathu Pan and Wonderwerk Cave, we used the tufa data and the archaeological record from Ga-Mohana Hill to show that before ~71 ka human occupation in the southern Kalahari was linked to water availability, whereas after this time, the relationship is decoupled. We argue that this decoupling, which may have occurred at ~32 ka but is clearly established after the Last Glacial Maximum, may represent early human adaptations to drier conditions. These journal articles are included in Appendix I.

1.3 Outline of the thesis

Chapters 2 and 3 provide the background and context for this research. In Chapter 2, I outline the geological and environmental setting of the study site and examine previous investigations into the palaeoenvironment of the interior region of southern Africa, with particular emphasis on archives linked to archaeological records. I describe the fundamentals of tufa deposits, their formation, and some of the methods applied to them that are relevant for this study, based on existing literature. In Chapter 3, I provide details on the methods used in this study.

In Chapter 4, I document the field, macro- and micromorphological observations of the tufas at Ga-Mohana Hill and use these to determine the depositional environment the tufas represent. In Chapter 5, I first characterise the mineralogy of the tufa deposits using XRD data, and then present trace element data collected using high resolution laser ablation inductively coupled plasma mass spectrometry (LA-ICP-MS), and comparatively low-resolution solution ICP-MS. In this chapter, I compare these two methods, and evaluate their utility to constrain processes relating to tufa formation. I also report the trace element concentrations in a small suite of water samples collected and use these to add to interpretations of the trace element contents in the tufa. In Chapter 6, I assess the concentrations and distribution of U and Th contents in the tufa samples, using the LA-ICP-MS data from Chapter 5, to select suitable material for U-Th dating. I then present the U and Th concentrations of samples selected and processed for U-Th analysis using solution ICP-MS and report the calculated U-Th age data. In Chapter 7, I present the results from the stable isotope analyses of water and tufa samples from Ga-Mohana Hill and use these to investigate patterns related to the depositional sub-environments (established in Chapter 4) and the timing of tufa formation (from Chapter 6). I also use the oxygen isotope data from the water and tufa samples to estimate the temperature at the time of tufa formation.

I discuss the findings presented in Chapters 4 to 7 in Chapter 8. The main findings are that the Ga-Mohana Hill tufas represent a perched spring-line tufa system that was active during at least five distinct periods over the last interglacial cycle, at ~114-100 ka,

~73-48 ka, ~44-32 ka, ~15-6 ka, and ~3 ka. This means that during these times, there was fresh water available on the landscape with the environment characterised by streams, waterfalls, and standing pools of shallow water on the hillside that would have supported vegetation growth, and human and animal activities. I discuss this record in context with global palaeoclimate records and relate my findings to regional and local archaeological and palaeoenvironment records. Finally, the main conclusions are summarised.

CHAPTER 2 BACKGROUND

This thesis is concerned with the palaeoenvironment represented by the tufa deposits at Ga-Mohana Hill, how this relates to existing palaeoclimate records, and the context the tufa deposits provide for the archaeological findings at the site. In the following sections, I provide background information on the geological setting of Ga-Mohana Hill (Section 2.1), the modern climate and vegetation (Section 2.2), and the archaeological context (Section 2.3). In Section 2.4, I review selected palaeoclimate records (global, regional and local), and in Section 2.5 I describe the formation of tufa deposits and their utility as palaeoclimatic proxies.

2.1 Geographical, geological and hydrological setting

Also known as Kurumankop, Ga-Mohana Hill is situated 12 km northwest of the town of Kuruman on the eastern edge of the Kuruman Hills, in the Northern Cape Province of South Africa (Figures 1.1 and 2.1). Ga-Mohana Hill has a maximum elevation of about 1530m asl, with a height of approximately 100-150 m above the surrounding landscape (Wilkins et al., 2020), and is a site of ritual significance for some members of the local community (Maape, 2021). Several small overhangs occur on Ga-Mohana Hill; the two largest have been termed Ga-Mohana Hill North (GHN) and Ga-Mohana Hill South (GHS). Both shelters have yielded archaeological material, but so far detailed investigations have been concentrated at GHN (Wilkins et al., 2020; Wilkins et al., 2021).

The Kuruman Hills are a prominent, NNE-SSW trending landform on the Ghaap Plateau (Figure 2.1). A notable archaeological site, Wonderwerk Cave, is hosted within the Kuruman Hills, south of Ga-Mohana Hill (Figure 2.1). East of the Kuruman Hills, the Ghaap escarpment straddles the Northern Cape and North West provinces of South Africa (Figure 1.1), along which extensive fossil and artefact-bearing tufa deposits have been documented (Peabody, 1954; Marker and Butzer, 1975; Marker, 1988; Beaumont and Vogel, 1993; McKee, 1993; Curnoe et al., 2006; Hopley et al., 2013; Doran et al., 2015).

Most notably, a skull identified as *Australopithecus africanus* and termed the Taung child, was recovered from a lime quarry along this escarpment (Dart, 1925).

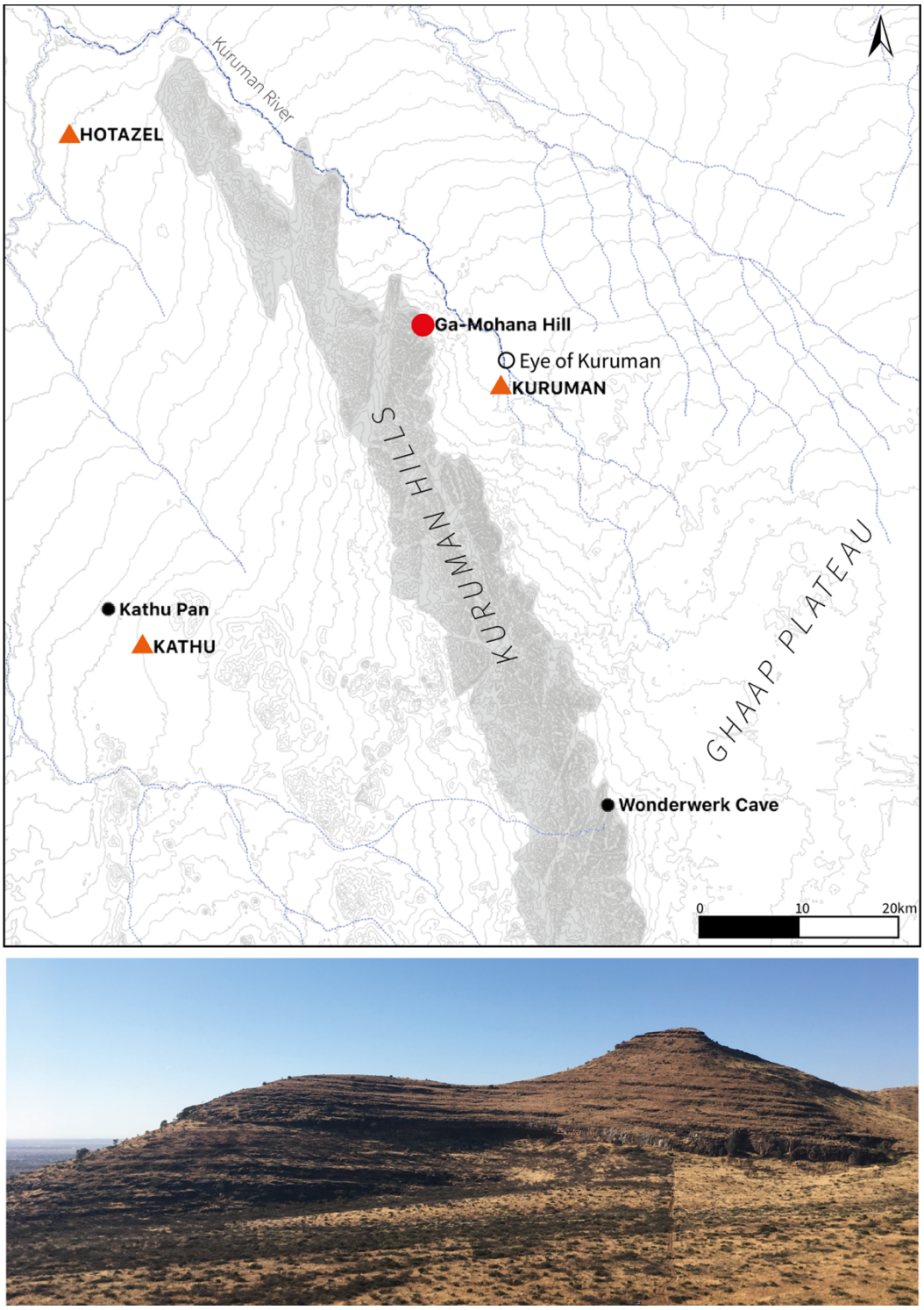

Figure 2.1 A topographic map showing the Kuruman Hills and the location of Ga-Mohana Hill, north of the town of Kuruman (a), and b) a photograph of Ga-Mohana Hill and the north rockshelter (GHN), taken facing south east.

The dominant lithologies outcropping on the Ghaap plateau are the dolomites of the Campbellrand Subgroup and the banded iron formations (BIF) of the Asbestos Hills Subgroup (Figure 2.2). These deposits belong to the Palaeoproterozoic Ghaap Group (Beukes, 1987), and were deposited in the Griqualand West Basin, one of three structural sub-basins which developed on the Kaapvaal Craton during the Archaean. The Transvaal Supergroup encompasses the deposits in these three sub-basins (Altermann and Wotherspoon, 1995). The Campbellrand Subgroup consists of an approximately 1500 m sequence of stromatolitic carbonate platforms, interbedded with limestone and chert. These dolomites correlate with the Malmani dolomites of the Chuniespoort Group in the adjacent Transvaal basin, within which are hosted the caves of the Cradle of Humankind World Heritage Site (Partridge, 2000). Together, these carbonates were deposited between 2600-2300 Ma with an initial extent of approximately 600,000 km^2, whereas presently, they cover an area of approximately 200,000 km^2 (Beukes, 1987).

Ga-Mohana Hill is predominantly composed of limestone, dolomite, and chert deposits of the Kogelbeen and Gamohaan Formations, belonging to the Campbellrand Subgroup, and is capped by a layer of banded iron of the Kuruman Formation (Sumner, 1997; Gandin et al., 2005). The rock shelters on the northern and southern sides of Ga-Mohana Hill are hosted within the dolomites of the Gamohaan Formation, positioned stratigraphically above the Kogelbeen Formation (Wilkins et al., 2020).

The ancient carbonate platforms of the Campbellrand Subgroup have been subjected to multiple phases of karstification (Eriksson and Altermann, 1998). This would have occurred during periods of erosion due to sub-aerial exposure of the deposits, with the percolation of meteoric waters through the BIF and into the carbonate rocks resulting in dissolution of the limestones and formation of underground cavities (Eriksson and Altermann, 1998). Multiple dolerite dykes cross-cut the dolomites with NNE and NNW strike directions (Smit, 1978; Rosewarne, 2006). These create large groundwater compartments and consequently, the dolomites act as important aquifers for the arid Northern Cape region (Smit, 1978; Altermann and Wotherspoon, 1995; Rosewarne, 2006). A large proportion of aquifer recharge occurs in the Kuruman Hills (Esterhuyse,

2003). The Kuruman BIFs are highly fractured and, as a result, collect and conduct rainfall run-off down into the dolomite aquifers (Rosewarne, 2006).

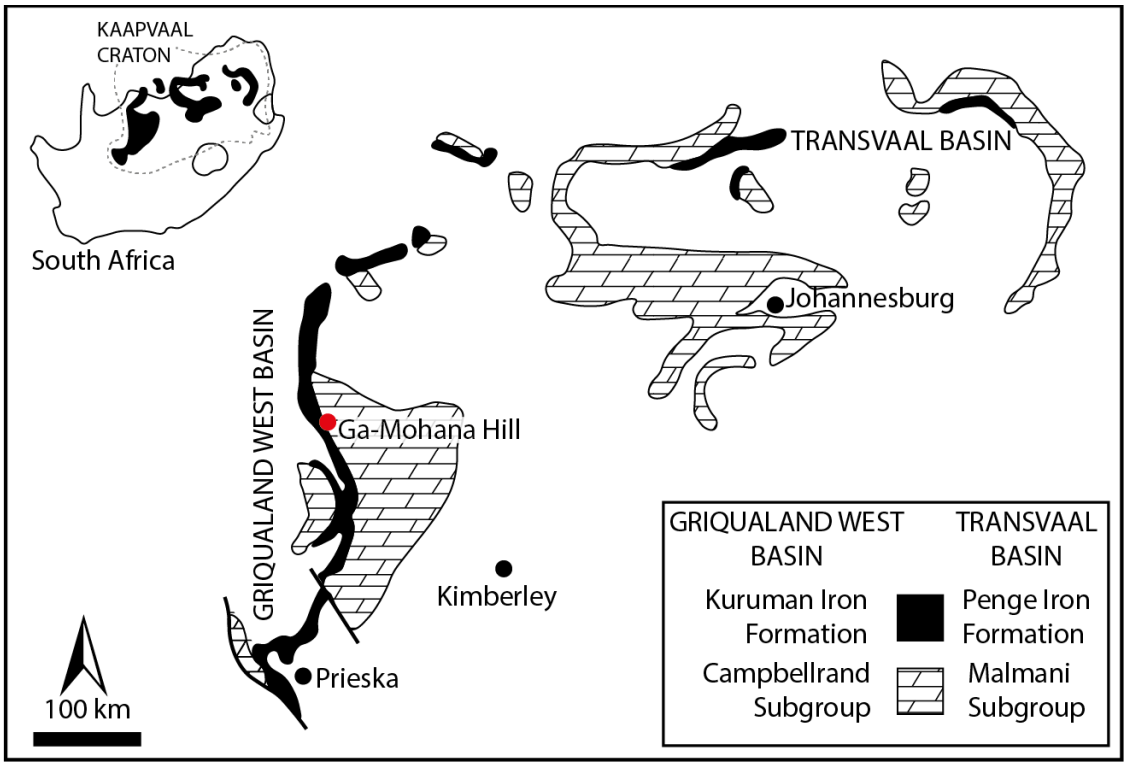

Figure 2.2 Simplified geological map of the Campbellrand Subgroup and Kuruman iron formation in the Griqualand West Basin, and equivalent deposits in the Transvaal Basin, adapted from Gandin et al. (2005). The approximate location of Ga-Mohana Hill is shown with a red dot.

Groundwater resurgence at several currently active springs in the area are a testament to this vast underground drainage network hosted within these dolomites (Smit, 1978). The Eye of Kuruman, also known as *Gasegonyane* in Tswana, is one such spring of particular significance, situated within the town of Kuruman (Figure 2.1). The ephemeral Kuruman River which drains the region is fed by the Eye of Kuruman spring (Figure 2.1). It has a discharge rate of 20-30 megalitres of fresh water daily and has been a historically important fresh water source for centuries (Smit, 1978; Jacobs, 1996). The presence and movement of the groundwaters in the dolomite aquifers is a vital precursor to the formation of surface carbonates, such as the tufas found on Ga-Mohana Hill.

Stratigraphically above the dolomitic bedrock are the deposits of the Kalahari Basin. The Kalahari Basin developed as a major sedimentary basin during the Cretaceous and covers an extensive region in southern Africa (Deacon and Lancaster, 1988; Matmon et al., 2015). It contains a thick succession of unconsolidated sediments and extensive duricrusts, broadly termed the Kalahari Group (Thomas and Shaw, 1991). A multitude of landforms characterise the Kalahari landscape, including vast dune systems, large palaeolakes, playas, and pans, all of which are evidence of considerable climatic fluctuations in the late Quaternary (Deacon and Lancaster, 1988; Thomas and Shaw, 1991; Burrough et al., 2009a, Matmon et al., 2015). Whereas the Kalahari as a whole is considered a semi-arid ecozone (Deacon and Lancaster, 1988), the south-eastern region, including Ga-Mohana Hill, is transitional since it lies on the boundary between the humid highveld regions in the eastern part of South Africa, and the semi-arid desert regions of the Kalahari to the north and west (Figure 2.3). Landforms at sites in transitional regions such as this are sensitive indicators of past global climate changes (Wasson et al., 2013).

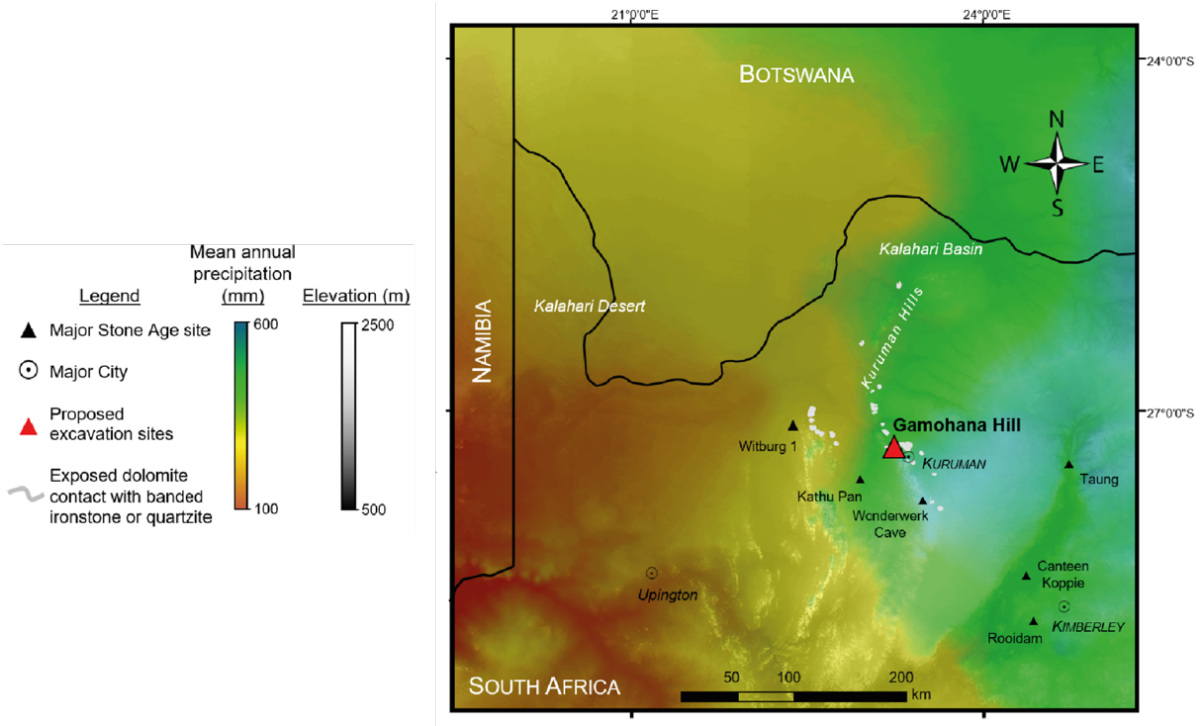

Figure 2.3 Precipitation map showing the location of Ga-Mohana Hill in the south-eastern region of the Kalahari Basin, and other nearby archaeological sites. Mean annual precipitation data from WorldClim V1 interpolations (Hijmans et al., 2005).

2.2 Modern climate and vegetation

Ga-Mohana Hill is located in the currently semi-arid south-eastern Kalahari region, which falls within the Summer Rainfall Zone (SRZ) of southern Africa (Figure 1.1 and Figure 2.4). The moisture source for summer rainfall in South Africa originates primarily from the southwestern Indian Ocean via convergent easterly winds (Tyson and Preston-Whyte, 2000) (Figure 2.5). Sea surface temperatures (SST) in the SW Indian Ocean are thought to influence the amount of rainfall in the SRZ of southeast Africa, as warmer SSTs generate increased moisture and correlate to periods of greater rainfall in southeastern Africa (Reason and Mulenga, 1999; Reason, 2001a; Reason, 2001b; Reason, 2002).

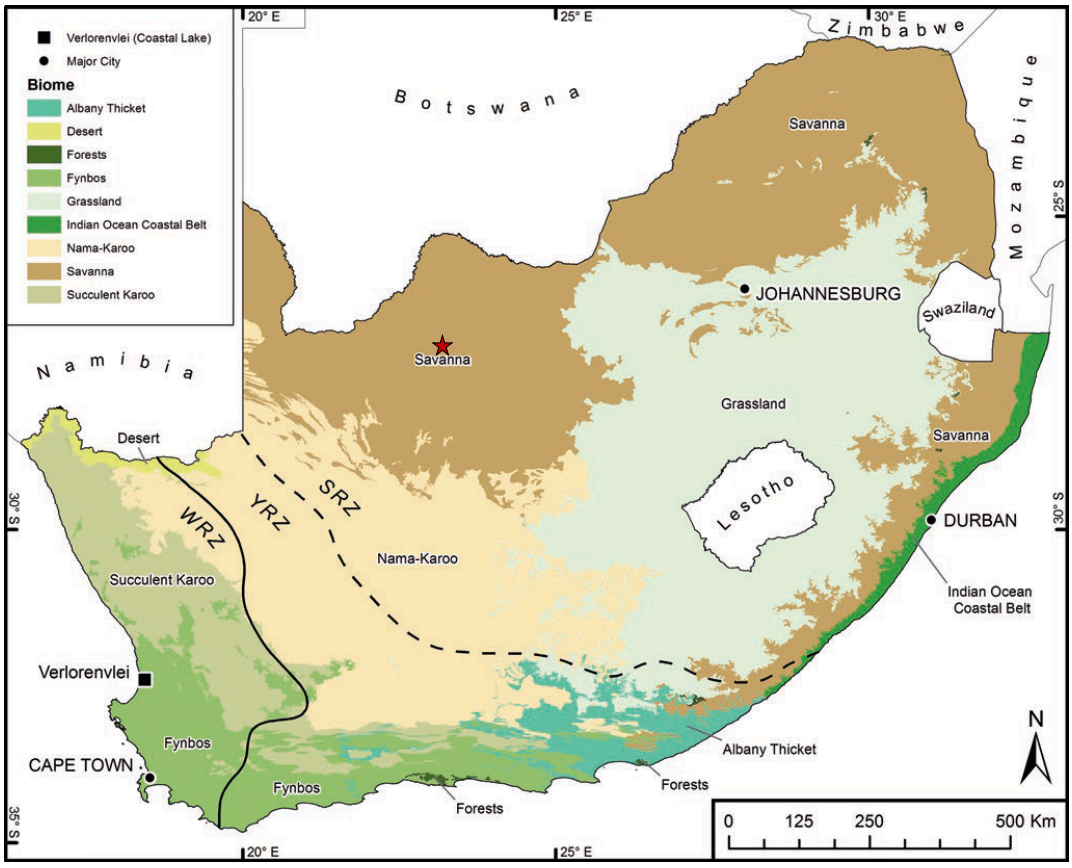

Figure 2.4 Biomes of South Africa, from Finch and Meadows (2019) after Mucina and Rutherford (2006). Ga-Mohana Hill (approximate location shown with the red star) falls within the Savanna biome.

The Kuruman area is characterised by a strongly seasonal climate, with a mean annual precipitation of ~300-400 mm during the austral summer months, i.e., October to March (Figure 2.3), whereas the winter months are dry with occasional frost (Scott and Thackeray, 2015). Ga-Mohana Hill falls within the Savanna biome with vegetation classified as grassy woodland belonging to the Kuruman Mountain Bushveld subdivision (Figure 2.4) (Mucina and Rutherford, 2006). Multiple factors that operate on different temporal and spatial scales are responsible for the varied climate across South Africa, see Lennard (2019) for a review. In short, South African climate is strongly influenced by 1) its latitudinal position at the southern tip of the African continent, 2) its topography, i.e., mountainous escarpments that separate the coastal plains in the east and west of the country from the elevated plateau in the interior, and 3) the oceans that surround it, i.e., the warm Indian Ocean and Aghulus current on the east and south coasts, and the colder Atlantic Ocean and Benguela current on the west coast (Figure 2.5).

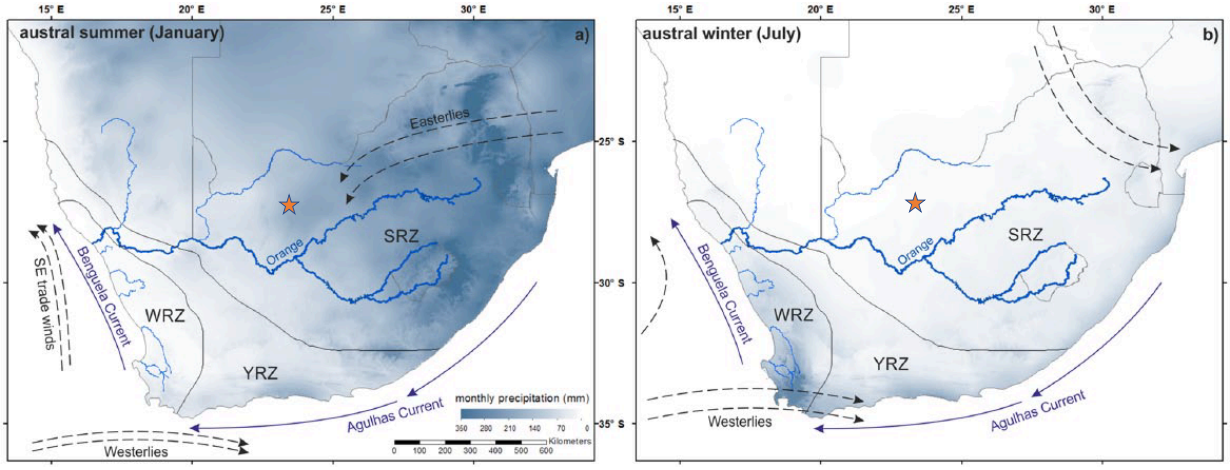

Figure 2.5 Map of southern Africa mean monthly precipitation in a) summer (January), and b) winter (July) from Burdanowitz et al. (2018). The approximate location of Ga-Mohana Hill is identified with an orange star. The Benguela (Atlantic Ocean) and Aghulas (Indian Ocean) currents are illustrated with solid arrows, and the major atmospheric circulation systems (SE trade winds, Westerlies, and Easterlies) are shown with dotted arrows.

2.3 Palaeoclimate records: global, regional, local

The scientific study of past climatic and environmental conditions is termed palaeoclimatology. The palaeoclimate of the Quaternary period (~2.6 Ma to present) is of particular interest, as it is during this time that the evolution of our species occurred against a backdrop of rapid and abrupt climate changes, characterised by orbitally-paced glacial (cold) and interglacial (warm) cycles (Hays et al., 1976; deMenocal, 2004; Caley et al., 2018). The Quaternary is divided into two epochs: the Pleistocene (~2.6 Ma to ~11.5 ka), and the Holocene (~11.5 ka to present). I briefly outline some key milestones during these periods below, as reviewed in Cronin (2010).

At the start of the Pleistocene, the periodic expansion and retreat of northern hemisphere continental ice sheets (driving glacial and interglacial states) occurred on ~40 ka cycles. The period between ~1.2 Ma to ~700 ka marks the Middle Pleistocene Transition (MPT), after which the pacing of glacial / interglacial cycles changed to ~100 ka. The Late Pleistocene encompasses the Last Interglacial (~130 ka to 115 ka), a period characterised by warm global temperatures and high sea levels, the end of which marks the start of the most recent glacial. This period is characterised by a series of millennial-scale climate fluctuations of abrupt warming and less-abrupt cooling events, culminating in the Last Glacial Maximum (LGM) at ~22 ka. The LGM is the most recent time that the ice sheets were at their maximum extent and thickness, and that global atmospheric temperatures were at a minimum. A period of gradual deglaciation followed the LGM, whereafter the start of the Holocene at ~11.5 ka marks the beginning of the present interglacial period.

The repository of geochemical proxy data from a variety of geological archives, such as marine sediments, ice cores, corals, and terrestrial deposits, e.g., speleothems and lake sediments, has informed our understanding of past global climate changes in response to glacial and interglacial cycles (Gascoyne, 1983; Broecker et al., 1985; Jouzel et al., 1987; Dansgaard et al., 1993; Lisiecki and Raymo, 2005). Some of these key records are introduced in the following section.

2.3.1 Global records

It is generally agreed that long-term variations in Earth's climate are driven by changes in insolation, i.e., the amount of solar energy received on the Earth's surface. Insolation is, in turn, influenced by the interaction of long-term variations in Earth's orbital parameters – precession, obliquity, and eccentricity. These parameters are termed Milankovitch cycles (Milankovitch, 1941) (Figure 2.6). Precession describes the wobble of the Earth around its axis of rotation and has a 23 ka cycle. Obliquity refers to the angle at which the Earth's axis of rotation is tilted relative to the plane of orbit. This angle varies between ~22° to ~25° on a 41 ka cycle. Eccentricity is the change in shape, i.e., circular to elliptical, of the Earth's orbit around the sun, which changes on timescales between 100 to 400 ka. Eccentricity influences insolation, and modulates the amplitude of insolation changes driven by precession and obliquity (Figure 2.6).

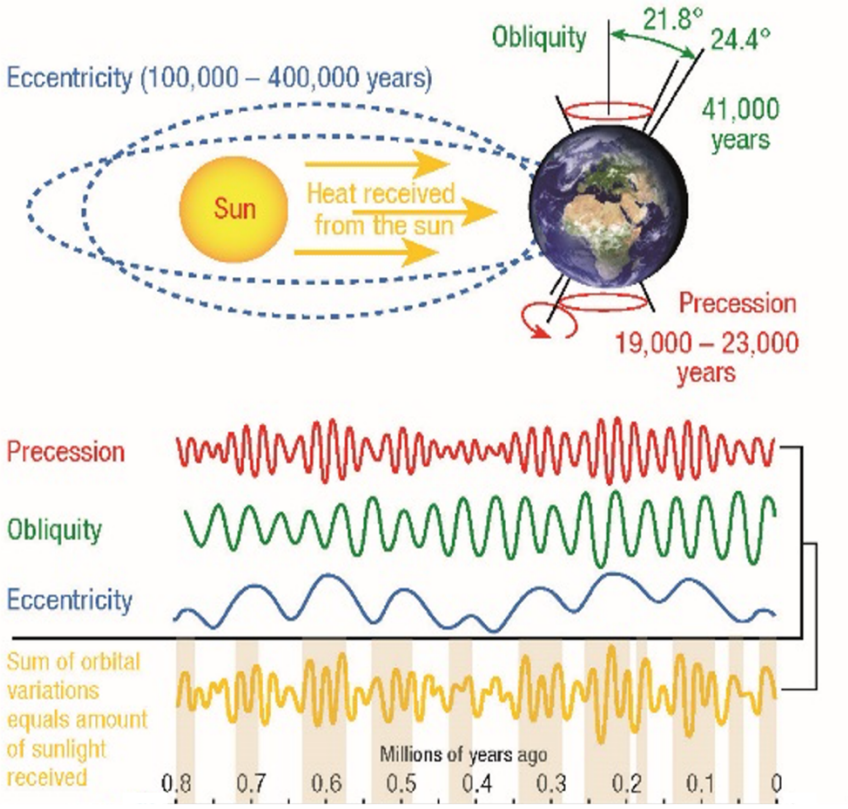

Figure 2.6 Schematic of the Milankovitch cycles, from Compton (2016). The top panel is an illustration of Earth's orbital parameters: eccentricity, obliquity and precession. The middle panel shows the amplitudes of their respective cycles, and the bottom panel shows their cumulative impact on insolation.

The distribution and intensity of insolation varies latitudinally and seasonally, and these changes in solar radiation drive the growth and retreat of ice sheets at the poles. This, in turn, influences the temperature and circulation of the oceans and atmosphere, initiating climate feedback loops (e.g. ocean and atmospheric circulation patterns, greenhouse gas concentrations, albedo effects etc.). These feedback loops generate and maintain glacial and interglacial cycles. Berger and Loutre (1991), and later Laskar et al. (2004), produced a computational model to calculate the amount of solar radiation received at any given latitude at a particular point in time, up to 250 Ma. This is an instrumental tool for relating palaeoclimate proxy data to orbital-scale climate forcing mechanisms.

The timing of glacial and interglacial cycles has been constrained primarily through measurements of oxygen isotope ratios recorded in gases trapped in polar ice cores (Grootes et al., 1993; Jouzel et al., 2007; Elderfield et al., 2012), and the calcium carbonate skeletons of organisms preserved in marine sediments, i.e. foraminifera (Imbrie et al., 1984; Shackleton et al., 1990; Lisiecki and Raymo, 2005). Fractionation of oxygen isotopes occurs during evaporation and precipitation processes and is temperature dependant. Thus, during glacial periods when ice sheets expand and the climate is colder, the ratio of oxygen isotopes in sea water, ^{18}O and ^{16}O, increases because the lighter ^{16}O isotope is stored in icesheets. During warmer, interglacial periods, excess ^{16}O flows into the seawater via run-off from melting glaciers, and this decreases the ratio of ^{18}O and ^{16}O in sea water. As such, the $\delta^{18}O$ value measured in marine carbonates reflects the $\delta^{18}O$ value of the seawater at the time of carbonate precipitation, which in turn is affected by the volume of ice and the storage of ^{16}O in ice sheets, and the temperature of the seawater. Consequently, marine carbonates are an ocean temperature proxy: higher $\delta^{18}O$ values measured in marine carbonates indicate cooler temperatures and glacial conditions, whereas lower $\delta^{18}O$ values indicate warmer temperatures and interglacial conditions (Dansgaard, 1964).

The main source of data relating to glacial / interglacial cycles, post 180 Ma, comes from the $\delta^{18}O$ value recorded in the calcitic skeletons, or tests, of foraminifera preserved in

deep-sea marine sediments. The $\delta^{18}O$ values of foraminifera tests are inherited from the sea water in which they form, and this in turn is a function of global ice volume, seawater temperature, and salinity through time. Imbrie et al. (1984) produced a stacked record of $\delta^{18}O$ measured in planktonic foraminifera from 5 sites for the last 750 ka. More recently, Lisiecki and Raymo (2005) generated a high-resolution stack of $\delta^{18}O$ measured from benthic foraminifera from 57 globally distributed locations. Termed the LR04 stack, the record spans the last 5.3 Ma, i.e. the entire Plio-Plesitocene (Figure 2.7) and has become the gold standard against which to compare palaeoclimate records.

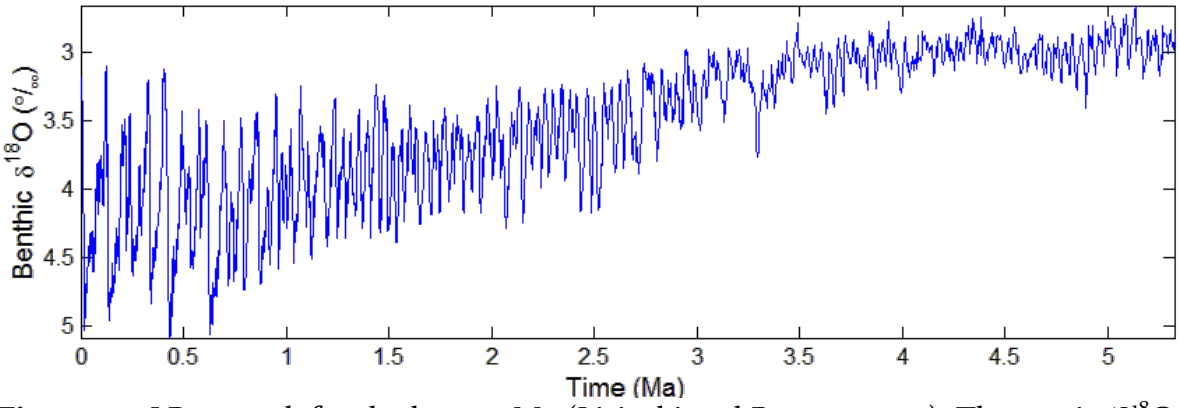

Figure 2.7 LR04 stack for the last 5.3 Ma (Lisiecki and Raymo, 2005). The y-axis ($\delta^{18}O$ values of benthic foraminifera) is inverted such that lower $\delta^{18}O$ values, i.e. warmer temperatures, are at the top, and higher values, i.e. cooler temperatures, are at the bottom.

The LR04 record shows the control of the different Milankovitch cycles over this time, and it delineates the timing of the Marine Isotope Stages (MIS) i.e., alternating warm / interglacial and cool / glacial periods in the Earth's climate (Emiliani, 1955). The odd numbered stages have lower $\delta^{18}O$ values, indicating a warmer interglacial climate, e.g., MIS 1 represents the present interglacial Holocene period. Even numbered stages have higher $\delta^{18}O$ values, indicating a colder glacial climate, e.g., MIS 2 represents the Last Glacial Maximum (LGM) (Figure 2.8).

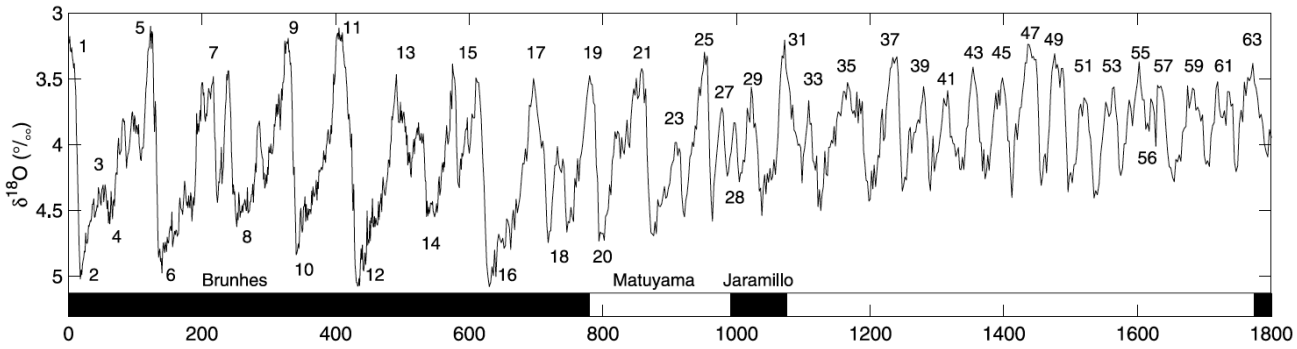

Figure 2.8 Portion of the LR04 stack from Lisiecki and Raymo (2005) showing changing $\delta^{18}O$ values over the last 1.8 Ma, and MIS stages numbered 1 to 63.

Ice cores from Antarctica and Greenland have been used to reconstruct temperatures through measurements of oxygen and hydrogen isotope ratios in the ice (Grootes et al., 1993; Jouzel et al., 2007; Elderfield et al., 2012), and to reconstruct past atmospheric composition using air trapped in gas bubbles (Raynaud et al., 1993; Siegenthaler et al., 2005). These data have been instrumental in improving our understanding of the role of greenhouse gases, particularly CO_2, in driving and amplifying large-scale climate change (Archer et al., 2000). Jouzel et al. (2007) present a high-resolution profile of δD from the European Project for Ice Coring in Antarctica (EPICA) Dome C ice core, from which surface temperature changes in Antarctica over the last 800 ka are inferred. Bereiter et al. (2015) provide the most up-to-date, composite reconstruction of atmospheric CO_2 for the last 800 ka from the EPICA Dome C ice cores in Antarctica.

The global-scale climate processes described above, i.e. Milankovitch cycles and summer insolation, glacial-interglacial phases, and atmospheric CO_2, all play a role in driving climate and environmental changes on multiple scales in continuous feedback loops. These global parameters have a variable and non-uniform effect on regional climate responses in southern Africa, and as such, interpretations of local palaeoclimate records cannot be easily correlated with global climate events and glacial/interglacial cycles (Chase and Meadows, 2007; Holzkämper et al., 2009; Chase, 2010). Robust and well-constrained terrestrial palaeoclimate proxy records are therefore critically important to provide direct information on environmental conditions in southern Africa at particular periods in the past (Bruch et al., 2012). With these, a clearer picture of the response of southern African environments to global climate drivers can emerge.

This is necessary to aid our understanding of the role climate played in driving the evolution of our species, how early humans adapted to these changing conditions, and how environments are likely to respond to the current climate changes we are experiencing.

2.3.2 Regional records

Multiple local and remote phenomena operating on different spatial and temporal scales influence the climate across southern Africa today, reviewed in Lennard (2019). How these may have been different in the past, and the impact of glacial-interglacial cycles on South African climate and vegetation, remains a matter of debate (Chase and Meadows, 2007; Gasse et al., 2008). Quaternary records of landscape changes, fluvial activity, and different pollen or faunal assemblages from particular sites have been used to reconstruct past environmental conditions that reflect changes in climate dynamics driven by a myriad local, regional and global processes that are inter-connected. For example, precession-driven changes in the position of the intertropical convergence zone (ITCZ), an area of low-pressure near the equator where the north- and south-easterly trade winds converge, is a primary control of rainfall seasonality in South Africa (Tyson and Preston-Whyte, 2000). This in turn impacts vegetation dynamics and the presence or absence of particular fauna in the region. Untangling these connections, and correlating environmental changes with regional-scale climatic processes is challenging, in part due to the lack of long, continuous and well-dated records. Palaeoclimate proxies that reflect regional-scale changes from selected sites in southern Africa (Figure 2.9) are described below, as these provide insight into how the various climate processes may have been different in the past.

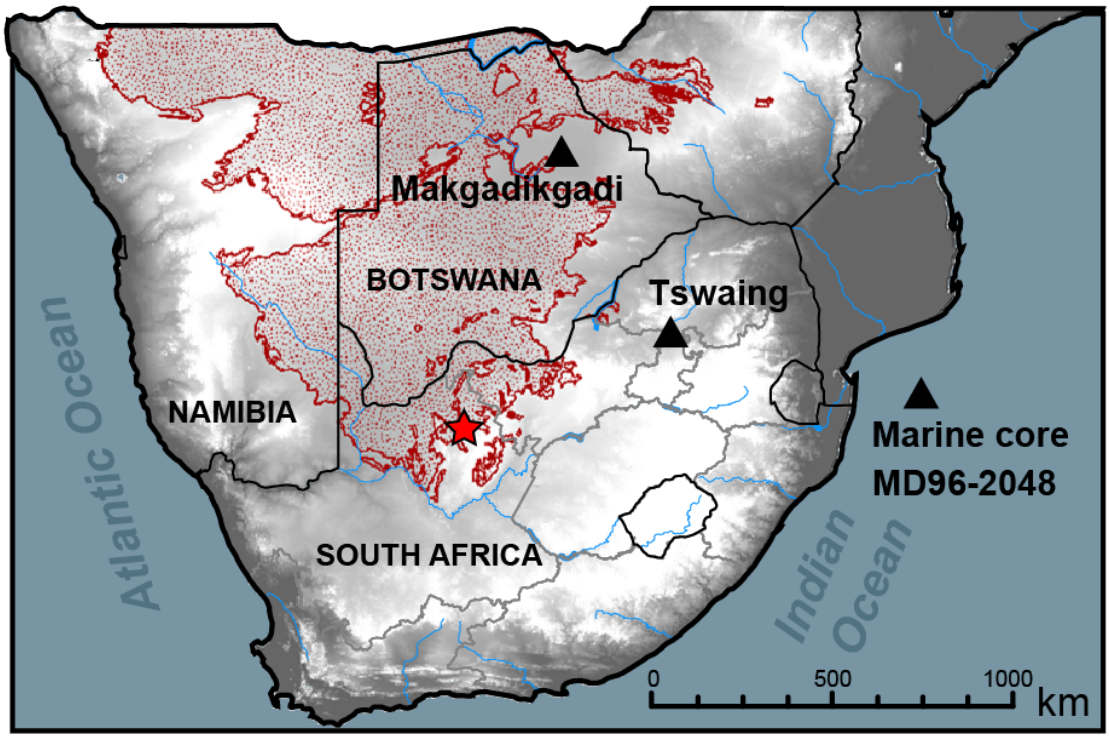

Figure 2.9 Map of southern Africa showing the extent of the Kalahari Basin (stippled red) and the location of palaeoclimate sites described in the text: marine core MD96-2048 (Caley et al., 2018), Tswaing meteorite crater (Partridge et al., 1997) and the Makgadikgadi palaeolake (Burrough et al., 2009a). The red star indicates the approximate location of Ga-Mohana Hill.

2.3.2.1 Marine core MD96-2048

Marine sediment cores from continental margins contain long and continuous records of environmental change from marine and terrestrial components, e.g. marine organisms and microfossils, clay minerals, pollen, and plant waxes. A chronology for marine cores can be established by tuning the $\delta^{18}O$ values of benthic foraminifera included in the core to the LR04 stack. In addition to their $\delta^{18}O$ values, element ratios of foraminifera can be used to investigate hydroclimate changes. Caley et al. (2018) measured the Mg/Ca ratios of foraminifera in marine core MD96-2048 collected off the east coast of South Africa near the Limpopo River mouth (Figure 2.9) and used this to reconstruct sea surface temperature (SST) changes for the southwest Indian Ocean over the last 2.14 Ma. They find a significant correlation between SSTs and variation in orbital parameters with 100 ka and 41 ka periodicity, but an absence of SST change on

processional timescales (~23 ka). Caley et al. (2018) interpret this as evidence that orbital-scale rainfall variability in South Africa is related to the contrast in temperatures between the land and sea, rather than by SSTs alone. Statistical analysis of the Fe/Ca ratios measured in terrestrial sediments in the same core indicate cycles of change that follow precession and eccentricity timescales. Through comparison with other studies of hydroclimate change in Lake Malawi, Caley et al. (2018) suggest that low-latitude insolation together with changes in ice volume exerted a strong control on hydrological changes in the Limpopo River catchment, and that SST change played a secondary role (Caley et al., 2018). This study highlights the combined effects of orbital-scale parameters and interhemispheric connections on hydroclimate variability in south-east Africa.

2.3.2.2 Tswaing crater

A 90 m sediment core from the Tswaing meteorite crater (Figure 2.9), also known as the Pretoria Salt Pan, is the longest continuous record for rainfall in South Africa, extending to ~200 ka (Partridge et al., 1997). The core, composed of lake sediments, has been partially dated based on radiocarbon ages (for the first ~40 ka). Fissure track analysis of the crater rim was used to estimate the age of the base of the core (~200 ka). A mean annual rainfall timeseries was derived using textural analysis of the lake sediments. An age model was produced based on sedimentation rates and by tuning the rainfall record to orbital insolation (30°S, January). With this, Partridge et al. (1997) interpret rainfall variation to be driven by precession with a periodicity of ~23 ka. Despite the poor chronology, the Tswaing sediment core has been adopted as evidence for orbital-scale forcing of regional climate and rainfall variability in South Africa, and serves a benchmark record for the region against which many other records have been compared. Recent analysis of the pollen, phytolith and diatom sequences preserved in the core sediments provide further palaeoenvironmental context from the palaeolake (McLean and Scott, 1999; Scott, 1999; Kristen et al., 2007).

2.3.2.3 Makgadikgadi palaeolake

Geomorphological features of the Makgadikgadi palaeolake system, situated in the Middle Kalahari (Figure 2.9), record fluctuating lake levels in this now arid region. Building on previous studies of these palaeolakes, an OSL-dating campaign of the palaeolake shoreline sediments, conducted by Burrough et al. (2007) and Burrough et al. (2009a) provide an improved and extensive chronology for the palaeolake developments over the last ~300 ka. Three component lake basins make up the Makgadigadi palaeolake system: Lake Ngami, Mababe depression, and Makgadigadi lake. Periodically, the three component lakes were so full that they coalesced to create a mega-lake, covering an area of approximately 66,000 km^2 at its largest extent (Burrough et al., 2009a).

Seven mega-lake high-stand phases occurred over the last glacial / interglacial cycle at 104.6 ± 3.1 ka, 92.2 ± 1.5 ka, 64.2 ± 2.0 ka, 38.7 ± 1.8 ka, 26.8 ± 1.2 ka, 17.1 ± 1.6 ka, and 8.5 ± 0.2 ka. The duration of these high-stands is unknown, however, and Burrough et al. (2009a) note that the resolution of the ages presented are insufficient to distinguish whether each of these times represent a single event (either brief of prolonged), or whether they encompass multiple fluctuations of the mega-lake on seasonal to thousand year time scales. Nevertheless, it is likely that these high-stand phases played an important role in influencing the regional hydrological dynamics. The existence of such a large body of surface water would have decreased surface albedo and increased air temperatures and evaporation, influencing the seasonal balance of precipitation and evaporation (P-E), and amplifying the availability of moisture in this region (Burrough et al., 2007; Burrough et al., 2009a). Burrough et al. (2009b) model this scenario using HadCM3 simulations and find that the presence of the mega-lake would have increased local annual precipitation by 10-15%. In response to these local increases in precipitation and temperature, they use the BIOME4 model to show that this would have impacted the broader environmental system, increasing primary productivity of vegetation in the region surrounding the lake by up to 50%. Based on these model outputs, Burrough et al. (2009b) propose that the intermittent lake high-stands would have significantly influenced the regional climate, and should be considered as an additional factor in the

interplay of complex feedback mechanisms that produced the palaeoclimate records from the Kalahari during the late Quaternary.

The cause of such a vast expanse of water is not only climatically driven, as the hydrological system that affects these lakes is influenced by multiple factors. Burrough et al. (2007) and Burrough et al. (2009a) consider the mega-lake palaeo-records alongside other local, regional and global proxies. In doing so, they note both correlations and contradictions, and discuss several points for consideration when comparing regional proxy records of 'wetness'. In particular, they highlight the influence of independent causal mechanisms driving regional and local rainfall conditions, and the discontinuity inherent in terrestrial records due to the range in accuracy of chronological techniques employed in deciphering these proxy records. Thomas and Burrough (2012) consider this issue further in a review paper, wherein several temporally and spatially overlapping geo-proxy records are critiqued.

2.3.3 Local records

The southern Kalahari region is characterised by a range of landscape features, evidence of the multitude of changes it has undergone in the past (Deacon and Lancaster, 1988). Changes in climate influence human-environment interactions and it is thought that shifts in climatic regimes are major drivers of early human adaptation (Barham and Mitchell, 2008; Trauth et al., 2009; Thomas and Burrough, 2012; Ziegler et al., 2013; Marean, 2015; Wilkins et al., 2020; Wilkins and Schoville, 2024). In order to test this hypothesis further, especially in light of the archaeological deposits at Ga-Mohana Hill, there is an urgent need for more, well dated local palaeoclimate records. While there is a growing body of palaeoclimate data from the southern Kalahari, reviewed below, gaps, contradictions and uncertainties remain (Lukich and Ecker, 2021). The absence of long and robust palaeoclimate records for the interior of southern Africa is a major hindrance to the development of a comprehensive model of climatic and environmental changes in this region during the late Quaternary. I introduce each of the key sites and their palaeoclimate proxies for the South African interior in below. The locations of these sites are marked on Figure 2.10.

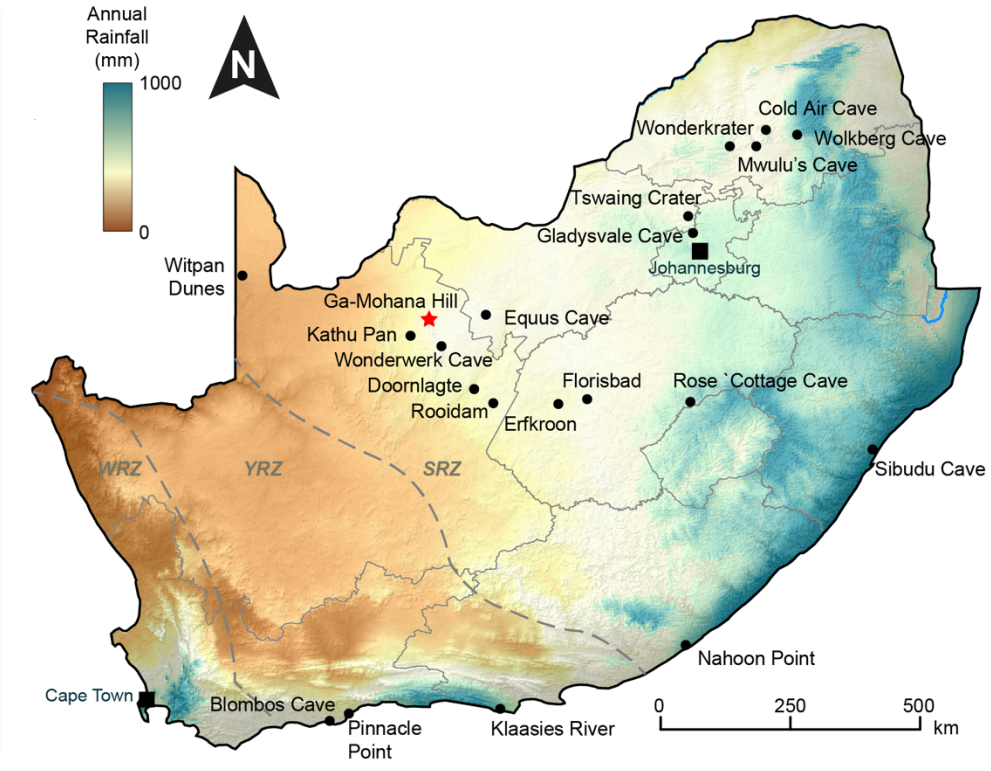

Figure 2.10 Map of South Africa showing the locations of sites with palaeoclimate proxy records from the Late Pleistocene and Holocene discussed in the text in relation to the study site, Ga-Mohana Hill (red star).

2.3.3.1 Wonderwerk Cave

Wonderwerk Cave is a flagship archaeological site in the southern Kalahari with a record of human occupation spanning the Early, Middle and Late Stone Ages over the last 2 Ma (Humphreys and Thackeray, 1983; Beaumont and Vogel, 2006; Herries, 2011; Chazan et al., 2012; Horwitz and Chazan, 2015; Chazan et al., 2020). The cave is hosted within the dolomites of the Kuruman Hills, ~60 km from Ga-Mohana Hill (Figure 2.10). Several studies demonstrate climatic shifts through the Pleistocene and Holocene at Wonderwerk Cave using various proxy materials, e.g. botanical and faunal remains (Bamford, 2015; Lee-Thorp and Ecker, 2015; Rossouw, 2016), pollen (van Zinderen Bakker Sr, 1983; Scott et al., 1995; Scott and Thackeray, 2015), stable isotope compositions of mammalian tooth enamel and ostrich eggshells (Ecker et al., 2018; Chazan et al., 2020), and speleothem deposits (Brook et al., 2010; Brook et al., 2015; Pickering, 2015). Stable isotopes of carbon and oxygen from tooth enamel, coupled with

faunal abundances and phytolith evidence from Wonderwerk Cave, is presented as evidence of persistent wetlands and lakes, and a mix of C3 and C4 grasses during the early Pleistocene (Ecker et al., 2018; Chazan et al., 2020).

Brook et al. (2010) present a combined speleothem isotope and pollen record for the last 35 ka based on a stalagmite core from the entrance of Wonderwerk Cave. Growth of the stalagmite, investigated through petrographic fabric analysis, and dated by radiocarbon, is interpreted to record wet conditions from ~35 - 33 ka, ~23 - 17 ka and 4 ka to present, with drier conditions represented by very slow growth between ~17 - 13 ka and depositional hiatuses between ~33 - 23 ka and ~13 - 4 ka (Brook et al., 2010). Radiocarbon has an upper age limit of ~40 ka, thereby limiting the timing of speleothem growth under investigation. There is also inherent uncertainty in this dating method as the incorporation of dead carbon into these deposits results in ages that are usually too old. In order to correct for this, calibration curves are employed, but these don't always account for variations due to local climate or atmospheric conditions (Brook et al., 2015). In addition to the age data, Brook et al. (2010) use oxygen and carbon isotopes, coupled with pollen assemblages preserved in the stalagmite and dung deposits, to situate these fluctuating climatic conditions at Wonderwerk Cave in a broader framework. They compare the record to other regional proxy data, and to palaeotemperature data from the Greenland Ice Sheet GISP2 ice core. They conclude that periods of rainfall and aridity at Wonderwerk Cave correspond to warm and cold periods in the Northern Hemisphere respectively (Brook et al., 2015). A hiatus in the stalagmite between 13-4 ka, and pollen evidence for dry conditions at ~12 ka corresponds to the Younger Dryas event recorded in the Northern Hemisphere. Brook et al. (2010) conclude that the stalagmite at Wonderwerk Cave reflects global-scale climate changes.

2.3.3.2 Kathu Pan

Kathu Pan is an open-air archaeological site in an ephemeral marshland located on the outskirts of the town of Kathu, ~50 km from Ga-Mohana Hill (Figure 2.10). Sinkholes in several localities have exposed the underlying stratified sediments which host archaeological material spanning the Early, Middle and Late Stone Ages (Beaumont, 1990; Beaumont and Morris, 1990; Beaumont, 2004; Wilkins and Chazan, 2012; Wilkins,

2017). The sediments, dated using optically stimulated luminescence (OSL), range from the mid-late Pleistocene to the Holocene (Porat et al., 2010; Lukich et al., 2019). Palaeoclimate investigations into these sediments reveal that the pan has experienced significant fluctuations in water and vegetation relating to groundwater recharge and the movement of the water table (Butzer, 1984). More recently, Lukich et al. (2020) conducted a detailed investigation of the sediments at Kathu Pan 1, 6 and 9, using OSL dating, micromorphology, loss-on-ignition and scanning electron microscopy techniques. Coupled with OSL ages for KP 6 (Lukich et al., 2019), this analysis provides a comprehensive record of semi-continuous paleoenvironmental changes at Kathu Pan over the last ~160 ka.

Lukich et al. (2020) describe three phases of deposition at the site and relate these to particular environmental conditions. The first depositional phase is characterised by Pleistocene sands which record a cyclic alternation of aeolian sands (dry conditions), the presence of palygorskite (a clay mineral used as a proxy for moderately wet conditions) and oxidised organic material (evidence of vegetation and the establishment of marshy conditions). Wet phases, represented by a high organic content in the sediments, are evident during MIS 5a and 5c. The second depositional phase is dated to the Last Glacial Maximum (LGM) and is characterised by extensive hardpan calcium carbonate deposits which suggest evaporative conditions and overall pan-wide drying. The presence of palygorskite in some layers implies a semi-arid environment with some moisture availability. The final phase of deposition during the Holocene preserves finely laminated alternations between organic and $CaCO_3$-rich deposits, suggesting rapid cycles of wet and dry conditions. Lukich et al. (2020) propose that this shift may be due to increasing seasonality with more severe aridity during the winter (dry) season, and the development of marshy conditions during the summer (rainy) season, whereas the Pleistocene may have been characterised by year-round rainfall. While the OSL-dated sediments allow for an extended chronology, i.e., beyond the limits of radiocarbon dating, the errors associated with the ages prohibits palaeoclimate reconstructions on seasonal time scales.

2.3.3.3 Ghaap escarpment

To the east of these sites, the north-east trending Ghaap escarpment (Figure 2.10) is ~275 km long with cliffs between 70-120 m high, and preserves important archaeological, faunal and palaeoenvironmental records (Peabody, 1954; Butzer et al., 1978; Marker, 1988; Klein et al., 1991; Beaumont and Vogel, 1993; Curnoe et al., 2006; Hopley et al., 2013; Doran et al., 2015; Kuhn et al., 2016). Extensive tufa deposits along the Ghaap escarpment, generated from karst springs at the intersection of faults or master joints, and along drainage lines, form relict cascades on the cliff fronts, as well as caves and breccia deposits. The tufas are host to many archaeological and faunal remains, and point to multiple periods of increased water availability and associated spring activity in the past (Butzer et al., 1978; Beaumont and Vogel, 1993; Curnoe et al., 2006).

Early attempts to constrain the timing of tufa deposition along the Ghaap escarpment using radiocarbon dating and geomorphological associations (Marker, 1974; Butzer et al., 1978) suggest tufa formation occurred on and off since the Pliocene, with cycles of both aggradation and erosion evident (Butzer et al., 1978; Curnoe et al., 2006). More recently, Doran et al. (2015) analysed tufas from three localities on the Ghaap escarpment: Buxton-Norlim Limeworks, Groot Kloof and Gorrokop, using a combination of radiocarbon and U-Th dating methods, and stable isotope analysis, to assess their utility as palaeoclimate archives. The tufas sampled in this study date to the Plio-Pleistocene, Middle Pleistocene, and terminal Pleistocene-Holocene. The $\delta^{18}O$ values increase over this time period, and this is interpreted to represent increasing evaporation from the Plio-Plesitocene to the Holocene (Doran et al., 2015). The $\delta^{13}C$ composition of the tufas is interpreted to reflect a higher proportion of C3 vegetation and well-developed soils in the Pliocene, whereas in the mid-late Pleistocene and Holocene, higher $\delta^{13}C$ values reflect a mix of C3 and C4 vegetation and thinner soils, suggesting increased aridity / decreased humidity. Doran et al. (2015) show that the Ghaap escarpment tufas are amenable to radiometric dating methods, and indicate wet periods dated to 2.1 ± 0.19 ka; 4.5 ± 0.2 ka; 5.4 ± 0.19 ka; 10.7 ± 0.23 ka; 40.03 ± 0.78 ka; 44.13 ± 0.76 ka; 44.27 ± 0.75 ka using radiocarbon (^{14}C), and at 5.8 ± 5.2 ka; 11.6 ± 6.2 ka; 127.4 ± 3.5 ka; 221.4 ± 6.3 ka; 275.4 ± 29.4 ka; 369.4 ± 12.3 ka dated using the ^{238}U-^{232}Th

disequilibrium method. Doran et al. (2015) conclude that the Ghaap tufas have potential to be useful palaeoclimate archives.

At Equus cave, another site along the Ghaap escarpment that preserves a rich faunal assemblage (Klein et al., 1991), palaeoclimate conditions for the last ~30 ka have been interpreted from pollen assemblages (Scott, 1987; Scott and Neumann, 2018), stable isotopes in tooth enamel (Lee-Thorp and Beaumont, 1995), and ostrich eggshells (Johnson et al., 1997). Analysis of oxygen and carbon isotopes in the tooth enamel of grazers indicates a predominance of C4 vegetation, i.e., an environment characterised by open grassland dependant on warm and wet summers, during the late Pleistocene to mid-Holocene (Klein et al., 1991; Lee-Thorp and Beaumont, 1995). However, an inclusion of C3 vegetation is recognised during several periods after ~15 ka and is interpreted to represent an increase in year-round rainfall as opposed to seasonal summer rainfall only (Lee-Thorp and Beaumont, 1995).

Ostrich eggshells (OES) dated using radiocarbon-calibrated amino acid racemization provide further insight for the last ~17 ka (Johnson et al., 1997). Stable nitrogen and oxygen isotopes measured in the OES point to temperature and rainfall minimums between ~17-14 ka, while an increase in rainfall is apparent between ~14-6 ka, and thereafter mean annual precipitation is interpreted to be similar to present conditions (Johnson et al., 1997). Building on the work of Scott (1987), a reassessment of pollen preserved in sediments and coprolites at Equus cave indicates cool conditions with variable moisture availability between ~31-23 ka (Scott et al., 2022). Drier conditions are indicated for ~27, ~23, ~16 and ~14.5 ka, and warm and dry conditions are indicated for the Holocene (Scott et al., 2022).

While there is some agreement between these records, all together, they provide a contradictory pattern of climate variation at this site. This is likely due to the unsecure chronology that underpins this palaeoclimate work, because of disturbance of sediments in the cave, as well as the range of proxies analysed, each of which responds differently to variable climate conditions.

2.3.3.4 Rooidam and Doornlaagte pans

Two pans, Rooidam and Doornlaagte, located about 200 km south of Ga-Mohana Hill (Figure 2.10), are composed of lacustrine and calcareous sediments that indicate fluctuating water levels during the mid-Pleistocene, associated with artefacts indicating early human occupation during the Early Stone Age (ESA) (Butzer, 1974). Building on earlier work by Netterberg (1969), Butzer (1974) provides a qualitative interpretation of oscillating lake levels at both sites through stratigraphic and geomorphological analysis of these pan sediments. Based on the archaeological artefacts and geomorphic associations between the pans, he estimated that the lacustrine sediments accumulated since the mid-Pleistocene and concluded that Doornlaagte is older than Rooidam. He also refers to one preliminary U-Th age of 115 ± 10 ka from a unit in which sediments represent low-energy aquatic sedimentation and deep lacustrine conditions, coupled with calcrete laminae that may represent periodic drying out during this time (Butzer, 1974).

2.3.3.5 Erfkroon

South-east of Ga-Mohana Hill, palaeoclimate reconstructions were carried out by Lyons et al. (2014) at the site of Erfkroon (Figure 2.10). Here, stacked palaeosols within an overbank alluvial succession are exposed in an incised channel along the Modder River. Climate affects soil formation (pedogenesis) and this influence is reflected in the variation of particular constituents within the soil, i.e. iron oxides, calcium carbonate and gypsum (Lyons et al., 2014). Using OSL dating and mineral magnetic and diffuse reflectance spectroscopy (DRS) to analyse these soil constituents, Lyons et al. (2014) inferred that from ~46-41 ka the local climate was characterised by warm temperatures and moderate seasonal rainfall (~200-400 mm per year), with a sharp and abrupt increase in precipitation (up to 600 mm per year) at ~42 ka. Between ~41-28 ka the climate remained warm and wet, with increased rainfall particularly apparent in the palaeosol horizon dated to ~32-28 ka. Lyons et al. (2014) note that this increase in rainfall does not correspond with elevated SSTs in the southwest Indian Ocean, which is expected to drive increased moisture in the SRZ. They discuss possible alternative mechanisms responsible for enhanced rainfall in the region, one of which is the expansion of the WRZ into the northern interior of South Africa, a scenario initially

proposed by Cockcroft et al. (1987) and refined by Chase and Meadows (2007). A progressive shift to cooler and drier conditions is identified between ~28-15.5 ka, with an indication for the lowest levels of rainfall between ~18-15.5 ka (~100-200mm per year) (Lyons et al., 2014). After ~15.5 ka, rising temperatures and seasonal rainfall into the Holocene are indicated, with moisture particularly enhanced during the onset and early stages of the Holocene. This finding is highlighted as being particularly important as it opposes the hypothesis that Northern Hemisphere cold events and direct insolation forcing exerted a control on southeast African climates during this time. Lyons et al. (2014) instead attribute the increase in rainfall to rising SSTs in the SW Indian Ocean, in agreement with a number of other studies (Dupont et al., 2011; Truc et al., 2013).

2.3.3.6 Florisbad

Florisbad is the site of a thermal spring, about 300 km south-east of Ga-Mohana Hill (Figure 2.10). It is located within a large (>30 km^2) depression, Soutpan, within a larger Pliocene pan field. A mound, part of a lunette dune belt, is adjacent to the spring; it is approximately 7 m high and 1.5 km wide and composed of layered organic and aeolian sediments which accumulated over the last ~300 ka (Grün et al., 1996). The mound is host to a rich archaeological and palaeoecological record, with well-preserved stone artefacts, and both human and animal fossils with age estimates from the Middle Pleistocene, Late Pleistocene and Holocene (Kuman and Clarke, 1986; Grün et al., 1996; Brink, 1997). Today, the area is semi-arid (mean annual rainfall ~450-530 mm), but a marsh, maintained by the Florisbad spring, is characterised by permanent shallow surface water and the growth of reeds and sedges on an organic-rich peat layer. Excavations into the mound reveal alternating lacustrine and peat layers, interpreted to represent past cycles of wet (lake) and drier (marsh) conditions, respectively (Toffolo et al., 2017).

Using sediment micromorphology, Fourier transform infrared spectrometry (FTIR) and x-ray diffraction (XRD), Toffolo et al. (2017) describe the sediment formational processes and present a geoarchaeological model of sediment accumulation and related palaeoclimate conditions for ~300-20 ka. Their results suggest fluctuating levels of standing water, with three alternating wet and drier stages paced at 50 ka intervals from

~300-150 ka, followed by two shorter drier and wet intervals of 20 ka each between 150-110 ka. A short dry stage is indicated by a peat layer at 110-100 ka, followed by a wet stage from ~100 - 40 ka, when a large paleolake covered the entirety of Soutpan. Thereafter, a dry stage from ~40-20 ka is represented by thick aeolian sand deposits and, in some parts, thin layers of peat. Artefact assemblages from the early Middle Stone Age (~259 ka), Middle Stone Age (MSA) (121 ± 6 ka), and Late Stone Age (LSA), indicate human activity associated with both wet and dry conditions, evidence for the persistence of a standing body of water, fed by the spring.

Renewed fossil pollen investigations by Scott et al. (2019) build on existing studies by Van Zinderen Bakker (1989) and Scott and Nyakale (2002). Although complex processes affect the accumulation and preservation of pollen at spring sites, the presence of grassy vegetation and a small fynbos component are interpreted to indicate cool and moist conditions during the Late Pleistocene. A shift to dry conditions, characterised by the presence of karroid vegetation (e.g. dwarf shrubs and succulents), occurred during the early Holocene (Scott et al., 2019). The pollen record is generally in agreement with the sedimentological record from Toffolo et al. (2017), but some contradictions are evident; this is attributed to the particular setting of Florisbad where fossil pollen from vegetation associated with the variable environment, i.e., spring, lake, and the surroundings combine, making it difficult to untangle the local and regional vegetation input, and to relate this to broader scale climate changes (Scott et al., 2019).

Age estimates for the Florisbad deposits were obtained through radiocarbon, electron spin resonance (ESR) and OSL methods (Grün et al., 1996; Brink, 1997). However, correlation of the layers across the site is challenging because of disturbance of the sediments related to the intrusion and migration of spring vents, as well as explosive earthquake activity. The age estimates therefore provide a broadly reliable chronological framework, but the absence of a precise absolute chronology limits reliable comparisons with other regional and global proxies (Scott et al., 2019).

2.3.3.7 Witpan dunes

Linear dunes are a characteristic feature of the southwestern Kalahari and represent periods of increased aeolian activity, sediment transport and accumulation. Situated approximately 400 km north-west of Ga-Mohana Hill, dune and pan sediments at the site of Witpan (Figure 2.10) have been investigated by Telfer and Thomas (2007) and Telfer et al. (2009) through geomorphology and optically stimulated luminescence (OSL) dating. Telfer and Thomas (2007) present evidence for dune development at Witpan around ~ 105-95 ka, 77-76 ka, 57-52 ka, 35-27 ka, 21-19 ka, and 15-9 ka. Palaeodunes have traditionally been utilised as a proxy for aridity in palaeoclimate studies. However, this interpretation is overly simplistic as it ignores the multiple factors involved in dune activation and accumulation, e.g. reduced rainfall, increased temperatures and evaporation, reduced soil moisture, increased windiness, and reduced vegetation (Hesse et al., 2004; Telfer and Thomas, 2007; Thomas, 2013). Compared with other regional climate proxy records, the timing of dune accumulation at Witpan mostly coincides with periods of aridity, but not always, e.g., the formation of Ghaap escarpment tufas (which are interpreted to represent wet periods) correspond to some periods of dune accumulation at Witpan. Telfer and Thomas (2007) consider the dune record from Witpan in relation to several other regional proxies for aridity and windiness. They argue that there is relative cohesion between these records, taking into account the coarseness of the resolution and disparate scales of processes, and the distances between the considered proxies. They ultimately conclude that strengthened anticyclonic winds promote aeolian activity and result in reduced moisture transport from the Indian Ocean, both of which supports dune accumulation.

2.3.3.8 Proxy data from north-eastern South African sites

Several sites in the north-east of South Africa, also in the SRZ, provide important palaeoclimate insights for the interior region during the Mid- to Late Pleistocene. These are Gladysvale Cave, Mwulu's Cave, Wonderkrater, Sudwala Cave, and Cold Air Cave (Figure 2.10). A brief account of the palaeoclimate records from these sites are given below.

Gladysvale Cave is host to hominin-bearing clastic sediments and flowstone deposits. The flowstones, which were dated with the U-Th method, indicate increased moisture availability during MIS 15 (571.4 ± 25 ka), 11 (393.0 ± 7.6 ka), 9 (307.5 ± 7.6 ka), 8 (255.3 ± 2.5 ka), 3 (56.8 ± .35 ka and 42.8 ± 6.7 ka), 2 (16.5 ± 0.15 ka and 14.4 ± 0.06 ka) and 1 (10.3 ± 2.7 ka and 7.5 ± 0.35 ka) (Pickering et al., 2007). The stable carbon isotope data also indicate generally higher proportions of C3 vegetation during these episodes, which are linked to warmer Indian Ocean sea surface temperatures and records of increased rainfall from the Tswaing crater (Pickering et al., 2007). The layers of clastic sediments sandwiched between the flowstone layers are interpreted to represent accumulation during drier periods, and carbon isotope data from these sediments indicates a higher proportion of C4 vegetation (Pickering et al., 2007).

Pollen analysis from sediments in Mwulu's Cave, a site associated with Middle Stone Age (MSA) archaeology, records swampy conditions at ~90 ka (dated using OSL) indicating local moisture availability during the latter stages of MIS (Esteban et al., 2020a). Esteban et al. (2020a) suggest that these wetter conditions may be due to decreased seasonality during MIS 5, and were perhaps related to an expansion of the WRZ into the interior during this time.

The pollen record from Wonderkrater, an open-air pan site, indicates the presence of grasslands, i.e. C4 vegetation, suggesting warm and dry conditions at ~45 ka, with a shift to cool and moist conditions at ~30 ka (Backwell et al., 2014). Thereafter, a hiatus in the record until ~16 ka exists, followed by indications for strongly evaporative but not necessarily low rainfall conditions between ~12 - 10 ka (Backwell et al., 2014).

A speleothem from Sudwala Cave, dated using the U-Th method, records growth phases between ~40 to 34 ka and between ~14 to 12 ka (Green et al., 2015). Based on oxygen and carbon isotope values, the early part of the first phase of growth is interpreted to have occurred under relatively dry conditions, i.e., sufficient moisture was available for speleothem formation, but oxygen isotope values indicate low rainfall amounts, and the carbon isotope values indicate a predominance of C4 vegetation (Green et al., 2015). Isotope values in the later portion of growth phase 1 are interpreted to indicate more

persistent rainfall and expansion of C3 vegetation. A hiatus in the speleothem is documented between ~34 to 14 ka. This interruption of speleothem growth is interpreted to have occurred due to an increased density of forest above the cave, i.e. dominance of C3 vegetation, as a result of high rainfall and cool temperatures, which restricted the flow of drip waters into the cave (Green et al., 2015). The second growth phase between ~14 to 12 ka coincides with the Antarctic Cold Reversal, a brief return to cold conditions during the overall warming period of deglaciation following the LGM (Green et al., 2015).

Holmgren et al. (2003) present oxygen and carbon isotopes underpinned by U-Th ages for a stalagmite from Cold Air Cave in the Makapansgat Valley (Figure 2.10), providing a high resolution record for the last ~25ka. The stable isotope data, in conjunction with complementary pollen records, track wet and dry periods and warming and cooling. Dry conditions, low temperatures, and sparse grass cover are recorded for ~23 - 21 ka, ~19.5 - 17.5 ka, and ~15 - 13.5 ka. Renewed warming is reported after ~13.5ka, and a hiatus in the stalagmite occurs between ~12.7 to 10.2 ka, indicating dry conditions. Warm and relatively dry conditions, i.e. wet enough to allow for resumption of stalagmite growth, continue between ~10 - 6 ka, followed by a gradual mid-Holocene cooling between 6 - 3 ka (Holmgren et al., 2003).

2.3.4 Concluding remarks

Clearly, the Late Pleistocene and Holocene record for the southern Kalahari and neighbouring areas of southern Africa is patchy, making it difficult to gain a cohesive sense of the spatial and temporal climate conditions that characterised this region in the past. Although some records point to evidence of orbital-scale controls impacting rainfall variability in southern Africa, many others suggest that Indian Ocean SST change plays a role in modulating orbital forcings. Increasingly, palaeoclimate records supported with modelling scenarios, suggest an inherent heterogeneity of past rainfall patterns in South Africa as a result of the interplay between multiple and complex factors operating on different scales (Singarayer and Burrough, 2015). More well-dated proxies with long and robust records need to be investigated in order to gain clarity on

these feedback mechanisms and their associated landscape expressions. There are even fewer well-dated palaeoclimate records linked to securely dated archaeological deposits; this is particularly important for placing archaeological findings in context, and to adequately address the question of how past climates and changing environments influenced early modern human behaviour and adaptation.

2.4 Archaeological background

Environmental variability has been proposed as a key driver of evolutionary adaptive change (Deacon, 1976; Ambrose and Lorenz, 1990; Trauth et al., 2009; Ziegler et al., 2013; Mackay et al., 2014; Maslin et al., 2014; Wilkins, 2017; Mackay et al., 2022; Wilkins and Schoville, 2024) but there is a need for more locations with robust geo-proxy and archaeological records to test this hypothesis and to establish the relationship between environmental and climate dynamics and human evolution and dispersal (Thomas and Burrough, 2012).

During the Quaternary, hunter-gatherer populations inhabited the South African landscape, and our understanding of their activity and behaviour is based primarily on interpretations of the remains of their material culture, i.e., the recovery of artefacts, such as stone tools. The variety of stone tools identified through time in the archaeological record have been grouped into various lithic assemblages that represent specific industries associated with particular technological and behavioural advances. These have been grouped into industrial complexes, also termed technocomplexes, and form the basis of the cultural-stratigraphic framework of the Earlier, Middle and Later Stone Ages of South Africa (Lombard et al., 2012; Wurz, 2013).

The Earlier Stone Age (ESA) is characterised by some of the earliest stone tool technologies that provide evidence of hominin activity in South Africa, and encompasses the Oldowan (>2 Ma to ~1.5 Ma), Acheulean (~1.5 Ma to ~300 ka) and transitional ESA (~600 ka to >200 ka) technocomplexes (Lombard et al., 2012). The tools from the early and middle stages of the ESA are relatively basic, large cutting tools e.g.

cores and hand axes. Many of the tools that typify these ESA technocomplexes are from sites in the southern Kalahari, e.g. Wonderwerk Cave, Rooidam, and Kathu Pan (Wilkins, 2021). The Middle Stone Age (MSA, ~300 ka to ~20 ka) is associated with technological and behavioural advances ascribed to the emergence of modern humans, *Homo sapiens* (McBrearty and Brooks, 2000; Henshilwood et al., 2004; Marean et al., 2007; Henshilwood et al., 2009; Wadley, 2015; Henshilwood et al., 2018). This stage is characterised by technological diversity and episodes of innovation and complexity reflected in smaller, more refined tools, the use of heat treatment, and hafting technologies (Wurz, 2013; Wadley, 2015). Notably, the Still Bay (~77 ka to 70 ka) and Howieson's Poort (~66 ka to 58 ka) technocomplexes include some of the most sophisticated and complex innovations during the MSA, and include the presence of other objects e.g. engraved ochre, bone artefacts, and beads (Henshilwood et al., 2002; Jacobs et al., 2008; Wadley et al., 2011). During the Later Stone Age (LSA; ~40-20 ka to recent) tools became even smaller, i.e. microlithic, and LSA assemblages include bone arrowheads and barbed points, ostrich eggshell beads, geometric engravings on rock slabs and ostrich eggshells, and ceramics (Thackeray et al., 1981; Robbins et al., 2007; Ecker et al., 2017; Wilkins, 2021).

A substantial amount of work has focused on MSA sites along the southern coast of South Africa, where systematic, high-resolution investigations have produced a robust record of early human behaviour and adaptations during the Late Pleistocene. Based largely on the archaeological records of flagships sites such as Pinnacle Point, Blombos Cave and Klassies River Mouth (Figure 2.10), the role of coastal resources is emphasised as the primary driver of innovation in human behaviour (Marean, 2010; Parkington, 2010; Marean, 2014; Will et al., 2016; Smith et al., 2018). This body of knowledge is informally known as the coastal adaptation hypothesis, with the main premise being that the southern coast served as a refuge for early human populations when the climate was cold and dry elsewhere. There is evidence at these sites that early humans expanded their diet to include shellfish and aquatic mammals, and this, coupled with the rich diversity of the Cape Floral Region and the now submerged Palaeo-Aghulus Plain, made these sites refugia with substantial and stable nutrition sources (Fisher et al., 2010; Copeland et al., 2016' Braun et al., 2020). This is proposed as a major factor in the

development of social and technological advances associated with *Homo sapiens*. Despite the evidence for an equally rich record in the interior region of South Africa, these deposits have received much less attention and have not been studied with the same rigour (Stewart et al., 2012; Backwell et al., 2014; Horwitz and Chazan, 2015; Wilkins et al., 2020; Wilkins et al., 2021). Consequently, there is a geographic bias towards coastal sites as loci for critical changes in early human behaviour.

Several important behavioural innovations are recorded at archaeological sites in the interior region of South Africa. In particular, a calcite crystal cache and assemblage of human-collected ostrich eggshells at Ga-Mohana Hill (Wilkins et al., 2021), early association of fire with artefacts (Berna et al., 2012) and early engraved portable art (Thackeray et al., 1981) at Wonderwerk Cave, early blade production and stone-tipped spear technologies at Kathu Pan (Chazan et al., 2012; Wilkins and Chazan, 2012), and the use of pigments for symbolic purposes, evident at many of these sites (Beaumont and Vogel, 2006; Watts et al., 2016). However, high resolution palaeoclimate data for Late Pleistocene archaeological sites in this region are lacking (Wilkins et al., 2020). Consequently, the existing records are as yet insufficient to meaningfully investigate the relationship between early *Homo sapiens* and palaeoenvironments away from the coast.

Wilkins et al. (2020) carried out a systematic, high-resolution archaeological excavation in Ga-Mohana Hill North Rockshelter to begin to correct the geographic bias, and to improve the Late Pleistocene archaeological record from the interior region of South Africa. Ga-Mohana Hill North has preserved stratified MSA and LSA sediments that have been the focus of systematic archaeological investigations, and each main artefact bearing horizon has been dated by OSL (Figure 2.11) (Wilkins et al., 2020; Wilkins et al., 2021). The lowest unit, Dark Brown Silt and Roofspall (DBSR), is dated to 105.3 ± 3.7 ka, and the archaeology is characterized by large MSA-type points and blades (Wilkins et al., 2021) (Figure 2.12). The overlying Orange Ashy Silt (OAS) unit is dated to 30.9 ± 1.8 ka with artefacts indicative of a flake and blade-based industry, consistent with a MSA designation (Wilkins et al., 2020). The top layer, Dark Brown Gravelly Silt (DBGS), is dated to 14.8 ± 0.8 ka and contains LSA-type lithic artefacts, such as bladelets and bladelet cores, as well as ostrich eggshell beads (Wilkins et al., 2020; Hatton et al., 2022).

These dated horizons are evidence of human occupation and activity at Ga-Mohana Hill during the Late Pleistocene.

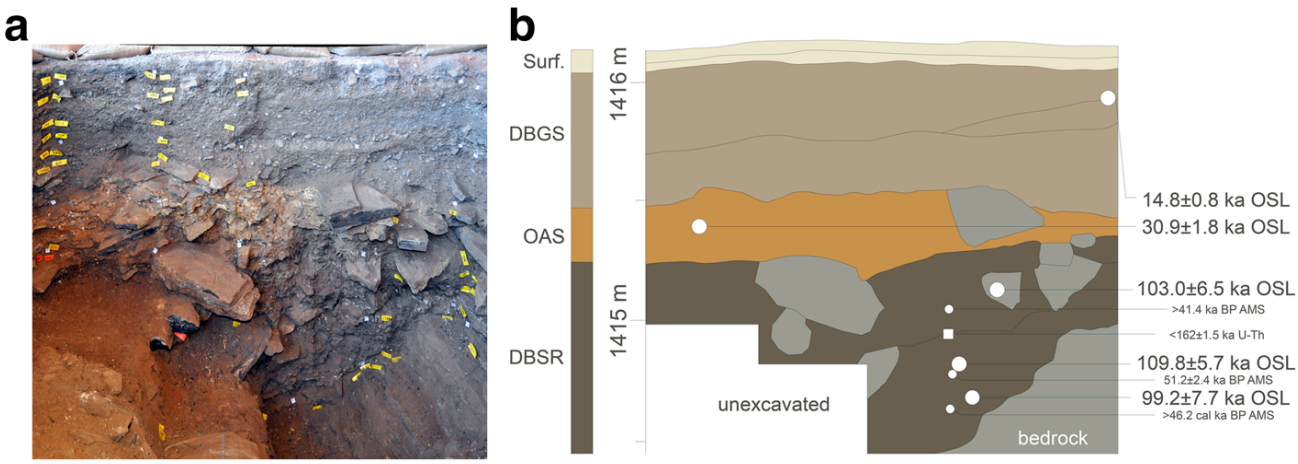

Figure 2.11 Portion of excavation Area A at Ga-Mohana North rockshelter, from Wilkins et al. (2020): a) photograph of the east wall, b) schematic of the stratigraphic boundaries seen in (a) with associated OSL ages.

Figure 2.12 Examples of lithic artefacts and ochre from the DBSR unit, from Wilkins et al. (2021): a) prepared core, b) ochre, c-d) points, e) blade.

2.5 Tufa: terminology, formation and palaeoclimate potential

2.5.1 Definitions and terminology

Tufa deposits are abundant on the Ga-Mohana Hillside and are the focus of this thesis. Although there is a long history of tufa documented in the region e.g., Ghaap Plateau and Eastern Transvaal (Peabody, 1954; Marker, 1988; McKee, 1993), the Ga-Mohana tufas have not been documented, mapped, or described in detail before. Tufa is defined here as terrestrial, ambient temperature (< 30°C), secondary carbonate deposits, which form from freshwater springs and streams, often in conjunction with botanical or microbial organisms (Marker, 1988; Pedley, 1990; Ford and Pedley, 1996; Pedley, 2009; Capezzuoli et al., 2014). Tufas are typically composed of low magnesian-calcite which precipitates from a solution enriched in calcium and bicarbonate ions, usually scavenged from carbonate bedrock in karst terrains (Ford and Pedley, 1996; Pentecost, 2005; Ford and Williams, 2007; Capezzuoli et al., 2014). In this case, the Archaean dolomites of the Campbellrand Subgroup would have been the precursor for the Ga-Mohana tufa deposits.

The terms travertine and tufa are used interchangeably in the literature, with distinctions made based on the porosity and density of the material, its degree of crystallinity, its environmental setting, and its location related to the water source (Julia 1983; Viles and Goudie 1990). Chafetz and Folk (1984), Pentecost and Viles (1994), and Pentecost (1995; 2005) use the term travertine to refer to all freshwater carbonate deposits. Pentecost (2005) proposed a differentiation of these based on the predominant source of carbon, i.e. carbon derived from meteoric sources, termed meteogene travertine, and carbon derived from hydrothermal sources, termed hypogene travertine. On the other hand, Pedley (1990) and Ford and Pedley (1996) suggested that travertine be restricted to calcareous deposits associated with hydrothermal environments, and recommended the term tufa be applied to all cool freshwater calcareous deposits, regardless of age or crystallinity. In accordance with this latter categorisation, the term tufa is used is in this study as there is no evidence of hydrothermal activity at Ga-Mohana Hill.

There is an extensive literature on tufas as there has been much interest in these deposits as short-term palaeoclimate archives, complementary to longer-term records from speleothem deposits (Hennig et al., 1983; Chafetz and Folk, 1984; Viles and Goudie, 1990; Ford and Pedley, 1996; Pentecost, 2005; Andrews, 2006; Pedley, 2009; Capezzuoli et al., 2014). The topic has been approached through a variety of disciplines including geomorphology, sedimentology, geochemistry, hydrology, and botany, as a range of factors contribute to and influence tufa formation. This complexity has made it difficult to achieve a consensus on the terminology used to describe these deposits, and to settle on a regulated method for classification (Capezzuoli et al., 2014). Despite this, the seminal works by Chafetz and Folk (1984), Viles and Goudie (1990), Pentecost and Viles (1994), Violante et al. (1994), Ford and Pedley (1996), Pedley (1990), and Pentecost (2005) provide a foundational framework for assessing tufa deposits. Although there is some disparity in the factors emphasised, these works provide a comprehensive basis for understanding and investigating tufa deposits and their palaeoclimatic significance.

2.5.2 Tufa formation

Tufas precipitate at the surface from calcium bicarbonate waters, facilitated by a combination of physico-chemical and bio-chemical processes (Chafetz and Folk, 1984; Ford and Pedley, 1996; Pentecost, 2005). Conditions controlling the precipitation of tufas include the temperature, pH, pCO_2, and chemical composition of the solution (Jacobson and Usdowski, 1975; Turi, 1986).

The primary requirements for tufa deposition are net moisture availability, i.e. precipitation > evaporation, CO_2 enrichment of groundwaters, and calcium saturation (Jacobson and Usdowski, 1975; Pentecost, 2005). Calcium is usually sourced via the dissolution of carbonate bedrock, e.g. dolomite, but may also be derived from evaporites and igneous rocks (Barnes and O'Neil, 1969; Pentecost, 2005; Stone et al., 2022). Hydration of carbon dioxide is required for dissolution of the carbonate bedrock, and the subsequent concentration of calcium and bicarbonate ions in the groundwater (Turi, 1986). This occurs in the soil zone, i.e. epikarst, where plant root respiration, the decay of organic matter, and bacterial activity produces high concentrations of CO_2 (g)

in the soil. This results in a higher partial pressure of CO_2 in the soil (pCO_2 ~21%) relative to the partial pressure of CO_2 in the atmosphere (pCO_2 ~0.038%) (Deines, 1980; Turi, 1986; Ford and Williams, 2007). Meteoric waters that infiltrate the soil zone dissolve this CO_2, and this enhances the dissolution capacity of the water. Temperature plays an important role in controlling the rate of tufa precipitation. Calcite becomes increasingly insoluble at higher temperatures, and consequently an increase in temperature increases the degree of calcium carbonate saturation, encouraging higher rates of precipitation (Pedley et al., 1996). Temperature and water availability are also important for soil productivity, which generates the CO_2 required for carbonate dissolution.

The principal processes leading to tufa precipitation are as follows. Meteoric waters that percolate the soil dissolve CO_2 (g) from the soil atmosphere (Equation 2.1). This results in an increase in the pCO_2 of the groundwater, and carbonic acid (H_2CO_3) is produced (Equation 2.2). The dissociation of carbonic acid occurs rapidly to produce bicarbonate ions, which further dissociates to produce carbonate ions (Equation 2.3). These carbon species make up the dissolved inorganic carbon (DIC) in meteoric waters (Ford and Williams, 2007). The DIC concentration in tufa-forming groundwaters is usually between 1-10 mmol/L (Pentecost, 1995; Capezzuoli et al., 2014).

Equation 2.1 $CO_2(g) \leftrightarrow CO_2(aq)$

Equation 2.2 $H_2O + CO_2 \rightarrow H_2CO_3$

Equation 2.3 $H_2CO_3 \rightarrow H^+ + HCO_3^-$ and $HCO_3^- \rightarrow H^+ + CO_3^{2-}$

The CO_2-rich waters then percolate into the underlying aquifer where they interact with the carbonate bedrock ($CaCO_3$). The carbonic acid dissolves the bedrock carbonate, whereby calcium and bicarbonate ions (Ca^{2+} and HCO_3^-) are incorporated into the groundwater (Equation 2.4).

Equation 2.4 $CaCO_3 + H_2O + CO_2 \rightarrow Ca^{2+} + 2HCO_3^-$

When these groundwaters emerge at the surface, the interaction of the solution with the atmosphere leads to degassing of carbon dioxide (CO_2) as a result of the different partial pressure between the CO_2 dissolved in the groundwater and the CO_2 of the atmosphere (Jacobson and Usdowski, 1975; Turi, 1986). Provided there is a sufficiently high calcium concentration in the groundwater (Ca^{2+} > 2mmol/L or > 80 ppm), this degassing disrupts the equilibrium (Pentecost, 2005). This leads to an increase in the pH and calcium saturation of the solution, triggering precipitation of calcium carbonate (Jacobson and Usdowski, 1975; Turi, 1986).

Degassing of CO_2 is most rapid close to the point of spring water emergence, and decreases with increasing distance from this point as precipitation proceeds and the stream water CO_2 equilibrates with atmospheric CO_2 (Jacobson and Usdowski, 1975). Other physical mechanisms that encourage CO_2 degassing, such as turbulent flow or evaporation, also lead to supersaturation of the groundwaters with respect to $CaCO_3$, resulting in tufa formation (Pedley et al., 1996).

Additionally, equilibrium conditions may be displaced via biotic mechanisms, for instance, when plants and microbial organisms are involved in extracting CO_2 from the water during photosynthesis or other metabolic processes (Chafetz and Folk, 1984; Viles and Goudie, 1990; Pedley, 2000). Semi-aquatic vegetation, such as bryophytes (mosses), and microbes, i.e., microscopic organisms encompassing bacteria, fungi, algae and protozoans, are often found in tufa forming environments, and this variety of biota can play an important role in the construction and precipitation of tufa deposits (Chafetz and Folk, 1984; Pedley, 2000; Riding, 2000; Pedley et al., 2009, Pedley and Rogerson, 2010). The extent to which biogenic factors are involved in tufa precipitation has long been debated (Ford and Pedley, 1996; Kano et al., 2003; Andrews and Brasier, 2005; Pedley et al., 2009). Nevertheless, it is clear that some level of biological activity is involved in tufa precipitation, particularly in slower flow circumstances (Merz-Preiz and Riding, 1999; Pedley, 2000; Pedley et al., 2009; Pedley and Rogerson, 2010). This role may either be active, e.g., removal of CO_2 from the fluid during metabolic processes facilitated by plants and microbes, or passive, in which case organic substrates, i.e., microbial mats and biofilms, provide sites for calcite nucleation on and within the

extracellular polymeric substance (EPS) material that they produce (Golubić, 1973; Riding, 2000; Andrews and Brasier, 2005). There is a growing body of work that explores the impact of these processes on tufa microfabrics and chemistry (Merz-Preiz and Riding, 1999; Rogerson et al., 2008; Arp et al., 2010; Pedley and Rogerson, 2010; Rogerson et al., 2010; Mercedes-Martín et al., 2021; Rogerson et al., 2022) but this is beyond the scope of this thesis.

It is generally acknowledged that tufa precipitation is facilitated by a combination of physico-chemical and biotic processes. Chen et al. (2004) show that physical CO_2 degassing is indeed the principle mechanism through which tufa precipitates at waterfall or cascade sites, where high flow velocity results in an enlarged air-water interface area. This causes CO_2 to diffuse into the atmosphere rapidly, leading to calcite precipitation. In areas of slower flow or stagnant water, however, CO_2 degassing is much less prevalent and it is likely that biological processes dominate in these environments (Ford and Pedley, 1996).

2.5.3 Tufa as a palaeoclimate archive

Both active and inactive tufa systems are found across a variety of climate zones (Pentecost, 1995; Pentecost, 2005; Capezzuoli et al., 2014). Tufa formation is reliant on a range of variables operating on multiple scales, e.g. local-scale geomorphology, biota, and water chemistry, regional-scale climate, i.e., rainfall patterns, temperature, and vegetation, and global-scale climate, i.e., ice volume, sea surface temperatures, atmospheric CO_2 concentrations, etc. As such, the relationship between tufa formation and climate is complex, and relating relict deposits to particular conditions or climatic events is challenging (Pentecost, 2005). Nevertheless, tufas do have the potential to record useful palaeoclimate information (Marker, 1974; Garnett et al., 2004a; Ordóñez et al., 2005; Andrews, 2006; Cremaschi et al., 2010; Domínguez-Villar et al., 2011; Dabkowski et al., 2012; Domínguez-Villar et al., 2012; Guo et al., 2013; Doran et al., 2015; Ibarra et al., 2015; Sancho et al., 2015).

On a first order, the presence of tufa on the landscape indicates spring or fluvial activity, which implies water availability (Marker, 1974; Gedda et al., 1999; Viles et al., 2007; Johnson et al., 2009; Stone et al., 2022). In addition to sufficient water, warm temperatures to support soil productivity creates favourable conditions for tufa formation. Consequently, tufa deposits have been linked to humid (warm and wet) phases associated with interglacial climate conditions (e.g. Horvatinčić et al., 2000; Auler and Smart, 2001; Soligo et al., 2002; Frančišković-Bilinski et al., 2004; Capezzuoli et al., 2010; Domínguez-Villar et al., 2011). In addition to signifying humid conditions, sedimentological features, mineralogy and trace element variation, and oxygen and carbon isotope data in tufas can provide indications of the hydrological conditions, temperature, and predominant vegetation at the time of formation (e.g. Pazdur et al., 1988a; Andrews, 2006; Arenas et al., 2007; Brasier et al., 2010; Cremaschi et al., 2010; Banks et al., 2012; Dabkowski et al., 2012, Doran et al., 2015).

The value of tufas as palaeoclimate archives relies on obtaining accurate and precise ages for the deposits so that proxy data, e.g. sedimentological models of the depositional environment, trace element contents, and carbon and oxygen isotope data, can be tied to a reliable chronology. This is crucial for Quaternary palaeoclimate reconstruction (Ford and Pedley, 1996; Andrews, 2006; Capezzuoli et al., 2014). Dated tufa found close to, or in association with, archaeological sites can provide an environmental context to the archaeological record, and shed light on the types of settings in which human populations thrived (Dabkowski, 2014; Doran et al., 2015; Hellstrom and Pickering, 2015). This is particularly important for understanding human-environment dynamics in the relatively understudied Kalahari region (Wilkins, 2021). While the bulk of terrestrial carbonate dating work has focused on speleothems, tufa has been shown to be amenable to U-Th dating (Auler and Smart, 2001; Mallick and Frank, 2002; Soligo et al., 2002; Garnett et al., 2004b; Sierralta et al., 2010).

In this thesis, I use a multi-proxy approach to investigate the Ga-Mohana Hill tufa deposits to provide a robust interpretation of the past climatic and environmental conditions at the time of their formation. Details on the methodologies applied are given in Chapter 3. The four results chapters follow, and each begins with a section

detailing the background and relevant case studies related to the proxy approach presented.

CHAPTER 3 METHODS

In the following sections in this chapter, I describe each of the methods I used to investigate the tufas at Ga-Mohana Hill and the past conditions they represent. The methods are presented in the order in which the results are reported in the subsequent chapters.

3.1 Field work

Field work at Ga-Mohana Hill was conducted over several years, beginning in August 2017. My first field visit involved a survey of the tufa deposits at Ga-Mohana and the surrounding hillsides and tufa sampling. Sample selection was partially informed by a pilot study conducted in 2016 by Dr R. Pickering in which six tufa samples had been collected and processed for U-Th dating. Subsequent field visits included modern water sampling, and further tufa sample collection.

3.1.1 Tufa mapping and sample collection

Mapping of tufa deposits at Ga-Mohana Hill and collection of samples was carried out over two field seasons. The initial visit in August 2017 involved a large-scale survey of Ga-Mohana Hill and the surrounding hillsides. Tufa deposits were documented, classified based on their gross morphology and occurrence on the hillside, and photographed. In a pilot study prior to the start of this project, six samples were collected and dated by Dr R. Pickering in 2016 (labelled GHN or GHS; Figure 3.1.1 and Table 3.1). These initial samples informed the sampling strategy for this first campaign, i.e., samples that resembled those that had been successfully dated were targeted, as one of the main objectives of the study is to investigate the ages of the tufa deposits. In addition, I collected representative tufa samples from each of the deposit categories that I noted during my survey to document their petrography in detail, and to investigate whether the various deposits were the same age. A total of twenty-six samples were collected during the survey. Eleven of these samples were collected from Ga-Mohana Hill and five from the hill slope to the west of Ga-Mohana (Figure 3.1.1 and Table 3.1).

Samples were collected using a geological hammer, mallet and chisel, and in some instances, were carefully removed using an angle grinder. Because of the tools available to collect samples, only surficial samples were collected during this field visit, i.e., tufas on the terraces and the outer layers of dome and tufa flows.

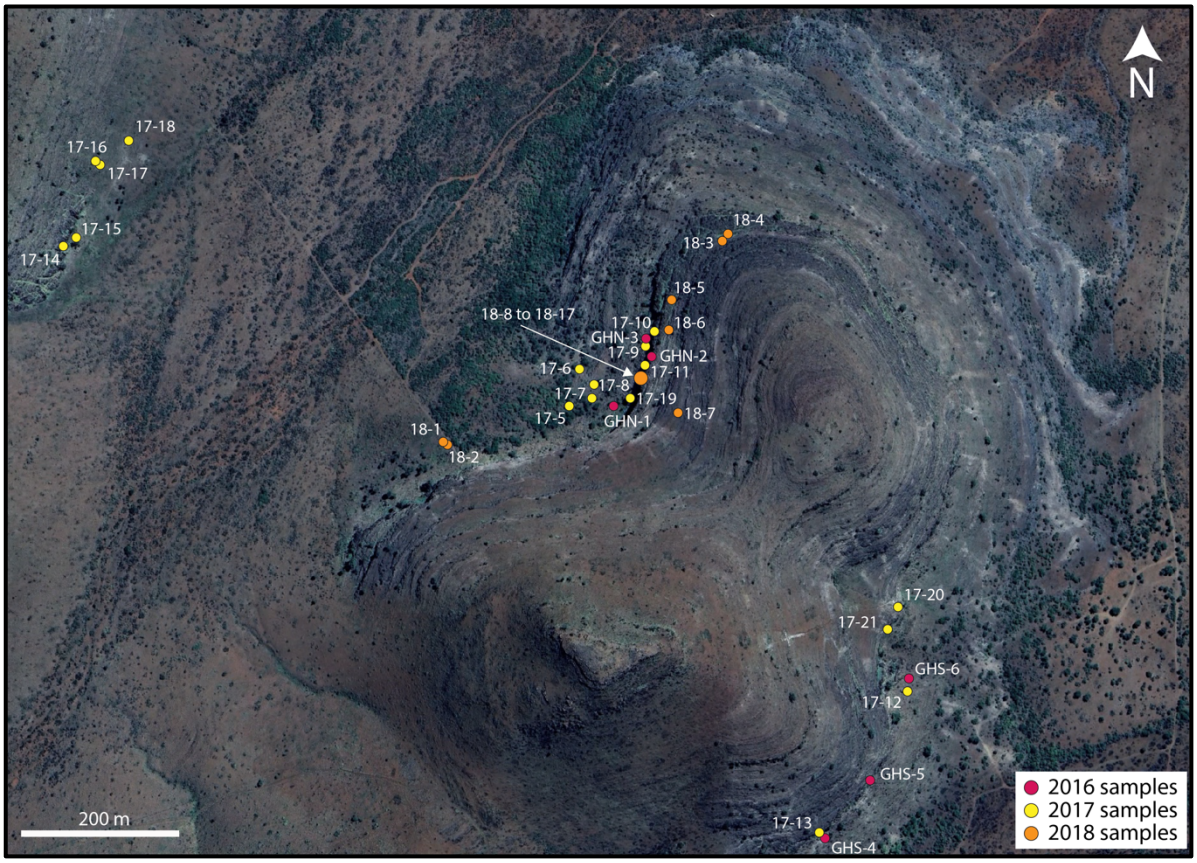

Figure 3.1.1 Satellite image of Ga-Mohana Hill showing the location of tufa samples collected during field campaigns in 2016, 2017 and 2018.

Tufa sampling during the second field visit in December 2018 involved targeted sample collection, informed by age data returned from samples collected in 2017. In an attempt to get a sense of an earlier initiation of the tufa system, a core drill was used to sample beyond the outer layers of the tufa mounds and flows, and tufa flows were sampled as close to their contact with the dolomite bedrock as possible. This sampling campaign was focussed on the northern side of the north shelter, as this location provided a high density of accessible and well-preserved deposits that appeared to present the best opportunity to obtain sequential ages (Figure 3.1.1). Ten tufa cores were collected from tufa mounds and flows using a modified Makita cordless hand drill fitted with a custom-

made core barrel (1 inch and 1.5 inches) (Figure 3.1.2). In addition, seven samples were collected from the terraces above and below the north shelter using a mallet and chisel. Three dolomite samples were also collected from the north shelter wall and the terraces to serve as a reference for the bedrock (Table 3.1).

Table 3.1 Record of analyses performed on tufa and dolomitic bedrock samples collected from Ga-Mohana Hill over several field visits, between 2017 to 2021.

Sample	Collected	Morphology	T/s	XRD	LA	SI	U-Th
GHN1	2016	rim-pool	✓	✓	✓	✓	✓
GHN2	2016	cascade	✓		✓		✓
GHN3	2016	dome	✓				✓
GHS4	2016	dome	✓	✓			✓
GHS5	2016	cascade	✓		✓		✓
GHS6	2016	rim-pool	✓		✓	✓	✓
17-5	2017	rim-pool				✓	
17-6	2017	barrage	✓	✓	✓	✓	✓
17-7	2017	terrace breccia				✓	
17-8	2017	terrace breccia	✓	✓	✓	✓	✓
17-9	2017	dome				✓	
17-10	2017	cascade	✓	✓		✓	
17-11	2017	cascade				✓	
17-12	2017	terrace breccia	✓			✓	
17-13	2017	dome	✓			✓	
17-19	2017	dolomitic bedrock				✓	
17-21	2017	cascade				✓	
18-2	2018	terrace breccia		✓			
18-4	2018	cascade	✓	✓	✓	✓	✓
18-6	2018	barrage	✓	✓	✓	✓	✓
18-7	2018	terrace breccia		✓	✓	✓	✓
18-10	2018	dome			✓	✓	✓
18-11	2018	cascade	✓		✓		
18-12	2018	cascade	✓	✓	✓	✓	✓
18-13	2018	cascade			✓	✓	✓
18-14	2018	cascade	✓		✓	✓	✓
18-15	2018	cascade	✓		✓	✓	✓
18-16	2018	cascade	✓		✓	✓	✓
18-17	2018	cascade			✓	✓	✓
GCC04	2021	dolomitic bedrock		✓			
GCC06A	2021	dolomitic bedrock		✓			

Figure 3.1.2 Sampling of tufa using modified hand drill fitted with custom core barrel.

In total, 43 tufa samples were collected over the course of this project, 28 of these were analysed (Table 3.1). Samples from Ga-Mohana Hill with dense micritic material and layering were prioritised for analysis to focus the scope of the project. The way-up was marked on all samples using a permanent marker, and the location was recorded using a roaming GPS. Although care was taken to select a representative collection of tufa samples, the 28 samples analysed in this study cannot be considered exhaustive.

3.1.2 Modern water sampling

Modern rain, ground, and drip waters from in and around Ga-Mohana Hill were collected on three separate field visits in January and July 2018, and February 2021. These water samples were collected to serve as proxies for the waters that formed the tufa deposits. Samples were collected in a combination of different sized plastic and glass bottles (5 – 45 ml) depending on the volume of water available for collection.

In January 2018, drip water was collected from actively dripping micro-stalactites within the GHN shelter. Bottles were positioned on a rock ledge beneath the micro-stalactites and the drip water allowed to accumulate overnight (Figure 3.1.3). The bottles were filled to the very top with no head space to avoid exchange between air and water oxygen isotopes, and then fastened with a screw cap lid. Drips from micro-stalactites which did not have a ledge beneath them were collected by securing a plastic bag to the micro-

stalactite using duct tape. The water collected in the bags was then transferred into bottles either by cutting a hole in the plastic bag and draining the water out, or by using a pipette. When possible, the bottles were initially rinsed with some of the water collected, filled to the top, and then closed tightly.

Figure 3.1.3 Photographs from water collection at Ga-Mohana Hill: a) actively dripping micro-stalactite, b) plastic bag strapped to dripping micro-stalactite, c) plastic bottle positioned on a ledge beneath a drip.

Rain water was collected on a large plastic drop sheet laid out on the ground during two short (approximately 10 to 15 minutes) rainfall events. The rainfall occurred during midday and late afternoon in January 2018. The temperature was approximately 32°C and the rainfall amount is unknown. The water was immediately transferred into bottles using a pipette. Rain water that had accumulated in shallow pools in the dolomite (classed as standing water) on Ga-Mohana Hill was also collected shortly after the rain event (time delay of approximately 30 minutes or less), either by submerging a vial in the water, or using a pipette to transfer the water into the bottle, depending on the depth of the pool. Ground water was collected from the Eye of Kuruman (-27.4632482, 23.4363511), and from several boreholes on two farms in the surrounding area, Red Sands Farm (-27.5103914, 23.3036016) and Rueben's Farm (-27.3885687, 23.2977902), by submerging the bottles into the water at the sites. The water samples were all stored in a dark container immediately after collection.

In July 2018, the collection process was repeated for drip water from stalactites in and around the shelter, and groundwater from the Eye of Kuruman. Different micro-stalactites to the ones sampled in January were actively dripping. No rain or standing water was collected as there were no rainfall events during the field visit. Water was not resampled from the boreholes on the farms due to time constraints. In February 2021, water was collected from several other actively dripping micro-stalactites, and again from the Eye of Kuruman Spring.

3.2 Petrography

Samples were cut using a diamond rock saw to expose a fresh surface and internal structures, and one half of each sliced sample was polished using various grits of sandpaper and water. The drill core samples were set in epoxy resin before being cut and polished due to their friable nature. Thin sections were prepared from fourteen samples, selected primarily on the basis of their potential for U-Th dating, i.e. samples composed of dense micritic material and low visible porosity, and samples with clear layering. Thin sections of three different sizes (7.5 x 11 cm, 5 x 7.5 cm and 3 x 4.5 cm) were prepared in the thin section lab at the University of Cape Town to identify and classify the micromorphological characteristics of the tufas. These thin sections were examined under a Nikon polarising microscope in plane polarised light and photos were taken using a Zeiss microphotographic microscope camera system. Micromorphological observations were described with reference to Perri et al. (2012).

3.3 X-ray diffraction

A subset of ten randomly selected tufa samples from each tufa category, and two dolomite samples, were processed for X-ray diffraction (XRD) at UCT to establish the whole bulk rock mineralogy. Sample preparation was done in the Department of Geological Sciences and analysis was conducted in the Chemical Engineering Department. A slice from each sample was cut using a saw and then crushed using a geological hammer. The crushed pieces were milled to a fine powder using a swing mill. The powders were measured on a Brucker D8 Advance instrument with a 2θ scan range

of 5–120 degrees using a cobalt source with wavelength of 1.78886 Å. The data obtained was then plotted using X'Pert Highscore Plus software (Degen et al., 2014), and peaks matched with reference to the PDF-4/Minerals 2020 database (Gates-Rector and Blanton, 2019).

3.4 Laser Ablation Inductively Coupled Plasma Mass Spectrometry

Trace element concentrations of layers within selected tufa samples were determined through *in-situ* laser-ablation using a HelEx 193nm ArF excimer laser-ablation system coupled to an Agilent 7700x Quadrupole ICP-MS at the University of Melbourne, following the method detailed in Woodhead et al. (2007). This was done primarily as a screening step to identify the best layers for U-Th dating (low detrital Th, high U), but additional trace element data were collected at the same time.

Sixteen tufa samples were selected for laser ablation analysis based on the following criteria: 1) samples composed of dense micritic material with low visible porosity based on the premise that these offered the best chance of returning a reliable U-Th age; 2) samples with layering since individual layers may represent separate growth periods and thus have the potential to provide sequential ages, and / or element variations that may provide information on changes in tufa growth and associated environmental conditions; 3) samples that had already been analysed for U-Th dating to serve as a benchmark for further U-Th sub-sampling.

Prior to laser-ablation, samples were washed in ultra-pure Milli-Q water in an ultrasonic bath for five minutes and allowed to air dry. The samples were mounted in a sample holder and high-resolution images (3200 dpi) were produced using a flat-bed scanner. The samples and sample holder were cleaned with high-pressure air before being placed in the laser cell. Using GeoStar software by Resonetics, the scanned image of each sample was then referenced to the co-ordinate system of the ablation cell. Several parallel lines, between 6 and 12 per sample, set 62 μm apart, were carefully chosen, perpendicular to the growth layers of the samples. The samples were then twice pre-ablated along these tracks, with a spot size of 60 μm and at a speed of 150 μm/s, to clean

the surfaces of the samples. Finally, the trace element ablation scans were performed with a circular spot size of 60 μm, a speed of 75 μm/s and a pulse rate of 10 Hz.

The ablation scans were carried out in an atmosphere of helium and the ablated material was then carried in an argon stream into the mass spectrometer to be measured. Elemental concentrations were calibrated against the NIST SRM 612 glass reference, with ^{43}Ca as an internal standard, and an estimated precision of ca <5%. NIST SRM 610 and JCp-1, a powdered coral standard, were also analysed.

The raw mass spectrometry data was reduced using the Iolite software package (Paton et al., 2011). A Ca concentration of 40 wt% was assumed for all samples. Maps of the element concentrations recorded along the laser ablation transects were then generated from this reduced data using data deconvolution (Paul et al., 2012). These maps allow extrapolation along similar layers from multiple line scans, providing greater confidence than a single line scan, due to the heterogeneity of the samples.

Further to the generation of the maps, processing of the trace element data was carried out in R version 4.2.1 (R Core Team, 2022). Negative values and those below detection were renamed as null. The time of analysis (s) was converted to length (mm) based on the sampling period and scan rate: 1 observation every ~12.5 um / 0.0125 mm. The element data collected from the multiple transects was plotted using Ggplot2 (Wickham et al. 2019) to visually assess lateral variations across each transect. High frequency outliers were removed by performing a 13-point moving average filter, followed by a 13-point moving median filter, following the method used in Carlson et al. (2018).

3.5 Solution ICP-MS

3.5.1 Tufa samples

Five tufa samples with laser ablation trace element data were drilled along layers associated with a U-Th age using a Dremmel hand-held hobby drill and a 0.8 mm carbide micro-drill bit. The drill and bit were carefully cleaned in between samples using

distilled water and dilute HCl. A total of 16 subsample powders (40 ± 10 mg each) were collected in plastic vials with screw-cap lids.

Twenty-five mg of powdered sample was weighed out and digested in stages following Tostevin et al. (2016). To avoid contributions from non-carbonate phases, I dissolved 20% of the sample by adding 446 µl of 1% HNO_3, corresponding to the calculated stoichiometric volume. The sample and acid were mixed manually and left to react for 1.5 hours. The samples were spun in a centrifuge at 3500 rpm for 12 minutes to separate the solid and supernate, and 90% of the supernate was removed using a pipette and discarded. The tubes with residual liquid were dried down in a warm oven for 2 hours. The second step, designed to dissolve the next 40% of the sample, was done by adding 892 µl of 1% HNO_3 to the solid residue. The sample and acid were mixed manually and left to react for 1 hour, before being spun in a centrifuge at 3500 rpm for 12 minutes to separate solid and supernate. Thereafter, 90–95% of the supernate was removed from each sample using a pipette. This was then filtered into a clean plastic tube using a 0.22 µm filter disc attached to a syringe, and then the filtered solution was pipetted into a clean centrifuge tube (with measurement accurately recorded). The solution was then dried down overnight in an oven.

Dried samples (10 mg) were taken back up into solution using 5% HNO_3. A dilution factor of ~43 was used to measure Mg, Sr, Mn, Fe, Zn and dilution factor of ~6 was used to measure Ba, Al, U and Pb. Samples were analysed on an iCAP RQ ICP-MS housed in the Geological Sciences Department at UCT. Calibration curves were obtained using synthetic stock solutions, and In, Rh, Re and Bi were used as internal standards.

3.5.2 Water samples

Water samples were stored in the fridge before being filtered through a 0.22 mm filter disc attached to a syringe. The filtered water samples were then analysed on an iCAP RQ ICP-MS housed in the Geological Sciences Department at UCT to establish their trace element compositions, and for comparison to trace element contents of the tufa

samples. Calibration curves were obtained using synthetic stock solutions, and In, Rh, Re and Bi were used as internal standards.

3.6 Uranium-Thorium dating

3.6.1 Sample selection and drilling

Six samples collected by Dr R. Pickering were dated in 2016 in a pilot study prior to the start of this project. Of the eight sub-samples analysed, five returned promising age data, confirming the potential of the tufas to be dated. These successfully dated samples were then used to inform subsequent sample collection for this project, which took place over two field seasons (detailed in section 3.1). Following the first round of sample collection, I selected tufa samples to sub-sample for U-Th analysis. Tufa composed of dense micritic material with little to no visible detrital material (to minimise Th contamination) were identified and then drilled using a Dremmel hand-held hobby drill and a 0.8 mm carbide micro-drill bit. The drill and bit were carefully cleaned in between samples using distilled water and dilute HCl. The powders were collected in plastic vials and sent to the University of Melbourne for U-Th analysis. The results from this analysis was used to inform subsequent sampling.

Guided by results from the laser ablation ICP-MS analysis described in section 3.4, I performed a second round of drilling at the University of Melbourne in 2019. Element distribution maps generated from LA-ICP-MS data (presented in Chapter 5) were used to evaluate each sample's potential for dating and to identify suitable layers to be sampled. In this case, layers with ^{238}U concentration > 0.1 ppm and ^{232}Th concentration < 0.01 ppm were targeted. In addition to these criteria, layers which were sufficiently wide and relatively continuous to allow for enough powder (60 mg) to be extracted were chosen in order to ensure a sufficient amount of ^{238}U, 5-15 ng/gram of sample, to be extracted. Prior to sampling, these layers were also physically examined and tested for integrity of the material to avoid permeable layers, so as to minimise the chance of U mobility. This was done by wiping a wet Kim wipe across the sample and observing where this water was absorbed; the layers which were slow to take up this water (i.e.

slow adsorption = low permeability, reducing the chance of U mobility) which also met the above-mentioned conditions, were selected to be subsampled for U-Th dating. Following these identification procedures, 60 ± 10 mg of powder from each selected layer was carefully drilled out using a hand-held hobby drill with a 0.5 mm carbide micro-drill bit, and collected in plastic vials. The samples, drill and burr were all cleaned with high-pressure air between sample collection.

3.6.2 U-Th analytical procedure

The powdered samples were chemically processed to purify and extract U and Th from the carbonate, and then analysed at the University of Melbourne, following the procedure detailed in Hellstrom (2003) and Hellstrom (2006). In brief, samples were weighed and then dissolved in concentrated nitric acid, and a mixed ^{236}U-^{233}U-^{229}Th spike was added to the solution. Once equilibrated, the solution was placed into columns containing Eichrom TRU-spec selective ion exchange resin in order to separate the U and Th from the calcite matrix, which was removed by further elution with 1 M HNO_3 and 4 M HCl. The separated U and Th were then collected together in 0.1 M HCl–0.2 M HF solution. This purified U-Th solution was dried down overnight and then dissolved in a mixture of dilute nitric and hydrofluoric acid. The resultant solution was loaded into an auto sampler coupled to a Nu Instruments Plasma multi-collector inductively coupled mass spectrometer (MC-ICPMS). An equilibrium reference material (HU-1) was used to correct for instrument drift and an in-house standard (YB-1) of known age was used to check for reproducibility of the results.

The measured activity ratio of $^{230}Th/^{232}Th$ (hereafter $(^{230}Th/^{232}Th)_A$) in the samples reflects the level of detrital Th contamination contained in the samples. Traditionally, a threshold of $(^{230}Th/^{232}Th)_A$ >20 was applied to determine acceptable levels of contamination (Bischoff and Fitzpatrick, 1991; Auler and Smart, 2001). However, this is based on measurements made using alpha spectrometry, and suggestions of a much higher threshold of >100-300 have been suggested to account for improved sensitivity in measurements made using mass spectrometry (Richards and Dorale, 2003). Hellstrom (2006) argues that even these threshold values are too low, and best practice

is to correct for all ages regardless of $(^{230}Th/^{232}Th)_A$, and to propagate the uncertainty through the age calculations. Following the recommendation in Hellstrom (2006), an *a priori* estimate of the isotopic composition for the initial $^{230}Th/^{232}Th$ at the time of deposition (hereafter $(^{230}Th/^{232}Th)_{A0}$) was applied to all of the samples in order to correct for the inherent detrital component. The estimated $(^{230}Th/^{232}Th)_{A0}$ value applied to all samples is 1.5 with a 100% uncertainty assigned to it, and fully propagated through.

3.7 Stable isotopes

3.7.1 Water isotope analysis

The hydrogen and oxygen (δD and $\delta^{18}O$) isotope values of the water samples were measured using wavelength-scanned cavity ring-down spectrometry (WS-CRDS) on a L2120-i (Picarro, Sunnyvale, Ca, USA) water isotope analyser in the Botany Department at the University of Cape Town, following the method outlined in Stowe et al. (2018). Two internal standards, Cape Town Millipore Water (ACTMP) and Rocky Mountain Water (RMW), calibrated to international standards, have δD and $\delta^{18}O$ values of +1.6‰ and -0.6‰, and -129.5‰ and -17.27‰, respectively. These were included in the analysis to correct for instrument drift and scale compression, as well as to convert the raw data to the Standard Mean Ocean Water (SMOW) scale. Repeat measurements of these standard materials (n=5) returned a precision better than 0.6‰ and 0.06‰ for δD and $\delta^{18}O$ respectively. Evian A water was analysed as a third standard to monitor accuracy and precision, and the values returned during the analysis for δD were -71.83‰ (1σ =0.28 , n=5) and for $\delta^{18}O$ were -10.32‰ (1σ=0.07, n=5). The accepted values for Evian A for δD and $\delta^{18}O$ are -71.7‰ and -10.2‰ respectively (Spangenberg and Vennemann, 2008).

3.7.2 Tufa isotope analysis

Carbon (C) and oxygen (O) isotope analyses were carried out using a Gasbench attached to an isotope ratio mass spectrometer (IRMS) in the Stable Light Isotope Lab in the Department of Archaeology at the University of Cape Town following the method detailed in Spötl and Vennemann (2003). Thirty-seven tufa subsamples were drilled

from selected layers from 26 hand samples, and one sub-sample was drilled from a dolomite sample using a Dremel hand-held hobby drill.

The powders drilled were collected in plastic vials, and then 0.15-0.18 mg of each sample was weighed out and placed into a clean, 12ml, borosilicate vial with a screw-top lid containing a septum. These vials were loaded into a temperature-controlled sampler set to 72°C and, using a CTC Analytics A200S autosampler, the vials were flushed with helium overnight to remove the atmospheric air present in them. Five drops of warm (72°C) acid (100% Orthophosphoric acid, specific gravity of solution = 1.92) was then manually added to each sample tube through the septum using a 1 ml syringe. The samples were left to react for three hours before starting the run. The gas, which evolved from each reaction, was then sampled by the autosampler and passed to a Thermo Finnigan II Gasbench, where the sample gas was passed through a Nafion water removal unit. It then passed through a gas chromatographic column (Poraplot Q) to separate the CO_2 from other gas compounds released by the reaction, and then through a second Nafion water trap. The gas was passed from the Gasbench to a Thermo Delta Plus XP IRMS. The gas flow was controlled to give 8 sample peaks and 5 reference peaks. The CO_2 reference gas was also introduced into the mass spectrometer via the Gasbench (Spötl and Vennemann, 2003).

Precision was monitored by repeated analysis of three standard materials; two international standards, IAEA-CO1 ($\delta^{13}C_{PDB}$ = 2.50‰ and $\delta^{18}O_{PDB}$ = -2.40‰ and Carrara Z marble (CZ new, $\delta^{13}C_{PDB}$ = 2.12‰ and $\delta^{18}O_{PDB}$ = -2.13‰) and an in-house calcite standard, Cavendish Marble (CM, $\delta^{13}C_{PDB}$ = 0.34‰ and $\delta^{18}O_{PDB}$ = -8.95‰). These standards were each included four times in both runs (Table 3.7.1). The mean and standard deviation for $\delta^{13}C$ and $\delta^{18}O$ of each standard was calculated (Table 3.7.1); the mean is used to calibrate the results and the standard deviation is a measure of the precision. For both runs the reproducibility of the repeated measurements of the standard materials was ≤ 0.2‰ for both C and O. The mean values of the measured standards were plotted against the known value for the standard to produce a straight-line graph, the equation for which was used to calibrate the raw data measured for the samples. The difference between the measured and expected values for these standards

was monitored to correct for instrument drift. Results were calibrated using the slope and intercept of the CM and IAEA-CO1 standards, calculated using the difference between the expected value of the standard material and the average of the actual measured values during the analyses. An additional correction for the dolomite $\delta^{18}O$ value was applied because, at the temperature of reaction (72°C), the correction results in an over-estimation of the dolomite $\delta^{18}O$ value by 1.47‰ (Rosenbaum and Sheppard, 1986; Vasconcelos et al., 2005).

Further analyses were carried out on an Analytical Precision AP2003 continuous-flow IRMS in at the University of Melbourne, following the method detailed in Tzedakis et al. (2017). A total of 32 subsamples were drilled from layers in 6 hand samples which were simultaneously sampled for U-Th dating. These were drilled using a hand-held hobby drill and collected in plastic vials. Thereafter, 0.7-0.8 mg of powder was weighed out and placed into 0.5 ml glass vials. Two in-house standards, NEW1 and NEW12, previously calibrated to the PDB scale using the international standard NBS19, were evenly spaced within the series of samples. The samples were flushed with helium overnight using a Cambridge Analytical device, and then 105% orthophosphoric acid was manually administered to the samples at 70°C. Measurements were made on the evolved CO_2 gas using an AP2003 CF-IRMS following the method described in Tzedakis et al. (2017). The in-house standard, NEW1, was included every 15 samples and used to correct for instrument drift and linearity, as well as to normalise the data to the PDB scale (Table 3.7.1). The two other standards, NEW12 and NBS18, were included seven and two times respectively to monitor precision (Table 3.7.1). The reproducibility of the repeated measurements of the standard materials was ≤ 0.14‰ for both C and O.

The $^{13}C/^{12}C$ and $^{16}O/^{18}O$ ratios are reported in the standard delta (δ) notation relative to the PeeDee Belemnite (PDB) standard in parts per million (‰), where $\delta^{13}C$ or $\delta^{18}O = [(R_{sample}/R_{standard} -1)*1000]$ with $R = {}^{13}C/{}^{12}C$ or $^{16}O/^{18}O$ respectively. The $\delta^{18}O$ values measured in the tufa samples were also converted to the Standard Mean Ocean Water (SMOW) scale using the following equation: $\delta^{18}O_{SMOW} = (\delta^{18}O_{PDB} \times 1.03086) + 30.86$. This was done to allow for comparison between the $\delta^{18}O$ measured in the tufas and the

$\delta^{18}O$ measured in water samples. In this thesis, PDB and SMOW are equivalent to VPDB and VSMOW as recommended by Coplen et al. (1983).

Table 3.7.1 Carbon and oxygen isotope data for standards Cavendish marble (CM), IAEA-CO1, Carrara Z new (CZ new), New 1, New 12 and NBS 18 for each of the three runs.

Run number	Standard	$\delta^{13}C_{PDB}$	$\delta^{18}O_{PDB}$
1	CM	0.21	-9.10
	CM	0.39	-9.78
	CM	0.49	-8.87
	CM	0.72	-8.65
	Mean	**0.45**	**-9.10**
	Known value	*0.34*	*-8.95*
	Std deviation	**0.19**	**0.18**
1	IAEA-CO1	2.28	-3.08
	IAEA-CO1	2.51	-3.78
	IAEA-CO1	2.52	-2.80
	IAEA-CO1	2.62	-2.59
	Mean	**2.48**	**-3.06**
	Known value	*2.50*	*-2.40*
	Std deviation	**0.12**	**0.20**
1	CZ new	1.98	-2.53
	CZ new	2.13	-2.52
	CZ new	2.15	-2.29
	CZ new	2.23	-2.21
	Mean	**2.12**	**-2.39**
	Known value	*2.12*	*-2.13*
	Std deviation	**0.09**	**0.14**
2	CM	0.38	-8.94
	CM	0.42	-8.98
	CM	0.49	-8.83
	CM	0.50	-8.78
	Mean	**0.45**	**-8.88**
	Known value	*0.34*	*-8.95*
	Std deviation	**0.05**	**0.07**
2	IAEA-CO1	2.42	-2.79
	IAEA-CO1	2.49	-2.83
	IAEA-CO1	2.60	-2.91
	IAEA-CO1	2.60	-3.18
	Mean	**2.53**	**-2.93**
	Known value	*2.50*	*-2.40*
	Std deviation	**0.08**	**0.16**
2	CZ new	2.10	-2.42
	CZ new	2.11	-7.37
	CZ new	2.24	-3.52

	CZ new	2.27	-2.39
	Mean	**2.18**	**-2.40**
	Known value	*2.12*	*-2.13*
	Std deviation	**0.08**	**0.01**
3	New1	2.34	-2.65
	New1	2.41	-2.43
	New1	2.38	-2.52
	New1	2.42	-2.43
	New1	2.42	-2.39
	New1	2.38	-2.32
	New1	2.40	-2.49
	New1	2.43	-2.52
	New1	2.42	-2.39
	New1	2.38	-2.58
	New1	2.48	-2.33
	New1	2.39	-2.47
	New1	2.40	-2.43
	New1	2.36	-2.47
	New1	2.43	-2.40
	New1	2.38	-2.54
	Mean	**2.40**	**-2.46**
	Std deviation	**0.03**	**0.09**
3	New12	-3.74	-9.46
	New12	-3.89	-9.75
	New12	-3.79	-9.49
	New12	-3.85	-9.68
	New12	-3.79	-9.55
	New12	-3.91	-9.55
	New12	-3.72	-9.56
	Mean	**-3.81**	**-9.58**
	Known value	*-3.80*	*-9.59*
	Std deviation	**0.07**	**0.10**
3	NBS18	-5.06	-22.98
	NBS18	-5.07	-22.78
	Mean	**-5.06**	**-22.88**
	Known value	*-5.01*	*23.20*
	Std deviation	**0.01**	**0.14**

CHAPTER 4 TUFA FACIES AND DEPOSITIONAL ENVIRONMENTS

The development and arrangement of tufa deposits depends on the interaction of a multitude of variables, such as topography, hydrology, temperature, and hydrochemistry. The interplay of these, along with small-scale factors, such as variable substrates, flow patterns, and the influence of biota, give rise to a wide variety of tufa macro-morphologies and internal fabrics (Pedley et al., 1996; Violante et al., 1994; Kano et al., 2003). Observation and identification of the sedimentological characteristics of a tufa system is an important step to understand the environment in which tufa deposits formed (Pedley, 1990; Pentecost and Viles, 1994; Violante et al., 1994; Pedley et al., 1996; Pentecost, 2005). In the following section, I provide an overview of tufa facies classification schemes (Section 4.1.1) and relevant environmental models from the literature (Section 4.1.2). In Section 4.2, I document and describe the macro-, meso- and micro-morphologies of the Ga-Mohana Hill tufa deposits to explore their architecture and decipher the depositional environment they represent. These observations are interpreted in Section 4.3.

4.1 Background and literature

The complex combination of factors that influence tufa deposits has made it difficult to establish a standard scheme for classifying them, and an array of facies classifications have been applied over the last fifty years (Capezzuoli et al., 2014). Early classification schemes were based on tufa formation processes (Julia, 1983), the geomorphology of deposits (Chafetz and Folk, 1984), botanical elements (Irion and Mueller, 1968; Pentecost and Lord, 1988), sedimentological criteria (Ordóñez and García del Cura, 1983; Pedley, 1990), petrographic features (Buccino et al., 1978; Violante et al., 1994), and geochemical criteria (Barnes and O'Neil, 1971; Pentecost, 1993; Pentecost, 2005). While many of these criteria are useful for holistically characterising tufa deposits, information related to tufa macrostructure and morphology is an important aspect, as it provides insights into depositional processes and the evolution of a tufa system (Pentecost, 1995). As the aim of this thesis is to investigate the palaeoclimatic context of the fossil tufas at

Ga-Mohana Hill, I focus on classification schemes relating to the macro-morphology of the deposit, supported by petrographic observations, in order to characterise the depositional environment of these tufas.

4.1.1 Tufa facies

Tufa facies constitute the main elements of a tufa's fabric and morphology. The major petrographic components of tufa are micrite, micro-sparite and sparite (Pedley, 1992). The variable arrangement of these internal components, along with other defining features, form the fabric of a deposit. A variety of tufa facies exist in the literature, based on an array of characteristics, e.g. sedimentation processes, petrology, associated vegetation, distance from source, porosity, etc. (Stirn, 1964; Irion and Mueller, 1968; Buccino et al., 1978; Ordóñez and García del Cura, 1983; Chafetz and Folk, 1984; Pentecost and Lord, 1988; Violante et al., 1994; Ordóñez et al., 2005; Arenas et al., 2007; Claes et al., 2017; Pla-Pueyo et al., 2017; Ukey and Pardeshi, 2019). Pedley (1990) provides a comprehensive description of tufa fabrics based on classifications developed by Buccino et al. (1978), Ordóñez and García del Cura (1983), and Chafetz and Folk (1984), who used petrographic approaches and terminology to identify and group tufa deposits.

The facies scheme that Pedley (1990) suggests is sub-divided into autochthonous and allochthonous (or clastic) deposits. Autochthonous tufas form *in situ* and comprise phytoherm framestones and phytoherm boundstones. The term phytoherm describes tufa formed in association with plant and bacterial components, i.e., tufa cemented vegetation. Autochthonous tufa are characterised by a high degree of porosity as a result of decayed organic matter (phytoherm framestones), and stromatolitic build-ups which result from cyano-bacterially mediated carbonate precipitation around algal filaments (phytoherm boundstones). Allochthonous tufa deposits are composed of clastic components, i.e., carbonate encrusted plant fragments (phytoclast tufa), carbonate-encrusted nuclei (oncoidal tufa), reworked deposits which include sand and silt-sized fragments (intraclast tufa), and structureless or clotted deposits of micrite and micritic peloids (microdetrital tufa). This has persisted as a popular method for categorising tufa fabrics, although countless variations using a combination of terms and categorisations

exist in the literature, such that a coherent and persistent scheme is difficult to find. Others have proposed entirely different schemes. For example, Arenas-Abad et al. (2010) proposed a facies system focused on textural characteristics identified in vertical tufa sequences in fluvial carbonate systems. Using these, they developed two models of tufa deposition related to sedimentary processes. While this rigorous facies classification scheme is valuable, such extensive and detailed sedimentary facies designations are beyond the scope of this thesis, particularly since there are no vertical sequences of tufa at Ga-Mohana Hill.

In their study of the relationship between biofilms and the associated carbonate precipitation fabrics that are produced, Perri et al. (2012) divide tufa into two basic types, laminated and porous. Laminated tufa comprises alternating layers of micrite, sparite, micro-spar, and / or dendritic layers, and form stromatolitic (i.e., undulating, dome-like layers) tufa, crusts, and oncoids (layers of carbonate around a nucleus). Porous tufa, as described by Perri et al. (2012), is composed of thin carbonate crusts around three main types of organic support: plant remains, algae, and bryophytes (mosses and liverworts). They observe that the three main petrographic components of tufa (micrite, micro-sparite and sparite) are variably arranged to create peloidal, aphanitic, laminar or dendrolitic fabrics, and that these fabrics occur in the macro-laminae that form the structure of both laminated and porous tufas. Perri et al. (2012) note that the variety of autochthonous and allochthonous tufa facies described in the literature are essentially composed of these simple components. On this basis, Perri et al. (2012) provide a neat and simplified method to classify tufa fabrics, regardless of facies or depositional setting. I use this approach to describe the petrology of the Ga-Mohana tufas.

4.1.2 Environmental models for tufa deposits

Pedley (1990) proposed an outcrop-scale classification scheme based on field observations, informed by earlier petrographic studies (Golubić, 1969; Buccino et al., 1978; Ordóñez and García del Cura, 1983). This scheme was adapted and refined by various workers (Pentecost and Viles, 1994; Violante et al., 1994; Ford and Pedley, 1996;

Pedley et al., 2003; Pedley, 2009). Ultimately, four end-member models provide the basis for the identification of tufa depositional environments: perched springline, fluvial, lacustrine, and paludal (swamp) (Pedley et al., 2003; Pedley, 2009). These models, summarised in Table 4.1 and illustrated in Figure 4.1.1, provide a flexible and widely applicable reference for identifying and interpreting fossil tufa deposits based on their macromorphologies and fabric associations, which can be related to formation processes and depositional environments (Pedley, 2000). Pedley (1990) notes that many deposits exhibit a combination of characteristics from these end-member models, and recognises that they are the minimum to be observed, i.e. no model can encompass all the variation in tufa deposits. Many workers describe tufa morphologies for individual depositional settings using a combination of schemes, often with Pedley's models as a starting point (e.g. Kano and Fujii, 2000; Carthew et al., 2003; Carthew et al., 2006; Viles et al., 2007; Keppel et al., 2011).

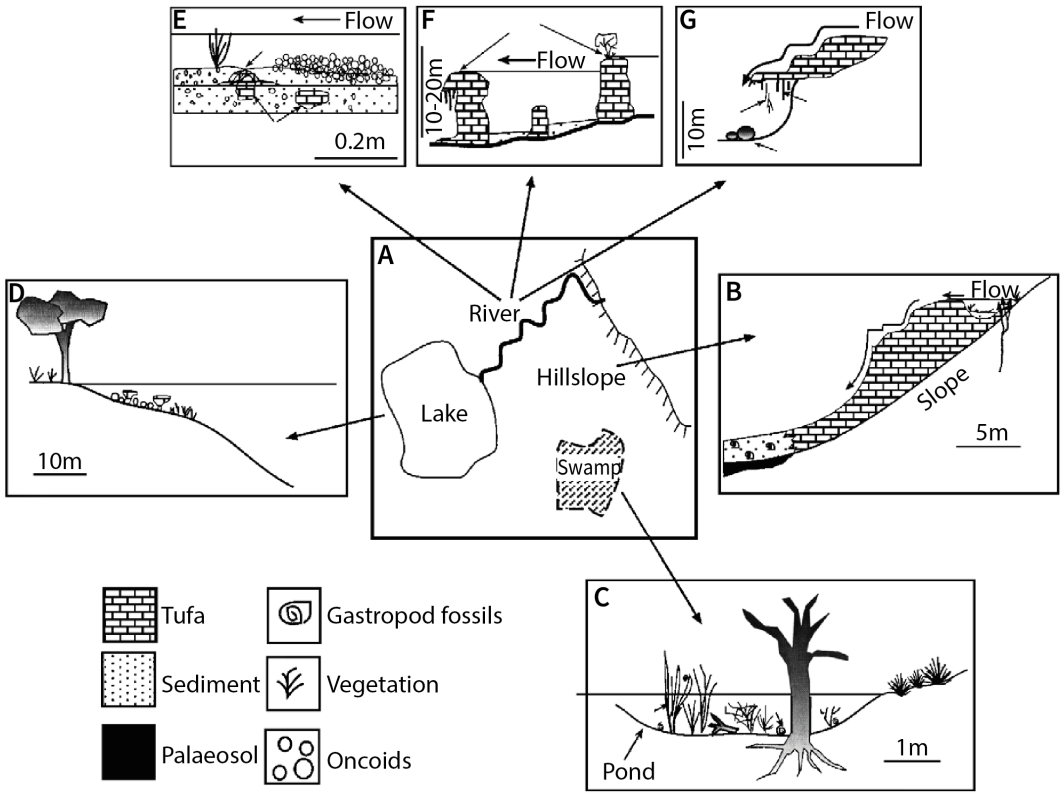

Figure 4.1.1 Schematic of tufa environmental models from Carthew et al. (2003), based on models described by Pedley (1990). A) Plan view of various tufa depositional settings, illustrated in profile view: hillslope, or perched springline (B), paludal / swamp (C), lacustrine / lake (D), and fluvial / river (E-G).

Table 4.1 Summary of environmental models and associated tufa facies (Pedley, 1990; Pedley et al., 2003; Pedley, 2009).

Model	Environmental setting	Characteristic morphologies	Characteristic facies	Typical flora / fauna	Notes
Perched springline	Hillslopes and valley sides, fed by emergent groundwaters at various points on hillside	Step-like terraces Cascades Shallow pools	Microdetrital tufa Intraclast tufa Phytoclastic lenses Sheet spreads	Liverworts Bryophytes Cyanobacteria Diatoms Leaf moulds Gastropods Ostracods Insect larvae	Radial water drainage Springs may coalesce to form sheet-like tufa covering hillside
Fluvial	Braided streams / rivers	Thick, clast-supported channel sequences	Cyanoliths Oncoids		
	Non-braided streams with barrages	Series of barrages (tufa barriers/ dams) Pools behind dams	Phytoherm framestones Stromatolites Sediment accumulations in pools: lithoclasts, phytoclasts, microdetrital tufa	Bryophytes Gastropods and ostracods in pools	
Lacustrine	Large deep water bodies / lake settings, shallow margin areas and deep water zones	Algal bioherms / stromatolites	Stromatolites Oncoids Phytoherms Intraclast tufa Microdetrital tufa	Reeds (shallow marginal)	
Paludal	Broad flat areas, poorly drained ground	Ephemeral ponds	Mix of fauna and flora encrusted in fringe cements Phytoherms Phytoclasts Microdetrital and intraclast tufa	Range of flora and fauna	
Cascade	High inclination slopes/cliffs Break points in cliffs Vigorous water flow/waterfalls	Wedge shaped or convex High angle cones and chutes (internal convolutions) Stalactites Hanging moss curtains Hemispherical moss cushions beneath	Internal laminations Phytoherms Phytoclasts	Bryophytes Algae	Initially proposed as a model, later recognised as a common feature across depositional settings Similar to barrages but without upstream pools

Although the environmental models developed by Pedley (1990) and Pedley (2009) provide a good foundation for identifying and defining the depositional environment of

a tufa system, they are predominantly based on tufa systems from temperate European settings. In their comparative study of two fluvial barrage tufa systems from different climatic settings, i.e. cool, temperate setting in the UK and warm, semi-arid setting in Spain, Pedley et al. (1996) note that climate, and temperature in particular, impacts the ultimate morphology of a tufa deposit. As such, several workers have proposed adapted or entirely new environmental models to better explain the processes of tufa formation in climatic settings different to European settings (e.g. Carthew et al., 2003; Viles et al., 2007; Keppel et al., 2011). Carthew et al. (2003) evaluated the applicability of Pedley's environmental models to tufa deposits in a tropical region of northern Australia, and subsequently developed a modified model to encompass the distinct features of tropical tufa deposits, based on the Gregory River tufa system in Queensland (Carthew et al., 2006). Viles et al. (2007) proposed a depositional model for fluvial barrage tufa deposits in arid environments, i.e., ~200 mm annual rainfall and ~20°C mean annual air temperature, based on observations of the Brandfontein River tufas in the Naukluft mountains of Namibia. A table comparing the different characteristics of fluvial barrage tufas from these four climatic zones (temperate, semi-arid European, tropical, and arid) is given in Viles et al. (2007). Since Ga-Mohana Hill is situated within the semi-arid southern Kalahari, the arid-zone model proposed by Viles et al. (2007) is most relevant for this study, and is thus described in detail below.

4.1.2.2 Arid environment tufa model

Viles et al. (2007) distinguish barrage, pool and cascade tufa morphologies within the a fluvial barrage tufa system in the Naukluft Mountains. Within these morphologies, the tufa facies they observed are:

1) **cemented gravel and boulder facies**: sub-rounded to angular clasts, local hillslope material, minimal fluvial reworking
2) **colluvial gravel facies**: *in situ* cemented weathered hillslope debris, angular clasts
3) **tufa moss facies**: bioconstructed material, bryophytes, complex morphology, at barrage sites, lack of allochthonous material
4) **laminated and reed facies**: reeds cemented *in situ*, associated with low-gradient slack water areas. Laminated tufa overlays coarse channel gravels

- gravel facies indicate high energy, low frequency flood events
- laminated facies indicate low energy, continuous and steady flow

5) **cascade facies**: high angle tufa cones and chutes, composed mainly of bryophyte facies with some detrital tufa and organic matter, internal morphology structurally complex, stacked sequences. Gross morphology of cascades commonly associated with seepage on hillslopes forming perched spring tufas, Naukluft cascades formed from waterfall driven by fluvial tufa

*difference between cemented gravel and boulder facies (cbg), and colluvial gravel facies (cg): cgb = clast supported, sub-rounded and angular / cg = matrix supported, angular.

Viles et al. (2007) note that the Brandfontein tufa deposits are composed of a relatively simple suite of sedimentary features compared to others from temperate, tropical and semi-arid settings. Based on their facies observations, they deduced that the tufa system was developed over a long period, characterised by highly variable flow regimes and hydroclimate shifts, and proposed a three phase model to describe this pattern of tufa deposition, erosion and quiescence. The key morphological features of their arid model are downstream, prograding barrages with forward-dipping fronts, and the presence of tufa-cemented gravels and boulders (Viles et al., 2007). The model is illustrated in Figure 4.1.2 and summarised below.

Phase 1: this is a building stage and involves constant (perennial) and steady, low-energy water flow that supports the growth of bryophytes (mosses). These provide a substrate upon which tufa is precipitated, forming a barrage. Continuous flow of water encourages the growth of bryophytes and further tufa precipitation, resulting in the gradual development of downstream sloping, prograding barrages. Behind these, slack-water pool environments develop. Here, slow flowing water supports the growth of reeds and laminated tufa deposits form. At the end of the stream, high angle cascades develop. This phase is characterised by the tufa moss facies which occur at barrage sites. The moss facies are recognised as calcified, bioconstructed material with complex morphologies and layers of dense tufa which mark the termination of a growth phase. Viles et al. (2007) note the lack of allochthonous material, e.g. leaves and woody debris.

Phase 2: this is a destructive stage characterised by episodes of very high-water flow, leading to erosion and transport of the dolomitic bedrock. This results in the production of colluvium on the hillside and spatially patchy erosion of tufa deposits.

Phase 3: this stage is characterised by ephemeral water flow and conditions similar to those observed at present. Temporary water availability restricts the development of streams and associated vegetation growth, and results in the precipitation of thin, discontinuous laminated tufa.

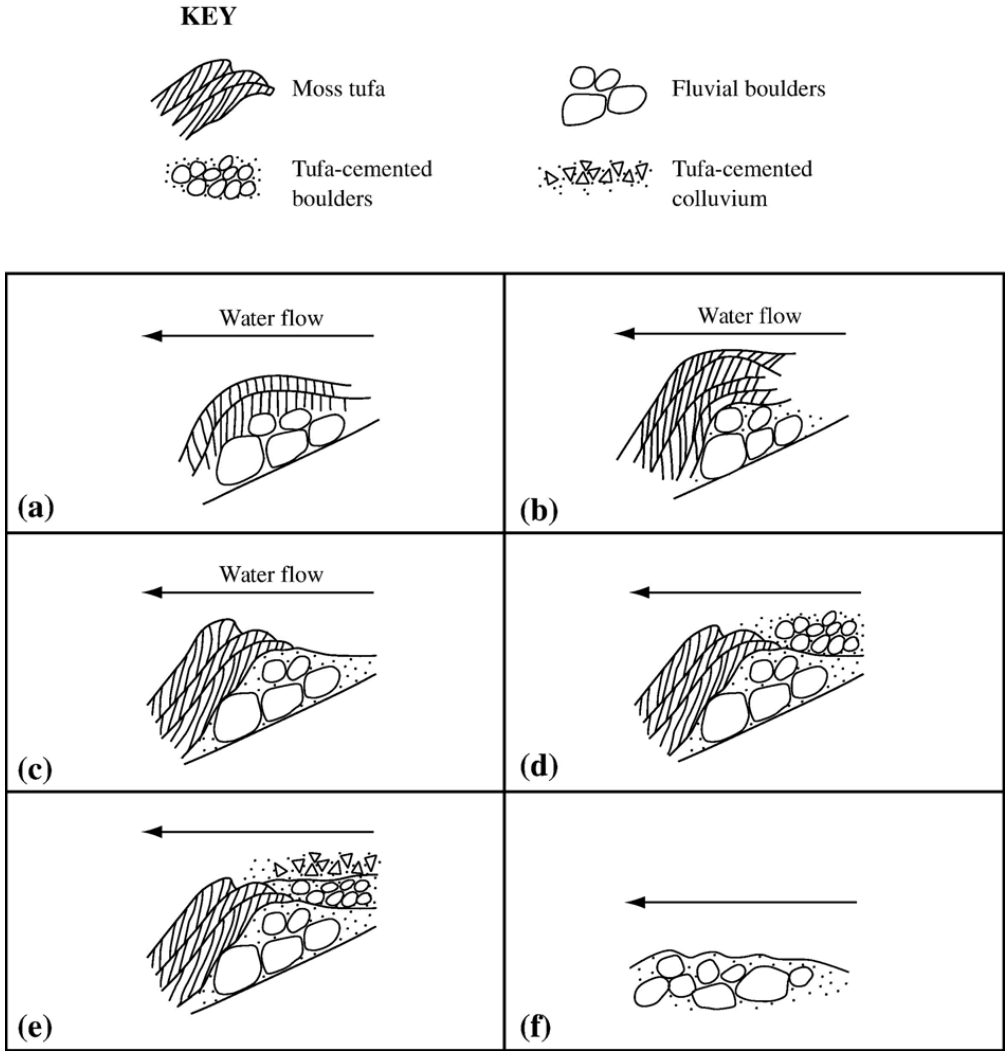

Figure 4.1.2 Conceptual model of fluvial barrage tufa formation along Brandfontein River, Naukluft from Viles et al. (2007). The panels illustrate: a) steady water flow, the growth of mosses and subsequent tufa precipitation; b) tufa cementation of boulders

and continued barrage growth; c) increase in water flow energy and consequent erosion of the tufa barrage; d) in-wash of boulders and further tufa cementation of them within the eroded barrage; e) collection of colluvial material around the barrage subsequently cemented by tufa; f) tufa-cementation of boulders at low-gradient sections of the river profile, the surfaces of which tend to be polished and eroded by further water flow.

4.2 Field and petrographic observations of Ga-Mohana tufa

Ga-Mohana Hill is a stand-out feature on the landscape as it extends east of the main north-south striking Kuruman Hills and has a distinctive double camel-hump shape (Figure 4.2.1). As described in Chapter 2, and schematically illustrated in Figure 4.2.1, Ga-Mohana Hill is characterised by a cap of resistant banded ironstone of the Kuruman formation, below which prominent dolomite terraces of the Ghaap group dip gently towards the south-west. The tufa deposits at Ga-Mohana Hill follow this stepped topography, appearing to flow out of the bedding planes in the dolomite, coating the dolomite steps and cascading down the terrace faces (Figure 4.2.1). The presence of large, lobe-shaped, orange-grey tufa 'flows' protruding from the steep dolomite cliffs adjacent to the shelters are the most visually striking of the Ga-Mohana tufa deposits (Figure 4.2.1), but these are only one component of the tufa complex at this site. Variable expressions of tufa are observed across the entire hillside, and these are classed as distinct morphology types, each of which relates to a different sub-environment. The whole assemblage forms a 'continuum' i.e., a series of related deposits or facies association.

Five main morphological types have been identified according to their field geometries and topographic associations, and named using descriptive terms commonly employed in the literature (Pedley et al., 2003; Viles et al., 2007). The Ga-Mohana tufa morphologies identified are: cascades, barrages, rim-pools, terrace breccias and domes (Figure 4.2.1). The term cascade is used here to mean waterfall-type deposits, and barrage means fluvial dam-like features, as in Pedley et al. (1996) and Viles et al. (2007). As in Perri et al. (2012), on a microscale the tufas consist of a few simple petrographic components common to each sample, regardless of depositional setting. These components are micrite (opaque, anhedral crystals <4 μm), microspar (sub- to euhedral transparent crystals between 5 to 15 μm) and sparite (euhedral, transparent crystals >15 μm), with some larger (>200 μm) detrital clasts (e.g. quartz) and iron and manganese oxides present to varying degrees.

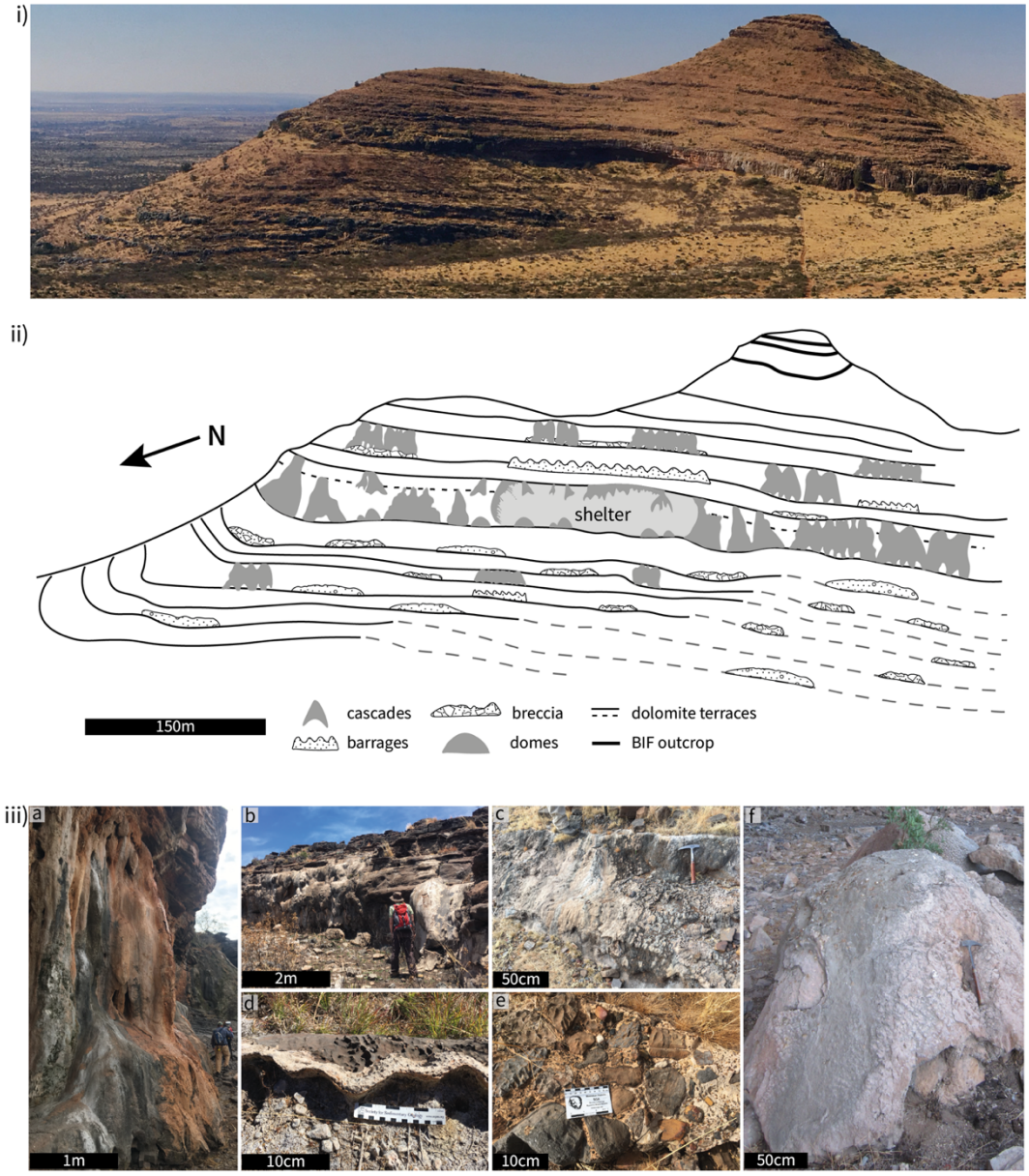

Figure 4.2.1 Summary of Ga-Mohana Hill and related tufa deposits. i) Photograph of Ga-Mohana Hill North, taken facing SE. ii) Schematic illustration of Ga-Mohana Hill showing the location of the north-facing rock shelter, the major geological units, and the location of different tufa types described in this chapter. iii) Photographs of examples of the various field expressions of tufa types: a) cascade b) step-front cascades and coatings, c) barrage, d) sinuous rim-pool edge, e) cemented terrace breccia, and f) dome tufa.

The variable organisation of these components within each sample results in distinct fabrics. These are classed as laminar (horizontally layered), peloidal, aphanitic, and stromatolitic (undulating, dome-like layering), adapted from the scheme by Perri et al.

(2012). Combinations of these fabrics are variably arranged within the tufa samples, giving rise to subtle differences in the texture and porosity. Samples from the same morphology type, or sub-environment, share common arrangements. Each of the morphologies identified at Ga-Mohana Hill are described in the following sub-sections based on their macro-, meso- and micro- morphologies and textures. In this case, I use macro to refer to centimetre to meter scale field observations, meso- to refer to centimetre to millimetre scale observations of cut slabs and hand samples, and micro- to refer to observations of thin sections on a micrometre to millimetre scale made using a petrographic microscope.

4.2.1 Cascades

4.2.1.1 Macromorphology

Cascades are lobe-shaped mounds of carbonate accumulation, which appear as 'flows' on vertical surfaces (Viles and Goudie, 1990). At Ga-Mohana Hill, cascades are observed on the cliff-fronts adjacent to the rock shelters, as well as on the fronts of the terraced dolomite steps above and below the rock shelters (Figure 4.2.2). These deposits are point-sourced at bedding planes within the dolomite, appearing to literally 'flow' out of these structures. Their sizes vary and they are streaky in appearance, exhibiting a range of colours from orange-brown, to grey-black and pinkish-white.

The most visually striking of the cascades are the large, approximately 3-5 m high, orange-brown and grey 'trunks', which cover the dolomite cliffs on either side of the Ga-Mohana Hill rock shelters (Figure 4.2.2). These cliff-front cascades are fan-shaped in plan view and measure up to 3 m across. In some instances, cascades have spread and coalesced with adjacent flows, creating a large apron of tufa (Figure 4.2.2). In profile, these cascades are generally wedge-shaped with bulging, mamillated fronts, which protrude from the dolomite cliff faces by approximately 2 m at their widest points. A variety of cavities and tongue-shaped stalactite-like features are common amongst the large cliff cascades (Figure 4.2.2). Large chunks of *ex situ* cascades, which have become detached from the cliff face, are commonly observed in close proximity to other *in situ* cascades and the cliff faces (Figure 4.2.2).

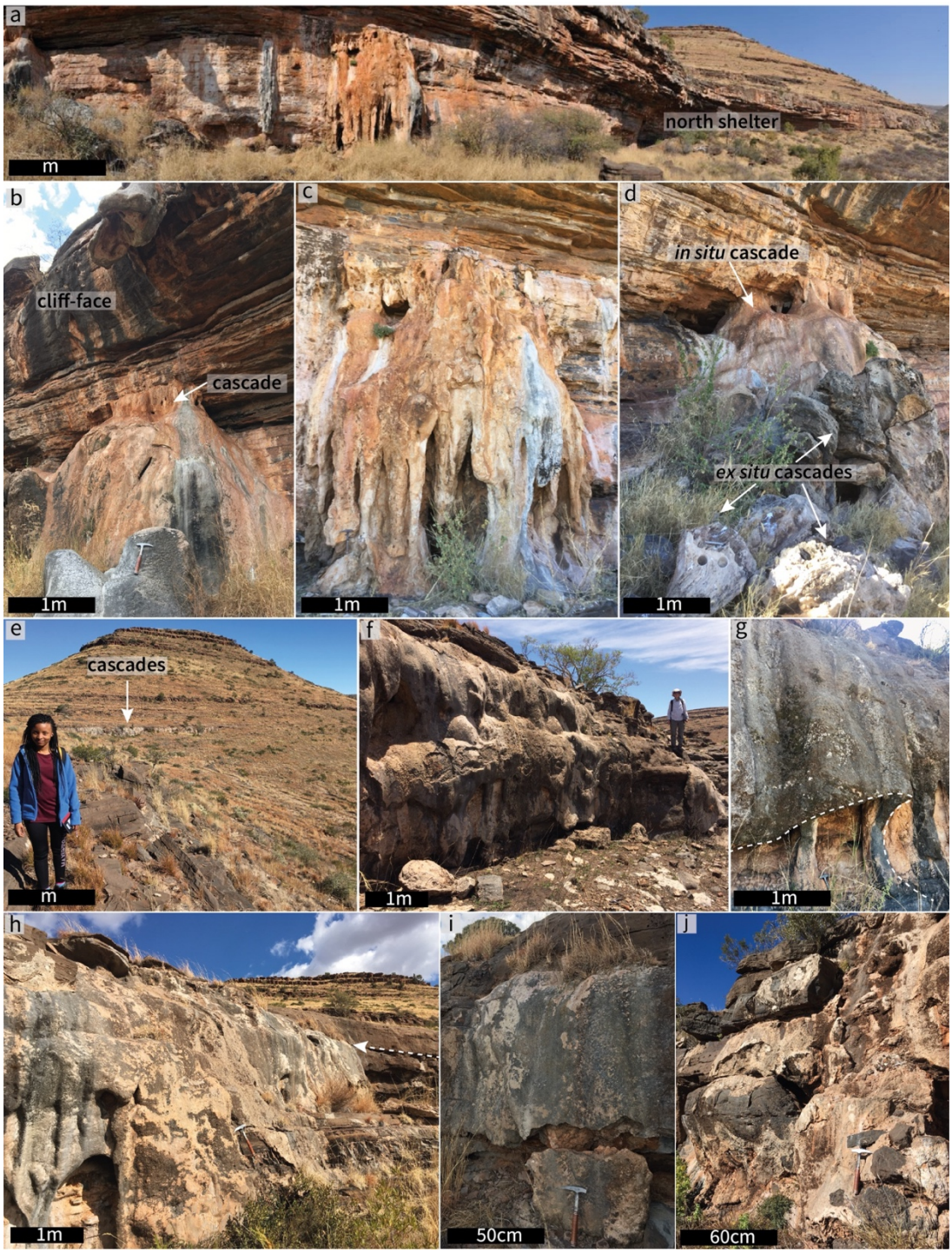

Figure 4.2.2 Field photographs of cascade tufa deposits at Ga-Mohana Hill. a-d) Cliff-front cascades on dolomite cliffs adjacent to the rockshelters. e-j) Cascades on dolomite step-fronts on terraces above the rockshelters. f-i) Examples of carapace and lobe tufa. Dotted white line in (g) illustrates the hollow carapace. Arrow in (h) highlights the connection of the cascade tufa with joints and bedding planes in the dolomite steps. j) Example of fluvial coating / seepage veneer i.e., thin carbonate coating over vertical dolomite surface.

Above and below the rock shelters, clusters of smaller tufa cascades occur on the fronts of the dolomite steps (Figure 4.2.2). These cascades vary in size and extent with average heights of 1-2 m and a lateral extent of up to approximately 4-5 m. They tend to have a stacked, mamillated morphology, and either protrude outward with a curved and partially hollow internal cavity, forming a carapace or a solid, tongue-shaped lobe with a tapered bottom section (Figure 4.2.2). The cascade tufas comprise a spectrum of morphologies, and associated with the above-described cascades are fluvial coatings or seepage veneers that form a thin carbonate coating over vertical dolomite surfaces (Figure 4.2.2). These are often adjacent to, or on the edges of thicker cascade deposits. The preservation of the cascade tufas is variable. They mostly have an indurated external layer which forms a crust, preserving their shape, but internally, some are well-preserved with a layered crystalline structure, whereas others lack any structure and are instead crumbly with a silty or chalky interior (Figure 4.2.2).

4.2.1.2 Meso- and micromorphology

On a meso-scale, the well-preserved cascades are composed of vertical to sub-vertical layering (Figure 4.2.3). The mm-scale layers are undulatory with irregular alternations between dense, crystalline layers, and irregular, porous, 'spongy' lenses (Figure 4.2.3). In some samples this layering is intermittently punctuated with thin, irregular and undulating orange-brown layers. On a micro-scale, the cascades display a combination of laminar, aphanitic and peloidal fabrics composed of alternating layers of oxide-rich micrite (brown), micrite (grey-brown), microspar, and sparite (white) (Figure 4.2.4). The laminae range from slightly wavy to steeply undulating and are sometimes discontinuous and irregular with poorly defined boundaries. Domal, stromatolite-like structures are commonly present in cascade samples (Figure 4.2.4). Others are composed of thicker, dense micritic laminae, which is generally sub-horizontal to vertical with gentle undulations and poorly defined boundaries. These laminae grade into an aphanitic mixed micrite-sparite mass with a somewhat porous and clotted texture. Cascade samples tend to have a very low detrital component with only a few small isolated detrital clasts identified (Figure 4.2.4).

Figure 4.2.3 Field context photographs and hand-sample slab scans of cascade tufa samples: a & b) Field context of cascade sample 18-14, white square in (a) indicates location of (b). c) Slice of hand sample 18-14. d) Dolomite cliff-front with *in situ* and *ex situ* cascade tufas, field context of cascade drill core samples 18-16 and 18-17. White square indicates location of (e). e) Drill holes for samples 18-16 and 18-17. f) Slice of sample 18-17 core. g) Slice of sample 18-16 core. h) Drill holes for samples 18-11 and 18-12. i) Slice of sample 18-11 core. j) Slice of sample 18-12 core.

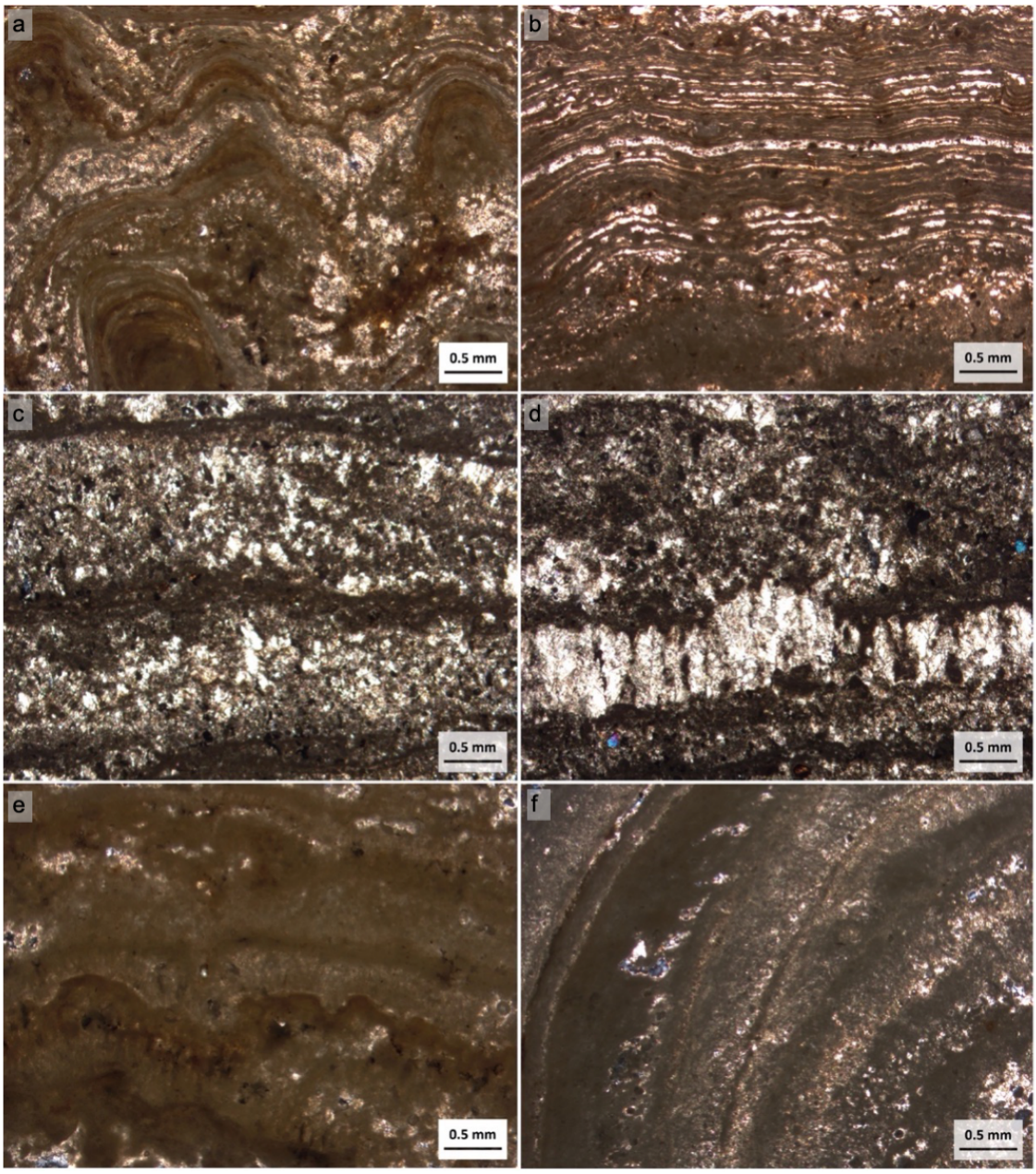

Figure 4.2.4 Photomicrographs of cascade tufa thin sections in plain polarized light (PPL) or with crossed polars (XPL), showing irregular and undulating laminations of micrite and sparite. a) Sample 18-11 in XPL, with stromatolite-like features. b) Sample 18-12 in XPL showing irregular and undulating laminations of micrite and sparite, with stromatolite-like features and some detrital inclusions. c) Sample 17-10 in XPL showing porous, grumulose layers of mixed sparite and micrite bound by thin, dense clotted micritic layers. d) Sample 17-10 in XPL showing a layer of columnar sparite with branching / feather textures. e) Sample 18-16 in PPL composed of dense and shrubby micrite and patches of micro-spar. f) Sample GHN2 in XPL, showing alternating layers of dense micrite and mixed micrite and micro-spar, with some detrital inclusions.

4.2.2 Barrages

4.2.2.1 Macromorphology

The term barrage is used to describe curved, sub-vertical, dam wall deposits, which act as barriers that impound water behind them (Viles and Goudie, 1990). At Ga-Mohana Hill, small-scale barrage tufas are down-hill sloping, arcuate structures, which occur at breaks in the slope on the hillside, both above and below the rock shelters (Figure 4.2.5). Some of the barrages are constructed on top of a dolomite step crest, and the tufa covers the front of the dolomite steps with a spongy, coralloid surface of variable thickness (between 2-10 cm).

The barrages are characterised by a curvilinear crest and exhibit a range of outer surfaces, i.e., smooth to lumpy, mamillated texture, sinuous 'brain' texture, and knobbly coralloid texture (Figure 4.2.5). They vary in size and extent, and are best preserved above the shelter, as barrages below the shelter tend to be partially buried and obscured by talus scree and vegetation (Figure 4.2.5). Barrages are smaller than cascades with heights ranging from several decimetres up to 1m. Instead of 'flowing' out of the bedding planes, they are preceded by flat, transverse areas filled with lightly compacted sediment, debris or vegetation, interpreted as remnants of previously filled rim pools (Figure 4.2.5). The barrages tend to be either laterally continuous, sub-vertical structures, around 0.5-1m in height, with a well-defined crest, or a series of small, terraced steps which extend downslope for a few meters. They are often associated with an irregular assortment of rim pools (Figure 4.2.5).

Figure 4.2.5 Field photographs of barrages and associated rim pool tufa at Ga-Mohana Hill. a) Barrage front with a lumpy outer surface that grades into sinuous 'brain' texture, and a curvilinear crest. b) Sub-vertical barrage preceded by a large flat area filled with sediment and scattered angular boulders. c) Barrage with mamillated to coralloid front and curvilinear barrage crest (dotted line), preceded by irregular, small (<50 cm) terraced rim pools (arrows). d) Path leading to the north rockshelter, white dotted outline indicates buried barrage remnant. e) Barrage crest / rim-pool lip ~10 cm high with coralloid texture. f) Series of small, irregular barrages with terraced rim pools.

4.2.2.2 Meso- and micromorphology

The internal structures of the barrages are characterised by sloping, irregular, mm-scale laminations (Figure 4.2.6). The layers are discontinuous and undulatory, and consist of a variety of colours: black, brown, white and pinkish-brown. The inside walls of the barrages are composed of pustular micro-stalactites which are 'inward' facing, some of which appear to have coalesced to form large black globular knobs at the base of the laminar sequence. In thin section, the barrages are characterised by a laminar fabric, with stromatolite-type layers i.e., multi-convex, domal laminae, which appear as discontinuous lenses of micrite, alternating with thicker layers of mixed micrite and microspar, and detrital and oxide-rich inclusions floating within these laminae (Figure 4.2.6). The layering is crinkly and has poorly defined boundaries, and in some instances an erosive contact is evident.

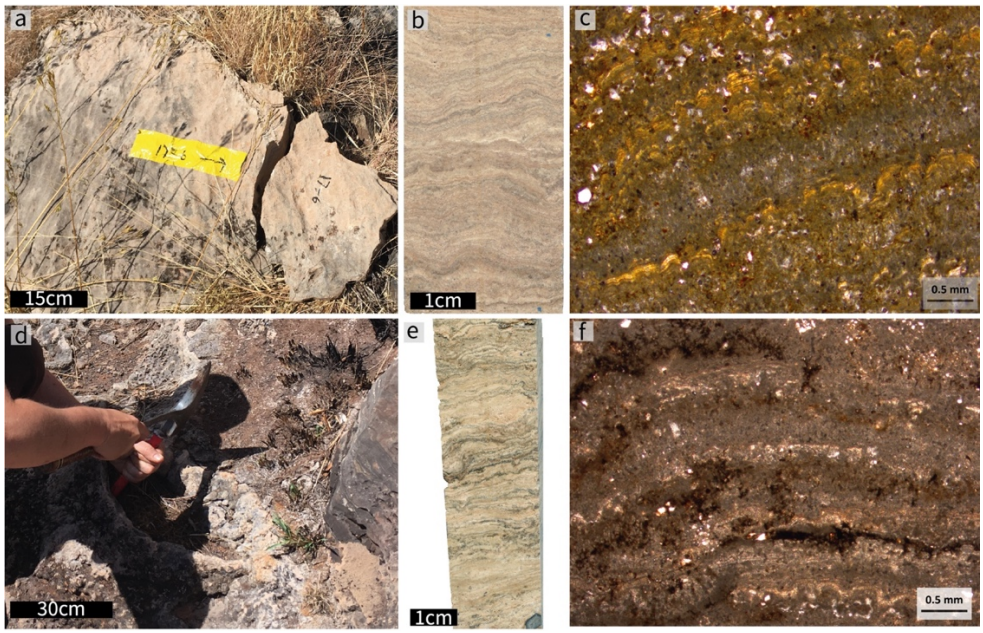

Figure 4.2.6 Field context photographs, hand-sample scans, and photomicrographs of barrage tufa from Ga-Mohana Hill. a-c) Sample 17-6, and d-e) sample 18-6. Hand sample scans (b,e) show irregular, undulating and discontinuous meso-scale layering. c) Thin section photomicrograph of a portion of sample 17-6 shows stromatolite-type micrite laminae alternating with layers of chaotic microspar with detrital and oxide inclusions. f) Thin section photomicrograph of a portion of sample 18-6 shows chaotic fabric of micrite with discontinuous remnants of crinkly microspar and dendritic oxide overprinting.

4.2.3 Rim-pools

4.2.3.1 Macromorphology

The term rim-pools, or rimstone pools, are used to describe flights of terraced pools, which occur on a range of scales in association with cascades and barrages (Viles and Goudie, 1990). At Ga-Mohana Hill, horizontal to gently sloping, transverse areas between dolomite steps are edged by a lip of sinuous carbonate, i.e., the crest of a barrage. As described above, these areas are either long and continuous, or consist of multiple, overlapping hemispherical 'pools' partitioned with carbonate rims (Figure 4.2.5). The remnant rim-pool areas are filled with lightly compacted sediment and debris, with the rim-pool edges, i.e. barrage crests, extending ~2-10 cm in height above this surface. No tufa was sampled directly from these clear rim-pool localities (as pictured in Figure 4.2.5), but some samples collected from terraces have been retrospectively classified as rim-pool tufas, primarily based on their meso- and micromorphological characteristics, described below.

4.2.3.2 Meso- and micromorphology

In hand sample, tufas classed as rim-pools consist of either massive creamy-brown carbonate, occasionally interrupted by a layer of detrital material, or a sequence of fine, wavy layers with small (0.5-5 cm), angular detrital fragments cemented at the base of the deposit, or within confined layers (Figure 4.2.7). The surfaces of some of these samples appear to consist of a series of domes, and sometimes display desiccation cracks (Figure 4.2.7). In thin section, rim-pool tufas consist of aphanitic micrite that grades to peloidal micrite (Figure 4.2.7). Laminoid fenestrae and circumgranular cracks filled with sparite are a common feature throughout these samples (Figure 4.2.7). The absence of a rim-pool lip or barrage associated with these samples make classification based solely on field observations difficult, and the macromorphology type of these samples was not clear in the field context. This was made more complicated due to partial burial in contemporary sediments, and scree and vegetation obstructions. In some instances, tufas classified as rim pool deposits include cemented clasts on their surface, blurring the distinction between rim pool and terrace breccia deposits (described in the next sub-section).

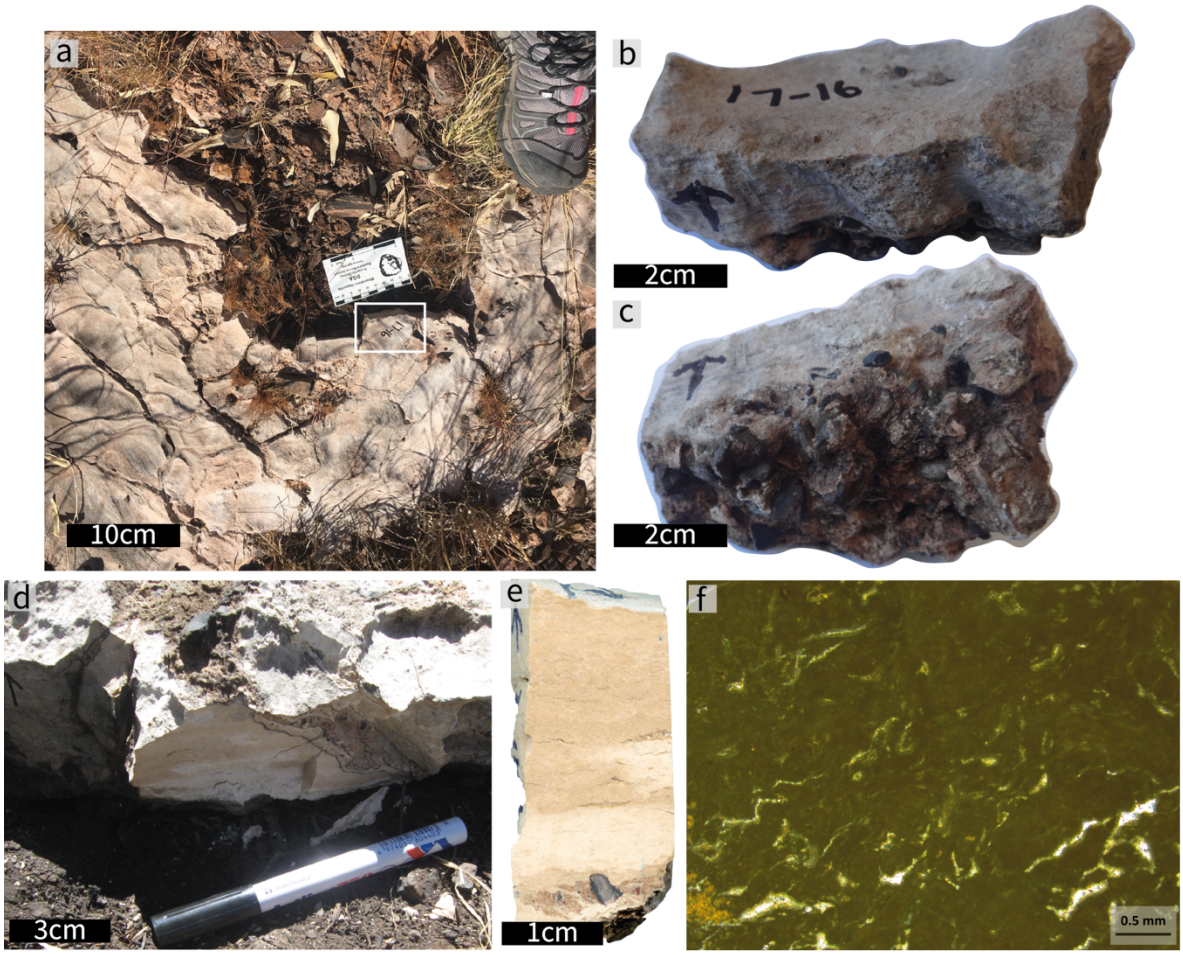

Figure 4.2.7 Field context photographs, hand-samples, and photomicrograph of rim-pool tufa from Ga-Mohana Hill. a) Field context of sample 17-16 showing surface desiccation cracks. b,c) Hand sample photographs of sample 17-16 showing ~4cm of finely layered tufa overlying tufa-cemented clasts on the underside. d) Field context photograph for sample GHN-1. e) Hand sample scan of sample GHN-1. c) Photomicrograph from portion of sample GHN-1 showing aphanitic micrite with spar-filled fenestrae.

4.2.4 Terrace breccias

4.2.4.1 Macromorphology

Terrace breccia deposits at Ga-Mohana Hill occur on the sub-horizontal terraces between the dolomite steps on the slopes above and below the rockshelters. They are sub-divided into two facies. The first consists of surface-cementations of sub-angular detritus of variable sizes from a few millimetres to tens of centimetres (Figure 4.2.8).

These occur as benches, pavements, or patches of carbonate-cemented hill-slope material. The cemented gravels range in size (0.5-20 cm) and are predominantly weathered BIF and dolomite fragments, gravels, and boulders. They are angular to sub-angular and poorly sorted, and in rare instances, stone tools are also cemented in these tufas (Figure 4.2.8). The carbonate cement is light grey to creamy brown and pinkish, and the deposits have a variable proportion of clast to matrix ratio across the hillslope. The second facies are composed of massive or laminar tufa, some of which include small (mm-scale) clasts distributed within the tufa or cemented at their base (Figure 4.2.10).

The lateral continuity of the terrace breccias is difficult to determine because of the density of vegetation and scree on the talus slope, which obscures the deposits, and no spatial pattern in the distribution of the various characteristics could be discerned. The carbonate cementing these clasts appears to have 'flowed' down portions of the slope, in some instances it is evident that cemented clasts have been transported down-slope, whereas in others, eroded hillslope material has been cemented in place, and *in situ* dolomite is coated in tufa, i.e. reworking of eroded material is limited (Figure 4.2.9). These are similar to the cemented gravel and boulder facies and colluvial gravel facies, respectively, of Viles et al. (2007).

Above the northern rock shelter, palaeochannels are incised in the bedrock (Figure 4.2.9). These channels, identified by smoothed scours in the dolomite, can be traced for several meters. They are fairly narrow with widths around 15-50 cm, and filled with loose sediment and detrital material, as well as patches of carbonate-cemented slope material. No further investigations into these channels were carried out.

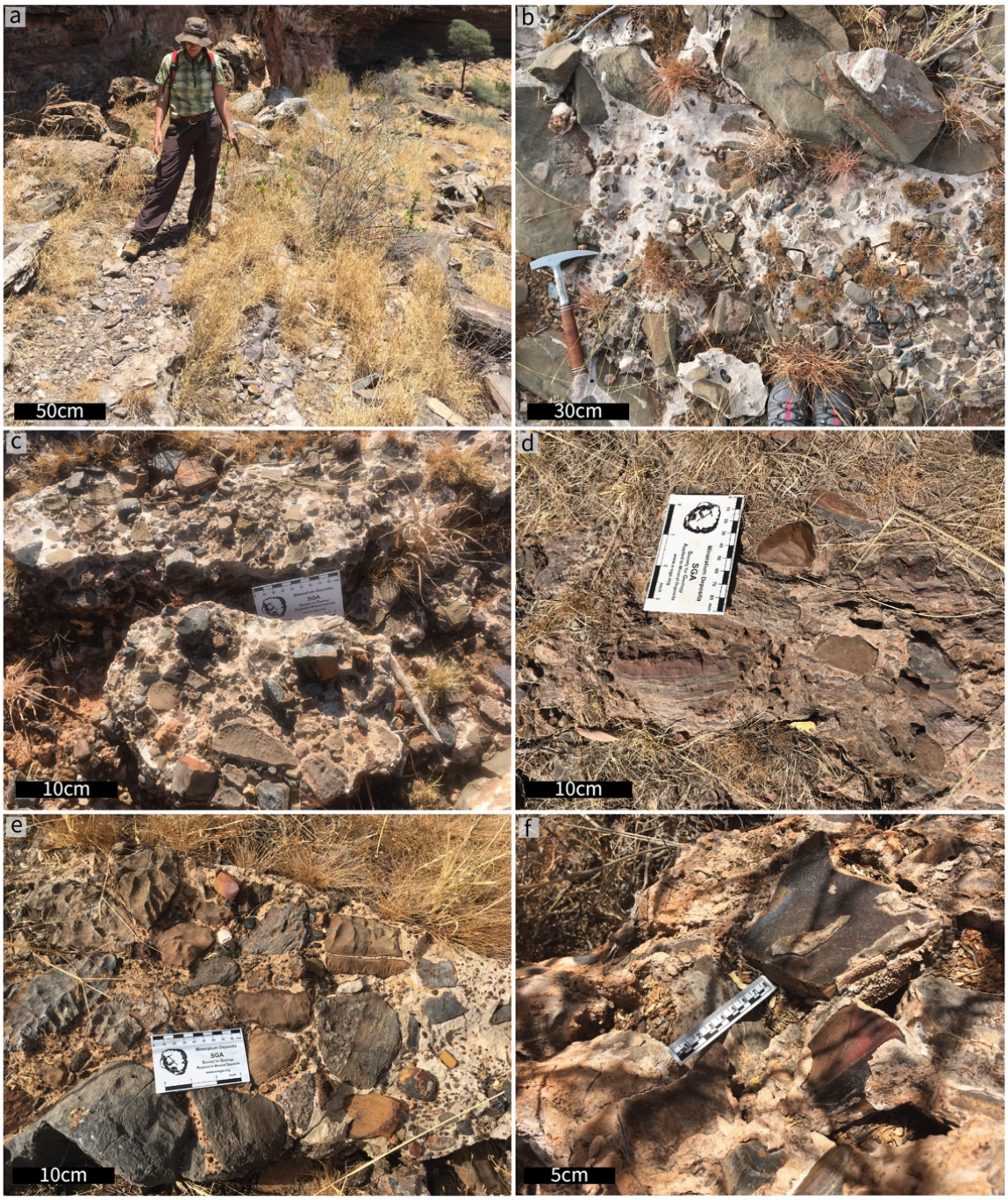

Figure 4.2.8 Field context photographs of terrace breccia tufa at Ga-Mohana Hill. a) Benches of terrace tufa adjacent to Ga-Mohana Hill North rockshelter. b-f) Pavements and patches of carbonate-cemented dolomite and BIF fragments, gravels and boulders on the hillslope below the rockshelters.

Figure 4.2.9 Field photographs of terrace tufa and scouring in dolomite bedrock on the terraces above and below the Ga-Mohana rockshelters. a) Remnants of tufa that appears to have precipitated while 'flowing' down the hillslope, exploiting cracks and joints. b) Dolomite boulder encrusted in tufa. c,d) Tufa crusted beneath dolomite step on hillslope. e-g) Palaeochannels scoured in dolomite bedrock with remnant tufa.

4.2.4.2 Meso- and micromorphology

On a meso-scale, the terrace tufas consist of either massive, creamy-brown micrite, occasionally interrupted by a layer of detrital material, or slightly wavy laminations with small (0.2-0.5 cm), sub-angular fragments cemented at the base of the deposit, or inclusions of small (0.2-0.5 cm), sub-rounded pebbles distributed throughout the sample (Figure 4.2.10). Crude layers of a few centimetres are evident with slight colour changes in the carbonate cement and a wavy contact (Figure 4.2.10). In some instances

brecciated tufa is also included (Figure 4.2.10). The surfaces of some of these samples have clear, well-preserved desiccation cracks. In thin section, terrace tufas consist of peloidal and aphanitic micrite with micro-spar filled in around peloids and in fenestrae and circumgranular cracks (Figure 4.2.10). In some samples, a nucleus, e.g. a quartz grain or oxide-rich clast, is coated in organic-rich micrite. Rounded, reworked tufa breccia is evident in some samples e.g. sample 17-8 (Figure 4.2.10). Tufa cemented beneath a dolomite boulder on the hillside was collected, sample 17-8. It is composed of massive, dense micrite on a meso-scale, and in thin section the micrite consists of peloids and spar-filled fenestrae (Figure 4.2.10).

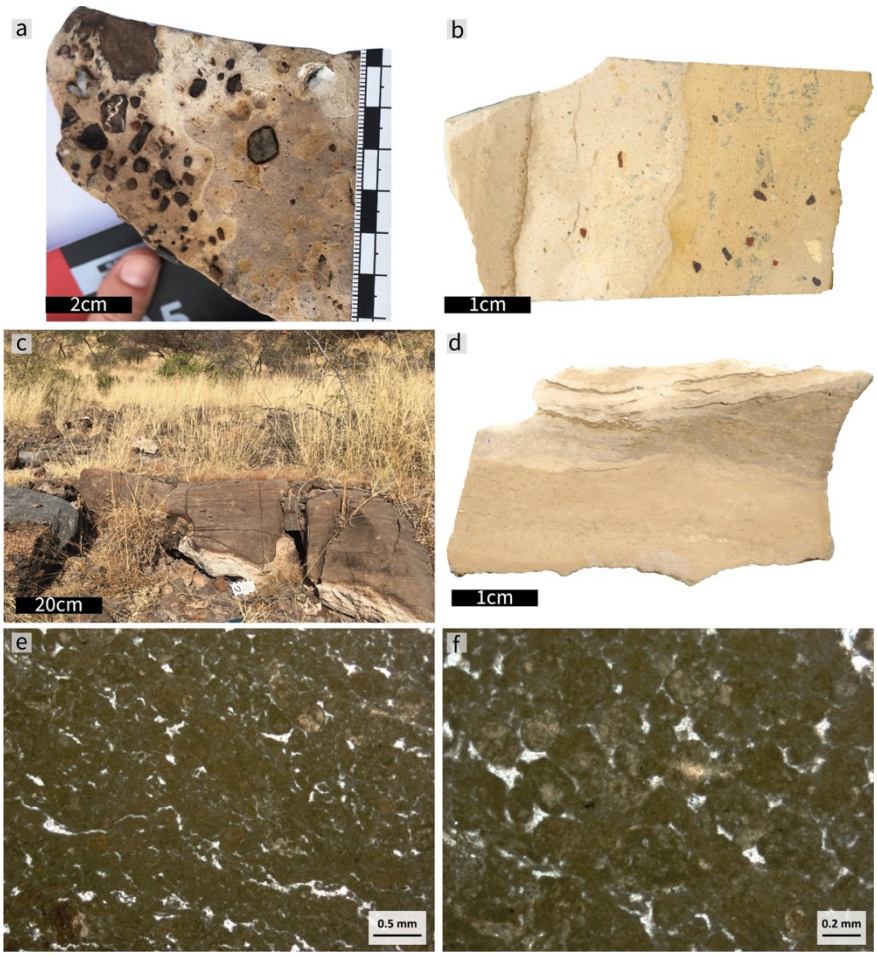

Figure 4.2.10 Field context photograph, hand-samples, and photomicrographs of terrace breccia tufa from Ga-Mohana Hill. a,b) Hand sample slabs with abundant detrital fragments, including tufa clasts (a). c) Field context of tufa sample 17-8. d) Slab of sample 17-8 composed of dense creamy micrite. e,f) Photomicrographs of sample 17-8 thin section showing aphanitic and peloidal micrite with microspar-filled void spaces.

4.2.5 Domes

4.2.5.1 Macromorphology

Domes are irregular, hemispherical tufa accumulations that occur along the edges of the Ga-Mohana rockshelters, below the drip-line of the overhangs and along the base of the cliff faces adjacent to the shelters (Figure 4.2.11). The domes range in size, with the width of the base measuring about 1.5 m on average, and up to 3 m for clustered domes. The tops of the domes tend to have a flattened, indurated surface, and are narrower than the bases, around 40 cm in diameter. The average height of the domes is about 1 m. The domes are variably preserved; several domes have a hemispherical hollowing at their base (Figure 4.2.11) and some are highly weathered, exposing a complex internal structure (Figure 4.2.11). Sections of the domes appear to have flaked off, exposing a layered internal configuration.

The outer surfaces of the domes are hard, consisting of an indurated, calcretised rind. These surfaces range from smoothly mamillated to lumpy, irregular and knobbly, characterised by a clotted raspberry or cauliflower texture i.e., small circular groupings of protruding bundles, approximately 2 mm in size (Figure 4.2.11). The domes are often paired with a second or third smaller dome, existing as a clustered aggregate, and exhibit a range of colours - grey, pink and orange-brown (Figure 4.2.11). Cone-shaped tufa 'noses' jut out over the lip of the rock shelters and are spread along the overhang. In some instances, domes are aligned with a 'nose' protruding from the cliff above (Figure 4.2.11). The noses are partially hollow with convoluted internal configurations. Due to their height, the noses are inaccessible and were consequently not sampled.

4.2.5.2 Meso- and micromorphology

On a meso-scale, layers of about 2-5 cm, and up to 10 cm in some instances, are exposed in a number of domes for which sections of the tops or sides have been eroded (Figure 4.2.12). Within these layers, thin (~1 mm), dense, undulating laminations are discernible in freshly exposed sections. These mm-scale laminations exist for ~1 cm successions, and alternate with spongy, porous layers. The hard calcretised layers flake off in sub-mm sheets and tiny circular indentations are visible on the undersides of these,

appearing to be pressed into the layer above (e.g. sample 17-13). These successive laminations sandwich the irregular, less-consolidated, porous layers between them. These layers tend to have a 'bubbly' texture and a gritty feel. This alternating pattern of dense micritic layers with a porous framework is sometimes also observed in cascade samples, but it is more regularly developed in the domes. Some dome samples, collected with the core drill, exhibit a highly reticulate structure, i.e., a framework of cream-coloured, dense tufa surrounding irregular angular voids (Figure 4.2.12).

In thin section, dome samples consist of well-developed successions of smooth, dense, horizontal microlaminae, interchanging with highly porous zones of clotted, aphanitic micrite and micro-spar (Figure 4.2.12). These porous zones are either sandwiched between microlaminae successions or a whole zone comprised of these, crudely layered and in variable orientations (vertical in Figure 4.2.12). The microlaminae consist of successions (approximately 1-3cm thick) of alternating brown and white lamina of variable thickness (<1 mm). Micro-oncoids with detrital quartz or iron-oxides as the nuclei are included in the porous micritic layers (Figure 4.2.12). In some instances, the laminae successions are abruptly truncated, evidence of mechanical erosion (Figure 4.2.12).

Figure 4.2.11 a-e) Photographs of various configurations of dome tufa in the field. a) Dashed line illustrates the hemispherical hollowing at the base of the dome. b) Tufa cone / nose associated with aggregated dome tufa below. c,d) Top of dome tufa, dashed line indicates growth zone of dome layer. e) Broken and weathered dome with layered internal structure visible. f,g) Close-up photographs of the outer surface of dome tufa to show clotted raspberry / cauliflower texture.

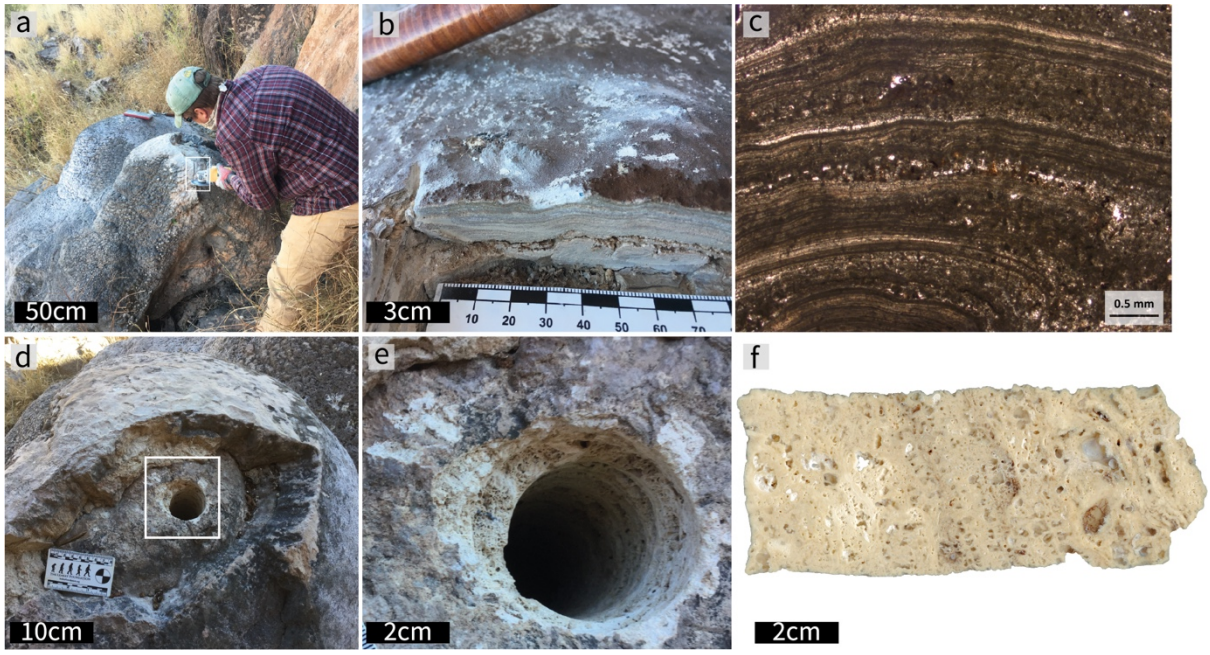

Figure 4.2.12 Photographs of sampled dome tufa. a) Dome tufa sampled using an angle grinder. b) Portion of dome sliced by angle grinder, meso-scale internal layered structure visible. c) Photomicrograph of sample GHN-3 thin section in PPL showing successions of thin, wavy laminations of micrite and micro-spar, alternating with layers of clotted micrite with detrital oxide inclusions. d,e) Drill hole for sample 18-10. f) Sample 18-10 core slab showing organic framework.

4.3 Depositional environment of Ga-Mohana Hill tufa

The relict tufa deposits at Ga-Mohana Hill indicate the past activation of a spring fluvial tufa system. The stepped topography of the dolomite hillside exerts a control on the macromorphologies of the tufa deposits described above. Each of these morphologies relate to a particular sub-environment, and together these form a tufa continuum or facies association, i.e. an inter-related series of deposits which altogether create a depositional environment.

Classification of the tufa system according to an environmental model is necessary to make useful interpretations of the depositional setting. At the field scale, the Ga-Mohana tufas appear to fit the perched springline model of Pedley (1990) and Pedley et al. (2003). The defining features of this model are a hillside setting, dominated by a step and terrace topography, the predominance of cascade deposits, and small-scale pools which form localised paludal (marshy) conditions. The tufa domes observed at Ga-Mohana are comparable to the moss cushions described by Pedley (1990). These are a common feature below tufa waterfalls, as described from the modern-day analogue site of Sitting Bull Falls in New Mexico, USA (Pedley, 1990). Based on field-scale components alone, the Ga-Mohana tufas can be classified as a perched springline deposit as they exhibit many of the features outlined above, as illustrated in Figure 4.1.3.

On an intermediate and microscale, however, there are a few key differences. In particular, oncoids, rhizoliths and macrophytes (plant, reed and root moulds) are absent in the Ga-Mohana tufa deposits. These features record evidence of vegetation growth and are typical features of tufa deposits in Europe and North America. It is likely that the absence of these in the Ga-Mohana tufas is due to local variations in climatic and environmental conditions which affect the growth of vegetation, or the preservation of such features. This study does not investigate the palaeobotany of this site, but it may be worth further investigation in the future.

The microfabrics of the Ga-Mohana tufas are predominantly composed of three basic petrographic components, i.e. micrite, microspar and sparite. and the arrangement of these into distinct fabrics: laminar, aphanitic and peloidal. Different combinations of these facies are present in each of the macro-morphologies. It has been proposed that these differences arise due to the variable substrates upon which the tufa precipitates, with the formation of the crystal habits being linked to the carbonate saturation state of the tufa forming waters, which in turn is controlled by (seasonal) temperature variations and the biota present (Pedley et al., 1996; Perri et al., 2012). The overall architecture of the Ga-Mohana tufa morphologies, and the depositional environments they represent, are discussed in relation to Figure 4.3.1, with reference to the field observations, hand samples and thin section figures presented in Section 4.2 above.

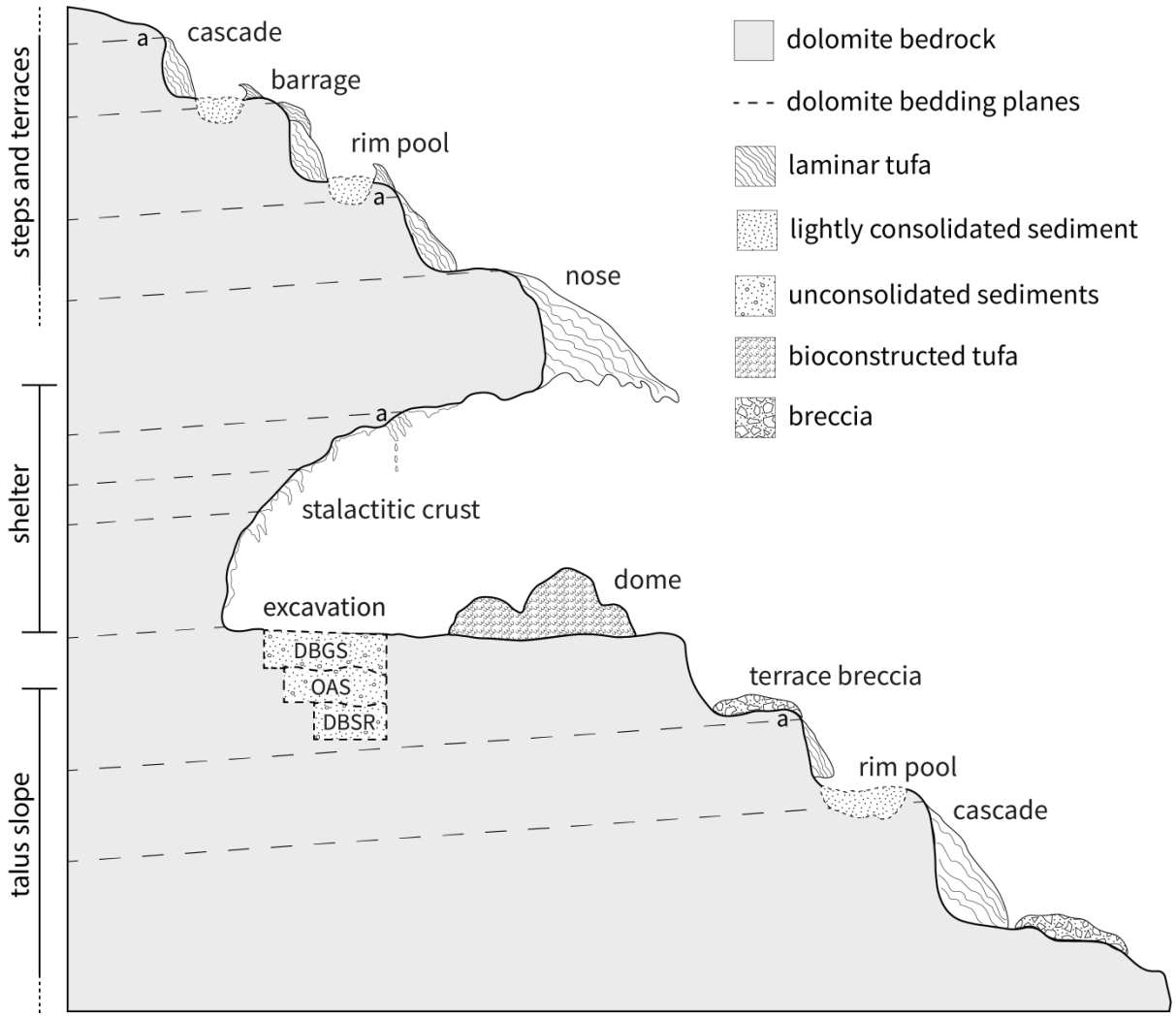

Figure 4.3.1 Schematic illustration of the tufa deposits at Ga-Mohana Hill.

Cascade, barrage, rim pool continuum (steps and terraces)

The cascade tufas are associated with bedding planes in the dolomite, on the dolomite step fronts, and on the cliff faces adjacent to the shelters (Figure 4.3.1), directly linking them to emergent spring waters. They are characterised by their convex mound shape and the vertical to subvertical layering identified in hand samples. The dolomites of the Campbellrand Subgroup have been extensively karstified (Eriksson and Altermann, 1998) and consist of a vast underground drainage network with significant storage capacity Smit (1978). Since Ga-Mohana is a topographic high, it is unlikely that it is tapping into these underground networks, but it may act as a perched aquifer, capable of storing rainwater for periods of time (Willimas, 2008). Actively dripping straw stalactites were observed at the site during field work in both the summer (wet) and winter (dry) months, which is further testament to the storage capacity of the dolomite. The tufa-forming waters likely emerged from bedding planes in the dolomite at particular times in the past when the maximum capacity of the aquifer was reached (Williams, 2008). The water source for the formation of the tufa deposits at Ga-Mohana is thus interpreted to be emergent groundwaters that exited the dolomite bedding, cleavage or fault planes at various positions on the hillside (Figure 4.3.1).

The resurgent groundwaters would have encountered a pCO_2 gradient as the atmospheric pCO_2 would have been lower than that of the groundwater. This would have led to a disruption of the equilibrium of the system, resulting in CO_2 degassing from the groundwater, triggering calcium carbonate precipitation. The atmospheric temperature is also likely to have been higher than that of the groundwaters, particularly in summer, causing the emergent waters to be warmed up at the surface. This would also trigger calcium carbonate precipitation as HCO_3^- becomes less soluble with increasing temperature. The steep angle of the step and cliff fronts will have encouraged turbulent flow of the ground waters, further promoting CO_2 degassing and carbonate precipitation (Marker, 1988; Violante et al., 1994; Chen et al., 2004). The cascade tufas are thus a direct result of groundwaters that have become saturated with respect to calcium carbonate, flowing out of the dolomite bedding planes and precipitating tufa.

While precipitation of the cascades was most likely triggered primarily by the physicochemical processes described above, tufa precipitation rarely occurs solely as a result of abiotic factors (Ford and Pedley, 1996; Pedley, 2009). In thin section, the cascade samples are composed of an predominantly stromatolitic fabric with layers of micrite and microspar. Void spaces and detrital inclusions are a minor component. This composition is interpreted to indicate tufa precipitation in the presence of algal communities and mosses, as observed in Arenas and Jones (2017), evidence for the involvement of organic activity in the precipitation of the cascades.

Cascades are commonly developed wherever vertical surfaces are available and are thus not restricted to a single environment, being instead a function of the underlying topography (Pedley, 2009). However, the cascades at Ga-Mohana Hill appear to play a central role as the starting point for the tufa system, displaying a direct link to the source of the tufa forming waters (Figure 4.2.4). These cascade or 'waterfall' features, present at multiple points on the hillside, likely fed the entire tufa system, contributing to surface flow (palaeochannels, fluvial crusts and terrace breccias), generating areas of ponded water on the terraces (rim pools and barrages), and waterfalls over the shelter overhang (noses and domes).

Shallow pools of standing water would have collected on the near-horizontal terraces, or on the horizontal tops of dolomite steps, impounded by barrage crests (or rim-pool edges), below which convex, dam-like barrage tufas formed on the slopeward pool fronts or the dolomite step fronts (Figure 4.2.5). Many of the barrages exhibit an irregular, knobbly or coralloid surface (Figure 4.2.5), and in hand sample, they are characterised by irregular, sloping, mm-scale laminations (Figure 4.2.6). In thin section, these tufas display thin, discontinuous lenses of dome-shaped calcitic crusts which point to the irregular nature of the growth surface. The crusts sandwich thicker, chaotic assemblages full of trapped grains and oxides (Figure 4.2.6). These features suggest that barrage construction occurred through precipitation of slow overflow of waters from the rim-pools. This slow and potentially intermittent flow likely generated a thin film of water that would have facilitated the growth of algae and other organisms, which

would have provided a substrate for tufa precipitation, as well as for the entrapment of wind-blown grains.

Tufa samples classified as rim-pool deposits are interpreted to be the products of tufa precipitated within shallow pools of standing water. In thin section, the predominant components of these samples are aphanitic micrite and micritic peloids (Figure 4.2.7). Components similar to these have previously been interpreted as products of biomediated tufa precipitation (Pedley et al., 2009). Thin, horizontal fenestrae, or 'wiggles' filled with micro-spar (Figure 4.2.7) are interpreted to be moulds left by decayed algal filaments.

The rim pool and barrage tufas together are interpreted to represent shallow pools of stagnant to slow-flowing water, fed and filled with water from preceding cascades that may have flowed directly into pools, or via channels down the hillslope with radial drainage. Groundwater resurgence through bedding planes at various positions on the hillslope would have activated this system of water flow and subsequent cascade, rim-pool, and barrage tufa formation. These points of resurgence may have been active simultaneously or at varying times, depending on the extent of aquifer recharge and epikarst flow paths. These proposed sub-environments of tufa formation will be further evaluated using carbon and oxygen isotopes in Chapter 7.

Tufa noses and domes (shelter)

Whereas the cascades are observed on the terraces both above and below the shelters, as well as on the cliff faces on either side of the shelters, the tufa noses and domes (Figure 4.2.11) are solely associated with the rockshelters. The rockshelters present a dramatic break in the hillslope topography and consequently provide a unique sub-environment for tufa depositing waters. Water flow over the cliffs above the rock shelters would likely have encouraged growth of vegetation, e.g. mosses, which would in turn have created a substrate and framework upon which tufa precipitated, producing the tufa 'noses' which jut out along the overhang (Figure 4.2.11). The noses (which were not investigated in detail) are interpreted to be remnants of tufa precipitation localised on moss curtains, based on their positioning on the overhanging

cliff lip, their cone-shaped morphologies and convoluted internal configurations; similar forms have been observed at analogous sites of active tufa formation (Golubić et al., 2008; Gradziński et al., 2018).

Dripping and splashing of waters flowing over the lip of the shelters, channelled via the noses, would have generated the growth of the large tufa domes, which are scattered below the drip line of the rock shelters, often observed in alignment with a tufa nose. The effect of water falling and splashing at these zones accelerates CO_2 degassing, promoting tufa precipitation. The morphology of the domes, i.e. clotted raspberry / cauliflower texture on the surface, layered, porous and spongy internal texture (visible on a macroscale), and capping of dense micritic crusts composed of a series of microlaminae (Figure 4.2.12), is evidence that they were constructed through precipitation of calcite on and within a framework of botanical material (Pedley, 1990).

On a meso-scale, some domes exhibit cm-scale successions of dense micritic laminae sandwiching spongy, porous layers, whereas others have a reticulate, mesh-like, internal framework with an assortment of irregular void spaces linked by layers of dense calcitic material (Figure 4.2.12). The spongy layers are interpreted to represent biotic activity and plant / moss growth. The void spaces are interpreted to be remnants of insect larvae or moss bundles. This alternating pattern may have been driven by seasonal changes, or by water flux. The growth of these biotic components provides a substrate upon and within which calcite nucleation and precipitation is facilitated and enhanced. The size and abundance of the tufa domes suggests multiple points of water flow and a sustained water source in the past.

The stalactitic crust on the walls inside the shelters were not sampled or investigated, but are interpreted to have formed from fluid exiting the dolomite bedding planes within the shelter, and subsequent flow down the shelter walls. Water was observed to be dripping from some of the microstalactites on the shelter walls on several field visits, but the low volume of water and absence of substantial tufa precipitation today is evidence of different environmental dynamics today than in the past.

Terrace breccia and fluvial crusts (talus slope)

The terrace breccia deposits, observed on the slopes both above and below the rock shelters, are composed of a variety of weathered material cemented in a tufa matrix. These deposits are patchy and somewhat obscured due to dense vegetation (particularly on the lower slopes) and contemporary scree, soil and detrital material. As such, it is difficult to trace their continuity and the deposits are relatively poorly preserved, most likely because they are exposed to weathering from run-off, soil and vegetation. The cemented clasts range in size and are poorly sorted (Figure 4.2.8), evidence of flash flood episodes in which variably sized clasts and scree material were rapidly transported down slope and then, either instantaneously or at a later stage, cemented in place. Tufa precipitation may have been instantaneous, driven by rapid and turbulent flow of fluids down slope, or it may have occurred through evaporation of calcium carbonate-saturated fluids pooled on flat sections of the terraces. Deposits with vertical, down-slope sorting of clasts (larger clasts higher up and smaller ones further down) are evidence for the former scenario and suggest simultaneous flow and cementation, whereas poorly sorted deposits are evidence of the latter scenario and suggest *in situ* cementation of talus scree. The dominant mechanism of tufa precipitation would have been determined by the flow regime, which likely varied over time, and the position on the slope, i.e. steep sections with high energy, turbulent flow versus flat sections where flow energy would have been reduced and water may have ponded.

The incised palaeochannels within the dolomite observed above the shelter are evidence of periods of sustained water flow. Fluvial crusts coating *in situ* dolomite boulders and joins between dolomite steps highlights periods of abundant and sustained water flow on the hillside, and multiple flow pathways. Further investigation focused on the terrace breccia deposits and palaeochannels (e.g. digging into the palaeochannels, mapping of cemented clasts distribution, sizes and sorting) is needed to elucidate the local hydrological dynamics to be able to confirm the hypotheses above. Nevertheless, terrace breccia deposits and fluvial crusts are evidence of flowing surface waters supersaturated with respect to calcium carbonate, and conditions for their precipitation i.e., high flow and degassing, or slow flow / stagnation and evaporation.

Aspects of the Ga-Mohana tufa system described above corroborate the model of arid-environment fluvial tufa deposition proposed by Viles et al. (2007) based on the Brandfontein River system in the Naukluft mountains of Namibia. Whereas tufa-encrusted reeds are observed on a macro-scale at Brandfontein, there is limited evidence for this at Ga-Mohana Hill, except in a few instances observed in thin section. The Ga-Mohana tufa deposits are predominantly features of a perched springline system with associated fluvial activity, whereas the Brandfontein tufas are fluvial barrage deposits with perched springs producing cascade tufas. Nevertheless, similarities in the facies at both sites suggests that the Ga-Mohana tufa system followed a similar three phase model of tufa formation to that described by Viles et al. (2007). That is, a phase of perennial, low energy water flow that supported growth of mosses in continuous flow areas, (associated with the development of cascade and dome tufas), and the development of slack-water environments (rim-pool and barrage tufas). A second phase of high flow, resulting in erosion and high energy transport of eroded clasts and boulders, and possibly instantaneous cementation of scree material (formation of terrace breccias), and a third phase of ephemeral flow with little to no tufa formation (present conditions).

CHAPTER 5 MAJOR AND TRACE ELEMENTS IN TUFA

Major and trace elements in carbonate deposits are commonly used as a palaeoclimate proxy tool, particularly in marine settings. However, the multiple and complex processes that govern the incorporation of trace elements into terrestrial carbonate deposits has made palaeoenvironmental reconstruction using trace elements challenging (Fairchild and Treble, 2009). In the following section, I first explore the range of factors that control trace element incorporation into calcite (Section 5.1.1), then review a selection of case studies for which trace element contents in tufa deposits have been analysed (Section 5.1.2), and in Section 5.1.3, I introduce the application of Laser Ablation ICP-MS to measure trace elements in tufas. In Section 5.2, I present the results of my analysis of major and trace element contents in the Ga-Mohana tufa deposits, as well as a small sub-set of present-day waters collected from the site. My primary focus is a high-resolution trace element dataset obtained from a selection of Ga-Mohana Hill tufa samples I analysed using LA-ICP-MS. This was carried out to test whether the trace elements in the tufa produce coherent trends, useful for palaeoclimate interpretations. These results are discussed in Section 5.3.

5.1 Background and literature

Monitoring studies and investigations of the chemistry of carbonate-forming waters and the associated modern precipitates aid in unravelling the mechanisms that influence trace element variability, and this has been done extensively in cave environments (Fairchild et al., 2000; Tooth and Fairchild, 2003; Treble et al., 2003; Fairchild and Hartland, 2011; Hartland et al., 2012; Baker et al., 2014; Rutlidge et al., 2014; Borsato et al., 2016). As such, a number of investigations of trace elements in speleothems have yielded high resolution palaeoclimate information (Johnson et al., 2006; Borsato et al., 2007; Frisia et al., 2012; Orland et al., 2014; Ban et al., 2018; Belli et al., 2017). However, in geochemical studies of tufa, the primary focus has been on using stable isotopes, $\delta^{18}O$ and $\delta^{13}C$, to infer climate signals (Andrews et al., 2000; Andrews and Brasier, 2005; Andrews, 2006). Although several geochemical investigations of modern tufa systems

have been conducted (Ihlenfeld et al., 2003; Leybourne et al., 2009; Lojen et al., 2009; Ritter et al., 2017), only a limited number of studies have combined isotope and trace element analysis to investigate palaeoclimate using relict tufas (Frančišković-Bilinski et al., 2004; Garnett et al., 2004a; Brasier et al., 2010; Dabkowski et al., 2012; Zavadlav et al., 2017). Altogether, these studies suggest that trace element contents in tufas do potentially provide additional climatic and hydrological information, but further application has been slow, and palaeoclimate records using high resolution element data lag that of speleothem studies.

5.1.1 Controls on trace element incorporation in calcite

One major control on trace element incorporation into carbonates is the mineralogy, with unique partitioning behaviour for calcite, aragonite and dolomite. The main constituent of tufa is calcium carbonate ($CaCO_3$), which can exist either as calcite or its less stable polymorph, aragonite. The formation of either of these two minerals depends on a variety of conditions, e.g. the chemical composition of the fluid from which they precipitate, temperature, pressure, and the rate of CO_2 degassing. Aragonite is a common component of travertine, i.e. $CaCO_3$ deposited from hot springs (> 40°), but is less frequently associated with cold water spring deposits, i.e. tufa (Folk, 1994; Pentecost, 2005).

Temperature control is not always the driver for aragonite vs. calcite precipitation though, and other factors, such as the addition of certain elements, may enhance or inhibit calcite or aragonite precipitation (Kitano and Kawasaki, 1958; Kitano, 1962; Jones and Renaut, 1995; Jones and Renaut, 2010). For example, precipitation of aragonite from ambient temperature spring waters has been linked to high Mg/Ca ratios in the source water (Müller et al., 1972; Kelts and Hsü, 1978; Popp and Wilkinson, 1983). Pentecost (2005) suggests that Mg concentrations >10 mmol/L could result in aragonite precipitation under ambient temperatures, but this threshold may not always be applicable because mineral precipitation can be affected by multiple other factors, including microbial activity (Guo and Riding, 1992). While Mg in solution favours aragonite precipitation, multiple other factors, such as water temperature, rate of CO_2

degassing, organic matter, and high levels of other solutes, e.g., Fe^{2+} and SO_4^{2-}, influence aragonite precipitation (Kitano, 1962; Meyer, 1984; Pentecost, 2005). Usually, calcite is the predominant mineral in tufa. This can be verified for individual deposits through X-ray diffraction (XRD).

In addition to calcite (or aragonite), many other elements that exist in natural systems can be co-precipitated with calcite either by incorporation into the crystal lattice, adsorption onto the crystal surface, as inclusions, or as a substitute for calcium or carbonate ions (Veizer, 1983; Pentecost, 2005). The concentration of these additional 'accessory' elements, usually present in minor or trace amounts (on the order of 10's–1000's ppm) reflect variations in the composition of parent waters, detrital input, as well as conditions during calcite precipitation, e.g. temperature and rate of precipitation influence the distribution of an element between the fluid and mineral phase. They can thus provide clues about the hydrological or environmental conditions during tufa formation.

Trace elements are derived from a variety of sources, and a multitude of complex processes govern their inclusion in carbonate deposits. Many elements enter groundwater during weathering of bedrock and soil and are present as divalent cations in solution. Divalent cations such as Mg^{2+}, Sr^{2+}, Ba^{2+}, can be incorporated into the calcite matrix, either by substitution of Ca^{2+} or at vacancies in the crystal lattice, and can occur up to several wt.%. Trace metals, such as Fe^{2+}, Mn^{2+} and Zn^{2+} have ionic radii less than that of Ca^{2+} and thus are preferentially co-precipitated in calcite, whereas Sr^{2+}, Ba^{2+} and $UO2^{2+}$ are larger than Ca^{2+} and thus are less likely to be incorporated into a calcite crystal (Speer, 1983).

The distribution of a divalent element between an aqueous solution and the mineral phase under equilibrium conditions is defined by a partition coefficient, Kd (Equation 5.1, where C denotes concentration). Partition coefficients depend on various factors, such as temperature, water chemistry, pH, precipitation rate, microbial communities, etc., and can be determined experimentally (Huang and Fairchild, 2001; Ritter et al., 2018). The dominant factor controlling the partition coefficient for individual elements

tends to vary, for example, the partition coefficient for Mg into calcite (Kd_{Mg}) is predominantly controlled by hydrological factors, whereas growth rate is a more important control on Kd_{Sr} (Treble et al., 2015).

Equation 5.1 $$Kd = \frac{C_{mineral}}{C_{solution}}$$

Less mobile elements, such as Pb, Al, Fe and Zn, can be transported in solution as solid particulates or colloidal material (molecules or particles with dimension between 1 nm and 1 μm) as a result of surface runoff from soil and bedrock erosion, or organic particulate matter. In particular, Fe and Zn are two of the most common metal ions in biological systems and may thus be associated with organic matter (Da Silva and Williams, 1991). Other non-carbonate constituents that contain a variety of trace elements may also be incorporated into carbonate deposits, thereby influencing the bulk rock chemistry (Veizer, 1983). These contributions may be from wind-blown particles, aerosols, or species associated with detritus.

Table 5.1 Typical range in trace element concentrations in tufa (Pentecost, 2005).

Element	Al	Ba	Fe	Mg	Mn	Pb	Sr	Th	U	Zn
Range (ppm)	100 - 15000	2 - 10000	46 - > 4000	180 - > 8000	5 - 1600	< 2 - 31	9 - > 2930	0.1 - 0.4	0.4 - 0.7	4 - 680

5.1.2 History of trace element work on tufas

Some of the earliest work on trace elements in tufas was conducted Chafetz et al. (1991) who documented seasonal variation using lamina-by-lamina trace element and C-O isotope data. Janssen and Swennen (1997) investigated diagenesis in tufas using trace elements. Frančišković-Bilinski et al. (2003) and Frančišković-Bilinski et al. (2004) reported mineralogical and geochemical compositions of tufa from China and Croatia respectively, using both XRF and solution ICP-MS analytical approaches.

Ihlenfeld et al. (2003) published a detailed study of a modern riverine tufa from the Gregory River catchment in Queensland, Australia, that acted as a test case for the

possibility of extracting high resolution climate records from tufas. They demonstrated the link between trace element concentrations in river waters, annually laminated tufa, and climate. They measured the $\delta^{18}O$ and $\delta^{13}C$ values, and trace elements Mg, Sr, Ba and U, in both river water samples and a recent tufa deposit to test whether variability was related to annual or interannual climate variations. Based on variation in the $\delta^{18}O$ values, they established a 14 year-long chronology for the tufa and used this chronology to frame their geochemical results. Ihlenfeld et al. (2003) found a significant anti-correlation between $\delta^{18}O$ values and Mg content, and interpreted this to result from a temperature-dependence for Mg partitioning into calcite. Based on this, they demonstrated the use of Mg as a paleothermometer for tufa-forming waters, using the Mg content in the tufa to calculate the annual temperature variation of the river water. Higher Mg contents were recorded for tufa formed during the warm and dry season relative to the wet season. They also reported a strong positive correlation between Sr and Ba content, and between both of these elements and $\delta^{13}C$, which they interpreted to reflect changes in water chemistry due to aquifer processes. Lower Sr, Ba and $\delta^{13}C$ were all attributed to increased rainfall, albeit with a lag on the order of 1–2 years due to water residence time. They documented annual and seasonal variation in U, which they interpreted to reflect U fluxes from the soil zone to the water table. An increase in U was suggested to be a consequence of intense rainfall events, during which U complexed to organic colloids is transported into the phreatic zone (Ihlenfeld et al., 2003).

Garnett et al. (2004a) published a study that combined stable isotope data and Mg and Sr content from a paludal Holocene tufa from Wateringbury, southern England. The tufa was dated with radiocarbon, and trace elements for each layer were analysed via solution ICP-MS. They determined that, whereas variations in the $\delta^{18}O$ values of the tufa reflect changes in the isotopic composition of rainfall, there was no relationship between $\delta^{18}O$ values and Mg/Ca. This finding is different to that of Ihlenfeld et al. (2003) in which an anti-correlated relationship between $\delta^{18}O$ values and Mg content was evident. Garnett et al. (2004a) did find a relationship between Mg/Ca and Sr/Ca ratios, which were also correlated with $\delta^{13}C$ values. They suggested that in this case, Mg content

was not related to temperature but was rather a reflection of in-aquifer processes, such as residence time, CO_2 degassing, and calcite dissolution/reprecipitation. As such, they argued that Mg, Sr and $\delta^{13}C$ in tufa record palaeorainfall intensity, with an increase in these values reflecting periods of low recharge, i.e. dry conditions.

Dabkowski et al. (2012) also presented combined stable isotope and Mg and Sr content for a tufa from the Seine Valley in northern France. The tufa in this study is much older than those sampled by Garnett et al. (2004a) and is dated to MIS 11 (424 to 362 ka) based on a combination of terrace morphology, biostratigraphy and U-Th methods. Consistent with Garnett et al. (2004a), they concluded that ambient rainfall was the predominant control on tufa chemistry at this site, with $\delta^{13}C$, Mg and Sr co-variation interpreted to reflect alternations in humidity and aridity.

Sierralta et al. (2010) analysed trace elements (Mg, Mn, Fe, Cu, Zn, Pb, Sr, Ba) in travertines from Hungary using an electron microprobe. While the microprobe method allowed for high spatial resolution of elements in the tufas, it is limited to Mg and occasionally Sr and Zn, the rest of the elements were below detection, i.e. <700 ppm. Sierralta et al. (2010) reported zoning of Mg in sparite and suggested that the low values of Mn in the samples indicated tufa formation under oxidising conditions.

These studies make general interpretations about alternations of humidity and aridity based on the co-variation of elements, predominantly Mg, Sr and Ba, and carbon or oxygen isotopes, but tufa systems are far more complex, and while co-variation of elements may arise as a result of an increase/decrease in rainfall, a variety of other factors impact the chemistry of tufa deposits and require consideration. In particular, the extent to which biological processes influence tufa geochemistry has been a subject of interest in recent years with a spate of studies attempting to address this question through *in vitro* experiments and chemical analysis of tufa-forming waters (Rogerson et al., 2008; Arp et al., 2010; Saunders et al., 2014; Ritter et al., 2018; Rogerson et al., 2022). In some tufa deposits, divalent ions, e.g. Ca^{2+}, Ba^{2+}, Sr^{2+} and Mg^{2+}, are accumulated in biofilms via chelation, i.e. bonding of divalent metal ions with an organic complexing agent. *In vitro* experiments have demonstrated that this process favours ions with low

charge densities, resulting in enrichment in divalent ions relative to equilibrium values in the order of Ba > Sr > Mg (Rogerson et al., 2008). This pattern is reflected in the trace element composition of a natural tufa forming system at Kaisinger Creek in Germany (Ritter et al., 2018). Ritter et al. (2018) also found that metals such as Cd, Zn, Co, Pb, Ni and Mn are highly compatible in tufa. They suggested that variations in these metals in tufa could track the lateral distribution of ancient tufa deposits relative to the water source because, at Kaisinger Creek, tufas are systematically depleted in these elements with increasing distance from the source.

Several attempts have been made to use Mg in tufa as a palaeotemperature proxy (Ihlenfeld et al., 2003, Zavadlav et al., 2017) based on the premise that the incorporation of Mg into calcite is temperature dependent (Katz et al., 1973). However, Saunders et al. (2014) showed that metabolic processes in the presence of exo-polymer substances (EPS), i.e., biofilm, can override the thermodynamic control on Mg partitioning. They also show that incorporation of cations into calcite is enhanced at low precipitation rates, and that this is regulated by the nature of the biofilm. These additional factors complicate the use of Mg in tufa as a paleothermometer. Additionally, in speleothem studies, it has been shown that hydrology exerts a greater control on Mg content than temperature, with increased Mg corresponding to longer groundwater residence time due to a decrease in rainfall (Fairchild et al., 2001; Treble et al., 2003; McDonald et al., 2004; Treble et al., 2005). Ultimately, the sources of elements in tufa and the mechanisms responsible for controlling their incorporation into calcite vary widely, and our understanding of these complex systems is still relatively limited.

5.1.3 Application of Laser Ablation ICP-MS to measure trace elements

The previous studies of trace elements in tufas are based on trace element data obtained via bulk sampling, dissolution and measurements made on a solution ICP-MS. The advancements of rapid, high-resolution analytical techniques, such as laser ablation inductively coupled plasma mass spectrometry (LA-ICP-MS), have made *in situ* trace element data on a high spatial resolution increasingly available. This has spurred studies of annual and sub-annual trace element variations in speleothems, allowing for high-

resolution, i.e., seasonal palaeoclimate reconstructions (Ayalon et al., 1999; Fairchild et al., 2000; Hellstrom and McCulloch, 2000; Treble et al., 2003; Desmarchelier et al., 2006; Johnson et al., 2006; Borsato et al., 2007; Fairchild and Treble, 2009; Orland et al., 2014; Belli et al., 2017). Others have applied the method to investigate speleothem growth processes (Treble et al., 2005), to facilitate U-series dating (Drysdale et al., 2012), or to generate a chronology based on element variations (Smith et al., 2009; Nagra et al., 2017; Ban et al., 2018; Carlson et al., 2018). Such an approach has not been robustly tested on tufa, and these studies provide a template for testing the applicability of LA-ICP-MS to tufas, which is the primary objective of this chapter.

5.2 Major and trace element contents in Ga-Mohana tufa and water

Here I report bulk XRD, LA-ICP-MS, and solution ICP-MS analysis of the Ga-Mohana tufas, as well as trace element concentrations in modern water samples. In Section 5.2.1, I summarise the bulk XRD results for a selection of tufa samples. In Section 5.2.2, I present high resolution trace element data from selected cascade, barrage, rim pool, terrace breccia and dome tufas (described in Chapter 4), measured using LA-ICP-MS. In section 5.2.3, I report trace element results from micro-drilled sub-samples from five tufa samples, GHN 1, 18-13, 18-14, 18-15 and 18-16, analysed via solution ICP-MS for comparison to the LA-ICP-MS data. In Section 5.2.4, I present trace element concentrations for a small set of modern waters. The data files for the results presented in this chapter are provided in Appendix II. The implications of these results are discussed in Section 5.3.

5.2.1 Mineral characterisation

A selection of samples analysed using bulk XRD confirm that the predominant mineral phase of the tufas is calcite, with minor dolomite present (Figure 5.2.1 and Table 5.2.1). Some of the samples have a minor component of quartz, e.g. sample 18-2 (Figure 5.2.1). These samples are from the terrace breccia and barrage morphologies where inclusions of lithic fragments were identified in the petrography section (Chapter 4), and so these non-carbonate phases would have contributed to this signal. Two of the samples, GCC04 and GCC06A, are from the dolomitic bedrock, i.e., Kogelbeen and Gamohaan Formations, and the mineralogy of these samples is confirmed to be calcite and dolomite (Figure 5.2.1).

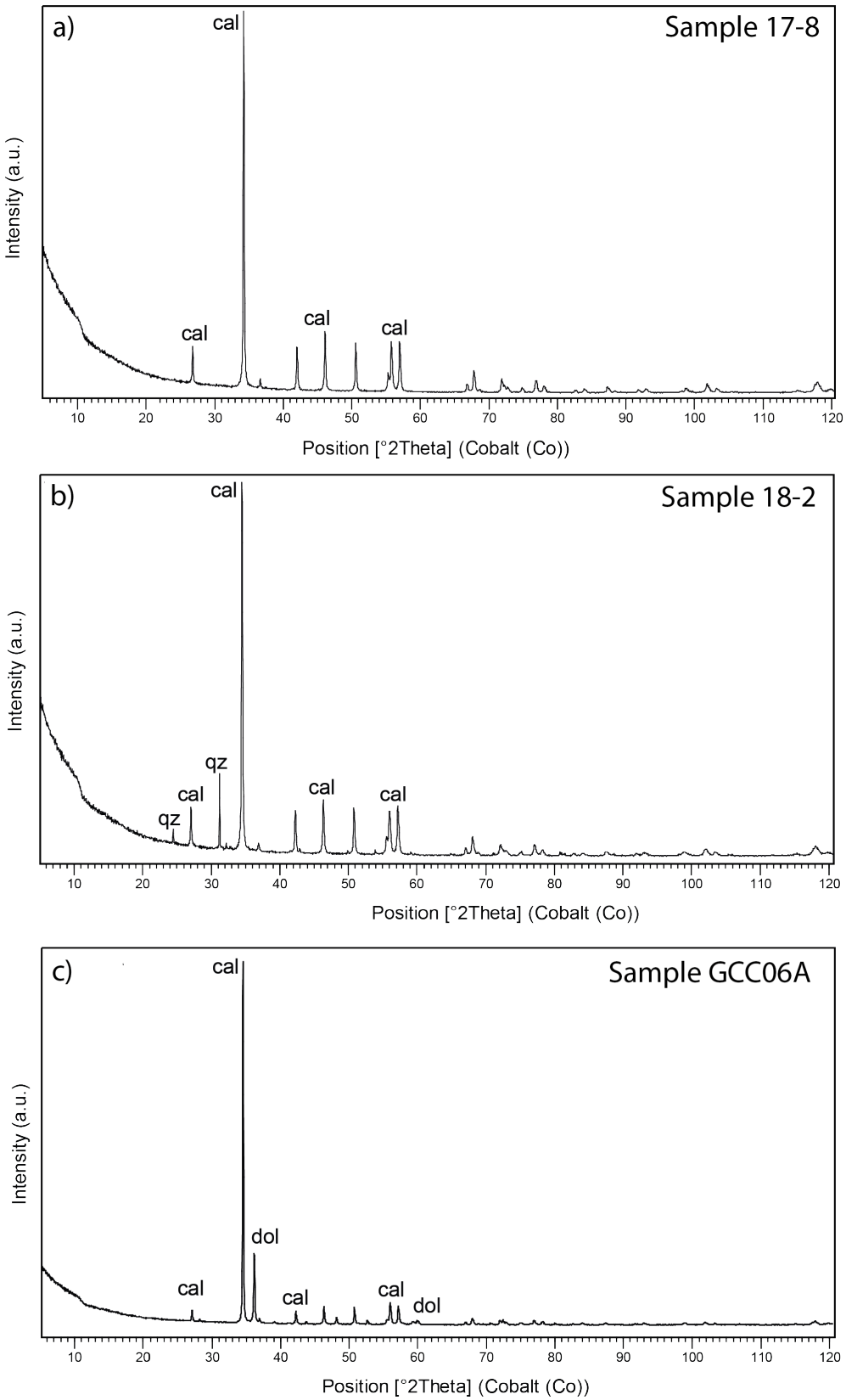

Figure 5.2.1 X-ray diffraction (XRD) patterns of representative tufa samples containing a) calcite with minor dolomite, and b) calcite, minor dolomite, and quartz. c) A bedrock sample from the Gamohaan Formation, shown for comparison.

Table 5.2.1. Summary of samples analysed using XRD for mineral identification

Sample no.	Macromorphology	Mineralogy
17-10	cascade	calcite
18-4	cascade	calcite
18-12	cascade	calcite
17-6	barrage	calcite and quartz
18-6	barrage	calcite and quartz
GHN1	rim pool	calcite
17-8	terrace breccia	calcite
18-2	terrace breccia	calcite and quartz
18-7	terrace breccia	calcite and quartz
GHS4	dome	calcite
GCC04	bedrock	calcite and dolomite
GCC06A	bedrock	calcite and dolomite

5.2.2 Trace element contents in Ga-Mohana tufa measured on LA-ICP-MS

Ten elements, Mg, Al, Mn, Fe, Zn, Sr, Ba, Pb, Th and U, were measured along several parallel transects through 16 tufa samples using LA-ICP-MS. Detailed descriptions of the analytical methods are reported in Chapter 3. Magnesium, Sr, Ba, and U are bedrock-derived, soluble elements that are sensitive to variations in hydrology. Particulate-colloidally bound elements (PCB) include Al, Fe, Mn, Pb, Zn and Th. Some of these elements can be incorporated into calcite in low amounts, e.g. incorporation of Fe and Mn, which is dependent on redox conditions. Since tufa generally forms under oxic conditions, Fe and Mn in calcite are generally low. As such, this suite of PCB elements in tufa are predominantly a proxy for detritus derived from silicates and clay minerals in soil and dust, and therefore most likely indicate ablation of non-carbonate phases.

The aim of this section is to describe the trace element content and inter-relationships for selected tufas from each of the morphologies described in Chapter 4. This will be used to identify any patterns that may relate to depositional processes, and to evaluate suitable material for U-Th dating (Chapter 6). The following representative samples

were selected: 18-4 and 18-16 (cascades), 17-6 (barrage), GHS-6 (rim-pool), 18-7 (terrace breccia), and 18-10 (dome). The full range, median, mean and standard deviation for each element measured in these samples is listed in Tables 5.2.2–5.2.7. Heat maps have been overlain on a scan of each sample to show the position of multiple transects and the relative trace element contents. For each sample, a single transect was selected for more detailed assessment. The criteria used for selection of the representative transect were minimal exaggerated/outlier peaks, and the lowest mean and standard deviation values for detrital-proxy elements (Al, Fe, Pb, Th). Trace element contents for the selected time series transects have been converted to sample length, with 0 mm marking the bottom of the samples. Notable variations and relationships between the elements are described. For each transect, a correlation matrix with cross-plots and their associated correlation coefficients, calculated after removal of extreme outlier values, is provided for each sample to complement the graphical observations. The results from the selected representative samples for each tufa type are presented below.

5.2.2.1 Cascade tufas

The stratigraphy of the cascade samples varies significantly, as described in Chapter 4, but they are broadly characterised by either crystalline material arranged in undulating and irregular layers, or a porous and poorly structured fabric, or a combination of these. Many of the cascade samples contain void spaces, and while care was taken to avoid large, visible holes in the sample, porous sections were sometimes impossible to avoid.

Sample 18-4

The concentration and stratigraphic distribution of elements measured in sample 18-4 along six parallel transects are shown overlaying the sample in Figure 5.2.2. The sample is composed of alternating dark and light undulating lamina of variable thickness. Some bands of dense, sub-mm laminae are grouped in the lower part of the sample, but most of the lamina are 0.5–1 mm thick, somewhat irregular, and discontinuous, and relatively porous (Figure 5.2.2).

Elevated Mg and Sr concentrations coincide with light-coloured laminae. In places, particularly toward the top of the sample, Mg and Sr are also elevated in darker laminae,

although enrichments are discontinuous along the layer (Figure 5.2.2). Magnesium and U maps are broadly similar. The Al, Fe, Ba, Pb and Th concentrations are generally low across the sample but display bands of enrichment, particularly in the top half of the sample where there appears to be a higher proportion of porosity. These enrichments occur in almost all the other elements as well (Figure 5.2.2).

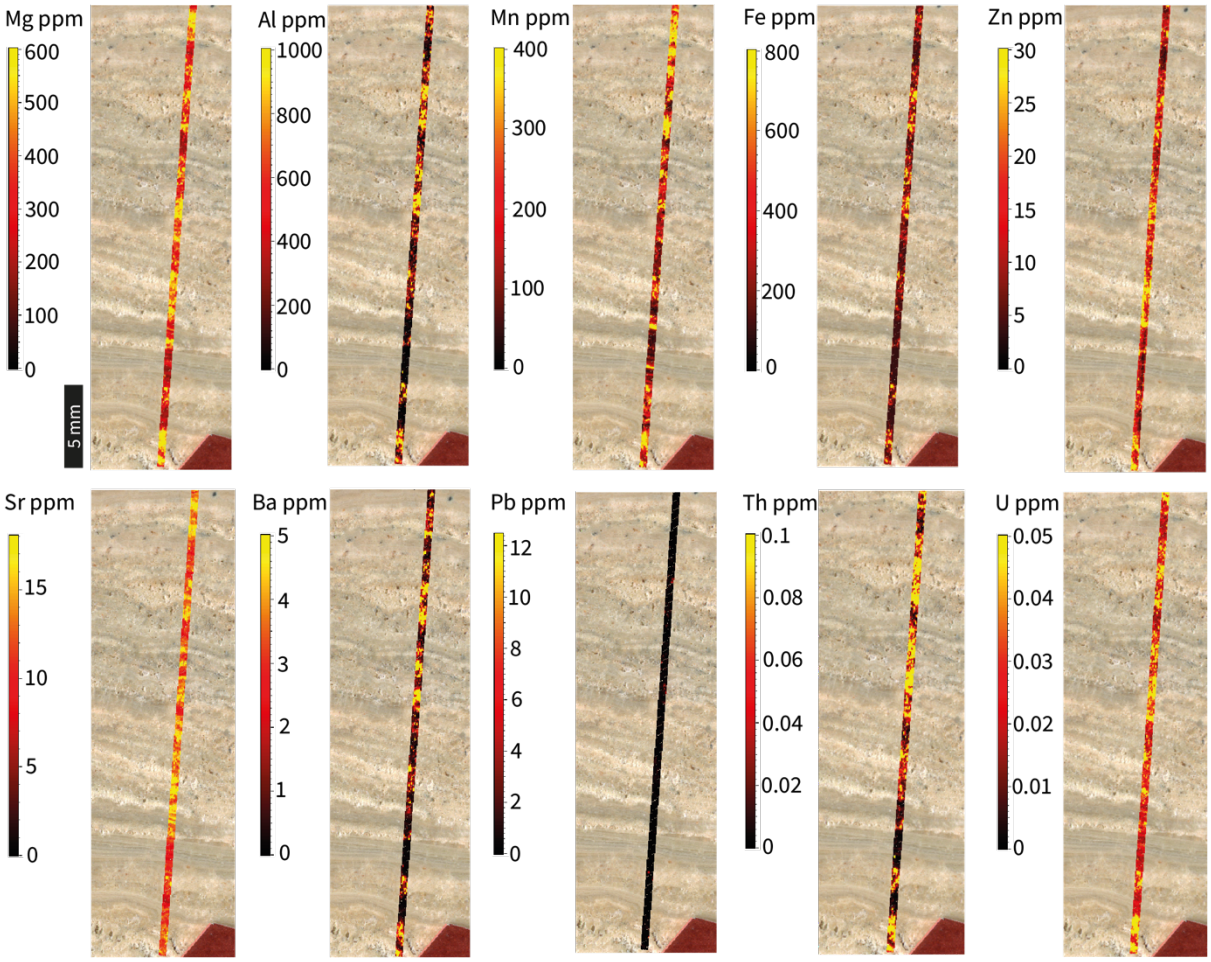

Figure 5.2.2 LA-ICP-MS trace element maps for sample 18-14 showing relative concentrations for each element measured along six parallel transects.

In the selected transect (transect 3; Figure 5.2.3), the elements all display a similar pattern in the first 5 mm of the sample, with a large single peak common to all elements. This may be due to the presence of an artefact, a clast contaminant, or high porosity in this region. Strontium shows the most variation across the sample, with a distinct increase to higher baseline values at ~6 mm. This variation is evident in Mg as well, which has a broadly similar pattern to Sr. Magnesium and Sr have a moderate but

statistically significant ($p < 0.001$) correlation coefficient ($r = 0.37$, $p < 0.001$; Figure 5.2.4). In profile, Mg and U have the most similar patterns with matching peaks and troughs. This is reflected in the strong positive correlation between them ($r = 0.74$, $p < 0.001$; Figure 5.2.4). Magnesium is moderately correlated with all other elements, except Mn (Figure 5.2.4).

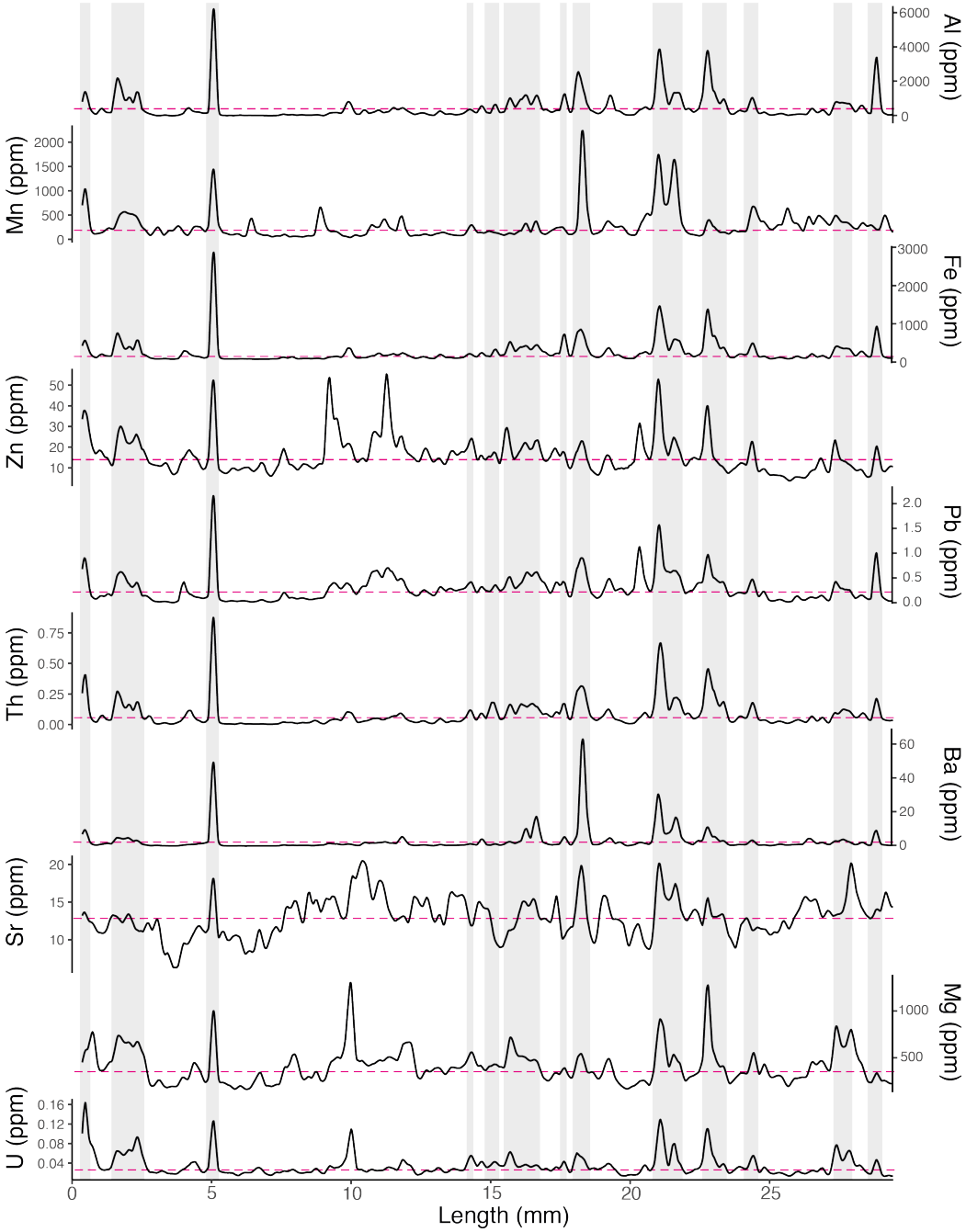

Figure 5.2.3 Stacked time series converted to sample length (where 0 mm = bottom of sample) for elements measured in sample 18-4 along transect 3. Data shown has been smoothed using a moving average of 13 points. The dotted pink horizontal lines

indicated the median concentration value for each element, and the grey vertical bars highlight Th-rich intervals, where Th > 0.1 ppm.

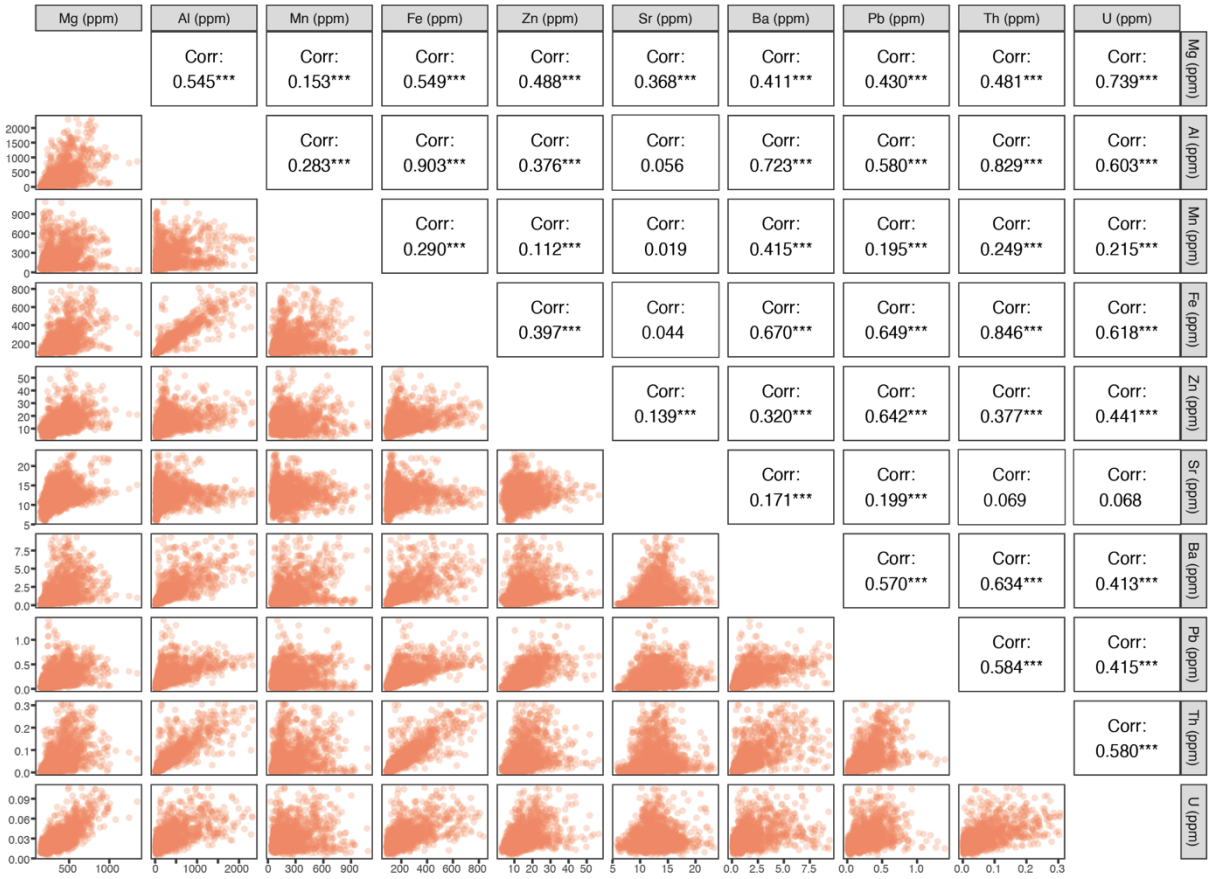

Figure 5.2.4 Correlation matrix showing cross-plots of each element and their corresponding Pearson correlation coefficients (r value) for sample 18-4-3. An outlier function of 4 times the interquartile range was applied to exclude extreme values that skew the plot. The stars next to the correlation coefficients are indications of the levels of significance related to the p-value i.e., the probability of observing a non-zero correlation coefficient in the sample data. A p-value of <0.05 is given one star (*), <0.01 is given two stars (**), and <0.001 is given three stars (***). No stars indicate no significant correlation.

Aside from the variability in the first 5 mm of the sample, Al, Fe, Ba and Th are relatively invariable until ~15 mm, with concentrations at or below their respective median values (Table 5.2.2; Figure 5.2.3). After ~15 mm, variability in these elements increases, and between 20–25 mm, several large peaks occur with concentrations of up to 4–10 times greater than their median values. The concentrations of these elements flatten out after

~25 mm, with the exception of a moderate peak at the top of the sample, which again occurs across almost all elements. Positive correlations exist between Al, Fe, Ba, Pb, Th and U (Figure 5.2.4). Lead and Zn have similar trends and cross-plots show a positive correlation ($r = 0.64$, $p < 0.001$; Figure 5.2.4). Manganese is moderately correlated with Ba ($r = 0.42$, $p < 0.001$; Figure 5.2.4), and some similarity in their profiles is evident, particularly between 15–25 mm (Figure 5.2.3).

Table 5.2.2 Summary statistics for each element measured across all six transects in cascade sample 18-4 (left) and for selected transect (right). Concentrations in ppm.

Cascade tufa	Min	Max	Median	Mean	1σ	Selected transect	Min	Max	Median	Mean	1σ
18-4						**18-4-3**					
Mg	127	3750	370	420	246	**Mg**	141	2202	374	418	228
Al	0.6	17667	219	547	1092	**Al**	7.60	16569	213	567	1161
Mn	17.4	24240	182	312	710	**Mn**	25.8	4657	192	305	421
Fe	76.8	24339	173	320	672	**Fe**	83.4	7148	174	295	440
Zn	1.8	473	14.3	17.8	14.6	**Zn**	2.90	201	13.7	17.0	12.9
Sr	5.0	183	12.8	13.3	5.02	**Sr**	5.80	34.0	12.8	13.2	3.21
Ba	<0.0007	589	1.01	4.43	18.6	**Ba**	<0.0007	152	1.11	3.86	11.6
Pb	<lld	56.5	0.221	0.371	0.830	**Pb**	<lld	6.51	0.221	0.333	0.431
Th	<0.0003	25.3	0.044	0.110	0.542	**Th**	<0.0003	6.95	0.045	0.097	0.228
U	<lld	27.6	0.028	0.040	0.259	**U**	<lld	0.458	0.028	0.037	0.034

*<lld = less than lower limit of detection

Sample 18-16

The concentration and stratigraphic distribution of elements measured in sample 18-16 along six parallel transects are shown in Figure 5.2.5. The sample is relatively unstructured and consists of creamy-brown crystalline calcite, punctuated with thin, undulating, orange-brown lamina and black splotchy oxide-rich layers. Rounded to sub-angular void spaces (~0.5 mm in diameter) tend to be associated with these layers, but also occur irregularly across the sample.

The Mg and Sr concentrations do not change significantly across the sample with elevated concentrations of Mg associated with oxide-rich layers or void spaces, while changes in Sr concentrations are less clearly associated with stratigraphic features (Figure 5.2.5). Like Mg, low U is associated with featureless, crystalline sections of the sample, and elevated concentrations coincide with void spaces and thin orange-brown lamina. Aluminium, Mn, Zn, Ba, Pb and Th are all low, with sharply elevated

concentrations, also associated with the thin orange-brown lamina, oxide-rich splotches, and void spaces. Iron is relatively consistent across the sample (Figure 5.2.5).

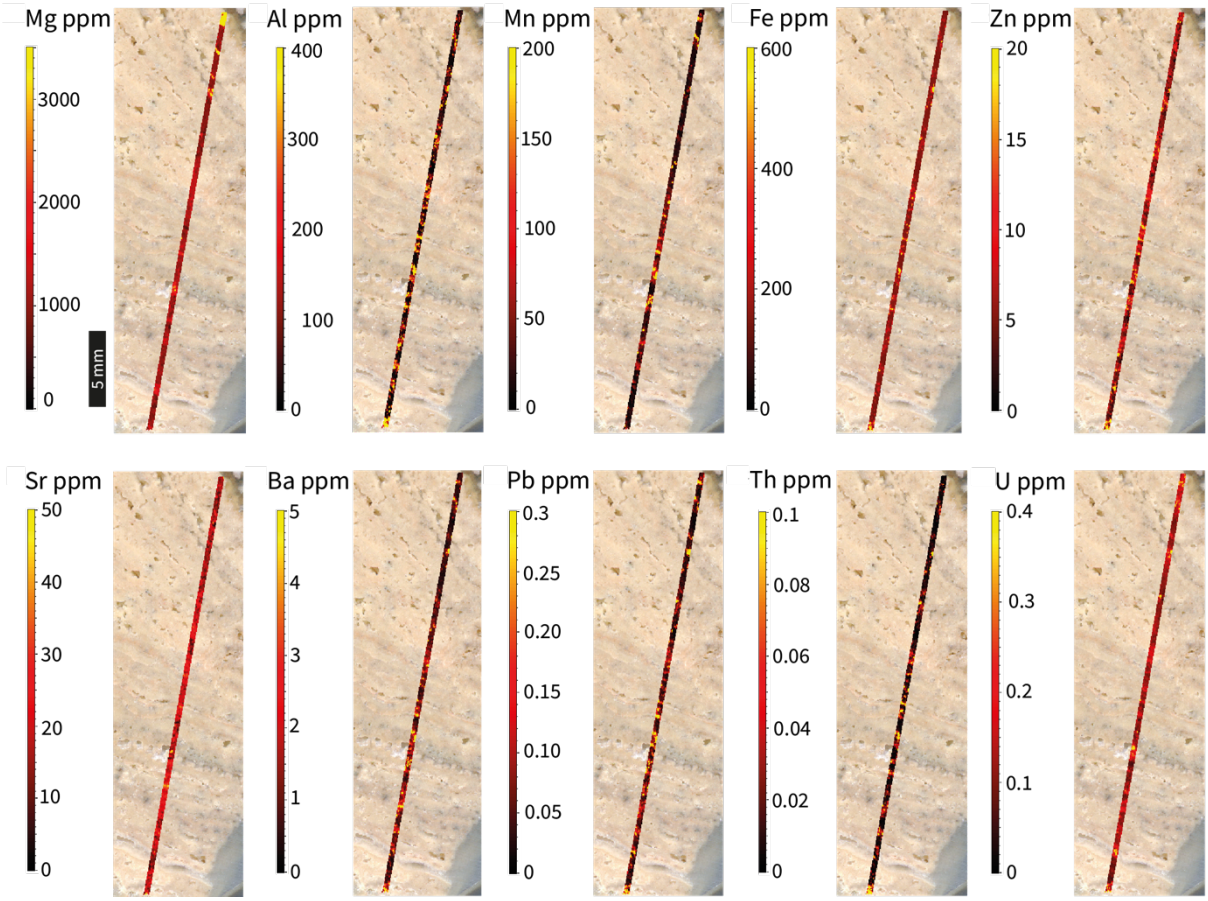

Figure 5.2.5 LA-ICP-MS trace element maps for sample 18-16 showing relative concentrations for each element measured along six parallel transects.

The Mg and U concentrations along the selected transect (transect 2, Figure 5.2.6) have near-identical profiles with several synchronous peaks and a positive correlation ($r = 0.50$, $p < 0.001$; Figure 5.2.7). Apart from these peaks, Mg is relatively consistent around its median value of 1088 ppm (Table 5.2.3; Figure 5.2.6). Strontium has greater variability with high frequency oscillations about its median, ~20 ppm (Table 5.2.3; Figure 5.2.6). While it does not clearly co-vary with any of the other element profiles, it is moderately correlated with Ba ($r = 0.35$, $p < 0.001$, Figure 5.2.7).

Aluminium, Fe, and Th concentrations are relatively low across the sample, with values generally at or below their respective median values, except in a few instances in which

these elements display synchronous peaks up to 4-10 times their medians (Table 5.2.3; Figure 5.2.6). These elements are also strongly correlated (Figure 5.2.7). The Mn profile has several large peaks that correspond with peaks in Ba and Pb, and Mn is strongly correlated with these elements ($r = 0.68$ and 0.52, respectively, $p < 0.001$; Figure 5.2.7). Lead and Zn display somewhat similar profiles, although in several instances one of them has a large peak while the other does not, and they are moderately correlated ($r = 0.36$, $p < 0.001$, Figure 5.2.7).

Table 5.2.3 Summary statistics for each element measured across all six transects in cascade sample 18-16 (left) and for selected transect (right). Concentrations in ppm.

Cascade tufa	Min	Max	Median	Mean	1σ	Selected transect	Min	Max	Median	Mean	1σ
18-16						**18-16-2**					
Mg	350	254910	1084	2178	8699	**Mg**	471	194377	1088	2034	8923
Al	0.9	120122	59.0	228	2108	**Al**	4	8095	57.6	193	507
Mn	0.7	5404	26.8	68	242	**Mn**	2.1	1267	27.2	49.5	88.0
Fe	41.7	62332	162	240	1316	**Fe**	43.5	2651	163	200	148
Zn	0.3	301	6.37	7.81	8.39	**Zn**	0.9	53.1	6.57	7.88	5.23
Sr	2.2	102	19.2	19.6	6.82	**Sr**	4.3	55.0	19.3	19.7	6.84
Ba	0.1	251	0.994	1.80	6.40	**Ba**	0.2	26.2	1.01	1.55	2.01
Pb	<lld	50.5	0.057	0.139	0.990	**Pb**	<lld	4.69	0.059	0.103	0.17
Th	<0.0003	11.2	0.011	0.033	0.237	**Th**	<0.0003	1.27	0.011	0.029	0.065
U	<lld	30.3	0.127	0.149	0.295	**U**	<lld	2.03	0.129	0.149	0.083

*<lld = less than lower limit of detection

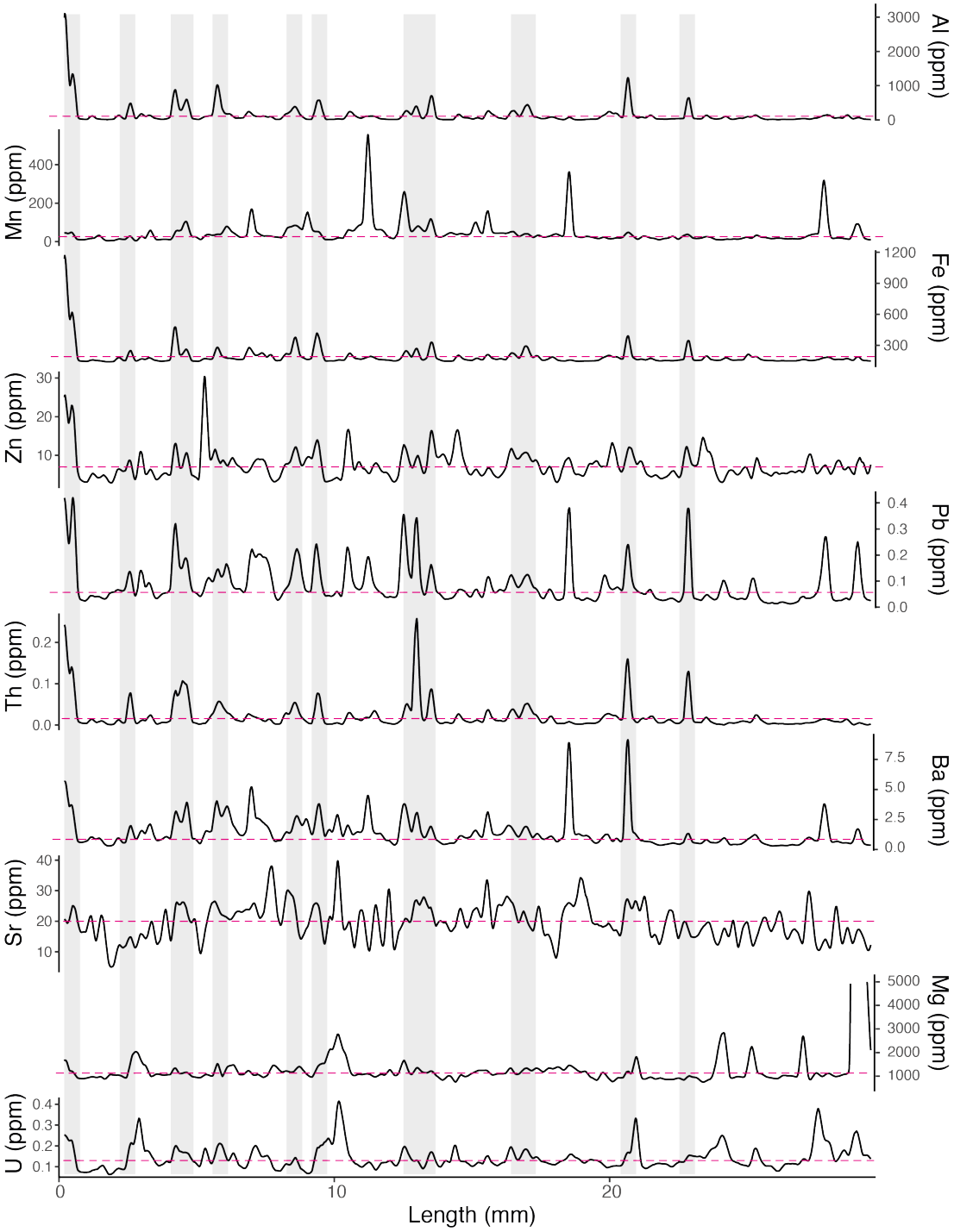

Figure 5.2.6 Stacked time series converted to sample length (where 0 mm = bottom of sample) for elements measured in sample 18-16 along transect 2. Data shown has been smoothed using a moving average of 13 points. The dotted pink horizontal lines indicated the median concentration value for each element, and the grey vertical bars highlight Th-rich intervals, where Th > 0.02 ppm.

Figure 5.2.7 Correlation matrix showing cross-plots of each element and their corresponding Pearson correlation coefficients (r value) for sample 18-16-2. An outlier function of 8 times the interquartile range was applied to exclude extreme values that skew the plots and correlation values. The stars next to the correlation coefficients are indications of the levels of significance related to the p-value (i.e., the probability of observing a non-zero correlation coefficient in the sample data. A p-value of <0.05 is given one star (*), <0.01 is given two stars (**), and <0.001 is given three stars (***). No stars indicate no significant correlation.

5.2.2.2 Barrage tufa

Barrage tufas are characterised by irregular, crenulated and high-frequency layering. They are composed of laminated micrite with micro- to meso-scale oxide and detrital inclusions (Chapter 4).

Sample 17-6

Twelve parallel transects were conducted on barrage sample 17-6, which consists of alternations of light-, orange-, and dark-brown, mm-scale lamina (Figure 5.2.8). Compositional heat maps illustrate the relative concentrations and stratigraphic distribution of each element measured along the transects (Figure 5.2.8).

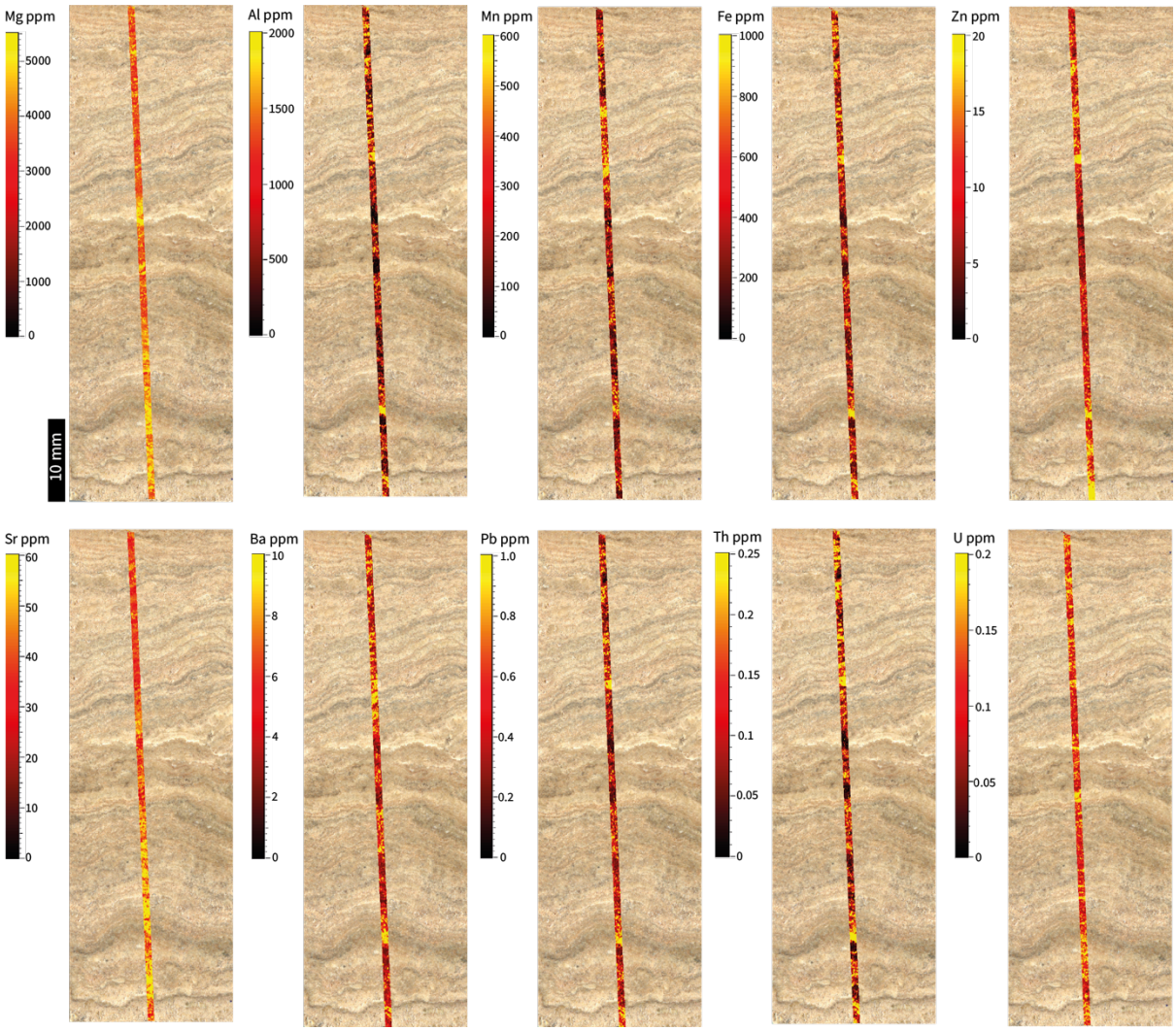

Figure 5.2.8 LA-ICP-MS trace element maps for sample 17-6 showing relative concentrations for each element measured along twelve parallel transects.

The Mg and Sr concentrations are not clearly associated with particular lamina, although in some parts of the sample, elevated Mg coincides with light lamina, and the opposite is observed in Sr (Figure 5.2.8). The Mg and Sr are higher in the bottom half of the sample and show an overall decrease toward the top of the sample. Elevated U coincides with light lamina, similar to Mg. Aluminium, Mn, Fe, Zn, Pb and Th all have similar profiles (Figure 5.2.8). Low concentrations in these elements generally coincide with light-coloured lamina, and higher concentrations are associated with dark lamina. This relationship is most apparent for Al, Fe, Pb and Th. The maps have a mottled appearance along several of the layers, suggesting some lateral heterogeneity on a micro-scale (Figure 5.2.8).

On closer inspection of element variability along the selected transect (transect 7, Figure 5.2.9), both Mg and Sr concentrations are elevated above their median values of ~4000 ppm and ~42 ppm, respectively, for the first 22 mm. After this point, Mg oscillates below ~4000 ppm with the exception of several sharp peaks that exceed ~5000 ppm (mean + 1σ), and Sr oscillates between ~30 – 50 ppm (mean +/- 1σ) with several peaks that exceed ~50 ppm. There is no correlation between Mg and Sr ($r = 0.18$, $p < 0.001$, Figure 5.2.10), but overall, both elements decrease along the length of the sample (Figure 5.2.9).

Peaks in U are aligned with several peaks in Mg, and the pattern of the U and Mg profiles are similar, particularly in the first ~35 mm of the sample. There is also a moderate correlation between them ($r = 0.49$, $p < 0.001$; Figure 5.2.10). There is a moderate anticorrelation between Sr and U ($r = -0.28$, $p < 0.001$; Figure 5.2.10). This relationship is not clear in their profiles, but several U peaks can be matched with Sr troughs, and vice versa (although this is not a consistent rule, i.e. some peaks match peaks; Figure 5.2.9).

Table 5.2.4 Summary statistics for each element measured across all 12 transects barrage sample 17-6 (left) and for selected transect (right). Concentrations in ppm.

Barrage tufa	Min	Max	Median	Mean	1σ	Selected transect	Min	Max	Median	Mean	1σ
17-6						**17-6-7**					
Mg	1521	57012	3998	4223	1150	**Mg**	1755	13857	4002	4218	1031
Al	21.3	53174	588	925	1226	**Al**	31.3	9202	616	869	861
Mn	8.00	11932	205	318	432	**Mn**	14.7	6507	203	305	404
Fe	67.2	67262	349	554	1063	**Fe**	80.1	8297	369	492	495
Zn	0.70	1045	9.32	12.5	11.4	**Zn**	1.10	105	9.17	12.1	10.1
Sr	11.6	837	42.4	43.5	12.8	**Sr**	11.6	82.1	42.1	43.1	10.7
Ba	0.60	899	4.26	7.34	18.0	**Ba**	0.600	169	4.35	6.38	9.13
Pb	<lld	52.4	0.370	0.530	0.709	**Pb**	<lld	7.65	0.363	0.498	0.528
Th	<0.0003	28.8	0.099	0.163	0.447	**Th**	<0.0003	1.21	0.101	0.138	0.133
U	<lld	10.8	0.112	0.131	0.154	**U**	<lld	0.654	0.111	0.126	0.065

*<lld = less than lower limit of detection

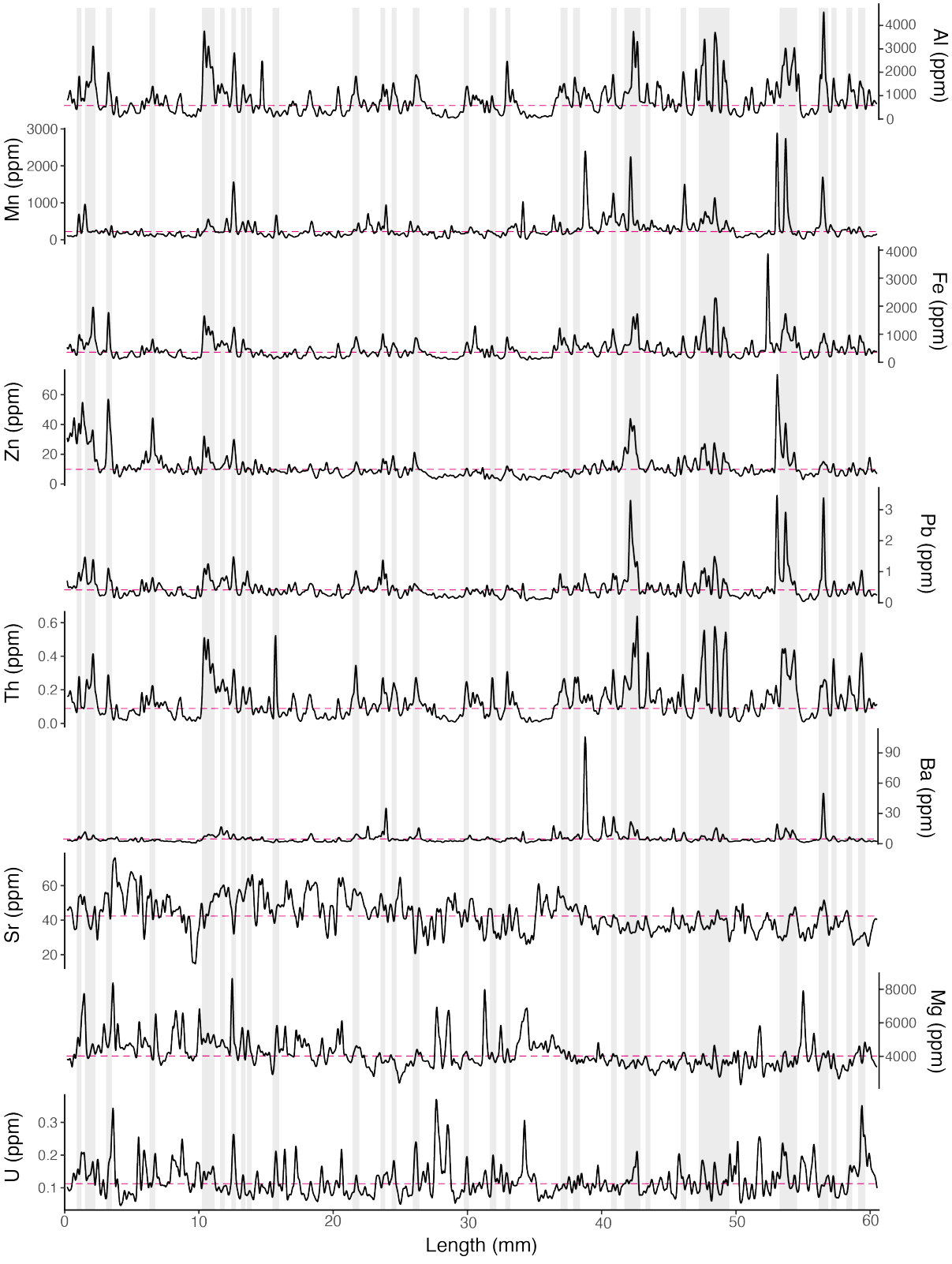

Figure 5.2.9 Stacked time series converted to sample length (where 0 mm = bottom of sample) for elements measured in sample 17-6 along transect 7. Data shown has been smoothed using a moving average of 13 points. The dotted pink horizontal lines

indicated the median concentration value for each element, and the grey vertical bars highlight Th-rich intervals, where Th > 0.2 ppm.

The Al, Fe, Pb, Zn and Th profiles all have a similar pattern with synchronous peaks that are between 4–10 times their mean values, and each of these elements have moderate to strong positive correlations with each other (Figure 5.2.10). The strongest of these is between Al and Fe and Al and Th, with r values of 0.89 ($p < 0.001$) and 0.83 ($p < 0.001$), respectively (Figure 5.2.10). Several peaks in the Mn profile are also aligned with some of the peaks in the aforementioned profiles, but overall the Mn profile has fewer large peaks, some of which correspond with peaks in Ba. This relationship between Mn and Ba is indicated with a strong correlation ($r = 0.59$, $p < 0.001$; Figure 5.2.10). Manganese is also strongly correlated with Pb ($r = 0.58$, $p < 0.001$; Figure 5.2.10) and moderately correlated with Al, Fe, Zn and Th. Zinc is moderately correlated with Al and Th, and most strongly correlated with Fe and Pb ($r = 0.56$ and 0.66, respectively, $p < 0.001$; Figure 5.2.10).

Figure 5.2.10 Correlation matrix showing cross-plots of each element against the other and their corresponding Pearson correlation coefficients (r value) for sample 17-6-7. The stars next to the correlation coefficients are indications of the levels of significance related to the p-value (i.e., the probability of observing a non-zero correlation coefficient in the sample data. A p-value of <0.001 is given three stars (***), and no stars indicate no significant correlation.

5.2.2.3 Rim-pool tufa

The rim-pool samples are characterised by texturally homogenous domains with cm-scale layering, mostly signalled by a colour change (e.g. Figure 5.10). Broad, gradual changes in the trace element concentrations generally reflect the layering.

Sample GHS-6

Element concentrations and their distributions measured in six parallel transects across sample GHS-6 are presented in Figure 5.2.11. The sample is predominantly composed of dense, creamy-brown micrite, interrupted by unusual features which separate layers with subtle differences. Based on these, the sample is divided into five sections: 1)

lowermost section with a thin, orange-brown layer bordered by splotchy black and brown inclusion- and oxide-rich features; 2) dense, creamy brown micrite inter-mingled with an irregular light /white feature; 3) smooth, homogenous creamy-brown micrite; 4) grainy micrite with sub-mm tufa fragments; 5) dense, homogenous, brown-grey micrite. The boundaries between these sections are gradational (sections 1–2 and 2–3), undulating (sections 3–4), and sharp (sections 4–5).

Magnesium concentration is variable and relatively low in sections 1 and 2, whereas it is relatively elevated and consistent in sections 3 and 4 (Figure 5.2.11). Peak Mg concentrations occur across the boundary between sections 2 and 3. An abrupt decrease in Mg occurs across the boundary into section 5, where it remains low. Strontium is consistently low across the sample, except in section 2, where it is significantly elevated in association with the white feature. This feature is also enriched in U, and to some extent in Zn and Ba (Figure 5.2.11). Aluminium, Fe, Mn, Zn, Ba, Pb and Th are all low across the sample, with the exception of elevated concentrations in sections 1 and 4 (Figure 5.2.11).

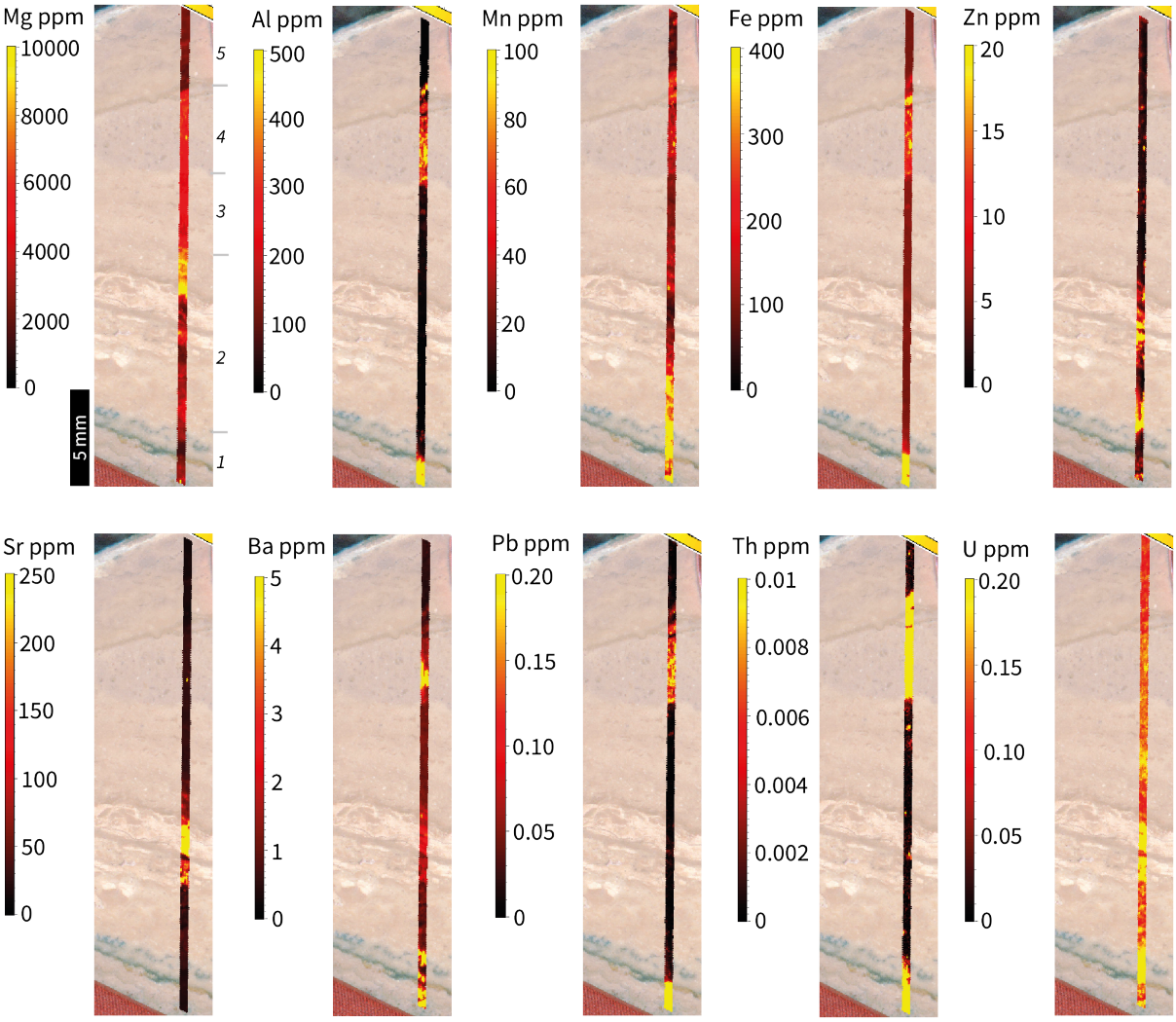

Figure 5.2.11 LA-ICP-MS trace element maps for sample GHS-6 showing relative concentrations for each element measured along six parallel transects.

Element concentrations measured along selected transect 6 are plotted in Figure 5.2.12. Magnesium and Sr concentration profiles are broadly similar, and their overall correlation co-efficient indicates a weak but statistically significant correlation ($r = 0.26$, $p < 0.001$; Figure 5.2.13). Magnesium and Sr concentrations are below their median values in section 1 and follow a similar pattern across the boundary into section 2. Mid-way through section 2, Mg and Sr concentrations are elevated, although Sr increases more rapidly and is characterised by broad peaks and a brief trough, and Mg enrichment lags behind Sr. There is no correlation between Mg and Sr in this section ($r = 0.095$, $p < 0.05$).

Magnesium and Sr values decrease across the boundary into section 3, and they remain relatively constant near their respective median values. In section 4, Mg concentration is elevated above its median value, but is relatively constant with only small, high-frequency oscillations, which are also apparent in Sr, but to a lesser extent. The correlation between Mg and Sr is strongest in sections 3 and 4 ($r = 0.68$ and 0.89, respectively, $p < 0.001$; Figure 5.2.13). Magnesium and Sr concentrations decrease abruptly to near-minimum values across the boundary into section 5. Uranium displays a fairly similar concentration profile to Sr with a moderate to strong correlation in sections 2 and 4 ($r = 0.52$ and 0.56, $p < 0.001$; Figure 5.2.13). Overall, U is anti-correlated with Mg and this relationship is strongest in sections 1 and 3 ($r = -0.72$ and -0.35, $p < 0.001$; Figure 5.2.13), whereas in section 4 they have a moderately positive correlation ($r = 0.50$, $p < 0.001$; Figure 5.2.13).

Table 5.2.5 Summary statistics for each element measured across all 12 transects in rim-pool sample GHS6 (left) and for selected transect (right). Concentrations in ppm.

Rim tufa	**Min**	**Max**	**Median**	**Mean**	**1σ**	**Selected transect**	**Min**	**Max**	**Median**	**Mean**	**1σ**
GHS6						**GHS6-6**					
Mg	1249	16511	3938	4244	2014	Mg	1272	10251	4147	4205	1951
Al	1	75005	24.7	319	1983	Al	1.1	12799	24.5	235	948
Mn	7.2	13152	34.3	106	460	Mn	9.5	13152	34.4	152	812
Fe	70.3	63005	106	254	1182	Fe	78.3	4566	106	206	372
Zn	0	93.8	2.93	6.18	8.92	Zn	0.4	87.8	2.61	7.34	12.1
Sr	11.3	1053	28.7	59.0	91.4	Sr	11.8	570	28.2	59.3	94.8
Ba	0.2	3873	1.22	5.3.1	83.7	Ba	0.3	235	1.19	3.48	14.0
Pb	0	9.88	0.012	0.086	0.30	Pb	0	2.41	0.013	0.078	0.21
Th	0	127	0.001	0.053	1.33	Th	0	1.11	0.001	0.031	0.108
U	0	59.5	0.144	0.169	0.63	U	0.1	0.598	0.143	0.155	0.052

Aluminium, Mn, Fe, Ba, Pb, and Th are at their maximum concentrations in section 1, and then decrease to concentrations at or below their median values in section 2, except Mn which remains elevated at the start of section 2, and then gradually decreases. Aluminium, and to some extent Ba, displays a gradual increase across section 2. Barium concentrations are generally low across this sample, except for a few large peaks in section 1 and section 4, and do not closely resemble any of the other element profiles. However, Ba is strongly correlated with Mg in sections 1 and 4, and with Sr in sections

2 and 4 (Figure 5.2.13). Lead and Th concentrations are predominantly below their median values, and frequently below detection, in sections 2, 3 and 5 (Figure 5.2.12). Aluminium, Fe, Pb and Th all display a broad increase above their respective median values across section 4, and then return to below-median values in section 5. Iron remains fairly constant below its median value across all sections, except section 4, and is correlated with Al across all sections, except section 5. Zinc has a singular pattern, with greatest variability in section 2 (Figure 5.2.12).

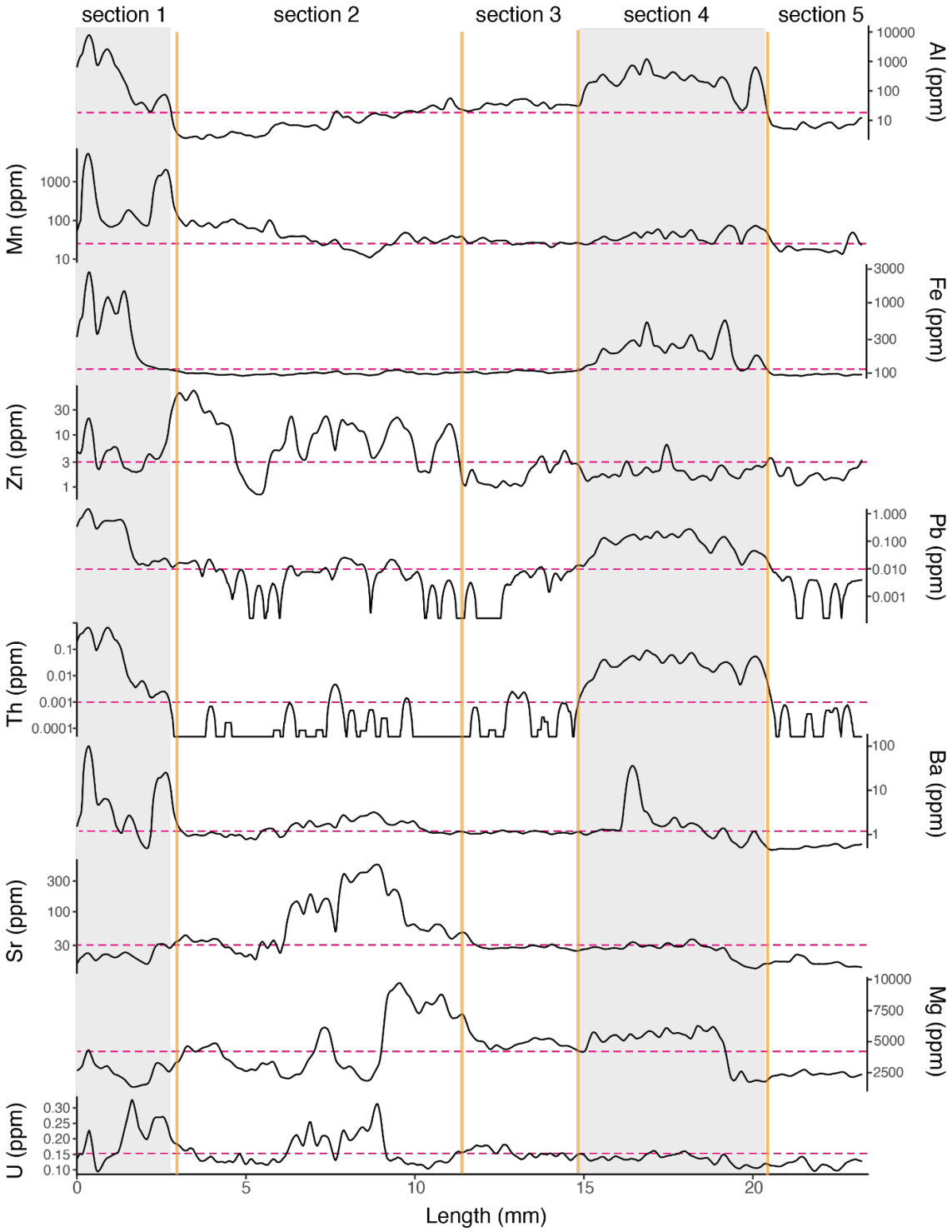

Figure 5.2.12 Stacked time series converted to sample length (where 0 mm = bottom of sample) for elements measured in sample GHS-6 along transect 6. Data shown has been smoothed using a moving average of 13 points. The dotted pink horizontal lines indicated the median concentration value for each element, and the grey vertical bars highlight Th-rich intervals, where Th > 0.002 ppm. All element axes, except Mg and U, are expressed on a logarithmic scale.

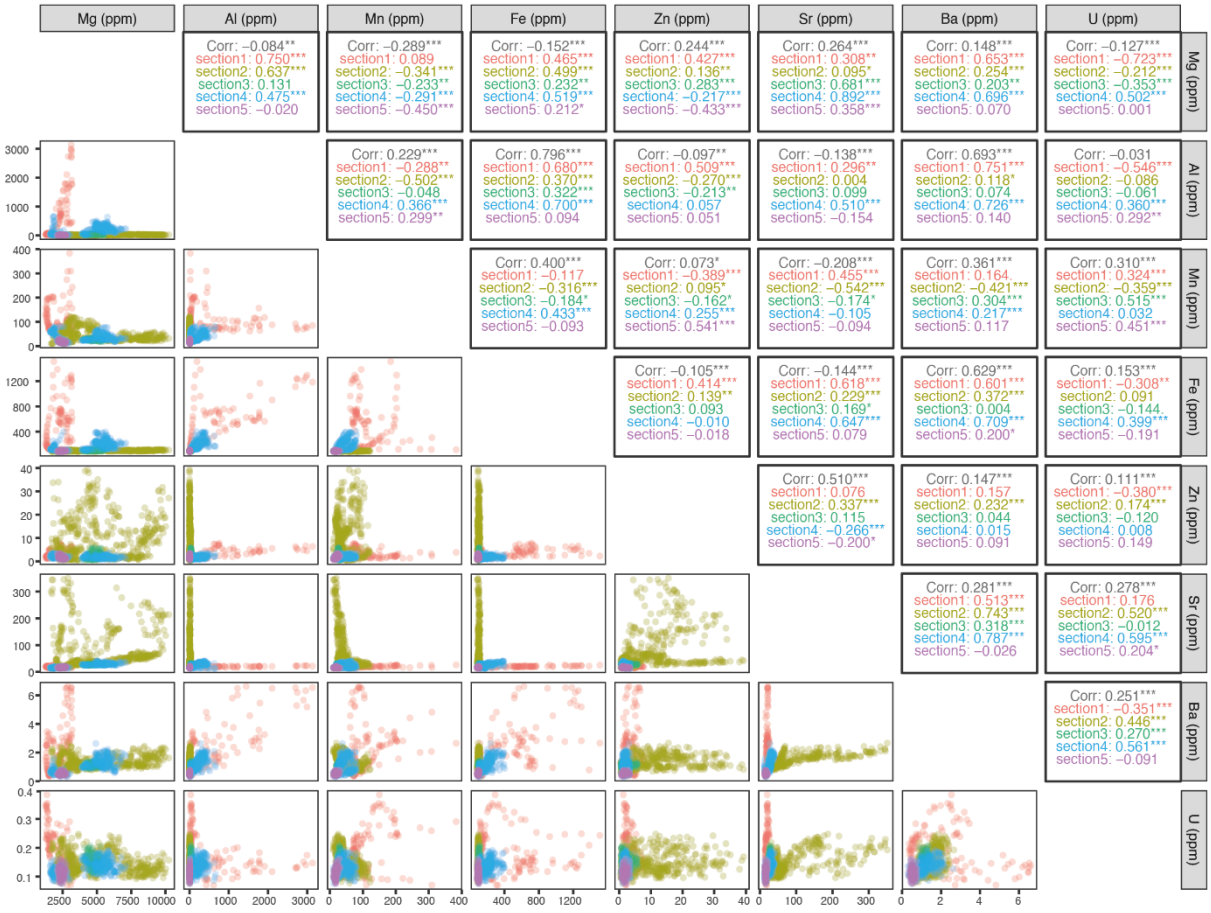

Figure 5.2.13 Correlation matrix showing cross-plots of each element against the other and their corresponding Pearson correlation coefficients (r value) for sample GHS-6-6. The data are broken into sections due to the variation in behaviour across the sample (Figure 5.2.12). The stars next to the correlation coefficients are indications of the levels of significance related to the p-value (i.e., the probability of observing a non-zero correlation coefficient in the sample data. A p-value of <0.05 is given one star (*), <0.01 is given two stars (**), and <0.001 is given three stars (***). No stars indicate no significant correlation. A function of 1.5 x IQR was applied separately to each section of this sample to remove any extreme values. Pb and Th are not included because their values are below detection for a large part of the sample, which obscured the data.

5.2.2.4 Terrace breccia tufa

Sample 18-7

Sample 18-7 is a terrace breccia, characterised by three distinct sections with large detrital clasts visible in the first two sections, and dense, creamy-brown micrite in the third (Figure 5.2.14). The trace element data have been divided into three sections, based on these distinctions, and are referred to as sections 1–3 (Figure 5.2.14). Elements were measured along six parallel transects, and their relative concentrations and distribution is shown in Figure 5.2.14.

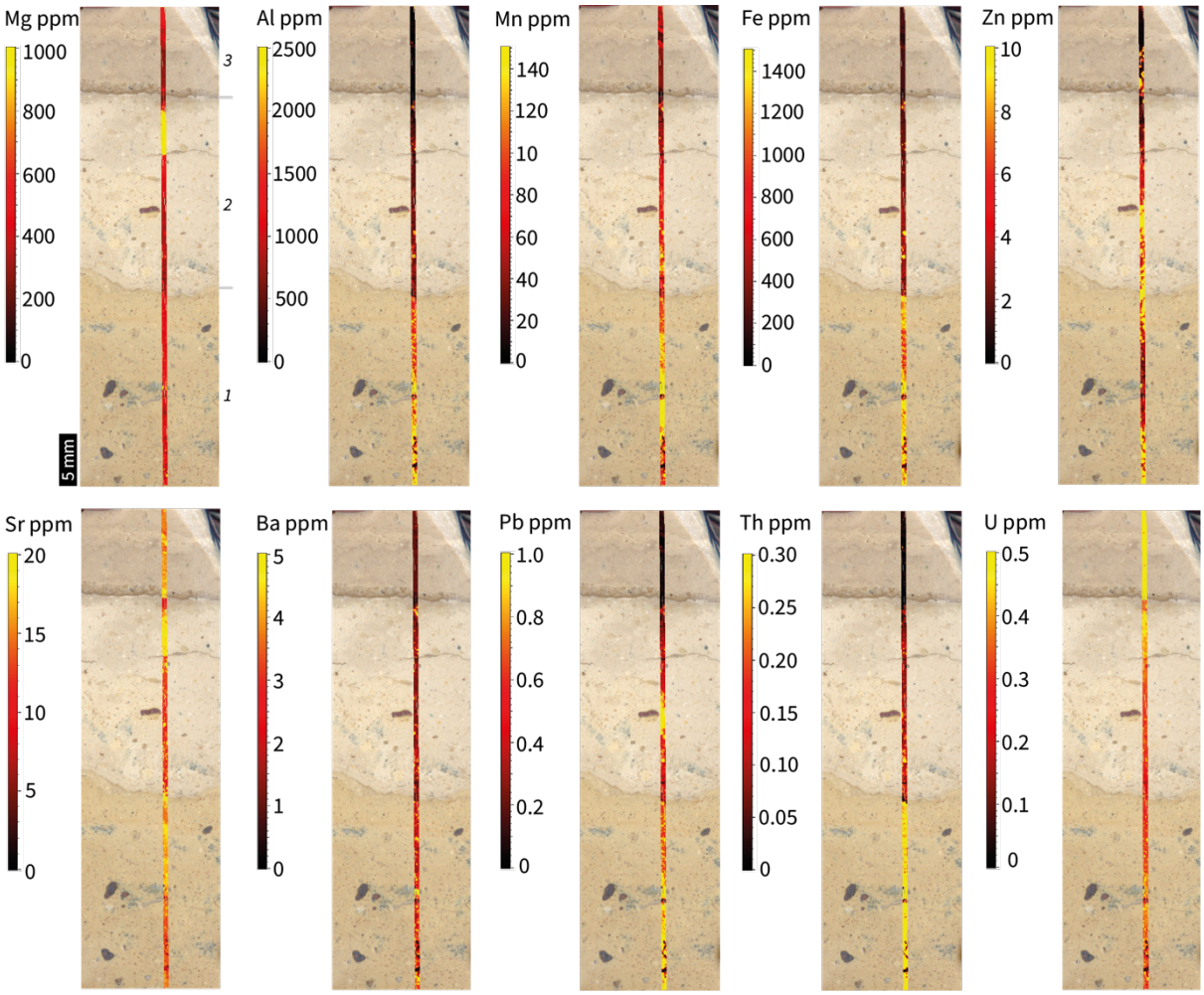

Figure 5.2.14 LA-ICP-MS trace element maps for sample 18-7 showing relative concentrations for each element measured along six parallel transects. Italicised numbers indicate the sections referred to in the text.

Magnesium is largely invariable across the sample with one exception, where elevated Mg occurs alongside elevated Sr toward the top of section 2 (Figure 5.2.14). Uranium concentration is low to moderate across the first two sections, with an increase in the

top portion of section 2, and at a maximum in section 3. Aluminium, Fe, Pb, Ba, and Th concentrations are highest in section 1, reflecting the visibly high proportion of detrital concentrations. These elements are lower in section 2, and section 3 contains little to no Al, Fe, Pb, and Th. Manganese and Zn concentrations follow a different pattern, with changes occurring within sections, rather than across them. Manganese and Zn also appear to be anti-phased, changing in opposite directions at the same points in the sample (Figure 5.2.14).

Element concentrations measured along selected transect 3 are plotted in Figure 5.2.15. Uranium concentrations in sections 1 and 2 are generally similar to the median U value for this transect, whereas there is a notable increase at the boundary between sections 2 and 3. Aluminium, Pb, Th and Fe show high amplitude variation in the first ~18 mm of the sample (section 1), with overall high concentrations in this section consistent with the presence of visible detrital inclusions. Manganese and Ba are relatively low and consistent around their median values, except for a few large spikes that predominantly occur in section 1 (Figure 5.2.15).

Aluminium, Mn, Fe, Ba, Pb and Th are all correlated across the three sections (Figure 5.2.16). Magnesium is strongly correlated with these elements in sections 1 and 2, and in section 3 they are moderately correlated (Figure 5.2.16). Strontium and U correlate with Mg in section 2 ($r = 0.76$ and 0.49, respectively, $p < 0.001$), whereas Sr and U are moderately correlated with each other in sections 1 and 2, and strongly correlated in section 3 ($r = 0.69$, $p < 0.001$; Figure 5.2.16). Strontium and U are moderately to strongly anti-correlated with PCB elements in section 3 (Figure 5.2.16).

Table 5.2.6 Summary statistics for each element across all six transects in terrace breccia sample 18-7 (left) and for the selected transect (right). Concentrations in ppm.

Terrace breccia	Min	Max	Median	Mean	1σ	Selected transect	Min	Max	Median	Mean	1σ
18-7						**18-7-3**					
Mg	170	2234	438	481	214	**Mg**	197	1368	440	477	206
Al	3.10	54302	631	1140	1726	**Al**	6	16623	589	1079	1210
Mn	2.70	9038	78.6	121	368	**Mn**	3	1905	74.7	95.5	102
Fe	97.3	27836	454	779	836	**Fe**	102	4198	432	740	646
Zn	<0.025	346	4.47	6.74	7.27	**Zn**	<0.025	70.4	3.93	6.11	6.53
Sr	3.70	1119	14.9	15.3	9.20	**Sr**	3.8	118	14.8	15.0	3.88
Ba	<0.0007	767	1.54	2.96	14.7	**Ba**	0.1	91.9	1.48	2.49	5.25
Pb	<lld	24.4	0.549	0.605	0.663	**Pb**	<lld	3.66	0.521	0.558	0.441
Th	<0.0003	11.9	0.128	0.223	0.285	**Th**	<0.0003	3.53	0.116	0.212	0.246
U	<lld	142	0.354	0.417	1.30	**U**	<lld	13.1	0.35	0.388	0.281

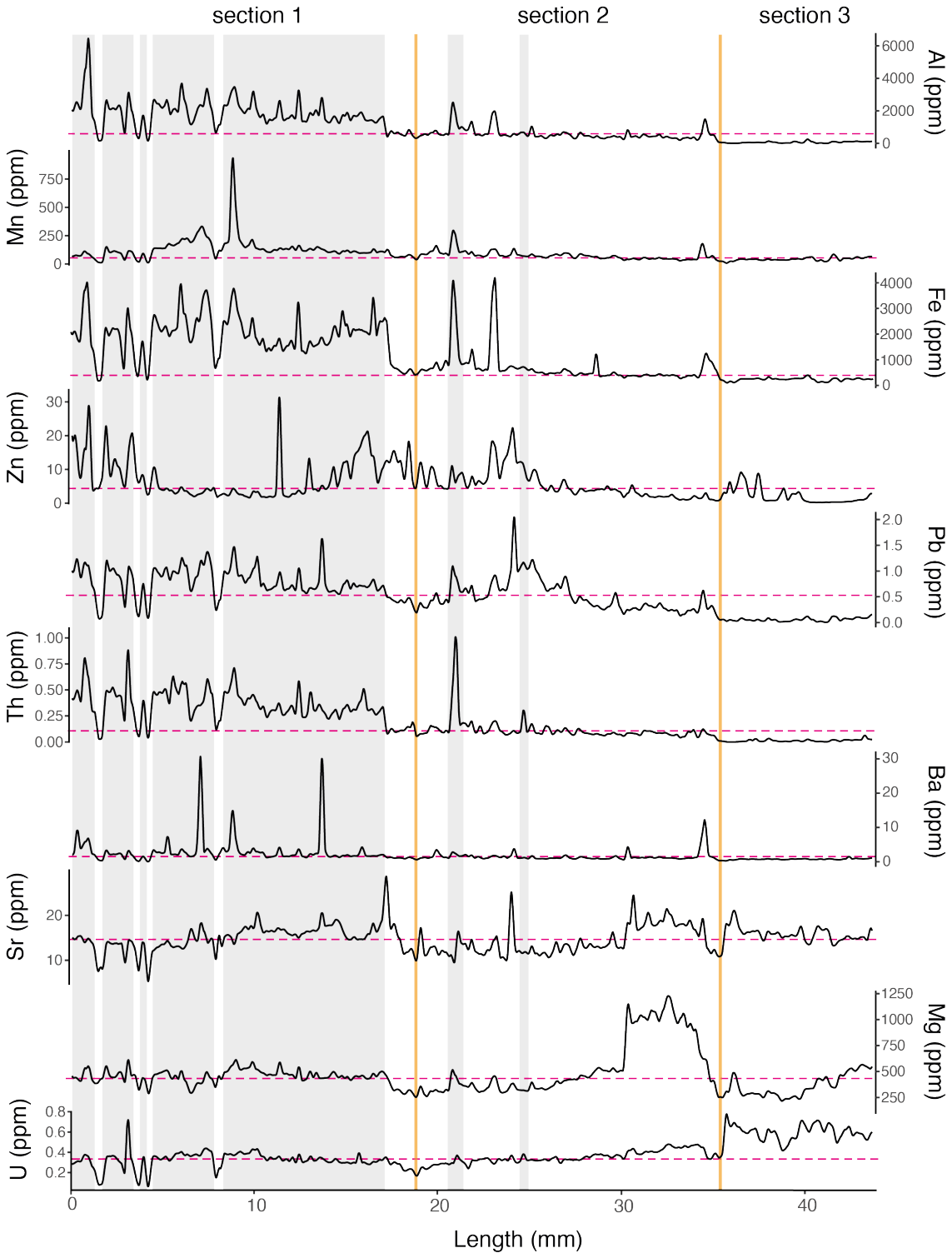

Figure 5.2.15 Stacked time series converted to sample length (where 0 mm = bottom of sample) for elements measured in sample 18-7 along transect 3. Data shown has been smoothed using a moving average of 13 points. The dotted pink horizontal lines indicated the median concentration value for each element, and the grey vertical bars highlight Th-rich intervals, where Th > 0.2 ppm.

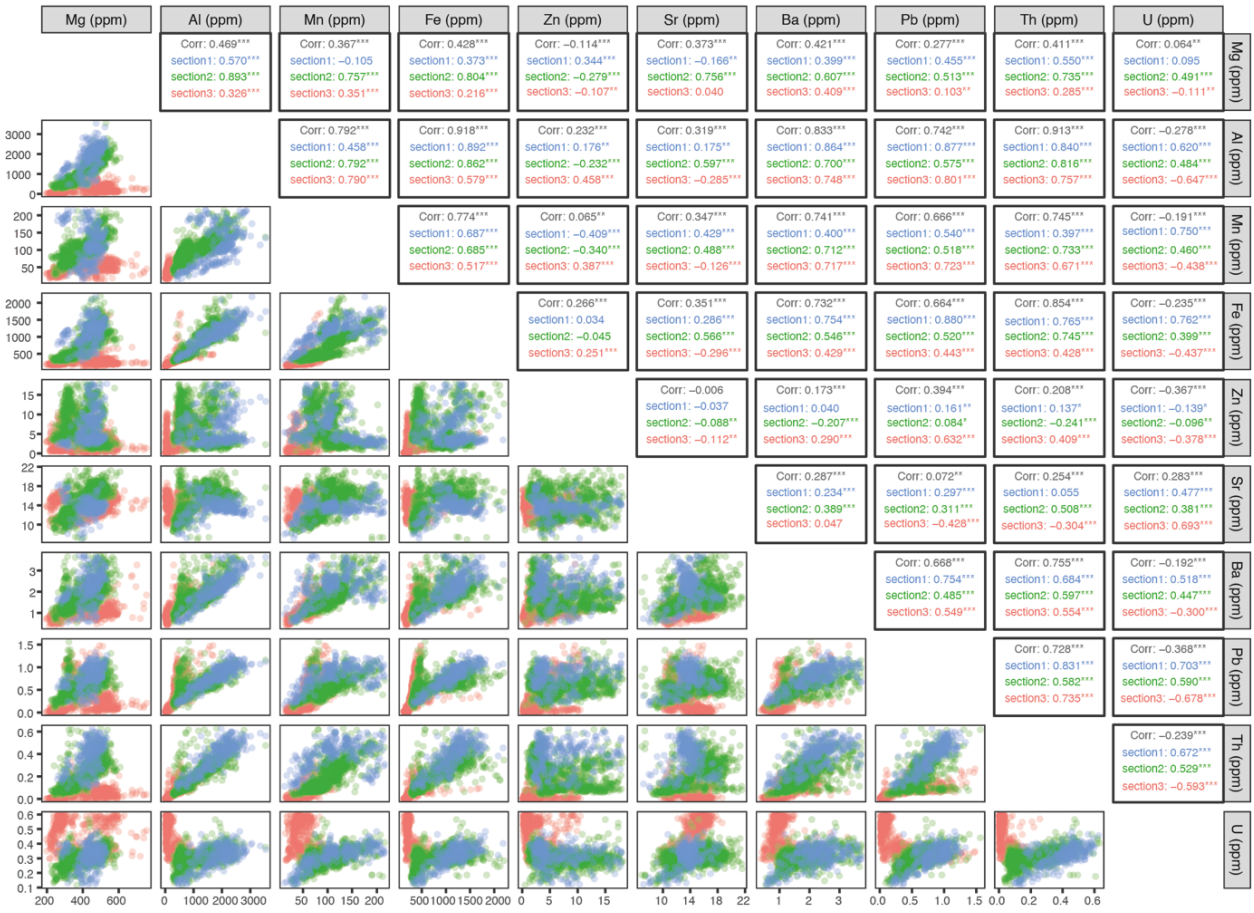

Figure 5.2.16 Correlation matrix showing cross-plots of each element against the other and their corresponding Pearson correlation coefficients (r value) for sample 18-7-3. The data are broken into sections due to the variation in behaviour across the sample (Figure 5.2.15). The stars next to the correlation coefficients are indications of the levels of significance related to the p-value (i.e., the probability of observing a non-zero correlation coefficient in the sample data. A p-value of <0.05 is given one star (*), <0.01 is given two stars (**), and <0.001 is given three stars (***). No stars indicate no significant correlation.

5.2.2.5 Dome tufa

The dome tufas are variably structured with complex, highly porous morphologies as described in Chapter 4.

Sample 18-10

Sample 18-10 broke into three pieces during extraction using the core drill. It is the only dome sample analysed using LA-ICP-MS. The top piece has a weakly layered structure,

with thin alternations of cream and brown-grey horizontal lamina that are semi-regular, although not clearly defined and porous. The middle piece has some horizontal layering that sandwiches a massive, porous layer. The bottom piece has near-vertical and sloping domains on either side of a large cavity. The portion above the cavity is porous and unstructured, while the material below the cavity is composed of dense, creamy micrite, with limited porous layers. Six parallel transects were conducted on each of these three pieces of tufa, referred to as traverse A (top), B (middle) and C (bottom).

Magnesium and Sr concentrations are invariable in traverses A and B, while in traverse C they are more variable, with elevated concentrations coinciding with lighter, less-dense portions of the sample (Figure 5.2.17). Aluminium, Mn, Fe, Ba, Pb and Th concentrations are highly variable and generally elevated across traverses A and B. However, in traverse C, these elements are consistently low (Figure 5.2.17). Transect 2 from traverse C was therefore selected for more detailed analysis (Table 5.2.7).

In selected transect 2 (Figure 5.2.18), U, Mg and Sr profiles are very similar, with synchronous peaks and troughs. These three elements are also strongly correlated, Mg and Sr in particular ($r = 0.88$, $p < 0.001$; Figure 5.2.19). Barium has a broadly similar pattern to these elements as well, although the variation in Ba is less pronounced, and Ba is not correlated with Mg, Sr, or U (Figure 5.2.19). In several instances, elevated Ba corresponds with elevated Th, with no response in U, Mg or Sr, and Ba is correlated with PCB elements, Pb and Th in particular ($r = 0.61$ and 0.62, respectively, $p < 0.001$; Figure 5.2.19).

Aluminium, Fe, Pb and Th are predominantly consistent about their respective median values, except in a few instances in which their values peak to concentrations 3 – 8 times their median (Figure 5.2.18). Lead and Th profiles are most similar, with synchronous peaks and a strongly correlated relationship ($r = 0.69$, $p < 0.001$; Figure 5.2.19). Manganese is elevated above its median value in the first ~5 mm of the transect. After this point, Mn concentration declines below its mean, with broad-scale variations between 0–50 ppm for the remainder of the transect, that appears to covary with Zn and Pb. Manganese is weakly correlated with these elements ($r = 0.25$ and 0.37, $p < 0.001$;

Figure 5.2.19) and moderately correlated with Ba (r =0.45, p < 0.001; Figure 5.2.19). Zinc oscillates about its median value, with a few elevations in concentration coinciding with Th peaks (Figure 5.2.18) and is moderately correlated with Pb (r = 0.48, p < 0.001, Figure 5.2.19).

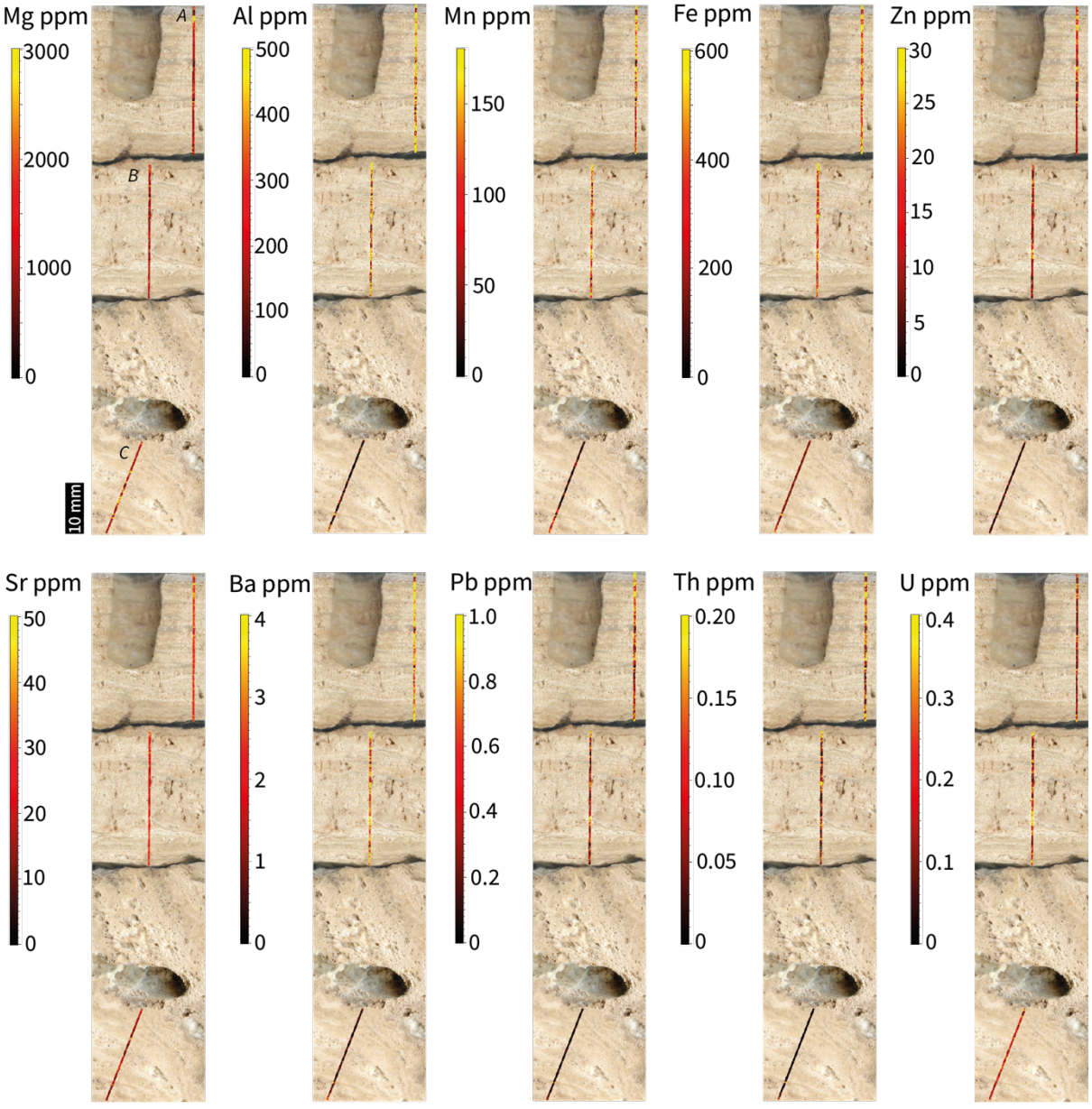

Figure 5.2.17 LA-ICP-MS trace element maps for sample 18-10 showing relative concentrations for each element measured along six parallel transects. Italicised letters A, B, C on the Mg heat map label the traverses referred to in the text.

Table 5.2.7 Summary statistics for each element across all six transects in dome sample 18-10 (left) and for the selected transect (right). Concentrations in ppm.

Dome tufa	Min	Max	Median	Mean	1σ	Selected transect	Min	Max	Median	Mean	1σ
18-10						**18-10-2**					
Mg	413	6164	1012	1422	943	**Mg**	447	6164	993	1391	954
Al	0	22328	39.6	125	437	**Al**	3.9	3660	37.3	114	280
Mn	0.5	8778	26.8	57.3	294	**Mn**	0.8	720	26.7	38.5	39.7
Fe	0	133683	143	266	2745	**Fe**	90	2211	143	189	161
Zn	0	251	3.58	4.30	5.85	**Zn**	0.5	25.6	3.41	3.92	2.35
Sr	6.3	64.2	14.2	16.8	8.07	**Sr**	7	62.2	13.8	16.1	7.96
Ba	<0.0007	311	0.465	0.892	4.39	**Ba**	0.1	13.7	0.42	0.631	0.757
Pb	<lld	37.8	0.054	0.139	1.09	**Pb**	<lld	0.74	0.05	0.08	0.098
Th	<0.0003	31.7	0.004	0.036	0.668	**Th**	<0.0003	0.326	0.004	0.014	0.03
U	<lld	1.40	0.154	0.174	0.086	**U**	0.1	0.54	0.145	0.161	0.07

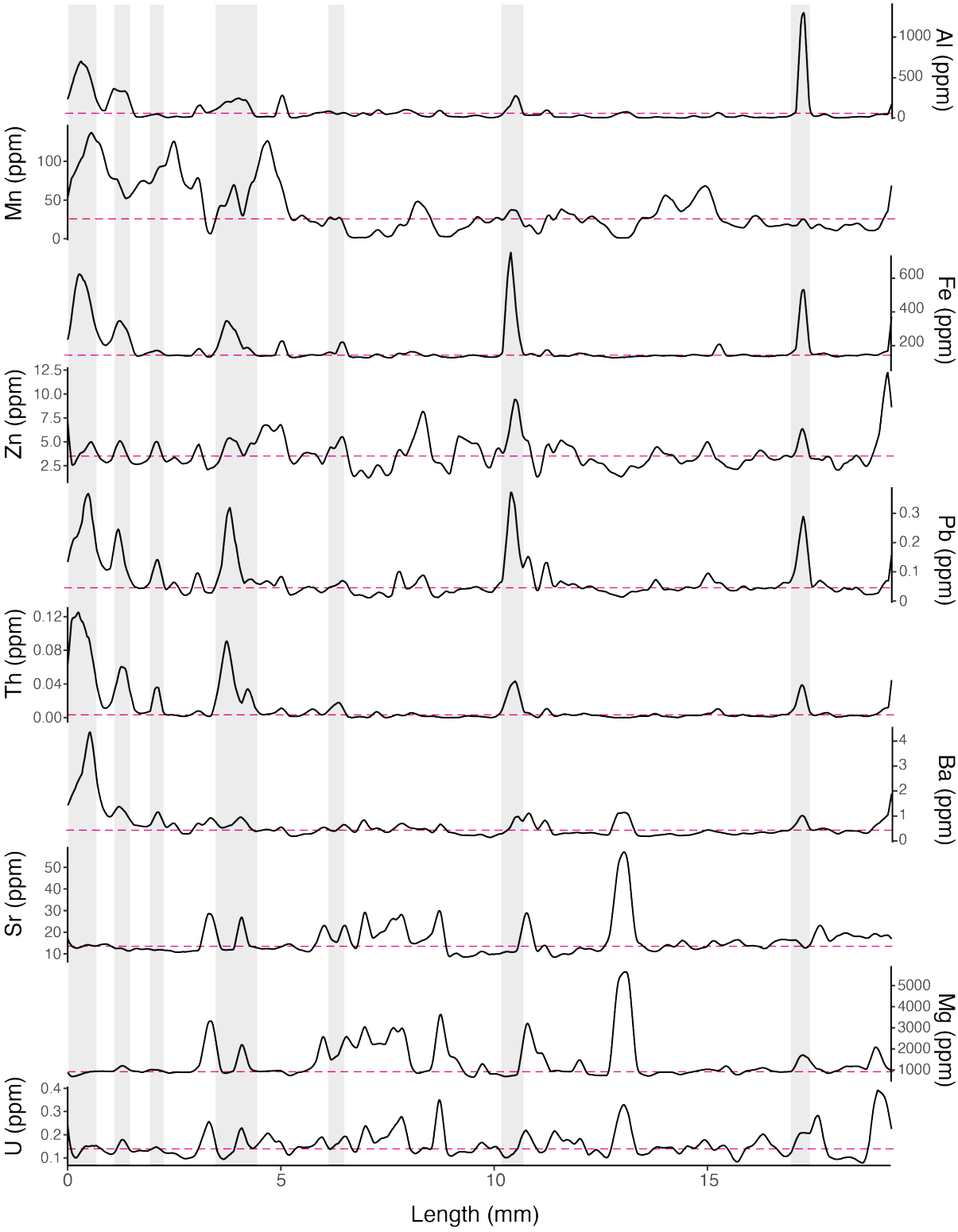

Figure 5.2.18 Stacked time series converted to sample length (where 0 mm = bottom of sample) for elements measured in sample 18-10 along transect 2. Data shown has been smoothed using a moving average of 13 points. The dotted pink horizontal lines indicated the median concentration value for each element, and the grey vertical bars highlight Th-rich intervals, where Th > 0.01 ppm.

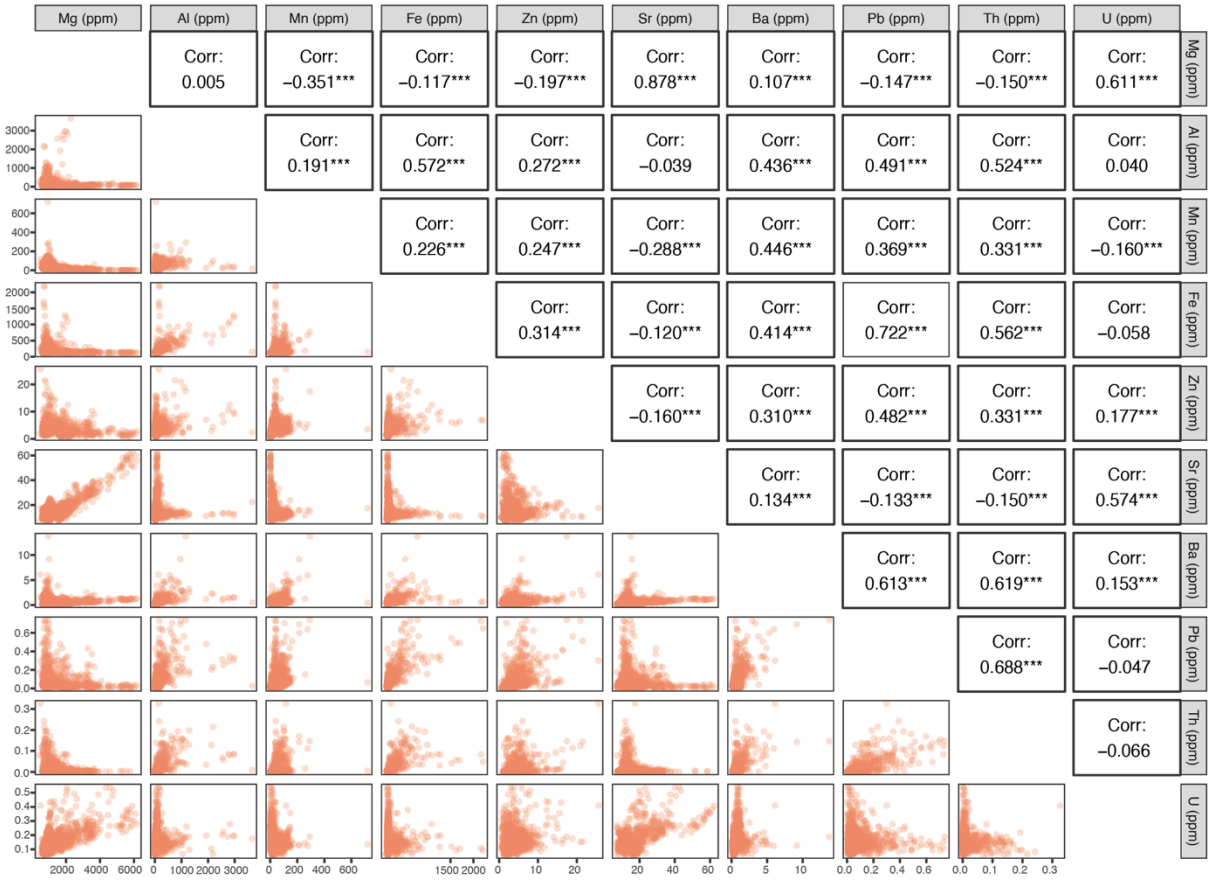

Figure 5.2.19 Correlation matrix showing cross-plots of each element against the other and their corresponding Pearson correlation coefficients (r value) for sample 18-10-2. The stars next to the correlation coefficients are indications of the levels of significance related to the p-value (i.e., the probability of observing a non-zero correlation coefficient in the sample data. A p-value of <0.05 is given one star (*), <0.01 is given two stars (**), and <0.001 is given three stars (***). No stars indicates no significant correlation. No outlier function was applied to this sample.

5.2.3 Trace element contents in tufa measured using solution ICP-MS

In addition to the trace element concentrations analysed via LA-ICP-MS, trace element contents were analysed via solution ICP-MS for comparison to the LA-ICP-MS data. The solution data from micro-drilled horizons in five tufa samples, GHN 1, 18-13, 18-14, 18-15 and 18-16, is presented in ppm in Table 5.2.8. The micro-drilled horizons were ~5 mm thick, and therefore encompass approximately 85 individual laser spot analyses. As such, the individual data points from solution analysis represent a homogenised section

of sample. These data are compared with the LA-ICP-MS data in Section 5.3.2 to evaluate the pros and cons of each technique.

Table 5.2.8 Trace element concentrations measured in selected tufas using solution ICP-MS method.

Sample	Mg (ppm)	Mn (ppm)	Fe (ppm)	Zn (ppm)	Sr (ppm)	Al (ppm)	Ba (ppm)	Pb (ppm)	U (ppm)
GHN1-1	1399	3.34	1747	10.2	27.4	6.07	1.78	0.0713	0.0985
GHN1-2	1287	11.0	1826	9.83	30.2	6.59	1.55	0.0887	0.0722
18-13-1	894	17.6	1817	17.8	20.8	4.07	1.43	0.0266	0.1248
18-13-2	727	16.0	1869	11.7	18.0	1.61	0.973	0.0245	0.1240
18-13-3	720	20.3	2243	13.7	14.1	1.37	1.20	0.0239	0.0683
18-13-4	611	4.91	2200	14.1	18.9	1.79	1.15	0.0301	0.1138
18-14-1	786	34.5	2123	8.78	23.8	1.33	1.30	0.1796	0.0739
18-14-2	551	8.60	2120	13.7	14.2	1.66	1.27	0.0401	0.0468
18-14-3	523	12.4	1985	10.6	14.8	2.72	0.684	0.1174	0.0612
18-14-4	681	6.65	2069	11.4	15.2	1.17	1.19	0.0316	0.0566
18-15-1	736	4.15	1800	4.52	11.9	1.02	0.991	0.0237	0.0728
18-15-2	622	8.85	2017	5.18	9.09	1.38	0.590	0.0217	0.0485
18-15-3	595	7.50	2027	13.8	16.9	2.84	1.01	0.0358	0.1687
18-16-1	1645	73.6	1732	8.44	35.0	3.94	2.94	0.0270	0.0624
18-16-2	1365	49.7	1980	9.06	31.3	2.65	1.92	0.0320	0.0843
18-16-3	1621	102	1756	4.92	35.3	1.69	2.61	0.0403	0.0856

5.2.4 Trace element concentration of modern waters

Trace elements measured in eight water samples collected from pools of standing water (n = 2) and drip waters (n = 5) at Ga-Mohana Hill, and ground water (n = 1) from the Eye of Kuruman spring are presented in Table 5.2.9 and Figure 5.2.20. Iron and Th concentrations were below the detection limit for all samples. Al and Mn were below detection in all samples except two: samples 18-3 and 21-1 have detectable levels of Al, and samples 18-13 and 21-1 have detectable levels of Mn. Strontium, Ba, U, Zn, Pb and Mg were above detection for all samples. Drip sample 21-1 has anomalously low Mg and Sr concentrations compared to the other drip samples, and instead the Mg and Sr values from this sample are similar to the concentrations seen in the surface water samples (Table 5.2.9). This sample also contains detectable amounts of Al and Mn and has

anomalously high Zn and Pb concentrations outside the range of all other samples. It is consequently treated as an outlier and excluded.

Table 5.9 Concentration of trace elements in water samples collected from shallow pools of fresh rainwater (surface), small stalactites on the inside, or adjacent to, the Ga-Mohana shelter (drips) and from the Eye of Kuruman spring (ground).

Sample	Type	Mg (μmol/L)	Sr (μmol/L)	Ba (μmol/L)	U (nmol/L)	Zn (μmol/L)	Pb (nmol/L)	Mg/Sr
18-3	surface	68.7	0.289	2.26	0.672	0.578	1.25	237
18-5	surface	105	0.128	0.029	0.042	0.196	0.770	823
18-17	ground	736	0.523	0.0023	0.336	0.107	0.190	1408
18-8	drip	1000	0.903	1.44	1.64	0.152	0.580	1107
18-11	drip	2263	0.624	0.0023	0.462	0.088	0.530	3624
18-13	drip	1893	0.467	0.361	0.210	0.254	0.340	4054
21-1	drip	99.6	0.211	0.027	0.168	1.56	9.70	471
21-6	drip	1024	0.661	0.0042	0.504	0.031	3.62	1550

The concentration of Mg in the water samples is two orders of magnitude greater than all the other trace elements measured in the water collected. This is expected since Mg is a major component of the dolomite host rock and is incorporated into ground water during rock-water interactions, resulting in enrichment of the ground and drip waters with respect to Mg. Overall, the drip waters have the highest Mg (1000 - 2263 μmol/L) and Sr (0.6 – 0.9 μmol/L) concentrations, with average values of 1545 ± 633 μmol/L (σ) and 17.6 ± 7.2 μmol/L (σ) for Mg and Sr respectively (Figure 5.2.20 and 5.2.21). The groundwater Mg and Sr concentrations are intermediate (736 μmol/L and 0.5 μmol/L, respectively), and the surface water samples have the lowest Mg and Sr values (~68 – 105 μmol/L and ~0.1 – 0.3 μmol/L, respectively). The drip waters and ground water sample also have high Mg/Sr ratios relative to the surface waters (Table 5.2.9).

Barium, U, Zn and Pb concentrations do not differ systematically between drip, surface and ground waters. However, drip sample 18-8 has anomalously high Ba and U concentrations (1.44 μmol/L and 1.64 nmol/L, respectively) compared to the other drip samples (0.0023 – 0.361 μmol/L and 0.168 – 0.504 nmol/L, respectively) (Figure 5.2.20). The trace element concentrations in the two surface water samples are different. Sample 18-3 has higher concentrations of all elements, except Mg, than sample 18-5. Sample 18-

3 also contains a trace amount of Al (18.3 ppb). Sample 18-3 and 21-1 both have detectable Al concentrations, and drip samples 18-13 and 21-1 have detectable Mn. These samples have the three highest concentrations in Zn, and samples 18-3 and 21-1 have both the two highest Zn and Pb concentrations.

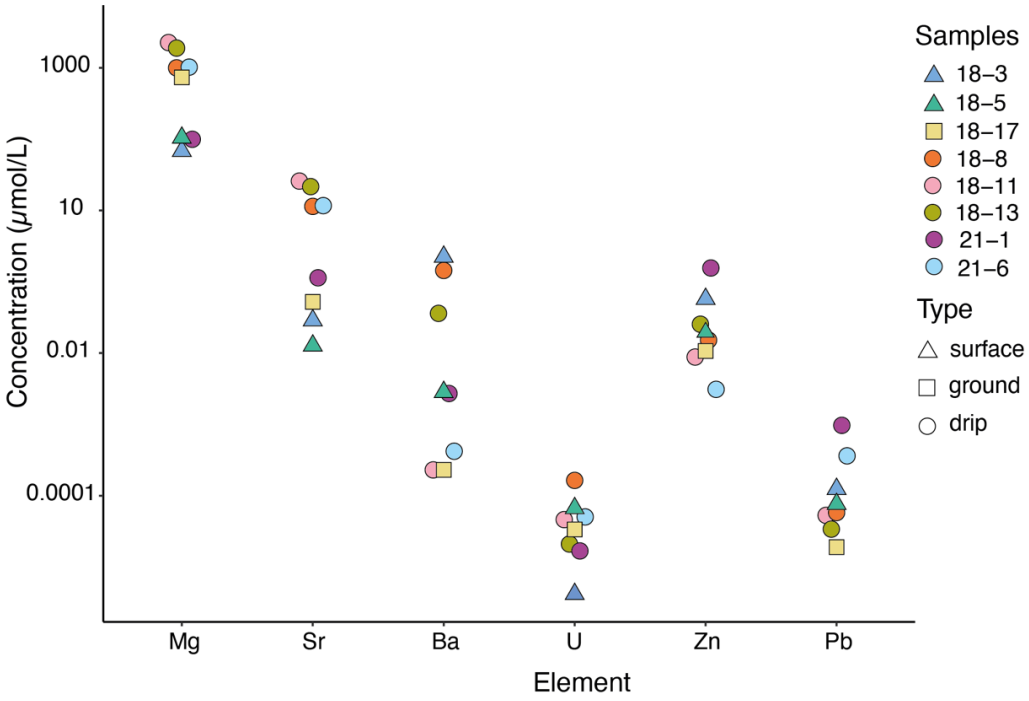

Figure 5.2.20 Distribution of trace element concentrations measured in each water sample on a log scale.

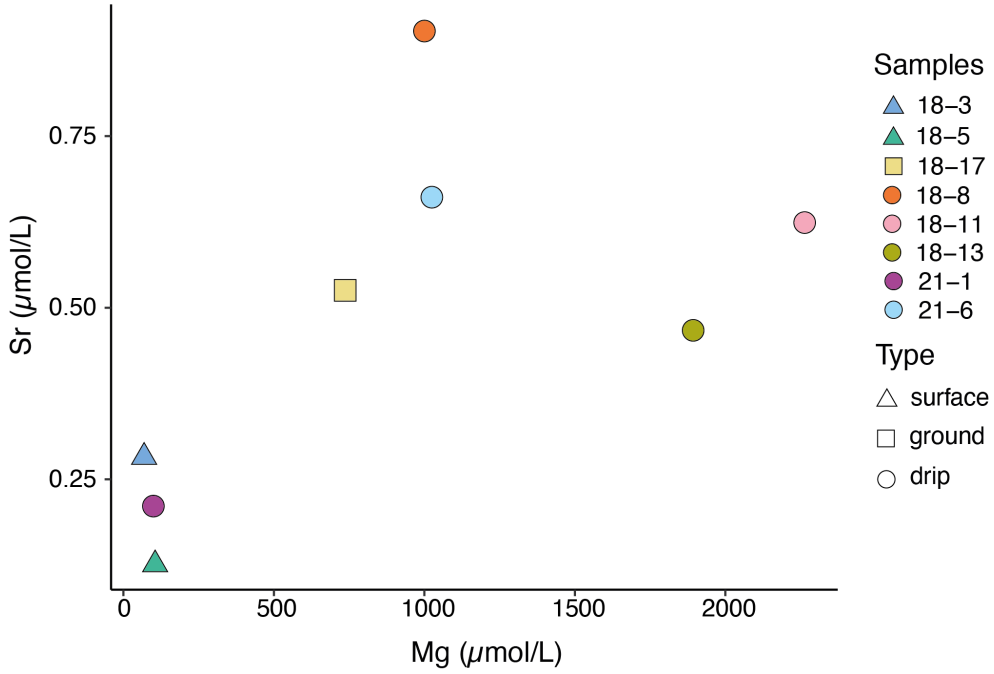

Figure 5.2.21 Concentration of Mg and Sr in the three types of water samples.

5.3 Utility of Ga-Mohana tufa and water trace element contents

In this section, I first evaluate the relationships between the measured trace elements that can aid in discriminating carbonate and non-carbonate phases in the tufas (Section 5.3.1). Thereafter, I compare the element concentrations measured using LA-ICP-MS and solution ICP-MS methods (Section 5.3.2), and then assess the utility of these trace element data as palaeoclimate proxies (Section 5.3.3). I briefly discuss the trace element concentrations measured in the modern water samples collected (Section 5.3.4) and finally conclude this chapter with Section 5.3.5.

5.3.1 Evaluation of carbonate vs non-carbonate phases

Magnesium, Sr, Ba, and U are generally soluble, bedrock-derived elements, and their concentration in tufa carbonate might be expected to aid in unravelling past hydrological conditions. However, interpreting variations in these elements is not straight-forward since partitioning of these elements into carbonate (i.e., the partition coefficient, Kd) is controlled by multiple factors, such as concentration in the fluid, temperature, precipitation rate, and whether equilibrium is achieved. The concentration of these elements in tufas may also reflect input from sources other than dissolution of the bedrock. For example, Mg can also be derived from undissolved bedrock fragments, soil and dust. Particulate, colloidally bound elements (PCB, e.g. Al, Fe, Pb, Th) are proxies for detritus derived from silicates and clays in soil and dust. Elevated concentrations of PCB elements indicate input from sources other than bedrock-derived dissolution, and as such, can be used to assess whether corresponding elevations in Mg and Sr are also partially derived from non-bedrock sources. For example, in cascade sample 18-4, Mg and U are moderately correlated with PCB elements (e.g., Mg-Th $r = 0.48$ and Mg-Pb $r = 0.43$, $p<0.001$), with peaks in Mg and U coinciding with elevated concentrations of Al, Th, Pb, and Fe (highlighted by grey bands in Figure 5.2.3). In these cases, Mg and U content in the tufas may be partially derived from detrital input. However, this is not the case in cascade sample 18-16, for example, where Mg, Sr and U vary independently of the PCB elements (Figure 5.2.6).

In almost all samples, Mg and U covary with moderate to strong, statistically significant ($p<0.001$) positive correlations. In some samples, Mg and Sr are correlated but this tends to occur in portions of the samples that contain detrital material or inclusions of brecciated tufa, e.g. cascade sample 18-4, rim-pool sample GHS-6 (sections 3 and 4 only) and terrace breccia 18-7 (section 2). Magnesium, Sr and U are most strongly correlated in traverse C of the dome sample, and in this case, detrital input is low.

For the most part, the Al, Fe, Pb and Th profiles are similar, and typically these elements display moderate to strong correlations (i.e., $r = 0.5\text{-}0.9$, $p<0.001$) in all the samples. This suggests either similar accumulation mechanisms in calcite, or ablation of additional phases that contain high concentrations of these elements. Barium, Mn and Zn are less straightforward; at times these elements co-vary with the PCB elements, while in other instances Ba is correlated with Sr and U. In several instances, Mn and Ba exhibit a moderate to strong positive correlation ($r = 0.4\text{-}0.7$, $p<0.001$). Zinc is most commonly correlated with Pb. Pb and Zn are both associated with organic matter complexes (Hartland et al., 2012), and in speleothem studies, are interpreted to increase during periods of elevated soil mobilisation and input (Borsato et al., 2007; Tan et al., 2014).

There are multiple potential sources for trace elements in tufa, and relationships between the elements need to be carefully evaluated before interpretations can be drawn. PCB elements such as Al, Th and Pb are clearly related to the inclusion of detritus in the tufas. Elevated concentrations of these elements therefore reflect ablation of non-carbonate phases, or $CaCO_3$-poor horizons. Magnesium and Sr concentrations in tufas are commonly used as proxies for palaeo-rainfall conditions (Garnett et al., 2004a; Dabkowski et al., 2012). However, these elements may be incorporated into tufa via non-primary sources, i.e. as solid particles incorporated into the tufa forming waters, obscuring the use of Mg and Sr as palaeoclimate proxies. In order to unravel primary ground-water signals from detrital input, a useful starting point is to assess correlations of these elements with PCB elements. For example, Belli et al. (2017) differentiated between Mg sourced from the dissolution of the host rock and Mg associated with particulates using the co-variation of Mg with PCB elements in speleothem samples from Savi Cave in Italy. They were able to define a threshold

concentration for Mg in the stalagmites in their study, above which the concentration is partially derived from particulate input. This is not possible for the tufa samples from Ga-Mohana Hill due in part to the large range in Mg concentration across the different tufa morphologies, and the heterogeneity of each sample. In this case, it would be necessary to evaluate each sample individually based on correlations with PCB elements in order to select portions of the samples that can be reliably used to infer palaeoclimate signals.

5.3.2 Comparison of LA-ICP-MS and solution ICP-MS methods

In Figures 5.3.1 to 5.3.5, the solution ICP-MS data is plotted as star symbols adjacent to box plots which represent the range in concentration for the equivalent section of the sample measured using LA-ICP-MS. The concentration of elements analysed via solution are generally within range of those measured using laser ablation, except for Al and Fe, which are systematically lower and higher than the laser data, respectively (Figures 5.3.1-5.3.5).

Aluminium is a major constituent of clays and silicate material observed as detritus in the tufa. This material will have been excluded during the sequential digestion of the carbonate, prior to solution analysis, whereas this material would have been ablated during the laser scan. Even layers that appear low in detrital material when inspected under an optical microscope contain elevated Al in laser data, compared with solution data from the same region. This suggests that clay and silicate material is finely disseminated within the tufa and visual assessment is not sufficient for excluding these phases. In addition, this confirms that sequential digestion techniques are effective at excluding non-carbonate phases in bulk tufa analyses, consistent with work on marine carbonates (Bailey et al., 2000; Zhang et al., 2015; Tostevin et al., 2016). The U concentration tends to be slightly lower in solution than the laser data for most of the samples too. This may indicate an association with non-carbonate phases, and this may have an implication for laser screening and U-Th dating.

Barium, Sr, Mg and particularly Fe show the opposite trend to Al, with systematically higher concentrations in the solution versus the laser ablation data for several samples. One explanation could be that these elements are hosted in the carbonate, and the carbonate signal is diluted by other phases during LA-ICP-MS analysis. While this is a reasonable explanation for Ba, Sr and Mg, it is difficult to reconcile with the Fe data. Although Fe^{2+} can be incorporated into calcite, Fe co-varies with Al, Mn, Th, and Pb in the LA-ICP-MS data, which suggests it is associated with detrital material. Under reducing conditions, Fe^{2+} can also be incorporated in organic matter, which may be present as a soil component or as microbial communities involved in tufa formation. Organic material is readily digested by nitric acid, a key component of the sample preparation for solution analysis, whereas Fe-rich oxides are not. The elevated Fe concentration in the solution data compared to the Fe concentration measured via laser ablation may indicate dissolution of organic material along with the carbonate. This could be tested with future analysis using an alternative acid, e.g. acetic, rather than nitric acid when performing solution analysis of tufa.

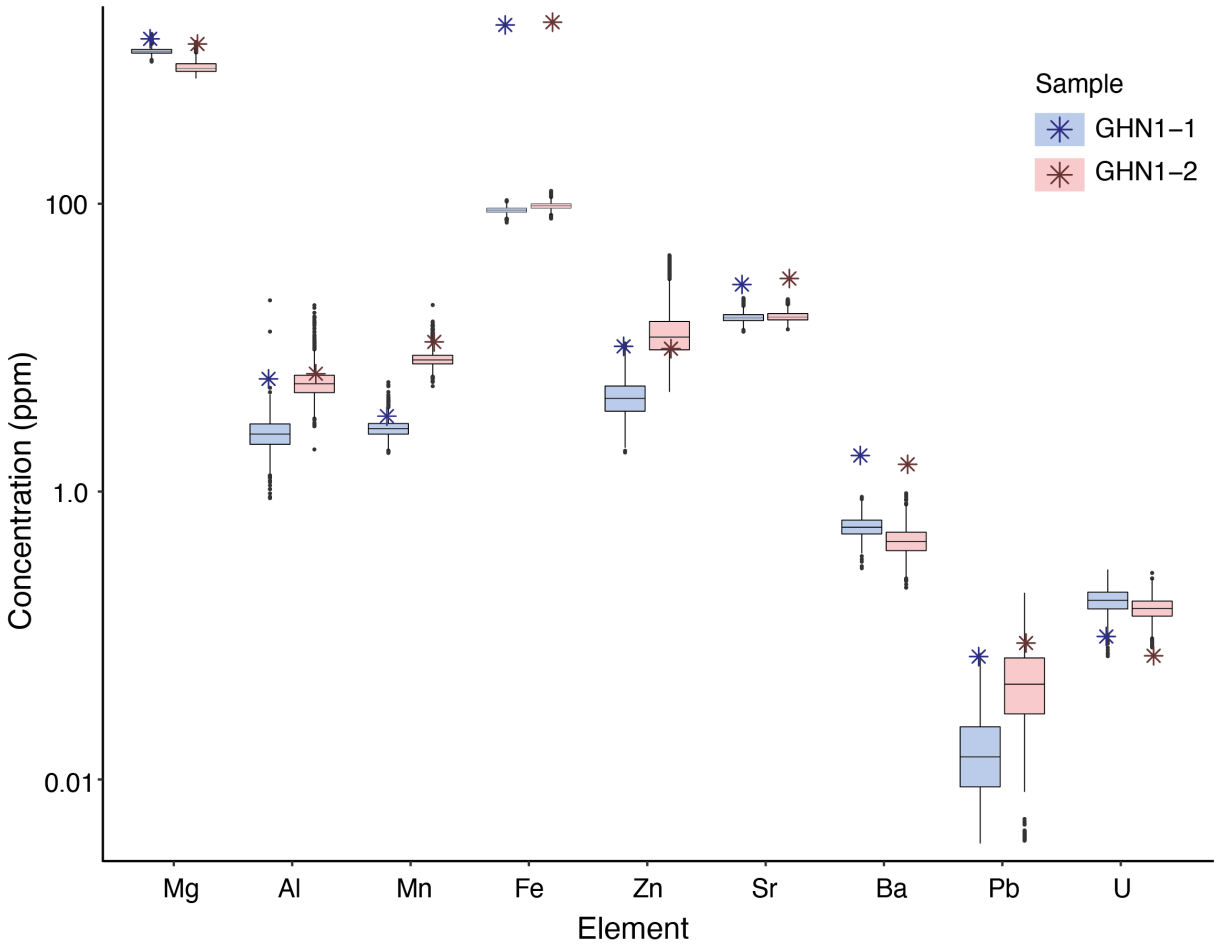

Figure 5.3.1 Comparison of solution ICP-MS point data (stars) and the range of concentration measured along the laser ablation transects for sections of tufa sample GHN1.

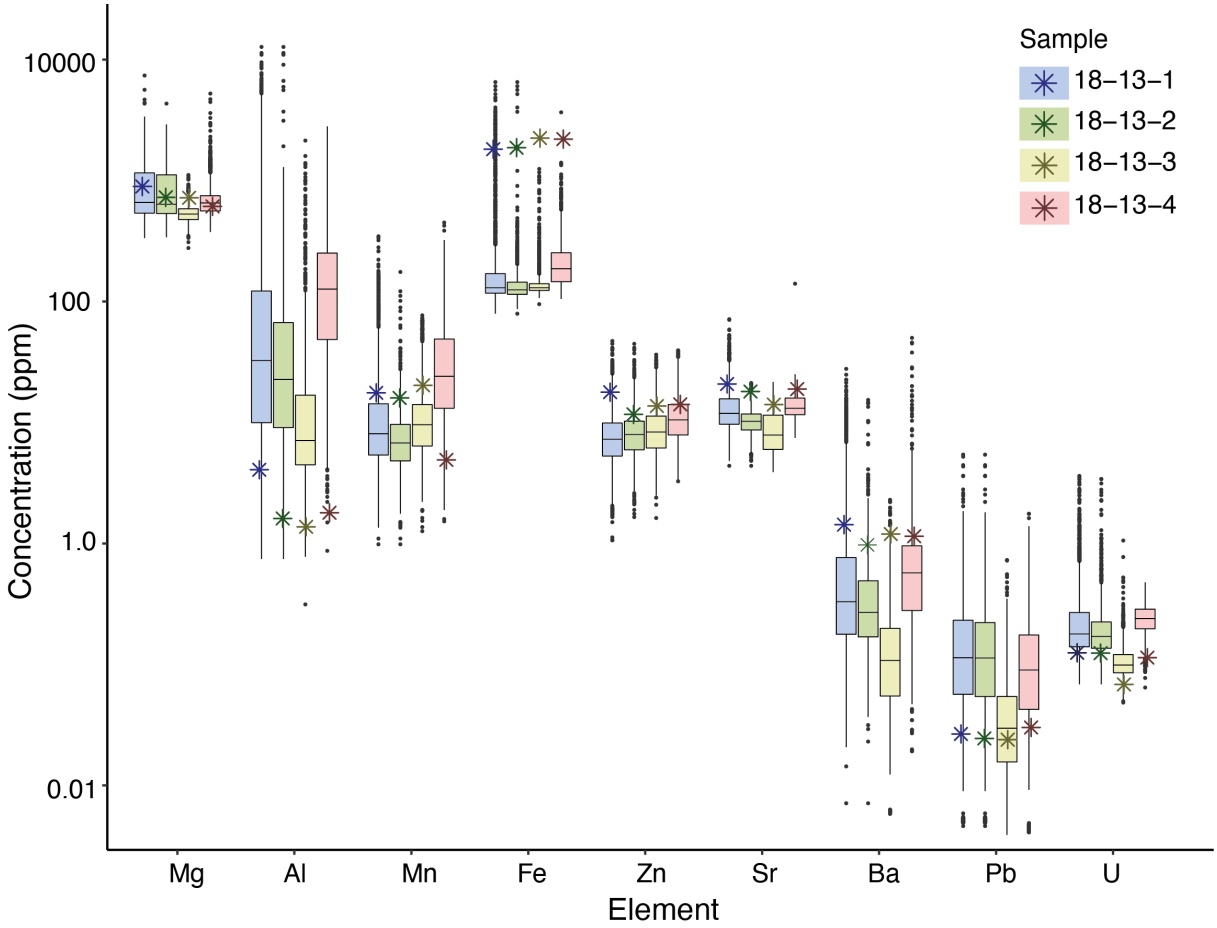

Figure 5.3.2 Comparison of solution ICP-MS point data (stars) and the range of concentration measured along the laser ablation transects for sections of tufa sample 18-13.

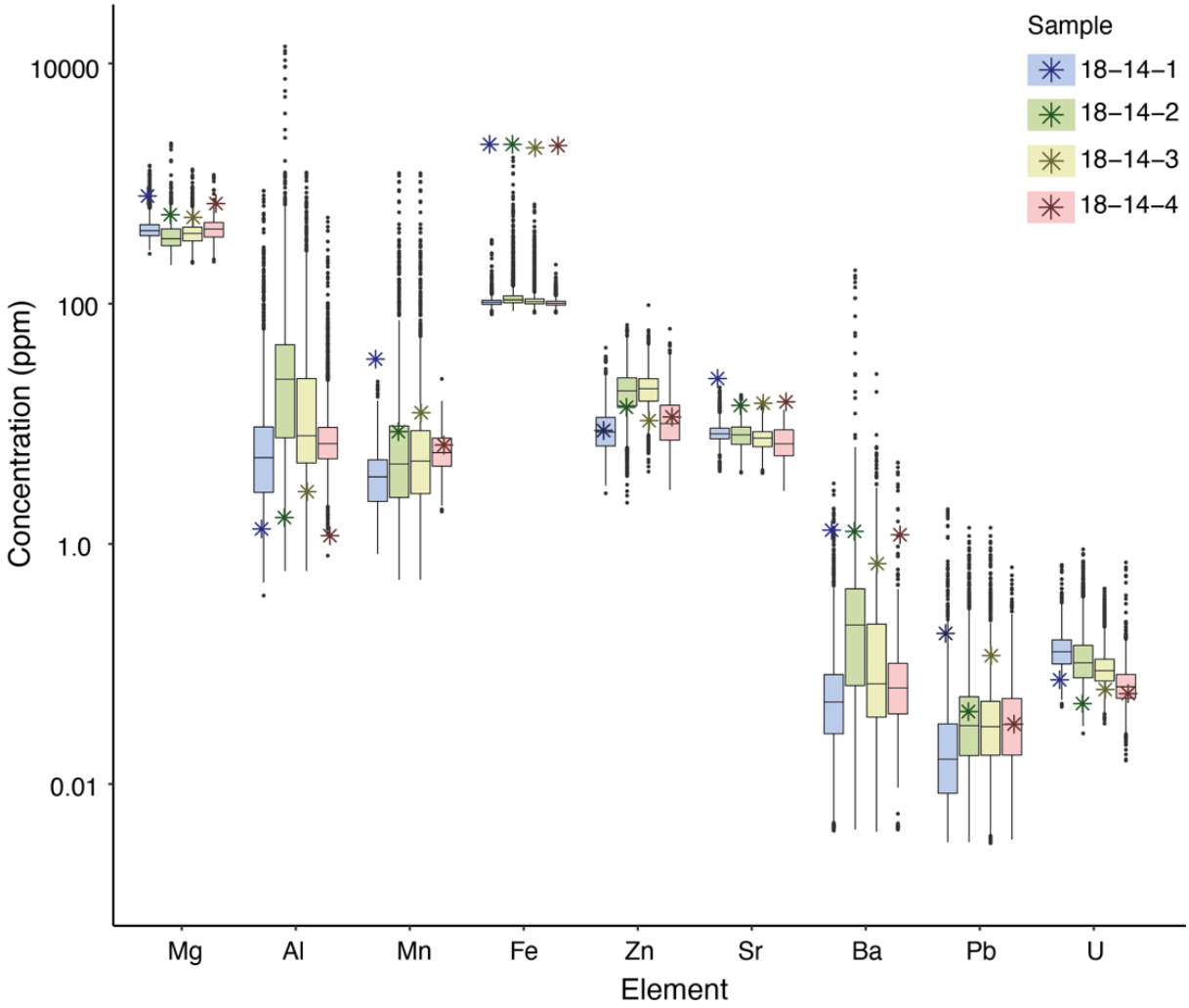

Figure 5.3.3 Comparison of solution ICP-MS point data (stars) and the range of concentration measured along the laser ablation transects for sections of tufa sample 18-14.

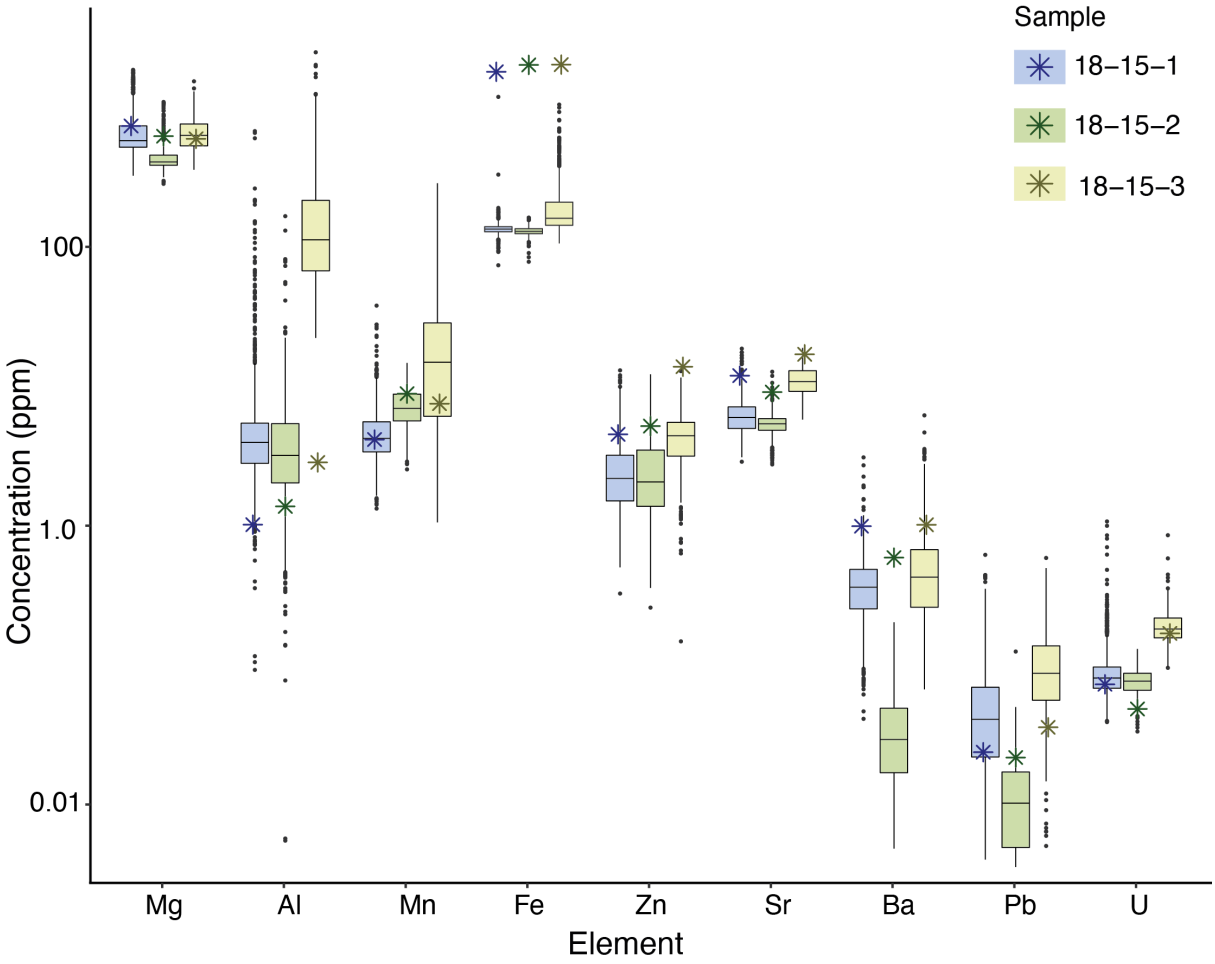

Figure 5.3.4 Comparison of solution ICP-MS point data (stars) and the range of concentration measured along the laser ablation transects for sections of tufa sample 18-15.

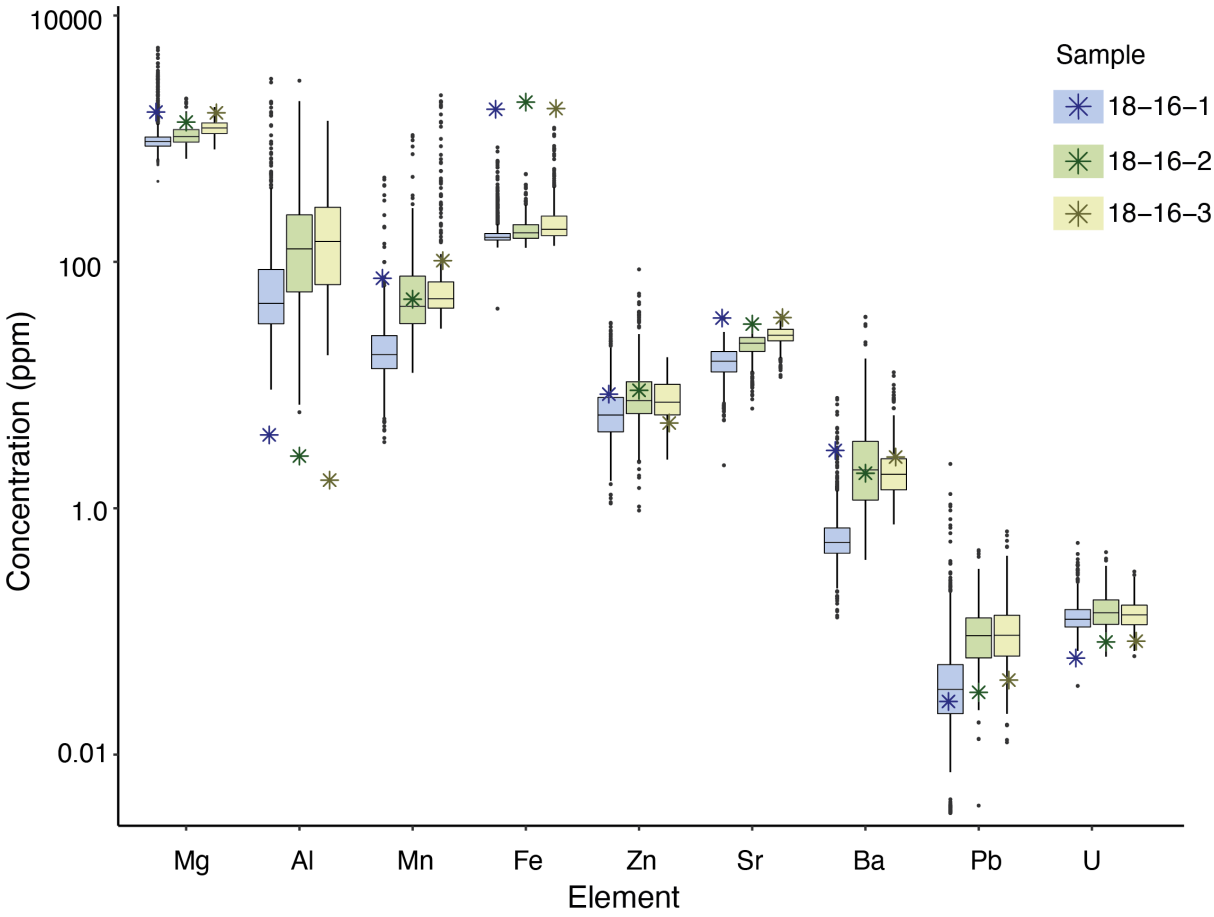

Figure 5.3.5 Comparison of solution ICP-MS point data (stars) and the range of concentration measured along the laser ablation transects for sections of tufa sample 18-16.

To date, trace element analysis of tufa samples have been conducted using the solution method (Ihlenfeld et al., 2003; Garnett et al., 2004a; Dabkowski et al., 2012). While this method is appropriate for material that is likely to contain detrital, non-carbonate phases, it does not allow for the continuous, high-resolution data generation granted by laser ablation. Digestion and solution analysis is therefore best-suited to address questions related specifically to the calcium carbonate component of the tufa deposits, whereas the LA-ICP-MS method allows for *in situ* sampling and returns high-resolution data of carbonate and other components, and their spatial variation, albeit on a very small scale. Such high-resolution data is helpful for evaluating whether there is any cyclicity in trace element input, and assessment of element variation with stratigraphic changes on a micrometre scale. Although this is a mixed mineralogy signal, it can still provide useful palaeoclimate information because the flux of PCB phases into the

environment can reflect variations in environmental parameters. For example, soil and particulates are mobilised during wetter conditions, so an increase in elements such as Pb, Zn and U may indicate high rainfall periods, whereas a period of aridity may result in a greater input of wind-blown detritus (Ihlenfeld et al., 2003; Borsato et al., 2007; Tan et al., 2014). However, unravelling which of these processes is responsible for the observed element variations remains a challenge. In order to harness the utility of the laser ablation method, constraints on the micro-fabric of the material being ablated should be well-established, so that element variation in the sample can confidently be assigned to either primary calcite or other non-carbonate phases. Ultimately, the method used to assess trace elements in tufas depends on the questions to address and the scale of investigation.

5.3.3 Trace elements in tufa as useful palaeo-proxies

The concentrations of trace elements in carbonate are controlled by both the composition of the parent solution, the inclusion of contaminants in both the tufa-forming water and as solid detrital matter, and the conditions under which precipitation occurs (Desmarchelier et al., 2006; Fairchild and Treble, 2009). This multitude of factors means that deciphering climate signals can be a complex task.

The Mg contents measured in the tufa using LA-ICP-MS are variable both within and between samples, and in many cases samples have relatively high mean values (~1000 to 4000 ppm). In some instances, samples have exceptionally high maximum values (up to ~250000 ppm). Although elevated Mg content in tufa is usually associated with aragonite precipitation, aragonite was not identified via XRD analysis (Section 5.2.1), nor was it observed in thin section analysis (Chapter 4). There is nevertheless potential that some of the calcite in the tufa recrystallised from aragonite, and that residual / remnant aragonite remains, which may affect trace element incorporation, and U-Th dating results (Ortega et al., 2005). The exceptionally high Mg contents in these tufa samples may also represent ablation of detrital material, e.g. undissolved dolomite bedrock fragments, as these are generally present as anomalous spikes along the laser transects.

The wide range in Mg content in the Ga-Mohana tufas is reportedly typical for tufas in general (Pentecost, 2005). Magnesium variation within a sample may reflect variable input sources, hydrological changes, i.e., changes in the residence time of tufa-forming water in the aquifer, variable precipitation conditions, microbial involvement, or, most likely, a combination of these (Pentecost, 2005). Magnesium variability in speleothems is commonly interpreted to represent aquifer residence time (Roberts et al., 1998; Fairchild et al., 2000; Musgrove and Banner, 2004; Desmarchelier et al., 2006). Periods of low groundwater recharge leads to longer in-aquifer residence times and the subsequent enrichment of Mg in the groundwater, ultimately reflected as elevated Mg in the carbonate deposit. In comparison, periods of high rainfall and groundwater recharge leads to a shorter residence time of the groundwater in the aquifer, and consequently lower Mg concentrations in the groundwater and resultant carbonate deposit.

In order to decipher which drivers are responsible for Mg variation in tufa, it is necessary to consider the element in relation to other elements, e.g. Sr and U. Garnett et al. (2004a) found correlations between Mg, Sr and $\delta^{13}C$ and inferred that low values represented dry conditions. In their study of modern tufas forming in a riverine setting in Australia, Ihlenfeld et al. (2003) determined that Sr and Ba, along with $\delta^{13}C$, recorded annual rainfall variability, characterised by a ~1-2 year lag. They found that low Sr and Ba concentrations in the tufa corresponded to an increase in rainfall. However, the relationship between Mg and Sr in the Ga-Mohana tufa samples is not straight-forward. While Mg and Sr show a strong correlation in some samples, this is not the case for the majority of Ga-Mohana tufa samples. The Sr contents also show inconsistent relationships with other elements, and this likely reflects variably dominating factors that control Sr incorporation in tufa. As a consequence, Sr in these samples has limited potential as a palaeohydrological record.

Magnesium and U show a more consistent positively correlated relationship in the Ga-Mohana tufa samples, e.g., samples 18-4, 18-16, 17-6, and 18-10. Ihlenfeld et al. (2003) found seasonal and annual variations in U and interpreted these as reflecting fluxes in U from the soil zone to the water table. They suggested that an increase in U is a

consequence of intense rainfall events during which U is complexed with organic colloids and is transported into the phreatic zone. However, if high Mg in the Ga-Mohana tufas is assumed to represent drier periods, the explanation from Ihlenfeld et al. (2003) contradicts the positive correlation between Mg and U observed in the Ga-Mohana tufas, and a different explanation is needed. Particulate and colloidally-bound elements (PCBs), i.e., Fe, Al, Mn, Ba, Pb, Th and Zn, are useful in determining portions of the samples with a high proportion of non-carbonate phases (as described in Section 5.3.1), and this is important in the selection of material for U-Th dating, detailed in the following Chapter 6.

5.3.4 Trace elements in water

Although the water analysed for trace element concentrations in this study consists of a small sample size, the data provides useful context for the element concentrations in the tufa samples. The surface waters are evaporated rainwater and did not interact with the dolomite aquifer, whereas the ground and drip waters would have become enriched in Mg and Sr during interaction with the dolomite bedrock. The ground water samples are 7 to 10 times enriched in Mg and 2 to 4 times enriched in Sr relative to the surface rainwater samples, and the drip waters are further enriched in these elements. The enrichment of the drip waters relative to the ground water may suggest that the drip waters were also subject to evaporation or prior calcite precipitation before exiting the dolomite as drips.

The drip waters are likely representative of the fluids from which the calcite precipitated, since the bed rock chemistry hasn't changed since tufa formation began. These data therefore provide some end member values for the tufa-forming fluid chemistry. Together with the tufa data, it allows a rough estimation of the partition coefficient of these elements to be calculated. Using Equation 5.1, the minimum, maximum and mean values for Mg and Sr contents in the tufa (using the solution data to avoid incorporating detrital Mg values), and the minimum, maximum and mean values for Mg in solution (calculated from ground and drip water values only), the $Kd_{Mg,calcite}$ value is estimated to be 0.3 (Table 5.10). This suggests that Mg preferentially

remains in the solution rather than being incorporated into the calcite mineral phase. Whereas the calculated *Kd* for Mg is constant, the calculated *Kd* for Sr is not. This suggests that the fluid was the main control of Mg partitioning into Ga-Mohana tufas, but other factors, such as growth rate, likely controlled the incorporation of Sr into the tufa.

Table 5.10 Partition coefficients calculated for Mg and Sr in calcite.

Element	C_{tufa} (µmol/L)	C_{fluid} (µmol/L)	Kd
Mg (mean)	38	1383	0.3
Mg (min)	21.5	736	0.3
Mg (max)	67.7	2263	0.3
Sr (mean)	0.9	0.2	4.5
Sr (min)	0.4	0.9	0.4
Sr (max)	1.5	0.6	2.5

5.3.5 Concluding remarks

Trace elements measured via solution are comparable to those measured using laser ablation, given the coarse resolution, and when the effect of sample digestion on various elements is taken into account. The visualisation of trace element contents in the tufa samples, obtained using LA-ICP-MS, is a useful tool to determine the spatial distribution of elements in tufa, and to distinguish CaCO3-rich vs CaCO3-poor horizons. This can aid in guiding sub-sampling for U-Th dating, whereas this is not possible using the coarser-resolution solution method, as Th was below the detection limit, and digestion removes the non-carbonate phases included in the tufa. As such, the solution method is best suited to questions relating to conditions of tufa formation based on elements incorporated into the calcite. Evidentially, colloidal and detrital material is finely disseminated throughout most of the tufa samples, even ones that appear to be composed of 'clean' calcium carbonate. This, together with the highly heterogenous nature of the samples means that interpretations based on this high-resolution element data cannot be inferred for other parts of a single sample, or across samples. As such, the LA-ICP-MS method would be best paired with high resolution

imaging of the samples, e.g. SEM and micro-sampling, and applied to questions related to processes on a micro scale.

CHAPTER 6 URANIUM-THORIUM DATING

The ability to date tufas, and thereby place a chronology on the palaeoenvironmental archive inherent within them, provides an opportunity to investigate the environmental contexts in which they formed. Uranium-thorium disequilibrium dating (U-Th dating) of carbonates is a well-established and widely applied technique that has greatly enhanced Quaternary studies (Schwarcz, 1992; Richards and Dorale, 2003; Walker, 2005; Reiners et al., 2017). In the following section, I describe the principles of U-Th dating (Section 6.1.1), introduce a method to screen tufa samples prior to sampling for U-Th dating (Section 6.1.2), and provide an account of some key studies in which U-Th dating has been applied to tufa. In Section 6.2, I present the results of my U -Th analysis of selected Ga-Mohana tufa samples, informed by screening the U and Th concentrations using LA-ICP-MS prior to sample selection. Thereafter, I discuss the age results in Section 6.3.

6.1 Background and literature

A range of methods have been applied in an attempt to date tufa deposits, including electron spin resonance (ESR), thermoluminescence, amino acid racemization (AAR), and various radiometric methods e.g. ^{14}C, $^{230}Th/^{234}U$ and $^{228}Ra/^{226}Ra$ (Capezzuoli et al., 2014). Many of the early attempts to obtain ages for tufas relied on ^{14}C radiocarbon dating (Marker, 1974; Butzer et al., 1978; Pazdur et al., 1988b; Beaumont and Vogel, 1993). ^{14}Carbon is restricted to deposits <40 ka old because ^{14}C has a short half-life, ~5700 years. Tufa is not an ideal target for ^{14}C dating though, with complications related to the preservation of organic material, the 'hard water' effect, and issues with 'dead carbon' (Ford and Pedley, 1996; Domínguez-Villar et al., 2012). Nevertheless, ^{14}C dating continues to be used to construct high-resolution chronologies for tufa <40 ka, Holocene deposits in particular (Domínguez-Villar et al., 2012; Brook et al., 2015; Ricci et al., 2015). It is also often combined with other methods, e.g. palynological analysis (Brook et al., 2010) and U-Th dating (Ordóñez et al., 2005; Doran et al., 2015).

Initially applied to dating marine carbonates (Barnes et al., 1956), U-Th dating is now routinely applied to dating speleothems, and is ideal for both Holocene and Pleistocene geoarchaeology and palaeoclimate studies as it can provide accurate and precise ages up to <600 ka (Cheng et al., 2013; Hellstrom and Pickering, 2015). It is particularly well-suited to terrestrial calcium carbonate deposits due to the solubility differences between uranium (U) and thorium (Th). Uranium is transported in natural water (i.e. water present in the environment, e.g. rain, groundwater, as opposed to tap or bottled water) as uranyl ions (UO_2^{2+}) and is co-precipitated with calcite, whereas Th is relatively insoluble and consequently not included in the calcite. As such, a state of disequilibrium is achieved, and it can be assumed that any Th in the calcite is produced from the decay of U. The U-Th sampling procedure is also relatively straight-forward as it involves sampling the carbonate directly, and it is applicable to deposits in a range of settings, i.e. it is not dependent on the presence or preservation of organic material like ^{14}C dating is.

Tufa has been shown to be amenable to U-Th dating and this method has been applied to a multitude of tufa deposits (Hennig et al., 1983; Kronfeld, 1988; Auler and Smart, 2001; Eikenberg et al., 2001; Mallick and Frank, 2002; Soligo et al., 2002; Garnett et al., 2004b; Sierralta et al., 2010; Sancho et al., 2015). While this is an increasingly popular methodology given its advantages over other methods, and the advances in technology that has allowed for vast improvements in precise measurements, the reliability of ages obtained is sometimes uncertain (Stone et al., 2010; Chellat, 2021). The two major challenges of U-Th dating tufa are U and Th mobility due to dissolution and leaching, and detrital contamination. These scenarios violate the essential prerequisites of U-Th dating that 1) the material has behaved as a 'closed system' and 2) no initial ^{230}Th is included (Ivanovich and Harmon, 1992; Bourdon et al., 2003).

6.1.1 U-Th disequilibrium dating

^{238}Uranium is the most abundant U isotope. This element's decay leads to the production of several daughter isotopes, with ^{234}U and ^{230}Th being the essential intermediate daughter products for the purpose of U-Th dating (Figure 6.1.1). These are

produced through the *in situ* decay of ^{238}U via ^{234}Th and ^{234}Pa. The life-spans of ^{234}Th and ^{234}Pa are on the order of days and minutes. This is a short enough time for these nuclides (distinct kinds of atoms with a specific number of protons and neutrons, and particular nuclear properties) to be assumed in secular equilibrium, i.e. the activity (the number of decay events per unit time) of the daughter nuclide is equal to the activity of the parent nuclide (Ivanovich and Harmon, 1992; Bourdon et al., 2003). On the other hand, the half-lives of ^{234}U and ^{230}Th are ~245 000 years and ~75 000 years, making them viable tools for dating (Bourdon et al., 2003; Reiners et al., 2017).

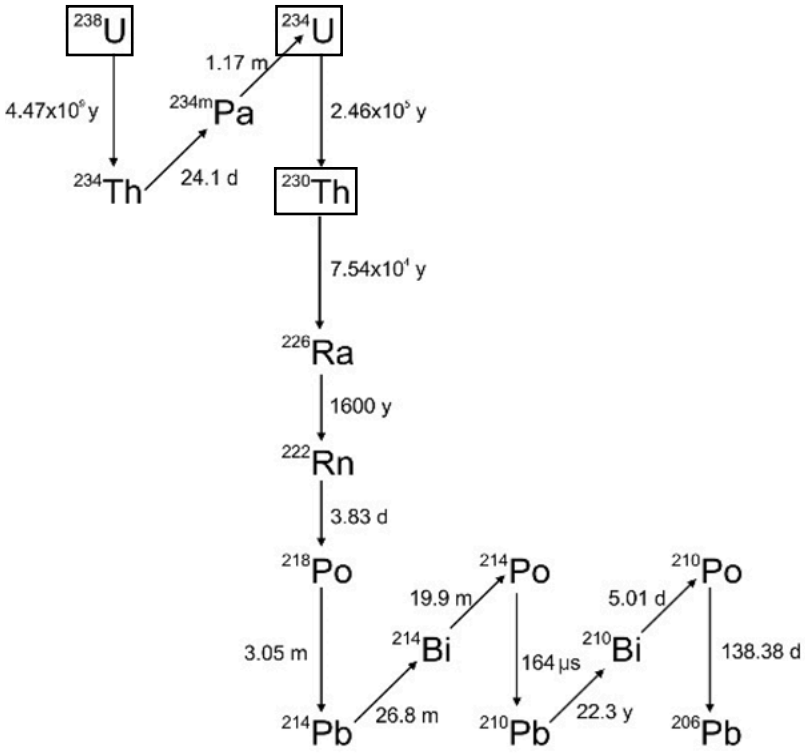

Figure 6.1.1 A schematic diagram of the uranium-series decay chain of ^{238}U, modified from Kölbel et al. (2020). The isotopes involved in U-Th dating are outlined in black.

A state of disequilibrium is generated when a closed system, in which the nuclides are considered to be in secular equilibrium, is disturbed (Bourdon et al., 2003, Richards and Dorale, 2003). This is fundamental to U-Th dating and occurs as a result of fractionation of the parent isotopes, in this case ^{238}U and ^{234}U, and daughter nuclide, ^{230}Th, due to their differences in solubility (Ivanovich and Harmon, 1992; Bourdon et al., 2003). This fractionation occurs during weathering and soil formation, and during crystallisation of minerals, e.g. calcite. Under oxidising conditions, U is transported in solution as soluble

uranyl ions (UO_2^{2+}) while Th, which is insoluble, is transported in minerals and adsorbed onto clay particles (Ivanovich and Harmon, 1992; Bourdon et al., 2003). Natural waters thus contain traces of dissolved U and almost no Th, and consequently, U is incorporated into carbonates that precipitate from natural water, whereas Th is excluded, resulting in an initial state of Th/U disequilibrium (Ivanovich and Harmon, 1992; Schwarcz, 1992; Bourdon et al., 2003).

Once precipitation has occurred and the system becomes 'closed', *in situ* radioactive decay of U to Th (and ultimately to stable Pb) changes the parent/daughter ratios over time, eventually leading to the return of secular equilibrium (Figure 6.1.2). This departure from, and subsequent return to secular equilibrium via radioactive decay forms the foundation of U-series dating (Ivanovich and Harmon, 1992; Schwarcz, 1992; Bourdon et al., 2003). Measurement of the present levels of these isotope ratios in the carbonate allows for ages to be calculated using the known decay constants (λ) of ^{234}U and ^{230}Th. These decay constants have been determined experimentally (Jaffey et al., 1971) and refined through further experimentation and recalculations (Cheng et al., 2013). Dating material in this way is possible until secular equilibrium between U and Th is re-established, at which point the upper limit of the U-Th dating method is reached (Figure 6.1.2).

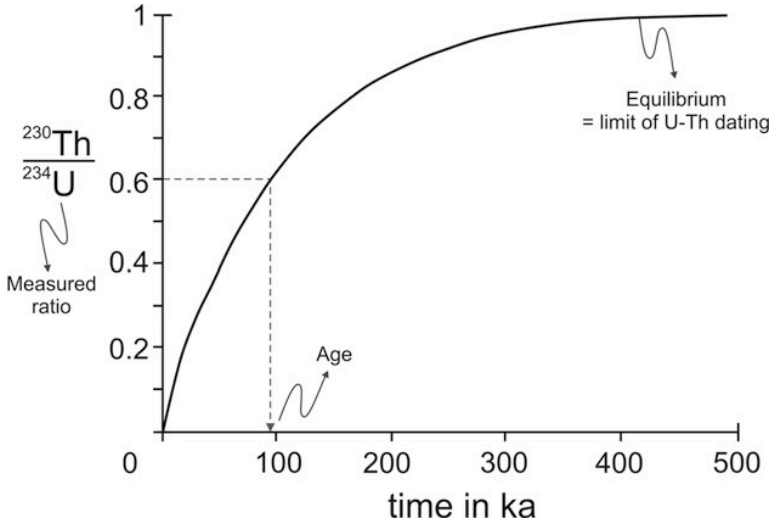

Figure 6.1.2 A plot of the ratio of daughter isotope ^{230}Th in relation to its parent isotope ^{234}U as a function of time, from Pickering (2017). As the $^{230}Th/^{234}U$ ratio approaches 1, i.e., secular equilibrium, the curve flattens out. This marks the upper limit for U-Th dating.

There are two principal assumptions for U-Th dating (Ivanovich and Harmon, 1992; Bourdon et al., 2003). The first is that the material, e.g. calcium carbonate, has behaved as a closed system, i.e., there has been no post-depositional disturbance to the U-series decay chain nuclides since carbonate formation, e.g. through dissolution and leaching or recrystallisation. In a closed system, the extent to which the U and Th activity ratios, denoted [$^{230}Th/^{238}U$], have returned to a state of secular equilibrium is a function of time (t) (Ivanovich and Harmon, 1992; Bourdon et al., 2003). This is expressed by Equation 6.1, and is based on the assumption that the activity of the U radionuclides are in equilibrium, i.e. $(^{234}U/^{238}U)_A = 1$.

Equation 6.1

$$\left[\frac{^{230}Th}{^{238}U}\right] = 1 - e^{-\lambda^{230}t}$$

However, in groundwaters the activity ratios of U are often in a state of disequilibrium, i.e. $(^{234}U/^{238}U)_A \neq 1$, due to fractionation of ^{234}U and ^{238}U during water-rock interactions (Cherdyntsev et al., 1955). During weathering and dissolution of rocks, groundwater preferentially accumulates ^{234}U. This arises as a result of alpha-emission recoil during ^{238}U decay, which damages the crystal lattice and makes ^{234}U more susceptible to leaching than ^{238}U. As a consequence, this increased mobility of ^{234}U during the weathering of host rocks adds extra ^{234}U to the groundwater, elevating the $(^{234}U/^{238}U)_A$ above 1 (Richards and Dorale, 2003). The $^{230}Th/^{238}U$ activity ratio varies with time, depending on the initial activity ratio of $^{234}U/^{238}U$ (Figure 6.1.3). As such, a term to account for initial $(^{234}U/^{238}U)_A > 1$ is necessary.

It is difficult to determine the initial $^{234}U/^{238}U$ ratio as the past U isotope ratios in groundwater cannot be measured. Consequently, the present $^{234}U/^{238}U$ in the sample needs to be measured as well as $^{230}Th/^{238}U$. The relationship between the initial $^{234}U/^{238}U$ activity ratio and measured $^{234}U/^{238}U$ activity ratio is given in Equation 6.2 and expressed in δ notation, where $(^{234}U/^{238}U)_m$ is the measured mass ratio, and $(^{234}U/^{238}U)_{eq}$ is the mass ratio at secular equilibrium. The additional term to account for initial $(^{234}U/^{238}U)_A$

> 1 produces the standard U-Th age equation (Equation 6.3) (Kaufman and Broecker, 1965).

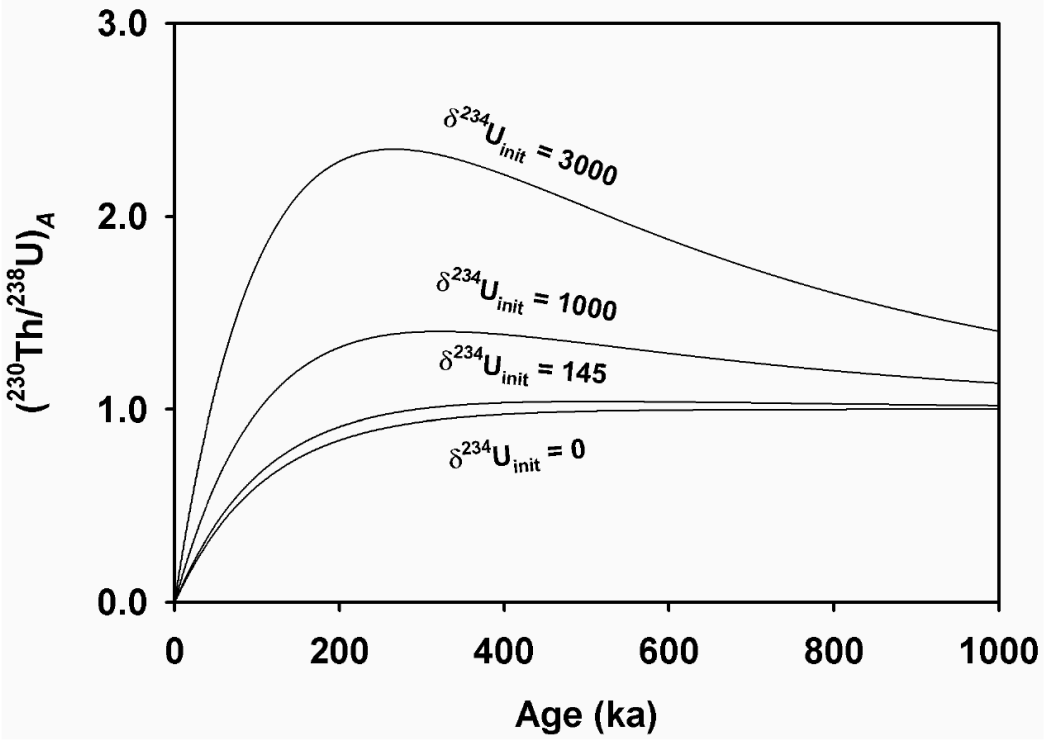

Figure 6.1.3 Plot from Richards and Dorale (2003) showing the variable activity ratio of $^{230}Th/^{238}U$ over time with different initial values of $\delta^{234}U$, assuming a closed system and the absence of initial ^{230}Th.

Equation 6.2

$$\delta^{234}U_m = (\delta^{234}U_i)e^{-\lambda^{234}t}$$

where $$\delta^{234}U_i = 1000 \times \left(\left(\frac{^{234}U}{^{238}U}\right)_m \Big/ \left(\frac{^{234}U}{^{238}U}\right)_{eq} - 1 \right)$$

Equation 6.3

$$\left[\frac{^{230}Th}{^{238}U}\right] = 1 - e^{-\lambda^{230}t} + \left(\frac{\delta^{234}U_m}{1000}\right)\left(\frac{\lambda^{230}}{\lambda^{230} - \lambda^{234}}\right) \times \left(1 - e^{-(\lambda^{230} - \lambda^{234})t}\right)$$

The second assumption is that the initial $^{230}Th/^{238}U$ activity ratio is zero (Ivanovich and Harmon, 1992; Bourdon et al., 2003). The ^{230}Th measured in the carbonate is therefore assumed to be produced by the *in situ* decay of U from the time of deposition, and the age of the sample is thus determined by the extent to which the $^{230}Th/^{234}U$ has returned to unity (or secular equilibrium). This is calculated using the known decay constants for ^{234}U and ^{230}Th (Cheng et al., 2013), and from the measured $^{230}Th/^{238}U$ and $^{234}U/^{238}U$ ratios in the sample (Hellstrom, 2003).

However, in nature it is seldom the case that the initial Th is zero, and ^{230}Th is often introduced into carbonates via clay detritus. The presence of this detritus introduces excess ^{230}Th i.e., not produced by U decay, violating the prerequisite of zero initial ^{230}Th (Bourdon et al., 2003). If not corrected for, this excess ^{230}Th distorts the calculated age of the sample making it appear older than it is (Hellstrom, 2006). It is not possible to distinguish between radiogenic ^{230}Th, i.e., produced via U decay, and detrital ^{230}Th, and because the source and amount of detritus varies for individual deposits, it is not possible to apply a universal correction to account for excess initial ^{230}Th.

In order to navigate the challenge associated with initial ^{230}Th, ^{232}Th is used as a proxy to estimate and correct for detrital ^{230}Th included in the sample. This works because ^{232}Th is the most abundant, naturally occurring Th isotope and is not produced by U decay, but it does co-precipitate with detrital ^{230}Th (Scholz and Hoffmann, 2008). It is therefore monitored during analysis and used as a proxy for detrital ^{230}Th contamination, i.e., the activity ratio of $^{230}Th/^{232}Th$ can be used to estimate how much detrital ^{230}Th is in the sample, and a correction can be applied to account for this contamination (Hellstrom, 2006).

Various methods to correct for initial Th are available. Initially, methods to correct for detrital ^{230}Th involved isochron techniques. This was done by analysing the isotopic composition of the detrital phase via selective leaching procedures (Ku and Liang, 1984; Schwarcz and Latham, 1989; Kaufman, 1993) or total sample dissolution (Bischoff and Fitzpatrick, 1991; Luo and Ku, 1991). An alternative method is to apply an *a priori* estimate of the initial $^{230}Th/^{232}Th$, and to subtract this from the measured isotopic

abundances, i.e., ^{238}U, ^{234}U and ^{230}Th (Dorale et al., 1998; Zhao et al., 2001; Hellstrom, 2006). Importantly, this estimated value must include an estimate of its uncertainty, and this uncertainty must be propagated through the age calculation (Hellstrom, 2003; Ludwig, 2003). Although this option is simpler than constructing an isochron, it can lead to considerable uncertainties associated with the corrected ages, particularly for highly contaminated samples.

An additional term to account for initial Th included in the U-Th age equation produces the standard U-Th age equation used in this study (Equation 6.4). The equation cannot be solved directly, and instead an iterative procedure to solve for t is applied. Square brackets indicate measured activity ratios, λ's are the decay constants, t is age, and i indicates initial ratio at $t = 0$.

Equation 6.4

$$\left[\frac{^{230}Th}{^{238}U}\right] = 1 - e^{-\lambda^{230}t}\left(1 - \left[\frac{^{230}Th}{^{232}Th}\right]_i \times \left[\frac{^{232}Th}{^{238}U}\right]\right) + \left(\left[\frac{^{234}U}{^{238}U}\right] - 1\right) \times \left(\frac{\lambda^{230}}{\lambda^{230} - \lambda^{234}}\right) \times \left(1 - e^{-(\lambda^{230} - \lambda^{234})t}\right)$$

6.1.2 LA-ICP-MS U-Th concentration screening

Another way to address the issue of initial ^{230}Th is to avoid sampling carbonate that has a high proportion of detrital material. Naked eye and thin section observations can assist with this, but this is not always reliable. With LA-ICP-MS, it is possible to 'screen' a sample, i.e., the concentrations of U and Th (and Pb) can be measured to assess the distribution and concentration of these elements in a sample, guided by the notion that layers with sufficiently high levels of U, and low levels of Th are the best targets for producing reliable age data (Richards and Dorale, 2003). This can provide information on the location of detrital components not visible on a meso- or micro-scale, and has proved a useful tool for targeted dating of speleothems (Woodhead and Pickering, 2012). As such, this screening step can inform on the optimum areas within a sample to target

for dating, thereby improving the reliability of the ages obtained and making the process more efficient.

Prior to my study, and to the best of my knowledge, this LA-ICP-MS screening approach has not been applied to tufas. However, tufas are an ideal medium to test this method as they are notoriously difficult to date due to a typically high detrital component. Tufa deposits are also often characterised by a high degree of porosity, and this enhances the chances for open system behaviour and U mobility (leaching or dissolution).

6.1.3 History of U-Th method applied to dating tufas

Early applications of U-Th dating to tufa deposits were based on alpha radiometric dating methods (e.g., Harmon et al., 1980; Hennig et al., 1983). With the exception of Hennig et al. (1983), who reported 140 U-Th tufa and travertine ages, datasets for U-Th dating via alpha spectrometry were small since it could take several days to obtain a single U-Th measurement (Latham, 2001). Ages calculated using this method usually had large associated errors, and the age determinations were limited by insufficient methods to correct for initial $^{230}Th/^{232}Th$ (Hennig et al., 1983; Smart, 1991).

Despite the improvement of mass spectrometry in the 1980s, and advances in analytical procedures for U-Th dating, measurements using alpha spectrometry were still applied to tufa deposits into the early 2000s (Horvatinčić et al., 2000; Auler and Smart, 2001; Eikenberg et al., 2001; Soligo et al., 2002). These were usually paired with a second dating technique, e.g. ^{14}C or ^{226}Ra, to verify the age determinations (Kronfeld, 1988; Horvatinčić et al., 2000; Eikenberg et al., 2001). Kronfeld (1988) used both ^{14}C and U-Th dating methods to determine the ages of the Bet Shean tufa deposit in Israel. They obtained U-Th age results for four of the seven samples analysed. They then applied four different values, between 1 to 2.3, as initial $^{230}Th/^{232}Th$ estimates to correct the U-Th ages. The age results varied by ~10 ka depending on the initial $^{230}Th/^{232}Th$ value applied, and ultimately a value of 2.3 returned U-Th ages that most closely matched the ^{14}C ages. Auler and Smart (2001) dated fossil tufa deposits and subaqueous speleothems in the semi-arid coastal region of north-eastern Brazil to investigate periods of increased

rainfall in the past. They sampled eleven tufas from five different sites and analysed these for U-Th dating using alpha-spectrometry. Four of the eleven samples had $^{230}Th/^{232}Th$ activity ratios <20, indicating a significant detrital component. Ages obtained for these samples were therefore corrected using an initial $^{230}Th/^{232}Th$ ratio of 1.7, following the recommendation of Kaufman (1993). Seven of the eleven tufas returned ages between 9.7 ± 0.3 ka and 21.4 ± 0.5 ka, while the rest indicated ages close to 400 ka. These older ages have large uncertainties, around 100 ka, and this is because these ages are close to the limit of alpha spectrometry, whereas the errors associated with the younger ages are smaller, <8% (Auler and Smart, 2001).

Currently, the dominant method for measuring U-series isotopes is with the use of inductively coupled plasma mass spectrometry (ICP-MS). Initially, thermo-ionisation mass spectrometry (TIMS), and later multi-collector inductively coupled plasma mass spectrometry (MC-ICP-MS), vastly improved the accuracy and precision of U-Th ages, the time it takes to measure, and the age limit (up to 600 ka) (Goldstein and Stirling, 2003). However, because of the common detrital component and often high porosity in tufa deposits, obtaining accurate and precise ages for tufa using the U-Th method remains a challenge. A more systematic approach was recommended by Mallick and Frank (2002) to identify primary calcite and to determine areas affected by detrital contamination and alteration, before sample selection for U-Th analysis. These prior investigations involved microscopic, mineralogical and geochemical investigations of tufa samples, e.g. XRD, cathodoluminescence, and trace element analysis, to identify primary calcite and avoid alteration phases and secondary cement. This greatly improved the success rate of obtaining reliable U-Th ages, and Mallick and Frank (2002) thus suggested the following criteria for U-Th sample selection: 1) micrite and/or spar should be the dominant phases, 2) luminescence of calcite phases should be weak or absent, 3) Fe, Al and Th levels should be low, and 4) Sr concentrations should be close to the average Sr values of the studied site.

Stone et al. (2010) carried out a study to assess the validity of the U-Th dating technique applied to tufa deposits in the Naukluft Mountains in Namibia, and they employed a rigorous approach in which multiple sub-samples from five distinct tufa units were

analysed. They measured the insoluble residues, used isochron mixing lines to correct for detrital Th, and carried out complimentary cathodoluminescence and micromorphological analyses. In total, they analysed 23 sub-samples using both a Nu Plasma multi-collector mass spectrometer (MC-ICP-MS) and a thermal ionisation mass spectrometer (TIMS). Stone et al. (2010) argue that, while many of the results obtained are geochemically acceptable when considered in isolation, problems with the ages are evident when considered in context of the deposit as a whole.

Doran et al. (2015) investigated tufa deposits at three localities along the Ghaap escarpment in South Africa to assess their potential as palaeoclimate indicators. Nine samples were dated using accelerated mass spectrometry (AMS) radiocarbon dating (^{14}C), and six samples were dated with the U-Th method using a MC-ICP-MS. Two of the samples were dated using both methods, and one sample dated using ^{14}C returned an infinite age. The resultant suite of twelve ages suggest that tufa formation occurred at these sites during the Middle and Late Pleistocene, and Holocene. The U-Th dated tufa returned the following ages from the Middle Pleistocene: 369.4 ± 12.3 ka, 275.4 ± 29.4 ka, 221.4 ± 6.3 ka, and 127.4 ± 3.5 ka, and the Holocene: 11.6 ± 6.2 ka and 5.8 ± 5.2 ka. The samples dated using U-Th have $^{230}Th/^{232}Th$ activity ratios of <3.5, indicating significant detrital contamination, which was corrected for using an estimated initial $^{230}Th/^{232}Th$ value of 1.5 ± 1.5, as recommended by Hellstrom (2006). Errors on the four Mid-Pleistocene ages are generally low (<10%), whereas the two Holocene ages have very large errors of 53% and 90%, respectively. These two samples were also dated with ^{14}C and the calibrated (cal) ages, 10.71 ± 0.2 cal ka BP and 5.4 ± 0.2 cal ka BP, are in good agreement with the U-Th ages, suggesting that the U-Th ages obtained provide a reliable chronology. Other tufa samples dated using the ^{14}C method date to the Late Pleistocene and Holocene (errors are given as 1σ): 44 ± 0.8 cal ka BP, 40 ± 0.8 cal ka BP, 4.5 ± 02 cal ka BP, 2.1 ± 0.2 cal ka BP, and 0.3 ± 0.1 cal ka BP.

6.1.4 Concluding remarks

The selected case studies outlined above illustrate the application of the U-Th dating method to tufa deposits. Advances in mass spectrometry has resulted in significant

improvements in the reliability and accuracy of ages, as well as pushing the technique to provide ages up to 600 ka. Careful sampling and a thorough knowledge of the context of tufa deposits is necessary in order to make reliable and meaningful age interpretations. However, in some instances it may simply not be possible to obtain a reliable U-Th age result from tufa because of a high detrital input (too much Th) and a high degree of porosity and permeability (leaching and U mobility). Despite the challenges associated with U-Th dating tufa, it remains the most promising option for acquiring ages for tufa deposits, and the effect of these issues can be partially mitigated through iterative field and lab campaigns and careful sample selection (Hellstrom and Pickering, 2015). Repeated sampling of material from a single stratigraphic layer is the best way to test for open or closed system behaviour (Hellstrom and Pickering, 2015), and a $^{232}Th/^{230}Th$ correction for detrital Th should be routinely applied to account for initial ^{230}Th (Hellstrom, 2006).

6.2 U and Th results for Ga-Mohana Hill tufa

This section documents the U and Th concentrations measured in the tufa samples using laser ablation inductively coupled plasma mass spectrometry (LA-ICP-MS), the U and Th activity ratios measured in solution using a MC-ICP-MS, and the resultant ages calculated. In Section 6.2.1, the U and Th data collected using LA-ICP-MS is reported as it informed the sample selection for U-Th dating, i.e. layers with low Th were targeted, and the concentration of U was used to calculate the amount of sample needed for U-Th analyses. The U and Th activity ratios measured in solution are reported in Section 6.2. Ultimately, the U and Th activity ratios measured in solution were used to calculate the U-Th ages, and the subsequent age results are reported in Table 6.1. The implications of the ^{238}U and ^{232}Th concentrations, activity ratios and ages reported are discussed in Section 6.3.

The primary aim was to obtain reliable U-Th age results for the Ga-Mohana tufa deposits. Once it was established that this was possible, tufa samples from each of the morphologies, i.e. cascades, barrages, rim pools, terrace breccias and domes, were selected for dating, with the aim being to determine when the tufa system had been active in the past, and to test the suitability of each of the morphologies to U-Th dating.

6.2.1 LA-ICP-MS screening of U and Th in Ga-Mohana tufa

The results of the screening process using LA-ICP-MS are presented in the composite Figures 6.2.1-6.2.3, which show an image of a small slab cut from each sample (to fit into the laser cell) overlain with U and Th element distribution maps. Each sample showed variability in the U and Th distributions, and these were used to identify layers most suitable for U-Th dating.

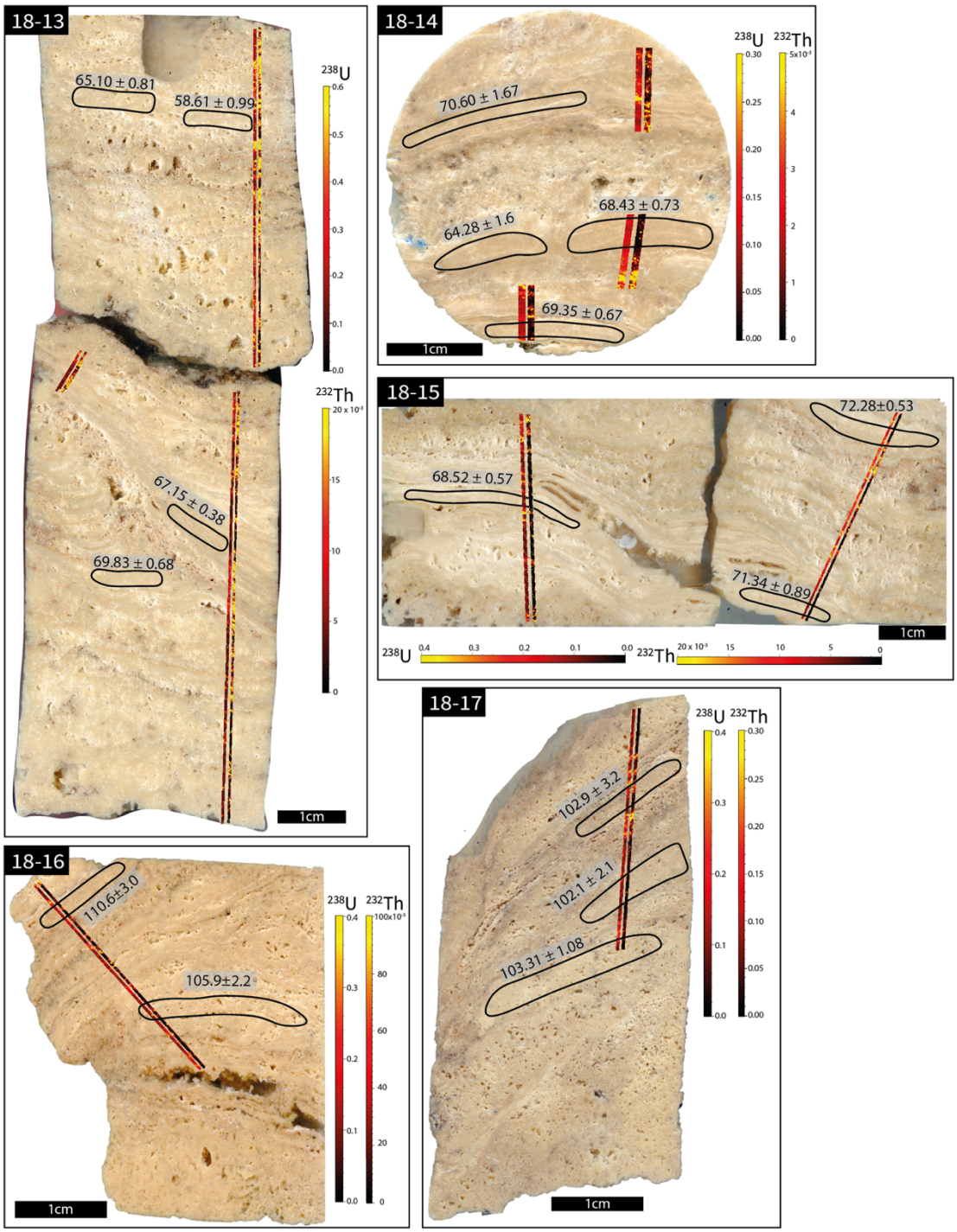

Figure 6.2.1 High resolution scans of cascade core sample slabs overlain by U (left) and Th (right) element distribution maps constructed using LA-ICP-MS data. The element concentrations for each sample are given by the colour scales in ppm. Black oblong shapes outline the location of sub-samples drilled for U-Th dating. The associated ages are given in thousands of years (ka), and these ages are reported in Table 6.1.

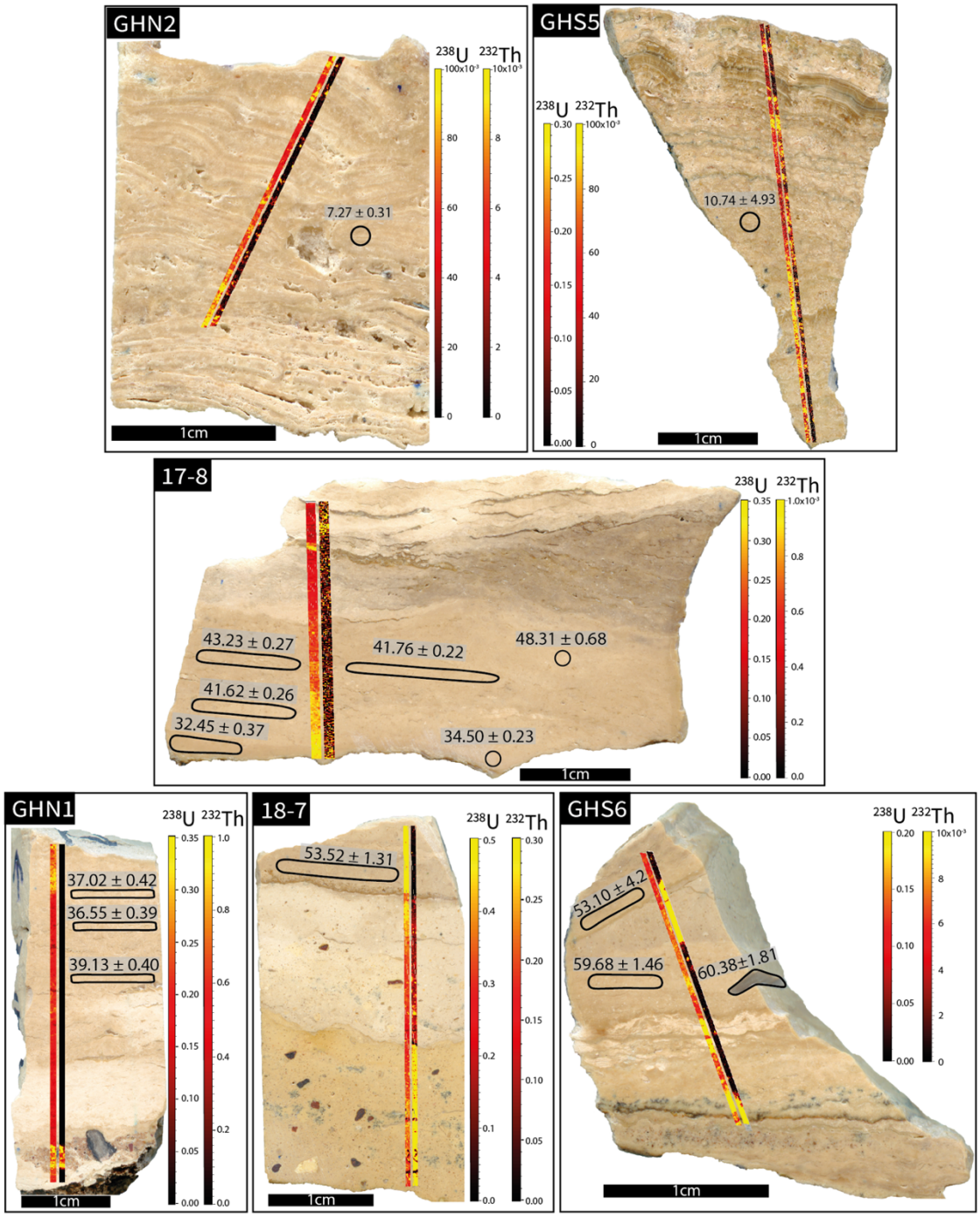

Figure 6.2.2 High resolution scans of cascade and terrace breccia sample slabs overlain by U (left) and Th (right) element distribution maps constructed using LA-ICP-MS data. The element concentrations for each sample are given by the colour scales in ppm. Black oblong shapes outline the location of sub-samples drilled for U-Th dating. The circles represent the approximate location of sub-samples drilled for U-Th dating prior to LA-ICP-MS screening. The associated ages are given in thousands of years (ka), and these ages are reported in Table 6.1.

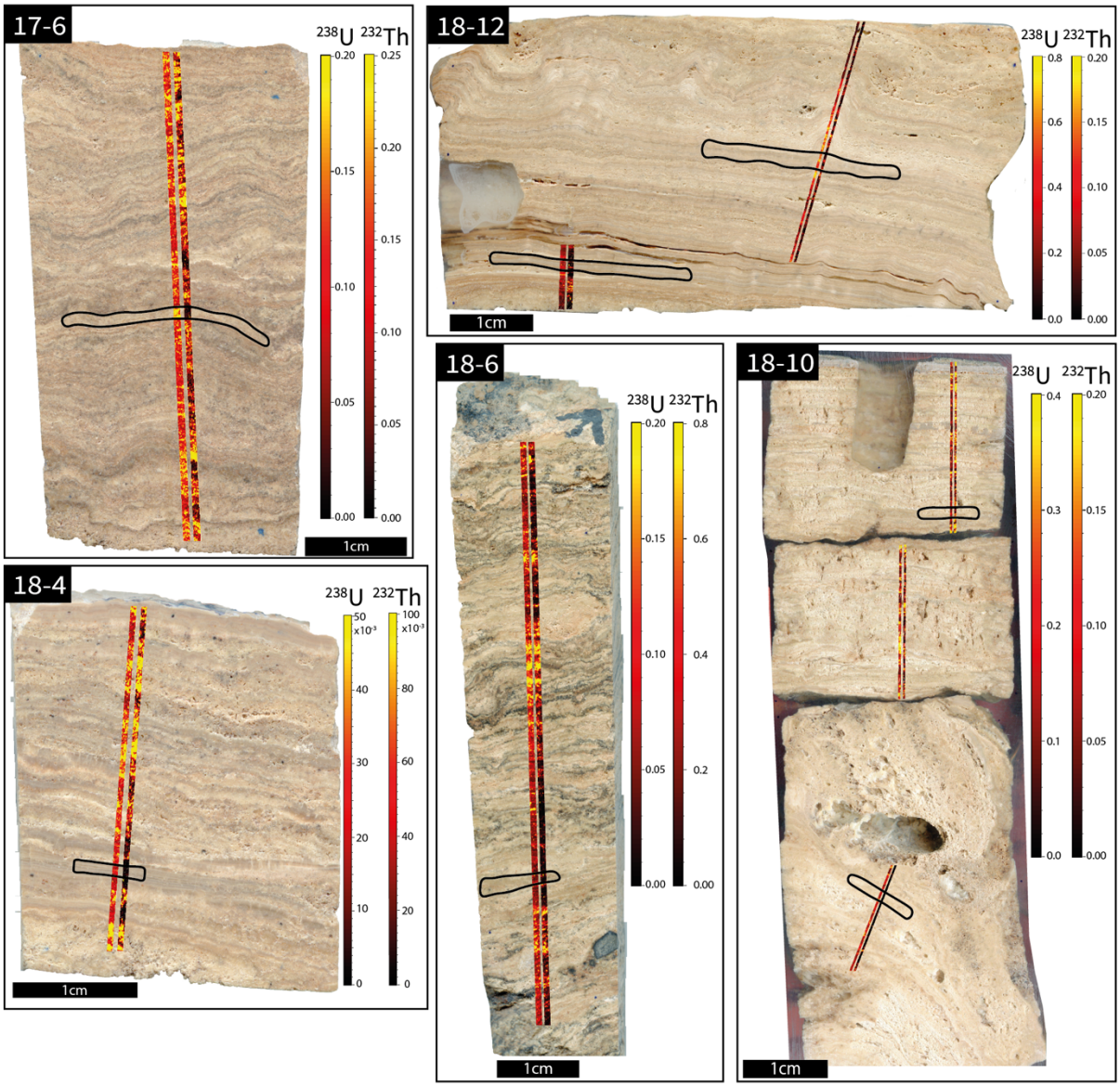

Figure 6.2.3 High resolution scans of cascade and terrace sample slabs overlain by U (left) and Th (right) element distribution maps constructed using LA-ICP-MS data. The element concentrations for each sample are given by the colour scales in ppm. Black oblong shapes outline the location of sub-samples drilled for U-Th dating. No age solution could be determined for sub-samples drilled from these samples, except 18-10.2. The U and Th activity ratios measured in these sub-samples are given in Table 6.2.

6.2.1.1 U concentration

In general, the U concentrations in the Ga-Mohana tufas measured by LA-ICP-MS are consistently low, with an average value of about 0.2 ppm, ranging between 0.1 to 0.6

ppm. Two cascade samples, GHN2 and 18-4, have U concentrations an order of magnitude lower than the average, with concentrations of between 20-100 ppb. Whereas abrupt changes in U concentrations across layers are clearly distinguishable in several samples, no clear or consistent relationship between the layering and U concentration distribution could be discerned, with variable U concentrations recorded in visually similar material within and between samples. The element distribution maps were constructed to get a sense of the continuity of the measured concentrations in each layer, and to extrapolate along the layers with some confidence, rather than relying on a single-point measurement. While the lateral distribution of the concentrations appears to be fairly consistent, this is on a very small scale (the laser tracks are about 0.5 mm in width) and many of the samples have lateral stratigraphic variations (Figures 6.2.1-6.2.3). This means that although the screening provides useful information, it is based on a very small portion of the sample and cannot be confidently extrapolated along layers.

6.2.1.2 Th concentration as an indicator of detrital ^{230}Th

As expected, the Th concentrations are generally lower than the U concentrations, with most samples reflecting a wide range in Th concentration of between 1-100 ppb. Several samples, 17-6, 18-6 and 18-7, record Th concentrations that are significantly higher, up to a maximum of 5 ppm in some layers. In the case of 18-7, the layers that record high levels of Th consist of clearly discernible detrital material, confirmation that Th effectively tracks detrital inputs. In samples 17-6 and 18-6, however, the layering is much finer and irregular, making it less obvious to visually determine the layer composition. These samples record alternating high and low levels of Th across the layers together with jagged and poorly defined contacts. Very frequent, small-scale alternations of Th concentrations are picked up in the laser maps where at times this sub-mm scale layering is not visible in the macroscale. This cautions against assumptions of homogeneity, even in layers that appear fairly uniform.

In some samples, such as 18-16 and 18-17, there is little to no Th except at a few points in the transect where the Th concentration recorded is as high as 0.3 ppm (18-17). These

anomalous peaks in Th concentration coincide with layers with a subtly different colour to the rest of the sample and correspond to elevated levels of U.

Overall, the Th concentrations appear to be lowest in samples with layers that are visually 'clean' i.e., layers that consist of dense creamy-brown carbonate with no visible grains or changes in colouring (e.g., samples GHN1 and 17-8). However, in some instances, material that appears 'clean' in the macroscale records relatively high Th concentrations (e.g., GHS5 and 18-12) (Figure 6.2.1). In some samples, the Th concentration maps pick out and highlight layers that are a different colour and thus confirm visual assessments. In other samples, e.g., 17-8, the Th concentration map is mottled, suggesting that the overall concentration is < 1 ppb, i.e., a negligible amount of Th and below detection limits. These observations highlight the limitations of selecting layers to date based on visual assessment alone and illustrate the utility of the LA-ICP-MS pre-screening process.

In many instances, the U and Th concentrations mirror each other, increasing or decreasing synchronously. These layers are generally not ideal for dating because a high U concentration, coupled with a high Th concentration, or vice versa - a low Th concentration accompanied by low U does not meet the criteria. In several instances, though, the element concentrations in a single layer are opposing, with elevated levels of U accompanied by little to no Th. It is these layers which were targeted for U-Th sampling.

6.2.2 U and Th ratios measured on MC-ICP-MS

Following the chemical preparation (described in Chapter 3) of the selected sub-samples illustrated with black oblong outlines in Figures 6.2.1-6.2.3, the U and Th activity ratios were measured on the multi-collector ICP-MS and used to calculate the age of each subsample, using the equations given in Section 6.1.1. These results are summarised in Table 6.1 and Table 6.2 and described in the following sub-sections.

Table 6.1 U and Th isotope ratios measured in tufa samples with reliable and precise ages. The samples are labelled according to the sequence they were collected in but are presented in stratigraphic order. Errors on all isotope activity ratios are reported with 2σ uncertainty. All ages have been corrected to account for the effect of detrital Th assuming an estimate for initial $^{230}Th/^{232}Th$ of 1.5 ± 1.5, and calculated using the ^{230}Th-^{238}U decay constants of Cheng et al. (2013) and equation 1 from Hellstrom (2006).

Sample ID	^{238}U ng/g	[$^{230}Th/^{238}U$]	2σ	[$^{234}U/^{238}U$]	2σ	[$^{232}Th/^{238}U$]	2σ	[$^{230}Th/^{232}Th$]	U-Th age (ka)	2σ	% error
18-10.3	174	0.088	0.001	2.443	0.006	0.013409	0.000268	6.5	3.0	0.9	30
GHN-2	75	0.184	0.002	2.728	0.009	0.005083	0.000089	36.2	**7.3**	0.3	4.1
GHS-5	263	0.251	0.002	1.866	0.007	0.054496	0.000692	4.6	**10.7**	4.9	45.8
17-8.1	363	0.707	0.002	1.895	0.003	0.008000	0.000104	88.4	**48.3**	0.7	1.4
17-8.2	273	0.528	0.002	1.894	0.003	0.002214	0.000019	238.3	**34.4**	0.2	0.6
17-8.3	321	0.621	0.002	1.896	0.005	0.000184	0.000004	3367.7	**41.8**	0.2	0.5
17-8.4	298	0.641	0.003	1.903	0.005	0.000142	0.000003	4516.0	**43.2**	0.3	0.7
17-8.5	307	0.618	0.003	1.895	0.005	0.000127	0.000003	4858.7	**41.6**	0.3	0.7
17-8.6	459	0.503	0.004	1.899	0.006	0.002320	0.000046	216.6	**32.5**	0.4	1.2
GHN-1	236	0.576	0.005	1.863	0.006	0.000805	0.000072	716.3	**39.1**	0.4	1.0
GHN-1.2	234	0.543	0.005	1.859	0.006	0.000080	0.000002	6818.5	**36.6**	0.4	1.1
GHN-1.3	240	0.551	0.005	1.868	0.007	0.000051	0.000001	10846.4	**37.0**	0.4	1.1
GHS-6	212	0.864	0.007	1.914	0.007	0.020890	0.000507	41.3	**60.4**	1.8	3.0
GHS-6.1	180	0.852	0.005	1.913	0.007	0.016957	0.000394	50.3	**59.7**	1.5	2.5
GHS-6.2	190	0.873	0.003	1.928	0.005	0.003473	0.000069	251.3	**61.9**	0.5	0.8
GHS-6.3	158	0.798	0.003	1.882	0.004	0.050119	0.001002	15.9	**53.1**	4.2	7.9
18-7	847	0.749	0.003	1.833	0.005	0.014829	0.000297	50.5	**53.5**	1.3	2.4
18-13.1	249	1.174	0.003	2.654	0.007	0.017183	0.000344	68.3	**58.6**	1.0	1.7
18-13.2	226	1.313	0.003	2.742	0.007	0.014022	0.000280	93.6	**65.0**	0.8	1.2
18-13.3	132	1.287	0.004	2.646	0.007	0.002075	0.000041	620.5	**67.2**	0.4	0.6
18-13.4	195	1.483	0.004	2.933	0.008	0.011902	0.000238	124.6	**69.8**	0.7	1.0
18-14.1	83	1.308	0.009	2.644	0.009	0.005376	0.000108	243.4	**68.4**	0.7	1.0
18-14.2	139	1.219	0.006	2.551	0.008	0.026423	0.000528	46.1	**64.3**	1.6	2.5
18-14.3	98	1.351	0.008	2.705	0.009	0.003077	0.000062	439.1	**69.4**	0.7	1.0
18-14.4	180	1.481	0.006	2.876	0.008	0.031531	0.000631	47.0	**70.6**	1.7	2.4
18-15.1	137	1.319	0.007	2.668	0.008	0.001688	0.000034	781.0	**68.5**	0.6	0.9
18-15.2	95	1.317	0.011	2.587	0.010	0.001764	0.000035	746.9	**71.3**	0.9	1.3
18-15.3	313	1.522	0.005	2.940	0.008	0.006626	0.000133	229.7	**72.3**	0.5	0.7
18-17.1	154	2.176	0.006	3.194	0.006	0.074913	0.001498	29.0	**102.9**	3.2	3.1
18-17.2	148	2.085	0.007	3.102	0.006	0.047194	0.000944	44.2	**102.1**	2.1	2.1
18-17.3	142	2.217	0.006	3.289	0.006	0.023170	0.000463	95.7	**103.3**	1.1	1.1
18-16.1	164	2.586	0.008	3.614	0.007	0.078583	0.001572	32.9	**110.6**	3.0	2.7
18-16.2	177	2.404	0.007	3.476	0.007	0.054789	0.001096	43.9	**105.9**	2.2	2.1

Table 6.2 U and Th isotope ratios measured in tufa samples which have unreliable or imprecise age solutions. Errors on all isotope activity ratios are reported with 2σ uncertainty. Upper limit is defined as corrected age plus 2σ uncertainty. All ages have been corrected to account for the effect of detrital Th assuming an estimate for initial $^{230}Th/^{232}Th$ of 1.5 ± 1.5, and calculated using the ^{230}Th-^{238}U decay constants of Cheng et al. (2013) and equation 1 from Hellstrom (2006).

Sample ID	^{238}U ng/g	$[^{230}Th/^{238}U]$	2σ	$[^{234}U/^{238}U]$	2σ	$[^{232}Th/^{238}U]$	2σ	$[^{230}Th/^{232}Th]$	U-Th age (ka)	2σ	Estimated upper limit (ka)
GHN3.1	209	0.238	0.004	2.396	0.007	0.202472	0.005325	1.2	-3.7	16.2	**<12.5**
GHN3.2	149	0.283	0.007	2.263	0.007	0.263966	0.007649	1.1	-7.2	24.0	**<16.8**
GHS4	207	0.242	0.003	1.75	0.007	0.314020	0.006247	0.8	-20.8	46.4	**<25.8**
17-6.1	196	0.295	0.002	1.949	0.003	0.315837	0.003331	0.9	-14.5	38.1	**<23.6**
17-6.2	219	0.162	0.001	2.009	0.004	0.098911	0.001978	1.6	0.7	8.8	**<9.5**
18-4	28	0.199	0.006	1.752	0.01	0.170880	0.003418	1.2	-4.6	19.1	**<14.5**
18-6	68	0.601	0.004	1.739	0.004	0.835852	0.016717	0.7	-	-	***infinity***
18-10.1	86	0.484	0.003	2.393	0.007	0.627906	0.012558	0.8	-	-	***infinity***
18-12.1	379	7.29	0.017	2.296	0.005	1.371873	0.027437	5.3	-1532.0	11145.3	***no age***
18-12.2	414	0.223	0.002	2.49	0.005	0.075426	0.001509	3	5.1	5.1	**<10.2**

6.2.2.1 U concentrations in solution

The mean ^{238}U concentration measured from the samples in solution is ~0.22ppm. A visual assessment of the element distribution maps (Figures 6.2.1-6.2.3) indicates that the U concentrations of the layers sub-sampled for dating generally reflect values comparable to those measured in solution (Table 6.1).

There is significant variation in the $^{234}U/^{238}U$ activity ratio, hereafter $[^{234}U/^{238}U]$, measured in the tufa sub-samples, with values ranging from 1.833 to 3.614, and a mean value of 2.443. The initial $[^{234}U/^{238}U]$ values, hereafter $[^{234}U/^{238}U]_i$, are back calculated using the measured $[^{234}U/^{238}U]$ and the calculated U-Th ages (Equation 6.3). The $[^{234}U/^{238}U]_i$ ratios range from 1.892 to 4.572, with a mean of 2.755. The initial ratios are slightly higher than the measured ratios, which is expected since these isotopes become gradually depleted over time as they decay to produce daughter isotopes ^{230}Th, and others in the U-series decay chain. Interestingly, there is an overall increase in both the initial and measured $[^{234}U/^{238}U]$ ratios with increasing age; i.e. young samples have low initial $[^{234}U/^{238}U]$ ratios while older samples have higher ratios, with the exception of

samples 18-10.2 and GHN2 (Table 6.2.1). Despite being the youngest samples, they have a [$^{234}U/^{238}U$] value of 2.455 and 2.728 respectively, both of which are higher than the mean value of 2.443.

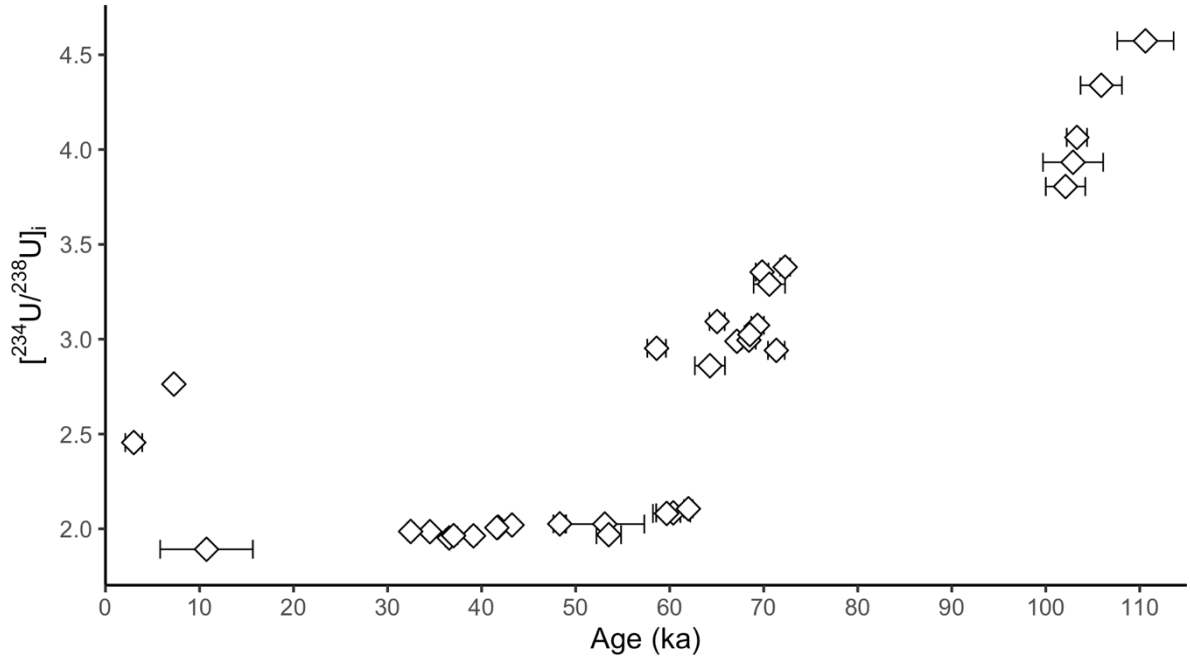

Figure 6.2.1 Plot of age in thousands of years against the measured $^{234}U/^{238}U$ activity ratio in Ga-Mohana tufa samples. Error bars represent error on the ages. The average error on the ($^{234}U/^{238}U$) measurement is 0.007 and contained within the symbols plotted.

6.2.2.2 $^{230}Th/^{232}Th$ activity ratio

The measured activity ratio of $^{230}Th/^{232}Th$, hereafter [$^{230}Th/^{232}Th$] in the samples reflects the level of detrital Th contamination contained in the samples, and as such serves as an index for the input of non-radiogenic ^{230}Th. Low [$^{230}Th/^{232}Th$] indicates a higher proportion of Th-bearing detritus, whereas high ratios signify 'clean' material i.e. little to no detrital contamination. Material with $^{230}Th/^{232}Th$ activity ratios less than 20 are generally considered too highly contaminated to return a reliable age estimate (Schwarcz and Latham, 1989; Hellstrom, 2006). The Ga-Mohana tufa samples contain a wide range of [$^{230}Th/^{232}Th$] values across several orders of magnitude. Minimum values of [$^{230}Th/^{232}Th$] less than 3.0 were recorded in sub-samples for which no age solution

could be determined (Table 6.2). An extreme maximum value of 10846.4 was measured in sub-sample GHN-1.3, illustrating the purity of the material sampled.

Interestingly, these [$^{230}Th/^{232}Th$] ratios vary considerably within samples, with sub-samples measuring values with a difference of as much as 4000 from a single sample, as can be seen in 17-8 for example, which has a range of [$^{230}Th/^{232}Th$] from 88.4 to 4858.7. This highlights the heterogeneity of the distribution of detrital Th within samples. Three of the samples that did return ages despite having [$^{230}Th/^{232}Th$] values <20 are 18-10.2, GHS-5 and GHS-6.3. The effect of these high levels of detrital contamination are reflected in the large errors associated with these age results (~30%, ~46% and ~8% respectively).

6.2.3 U-Th age results

The resultant ages calculated using the activity ratios $^{230}Th/^{238}U$ and $^{234}U/^{238}U$ and Equation 6.4 are given in Table 6.1. A total of thirty-three resolvable ages were obtained, spanning a time range from 110.6 ± 3.0 ka to 3.0 ± 0.9 ka. The 2σ uncertainties associated with the ages vary considerably from 220 years (0.5% precision) to as much as ~4.93 ka (49% precision), with an average uncertainty of ~1.2 ka, equivalent to 3.2% precision.

The U-Th ages are plotted in Figure 6.2.5, and based on clusters of overlapping ages, I have identified five tufa formation stages. These formation stages are based on the available age data collected to date from a comprehensive but limited suite of samples. I note that the ages and the samples they come from may not represent tufa formation at Ga-Mohana Hill in its entirety, and there may be gaps in the record. The bounds of these groupings are defined by the minimum and maximum ages within a cluster, calculated using the uncertainties of the ages. The location of the ages obtained for each sample are illustrated in Figures 6.2.1 and 6.2.2. Samples with no age solution (Table 6.2) are shown in Figure 6.2.3. Below, I describe the U-Th ages in relation to the samples they come from and their field and stratigraphic contexts, organised according to the tufa stages identified, from oldest to youngest. Samples for which reliable age estimates could not be determined are also briefly discussed at the end.

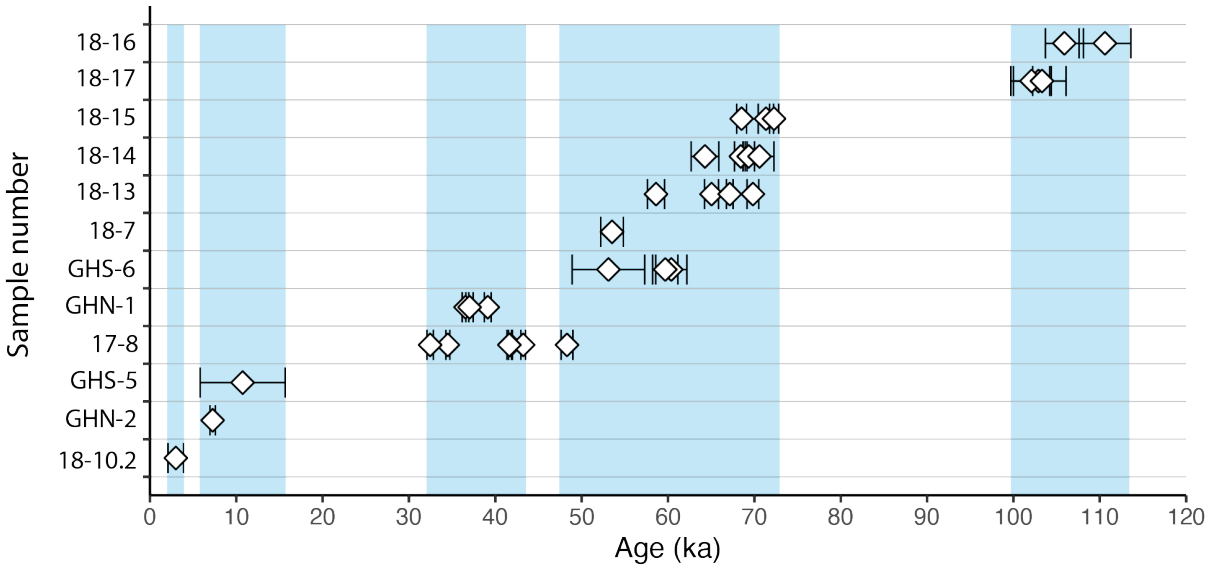

Figure 6.2.5 Plot of Ga-Mohana tufa U-Th ages, grouped according to their sample numbers. The blue bars highlight the clusters of ages identified.

6.2.3.1 Tufa stage 1 (~114 - 100 ka)

The oldest tufas sampled from Ga-Mohana Hill have the following ages: 110.6 ± 3 ka and 105.9 ± 2.2 ka (sample 18-16), and 103.31 ± 1.08 ka, 102.1 ± 2.1 ka and 102.9 ± 3.2 ka (sample 18-17). Age results from sample 18-16 have precisions of 2.1% and 2.7%, respectively, and ages from sample 18-17 have precisions of 1%, 3%, and 2%, respectively. These samples were collected by drilling adjacent (about 40 cm apart) short cores from a single *ex-situ* cascade tufa, sampled specifically to target older material (detailed in Chapter 3). These cascades are likely not far from their original positions and are still relatively intact with clearly preserved crystalline layering (Figure 6.2.6).

Sample 18-16 is from a section of the cascade interpreted to be close to the base of the cascade, i.e., previously attached to the dolomite cliff or an older layer of tufa, and 18-17 is from a stratigraphically higher position, i.e. closer to the outer / younger edge of the cascade. Because the cascade tufa is *ex-situ*, it isn't easy to know the orientation of the samples with absolute certainty, and so, while the two ages from sample 18-16 appear to be in stratigraphic order, only a third subsample from between the two ages would provide further confirmation. The three ages obtained from sample 18-17 are all within error of one another. Together, these two cascade samples represent semi-continuous

tufa formation over a period spanning approximately 10 ka, with a maximum age range of 113.6 to 103.7 ka for sample 18-16 and 104.39 to 99.7 ka for sample 18-17.

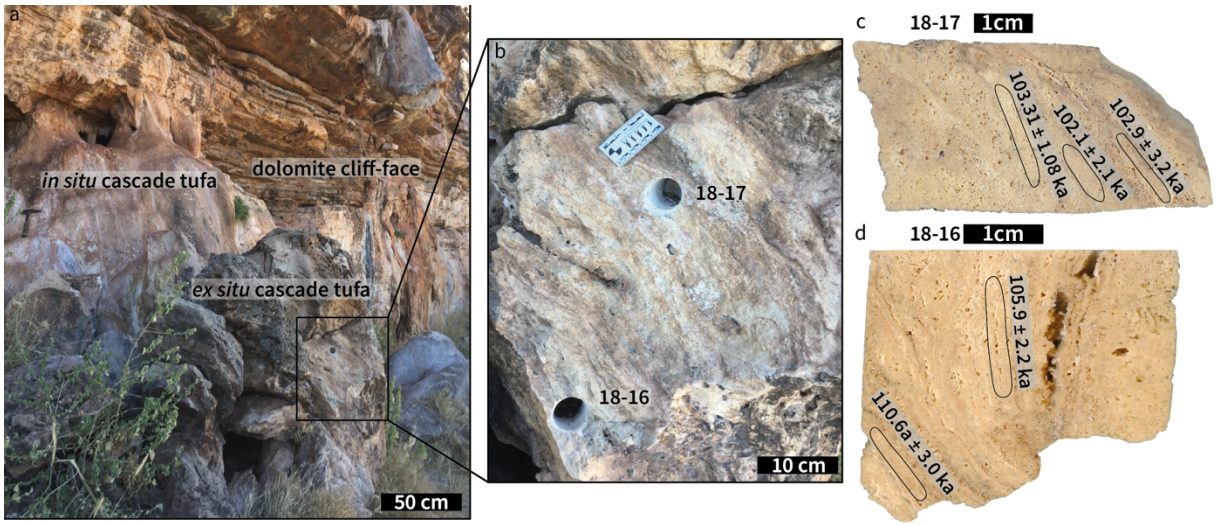

Figure 6.2.6 a) Field context of *ex-situ* cascade tufa in relation to the dolomite cliff and another *in situ* cascade deposit. The black square outlines the location of drill holes for samples 18-16 and 18-17, shown in the close-up photograph (b). Core sample slabs of samples 18-16 and 18-17 and the location of U-Th ages obtained.

6.2.3.2 Tufa stage 2 (~73-48 ka)

The second stage indicates tufa formation from ~73 to 48 ka, defined by ages from the following six tufa samples: 18-13, 18-14, 18-15, 18-7, GHS-6, and 17-8. Samples 18-13, 18-14, and 18-15 are short cores drilled from *ex-situ* cascades and together record an age range between ~73-58 ka. A sequence of ages from the other three samples, GHS-6 (53.10 ± 4.2 ka), 18-7 (53.52 ± 1.31 ka), and 17-8 (48.31 ± 0.68), which formed on the terraces above and below the shelters, partially overlap with the timing of tufa formation recorded in the cascade cores, with an age range between ~62-48 ka.

Sub-samples from sample 18-13 returned the following ages: 58.61 ± 0.99 ka, 65.04 ± 0.81 ka, 67.15 ± 0.38 ka, and 69.83 ± 0.68 ka. The core is porous with organic structures visible, although some dense layering is evident in the mid-section of the sample, which was dated (Figure 6.2.1). The ages are in stratigraphic agreement, except for 18-13.1 (58.61 ± 0.99 ka), which is an obvious outlier. Four sub-samples drilled from sample 18-14

produced ages of 68.43 ± 0.73 ka, 64.28 ± 1.60 ka, 69.35 ± 0.67 ka and 70.60 ± 1.67 ka (Figure 6.2.1). Three of these ages are in stratigraphic agreement, except for 18-14.2, which is another obvious outlier. The layering in this sample is convoluted and suggests a complex flow pattern, making it difficult to determine a simple stratigraphy through this sample. The ages returned from three sub-samples from sample 18-15 are 68.52 ± 0.57. ka, 71.34 ± 0.89 ka and 72.28 ± 0.53 ka. The youngest of the three ages, 18-15.1, is from a layer that appears to be sandwiched between the older two.

GHS-6 was sampled from a terrace on the south side of Ga-Mohana Hill. Four sub-samples, GHS-6, GHS-6.1, GHS-6.2, and GHS-6.3, returned ages of 60.38 ± 1.81 ka, 59.68 ± 1.46 ka, 61.9 ± 0.5 ka, and 53.10 ± 4.20 ka respectively (Figure 6.2.2). GHS-6 and GHS-6.1 are sub-samples from a single layer, and the precisions of the age results obtained are 3.0% and 2.4%, respectively. These ages are within error of each other, which means the ages are reproducible. GHS-6.2 is the oldest sub-sample from the lowest stratigraphic position in the sample, and has the tightest age precision, 0.8%, while the youngest age from sub-sample GHS-6.3 is the least precise with an uncertainty of 4.2 ka (7.9%) associated with the age. It is stratigraphically above the other three sub-samples, separated by a layer with a high level of Th contamination (Figure 6.2.2). While this is a large error, the age result remains in stratigraphic agreement with the older three ages sampled from stratigraphically lower layers.

Sample 18-7 was collected from the terrace above the north shelter. This sample has three clearly distinct cm-scale layers (Figure 6.2.2). The lower two layers contain significant detrital material, visible in hand sample and reflected in the high Th concentrations (0.1-3ppm) measured by LA-ICP-MS (Figure 6.2.2). The top layer has desiccation cracks preserved on the surface and no detrital material. Consequently, it proved suitable for dating and returned an age result of 53.52 ± 1.31 ka. Finally, the tufa sub-sample that marks the end of this tufa stage is the oldest age from sample 17-8. It is included in this tufa formation stage as it overlaps with the error associated with the youngest age from sample GHS-6, i.e. GHS-6.3 (53.10 ± 4.20 ka). Sub-sample 17-8.1 returned an age result of 48.3 ± 0.7 ka (Figure 6.2.2).

6.2.3.3 Tufa Stage 3 (44-32 ka)

Sub-samples from two terrace samples, GHN-1 and 17-8 (Figure 6.2.2) returned ages between ~44-32 ka. Sample GHN-1 yielded the following age results from three sub-samples: 39.13 ± 0.40 ka, 37.02 ± 0.42 ka and 36.55 ± 0.39 ka. These were drilled within 1 cm of each other from a layer of massive, dense micritic material (Figure 6.2.2). The sample itself is from the terrace below the north shelter, and, as described previously in Chapter 4, thin section analysis suggests that it formed in a shallow pool. The ages are in stratigraphic agreement, with the oldest age (GHN-1) being derived from lower down in the layer, and the two younger ages (GHN-1.2 and GHN-1.3) within error of each other. The uncertainties associated with each of the ages are fairly low (~1%) and consistent across the sub-samples.

Sample 17-8 was taken from the underside of an *in-situ* dolomite boulder, mid-way up the talus slope on the north side of Ga-Mohana Hill. Initial sub-samples drilled from two subtly distinguishable layers within the sample, 17-8.1 (tufa stage 2) and 17-8.2 are (indicated as circles on Figure 6.2.2), returned ages of 48.31 ± 0.68 ka and 34.50 ± 0.23 ka respectively, demonstrating the potential for high precision ages. Following LA-ICP-MS screening, a second round of sub-samples, 17-8.3 to 17-8.6, returned the following ages: 43.23 ± 0.27 ka, 41.76 ± 0.22 ka, 41.62 ± 0.26 ka, and 32.45 ± 0.37 ka, all with good precision (0.5-1.1%). Sub-samples 17-8.3, 17-8.4, and 17-8.5 are fairly closely spaced, both in space and time, with up to ~1500 years between them (Figure 6.2.2). The two sub-samples from the lowermost portion of the sample (17-8.2 and 17-8.6) have an age difference of ~2000 years between them.

These terrace samples are evidence that water was flowing down the hillside and forming pools on the slopes of Ga-Mohana Hill between ~44-32 ka. Despite the relatively low resolution of the ages within individual samples, i.e. errors on the order of hundreds of years, together they suggest semi-continuous tufa formation over a period of ~ 14 ka. Sample 17-8 records three distinct periods of tufa formation, with the oldest age being 48.31 ± 0.68 ka (tufa stage 2), followed by three ages spanning ~41-43 ka, and two ages spanning ~32-34 ka. An abrupt contact separates the ages of 41.62 ± 0.26 ka and 34.50 ± 0.23 ka, representing a gap of approximately 6000 years. Ages from

sample GHN-1 suggest a semi-continuous period of tufa accumulation for around 3000 years, from ~39 to 36 ka. This time period falls into the ~6000 year hiatus recorded in sample 17-8. Given this, it is likely that the hiatus recorded in sample 17-8 represents a localised change, i.e. water flow may have been diverted away from the site of deposition for a period, potentially leading to erosion of part of the deposit. It may also represent a site-wide diminishment of the tufa system at Ga-Mohana, resulting from a decrease in the energy of the water flow. The fact that sample GHN-1 records tufa precipitation during at least some of this time suggests that the tufa system was still active, albeit to a lesser degree.

6.2.3.4 Tufa stage 4 (15 - 6 ka)

Samples GHS5 and GHN2 record early Holocene tufa formation at 10.74 ± 4.93 ka and 7.27 ± 0.31 ka, respectively. They were both collected from the outermost layers of *in situ* cascade tufas from areas adjacent to the rock shelters. Sample GHS-5 is from a cascade on the south side of Ga-Mohana Hill. While the material sampled appears 'clean' and dense (Figure 6.2.2), the very low measured $^{230}Th/^{232}Th$ value of 4.6 indicates considerable detrital input. This is far below any acceptable threshold for Th contamination and is thus reflected in the very poor precision of only ~50% for the age. Sample GHN-2 was taken from the base of a cascade on the north side of the hillside, and is a relatively clean sample compared to GHS-5, with a $^{230}Th/^{232}Th$ value of 36.2, and consequently a more precise age (4% precision).

Based on the premise that the cascades developed with successive layers built outward from the host dolomite cliff face over time, it is expected that the outermost layers of the cascade tufas would record the most recent period of tufa formation, while the layers closest to the dolomite should record the earliest period of tufa formation. This is confirmed with the young ages obtained from these samples, and older ages from the *ex situ* cascades discussed above.

6.2.3.5 Tufa stage 5 (~4-2 ka)

A single age from dome sample 18-10 defines this youngest tufa stage, with an age of 3.0 ± 0.9 ka from sub-sample 18-10.2. While the uncertainty associated with this age is small, i.e. 0.9 ka, it is relatively imprecise as it represents ~30% of the age. A second sub-sample drilled from this dome core, sample 18-10.1, yielded an unresolvable age estimate (Table 6.2).

The fact that there are only three ages that form the last identified tufa stages, and that these are from the outer layers of cascades near the shelters, and a dome tufa, may suggest that Holocene tufa formation was less extensive than in previous stages. The energy of the water flow may have been reduced, and restricted to the areas around the rock shelters, such that pools and barrages on the hillside were not established.

6.2.3.6 Unresolvable age estimates

No reliable age solution could be calculated for ten sub-samples drilled from the following seven samples: GHN3, GHS4, 17-6, 18-4, 18-6, 18-10 and 18-12 (Table 6.2; Figure 6.2.3). Samples 18-4, 18-6 and 18-10.1 contain very low levels of U with concentrations of 28, 68 and 86 ng/g measured in each sub-sample, respectively. These low levels of U in turn result in very low levels of ^{230}Th being produced, likely resulting in concentrations below detection. This material is also more likely to be vulnerable to ^{232}Th contamination. The ^{230}Th/^{232}Th measured in all these subsamples, except 18-12.1 and 18-12.2, is less than 1.5, indicating a significant detrital Th component. In these instances, the assumption of an initial ^{230}Th/^{232}Th of 1.5 is inappropriate, as applying this correction means taking away more Th than there was to begin with.

Although the layers in the samples selected for sub-sampling were chosen on the basis of little to no Th, the laminations are very fine and highly irregular and it is possible that, despite very careful drilling, cross-cutting of the adjacent layers may have occurred, contaminating the powdered samples (Figure 6.2.3). Samples GHN-3 and GHS-4 are from dome tufas which are highly porous. This makes them less suitable candidates for U-Th age sampling as this porosity creates an opportunity for water to dissolve parts of the sample and mobilise U. As such, these samples may not have acted

as closed systems. The $^{230}Th/^{232}Th$ activity ratios for these dome samples are also extremely low (Table 6.2), indicating a significant detrital Th component. Nevertheless, some of the corrected ages for these samples provide a useful upper limit age estimate, i.e. the corrected age plus the associated 2σ uncertainty (Table 6.2).

6.3 Implications of U-Th age results

In this section, I first discuss the significance of the uranium isotopes measured in the tufas, and then evaluate the validity of the U-Th ages presented above (Section 6.3.1). Following this, I assess whether the age results indicate that a particular morphology is best suited to U-Th dating (Section 6.3.2).

6.3.1 Validity of U-Th ages

In order to compare and correlate the Ga-Mohana tufa ages with other palaeoclimate records, it is necessary to first establish their reliability. In the following discussion, I argue that the majority of ages obtained in this study are valid and do provide a robust chronological framework for interpreting tufa deposition at Ga-Mohana Hill. Thus, they can be reliably employed as a proxy for local hydroclimate changes during the late Pleistocene and early Holocene in the southern Kalahari region (discussed in Chapter 8).

A first order method for assessing the validity of the U-Th ages is to check that stratigraphic order is preserved, and that the ages are reproducible across the same layer. As presented in section 6.2.3 above, and illustrated in Figures 6.2.1 and 6.2.2, twenty-eight of the thirty-one tufa ages obtained are in stratigraphic order. In the case in which only single ages were obtained from samples (due to limited material; e.g. sample GHN2, GHS5 and 18-7), the ages are deemed reliable based on their stratigraphic context in the field (samples GHN2 and GHS5, both from outer layers of cascade tufas), and the integrity of the material sampled, i.e. lack of detrital Th (sample 18-7).

Three samples, 18-13, 18-14 and 18-15 (Figure 6.2.1), deviate from this general pattern and are discussed in detail here. These samples were cored from a single *ex situ* cascade tufa; while the ages from all three samples overlap with one another, it is difficult to untangle the flow pattern and relate the layers within each sample to one another. There are some inconsistencies within each of these three samples as layers for which the youngest ages were obtained appear to be sandwiched between layers with older ages (samples 18-14

and 18-15), and more problematic are sub-samples across the same layer which returned inconsistent ages (samples 18-14 and 18-13).

6.3.1.1 Sample 18-15

On initial assessment of the three ages from sample 18-15, it appears that the ages in stratigraphic order of 71.34 ± 0.89 ka, 68.52 ± 0.57 ka, and 72.28 ± 0.53 ka, are not in sequence, as the youngest age appears to be sandwiched between two older layers. However, considering the irregularity of the layers in sample 18-15, a case is made for the stratigraphic agreement of these ages as the layer from which the youngest age was sampled can be traced to a stratigraphic position above the older age. This makes the maximum age range for this sample almost 5000 years, from 67.95 ka to 72.81 ka.

6.3.1.2 Samples 18-14 and 18-13

Four ages were obtained from each of the two adjacent core samples 18-14 and 18-13: 64.28 ± 1.6 ka, 68.43 ± 0.73 ka, 69.35 ± 0.67 ka, and 70.60 ± 1.67 ka (sample 18-14) and 69.83 ± 0.68 ka, 67.15 ± 0.38 ka, 65.10 ± 0.81 ka, and 58.61 ± 0.99 ka (sample 18-13). In both samples, three of the four ages are in stratigraphic agreement, however, two of the four ages from each of these samples are not consistent across the same stratigraphic layer; this suggests U mobility in these layers, and potentially across the whole sample.

In the case of 18-14, the ages under suspicion border a highly porous layer, sandwiched by layers of crystalline carbonate. The ages from the top and bottom of the sample, and one of the two ages from the middle layer, are within error of one another, but the fourth age of 64.28 ± 1.6 ka, also from the mid-section of the sample, is anomalous. It is possible that the layers sampled in the mid-section may have been more susceptible to U remobilisation due to their proximity to the porous layer.

In sample 18-13, the ages from the lower part of the sample are from dense crystalline layers, and are in stratigraphic agreement, along with an age from the top of the sample. However, an adjacent sub-sample from this top layer differs significantly. Again, this may be due to the more porous nature of the material sampled from the top part of this

core, but it nevertheless calls into question the reliability of the ages contained within the entire sample. In order to confirm the validity of the other ages, it is necessary to analyse two more sub-samples from those same layers, however this was beyond the scope of this study.

The stratigraphy of these cascade samples is highly irregular and there is a high possibility that precipitation of the flows occurred heterogeneously across a surface. However, given the large age discrepancies between the samples in 18-13 and 18-14, and their close proximity, this is hard to reconcile. The ages from these samples are included in the following discussion as, taken all together, the ages from these three samples do overlap and as a whole are consistent.

The laser ablation data provides further evidence for the reliability of the ages; the element concentration maps generated from the laser ablation data (Figures 6.2.1 and 6.2.2) show sharp boundaries between areas of higher and lower U concentration, indicating that the U has not been subject to remobilisation and diffusion. Had this been the case, blurred boundaries and clear diffusive profiles (high concentrations on the edges and low concentrations toward the middle) would be expected (Millard and Hedges, 1996; Pike and Hedges, 2002; Pickering, 2015). It is for these reasons that the ages obtained in this study are deemed to be reliable.

6.3.2 Morphologies best suited to U-Th dating

It has been suggested that tufas which form in pools are ideal targets for acquiring a chronology because, unlike waterfall / cascade tufas that tend to be porous and have a highly convoluted stratigraphy, pool tufas offer the best option for the recovery of a simple stratigraphy, important for interpreting geochemical changes over time (Garnett et al., 2004b). However, because of the nature of their formation, i.e. accumulation in a pool which may also be a sink for debris, such deposits may be affected by a significant detrital component. Ga-Mohana tufa samples interpreted to have formed in shallow pools of water are composed of clean, dense micrite and returned ages with low errors, supporting the assertion by Garnett et al. (2004b) that pool tufas are good candidates

for U-Th dating. However, the limited sample material and massive nature of the Ga-Mohana pool tufas do not allow for a substantial chronology to be obtained. Consequently, the age results obtained from the rim pool tufas are limited to a small window of time. This may be because older rim tufas were more prone to dismantling and erosion due to their exposed positions on the talus slope, and susceptibility to burial beneath soil cover and subsequent dissolution.

The majority of ages obtained in this study are from cascade deposits. Despite the significant porosity in several of these cascade samples, they proved to be the best candidates for obtaining both reliable ages, and a record of the longevity of the system, as they are the most intact of the tufa morphologies at Ga-Mohana Hill. The cascade tufas comprise dense micrite and micro-spar and generally have a low detrital content, thus offering the best chance to obtain a sequential chronology. They are also comparatively well-preserved and protected from burial beneath soil and alteration from vegetation due to their positions on vertical cliff and step fronts, unlike barrage, rim pool and terrace tufas. Cascades are only susceptible to alteration or dissolution from meteoric waters, and burial by subsequent tufa precipitation. Nevertheless, careful sample selection was required as some cascade samples contain thin layers with a high detrital Th content, despite appearing to be composed of 'clean' and dense crystalline carbonate when viewed in hand sample.

Several cascade samples which did not return U-Th ages are composed of laminar fabrics with gently undulating convex and multiconvex composite lamina made up of mm-thick successions of microlaminae. The microlaminae alternate between grey and oxide-rich, brown micrite and are interspersed with thin lenses of microspar. Others exhibit a more 'open' laminar fabric, i.e. thin (0.1 mm) aphanitic to clotted micrite crusts sandwich thicker (0.5 mm) layers. These samples also exhibit a high proportion of small void spaces. In comparison, the successfully dated cascade samples comprise thicker (2 mm), more homogenous laminae of dense, aphanitic micrite and mixed micrite-microspar layers with only a few isolated void spaces. Thus, while cascade samples represent the best candidates for obtaining sequential chronology of tufa formation,

care must be taken to avoid layers with high detrital Th concentrations and the laser ablation pre-screening in particularly useful here.

The terrace breccia tufa deposits also proved to be good candidates for U-Th dating, given careful sample selection. For example, sample 17-8, returned a series of ages, all within error of each other. This sample is composed of aphanitic to peloidal micrite with microspar infilling fenestral pore spaces, and the laser ablation data revealed little to no detrital Th content (Figure 6.2.2). Most of the other terrace breccia samples collected contained a tufa matrix with a high detrital component, visible in hand sample, e.g. sample 18-7 (Figure 6.2.2). In this instance, an age was obtained from the uppermost layer of the sample, which was composed of clean, dense micrite, while the two lower layers were not sampled given their chaotic assemblage of detrital grains.

The barrage tufa samples are characterised by fine, irregular layering, and have a high level of detrital contamination (Figure 6.2.3). As such, neither of the barrage samples returned a U-Th age result. Although the dome tufas exhibit interesting microfabrics and can contain dense successions of micritic laminae, they too were not good candidates for obtaining U-Th ages. This is likely due to the highly porous nature of the material and inclusion of detritus. Only one sample from a dome (18-10) returned an age of ~3 ka.

While some morphologies may be better suited to U-Th dating than others, it is difficult to apply a general rule as successful dating is reliant on obtaining sufficient, clean material, and some sites may be limited in terms of which morphologies are preserved etc. So although it may be useful to be guided by some sense of morphological suitability, a thorough knowledge of the depositional setting and stratigraphic relations of the deposits is important. Prior analysis, e.g. petrographic observations, laser ablation pre-screening, remain key to obtaining reliable age data (Mallick and Frank, 2002).

CHAPTER 7 STABLE ISOTOPES

Stable isotopes are an invaluable tool in the Earth sciences. As the major constituents of water, hydrogen (H) and oxygen (O) isotopes, specifically ^{2}H (also referred to as deuterium, D) and ^{1}H, and ^{18}O and ^{16}O, are important tracers of hydrological patterns and processes (Gat, 1996). These isotopes are applicable to a wide variety of disciplines and have long been used as geochemical proxies in palaeoclimate research (Emiliani, 1966; Epstein et al., 1965; Johnsen et al., 1972; Emiliani and Shackleton, 1974). Tufas precipitate from bicarbonate in solution (H_2CO_3), and as such, calcium-saturated water is an important precursor for tufa formation. Two of the three main constituents of calcium carbonate deposits are oxygen and carbon (C), and their stable isotopes, ^{13}C and ^{12}C, and ^{18}O and ^{16}O, serve as the main source of geochemical proxy data in palaeoclimate studies on terrestrial carbonates (Sharp, 2007). In the following section, I first provide an overview of stable isotope principles and terminology, then detail the controls of oxygen and hydrogen isotopes in meteoric waters (Section 7.1.1), and oxygen and carbon isotopes in tufa deposits (Section 7.1.2). In Section 7.2, I report the results of H and O isotopes measured in water samples and C and O isotopes measured in tufa samples collected from Ga-Mohana Hill. I then explore the implications of these results in Section 7.3.

7.1 Background and literature

Variations in the stable isotope ratios of a given element occur as a result of fractionation during physical and/or chemical reactions, e.g. water-liquid to water-vapour (hydrogen and oxygen), or photosynthesis (carbon) (Urey, 1947). Fractionation, i.e. the preferential incorporation of the light (or heavy) isotope into one phase relative to another co-existing phase, is caused by the mass difference between isotopes, and is expressed as a fractionation factor, $a_{A\text{-}B}$ (Equation 7.1), where R_A and R_B are isotope ratios of different phases, e.g. water and vapour. Fractionation is driven by a multitude of physical and chemical processes, and these, together with fractionation effects, i.e.

equilibrium or kinetic processes, impact isotope ratios to varying degrees as they are cycled through the hydrological, terrestrial and biological systems.

Equation 7.1 $$\alpha_{A-B} = \frac{R_A}{R_B}$$

In palaeoclimate studies, the isotopes of hydrogen (^{2}H and ^{1}H), oxygen (^{18}O and ^{16}O) and carbon (^{13}C and ^{12}C) are of interest. Stable isotope data are usually reported in delta (δ) notation in per mil (‰), i.e. parts per thousand. The delta value is given by Equation 7.2, where R is the ratio of the abundance of the heavy to light isotope, x denotes the sample, and *std* refers to the reference standard against which the sample is compared.

Equation 7.2 $$\delta = \left(\frac{R_x - R_{std}}{R_{std}}\right) \times 1000$$

With this notation, the small relative difference in isotopic ratios between a sample and standard are expressed with respect to Standard Mean Ocean Water (SMOW) for hydrogen and oxygen isotopes in water, and Pee Dee Belemnite (PDB) for carbon and oxygen isotopes in carbonates. The δD and $\delta^{18}O$ values for SMOW and $\delta^{13}C$ values for PDB are by definition equal to 0‰ because $R_{std} - R_{std}$ = zero.

7.1.1 Oxygen and hydrogen isotopes in meteoric water

Fractionation of H- and O- isotopes occurs semi-predictably during physical processes that drive the exchanges between oceans, bodies of water on land, the atmosphere, and groundwater systems as water is cycled through the hydrological system. These processes result in spatial variation of the H- and O- isotopes (Craig, 1961; Dansgaard, 1964; Bowen and Revenaugh, 2003), and this forms the basis of isotope hydrology (Clark and Fritz, 1997). Craig (1961) recognised a linear relationship between the H- and O-isotope ratios (δD and $\delta^{18}O$) in rainwater world-wide and termed the line of best fit the Global Meteoric Water Line (GMWL; Figure 7.1.1). Although most of the rainfall world-wide has isotope compositions that lie on or close to the GMWL, individual areas have their own Local Meteoric Water Line (LMWL) as a result of physical processes and local

conditions specific to a particular site. The GMWL represents a weighted mean of LMWLs (Gat, 1996).

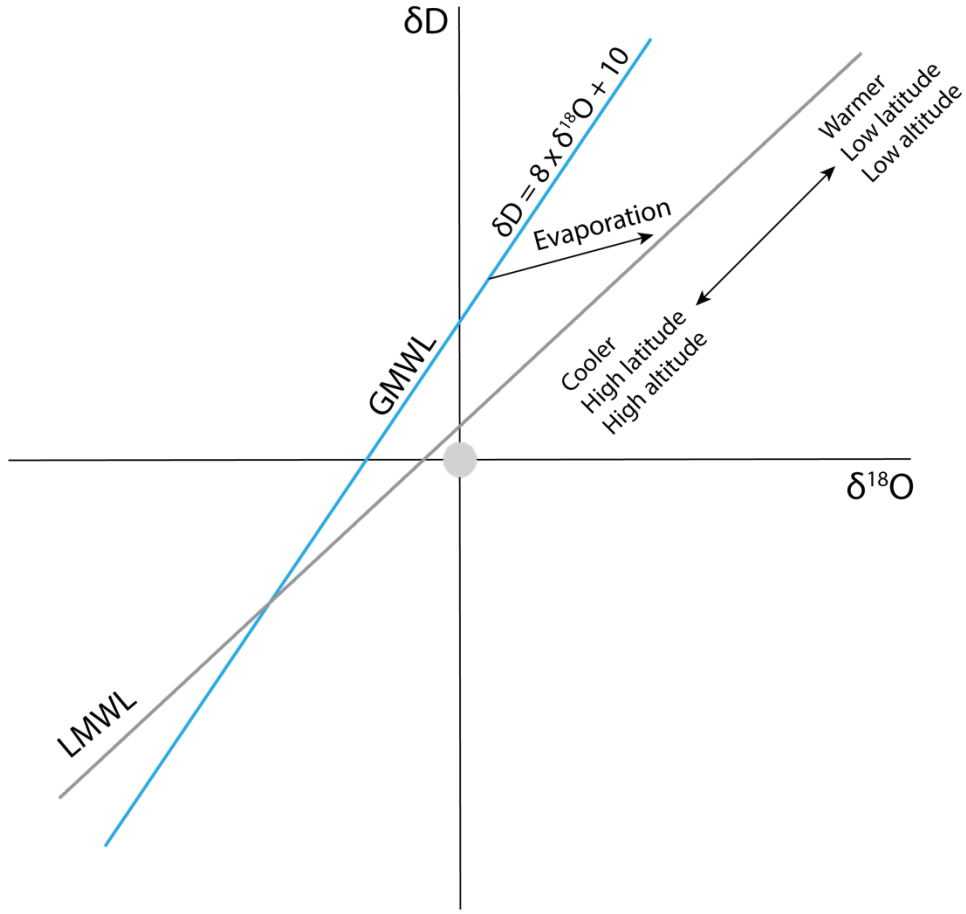

Figure 7.1.1 Plot of the Global Meteoric Water Line (GMWL) with its associated equation (Craig, 1961), and a hypothetical Local Meteoric Water Line (LMWL) (Rozanski et al., 1993). Ocean water (SMOW) is the standard reference point for isotope ratios in water and has δD and $\delta^{18}O$ values equal to ~0‰.

Variations in the δD and $\delta^{18}O$ values of meteoric waters are driven by several geographical factors detailed in Table 7.1 (Dansgaard, 1964; Rozanski et al., 1993). The principal factor affecting the isotope composition of meteoric water is water temperature (Dansgaard, 1964). As a result of this temperature control, global H and O isotope ratios in rainfall have a distinct spatial distribution that varies with latitude, i.e., lower temperatures, which occur with increasing distance from the tropics, result in lower $\delta^{18}O$ values, and vice versa (Dansgaard, 1964; Rozanski et al., 1993) (Figure 7.1.2).

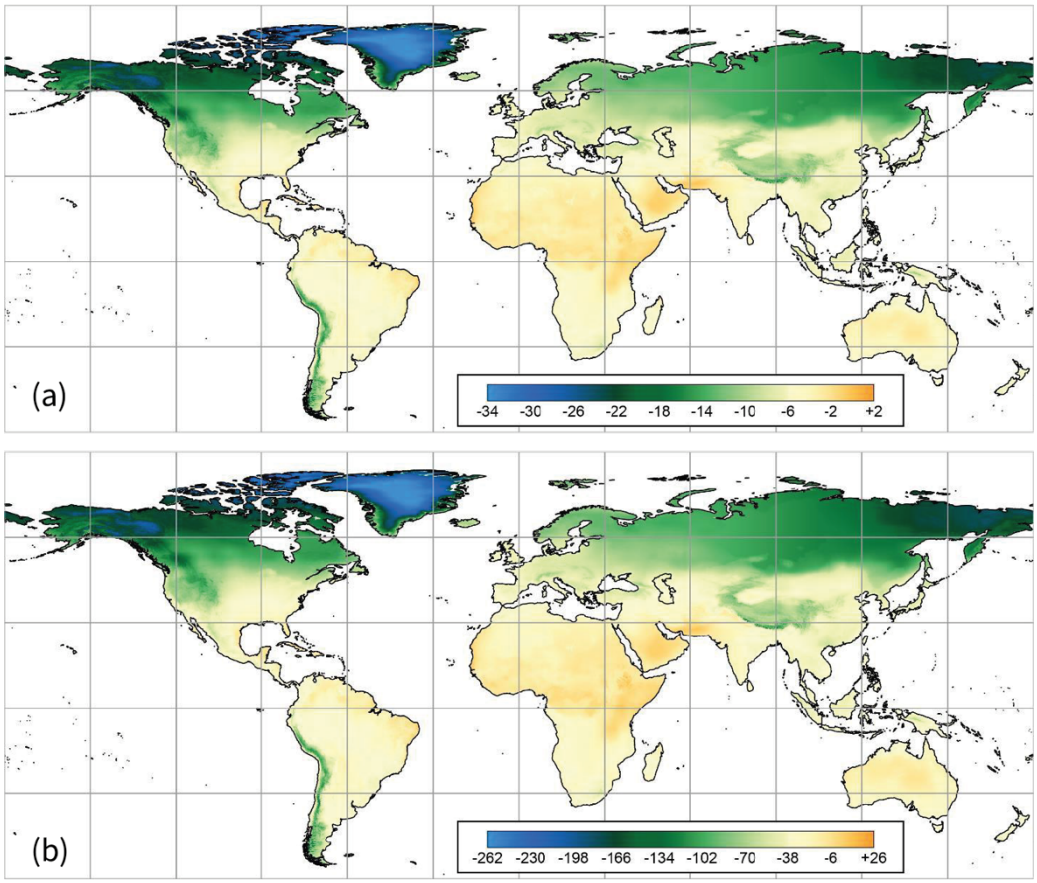

Figure 7.1.2 Global isoscape RCWIP2 (Regionalized Cluster-Based Water Isotope Prediction Model) of mean annual $\delta^{18}O$ (a) and δD (b) in precipitation, from Terzer-Wassmuth et al. (2021).

Groundwater δD and $\delta^{18}O$ values at Ga-Mohana Hill are inherited from rainwater that recharges the karst aquifer. Although evaporation prior to recharge can alter the δD and $\delta^{18}O$ values of the meteoric water (Gat and Dansgaard, 1972), groundwater isotope compositions can be used as a proxy for rainfall (Wassenaar et al., 2009). However, short-term variations in the δD and $\delta^{18}O$ of rain waters, driven by the amount effect or seasonal changes, are generally not reflected in the groundwater isotope composition. Instead, groundwater tends to have fairly constant isotope compositions as a result of long residence times, generally large volumes within the aquifer relative to the volume of recharge, and mixing with older waters in the aquifer (Gat, 1971; Chafetz et al., 1991; Andrews, 2006).

The oxygen in meteoric water (rainwater and karst groundwaters) is a principal source of oxygen in tufas. Knowledge of the δD and $\delta^{18}O$ values for the meteoric water at a given tufa site can aid interpretations of the $\delta^{18}O$ values measured in the tufa, as fractionation between $\delta^{18}O_{water}$ and $\delta^{18}O_{calcite}$ is temperature dependent (Urey et al., 1951; Hendy, 1971). Theoretically, the past temperature (*T*) of the tufa formation can therefore be calculated using the known water-calcite fractionation equation and the $\delta^{18}O$ values for both the tufa deposit ($\delta^{18}O_{calcite}$) and the water from which it formed ($\delta^{18}O_{water}$) (Epstein et al., 1953; Craig, 1965). Multiple derivations of this equation are available (e.g. O'Neil et al., 1969; Hays and Grossman, 1991; Kim and O'Neil, 1997; Coplen, 2007). There is some debate as to which equation is best suited to various types of deposits, and calculated temperature estimates vary depending on which equation is used. For the purpose of this study, I refer to the temperature equation from O'Neil et al. (1969) (Equation 7.3).

Equation 7.3 $$1000ln\alpha = {}^{2.78 \times 10^6}/_{T^2} - 2.89$$

where

$$\alpha = (1000 + \delta^{18}O_{calcite})/(1000 + \delta^{18}O_{water})$$

In the case of relict tufa deposits that are no longer active, the $\delta^{18}O$ value of the tufa-forming water is unknown. Present-day isotope values from rainwater and/or groundwater can be used as an estimate, but may be quite different from the tufa formation water (Clark and Fritz, 1997).

7.1.1.1 Southern Africa rainwater

Knowledge of long-term rainfall data aids in understanding and characterising groundwater stable isotopes, which is fundamental to understanding oxygen isotope variations in tufa deposits. Records of modern rainwater and groundwater across southern Africa are limited. Ongoing global monitoring of monthly rainwater and associated isotope data is conducted by The Global Network of Isotopes in Precipitation (GNIP), initiated by the International Atomic Energy Agency (IAEA) and the World Meteorological Organisation (WMO) (IAEA/WMO, 2015). In southern Africa, GNIP

stations with long-term, semi-continuous, records of rainfall isotope data are sparse, based only in major centres e.g., Pretoria, Cape Town, Windhoek, and Harare (IAEA/WMO, 2015). Individual studies supplement this data (e.g. Midgley and Scott, 1994; Weaver et al., 1999; Weaver and Talma, 2005). In particular, Harris (2023) conducted rainfall monitoring and isotope data collection in Cape Town over a period of 27 years to characterise the groundwater recharge of the Table Mountain aquifers.

7.1.1.2 Southern Africa groundwater

Innovative studies to survey and model the spatial variability of isotope compositions of meteoric water across South Africa have been conducted through the collection and analysis of both ground and tap water samples (West et al., 2014; de Wet et al., 2020). de Wet et al. (2020) investigated seasonal variability in tap water across South Africa. Tap water isotope data collected from the Northern Cape was found to be seasonally invariant, essentially reflecting a stable groundwater source. These data can therefore be used as a proxy for groundwater isotope composition in the Northern Cape, the region of interest in this study.

The aquifers hosted in the dolomite bedrock in the Northern Cape are an important water source in this semi-arid region of South Africa and have been the focus of several studies since the 1970s (Bredenkamp and Vogel, 1970; Bredenkamp et al., 1974; Verhagen et al., 1979). Recently, Xiao et al. (2019) investigated flow dynamics and hydrochemistry of spring waters from several Ghaap Plateau springs. They collected water samples from thirty-three springs across the dolomite aquifer in northern South Africa (Figure 7.1.3), eight of these were from the Ghaap Plateau (Figure 7.1.4).

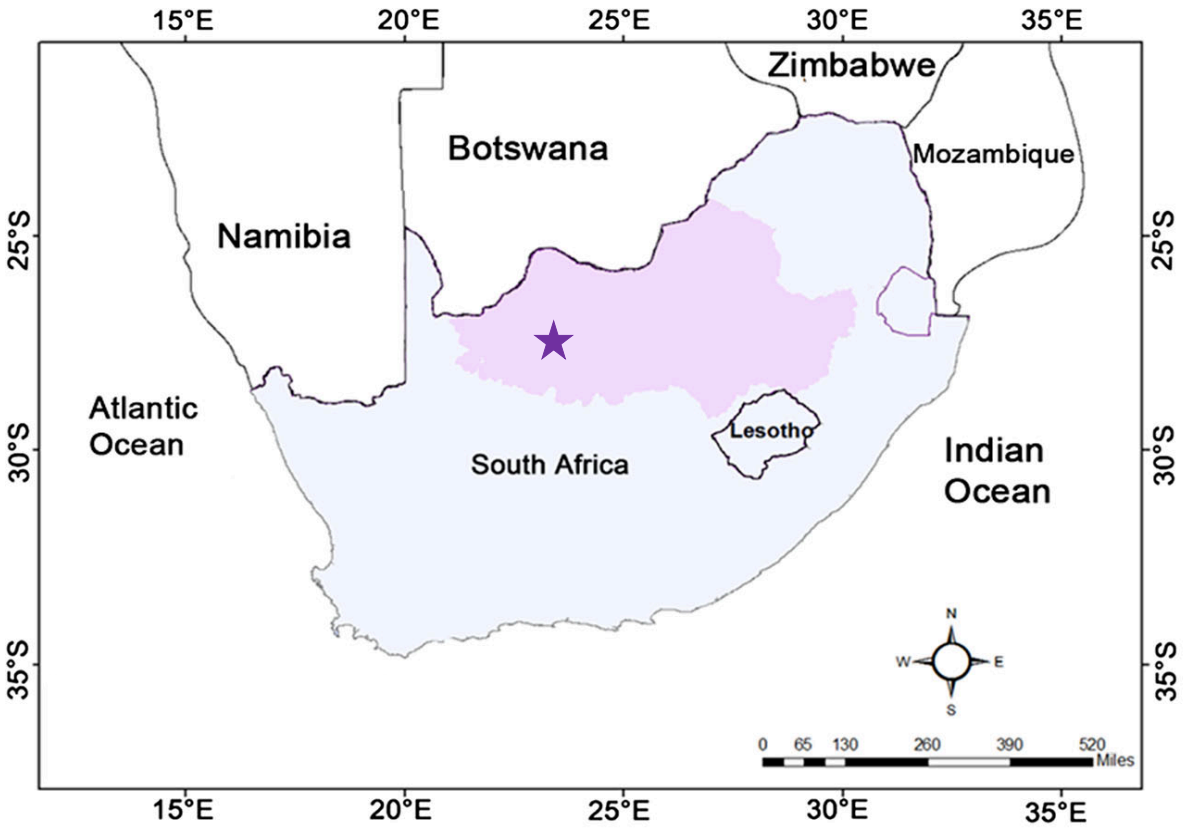

Figure 7.1.3 Map from Xiao et al. (2019) showing the location and extent of the dolomite aquifer (purple shading) in northern South Africa. The star marks the approximate location of Ghaap Plateau.

The Ghaap Plateau spring water temperatures ranged between 18°C to 21°C, and for each of the water samples, they measured the δD and $\delta^{18}O$ values, and the $\delta^{13}C$-DIC values. The δD values ranged between -38.9 and -16.5‰, $\delta^{18}O$ values between -6.13 and -2.75‰, and $\delta^{13}C$-DIC values between -12.1 and -10‰. The line of best fit for the δD and $\delta^{18}O$ values measured across the dolomite aquifer region is plotted in Figure 7.1.5 (Xiao et al., 2019). They compare this to a LMWL from Mekiso et al. (2015), and the GMWL (Figure 7.1.5).

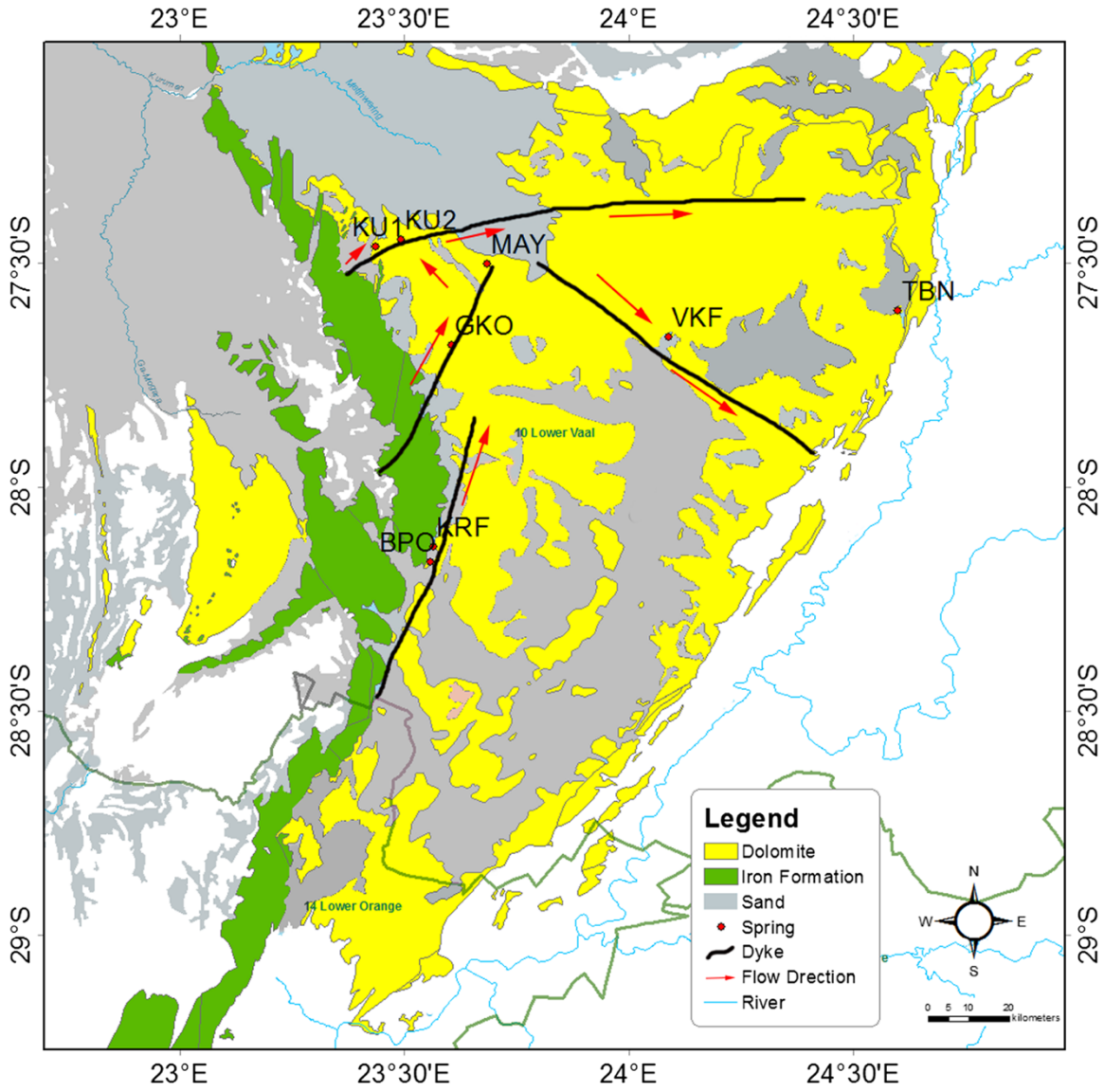

Figure 7.1.4 Map of the Ghaap Plateau from Xiao et al. (2019) showing geological outcrops (dolomite, iron formation and Kalahari sand), dykes, spring locations and their associated subsurface flow directions.

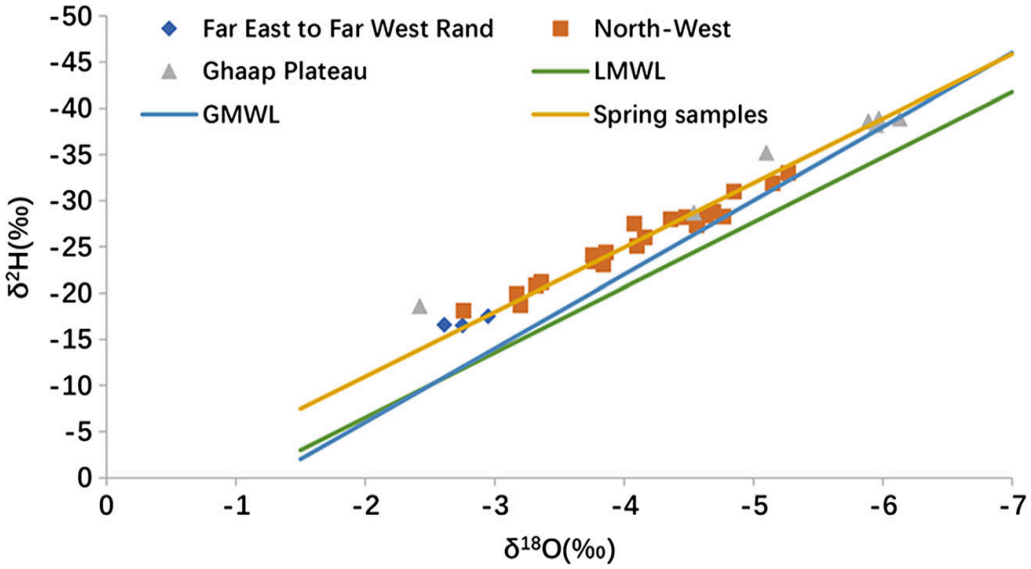

Figure 7.1.5 δ^2H and δ^{18}O values for the dolomite aquifer spring waters collected and plotted by Xiao et al. (2019). The y-axis is inverted with negative values at the top, as presented by the original authors. The line of best fit for these spring water samples (orange) has equation $\delta D = 6.98 \times \delta^{18}O + 3.5$. The LMWL (green) from Mekiso et al. (2015) has equation $\delta D = 7.05 \times \delta^{18}O + 7.6$, and the GMWL (blue) shown for reference (from Xiao et al. 2019).

The δD and δ^{18}O values of the spring waters plot below the LMWL from Mekiso et al. (2015), and their slope is shallower than that of the GMWL (Figure 7.1.5). Based on this shallower slope, Xiao et al. (2019) infer that the springs were recharged during conditions of low rainfall and high evaporation. Low SO_4^{2-} values of the spring waters are interpreted to indicate that the groundwater δ^{13}C-DIC values are mainly controlled by rock-water interactions (Xiao et al., 2019). Xiao et al. (2019) assume a starting value of -13‰ for the δ^{13}C-DIC from the soil zone, based on typical δ^{13}C-DIC values for soils in semi-arid regions with a predominance of C4 vegetation (Vogel, 1993). They thus interpret the Ghaap Plateau spring water δ^{13}C-DIC values of -12.1 to -10‰ to indicate only slight dolomite dissolution.

Xiao et al. (2019) also modelled the mean residence times (MRTs) of the spring waters using ^{14}C measurements of spring waters collected between 1970 and 2002 and found that residence times range from 20-50 years. They compare the MRTs of the spring waters with historical records of rainfall and note that a decrease in rainfall results in

longer residence times. They concluded that the Ghaap Plateau springs are sensitive to rainfall variability (Xiao et al., 2019).

7.1.1.3 Southern Africa palaeo-groundwater

While modern precipitation and groundwater data is a useful reference to aid interpretations of the Ga-Mohana tufa isotope values, it is likely that these values differed in the past. Kulongoski et al. (2004) investigated palaeo-groundwaters in the southern Kalahari in Botswana to investigate climate variability in southern Africa from during the late Pleistocene to present. Currently, their study site experiences a similar rainfall regime to that of Ga-Mohana Hill, with ~400mm of mean annual rainfall during the Austral summer months (December to April) sourced from the Indian Ocean (Kulongoski et al., 2004). They analysed dissolved noble gas concentrations, ^{14}C, and oxygen isotopes in groundwater collected from eleven wells. Their results reveal that the waters date from ~45 ka to present. The groundwaters that are between ~45 and 24 ka have distinctly lower $\delta^{18}O$ values than those from 24 ka to present, with mean $\delta^{18}O$ values of -5.62‰ prior to the last glacial maximum (LGM), compared to the modern groundwater mean $\delta^{18}O$ value of -4.65‰.

Based on these results, Kulongoski et al. (2004) asserted that the Indian Ocean has remained the primary moisture source for rainfall in the southern Kalahari over the last ~45 ka. They concluded that the temporal shift to higher $\delta^{18}O$ values from the late Pleistocene to present is a consequence of increasing atmospheric temperatures following the LGM, combined with the ice volume effect, i.e. prior to the LGM, the greater volume of ice globally would have produced rainfall with a $\delta^{18}O$ value ~1‰ lower. The noble gas data indicates that mean annual atmospheric temperatures were ~5.2 ± 1.2°C lower in the southern Kalahari between 45-24 ka than present, with recharge temperatures of ~18.3 ± 0.5°C between 45 to 24 ka, and ~23.4 ±. 1.5°C after ~16 ka (Kulongoski et al., 2004).

7.1.2 Oxygen and carbon isotopes in tufas

Carbon and oxygen isotopes undergo fractionation between the water and calcite phases during precipitation of calcium carbonate, and various environmental conditions impact this, e.g. oxygen fractionation is dependent on temperature (Urey et al., 1951), and carbon fractionation is affected by rate of precipitation (Turner, 1982). As such, the ratios of carbon and oxygen isotopes in tufa deposits can be expected to provide information about the physical and chemical conditions during formation (Gonfiantini et al., 1968; Pentecost, 2005). However, the isotope ratios that are ultimately recorded in tufa deposits depend on the combination and relative contribution of a multitude of factors prior to calcite precipitation, and unravelling these in order to make palaeoclimate interpretations is a challenge (Figure 7.1.6) (Andrews, 2006). The various factors involved in the carbon and oxygen isotope composition of tufas are discussed in the following sub-sections.

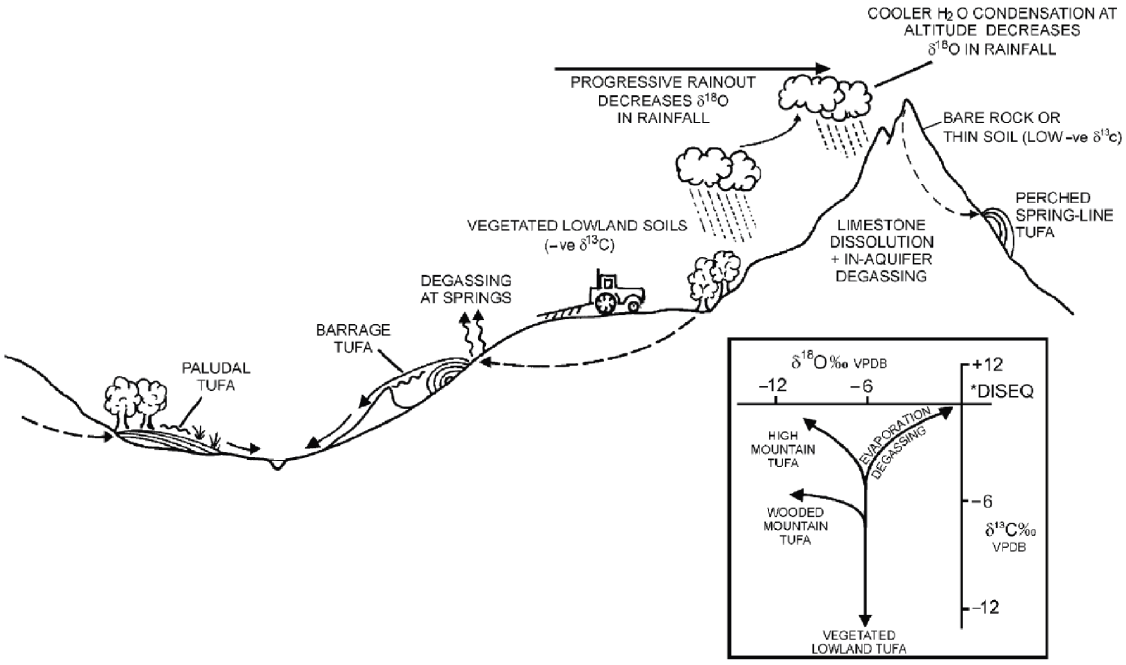

Figure 7.1.6 Schematic illustration of regional-scale factors that affect the $\delta^{18}O$ and $\delta^{13}C$ values of tufa at various deposition sites from Andrews (2006).

7.1.2.1 Equilibrium and kinetic fractionation

Both equilibrium and kinetic processes produce fractionation effects. In carbonate systems, precipitation of calcite occurs when a solution saturated in calcium carbonate becomes supersaturated with respect to calcite through the removal of CO_2. This can be triggered by a myriad of processes, e.g. a pressure change upon emergence of ground water at the surface, turbulent water flow, or an increase in temperature (Jacobson and Usdowski, 1975; Usdowski et al., 1979; Turi, 1986). If the rate of CO_2 loss is sufficiently slow to maintain equilibrium between the carbon species in the solution, i.e. HCO_3^- and $CO_{2(aq)}$, the calcite that precipitates remains in oxygen isotopic equilibrium with the water from which it forms (Hendy, 1971). Maintenance of isotopic equilibrium between calcite and the parent water is related to the rate of CO_2 degassing from the bicarbonate solution, i.e. a sufficiently slow rate of degassing will allow for oxygen in the calcite and oxygen in the water to be in equilibrium (Hendy, 1971). Equilibrium fractionation is temperature dependent, and the equilibrium calcite-water fractionation factor for oxygen is inversely proportionate to temperature ($1/T^2$), such that at low temperatures the fractionation factor is high, and vice versa (Sharp, 2007 and references therein). Thereby, oxygen isotopes in calcite deposits, precipitated under equilibrium conditions, provide a tool to determine the temperature of the water from which the calcite precipitated (Urey et al., 1951; Epstein et al., 1953).

In contrast, disequilibrium processes, i.e. kinetic fractionation, are uni-directional and occur when the rate of exchange is too fast to maintain equilibrium, e.g. rapid CO_2 degassing, evaporation, or photosynthesis (Jacobson and Usdowski, 1975). This leads to preferential loss of the lighter isotopes, ^{16}O and ^{12}C, and results in higher $\delta^{18}O$ and $\delta^{13}C$ values in the residual fluid, and hence the calcite that later precipitates. This significant fractionation of the oxygen and carbon isotopes means that the calcite precipitate has higher $\delta^{18}O$ and $\delta^{13}C$ values than equilibrium precipitation (Turi, 1986). In such cases, oxygen isotope fractionation is not only a function of temperature, and the oxygen isotope values cannot be reliably used as a palaeothermometer. Kinetic processes are reflected as simultaneous enrichment of $\delta^{18}O$ and $\delta^{13}C$ values in the calcite (Gonfiantini et al., 1968; Hendy, 1971; Usdowski et al., 1979).

Although it is usually assumed that isotopic equilibrium effects dominate the incorporation of C and O atoms into carbonates, it is known that in natural systems, precipitation seldom occurs under equilibrium conditions (Gonfiantini et al., 1968; Lojen et al., 2004; Daëron et al., 2019). A positive correlation between $\delta^{13}C$ and $\delta^{18}O$ in carbonates indicates the predominance of fractionation driven by kinetic processes, i.e., rapid degassing via turbulent water flow or evaporation (Craig et al., 1963; Hendy, 1971; Andrews et al., 1997; Andrews et al., 2000; Pentecost, 2005). Covariance of $\delta^{18}O$ and $\delta^{13}C$ values is common in tufa samples, particularly in semi-arid/arid environments (Pazdur et al., 1988a; Andrews et al., 1997; Smith et al., 2004). Nevertheless, numerous studies have shown that useful palaeoclimate information can be derived from $\delta^{18}O$ and $\delta^{13}C$ values measured in tufas (Pazdur et al., 1988a; Andrews et al., 2000; Smith et al., 2004; Cremaschi et al., 2010; Doran et al., 2015).

7.1.2.2 Controls on oxygen isotopes in tufas

The $\delta^{18}O$ value of tufa is a function of the tufa-forming water $\delta^{18}O$ and the temperature of the water at the time of formation, and hence the calcite-water fractionation factor (Epstein et al., 1951). The tufa-forming water reflects the $\delta^{18}O$ value of groundwater, which in turn is influenced by the $\delta^{18}O$ of meteoric waters that recharge the aquifers. The main controls on the tufa-forming water are related to those that control the isotope values of meteoric water plus local climatic factors (Figure 7.1.7). These are summarised in Table 7.1 and briefly described below.

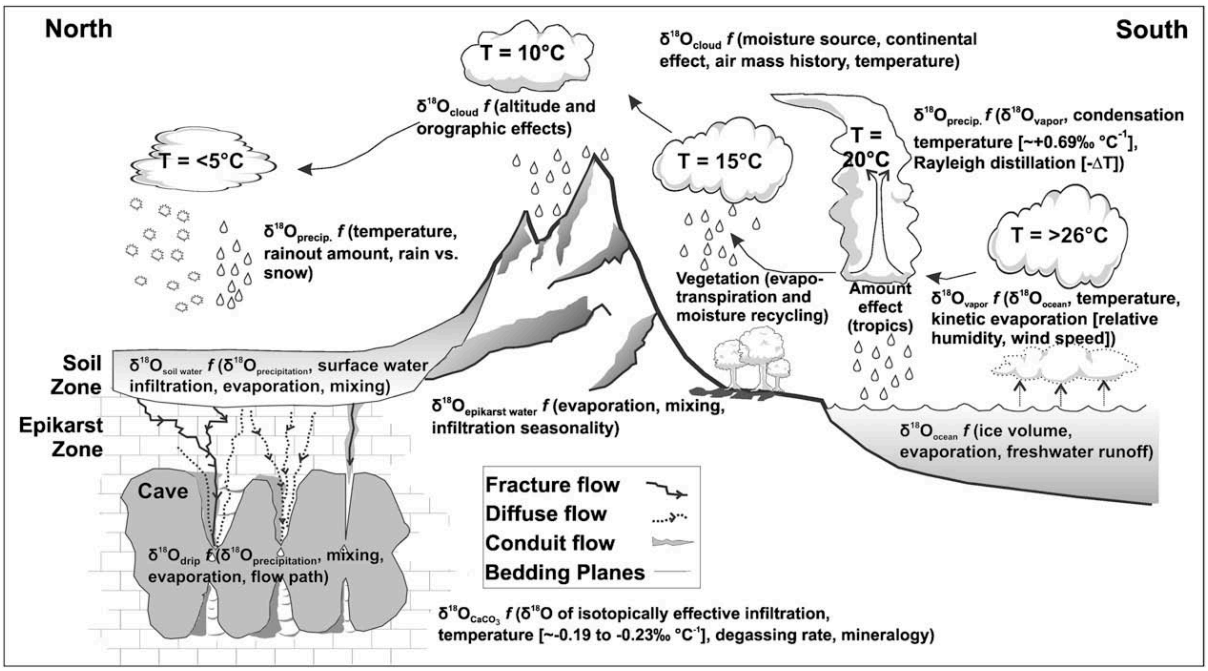

Figure 7.1.7 Schematic illustration of factors that affect the $\delta^{18}O$ values of rainwater and terrestrial carbonates, from Lachniet (2009).

Fluctuations in water temperature, driven by solar insolation and air temperature variations, drives short-term $\delta^{18}O$ variation in tufa deposits, with warmer/colder temperatures resulting in lower/higher $\delta^{18}O$ values (Chafetz et al., 1991; Matsuoka et al., 2001; Andrews and Brasier, 2005; Vázquez-Urbez et al., 2011). Warmer temperatures are also likely to intensify the effect of evaporation, which leads to tufa-forming waters enriched in ^{18}O, and subsequent tufa formation with higher $\delta^{18}O$ values.

Many tufa environments are characterised by hydrologically open systems with low residence times and minimal evaporation, such that the tufa $\delta^{18}O$ values reflect the $\delta^{18}O$ of the meteoric waters recharging the aquifer (Arenas et al., 2000; O'Brien et al., 2006). However, this is not the case in semi-arid settings where processes such as evaporation dominate due to high insolation coupled with slow aquifer recharge and low outflow rates (Bar-Matthews et al., 1996). This results in higher tufa $\delta^{18}O$ values than expected based on the groundwater composition (Smith et al., 2004; Cremaschi et al., 2010). Variations in $\delta^{18}O$ may in part also reflect different moisture sources that contribute to recharging the aquifer (Makhnach et al., 2004; Andrews, 2006).

Table 7.1 Environmental and climatic influences on $\delta^{18}O$ of meteoric waters and tufas.

Factor	Effect on $\delta^{18}O$
ATMOSPHERE – RAIN WATER	
Altitude	The $\delta^{18}O$ value of rainfall is lower at higher altitudes. This is related to the decrease in mean annual temperature with increased elevation (Dansgaard, 1964).
Latitude	The $\delta^{18}O$ value of rainfall decreases with increasing distance from the tropics (Dansgaard, 1964). As such, $\delta^{18}O$ is lowest at the poles.
Temperature	Lower average temperatures result in lower rainfall $\delta^{18}O$ values; higher average temperatures result in higher rainfall $\delta^{18}O$ values (Dansgaard, 1964).
Continental effect	The $\delta^{18}O$ value of rainfall decreases with increased distance away from the coast, i.e. the further inland the moisture travels, the lower the $\delta^{18}O$ value of the rainfall (Rayleigh fractionation process) (Dansgaard, 1964).
Reservoir / source	Different sources, e.g. sea water versus fresh water, have different isotopic values. Rainfall $\delta^{18}O$ value changes depending on the air mass moisture source (Dansgaard, 1964).
Amount	The $\delta^{18}O$ value decreases with an increase in the amount of precipitation (Dansgaard, 1964)..
Seasonality	Rainfall in cooler months has a lower $\delta^{18}O$ value, related to temperature and amount (Dansgaard, 1964).
Ice volume	Changes in the $\delta^{18}O$ value of seawater is regulated by long-term changes in global ice volume; an increase (decrease) in ice volume leads to a colder (warmer) global climate and a higher (lower) $\delta^{18}O$ value (Dansgaard, 1964).
SOIL ZONE & EPIKARST – GROUNDWATER	
Evaporation	Low net moisture availability and / or high temperatures lead to evaporation of soil moisture and higher $\delta^{18}O$ values of groundwaters (Gat and Dansgaard, 1972).
Residence time and mixing	Slow rates of groundwater percolation and longer residence time allows for mixing of groundwaters which changes the $\delta^{18}O$ value and attenuates the climate signal (Andrews, 2006, Arenas et al., 2000).
SURFACE – TUFA-FORMING WATERS	
Temperature	The equilibrium water-calcite fractionation factor is temperature dependent (Epstein et al., 1951, Urey et al., 1951). Temperature and the water $\delta^{18}O$ value are related to the $\delta^{18}O$ of calcite by the palaeotemperature equation (Equation 7.3) (Epstein et al., 1953). Under equilibrium conditions, a 1°C change in temperature equates to a 0.24‰ change in the $\delta^{18}O$ value of the calcite (Craig, 1965, Hays and Grossman, 1991). Warmer temperatures result in higher tufa $\delta^{18}O$ values, and vice versa (Andrews, 2006).
Distance from point of resurgence	Tufa-forming waters become progressively warmer with increasing distance from the point of resurgence due to solar insolation and equilibration with ambient air temperature (Chafetz et al., 1991, Fritz, 1965, Gonfiantini et al., 1968). This leads to higher tufa $\delta^{18}O$ values (Andrews, 2006).
Evaporation	Low moisture availability and / or high temperatures result in evaporation and kinetic fractionation, which leads to higher $\delta^{18}O$ values in the tufa-forming waters and the subsequent deposits (Hendy, 1971, Smith et al., 2004, Turi, 1986).

7.1.2.3 Controls on carbon isotopes in tufas

Carbon plays a crucial role in geological and biological processes, and its stable isotopes, ^{12}C and ^{13}C, are valuable tracers of these processes as they are cycled through the earth's reservoirs, i.e. the atmosphere, ocean, soil, and living organisms (Clark and Fritz, 1997). The predominant sources of carbon in tufa are atmospheric CO_2 ($\delta^{13}C$ ~-7‰) (Keeling, 1958), soil zone CO_2 ($\delta^{13}C$ ~-15‰ to -25‰) (Deines, 1980), and the underlying carbonate bedrock ($\delta^{13}C$ ~-4‰ to +4‰) (Clark and Fritz, 1997; Pentecost, 2005) (Figure 7.1.8). Each source of carbon has a different $^{13}C/^{12}C$ ratio, and fractionation during processes involved in the sequestration and transport of C from the various sources to the final tufa deposit depends on a multitude of environmental and climatic factors, e.g. the type of vegetation, soil profile, and the level of biogenic activity, many of which are linked to rainfall and temperature (Andrews, 2006). Consequently, $\delta^{13}C$ values in tufa deposits are highly variable, ranging from -12‰ to +2‰ (Pentecost, 2005). The effects of various factors on the $^{13}C/^{12}C$ ratio are summarised in Table 7.2 and briefly described below.

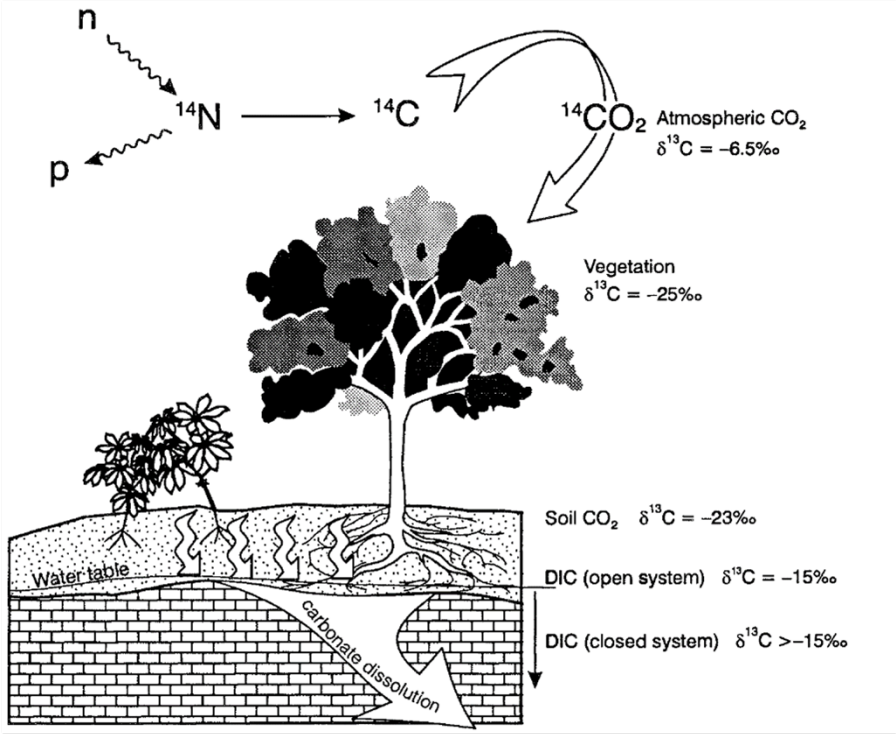

Figure 7.1.8 Schematic illustration of the pathway and fractionation of ^{13}C during photosynthesis, soil respiration and bedrock dissolution by groundwaters, from Clark and Fritz (1997).

Atmospheric CO_2 is fixed in soils via photosynthesis and respiration of vegetation, including decomposition of organic matter, during which carbon is significantly fractionated (Andrews et al., 1993; Andrews et al., 2000; Arp et al., 2001) (Figure 7.1.8). Carbon isotope fractionation during photosynthetic uptake of atmospheric CO_2 leads to a decrease of $\delta^{13}C$, the extent of which depends on the photosynthetic pathway. Photosynthetic pathway refers to the different biochemical processes that plants, algae and some bacteria use to convert CO_2 into organic compounds. Depending on the process used to store and metabolise CO_2, plants are classed as either C3 plants, C4 plants, or plants using the Crassulacean Acid Metabolism (CAM). The distribution of these vegetation types depends on climatic and environmental conditions. Vegetation with a C3 photosynthetic pathway converts atmospheric CO_2 into a three-carbon compound called 3-phosphoglycerate and includes trees, shrubs, and grasses that thrive in cool and moist environments. In contrast, CAM and C4 plants have adapted their photosynthetic processes to minimise water loss in hot and dry environments (Ehleringer and Monson, 1993). Vegetation with a C4 photosynthetic pathway converts CO_2 into a four-carbon compound, oxaloacetate, which reduces photorespiration, whereas CAM vegetation converts CO_2 into malate at night to reduce water loss through transpiration. Plants that utilise the C4 pathway are predominantly warm-season grasses that grow in tropical and subtropical grasslands and semi-arid regions, whereas CAM plants are predominantly succulents that grow in arid, desert environments (Collatz et al., 1998; Ehleringer and Cerling, 2001). The different photosynthetic pathways result in distinct carbon isotope values of the plants tissues; plants with a C3 pathway have a mean $\delta^{13}C$ value of ~-27‰, those with a C4 pathway have a mean $\delta^{13}C$ value of ~-12.5‰, and CAM plants have an intermediate $\delta^{13}C$ value (Vogel et al., 1978; Cerling et al., 1991, Vogel, 1993). In the sub-tropical Northern Cape, the vegetation is categorised as savanna, i.e., a mix of predominantly C4 grasses and C3 woodland (Mucina and Rutherford, 2006; SANBI, 2021).

Decaying plant material is converted back to CO_2 in the soil via respiration of bacteria, and the soil inherits the $\delta^{13}C$ of the vegetation (Cerling et al., 1991). The soil CO_2 is then dissolved in percolating rainwater, producing carbonic acid (H_2CO_3), which dissociates into H^+ and HCO_3^- ions, lowering the pH of the groundwater which increases its

weathering capacity (Clark and Fritz, 1997; Pentecost, 2005). The proportions of the carbon species in groundwater, i.e. $CO_{2(aq)}$, HCO_3^-, and CO_3^{2-} vary depending on temperature, pH, and ionic strength (Turi, 1986). This solution is transported into the underlying karst aquifer where further carbon is incorporated into the dissolved inorganic carbon (DIC) pool during carbonate bedrock dissolution (Clark and Fritz, 1997).

The proportion of CO_2 derived from the soil-zone versus the bedrock depends on open or closed system dissolution (Hendy, 1971; Clark and Fritz, 1997). In the case of open system dissolution, the percolating waters are in contact with the soil atmosphere and there is continuous equilibration between the water dissolving the bedrock and the soil CO_2, and as such, the $\delta^{13}C$ value of the tufa would reflect the input of soil CO_2. In contrast, closed system conditions result in greater input of carbon from the carbonate bedrock with a higher $\delta^{13}C$ value (Craig, 1953; Clark and Fritz, 1997; Pentecost, 2005). These systems are extreme end-member scenarios, in reality there is usually a mixture of open and closed systems (Hendy, 1971; Clark and Fritz, 1997; McDermott, 2004), and distinction between them is best determined through measurements of the soil and bedrock $\delta^{13}C$ and assessed from the DIC in the water rather than from the tufa (Usdowski et al., 1979; Pentecost, 2005).

When the ground water emerges at the surface, the carbon isotopes are further fractionated via degassing of CO_2, which increases the saturation of the solution with respect to $CaCO_3$ (Jacobson and Usdowski, 1975; Andrews, 2006). This degassing occurs through interaction with the atmosphere, the landscape morphology, and photosynthesis of biota such as mosses or algae that may be passively or actively involved in calcite precipitation (Andrews, 2006) (Table 7.2). These processes affect the $\delta^{13}C$ of the DIC in the water, and subsequently the tufa that forms.

Table 7.2 Environmental and climatic influences on $\delta^{13}C$ in tufas

Factor	Effect on $\delta^{13}C$
VEGETATION, SOIL ZONE, EPIKARST & BEDROCK	
Type of vegetation	The dominant vegetation type can influence the $\delta^{13}C$ of the tufa (Cerling and Quade, 1993). Plants with a C3 pathway ($\delta^{13}C$ ~-27‰) prefer cool and moist climates and are depleted in ^{13}C relative to those with a C4 pathway ($\delta^{13}C$ ~-11‰ to +2‰), which are adapted to warmer and drier conditions (Cerling et al., 1991, Smith and Epstein, 1971).
Biogenic activity	Productive soils, i.e. soils with a higher biological activity and organic matter decay, contribute ^{12}C (leading to low $\delta^{13}C$ values) (Craig, 1953). Soil productivity and the associated vegetation is linked to moisture availability (Andrews, 2006, Cerling, 1984, Cerling and Quade, 1993, Quade et al., 1989).
Soil pCO_2	CO_2 in the soil, produced by biogenic activity / soil respiration, is dissolved by percolating rainwater. This produces carbonic acid (HCO_3^-) which contributes ^{12}C to the DIC, i.e., lower $\delta^{13}C$ values (Pentecost, 2005). Changes in the soil pCO_2 depends on the relative contribution of atmospheric CO_2 vs soil-derived CO_2. A higher proportion of atmospheric CO_2 leads to higher $\delta^{13}C$ values of the DIC.
Bedrock dissolution	Carbonate bedrock dissolution contributes ^{13}C (low negative or low positive $\delta^{13}C$ values) to the DIC of the water. The extent of this is determined by the residence time of the water in the aquifer, and also on whether there is open (in contact with soil CO_2) or closed (water is not in contact with soil atmosphere) system dissolution. In open system conditions, soil $\delta^{13}C$ is dominant, whereas in closed system conditions the bedrock $\delta^{13}C$ prevails. In reality, there is usually a mixture of these conditions (Hendy, 1971). Longer groundwater residence times (likely during drier conditions) leads to more dissolution of the bedrock and higher input of ^{13}C. CO_2 degassing and calcite precipitation in the aquifer also lead to higher DIC $\delta^{13}C$ values in the groundwater.
SURFACE	
Atmospheric CO_2	Equilibration of emergent spring & stream waters with atmospheric CO_2 leads to CO_2 degassing from the groundwater, and higher DIC $\delta^{13}C$ values in the remaining water (Andrews et al., 1993).
Distance from source	As the emergent groundwater travels away from its point of resurgence, the water re-equilibrates with surface conditions, and the DIC becomes progressively enriched in ^{13}C as ^{12}C is preferentially lost during degassing, such that tufa precipitated further downstream from the source has higher $\delta^{13}C$ values (Chafetz and Lawrence, 1994, Spiro and Pentecost, 1991, Usdowski et al., 1979).
Photosynthesis	Photosynthesis and microbial metabolic processes preferentially extract ^{12}C from the DIC in the tufa-forming waters. This causes an increase in the $\delta^{13}C$ value of the remaining water and leads to calcite precipitation from a DIC pool enriched in ^{13}C (higher / more positive $\delta^{13}C$ values). Whereas the effect of photosynthesis on the $\delta^{13}C$ value of tufa has been shown to be negligible (Arp et al., 2010), it may be more pronounced when there is a slow rate of flow and warm temperatures (Chafetz et al., 1991, Spiro and Pentecost, 1991) and in micro-environments where cyanobacteria and other algal species are actively involved in calcite precipitation (Andrews et al., 1993, Andrews et al., 2000, Arp et al., 2001). Instances in which microbial communities actively precipitate calcite, i.e., biomineralization, the resultant tufa has lower $\delta^{13}C$ values (Merz-Preiz and Riding, 1999).

7.1.3 Oxygen and carbon isotopes in tufas as palaeoclimate proxies

Oxygen and carbon isotopes in carbonate deposits have long been recognised as useful tools for unravelling palaeoclimates. In terrestrial settings, much of the focus has been on speleothems, and consequently there have been great advances in this area with long and detailed records constructed (Hendy and Wilson, 1968; Hendy, 1969; Hennig et al., 1983; Bar-Matthews et al., 1997; McDermott, 2004). Unlike speleothems that form over potentially long periods of time and in fairly stable cave environments with generally high humidity and low pCO_2, tufas form rapidly and in the open, and are thus exposed to variable surface conditions. This means that they have the potential to record short-term variability, e.g. seasonal temperature changes, making tufas complimentary archives to longer-term records from speleothem and lake deposits (Andrews, 2006). However, tufas are affected by a variety of local factors and site characteristics that complicate their geochemistry, e.g. microbial activity, entrapment of dust and debris, and kinetic fractionation effects (Andrews et al., 1997; Andrews, 2006).

Numerous investigations of active and sub-recent tufa deposits, coupled with measurements of the tufa-forming spring/stream waters, have demonstrated that $\delta^{18}O$ and $\delta^{13}C$ values in tufas do have the potential to reliably record temperature variability and climatic conditions, confirmed through comparison against observed values of these variables (Pentecost and Spiro, 1990; Chafetz et al., 1991; Andrews et al., 1997; Drysdale, 2001; Matsuoka et al., 2001; Ihlenfeld et al., 2003; Kano et al., 2007; Lojen et al., 2009; Koltai et al., 2012; Osácar et al., 2016). This has been shown to be particularly true for well-laminated tufas, which have the potential to record seasonal climatic variation (Chafetz et al., 1991; Matsuoka et al., 2001; Ihlenfeld et al., 2003; Andrews and Brasier, 2005).

The palaeoclimate proxy potential of $\delta^{18}O$ and $\delta^{13}C$ values in fossil tufas has been recognised since the 1980s. In particular, Pazdur et al. (1988a) used $\delta^{18}O$ and $\delta^{13}C$ values measured in Holocene tufa samples from Poland to reconstruct environmental conditions at the site. They found good agreement between their reconstruction and other records of environmental change in Europe for the same time period.

Subsequently, isotope studies on fossil tufa deposits have provided the basis for environmental reconstruction at numerous tufa sites world-wide (Andrews et al., 2000; Makhnach et al., 2004; Smith et al., 2004; O'Brien et al., 2006; Ortiz et al., 2009; Cremaschi et al., 2010). However, most of these studies have coarse sampling resolution, and this averages out short-term / seasonal variations (Garnett et al., 2004a, Makhnach et al., 2004). A study on tufas in the Grand Canyon, Arizona, conducted by O'Brien et al. (2006) is one example of older tufas with resolvable isotope data on seasonal time-scales. Brasier et al. (2010) used petrographic analysis together with high resolution measurements of oxygen and carbon isotope ratios to investigate seasonal variation in laminated tufas from Greece (dated ~100 ka).

Whereas interpretations of fossil tufa $\delta^{18}O$ and $\delta^{13}C$ values are often made based on comparisons with modern tufas or analysis of water from the same hydrological system (e.g. Pazdur et al., 1988a; Andrews et al., 2000; O'Brien et al., 2006), this is seldom possible in the case of fossil tufas from semi-arid and arid regions where the tufa-forming system is no longer active, and the past environment was likely characterised by different climatic conditions than regions in which modern tufas have been studied. The following sections detail selected studies of isotope records from fossil tufas in semi-arid and arid settings, relevant to the tufas at Ga-Mohana Hill.

7.1.3.1 Semi-arid environment tufa isotopes

Despite the prevalence of evaporation and disequilibrium effects, fossil tufas from arid and semi-arid environments have been shown to be useful palaeoclimate archives and a valuable tool for filling in gaps in areas where other palaeoclimate proxy data is sparse (Pazdur et al., 1988a; Smith et al., 2004; Moeyersons et al., 2006; O'Brien et al., 2006; Cremaschi et al., 2010; Diniz et al., 2022; Stone et al., 2022). Oxygen isotope values measured in tufas that formed in semi-arid / arid settings tend to have a wider range than fossil-tufas from temperate regions and modern settings, with the upper range of $\delta^{18}O$ values extending towards more positive values (>-5‰) (Figure 7.1.9 and references given in the caption). This is attributed in part to enhanced evaporation and variable

rainfall isotope compositions in settings with higher mean annual temperatures (Smith et al., 2004; Diniz et al., 2022; Stone et al., 2022).

Interpretation of carbon isotopes in tufas is more complicated than interpreting oxygen isotopes, as $\delta^{13}C$ values tend to vary widely, regardless of climatic setting (Figure 7.1.10 and references given in the caption). Overall, though, tufas from semi-arid / arid settings do tend to have higher $\delta^{13}C$ values than those from temperate regions. This is interpreted to result from sparse vegetation cover or vegetation predominantly with C4 photosynthetic pathways (Smith et al., 2004), as well as greater influence of bedrock-derived carbon due to longer water residence times. Temporal variations in $\delta^{13}C$ values in tufas from semi-arid settings can thereby aid in constraining local environmental shifts (Cremaschi et al., 2010).

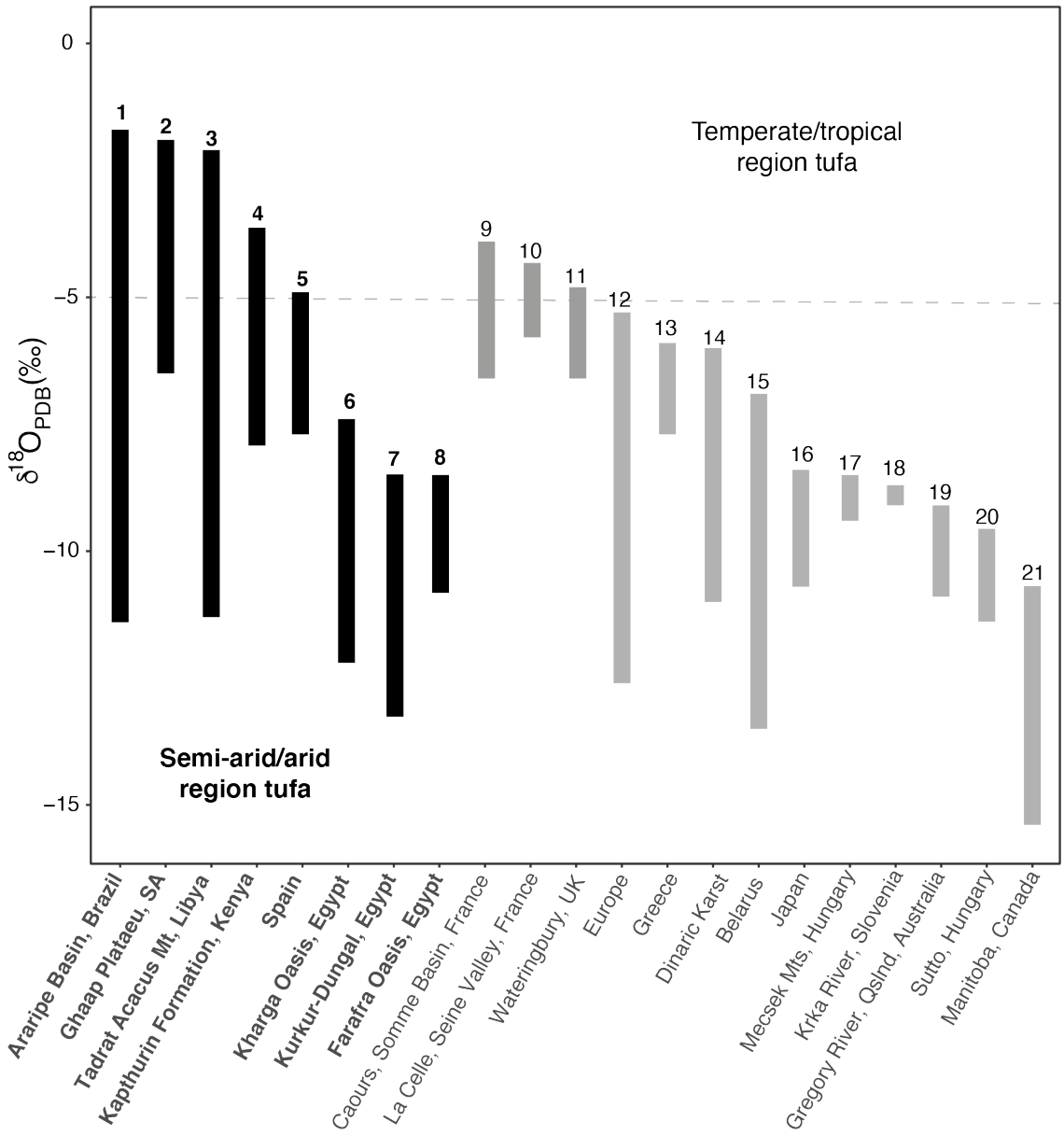

Figure 7.1.9 Comparison between the range of tufa $\delta^{18}O_{PDB}$ values from various global localities grouped by semi-arid/arid (black) and temperate/tropical climates (grey): 1.Araripe Basin, Brazil (Diniz et al., 2022); 2.Ghaap Plateau, South Africa (Doran et al., 2015); 3.Libya (Cremaschi et al., 2010); 4.Kapthurin Formation, Kenya (Johnson et al., 2009); 5. Spain (Andrews et al., 2000); 6. Kharga Oasis, Egypt (Smith et al., 2004); 7. Kurkur-Dungal, Egypt (Kele et al., 2021); 8. Farafra Oasis, Egypt (Wanas and Armenteros, 2019); 9.Caours, Somme Basin, France (Dabkowski et al., 2015); 10.La Celle, Seine Valley, France (Dabkowski et al., 2012); 11.Wateringbury, UK (Garnett et al., 2004a); 12.Various localities in western Europe (Andrews et al., 1997); 13.Greece (Brasier et al., 2010); 14.Dinaric Karst, eastern Europe (Horvatinčić et al., 2003); 15.Belarus (Makhnach et al., 2004); 16.Japan (Matsuoka et al., 2001); 17.Mecsek Mountains, Hungary (Koltai et al., 2012); 18.Krka River, Slovenia (Zavadlav et al., 2017); 19.Gregory River, Queensland, Australia (Ihlenfeld et al., 2003); 20.Sutto, Hungary (Sierralta et al., 2010); 21.Manitoba, Canada (Leybourne et al., 2009).

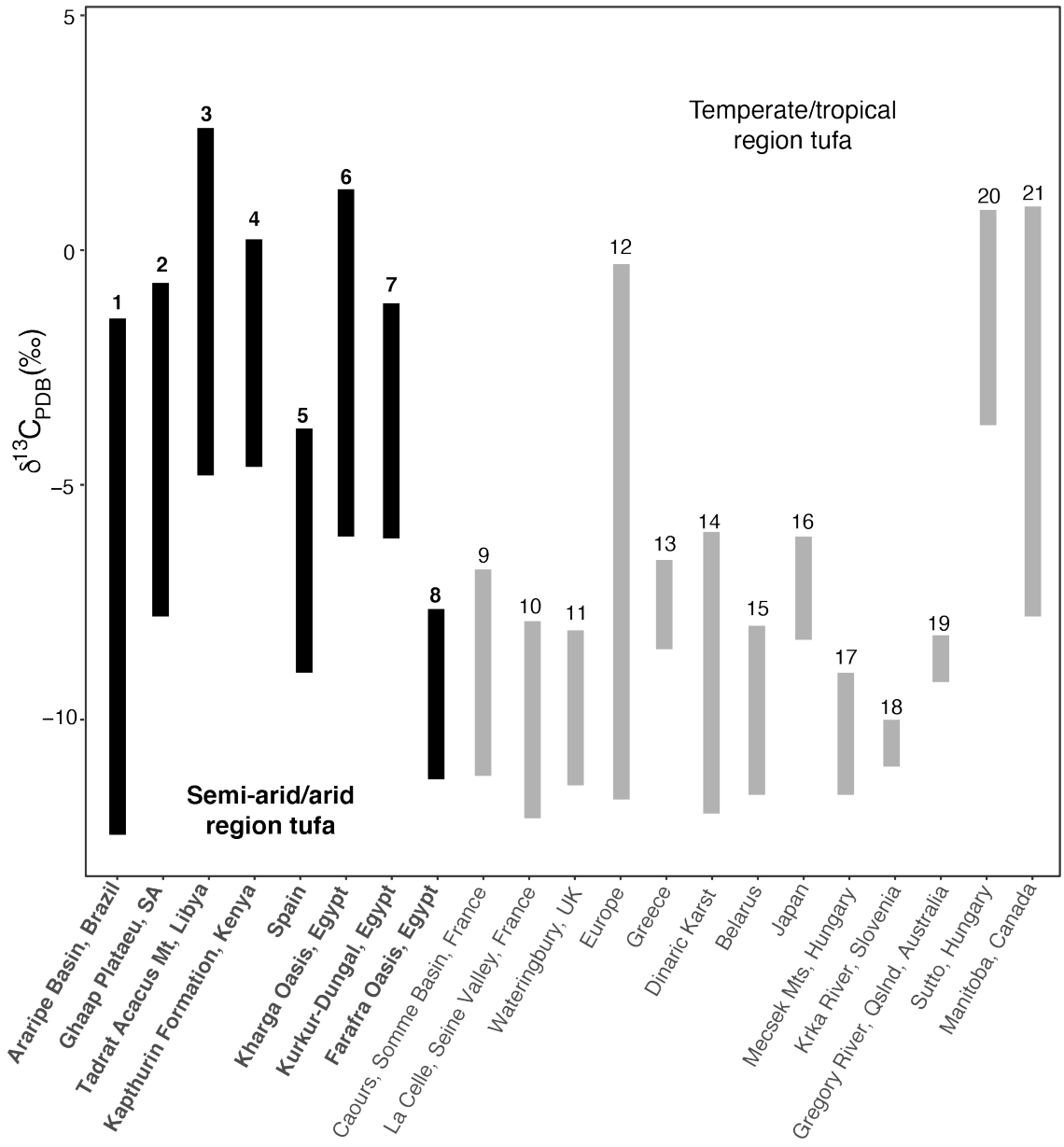

Figure 7.1.10 Comparison between the range of tufa $\delta^{13}C_{PDB}$ values from various global localities grouped by semi-arid/arid (black) and temperate/tropical climates (grey): 1.Araripe Basin, Brazil (Diniz et al., 2022); 2.Ghaap Plateau, South Africa (Doran et al., 2015); 3.Libya Libya (Cremaschi et al., 2010); 4.Kapthurin Formation, Kenya (Johnson et al., 2009); 5. Spain (Andrews et al., 2000); 6. Kharga Oasis, Egypt (Smith et al., 2004); 7. Kurkur-Dungal, Egypt (Kele et al., 2021); 8. Farafra Oasis, Egypt (Wanas and Armenteros, 2019); 9.Caours, Somme Basin, France (Dabkowski et al., 2015); 10.La Celle, Seine Valley, France (Dabkowski et al., 2012); 11.Wateringbury, UK (Garnett et al., 2004a); 12.Various localities in western Europe (Andrews et al., 1997); 13.Greece (Brasier et al., 2010); 14.Dinaric Karst, eastern Europe (Horvatinčić et al., 2003); 15.Belarus (Makhnach et al., 2004); 16.Japan (Matsuoka et al., 2001); 17.Mecsek Mountains, Hungary (Koltai et al., 2012); 18.Krka River, Slovenia (Zavadlav et al., 2017); 19.Gregory River, Queensland, Australia (Ihlenfeld et al., 2003); 20.Sutto, Hungary (Sierralta et al., 2010); 21.Manitoba, Canada (Leybourne et al., 2009).

7.1.3.2 Oxygen and carbon isotopes from local tufa deposits

Tufa isotope data have been reported from two localities near Ga-Mohana Hill: Wonderwerk Cave (Brook et al., 2010; Brook et al., 2015) and the Ghaap escarpment (Doran et al., 2015). The findings from these studies are summarised below as they provide a useful comparison for the Ga-Mohana tufa isotope data.

Wonderwerk Cave

At Wonderwerk Cave, isotope data from stalagmite WW1-3 near the cave entrance, dated using radiocarbon, provides a basis for palaeoenvironmental reconstruction spanning the last 35 ka (Brook et al., 2010). The $\delta^{13}C$ values from WW1-3 range from -5.1‰ to +4.2‰ with a mean of -1.4‰. Brook et al. (2010) interpreted lower $\delta^{13}C$ values, associated with calcite precipitation between ~23 to 17 ka, to represent a predominance of C3 vegetation. They interpreted this to imply cooler and wetter conditions with more regular winter rainfall and greater input of soil-derived CO_2. On the other hand, higher $\delta^{13}C$ values are interpreted to represent an increase in C4 grasses with reduced vegetation cover and decreased soil productivity, resulting in lower input of soil-derived CO_2. Altogether this is interpreted as representing warmer and drier conditions related to the ~32 ka, ~24 ka, ~15 ka and ~4 ka time periods.

Using rainfall data from IAEA stations in Pretoria and Windhoek, Brook et al. (2010) note a negative correlation between the average monthly rainfall amount and the $\delta^{18}O$ value of the rainfall. They infer that the amount effect is the principal factor influencing the $\delta^{18}O$ value of rainfall at these locations and extrapolate this to Wonderwerk Cave. They therefore interpret lower $\delta^{18}O$ values in the stalagmite to represent a higher amount of summer rainfall coupled with cooler conditions and lower rates of evaporation. This is corroborated by other proxy records from the site, including pollen and isotope data from faunal tooth enamel (Brook et al., 2010). The authors note that their interpretation of the oxygen isotope data differs from that of Holmgren et al. (2003) who interpret lower $\delta^{18}O$ values from the Cold Air Cave speleothem as evidence for cooler and drier climatic conditions.

In a second study, Brook et al. (2015) report high resolution isotope data for late Holocene (<3500 years) samples from stalagmite WW1-3 and a cave entrance tufa, WW3. In these two samples, the $\delta^{13}C$ and $\delta^{18}O$ values exhibit a strong correlation (R^2 = 0.83 for WW1-3 and R^2 = 0.82 for WW3), which indicates kinetic fractionation effects likely related to high rates of evaporation (Brook et al., 2015). However, a similar relationship is noted for isotope values of speleothems from Cold Air Cave and Dante Cave, where evaporation is less likely to have had an impact on the isotope values given that they are situated deep within caves. In light of this, Brook et al. (2015) argued that the sympathetic relationship between carbon and oxygen isotope values in the samples from all three localities indicates that soil pCO_2, impacted by the rainfall amount, is the predominant control on the $\delta^{13}C$ value, rather than the type of vegetation. In this context, they interpret low $\delta^{18}O$ and $\delta^{13}C$ values as evidence of increased rainfall and lower rates of evaporation together with increased vegetation and higher soil productivity, versus high $\delta^{13}C$ and $\delta^{18}O$ values interpreted as evidence of decreased rainfall and higher rates of evaporation leading to less vegetation and associated soil productivity (Brook et al., 2015).

Ghaap escarpment

Tufa deposits along the Ghaap escarpment have a long history of investigation having been recognised as hosts of faunal and hominin fossil accumulations since the early 20th century (Peabody, 1954), and as useful deposits for landscape and climate reconstruction (Butzer, 1974, Marker, 1974; Butzer, 1984). Recently, Doran et al. (2015) successfully applied radiometric methods (^{14}C and U-Th) to date some of the Ghaap escarpment tufas and measured their oxygen and carbon isotope values to assess their potential to record useful palaeoclimate information. They report eleven tufas, sampled from three different localities along the Ghaap escarpment, that represent tufa growth during three temporal periods: the Pliocene, Middle Pleistocene, and Holocene. These were sampled on a cm-scale for oxygen and carbon isotope analysis (n = 85). The results show a distinct grouping of isotope values for each time period, with both oxygen and carbon values becoming less negative from the Pliocene through to the Holocene deposits (Doran et al., 2015).

The Pliocene deposits have a mean $\delta^{18}O$ value of -5.8‰ and $\delta^{13}C$ value of -6‰, the Middle Pleistocene samples have a mean $\delta^{18}O$ value of -3.7‰ and $\delta^{13}C$ value of -3.6‰, and the Holocene tufas have a mean $\delta^{18}O$ value of -2.3‰ and $\delta^{13}C$ value of -0.5‰ (Doran et al., 2015). They attribute the trend of increasing $\delta^{18}O$ values with decreasing age primarily to an increasing effect of evaporation on tufa formation, related to increasing temperatures and aridity from the Pliocene through to the Holocene. They also observe that this trend is consistent with speleothem records in South Africa, which show a similar temporal pattern, and suggest that this can be partially explained by the increase in global ice volume over this time. The lower $\delta^{13}C$ values in the Pliocene tufas are interpreted as reflecting a predominance of C_3 vegetation, and the increasing $\delta^{13}C$ values through time is attributed to an expansion of C_4 vegetation into the Holocene. The $\delta^{18}O$ and $\delta^{13}C$ variability in these tufas thus both point to increasing aridity through this time period. Finally, Doran et al. (2015) conclude that the Ghaap escarpment tufas demonstrate excellent potential for further palaeoclimate investigations.

Altogether, the theory and case studies presented above provide context and useful comparisons for the Ga-Mohana tufa isotope data presented in the following section.

7.2 Isotope results for Ga-Mohana Hill water and tufa samples

A sample set (n = 62) of δD and $\delta^{18}O$ values measured in modern groundwater, rainfall, and drip water samples from Ga-Mohana Hill and surrounds are reported in Section 7.2.1. These data were collected in January (wet summer) and July (dry winter) of 2018 to complement the tufa isotope data. Groundwater samples were collected from boreholes on farms in the Kuruman area, and from the Eye of Kuruman spring (Figure 2.1). The rain waters were collected during two brief (~15 minute) rain events, and the drip water samples were collected from actively dripping mini-stalactites along the Ga-Mohana north shelter walls and cliff-faces. The isotope data for the modern waters collected are presented in Table 7.3. The data is summarised according to category in Table 7.4 and presented graphically in Figure 7.2.1.

The $\delta^{18}O$ and $\delta^{13}C$ values of 75 sub-samples drilled from 26 tufa samples are reported relative to PDB in section 7.2.2. These were investigated to assess whether there are any patterns related to the individual tufa morphologies and their associated depositional settings, or if any temporal patterns in the $\delta^{18}O$ and $\delta^{13}C$ values are evident. A dolomite sample from the rock shelter wall was also collected and analysed for its isotope composition for comparison. The results of the tufa isotope analyses are given in Table 7.5 and summarised according to morphology in Table 7.6, wherein the $\delta^{18}O$ tufa values are reported relative to both PDB and SMOW for ease of comparison between $\delta^{18}O_{tufa}$ and $\delta^{18}O_{water}$.

The data presented here is interpreted in Section 7.3, and discussions therein relating to conditions of precipitation from water of different $\delta^{18}O$ values use water and carbonate relative to SMOW.

7.2.1 Hydrogen and oxygen isotopes measured in water

The δD and $\delta^{18}O$ values of modern waters collected from Ga-Mohana Hill and the surrounding area of Kuruman were analysed, as the $\delta^{18}O$ values of the tufas are related to the $\delta^{18}O$ value of the waters from which they formed. Although there is a difference

between the time of tufa formation and the time of water sample collection, the δD and $\delta^{18}O$ values for the modern rain, groundwater and drip waters may provide some insight into the potential variation in δD and $\delta^{18}O$ at the time of tufa formation. The δD and $\delta^{18}O$ values of the water samples from all sources have a range of 89.41‰ (min = -39.71‰, max = +49.70‰) and 18.03‰ (min = -6.59‰, max = +11.44‰), respectively. The mean δD and $\delta^{18}O$ values are -0.77‰ (σ = 5.34, n=43) and -10.84‰ (σ = 27.92, n= 43), respectively.

The groundwaters collected (n=15) are relatively consistent and show the least amount of variation. This is expected as they represent a large reservoir which is not prone to evaporation. The range in δD and $\delta^{18}O$ values for these samples are 4.05‰ (min = -39.71‰, max = -35.66‰) and 1.04‰ (min = -6.59‰, max = -5.55‰), respectively. The mean δD and $\delta^{18}O$ values for groundwater are -37.78‰ (σ = 1.44) and -6.14‰ (σ = 0.33) respectively. The groundwater plots just below the Windhoek LMWL and slightly above the GMWL, with a few samples plotting on the GMWL (Figure 7.2.1).

The drip water sampled (n=11) has higher δD and $\delta^{18}O$ values than the groundwater with a range of 27.38‰ (min = -31.82‰, max = -4.44‰) and 6.26‰ (min = -5.26‰, max = -1.00‰), respectively. The mean drip water δD and $\delta^{18}O$ values are 24.35‰ (σ = 9.43) and -3.45‰ (σ = 2.25), respectively. The low end of the data array plots on the GMWL but has a less steep gradient than the GMWL (Figure 7.2.1).

The rainwater collected directly as fresh rainfall (n=4) and from pools of shallow standing water about 20 minutes after rainfall events (n=13) shows the greatest spread, with significantly more positive δD and $\delta^{18}O$ values than the ground and drip waters. The range of δD and $\delta^{18}O$ values in the rainwater collected are 56.1‰ (min = -1.9‰, max = 49.7‰) and 10.9‰ (min = 0.54‰, max = 11.44‰), respectively. The mean δD and $\delta^{18}O$ values for rainfall collected during this study near Ga-Mohana Hill are 30.29‰ (σ =15.66) and 6.57‰ (σ = 3.47) respectively. The rainwater samples all plot below the GMWL (Figure 7.2.1).

Table 7.3 δD and $\delta^{18}O$ values measured in waters collected at and around Ga-Mohana Hill. Values reported relative to SMOW in per mil (‰).

Sample no	Month	Category	δD_{SMOW} (‰)	$\delta^{18}O_{SMOW}$ (‰)
2.1	January	rain	+19.7	+3.38
2.2	January	rain	+21.0	+3.47
3.1	January	standing	+24.2	+6.00
3.2	January	standing	+22.4	+5.84
4.1	January	standing	+46.6	+10.54
4.2	January	standing	+47.6	+10.78
5.1	January	standing	-1.9	+0.61
5.2	January	standing	-0.8	+0.54
6.1	January	standing	+48.5	+11.44
6.2	January	standing	+48.3	+11.22
7.1	January	drip water	-22.6	-2.64
7.2	January	drip water	-14.9	-0.94
8.1	January	drip water	-29.8	-4.96
8.2	January	drip water	-31.6	-5.07
8.3	January	drip water	-31.3	-5.20
8.4	January	drip water	-31.8	-5.26
9.1	January	standing	+49.7	+10.95
10.1	January	drip water	-4.4	+1.00
11.1	January	drip water	-12.8	-0.66
13.1	January	drip water	-29.8	-4.88
13.2	January	drip water	-29.4	-4.75
13.3	January	drip water	-29.4	-4.57
14.1	January	standing	+32.7	+6.67
14.2	January	standing	+33.3	+6.65
15.1	January	standing	+31.8	+6.29
15.2	January	standing	+32.5	+6.25
16.1	January	rain	+29.5	+5.49
16.2	January	rain	+29.8	+5.65
17.1	January	groundwater	-37.9	-6.09
17.2	January	groundwater	-38.2	-6.07
18.1	January	groundwater	-37.8	-6.28
18.2	January	groundwater	-38.6	-6.29
19.1	January	groundwater	-38.5	-6.17
19.2	January	groundwater	-37.4	-6.21
19.3	January	groundwater	-37.6	-6.25
20.1	January	groundwater	-35.9	-5.55
20.2	January	groundwater	-35.7	-5.72
20.3	January	groundwater	-35.8	-5.72
20.4	January	groundwater	-35.7	-5.73
21.1	January	groundwater	-39.3	-6.48
21.2	January	groundwater	-39.2	-6.46
21.3	January	groundwater	-39.7	-6.59
21.4	January	groundwater	-39.4	-6.56

22.1	July	drip water	-4.9	+2.64
22.2	July	drip water	-11.4	+0.43
23.2	July	drip water	-14.4	-0.21
22.4	July	drip water	-16.6	-1.31
23.1	July	drip water	-24.1	-3.88
23.1.1	July	drip water	-16.7	-1.34
23.1.2	July	drip water	-13.3	-0.40
23.1.3	July	drip water	-11.4	+0.40
23.1.4	July	drip water	-10.7	+0.49
23.2	July	drip water	-21.8	-2.83
24.1	July	drip water	-22.5	-3.11
24.2	July	drip water	-24.1	-3.47
24.3	July	drip water	-23.9	-3.56
24.4	July	drip water	-23.6	-2.90
25.1	July	drip water	-15.3	-0.64
25.2	July	drip water	-13.5	+0.27
26.1	July	drip water	-2.6	+1.71
28.1	July	groundwater	-37.2	-6.10
28.2	July	groundwater	-37.5	-6.10

Table 7.4 Summary of hydrogen and oxygen isotope data measured in water samples according to category.

		δD_{SMOW} (‰)				$\delta^{18}O_{SMOW}$ (‰)			
Category	**n**	**min**	**max**	**mean**	**σ**	**min**	**max**	**mean**	**σ**
groundwater	17	-39.71	-35.66	-37.72	1.36	-6.59	-5.55	-6.14	0.31
drip water	28	-31.82	-2.59	-19.24	8.78	-5.26	+2.64	-1.99	2.37
rain water	17	-1.9	+49.7	+30.29	15.66	+0.54	+11.44	+6.57	3.47
all waters	62	-39.71	+49.7	-10.72	28.36	-6.59	+11.44	-0.78	5.42

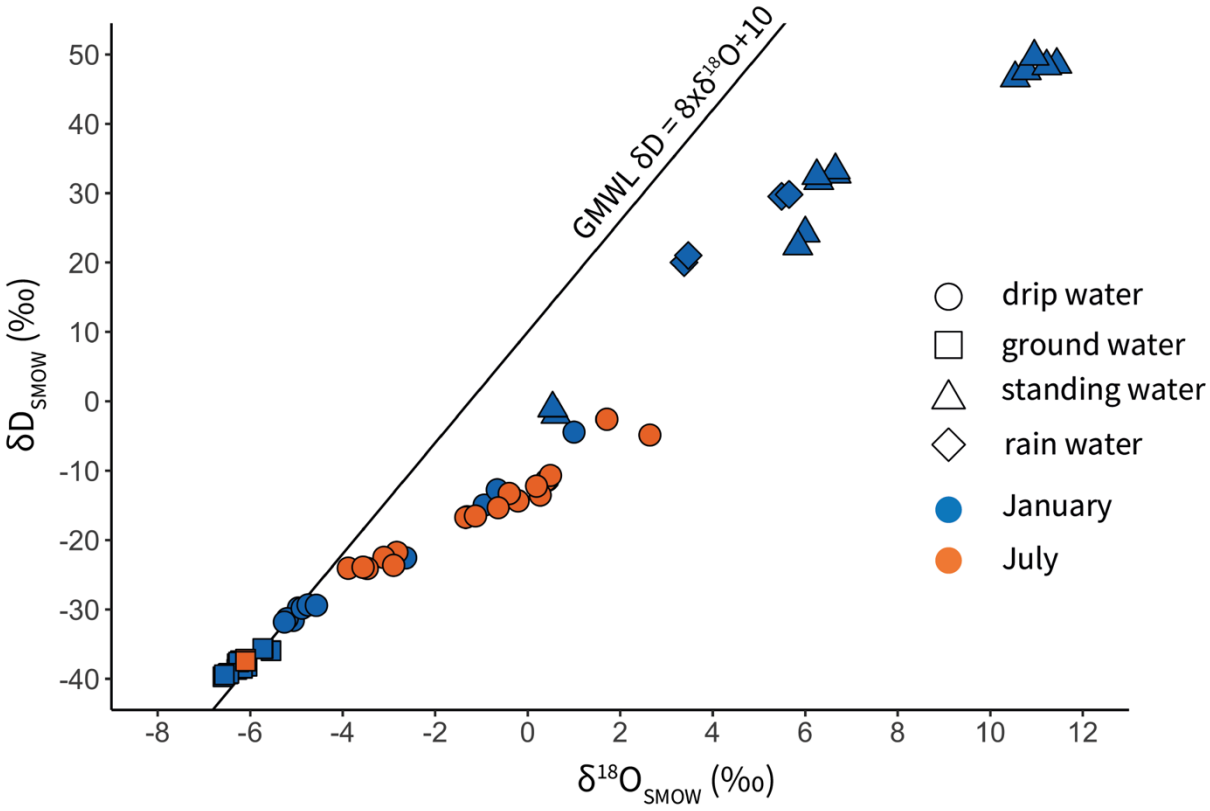

Figure 7.2.1 Plot of δD against $\delta^{18}O$ values for groundwater, precipitation (rain and standing water), and drip waters collected from Ga-Mohana Hill and Kuruman surrounds in January and July 2018. The shape of the symbols represents the type of water, and the colour represents the time of year the water was collected. GMWL = Global Meteoric Water Line (Craig, 1961).

There is a strong positive correlation between the δD and $\delta^{18}O$ values for the groundwaters (r = 1, n = 17), drip waters (r = 0.97, n = 28), and rain waters (r = 0.95, n= 17). This strongly linear relationship is expected for waters of meteoric origin (Craig, 1965). The groundwaters and some of the drip waters collected in January plot on or near the GMWL. The majority of July drip waters, as well as the rain and standing waters, plot below the GMWL, which suggests evaporation either as the rain fell, or evaporation of the standing water on the surface (Gat, 1996).

7.2.2 Carbon and oxygen isotopes measured in Ga-Mohana tufas

The $\delta^{13}C_{PDB}$ values of the tufa samples have a range of 12.38‰ with a minimum of -8.83‰ and a maximum of +3.55‰. The $\delta^{18}O_{PDB}$ values have a range of 6.09‰, with a minimum of -6.14‰ and a maximum of -0.05‰. The mean $\delta^{13}C_{PDB}$ and $\delta^{18}O_{PDB}$ values are -3.82‰ (σ = 3.19, n=74) and -3.57‰ (σ = 1.40, n=74), respectively. The $\delta^{13}C_{PDB}$ and $\delta^{18}O_{PDB}$ values for the Campbellrand dolomite sample are -0.03‰ and -10.60‰, respectively. These data are presented in Table 7.5.

Four subsamples (marked with an * in Table 7.5) were analysed twice to assess the reproducibility of the data. The repeat subsamples were all run in the second round of analyses. Subsample 17-11.3 is a repeat of subsample 17-11.1; the $\delta^{13}C_{PDB}$ and $\delta^{18}O_{PDB}$ values for 17-11.1 are -6.14‰ and -5.01‰, respectively, while $\delta^{13}C_{PDB}$ and $\delta^{18}O_{PDB}$ values for 17-11.3 are -5.74‰ and -5.81‰, respectively. There is a difference of 0.4‰ and 0.8‰ for the $\delta^{13}C$ and $\delta^{18}O$ measurements. Subsamples 17-13.4, 17-13.5 and 17-13.6 are repeats of 17-13.1, 17-13.2 and 17-13.3, respectively. A difference of 0.06‰ for both the $\delta^{13}C$ and $\delta^{18}O$ values measured in subsamples 17-13.2 and 17-13.5 is negligible, whereas there is a relatively substantial difference of 0.93‰ and 1.42‰ for the $\delta^{13}C$ and $\delta^{18}O$ values measured in samples 17-13.1 and 17-13.4. A difference of 0.2‰ and 0.43‰ is recorded for the $\delta^{13}C$ and $\delta^{18}O$ values in subsamples 17-13.3 and 17-13.6. These differences in values for the same samples between run 1 and run 2 are partially reflected in the difference in values in the standard repeats for each of the two runs. As with the subsamples, a larger difference in $\delta^{18}O$ values in samples across the two runs is recorded, with the largest being 0.22‰ for in-house standard CM, followed by 0.13‰ for the IAEA standard. The difference in $\delta^{13}C$ values measured in the standard repeats between the two runs is much less, with a 0.05‰ difference for the IAEA standard, a 0.06‰ difference for in-house standard CZ and a 0.00‰ difference for CM. The repeated subsamples thus display a comparatively higher difference to the standards, but, overall, these values indicate the data are reproducible and reliable.

Table 7.5 $\delta^{13}C$ and $\delta^{18}O$ values measured in tufa carbonate samples, reported in per mil (‰). Sub-samples in italics and labelled with *SI* were run at the University of Melbourne, the rest were run at the University of Cape Town.

Location	Morphology	Sample	Subsample	$\delta^{13}C_{PDB}$	$\delta^{18}O_{PDB}$	$\delta^{18}O_{SMOW}$
GHN cliff	dolomite	17-19	17-19.1	-0.03	-10.60	19.93
GHN cliff	cascade	GHN2	GHN 2.1	-4.92	-3.33	27.42
GHN cliff	cascade	GHN2	GHN 2.2	-4.45	-3.27	27.49
GHN cliff	cascade	GHN2	GHN 2.3	-4.92	-3.01	27.75
GHN cliff	cascade	17-10	17-10.1	-5.73	-4.65	26.07
GHN cliff	cascade	17-10	17-10.2	-6.10	-3.75	26.99
GHN cliff	cascade	17-10	17-10.3	-5.39	-3.62	27.13
GHN cliff	cascade	17-11	17-11.1	-6.14	-5.01	25.69
GHN cliff	cascade	17-11	17-11.2	-5.41	-5.19	25.51
GHN cliff	cascade	17-11	17-11.3*	-5.74	-5.81	24.87
GHN cliff	*cascade*	*18-12*	*18-12-SI-1*	*+1.92*	*-1.77*	*29.04*
GHN cliff	*cascade*	*18-12*	*18-12-SI-2*	*+2.10*	*-0.79*	*30.04*
GHN cliff	*cascade*	*18-13*	*18-13-SI-1*	*-6.84*	*-3.99*	*26.75*
GHN cliff	*cascade*	*18-13*	*18-13-SI-2*	*-7.53*	*-4.36*	*26.37*
GHN cliff	*cascade*	*18-13*	*18-13-SI-3*	*-8.59*	*-5.00*	*25.71*
GHN cliff	*cascade*	*18-13*	*18-13-SI-4*	*-8.83*	*-4.69*	*26.02*
GHN cliff	*cascade*	*18-14*	*18-14-SI-1*	*-7.91*	*-4.19*	*26.54*
GHN cliff	*cascade*	*18-14*	*18-14-SI-2*	*-8.18*	*-3.95*	*26.79*
GHN cliff	*cascade*	*18-14*	*18-14-SI-3*	*-7.08*	*-3.59*	*27.16*
GHN cliff	*cascade*	*18-14*	*18-14-SI-4*	*-5.55*	*-2.79*	*27.98*
GHN cliff	*cascade*	*18-15*	*18-15-SI-1*	*-7.63*	*-4.47*	*26.25*
GHN cliff	*cascade*	*18-15*	*18-15-SI-2*	*-8.16*	*-4.85*	*25.86*
GHN cliff	*cascade*	*18-15*	*18-15-SI-3*	*-8.71*	*-4.75*	*25.97*
GHN cliff	*cascade*	*18-16*	*18-16-SI-1*	*-4.77*	*-3.94*	*26.80*
GHN cliff	*cascade*	*18-16*	*18-16-SI-2*	*-5.22*	*-4.20*	*26.53*
GHN cliff	*cascade*	*18-17*	*18-17-SI-1*	*-4.36*	*-3.44*	*27.32*
GHN cliff	*cascade*	*18-17*	*18-17-SI-2*	*-4.44*	*-5.22*	*25.48*
GHN cliff	*cascade*	*18-17*	*18-17-SI-3*	*-4.67*	*-5.48*	*25.21*
GHN cliff	cascade	17-21	17-21.1	-3.10	-4.29	26.43
GHN cliff	cascade	GHS5	GHS 5.1	-4.40	-4.22	26.51
GHN cliff	cascade	GHS5	GHS 5.2	-3.02	-1.61	29.20
GHN terrace	*cascade*	*18-4*	*18-4-SI-1*	*-4.96*	*-6.14*	*24.53*
GHN talus	barrage	17-6	17-6.1	+0.63	-4.19	26.54
GHN talus	barrage	17-6	17-6.2	-1.86	-4.84	25.88
GHN talus	barrage	17-6	17-6.3	-0.40	-3.56	27.19
GHN talus	barrage	17-6	17-6.4	-0.68	-5.26	25.43
GHN talus	*barrage*	*17-6*	*17-6-SI-1*	*+0.14*	*-2.46*	*28.32*
GHN terrace	*barrage*	*18-6*	*18-6-SI-1*	*-0.99*	*-1.10*	*29.73*
GHN talus	rim pool	GHN1	GHN 1.1	-3.74	-3.66	27.08
GHN talus	rim pool	GHN1	GHN 1.2	-2.86	-3.33	27.42
GHN talus	rim pool	GHN1	GHN 1.3	-3.04	-2.98	27.79

GHN talus	rim pool	GHN1	GHN 1.4	-4.53	-3.04	27.73
GHN talus	*rim pool*	*GHN1*	*GHN1-SI-2*	*-4.28*	*-3.75*	*26.99*
GHN talus	*rim pool*	*GHN1*	*GHN1-SI-3*	*-4.53*	*-3.74*	*27.01*
GHN talus	rim pool	17-5	17-5.1	-5.57	-3.60	27.15
GHN talus	rim pool	17-5	17-5.2	-4.14	-3.00	27.77
GHS talus	rim pool	GHS-6	GHS6.1	-5.06	-4.03	26.71
GHS talus	rim pool	GHS-6	GHS6.2	-4.27	-4.12	26.61
GHS talus	*rim pool*	*GHS-6*	*GHS6-SI-1*	*-4.92*	*-4.06*	*26.67*
GHS talus	*rim pool*	*GHS-6*	*GHS6-S1-3*	*-4.65*	*-4.29*	*26.44*
GHN talus	terrace breccia	17-7	17-7.1	-1.47	-3.18	27.58
GHN talus	terrace breccia	17-7	17-7.2	-4.43	-3.66	27.09
GHN talus	terrace breccia	17-8	17-8.1	-5.68	-4.34	26.38
GHN talus	terrace breccia	17-8	17-8.2	-6.35	-3.96	26.77
GHN talus	*terrace breccia*	*17-8*	*17-8-SI-3*	*-5.36*	*-4.30*	*26.43*
GHN talus	*terrace breccia*	*17-8*	*17-8-SI-4*	*-5.50*	*-4.32*	*26.41*
GHN talus	*terrace breccia*	*17-8*	*17-8-SI-5*	*-5.34*	*-4.41*	*26.32*
GHN talus	*terrace breccia*	*17-8*	*17-8-SI-6*	*-4.91*	*-3.96*	*26.78*
GHS talus	terrace breccia	17-12	17-12.1	-3.97	-3.69	27.06
GHN terrace	*terrace breccia*	*18-7*	*18-7-SI-1*	*-7.29*	*-4.35*	*26.38*
GHN	dome	GHN3.2	GHN 3.2.1	-4.49	-3.13	27.64
GHN	dome	17-9	17-9.1	-3.73	-2.91	27.86
GHN	dome	17-9	17-9.2	-5.48	-5.07	25.63
GHN	dome	17-9	17-9.3	-4.47	-3.18	27.58
GHN	*dome*	*18-10*	*18-10-SI-1*	*-5.91*	*-5.89*	*24.78*
GHN	*dome*	*18-10*	*18-10-SI-2*	*-5.02*	*-4.57*	*26.15*
GHN	*dome*	*18-10*	*18-10-SI-3*	*-0.48*	*-0.92*	*29.91*
GHS	dome	GHS4	GHS 4.1	+3.40	-1.18	29.64
GHS	dome	GHS4	GHS 4.2	+1.33	-2.35	28.44
GHS	dome	17-13	17-13.1	+1.71	-2.18	28.61
GHS	dome	17-13	17-13.2	+2.20	-0.38	30.46
GHS	dome	17-13	17-13.3	+3.55	-0.48	30.37
GHS	dome	17-13*	17-13.4*	+2.64	-0.76	30.07
GHS	dome	17-13*	17-13.5*	+2.26	-0.44	30.41
GHS	dome	17-13*	17-13.6*	+3.35	-0.05	30.81

* represents repeat subsample analysed in second run to assess reproducibility

7.2.2.1 C and O isotope results according to tufa morphology

The carbon and oxygen isotope ratios measured in the tufas are reported below according to the various morphologies that are described in Chapter 4. Isotope data from each of the morphologies is summarised in Table 7.6, and the $\delta^{18}O_{PDB}$ and $\delta^{18}O_{SMOW}$ values are plotted against the $\delta^{13}C_{PDB}$ values in Figure 7.2.2. In the results below, I plot the C and O isotope data for individual samples from each morphology, wherein I include correlation coefficients for data from individual samples. These are

based on a small number of data points (n < 4) which is typically insufficient for a reliable statistical test, and this is a limitation in this study. However, they represent a starting point to evaluate equilibrium versus kinetic fractionation in the tufas.

Table 7.6 Summary of carbon and oxygen isotope data measured in tufa samples according to morphology.

		$\delta^{13}C_{PDB}$ (‰)				$\delta^{18}O_{PDB}$ (‰)				$\delta^{18}O_{SMOW}$ (‰)			
Macrofacies	**n**	**min**	**max**	**mean**	**σ**	**min**	**max**	**mean**	**σ**	**min**	**max**	**mean**	**σ**
cascades	31	-8.83	+2.1	-5.44	2.56	-6.14	-0.79	-4.04	1.19	24.53	30.04	26.69	1.23
barrages	6	-1.86	+0.63	-0.53	0.88	-5.26	-1.10	-3.57	1.56	25.43	29.73	27.18	1.61
rim pools	12	-5.57	-2.86	-4.30	0.79	-4.29	-2.98	-3.63	0.46	26.44	27.79	27.12	0.47
terrace breccia	10	-7.29	-1.47	-5.03	1.56	-4.41	-3.18	-4.02	0.41	26.32	27.58	26.72	0.42
domes	15	-5.91	+3.55	-0.61	3.74	-5.89	-0.05	-2.23	1.86	24.78	30.81	28.56	1.92
all tufas	74	-8.83	+3.55	-3.82	3.19	-6.14	-0.05	-3.57	1.40	24.53	30.81	27.18	1.44

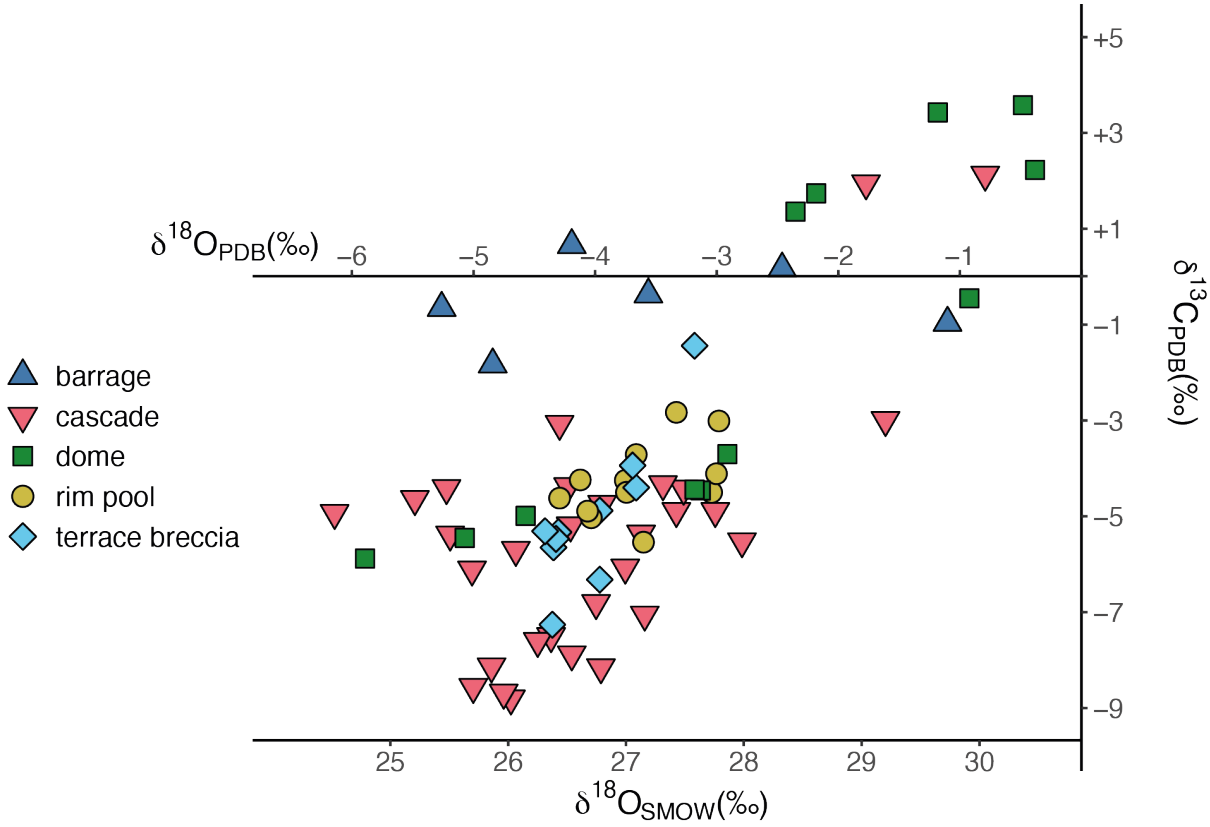

Figure 7.2.2 Plot of $\delta^{18}O_{PDB}$ and $\delta^{18}O_{SMOW}$ against $\delta^{13}C_{PDB}$ for all tufa isotope data. The data are categorised according to their respective morphologies described in Chapter 4.

Cascades

This morphology has the largest spread in isotope values compared to the other morphologies (Figure 7.2.2), with the largest number of subsamples drilled from 12 hand samples (n = 31; Figure 7.2.3 and 7.2.4). The range in $\delta^{13}C$ values is 10.93‰ (min = -8.83‰, max = 2.1‰) and the range in $\delta^{18}O$ values is 5.35‰ (min = -6.14‰, max = -0.79‰) (Figure 7.2.5). The mean $\delta^{13}C$ and $\delta^{18}O$ values are -5.43‰ (σ = 2.60) and -3.99‰ (σ = 1.17) respectively (Table 7.6). The majority of the cascade $\delta^{13}C$ and $\delta^{18}O$ values are negative, whereas sample 18-12 is a noticeable outlier with positive $\delta^{13}C$ and high $\delta^{18}O$ values relative to the rest of the cascade samples (Figure 7.2.5). Of the six cascade samples with isotope data from 3 or more sub-samples, the following four samples exhibit moderate to strong positive correlations between their $\delta^{18}O$ and $\delta^{13}C$ values: 18-15 (n = 3, r^2 = 0.48), 18-17 (n = 3, r^2 = 0.61), 18-13 (n = 4, r^2 = 0.85), and 18-14 (n = 4, r^2 = 0.94) (Figure 7.2.5). The other two samples, GHN-2 and 17-10, have almost no correlation between their respective $\delta^{18}O$ and $\delta^{13}C$ values (n = 3, r^2 = 0.1 and 0.01, respectively) (Figure 7.2.5).

Figure 7.2.3 The $\delta^{18}O_{PDB}$ and $\delta^{13}C_{PDB}$ values of material drilled at the indicated position for cascade samples 18-17, 18-13 and GHS5.

Figure 7.2.4 The $\delta^{18}O_{PDB}$ and $\delta^{13}C_{PDB}$ values of material drilled at the indicated position for cascade samples GHN2, 18-12, 18-4, 18-14, 18-16 and 18-15.

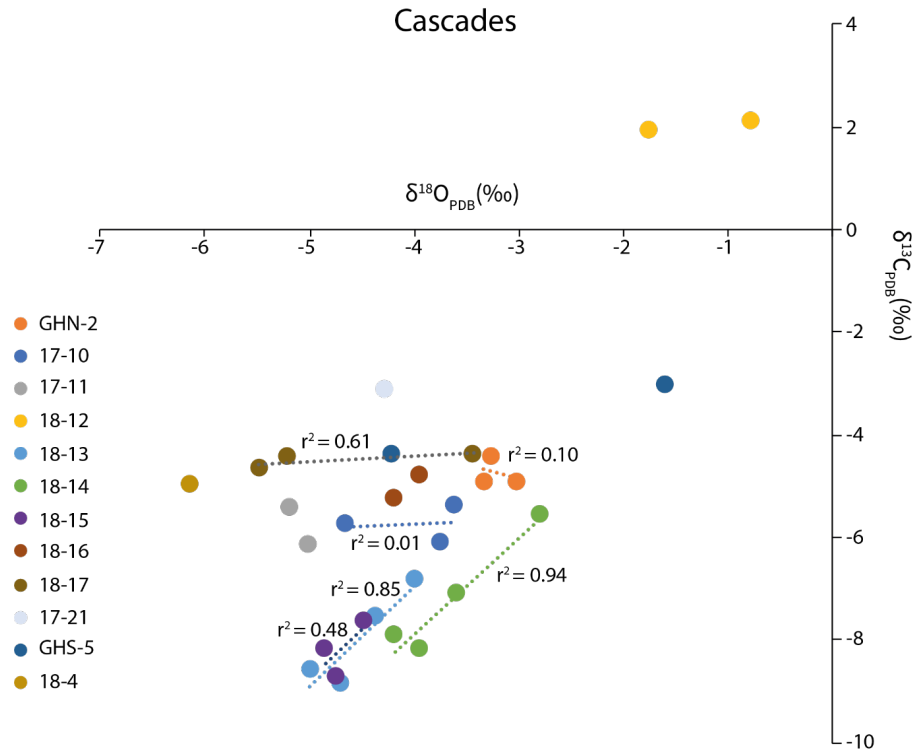

Figure 7.2.5 Bivariant plot of $\delta^{18}O_{PDB}$ and $\delta^{13}C_{PDB}$ values measured in cascade samples. Dotted lines and associated r^2 values indicate the correlations between sub-samples from individual samples with more than two sub-samples.

Barrages

The isotope values from the barrage samples have the following ranges: $\delta^{13}C$ = 2.49‰ (min = -1.86‰, max = 0.63‰) and $\delta^{18}O$ = 4.16‰ (min = -5.26‰, max = -1.10‰), with mean $\delta^{13}C$ and $\delta^{18}O$ values of -0.53‰ (σ = 0.88) and -3.57‰ (σ = 1.56) respectively (Table 7.6). These data are from two barrage samples, 18-6 (n=1) and 17-6 (n=5) (Figure 7.2.6). The $\delta^{18}O$ and $\delta^{13}C$ values in sample 17-6 are weakly correlated (n = 5, r^2 = 0.23) (Figure 7.2.7).

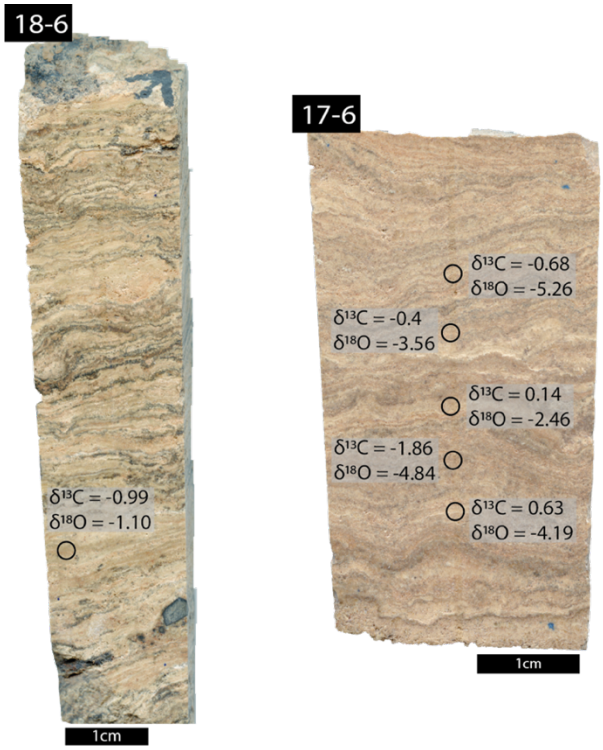

Figure 7.2.6 The $\delta^{18}O_{PDB}$ and $\delta^{13}C_{PDB}$ values of material drilled at the indicated position for barrage samples 18-6 and 17-6.

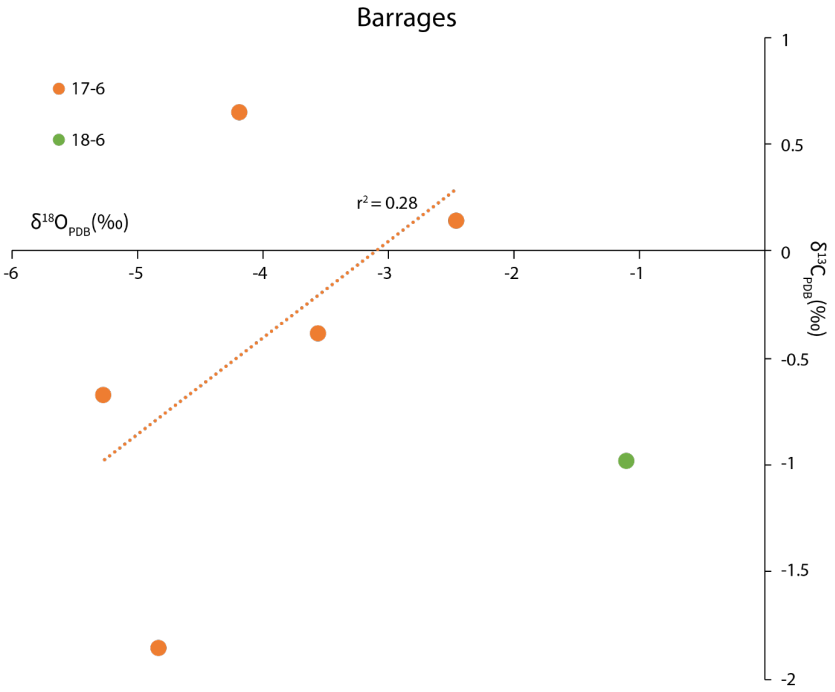

Figure 7.2.7 Bivariant plot of $\delta^{18}O_{PDB}$ and $\delta^{13}C_{PDB}$ values measured in barrage samples. The dotted line and associated r^2 value indicate the correlation between sub-samples from sample 17-6 (n>2).

Rim pools

Three rim pool samples were subsampled for isotope analysis (n=12), two of which are shown in Figure 7.2.8. The range of $\delta^{13}C$ values is 2.71‰ (min = -5.57‰, max = -2.86‰) and the range in $\delta^{18}O$ values is 1.31‰ (min = -4.29‰, max = -2.98‰), with mean $\delta^{13}C$ and $\delta^{18}O$ values of -4.30‰ (σ = 0.78) and -3.63‰ (σ = 0.46), respectively (Table 7.6). There is little to no correlation between the $\delta^{13}C$ and $\delta^{18}O$ values from these samples (Figure 7.2.9).

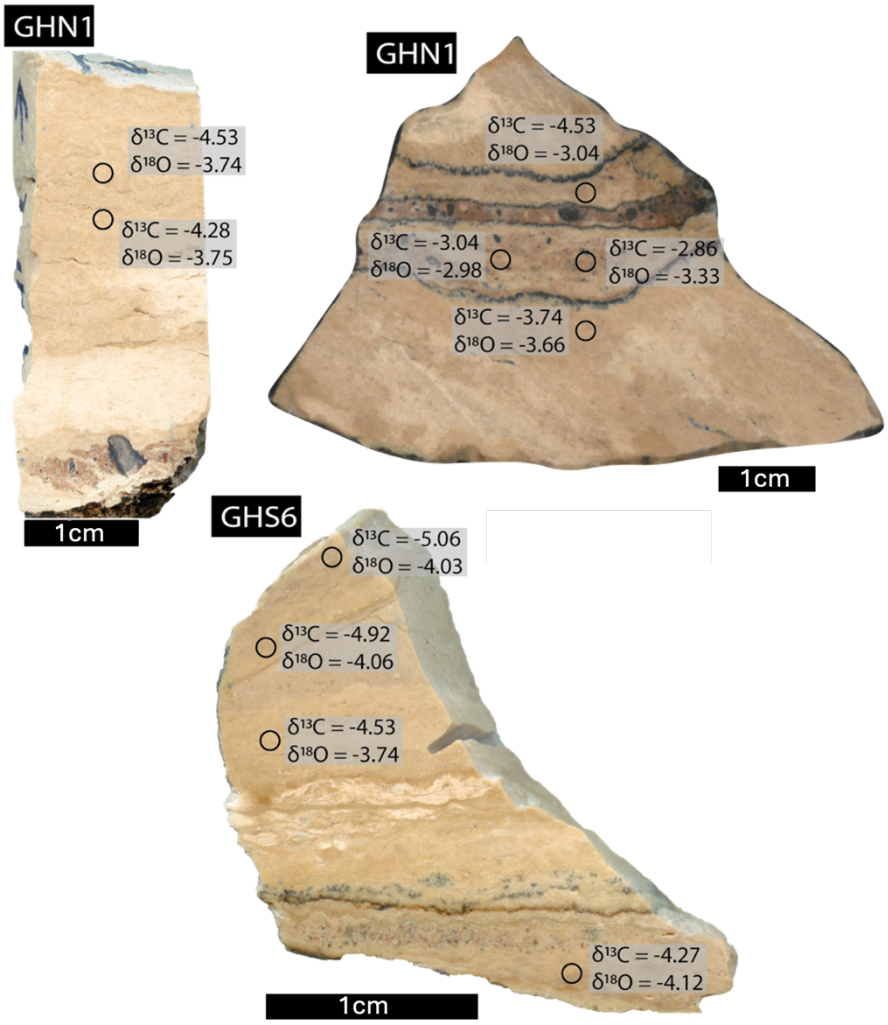

Figure 7.2.8 The $\delta^{18}O_{PDB}$ and $\delta^{13}C_{PDB}$ values for material drilled from the positions indicated with a circle for rim pool samples GHN1 and GHS6.

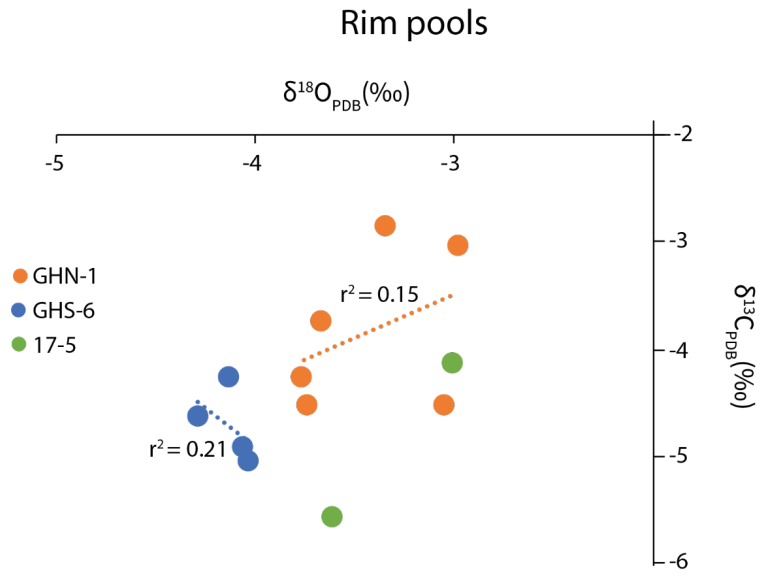

Figure 7.2.9 Bivariant plot of $\delta^{18}O_{PDB}$ and $\delta^{13}C_{PDB}$ measured in rim pool samples. The dotted lines and associated r^2 values indicate the correlation between sub-samples from individual samples with more than two sub-samples.

Terrace breccias

Four terrace breccia samples were subsampled (n=10), two of which are shown in Figure 7.2.10. The majority of data for the terrace samples are from sample 17-8 (n = 6, Figure 7.2.10). The range in $\delta^{13}C$ values is 5.82‰ (min = -7.29‰, max = -1.47‰) and the range in $\delta^{18}O$ values is 1.23‰ (min = -4.41‰, max = -3.18‰), with mean $\delta^{13}C$ and $\delta^{18}O$ values of -5.03‰ (σ = 1.56) and -4.02‰ (σ = 0.41), respectively (Table 7.6). Sample 17-8 is the only terrace breccia sample with enough data points to assess correlation, and in this case there is no relationship between the $\delta^{13}C$ and $\delta^{18}O$ values (n = 6, r^2 = 0.03; Figure 7.2.11).

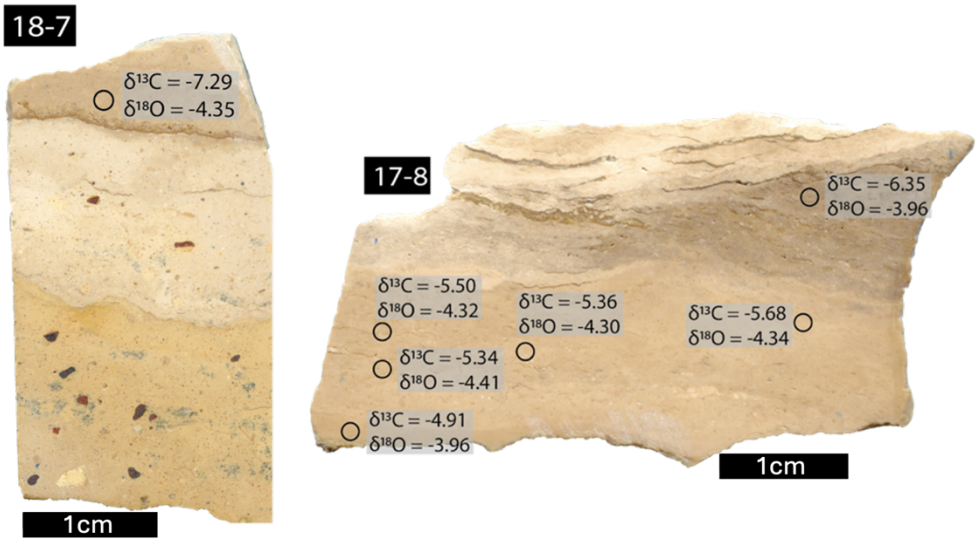

Figure 7.2.10 The $\delta^{18}O_{PDB}$ and $\delta^{13}C_{PDB}$ values for material drilled at the positions indicated with a circle for terrace breccia samples 18-7 and 17-8.

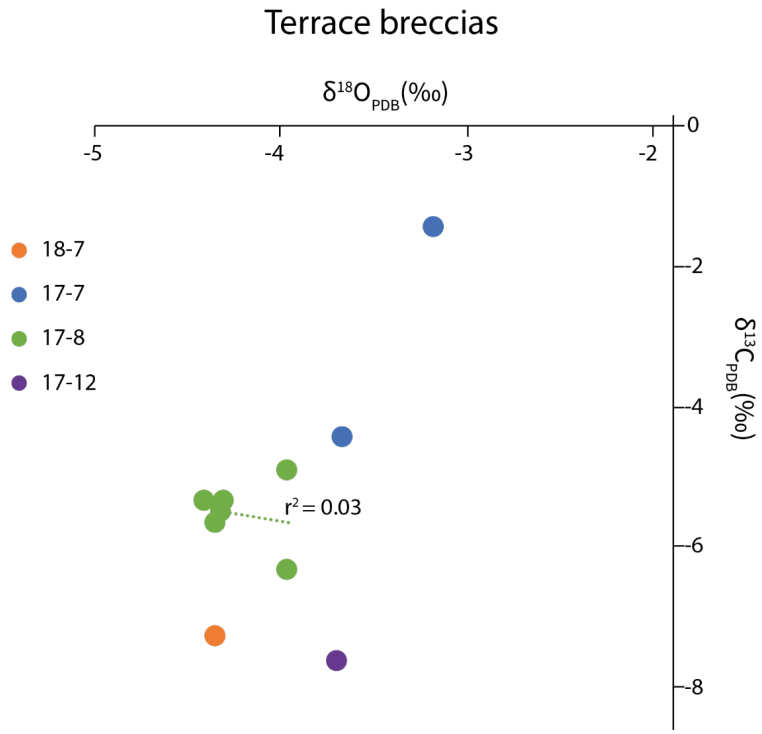

Figure 7.2.11 Bivariant plot of $\delta^{18}O_{PDB}$ and $\delta^{13}C_{PDB}$ values measured in terrace breccia samples. The dotted line and associated r^2 value indicate the correlation between sub-samples from sample 17-8 (n>2).

Domes

Fifteen sub-samples (n=15), including 3 repeats, were drilled from five dome samples. The location of sub-samples from sample 18-10 is shown in Figure 7.2.12. The dome samples have the second largest spread in isotope values (Figure 7.2.2). The range in $\delta^{13}C$ values is 9.46‰ (min = -5.91‰, max = +3.55‰) and the range in $\delta^{18}O$ values is 4.97‰ (min = -5.89‰, max = -0.92‰), with mean $\delta^{13}C$ and $\delta^{18}O$ values of -0.61‰ (σ = 3.74) and -3.25‰ (σ = 1.68) respectively (Table 7.6). There is a moderate to strong positive correlation between the $\delta^{18}O$ and $\delta^{13}C$ values three of the dome samples with n = 3: sample 17-13 (r^2 = 0.45), sample 17-9 (r^2 = 0.90), sample 18-10 (r^2 = 0.99) (Figure 7.2.13).

Figure 7.2.12 The $\delta^{13}C_{PDB}$ and $\delta^{18}O_{PDB}$ values of material drilled at the indicated position from dome sample 18-10.

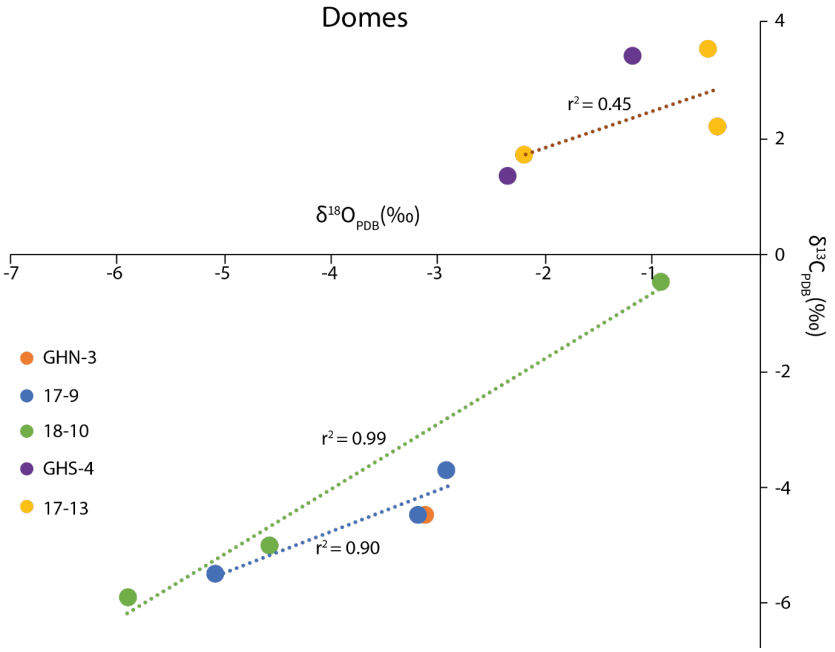

Figure 7.2.13 Bivariant plot of $\delta^{18}O_{PDB}$ and $\delta^{13}C_{PDB}$ values measured in terrace breccia samples. Dotted lines and r^2 values indicate the correlation between sub-samples from individual samples with more than two sub-samples.

7.3 Implications of oxygen and carbon isotope data

In sections 7.3.1 and 7.3.2, I discuss the results for the water and tufa isotope data respectively. Finally, in section 7.3.3, I use the oxygen isotope data from the modern water samples and the tufas to model the likely temperature and oxygen isotope value of the waters during tufa formation.

7.3.1 Water isotopes

There is limited rainfall data available for the Northern Cape province. Rainwater samples collected during this study (n=4) during brief downpours in January 2018 form a small sample set. The δD and $\delta^{18}O$ values are very high and plot well below the GMWL, which suggests a high degree of evaporation (Figure 7.3.1). This is to be expected considering the nature of the rain events sampled (~10-15-minute afternoon thunderstorm in late summer). Given the short duration of the rain events sampled, the δD and $\delta^{18}O$ values of the rainwater collected in this study are likely also affected by the amount effect, i.e., a small amount of precipitation results in high δD and $\delta^{18}O$ values (Dansgaard, 1964). It is likely that the high summer temperatures on the days of sampling (~32°C), coupled with evaporation, also contributed to the high $\delta^{18}O$ values of the rainwater. In light of these factors, the rainwater isotope data collected in this study cannot be considered representative of the δD and $\delta^{18}O$ value of rainfall in the area, but it does provide a useful end member composition for the effects of kinetic fractionation on hydrogen and oxygen stable isotopes in the region.

Pretoria is the nearest area to Kuruman with a long-term record of rainfall data (IAEA/WMO, 2015). The climate is characterised by a mean annual temperature of 18.4°C and 671mm of average annual rainfall (IAEA, 1981). In comparison, Kuruman experiences a mean annual temperature of ~18°C and ~450mm of average annual rainfall. Data from Pretoria and several other rainfall monitoring stations in southern Africa - Windhoek, Cape Town and Harare, is plotted in Figure 7.3.1 for comparison to water data collected in this study. Rainfall with compositions most similar to the high positive water samples collected in this study come from Windhoek, an arid region that

experiences a mean annual temperature of 18.5°C and 534mm of average annual rainfall (Bean, 2003). The groundwater samples collected in this study from the area near Ga-Mohana Hill have much lower δD and $\delta^{18}O$ values than the rainwater samples, and the drip water isotope data have an intermediate composition between the groundwater samples and the rainwater samples (Figure 7.3.1).

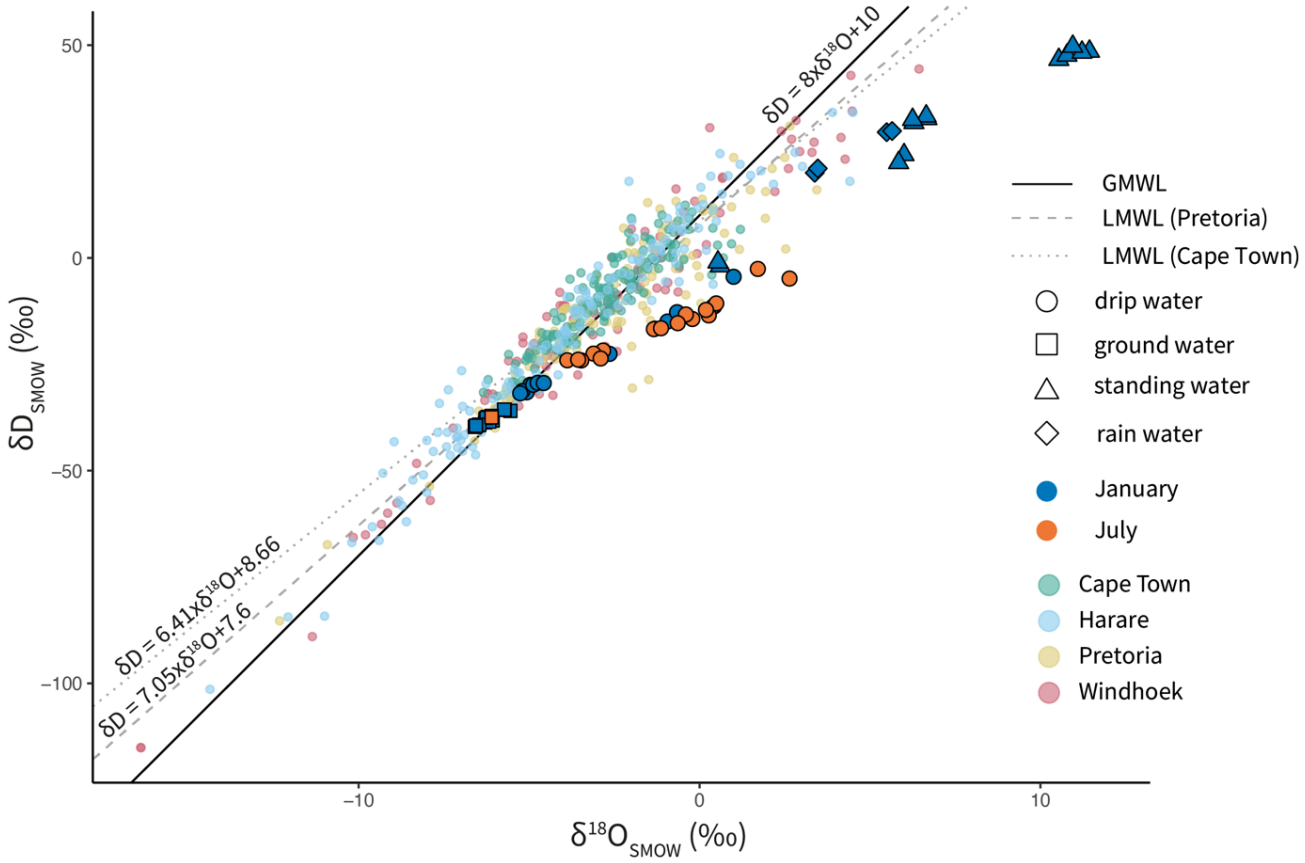

Figure 7.3.1 Isotope data for water samples collected at and around Ga-Mohana Hill plotted with isotope data from rainfall collected at IAEA stations in southern Africa. The Global Meteoric Water Line (GMWL) (Craig, 1961) and two local meteoric water lines from Pretoria and Cape Town (IAEA/WMO, 2015) are plotted for reference.

The ground and drip waters collected in this study are presented without the rain water data in Figure 7.3.2 for better resolution. Isotope data from groundwaters collected by Xiao et al. (2019) from several springs along the Ghaap Plateau, and tap water collected from various places in the Northern Cape that can be used as a proxy for groundwater (de Wet et al., 2020), are included in this plot for comparison. The groundwater data

from this study plot in a tight cluster close to (on or slightly above) the GMWL, irrespective of the month collected (Figure 7.3.2). Most of the Ghaap Plateau spring water samples have similar isotopic compositions, except for three samples which have more positive δD and $\delta^{18}O$ values and an evaporative signature. The Ga-Mohana drip waters and the NC tap water samples have a similarly wide range of δD and $\delta^{18}O$ values that are more positive than the ground and spring water samples, and track below the GMWL, which suggests that they have been affected by evaporation. This evaporative signature may be inherited from rainwaters that were affected by evaporation during precipitation, or it may be due to evaporation that occurred prior to and/or during infiltration of the water through the soil zone (Gat, 1996). In the case of the tap waters, the variation is consistent with evaporation that likely occurred in the tap water reservoir (de Wet et al., 2020).

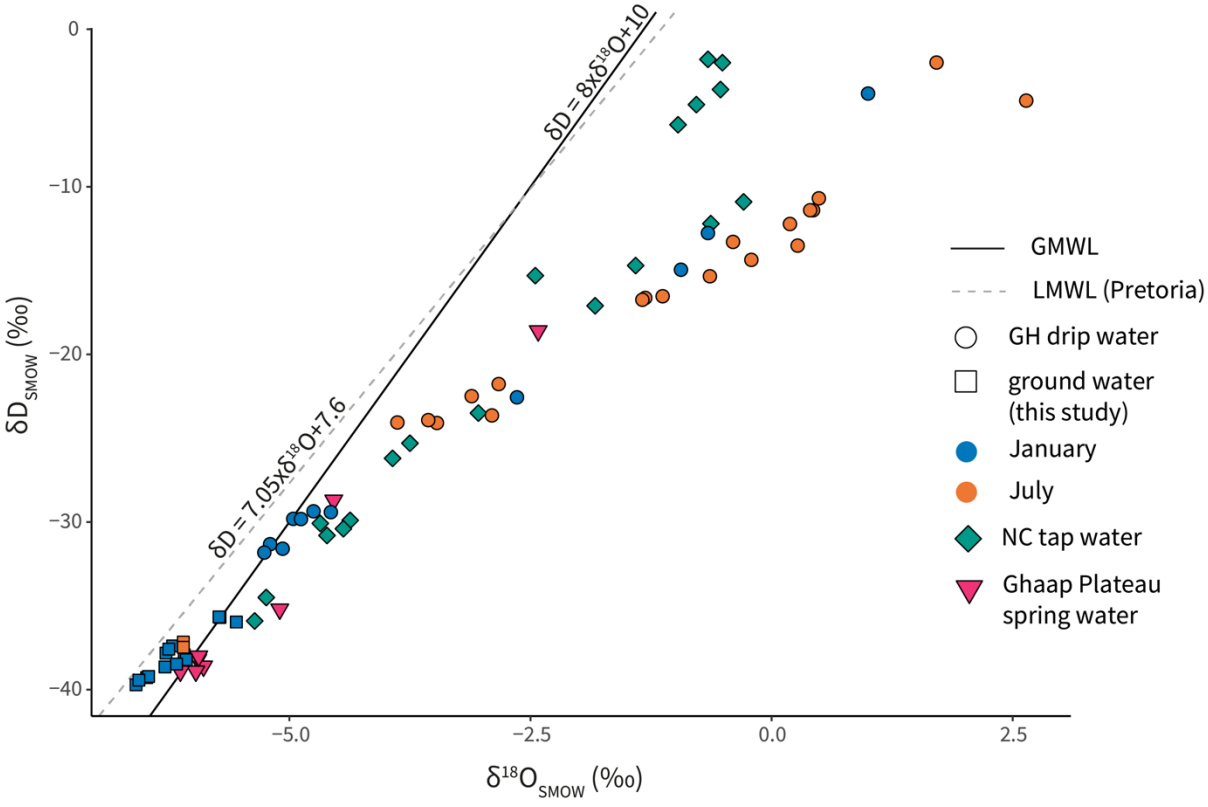

Figure 7.3.2 Isotope data from ground and drip waters collected at and around Ga-Mohana Hill plotted with isotope data measured in tap water collected from multiple locations in the Northern Cape (de Wet et al., 2020) and ground water collected from springs on the Ghaap Plateau (Xiao et al., 2019). The Global Meteoric Water Line (GMWL) (Craig, 1961), and the LMWL from Pretoria are plotted for reference.

7.3.2 Tufa isotopes

Tufa $\delta^{18}O$ values are expected to reflect the ambient temperature and $\delta^{18}O$ value of the waters from which they formed, plus/minus additional effects such as evaporation (Andrews, 2006). Tufa $\delta^{13}C$ values reflect the $\delta^{13}C$ value of the groundwater DIC, which in turn reflects the isotopic composition of the predominant source of C and the prevalent vegetation, plus/minus additional effects such as atmospheric equilibration and photosynthesis (Andrews, 2006). In the following sub-sections, I explore the various processes and factors that may have contributed to the range of isotope values and patterns observed in the Ga-Mohana tufa data with respect to equilibrium fractionation, the various tufa morphologies (identified in Chapter 4), and the ages of the tufa samples (from Chapter 6).

7.3.2.1 Equilibrium vs kinetic fractionation

In order to make quantitative interpretations from the O and C isotope data, e.g. palaeotemperature determinations using $\delta^{18}O$ values, or estimation of the relative sources of carbon input into the tufa system using $\delta^{13}C$ values, it is necessary to establish first whether the tufa precipitated in isotopic equilibrium with the tufa-forming water. It is known that tufa-precipitating systems are commonly affected by kinetic fractionation effects, particularly in semi-arid environments (Pazdur et al., 1988a; Andrews et al., 1997; Smith et al., 2004). Disequilibrium conditions are likely to occur close to the point of groundwater discharge, whereas further downstream the system re-equilibrates with surface conditions and disequilibrium effects are reduced (Usdowski et al., 1979; Andrews et al., 1993; Turi, 1986). Whether the oxygen and carbon isotope values in a carbonate deposit have been affected by kinetic fractionation can be established by testing for correlation between them. If there is no / low correlation, it is likely that calcite precipitation occurred at a sufficiently slow rate for equilibrium to be maintained, whereas kinetic fractionation effects will produce a strong correlation between the oxygen and carbon isotope values (Hendy, 1971). However, patterns attributed to kinetic fractionation do not necessarily mean that tufa $\delta^{18}O$ or $\delta^{13}C$ values are unreliable as palaeoenvironmental or palaeoclimatic indicators, and there are instances in which correlation between $\delta^{18}O$ and $\delta^{13}C$ values occur other than as a result

of kinetically-driven precipitation. For example, correlated $\delta^{18}O$ and $\delta^{13}C$ values may reflect a downstream trend, i.e. as the tufa-forming water flows away from the point of resurgence, simultaneous evaporation and CO_2 degassing of the tufa-forming water would raise the $\delta^{18}O$ and $\delta^{13}C$ values of the water, respectively, and lead to precipitation of calcite in equilibrium with the tufa-forming water. In such an instance, however, evaporation of the tufa-forming water makes it difficult to calculate temperature from the $\delta^{18}O$ value subsequently recorded in the tufa deposit. Nevertheless, useful interpretations can be made from tufa $\delta^{18}O$ and $\delta^{13}C$ values, regardless of the presence of kinetic effects.

Overall, there is a positive correlation between the $\delta^{18}O$ and $\delta^{13}C$ values measured in the Ga-Mohana tufas as a whole ($r^2 = 0.72$, $n = 74$), but the strength of this correlation varies between individual samples, with some samples having almost perfect correlation ($r^2 = 1$) and others showing no relationship between the $\delta^{18}O$ and $\delta^{13}C$ values ($r^2 = 0$). The ability to test for correlations within samples is limited by the number of sub-samples collected from an individual sample, i.e. it is only meaningful to assess for correlations in samples that have more than two data points. Of the twelve cascade samples, only six meet this criteria, and of these six samples, four have moderate to strong correlations between their $\delta^{18}O$ and $\delta^{13}C$ values ($r^2 = > 0.5$) and two have little to no correlation ($r^2 = < 0.1$) (Figure 7.2.5). The $\delta^{18}O$ and $\delta^{13}C$ values in the barrage and rim pool samples are weakly correlated ($r^2 = < 0.3$) (Figures 7.2.7 and 7.2.9), and the $\delta^{18}O$ and $\delta^{13}C$ values in the terrace breccia sample are not correlated ($r^2 = 0.03$) (Figure 7.2.11). All three dome samples are positively correlated ($r^2 = > 0.5$) (Figure 7.2.13). This suggests that for the barrages, rim pools, terrace breccias, and some cascade samples, calcite precipitation occurred not far from isotopic equilibrium, whereas kinetic fractionation likely dominated the precipitation of the dome tufas and some cascade samples. The sample sizes used to evaluate correlations between the $\delta^{18}O$ and $\delta^{13}C$ values in individual samples are small ($n < 4$) and this is a limitation in this study. Nevertheless, disequilibrium processes, such as evaporation and rapid degassing, evidently played a variable role in the precipitation of the Ga-Mohana tufas, depending on the sub-

environment of tufa formation and conditions at the time. This is taken into account in the ensuing discussion.

7.3.2.2 Isotope variation for each morphology and implications for formation processes

Here, I discuss the possible processes responsible for the variations in $\delta^{18}O$ and $\delta^{13}C$ values for each of the tufa morphologies in conjunction with field and petrographic observations described in Chapter 4.

Cascades

The cascade tufas are the biggest sample group and also have the widest range of isotope values compared to the other morphologies (Figure 7.2.2). They are the dominant tufa morphology on the hillside, found along the terraces above and below the shelter, as well as along the cliff faces adjacent to the shelters, forming the largest tufa deposits relative to the other Ga-Mohana tufa morphologies. Cascades are directly linked to emergent groundwaters (Chapter 4) and their $\delta^{18}O$ values are thus expected to most closely resemble the $\delta^{18}O$ value of groundwater, modified by local effects such as surface temperature, flow rate and presence of organisms. These tufas are also dated to three of the five tufa stages (Chapter 6), so variation in their $\delta^{18}O$ values may be expected to represent hydroclimate and temperature shifts over time. However, the range of isotope values associated with each of the cascade samples suggests variable conditions and processes affected individual cascade tufa formation (Figure 7.2.5), and this is reflected in the variety of meso- and micro-morphologies identified from samples in this morphology (Chapter 4). It is likely that localised conditions and processes played a role in the isotope values recorded in each of the cascade samples. For example, the ambient temperature, flow rate and type of organisms present varies depending on the season, and these factors influence the resultant isotope composition of calcite (Matsuoka et al., 2001; Arenas and Jones, 2017).

Barrages

The barrage tufas are characterised by a wide range in $\delta^{18}O$ values (~-5‰ to -1‰), and a relatively narrow range of $\delta^{13}C$ values (> -2‰, < +1‰; Figure 7.2.2). Considering that

these data are mostly from one sample, this range in $\delta^{18}O$ values suggests large shifts in the $\delta^{18}O$ value of the tufa-forming water, and this variation is most likely to have been driven by changes in temperature, and possibly evaporation effects prior to tufa formation (if there had been evaporation-driven tufa formation, the $\delta^{18}O$ and $\delta^{13}C$ values should be correlated).

The barrages formed on steps below pools of water that ponded on flat sections of the hillslope, and were fed from spill-over waters from these pools (Chapter 4). Prior to forming the barrages, the water in the pools would have been exposed to solar insolation which may have increased the temperature of the water, and likely also caused some evaporation, resulting in an increase of the $\delta^{18}O$ value of the water. This effect is evident in the high $\delta^{18}O$ values of the modern standing water collected in pools on the Ga-Mohana hillslope (Figure 7.3.1). Spill-over flow from the pools would have created a thin film of water on the pool fronts, during which loss of CO_2 would have facilitated precipitation of calcite, forming barrage tufa. The variable temperature and evaporation that influenced the pooled waters is likely to have generated the variation in the $\delta^{18}O$ value of the barrages.

The relatively high $\delta^{13}C$ values (-1.83‰ to +0.6‰) indicate that either the $\delta^{13}C$ value of the tufa-forming water was quite high to begin with, for example as a result of a high proportion of bedrock carbon input and/or a predominance of C_4 vegetation, or that micro-environmental processes altered the DIC of the water after resurgence on the landscape, but before tufa precipitation. For example, photosynthetic activity or equilibration with atmospheric CO_2 preferentially extracts ^{12}C, leading to an increase in the $\delta^{13}C$ of the carbon species in the tufa-forming water. The barrage sites would have been conducive to microbial organism growth, which would have served as a substrate for calcite precipitation. This micro-environment may have generated an increase in the $\delta^{13}C$ value of the tufa-forming water by preferentially extracting ^{12}C from the DIC component of the water (Arp et al., 2010). This effect is most pronounced in instances of slow flow rate and warm temperatures (Chafetz et al., 1991; Spiro and Pentecost, 1991).

It is most likely that physico-chemical degassing of CO_2 from the tufa forming waters drove the high $\delta^{13}C$ values in the resultant barrage tufa.

Rim pools

The rim pool tufas have the smallest spread in isotope values ($\delta^{18}O$ = -4.3‰ to -2.98‰; $\delta^{13}C$ = -5.6‰ to -2.86‰) (Figure 7.2.2). These tufas represent shallow bodies of standing water that may have been prone to warming from solar insolation and evaporation. Warmer temperatures would have decreased the calcite-water fractionation factor and lead to a decrease in the $\delta^{18}O$ value of the tufa (Equation 7.3). On the other hand, evaporation of these waters would drive an increase in the $\delta^{18}O$ value.

Terrace breccias

The terrace breccias have a relatively small spread in $\delta^{18}O$ values ($\delta^{18}O$ = -4.4‰ to -3.18‰), whereas the $\delta^{13}C$ values are more variable ($\delta^{13}C$ = -7.3‰ to -1.47‰) (Figure 7.2.2). Terrace breccia deposits are found on the slopes above and below the Ga-Mohana shelters. They are interpreted to have formed from relatively high-energy waters that flowed down the hillside, transporting weathered material down-slope and cementing it on flat sections (Chapter 4). It is therefore likely that these tufa-forming waters travelled some distance from their point of emergence before precipitating, allowing time for warming of the waters and equilibration with atmospheric CO_2. These processes would drive increases in both $\delta^{18}O$ and $\delta^{13}C$ values, relative to the initial isotope values of the groundwater. Turbulence along the flow path is likely to have encouraged CO_2 degassing, which would have facilitated calcite precipitation, and some evaporation may also have occurred.

Domes

The dome tufa isotope values form two distinct groups: samples GHN3.2, 18-10, and 17-9 have negative $\delta^{18}O$ and $\delta^{13}C$ values ($\delta^{18}O$ = -5.9‰ to -2.1‰ and $\delta^{13}C$ = -5.9‰ to -3.7‰), whereas samples GHS-4 and 17-13 have low negative $\delta^{18}O$ values and positive $\delta^{13}C$ values ($\delta^{18}O$ = -2.4‰ to -0.05‰ and $\delta^{13}C$ = +1.3‰ to +3.6‰) (Figure 7.2.2). The dome tufas formed from waters dripping from the shelter overhang above them, channelled via the

vegetation curtains draped along the shelter ledges (now observed as tufa 'noses' protruding from the overhang, as described in Chapter 4). This drip and splash process can be described as turbulent, as water tumbling over the overhang would encounter rapid degassing. The physical process of dripping and splashing of waters results in kinetic fractionation of the isotopes (Hendy, 1971), and this is supported by moderate to strong correlations between the $\delta^{18}O$ and $\delta^{13}C$ values within individual dome samples (Figure 7.2.13). Only one dome sample was successfully dated, sample 18-10.3, with an age of 3.0 ± 0.9 ka (Chapter 6). It is thus unclear whether the distinct isotope values are a result of changing conditions over time. The difference may be related to microbial activity and photosynthetic influences on the DIC of the tufa-forming water, which would result in an increase in $\delta^{13}C$ values. It is evident that vegetation and microbial organisms played a role in the formation of dome deposits (Chapter 4), and more detailed microscopic investigations of the layers associated with isotope data are needed to determine the various biota and their impact on the isotope values, e.g. Arenas et al. (2019).

7.3.2.3 Temporal variations in isotope composition

Of the 74 tufa sub-samples with carbon and oxygen isotope data, 32 of them have an associated U-Th age, listed in Table 7.7. The $\delta^{18}O$ and $\delta^{13}C$ values associated with dated tufa samples are plotted against age in Figures 7.3.4 and 7.3.5, respectively, to assess whether there are any temporal patterns in the isotope data. I use these figures to explore the isotope data in the context of the associated ages. It must be noted that time is one aspect that can affect the variability of the isotope values in tufas. In reality, there are multiple, inter-related factors that drive variability in oxygen and carbon isotopes in tufa, e.g. distance of tufa precipitation from the point of resurgence and flow rate.

Tufa $\delta^{18}O$ vs age

At first glance, the $\delta^{18}O$ values appear to be relatively consistent over time (Figure 7.3.4). However, there does appear to be an increase in the $\delta^{18}O$ values with decreasing age, particularly if the $\delta^{18}O$ values from samples at the end of each tufa stage are compared with one another (Figure 7.3.4). This may have resulted from an increase in the $\delta^{18}O$

values of ambient rainfall, or a decrease in ambient temperature, and hence an increase in the O-isotope fractionation factor over time (Table 7.1).

Table 7.7 $\delta^{13}C$ and $\delta^{18}O$ values for tufa sub-samples with an associated U-Th age. The U-Th ages and their associated 2σ errors are given in thousands of years (ka).

Sample	Group	Morphology	$\delta^{13}C_{PDB}$ (‰)	$\delta^{18}O_{PDB}$ (‰)	Age ± 2σ (ka)
18-16-SI-1	2	cascade	*-4.77*	*-3.94*	*110.6 ± 3.0*
18-16-SI-2	2	cascade	*-5.22*	*-4.20*	*105.9 ± 2.2*
18-17-SI-3	2	cascade	*-4.67*	*-5.48*	*103.3 ± 1.1*
18-17-SI-1	2	cascade	*-4.36*	*-3.44*	*102.9 ± 3.2*
18-17-SI-2	2	cascade	*-4.44*	*-5.22*	*102.1 ± 2.1*
18-15-SI-3	1	cascade	*-8.71*	*-4.75*	*72.3 ± 0.5*
18-15-SI-2	1	cascade	*-8.16*	*-4.85*	*71.3 ± 0.9*
18-15-SI-1	1	cascade	*-7.63*	*-4.47*	*68.5 ± 0.6*
18-14-SI-4	2	cascade	*-5.55*	*-2.79*	*70.6 ± 1.7*
18-14-SI-3	1	cascade	*-7.08*	*-3.59*	*69.4 ± 0.7*
18-14-SI-1	1	cascade	*-7.91*	*-4.19*	*68.4 ± 0.7*
18-14-SI-2	1	cascade	*-8.18*	*-3.95*	*64.3 ± 1.6*
18-13-SI-4	1	cascade	*-8.83*	*-4.69*	*69.8 ± 0.7*
18-13-SI-3	1	cascade	*-8.59*	*-5.00*	*67.2 ± 0.4*
18-13-SI-2	1	cascade	*-7.53*	*-4.36*	*65.0 ± 0.8*
18-13-SI-1	1	cascade	*-6.84*	*-3.99*	*58.6 ± 1.0*
18-7	1	terrace breccia	*-7.29*	*-4.35*	53.5 ± 1.3
GHS6.1	2	rim pool	-5.06	-4.03	60.4 ± 1.8
GHS6.2	2	rim pool	-4.27	-4.12	59.7 ± 1.5
GHS6-SI-1	2	rim pool	*-4.92*	*-4.06*	61.9 ± 0.5
GHS6-S1-3	2	rim pool	*-4.65*	*-4.29*	*53.1 ± 4.2*
17-8.1	2	terrace breccia	-5.68	-4.34	48.3 ± 0.7
17-8-SI-4	2	terrace breccia	*-5.50*	*-4.32*	*43.2 ± 0.3*
17-8-SI-3	2	terrace breccia	*-5.36*	*-4.30*	*41.8 ± 0.2*
17-8-SI-5	2	terrace breccia	*-5.34*	*-4.41*	*41.6 ± 0.3*
17-8.2	2	terrace breccia	-6.35	-3.96	34.4 ± 0.2
17-8-SI-6	2	terrace breccia	*-4.91*	*-3.96*	*32.5 ± 0.4*
GHN1.1	2	rim pool	-3.74	-3.66	39.1 ± 0.4
GHN1-SI-2	2	rim pool	*-4.28*	*-3.75*	*36.6 ± 0.4*
GHN1-SI-3	2	rim pool	*-4.53*	*-3.74*	*37.0 ± 0.4*
GHS 5.1	2	cascade	-4.40	-4.22	10.7 ± 4.9
GHN 2.1	2	cascade	-4.92	-3.33	7.3 ± 0.3
18-10-SI-3	2	dome	*-0.48*	*-0.92*	3.0±09

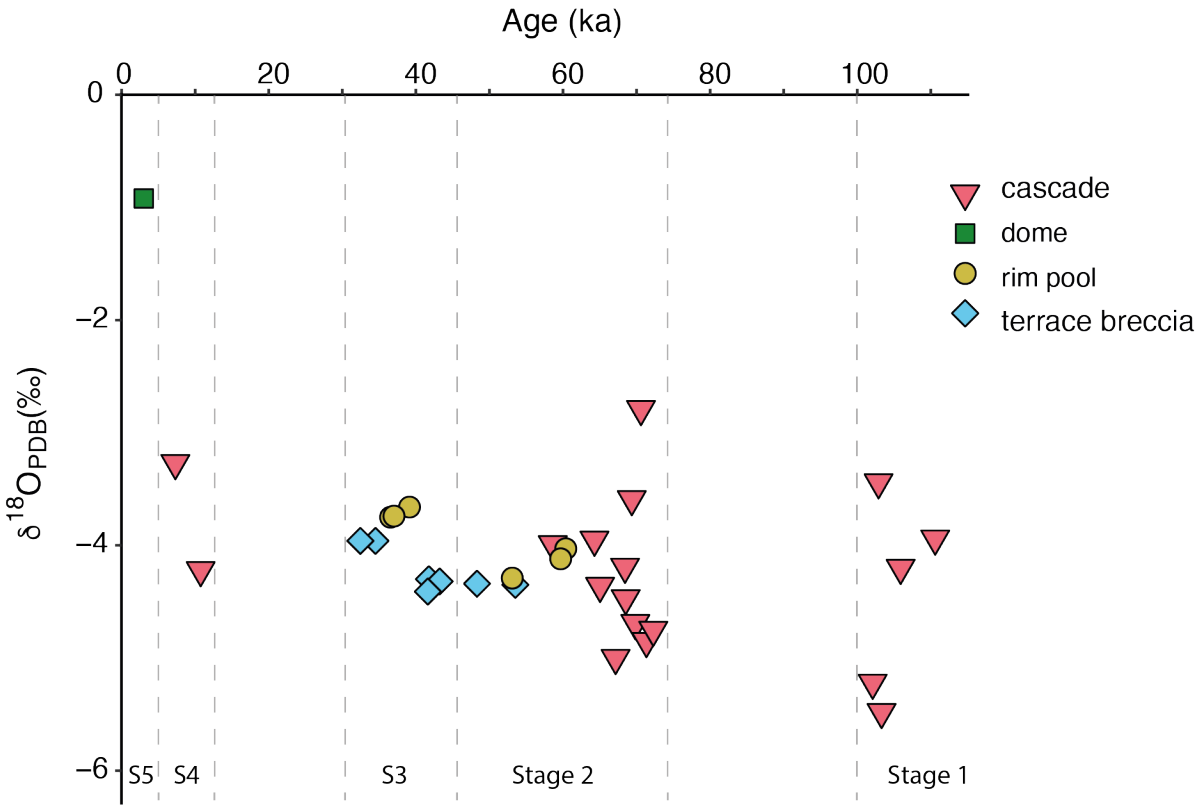

Figure 7.3.4 Plot of dated tufa $\delta^{18}O_{PDB}$ against the age of each tufa sample in thousands of years. Samples are colour-coded according to their respective macrofacies, and dotted lines separate the tufa formation stage (described in Chapter 6).

There is also some variation between the $\delta^{18}O$ values within each tufa stage, predominantly among samples within the cascade morphology (Figure 7.3.4). Since the equilibrium water-calcite fractionation factor is temperature dependent (Urey, 1951; Epstein, et al., 1951), and a 1°C change in temperature results in a 0.24‰ change in the resultant calcite $\delta^{18}O$ value (Craig, 1965; Hays and Grossman, 1991), these variations may indicate variable temperature changes within each stage of tufa formation.

The $\delta^{18}O$ values for the cascade samples in the first stage of tufa formation (samples 18-16 and 18-17) appear to decrease from moderate $\delta^{18}O$ values (~ -4‰) between ~110-105 ka, to lower $\delta^{18}O$ values (~ -5.2‰) between ~104-100 ka (Table 7.7). This decrease in tufa $\delta^{18}O$ may have been driven by an increase in the temperature of the tufa-forming water which results in a smaller fractionation factor, assuming the $\delta^{18}O$ value of the rainwater remained constant. Alternatively, a decrease in the $\delta^{18}O$ value of the tufa may indicate

that the $\delta^{18}O$ value of the tufa-forming water was lower during the second phase of tufa formation, perhaps caused by a higher rainfall amount, and / or decrease in temperature. Sample 18-17-1 is an outlier during this period, with a relatively higher $\delta^{18}O$ value of -3.4‰, perhaps due to variable temperatures (e.g. seasonal) or strong evaporation effects. However, the resolution of the ages is too coarse to verify this.

In tufa formation stage 2, there is an overall increase in the cascade $\delta^{18}O$ values from ~ -4.8‰ at ~72 ka to ~ -4‰ at ~58 ka, with variations within this time frame, i.e., three sub-samples, 18-13-3, 18-14-3 and 18-14-4, don't follow this general trend. Sub-sample 18-13-3, dated to ~67 ka, has the lowest $\delta^{18}O$ value within the tufas from this stage (-5‰), and the two latter samples, dated to ~70 ka, have the highest $\delta^{18}O$ values in this tufa formation stage (-3.6‰ and -2.8‰ respectively; Figure 7.3.4). This may indicate short term (possibly millennial scale) temperature variations, with an overarching increase in temperature over a period of ~14 ka. The oldest rim pool and terrace breccia tufas occur from ~61 ka. Their $\delta^{18}O$ values are similar to the $\delta^{18}O$ values from cascade samples of the same age, and thereafter the rim pool and terrace breccia $\delta^{18}O$ values decrease slightly, from ~ -4‰ to -4.3‰, possibly indicating an increase in temperature towards the end of this stage. They remain relatively consistent during the rest of tufa stage 2 and into the early part of stage 3 (~55-40 ka).

During the late stage 3 (~40-32 ka), the rim pool and terrace breccia $\delta^{18}O$ values increase slightly, from ~ -4.3‰ to between ~ -4‰ and -3.7‰, indicating lower temperatures, and / or higher $\delta^{18}O$ values of the tufa-forming water, at the end of tufa stage 3 (Figure 7.3.4). There is a marked rise in $\delta^{18}O$ values over the last two stages of tufa formation, represented by two cascade samples dated to 10.7 ± 4.9 ka and 7.3 ± 0.3 ka (stage 4), and one dome sample dated to 3.0 ± 0.9 ka (stage 5). The large difference of ~ 3.5‰ between the $\delta^{18}O$ values from each of these samples (-4.4‰, -3.3‰ and -0.9‰, respectively), indicates a large change in temperature (~14.5°C) over ~11 ka, assuming equilibrium precipitation. Since the youngest tufa sample is from a dome tufa which precipitated under disequilibrium conditions, this temperature change is likely an over-estimation.

Overall, the temporal variations in the tufa $\delta^{18}O$ values described indicate variable local temperature and evaporation effects, but may also reflect regional temperature changes over time. This is explored in the final discussion (Chapter 8). The overall increase in $\delta^{18}O$ values from ~100 ka to ~3 ka may indicate a change in the $\delta^{18}O$ value of the tufa-forming water over time, possibly due to a decrease in rainfall amount and an increase in atmospheric temperature over time. Warmer atmospheric temperatures do not only impact the temperature of tufa formation and lead to higher rates of evaporation, driving an increase in the tufa $\delta^{18}O$ values, but also affect vegetation growth and type, and soil productivity, which in turn impacts the $\delta^{13}C$ values of the tufa.

Tufa $\delta^{13}C$ vs age

Variations temperature affect vegetation growth and type (C3 vs C4), and soil productivity, which in turn impacts the $\delta^{13}C$ values of the tufa. There appears to be an increase in $\delta^{13}C$ values with decreasing age, from ~72 ka to ~30 ka, with the lowest $\delta^{13}C$ values represented in the second-oldest group of tufas during formation stage 2. The highest $\delta^{13}C$ value is associated with the youngest tufa in stage 5 (~8‰ difference, Figure 7.3.5), although this tufa formation stage is only represented by one dated tufa sample. The $\delta^{13}C$ values from the two oldest cascades in the first stage of tufa formation (~114-100 ka) do not follow this trend, and instead have $\delta^{13}C$ values that are most similar to the rim pool tufas in stages 2 and 3, and the cascade tufas in stage 4 (Figure 7.3.5).

In comparison to the stage 1 tufa $\delta^{13}C$ values, most of the samples in tufa formation stage 2 (~72-48 ka) have low $\delta^{13}C$ values, between -8.83‰ and -6.84‰ (n = 11/16 samples, Figure 7.3.5). These $\delta^{13}C$ values indicate ^{12}C input from the soil with a mixed C3/C4 vegetation cover, whereas the samples in tufa formation stage 1 have $\delta^{13}C$ values that reflect input from a source with more ^{13}C, i.e. dolomitic bedrock (-0.03‰; Table 7.5) and / or a higher proportion of C4 vegetation. The ~2‰ difference between stage 1 and the stage 2 cascade tufa $\delta^{13}C$ values may suggest a shift to conditions that favour C3 vegetation growth, which would lead to lower soil $\delta^{13}C$ values (Cerling et al., 1991). This shift is likely to have been driven by higher rainfall amounts, and / or lower temperatures, which may have increased soil productivity and groundwater recharge

and flow, thereby decreasing the residence time of groundwater and minimising the input of carbon from the dolomitic bedrock (Table 7.2).

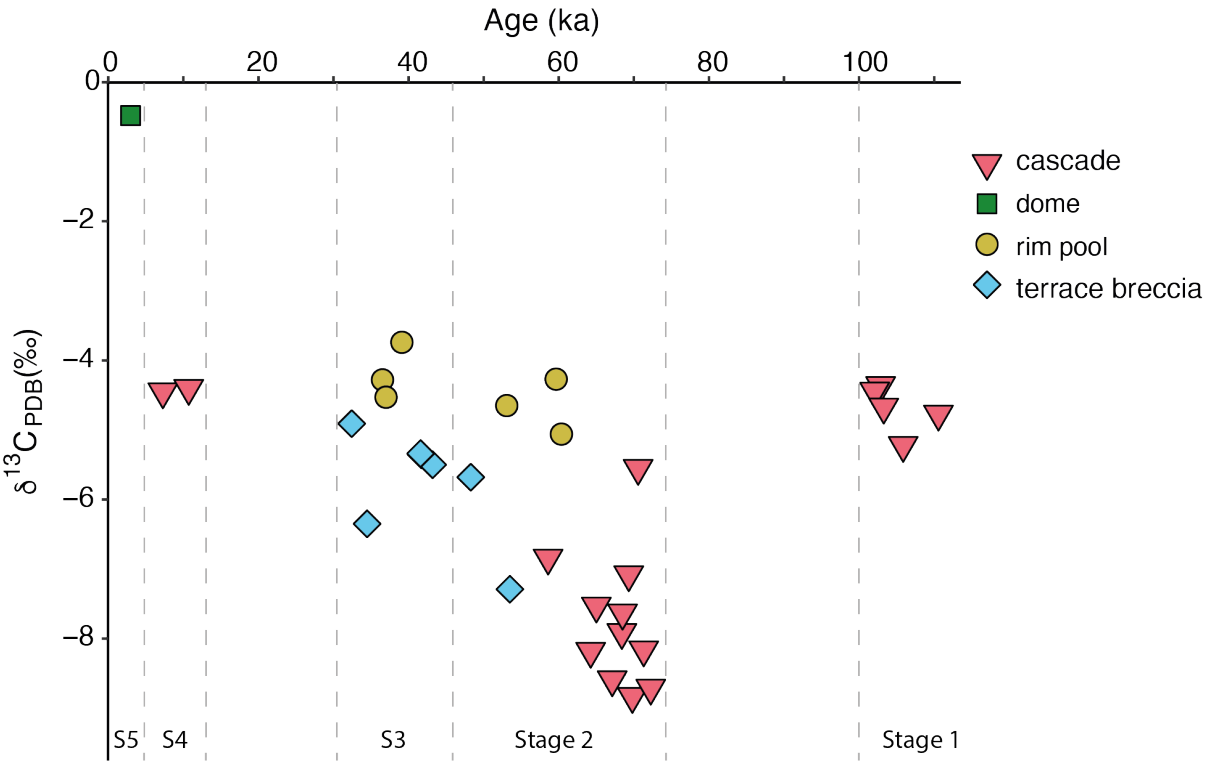

Figure 7.3.5 Plot of dated tufa $\delta^{13}C_{PDB}$ against the age of each tufa sample in thousands of years. Samples are colour-coded according to their respective macrofacies.

The five samples in stage 2 with $\delta^{13}C$ values > 6.5‰ are cascade sub-sample 18-14-4, terrace breccia sub-sample 17-8.1, and rim pool sample GHS-6 (n = 3). Cascade sample 18-14-4 also has an anomalously high $\delta^{18}O$ value relative to the other cascade samples with a similar age, and this may indicate that this sample was affected by kinetic processes during precipitation, resulting in high $\delta^{18}O$ and $\delta^{13}C$ values relative to the rest of the sample. Terrace breccia sample 17-8.1 is the youngest of the tufas in this stage (48.31 ± 0.68 ka), so its relatively high $\delta^{13}C$ value fits with the trend of increasing $\delta^{13}C$ with decreasing age. The sub-samples from the GHS-6 rim pool tufa are dated to between ~61 to 53 ka and their associated $\delta^{13}C$ values are consistently higher than the cascade and terrace breccia tufas of similar age (Figure 7.3.5). In this instance, the relatively higher $\delta^{13}C$ values in this sample may be a function of their greater distance from the point of resurgence compared to the cascade samples, which would have

allowed more time for degassing and equilibration of CO_2 in the fluid with atmospheric CO_2, driving an increase in the $\delta^{13}C$ value of the resultant tufa precipitate. The higher $\delta^{13}C$ values in these samples may also reflect the impact of metabolic processes on the $\delta^{13}C$ value of the DIC in the water, which would result in an increase in the $\delta^{13}C$ value of the tufa (Table 7.2).

Stage 3 tufa formation (~44-32 ka) comprises terrace breccia sample 17-8 (n = 5) and rim pool sample GHN-1 (n = 3). Together, the $\delta^{13}C$ values of these samples appear to continue the trend of increasing $\delta^{13}C$ with decreasing age, except for 2 anomalous sub-samples, GHN1.1 (rim) and 17-8.2 (terrace). These samples have extreme high (-3.74‰) and low (-6.35‰) $\delta^{13}C$ values respectively, relative to the other sub-samples in this tufa stage (Figure 7.3.5). The rim pool samples do generally have higher $\delta^{13}C$ values relative to the terrace breccia tufas, despite similar ages, and this may be related to micro-environmental factors during their formation, as described above for sample GHS-6.

Following a hiatus in tufa deposition between ~32 ka and ~15 ka, the $\delta^{13}C$ values associated with the two cascade samples in tufa stage 4 (~15-7 ka, sample GHS-5 and GHN-2) are similar to the $\delta^{13}C$ values in samples dated to the end of tufa stage 3 (~-4.5‰; Figure 7.3.5). This suggests a similar mix of soil-zone and bedrock CO_2 input, and / or a similar C3/C4 vegetation ratio at the end of tufa stage 3 and at the start of tufa stage 2. The $\delta^{13}C$ value for the dome tufa in the final stage of tufa formation (stage 5) is much higher than all the previous values ($\delta^{13}C$ = -0.48‰; Figure 7.3.5). Since both $\delta^{13}C$ and $\delta^{18}O$ values in this final stage tufa are high, it is possible that the formation of this tufa was driven predominantly by disequilibrium effects. It is also the only dome tufa with a resolvable age (3 ± 0.91 ka).

The pattern of increasing $\delta^{13}C$ values with decreasing age, from ~72 ka suggests a decrease in the input of isotopically light soil CO_2 and / or higher input of isotopically heavier sources, e.g., increased dissolution of host dolomite with high $\delta^{13}C$ (-0.03‰) and expansion of C4 vegetation over time. This may have been driven by warmer temperatures and reduced humidity, which would have impacted soil productivity and

prolonged water residence time in the aquifer, resulting in higher $\delta^{13}C$ values in the groundwater. Altogether, this shift to higher tufa $\delta^{13}C$ values over time suggests a gradual increase in temperatures and / or decrease in humidity from ~72 ka to present.

7.3.2.4 Comparison with other tufa deposits

In Figure 7.3.3, Ga-Mohana Hill tufa $\delta^{18}O$ and $\delta^{13}C$ values are plotted, along with isotope data for carbonate deposits from a selection of other local and regional sites for comparison. The Ga-Mohana tufa isotope values can be grouped into four distinct clusters, and these are highlighted by the shaded circles in Figure 7.3.3. The first group (green) consists of 11 sub-samples characterised by tufa with the lowest $\delta^{13}C$ values (< -6.5‰) and moderate $\delta^{18}O$ values (> -5‰ and < -3.5‰). All of the samples in this group are associated with a U-Th age, and most of these fall within tufa formation stage 2 (~73-48 ka). The second group (yellow) consists of the majority of tufa samples, and these are characterised by moderate $\delta^{13}C$ values (> -6.5‰, < -2.5‰), and a wider range of $\delta^{18}O$ values (> -6.2‰ and < -1.5‰). Almost all of the remaining samples with a U-Th age fall within this group, and comprise samples from each of the tufa formation stages. The third group (orange) encompasses 8 sub-samples with relatively high $\delta^{13}C$ values (> -2.5‰, < +1‰) and a wide range of $\delta^{18}O$ values (> -6‰ and < -1‰). Most of these come from barrage samples. The only sample in this group that returned a reliable age is dome sample 18-10.3, the youngest of the tufa dated in this study with an age of 3.0 ± 0.9 ka. Lastly, the fourth group (pink) consists of 10 sub-samples with the highest $\delta^{13}C$ values (> +1‰, < +4‰) and relatively high $\delta^{18}O$ values (> -2‰ and < 0‰). The tufas in this group are mostly dome samples, with two sub-samples from cascade sample 18-12. Interestingly, none of the samples in groups 3 and 4, except dome sample 18-10.3, returned a reliable U-Th age result. However, of the samples within these groups that were sampled for U-Th dating, one from isotope group 3, sample 17-6, and two from isotope group 4, GHS-4 and 18-12, have estimated upper age limits of <23.6 ka (17-6.1), <9.5 ka (17-6.2), <25.8 ka (GHS-4.2), and <10.2 ka (18-12.2), respectively (Table 6.2). This suggests that the tufa samples in isotope groups 3 and 4 formed after ~26 ka.

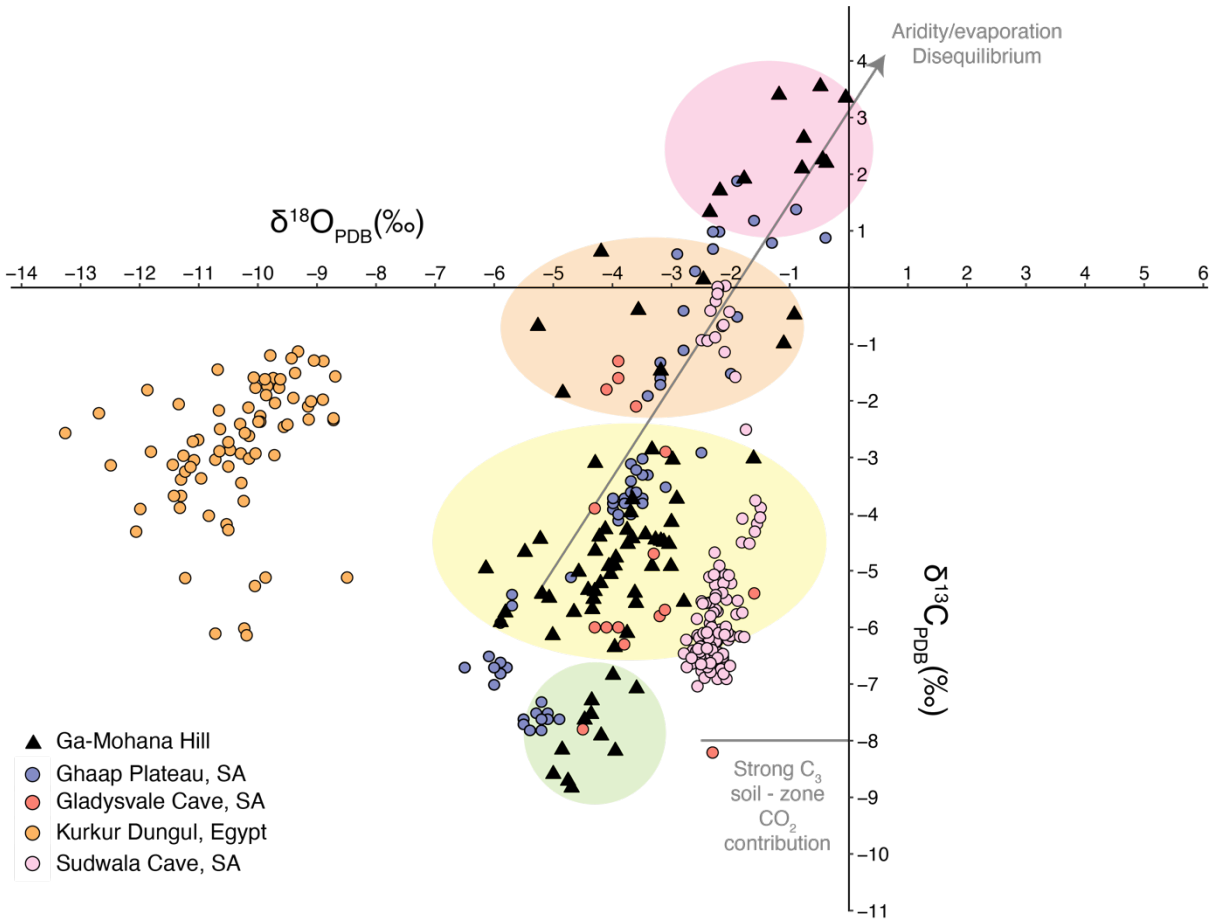

Figure 7.3.3 Bivariant plot of $\delta^{18}O$ and $\delta^{13}C$ values from Ga-Mohana Hill (this study) and tufa data from other semi-arid sites for comparison: the Ghaap Plateau, South Africa (Doran et al., 2015) and Kurkur-Dungal, Egypt (Kele et al., 2021). Speleothem $\delta^{18}O$ and $\delta^{13}C$ data from South African sites in the Summer Rainfall Zone, Gladysvale Cave (Pickering et al., 2007) and Sudwala Cave (Green et al., 2015), are also included for comparison. Aridity / evaporation arrow and demarcation of strong C3 / soil-zone CO2 contribution is after Andrews (2006). The shaded circles highlight four groups of Ga-Mohana tufa isotope data that represent distinct conditions of formation discussed in the text: group 1 = green, group 2 = yellow, group 3 = orange, group 4 = pink.

The Ga-Mohana tufa $\delta^{18}O$ and $\delta^{13}C$ values are similar to the range in values from the nearby Ghaap Plateau tufas (Doran et al., 2015; Figure 7.3.3). This makes sense given the proximity of these sites (Figure 2.10); both sites likely experienced comparable shifts in temperature and vegetation type, and would also have had similar rainfall and groundwater $\delta^{18}O$ values. Although the lowest isotope values of the Ghaap Plateau tufas

are older (Pliocene and Mid-Pleistocene) than the Ga-Mohana tufas (Late Pleistocene), there is some overlap in the timing of tufa formation, and the tufas from both sites show an aridity / evaporation trend, i.e., a trend towards higher $\delta^{18}O$ and $\delta^{13}C$ values over time (Figure 7.3.3).

The range in $\delta^{18}O$ values of the Ga-Mohana tufa encompass the $\delta^{18}O$ values from the Late Pleistocene flowstone and speleothem deposits from Gladysvale Cave (~ -5‰) (Pickering et al., 2007) and Sudwala Cave (~ -2.8 to -1.5‰) (Green et al., 2015) (Figure 7.3.3). Although these cave sites are ~500 and 850 km from Ga-Mohana Hill respectively, they fall within the Summer Rainfall Zone and likely experienced a similar regional hydroclimate. The relatively narrower range in the $\delta^{18}O$ values of the speleothem deposits reflects the more stable temperatures in a cave environment, and unlike the tufas, the speleothem isotope values do not follow the aridity / evaporation trend as speleothems are less prone to the effects of evaporation. The range in Ga-Mohana tufa $\delta^{13}C$ values is comparable to the Gladysvale and Sudwala Cave speleothem $\delta^{13}C$ values, although only the Ga-Mohana and Ghaap plateau tufas extend to positive $\delta^{13}C$ values (Figure 7.3.3). Again, this is likely due to the prevalence of disequilibrium processes involved in tufa formation compared to speleothem growth. At Gladysvale Cave, the flowstone $\delta^{13}C$ values are interpreted as reflecting persistent C4 vegetations, combined with variable proportions (between 40-75%) of C3 vegetation (Pickering et al., 2007).

Tufa isotope data from the semi-arid Kurkur-Dungal region in southern Egypt is included for comparison (Kele et al., 2021) (Figure 7.3.3). These tufa were U-Th dated and indicate tufa formation and spring activity between MIS 11 to MIS 1. The $\delta^{18}O$ values of the Kurkur-Dungul tufa are distinctly lower than the Ga-Mohana $\delta^{18}O$ values, and this distinction represents the different processes that affect rainfall, and hence groundwater, in the respective regions. The range in $\delta^{13}C$ values of the Kurkur-Dungal tufa (~ -6‰ to -1‰) are comparable to the Ga-Mohana $\delta^{13}C$ values (Figure 7.3.3). Kele et al. (2021) interpret the lower end of this range to indicate humid conditions with CO_2 input from soil-zone and mixed C3–C4 type vegetation. They conclude that altogether these data indicate that semi-arid conditions in this region prevailed during tufa

formation, despite episodes of spring activity and the associated increase in water availability.

In summary, tufas from Ga-Mohana with $\delta^{13}C$ values < -6‰, i.e. isotope group 1 tufa, likely formed from fluids with a DIC content inherited from soil-zone derived CO_2 and/or a higher proportion of C3 vegetation (Figure 7.3.3), whereas modern and fossil tufas from temperate European settings tend to have mean $\delta^{13}C$ values < -6‰, reflecting the predominance of C3 vegetation and well-developed soil profiles (Figure 7.1.10) (Usdowski et al., 1979; Chafetz et al., 1991; Andrews et al., 2000; Horvatinčić et al., 2003; Andrews, 2006; Brasier et al., 2010; Dabkowski et al., 2015). The less negative tufa $\delta^{13}C$ values (> -6‰, i.e. isotope groups 2 and 3) likely represent a higher proportion of C4 vegetation, reduced input of soil-zone C, possibly linked to thinner and less-productive soils, and a greater input of bedrock-derived C linked to longer groundwater residence times (Figure 7.3.3). These conditions occur as a result of reduced moisture availability, either through lower amounts of rainfall, or higher temperatures which increase the effect of evaporation and impede groundwater recharge. Ga-Mohana tufa samples with relatively high $\delta^{18}O$ values, > -2‰, coupled with high $\delta^{13}C$ values, i.e., group 4 tufa, are interpreted to indicate disequilibrium precipitation as a result of kinetic effects (Figure 7.3.3).

7.3.3 Oxygen isotope temperature modelling

The $\delta^{18}O$ values of the rainfall and groundwaters that formed the Ga-Mohana tufas is unknown, as are the temperatures of the water and atmosphere at the time of tufa formation. Thus, substituting these values to calculate the temperature of calcite formation using the calcite-water fractionation equation does not lead to reliable temperature estimates. However, the range of temperature and water $\delta^{18}O$ values during tufa formation can be estimated using the measured $\delta^{18}O$ values from the tufa samples and the palaeotemperature equation (Craig, 1965; O'Neil et al., 1969; Equation 7.3). The reliability of a temperature estimate depends on whether calcite precipitation occurred under equilibrium conditions, and even then, it is not straight-forward because of the varied influences that affect $\delta^{18}O$ (Lachniet, 2009). With these caveats in mind, I use the

equations below to calculate 1) the range of temperatures required to produce the measured range in calcite $\delta^{18}O$ values, assuming a fixed $\delta^{18}O$ value of the water, and 2) the range in water $\delta^{18}O$ values required to explain the range in calcite $\delta^{18}O$ at a fixed temperature.

1)

$$T°C = \left(\left.(2.78 \times 10^6)\right/ +(1000 \times ln\alpha + 2.89)\right)^{0.5} - 273$$

where

$$\alpha = (1000 + \delta^{18}O_{calcite})/(1000 + \delta^{18}O_{water})$$

2)

$$\delta^{18}O_{water} = \left(\left.(1000 + \delta^{18}O_{calcite})\right/_{\alpha}\right) - 1000$$

where

$$\alpha = e^{\frac{\left.2.78\times10^6\right/_{T°C^2} - 2.89}{1000}}$$

The average $\delta^{18}O$ value of the modern groundwaters near Ga-Mohana Hill is ~-6‰, and this value is used as a proxy for the present-day mean annual rainfall $\delta^{18}O$ value. The average drip water $\delta^{18}O$ value is ~-2‰. Drip waters are enriched in $\delta^{18}O$ relative to the groundwaters. This may be due to the fact that the drip waters represent waters that were initially pooled on the surface and exposed to evaporation, or they may reflect the most recent rainfall events, whereas the groundwater values represent a mean value for multiple rainfall events. Temperatures for tufa formation are calculated using $\delta^{18}O_{water}$ values that cover the range of average drip and ground waters (-2 to -7‰; Table 7.7).

Three fixed temperatures of 12°C, 18°C and 25°C are used to calculate the $\delta^{18}O$ values of the waters required to produce the range of $\delta^{18}O$ values measured in the tufas (Table 7.8). These temperatures were chosen based on the present-day mean annual temperature of 18°C for Kuruman, which is also the temperature measured in spring waters on the Ghaap Plateau (Xiao et al., 2019). A lower limit of 12°C was chosen based on the fact that temperatures during the LGM are suggested to have been ~5°C lower

than present day (Kulongoski et al., 2004 and references therein), and a realistic upper limit temperature of 25°C was chosen.

The range of $\delta^{18}O_{SMOW}$ values measured in the tufas is 24.5‰ to 30.8‰. Tufa samples with $\delta^{18}O_{SMOW}$ values >28‰ (highlighted in yellow in Tables 7.7 and 7.8) are interpreted to have formed under disequilibrium conditions, and as such, are likely to produce calculated temperatures or $\delta^{18}O_{SMOW}$ water values that do not accurately reflect the conditions during precipitation. They are thus not included in the possible temperature and $\delta^{18}O_{water}$ estimates reported here.

7.3.3.1 Temperature estimates

Five different $\delta^{18}O$ values that range between average drip water and average groundwater $\delta^{18}O$ measured at Ga-Mohana Hill (-2‰ to -7‰) were used to calculate the possible range in temperatures that might have produced the $\delta^{18}O$ values measured in the tufa samples (Table 7.7). The calculated range in temperatures required to form tufa from $\delta^{18}O_{water}$ values of 1) -2‰, T = 11.4°C to 35.9°C (average ~26°C); 2) -3‰, T = 7.4°C to 30.8°C (average ~21°C); 3) -4‰, T = 3.5°C to 25.8°C (average of ~16°C); 4) -5‰, T = -0.3°C to 21.1°C (average of ~12°C); 5) -6‰, T = -3.9°C to 16.6°C (average of ~6°C); 6) -7‰, T = -7.3°C to 12.3°C (average of ~4°C).

A range of realistic formation temperatures between 10°C to 25°C are highlighted in Table 7.7. These temperatures occur mostly for waters with values of -3‰ (82%), -4‰ (95%) and -5‰ (74%). It is therefore likely that the waters precipitating the Ga-Mohana tufas had $\delta^{18}O$ values within this range (-5‰ to -3‰), assuming formation temperatures between 10°C to 25°C and isotopic equilibrium conditions.

Table 7.7 Predicted temperature* of tufa formation based on fixed water $\delta^{18}O$ values (-2‰; -3‰; -4‰; -5‰; -6‰ and -7‰).

Sample	Type	Age (ka)	$\delta^{18}O_{tufa}$ (‰)	T °C (-2‰)	T °C (-3‰)	T °C (-4‰)	T °C (-5‰)	T °C (-6‰)	T °C (-7‰)
GHN 2.1	cascade	-	27.42	22.0	17.5	13.1	9.0	5.0	1.2
GHN 2.2	cascade	7.30	27.49	21.7	17.2	12.9	8.7	4.8	1.0
GHN 2.3	cascade	-	27.75	20.5	16.1	11.8	7.7	3.8	0.0
17-10.1	cascade	-	26.07	28.3	23.5	18.9	14.5	10.3	6.3
17-10.2	cascade	-	26.99	23.9	19.3	14.9	10.7	6.7	2.8
17-10.3	cascade	-	27.13	23.3	18.7	14.4	10.2	6.1	2.3
17-11.1	cascade	-	25.69	30.1	25.2	20.5	16.1	11.8	7.7
17-11.2	cascade	-	25.51	31.0	26.0	21.3	16.8	12.5	8.4
17-11.3	cascade	-	24.87	34.2	29.1	24.2	19.6	15.2	10.9
18-12-SI-1	cascade	-	29.04	15.0	10.8	6.8	2.9	-0.8	-4.4
18-12-SI-2	cascade	-	30.04	10.9	6.9	3.0	-0.7	-4.3	-7.8
18-13-SI-1	cascade	58.61	26.75	25.1	20.4	15.9	11.7	7.6	3.7
18-13-SI-2	cascade	65.04	26.37	26.9	22.1	17.6	13.3	9.1	5.1
18-13-SI-3	cascade	67.15	25.71	30.0	25.1	20.5	16.0	11.7	7.6
18-13-SI-4	cascade	69.83	26.02	28.5	23.7	19.1	14.7	10.5	6.4
18-14-SI-1	cascade	68.43	26.54	26.1	21.3	16.9	12.6	8.4	4.5
18-14-SI-2	cascade	64.28	26.79	24.9	20.2	15.8	11.5	7.5	3.5
18-14-SI-3	cascade	69.35	27.16	23.2	18.6	14.2	10.1	6.0	2.2
18-14-SI-4	cascade	70.60	27.98	19.5	15.1	10.9	6.8	3.0	-0.8
18-15-SI-1	cascade	68.52	26.25	27.4	22.6	18.1	13.7	9.6	5.6
18-15-SI-2	cascade	71.34	25.86	29.3	24.4	19.8	15.4	11.1	7.1
18-15-SI-3	cascade	72.28	25.97	28.8	23.9	19.3	14.9	10.7	6.6
18-16-SI-1	cascade	110.60	26.80	24.8	20.2	15.7	11.5	7.4	3.5
18-16-SI-2	cascade	105.90	26.53	26.1	21.4	16.9	12.6	8.5	4.5
18-17-SI-1	cascade	102.90	27.32	22.5	17.9	13.6	9.4	5.4	1.6
18-17-SI-2	cascade	102.10	25.48	31.2	26.2	21.5	17.0	12.7	8.5
18-17-SI-3	cascade	103.31	25.21	32.5	27.5	22.7	18.1	13.8	9.6
17-21.1	cascade	-	26.43	26.5	21.8	17.3	13.0	8.8	4.9
GHS 5.1	cascade	10.75	26.51	26.2	21.5	17.0	12.7	8.5	4.6
GHS 5.2	cascade	-	29.20	14.3	10.2	6.1	2.3	-1.4	-5.0
18-4-SI-1	cascade	-	24.53	35.9	30.8	25.8	21.1	16.6	12.3
18-6-SI-1	barrage	-	29.73	12.2	8.1	4.1	0.4	-3.2	-6.7
18-7-SI-1	breccia	53.52	26.38	26.8	22.1	17.5	13.2	9.1	5.1
GHN 1.1	pool	39.13	27.08	23.5	18.9	14.6	10.4	6.3	2.5
GHN 1.2	pool	-	27.42	22.0	17.5	13.1	9.0	5.0	1.2
GHN 1.3	pool	-	27.79	20.4	15.9	11.6	7.6	3.7	-0.1
GHN 1.4	pool	-	27.73	20.6	16.2	11.9	7.8	3.9	0.1

GHN1-SI-2	pool	36.55	26.99	24.0	19.3	14.9	10.7	6.7	2.8
GHN1-SI-3	pool	37.02	27.01	23.9	19.3	14.9	10.6	6.6	2.7
17-5.1	pool	-	27.15	23.2	18.6	14.3	10.1	6.1	2.2
17-5.2	pool	-	27.77	20.4	16.0	11.7	7.7	3.7	0.0
17-6.1	barrage	-	29.44	13.3	9.2	5.2	1.4	-2.2	-5.8
17-6.2	barrage	-	26.54	26.0	21.3	16.8	12.5	8.4	4.5
17-6.3	barrage	-	25.88	29.2	24.4	19.7	15.3	11.1	7.0
17-6.4	barrage	-	27.19	23.0	18.5	14.1	9.9	5.9	2.1
17-6.5	barrage	-	25.43	31.4	26.4	21.7	17.2	12.8	8.7
17-6-SI-1	barrage	-	28.32	18.0	13.7	9.5	5.5	1.7	-2.0
17-7.1	breccia	-	27.58	21.3	16.8	12.5	8.4	4.4	0.6
17-7.2	breccia	-	27.09	23.5	18.9	14.5	10.3	6.3	2.5
17-8.1	breccia	48.31	26.38	26.8	22.0	17.5	13.2	9.0	5.1
17-8.2	breccia	34.50	26.77	25.0	20.3	15.8	11.6	7.5	3.6
17-8-SI-3	breccia	41.76	26.43	26.6	21.8	17.3	13.0	8.9	4.9
17-8-SI-4	breccia	43.23	26.41	26.7	21.9	17.4	13.1	8.9	5.0
17-8-SI-5	breccia	41.62	26.32	27.1	22.3	17.8	13.5	9.3	5.3
17-8-SI-6	breccia	32.45	26.78	24.9	20.3	15.8	11.6	7.5	3.6
17-12.1	pool	-	27.06	23.6	19.0	14.7	10.4	6.4	2.5
GHS6.1	pool	60.38	26.71	25.3	20.6	16.1	11.9	7.8	3.8
GHS6.2	pool	59.68	26.61	25.7	21.0	16.5	12.2	8.1	4.2
GHS6-SI-1	pool	61.90	26.67	25.4	20.7	16.3	12.0	7.9	4.0
GHS6-S1-3	pool	53.10	26.44	26.5	21.8	17.3	12.9	8.8	4.8
GHN 3.2.1	dome	-	27.64	21.0	16.6	12.3	8.2	4.2	0.5
17-9.1	dome	-	27.86	20.1	15.6	11.4	7.3	3.4	-0.3
17-9.2	dome	-	25.63	30.4	25.5	20.8	16.3	12.0	7.9
17-9.3	dome	-	27.58	21.3	16.8	12.5	8.4	4.4	0.7
18-10-SI-1	dome	-	24.78	34.6	29.5	24.6	20.0	15.5	11.3
18-10-SI-2	dome	-	26.15	27.9	23.1	18.5	14.1	10.0	5.9
18-10-SI-3	dome	3.00	29.91	11.4	7.4	3.5	-0.3	-3.9	-7.3
GHS 4.1	dome	-	29.64	12.5	8.4	4.5	0.7	-2.9	-6.4
GHS 4.2	dome	-	28.44	17.5	13.2	9.1	5.1	1.3	-2.4
17-13.1	dome	-	28.61	16.8	12.5	8.4	4.5	0.7	-3.0
17-13.2	dome	-	30.46	9.2	5.3	1.5	-2.2	-5.7	-9.1
17-13.3	dome	-	30.37	9.6	5.6	1.8	-1.9	-5.4	-8.8
17-13.4	dome	-	30.07	10.8	6.7	2.9	-0.8	-4.4	-7.9
17-13.5	dome	-	30.41	9.4	5.5	1.7	-2.0	-5.5	-8.9
17-13.6	dome	-	30.81	7.9	4.0	0.2	-3.4	-6.9	-10.2

* Tufas are assumed to have formed in equilibrium with the water. Realistic temperatures between 10 to 25°C are highlighted in green, less realistic temperatures (<10 and >25°C) are highlighted in orange. Tufa $\delta^{18}O$ values are given relative to SMOW, and $\delta^{18}O_{tufa}$ with values > 28‰ are highlighted in yellow.

7.3.3.2 Water $\delta^{18}O$ estimates

Three fixed temperatures of 12°C, 18°C and 25°C were selected to explore the possible range in water $\delta^{18}O$ values that might have produced the $\delta^{18}O$ values measured in the tufas (under equilibrium conditions). The $\delta^{18}O$ values for 1) T = 12°C are between -7.08‰ and -3.73‰ (average = -5.06‰); 2) T = 18°C are between -5.69‰ and -2.34‰ (average = -3.67‰); 3) T = 25°C are between -4.17‰ and -0.82‰ (average = -2.15‰). Assuming tufas formed from waters with $\delta^{18}O$ values equivalent to the present-day groundwater $\delta^{18}O$ value (-6‰ ± 1‰), then the water temperature must have been on the lower end, around 12°C, to produce the measured tufa $\delta^{18}O$ values (Table 7.8). Conversely, if tufas formed from waters with $\delta^{18}O$ values similar to the present-day drip water values (-2‰ ± 1‰), then the temperature of formation will have been higher, i.e., around 18°C to 25°C (Table 7.8).

The average $\delta^{18}O$ values for each of the temperature options are slightly higher than the range in measured $\delta^{18}O$ values for groundwater (-6.6‰ to -5.5‰) and overlap with the lower range of present-day drip waters measured at Ga-Mohana Hill (-5.3‰ to +2.6‰). The samples that fall outside of this range (<-5 and >-2) are those with high $\delta^{18}O$ values in the tufa, unlikely to have precipitated under equilibrium conditions.

Based on the temperature and water $\delta^{18}O$ estimates presented above, it is likely that the Ga-Mohana tufas precipitated from waters with a $\delta^{18}O$ range of -5‰ to -3‰. This calculated range is 1.5‰ to 2.5‰ higher than the range of measured ground water values (-6.5‰ to -5.5‰), and similar to the lower end of the measured drip water $\delta^{18}O$ values (-5.4‰ to ~-2‰; Table 7.4). The temperature range of tufa-formation is less clear as $\delta^{18}O_{water}$ values within the likely range determined above (-5‰ to -3‰) are estimated across the fixed tufa-forming water temperatures of 12°C, 18°C and 25°C, with some exceptions. The highest proportion of data that falls within the -5‰ to -3‰ range is for the fixed temperature of 18°C, which is the present-day temperature of groundwater in the region.

Table 7.8 Predicted $\delta^{18}O$ values for tufa forming waters*, based on $\delta^{18}O$ of tufa samples and a fixed temperature (T = 12°C, T = 18°C and T = 25°C).

Sample	Type	Age (ka)	$\delta^{18}O_{tufa}$ (‰)	$\delta^{18}O_{water}$ (‰) (12°C)	$\delta^{18}O_{water}$ (‰) (18°C)	$\delta^{18}O_{water}$ (‰) (25°C)
GHN 2.1	cascade	-	27.42	-4.27	-2.88	-1.36
GHN 2.2	cascade	7.30	27.49	-4.20	-2.81	-1.29
GHN 2.3	cascade	-	27.75	-3.95	-2.56	-1.04
17-10.1	cascade	-	26.07	-5.59	-4.20	-2.68
17-10.2	cascade	-	26.99	-4.69	-3.30	-1.78
17-10.3	cascade	-	27.13	-4.56	-3.16	-1.64
17-11.1	cascade	-	25.69	-5.95	-4.56	-3.04
17-11.2	cascade	-	25.51	-6.12	-4.73	-3.22
17-11.3	cascade	-	24.87	-6.74	-5.35	-3.84
18-12-SI-1	cascade	-	29.04	-2.71	-1.31	0.21
18-12-SI-2	cascade	-	30.04	-1.73	-0.34	1.19
18-13-SI-1	cascade	58.61	26.75	-4.92	-3.53	-2.01
18-13-SI-2	cascade	65.04	26.37	-5.30	-3.91	-2.39
18-13-SI-3	cascade	67.15	25.71	-5.94	-4.55	-3.03
18-13-SI-4	cascade	69.83	26.02	-5.63	-4.24	-2.72
18-14-SI-1	cascade	68.43	26.54	-5.13	-3.74	-2.22
18-14-SI-2	cascade	64.28	26.79	-4.89	-3.50	-1.98
18-14-SI-3	cascade	69.35	27.16	-4.53	-3.14	-1.62
18-14-SI-4	cascade	70.60	27.98	-3.73	-2.34	-0.82
18-15-SI-1	cascade	68.52	26.25	-5.41	-4.02	-2.50
18-15-SI-2	cascade	71.34	25.86	-5.79	-4.40	-2.88
18-15-SI-3	cascade	72.28	25.97	-5.69	-4.30	-2.78
18-16-SI-1	cascade	110.60	26.80	-4.88	-3.49	-1.97
18-16-SI-2	cascade	105.90	26.53	-5.14	-3.75	-2.23
18-17-SI-1	cascade	102.90	27.32	-4.37	-2.98	-1.46
18-17-SI-2	cascade	102.10	25.48	-6.16	-4.77	-3.25
18-17-SI-3	cascade	103.31	25.21	-6.42	-5.03	-3.51
17-21.1	cascade	-	26.43	-5.23	-3.84	-2.32
GHS 5.1	cascade	10.75	26.51	-5.16	-3.77	-2.25
GHS 5.2	cascade	-	29.20	-2.55	-1.16	0.36
18-4-SI-1	cascade	-	24.53	-7.08	-5.69	-4.17
18-6-SI-1	barrage	-	29.73	-2.04	-0.64	0.88
18-7-SI-1	terrace breccia	53.52	26.38	-5.28	-3.89	-2.38
GHN 1.1	rim pool	39.13	27.08	-4.60	-3.21	-1.69
GHN 1.2	rim pool	-	27.42	-4.27	-2.88	-1.36
GHN 1.3	rim pool	-	27.79	-3.92	-2.52	-1.00
GHN 1.4	rim pool	-	27.73	-3.98	-2.59	-1.06
GHN1-SI-2	rim pool	36.55	26.99	-4.69	-3.30	-1.78

GHN1-SI-3	rim pool	37.02	27.01	-4.67	-3.28	-1.76
17-5.1	rim pool	-	27.15	-4.54	-3.15	-1.63
17-5.2	rim pool	-	27.77	-3.94	-2.54	-1.02
17-6.1	barrage	-	29.44	-2.32	-0.93	0.60
17-6.2	barrage	-	26.54	-5.13	-3.74	-2.22
17-6.3	barrage	-	25.88	-5.77	-4.38	-2.86
17-6.4	barrage	-	27.19	-4.50	-3.11	-1.59
17-6.5	barrage	-	25.43	-6.20	-4.81	-3.29
17-6-SI-1	barrage	-	28.32	-3.40	-2.01	-0.48
17-7.1	terrace breccia	-	27.58	-4.12	-2.73	-1.20
17-7.2	terrace breccia	-	27.09	-4.60	-3.21	-1.69
17-8.1	terrace breccia	48.31	26.38	-5.28	-3.89	-2.37
17-8.2	terrace breccia	34.50	26.77	-4.90	-3.51	-1.99
17-8-SI-3	terrace breccia	41.76	26.43	-5.24	-3.85	-2.33
17-8-SI-4	terrace breccia	43.23	26.41	-5.26	-3.87	-2.35
17-8-SI-5	terrace breccia	41.62	26.32	-5.34	-3.95	-2.44
17-8-SI-6	terrace breccia	32.45	26.78	-4.90	-3.51	-1.99
17-12.1	rim pool	-	27.06	-4.63	-3.23	-1.71
GHS6.1	rim pool	60.38	26.71	-4.97	-3.58	-2.06
GHS6.2	rim pool	59.68	26.61	-5.06	-3.67	-2.15
GHS6-SI-1	rim pool	61.90	26.67	-5.00	-3.61	-2.09
GHS6-S1-3	rim pool	53.10	26.44	-5.22	-3.83	-2.31
GHN 3.2.1	dome	-	27.64	-4.06	-2.67	-1.15
17-9.1	dome	-	27.86	-3.85	-2.46	-0.94
17-9.2	dome	-	25.63	-6.01	-4.62	-3.10
17-9.3	dome	-	27.58	-4.12	-2.73	-1.20
18-10-SI-1	dome	-	24.78	-6.83	-5.44	-3.93
18-10-SI-2	dome	-	26.15	-5.51	-4.12	-2.60
18-10-SI-3	dome	3.00	29.91	-1.86	-0.47	1.06
GHS 4.1	dome	-	29.64	-2.12	-0.73	0.80
GHS 4.2	dome	-	28.44	-3.29	-1.90	-0.37
17-13.1	dome	-	28.61	-3.12	-1.73	-0.21
17-13.2	dome	-	30.46	-1.33	0.07	1.60
17-13.3	dome	-	30.37	-1.42	-0.02	1.50
17-13.4	dome	-	30.07	-1.70	-0.31	1.22
17-13.5	dome	-	30.41	-1.38	0.02	1.54
17-13.6	dome	-	30.81	-0.99	0.41	1.93

* Tufas are assumed to have formed in equilibrium with the water. $\delta^{18}O$ values that are within the range of groundwater (-6.5‰ to -5.5‰) are highlighted in light green, $\delta^{18}O$ values that are within the lower range of drip water values (-5.5‰ to -2‰) are highlighted in darker green, and values outside of these ranges (<-6.5‰ and >-2‰) are highlighted in orange. Tufa $\delta^{18}O$ values are given relative to SMOW, and $\delta^{18}O_{tufa}$ with values > 28‰ are highlighted in yellow.

The calculated range of $\delta^{18}O_{water}$ values at the fixed tufa-forming water temperature of 18°C, i.e. emergent groundwater temperature, is plotted against age in Figure 7.3.4 to explore the relationship between the $\delta^{18}O$ of the tufa-forming water and time. There is a weak correlation between age and $\delta^{18}O_{water}$ (r^2 = 0.23, n = 33), with a slight increase in the $\delta^{18}O_{water}$ value with decreasing age. This increase could reflect a change in the tufa-forming waters over time, i.e. the emergent groundwater $\delta^{18}O$ value increased, which can be achieved through a change in the $\delta^{18}O$ value of the rainfall. An increase in the $\delta^{18}O_{rainfall}$ value at this site over the last 100 ka is likely to have been driven by increasing atmospheric temperatures, or a decreasing amount of rainfall over time, both of which would lead to higher $\delta^{18}O_{water}$ values. Evaporation of rainwater prior to recharge may also have resulted in an increase in the $\delta^{18}O_{water}$ value. All three factors, i.e. higher atmospheric temperatures, lower rainfall amount, and higher evaporation, indicate an aridity trend with time.

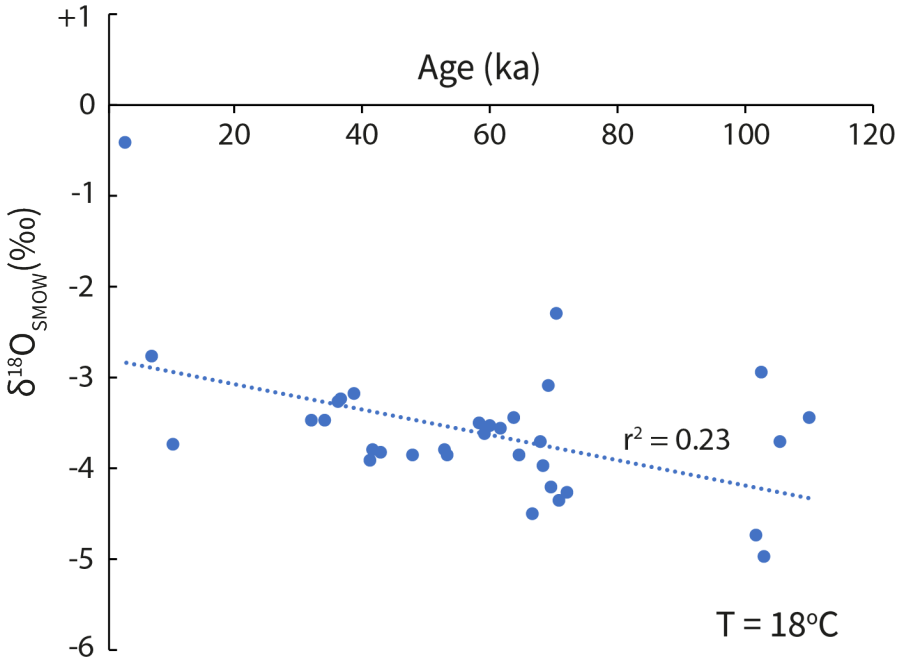

Figure 7.3.4 Age in thousand years (ka) plotted against the calculated tufa-forming water $\delta^{18}O$ value (Table 7.8) at a fixed tufa-forming water temperature of 18°C.

Although the individual tufas sampled provide a discontinuous record of isotope variation through time, together they provide some insight into tufa formation processes and palaeoenvironmental conditions over the last ~110 ka. Oxygen-water

modelling allows for an estimation of the hydrological conditions at the time of tufa formation, and the carbon isotope values track shifts in soil-productivity and associated vegetation, which are linked to temperature and moisture availability. These are discussed in relation to other regional records of environmental change in the following chapter.

CHAPTER 8 DISCUSSION AND CONCLUSIONS

Tufa formation is sensitive to multiple environmental parameters, but ultimately provides direct evidence of fresh water and associated productivity on the landscape. I have shown that the Ga-Mohana Hill tufa deposits indicate past spring activity that produced shallow streams, cascading waterfalls, and pools of standing water during five time intervals in the southern Kalahari during the Late Pleistocene and Holocene, from ~114 to ~2 ka. The principal conditions required for tufa formation are sufficient effective precipitation to recharge the aquifers, productive soil and vegetation cover to enhance the pCO_2 of the percolating waters, $CaCO_3$ supersaturation of those waters through dissolution of a carbonate host rock, and moderate temperatures which balance productivity, moisture and evaporation (Martín-Algarra et al., 2003; Pentecost, 2005; Cremaschi et al., 2010; Sancho et al., 2015).

The primary objective of this thesis was to investigate the palaeoenvironment that the Ga-Mohana Hill tufa deposits represent, and to relate this to the archaeological record of Late Pleistocene and Holocene human occupation in the region. In the following sections, I discuss the timing of tufa formation within a global and regional context, and compare the Ga-Mohana Hill archaeological and palaeoenvironment records to those of the nearby sites of Wonderwerk Cave and Kathu Pan.

I first situate the periods of tufa occurrence at Ga-Mohana Hill within a global context and discuss the aspects of global climatic conditions that may have influenced tufa precipitation (Section 8.1). To do this, I compare the timing of tufa formation and the oxygen isotope values recorded in the tufa at Ga-Mohana Hill to records of global ice (Lisiecki and Raymo, 2005), austral summer insolation (Laskar et al., 2004), changes in sea surface temperature in the southwest Indian Ocean (Caley et al., 2018), and changes in atmospheric CO_2 based on the EPICA Dome C ice core record (Bereiter et al., 2015) (Figure 8.1). I then compare the timing of tufa formation at Ga-Mohana Hill, and the depositional environment the tufas represent, with other selected proxy records of local and regional climate in southern Africa (Section 8.2). I structure this section of the

discussion using the Marine Isotope Stage (MIS) framework based on the Lisiecki-Raymo benthic stack (LR04) (Lisiecki and Raymo, 2005). I also explore the relationship between human occupation and changing environmental conditions in the southern Kalahari region based on records from Ga-Mohana Hill, Kathu Pan and Wonderwerk Cave (Figure 8.3). I conclude this chapter with Section 8.3, in which I summarise the main findings of this thesis and suggest directions for future research.

8.1 Ga-Mohana tufa compared to global palaeoclimate records

The individual tufa ages are clearly clustered into several distinct groups (Chapter 6). In Figure 8.1, blue bars highlight these clusters of tufa ages, which represent periods of water availability and conditions suitable for tufa formation at Ga-Mohana Hill. Taken at their maximum duration, the periods are: ~114 to 100 ka, ~73 to 48 ka, 44-32 ka, 15-6 ka, and ~4 to 2 ka.

Here, I compare the timing of tufa formation and the associated $\delta^{18}O$ values at Ga-Mohana Hill to the following selected global and regional climate records: 1) The LR04 $\delta^{18}O$ benthic stack, which is a composite record reflecting orbital-scale changes in global ice volume, and thus cycles of interglacial / glacial climate (Figure 8.1a; Lisiecki and Raymo, 2005). This record provides the marine isotope stage (MIS) framework within which the episodes of tufa formation are later discussed. 2) Insolation curve from 21 February for 27 degrees latitude (Figure 8.1b; Laskar et al., 2004). 3) A composite record of changing atmospheric CO_2 from the Antarctic ice core record (Figure 8.1c; Bereiter et al., 2015). 4) Antarctic temperature changes measured from EPICA Dome C (Figure 8.1d; Jouzel et al., 2007). 5) A record of SST variation constructed from a southwest Indian Ocean sediment core MD96-2048 collected from the Limpopo catchment off the north-east coast of South Africa (Figure 8.1e; Caley et al., 2018).

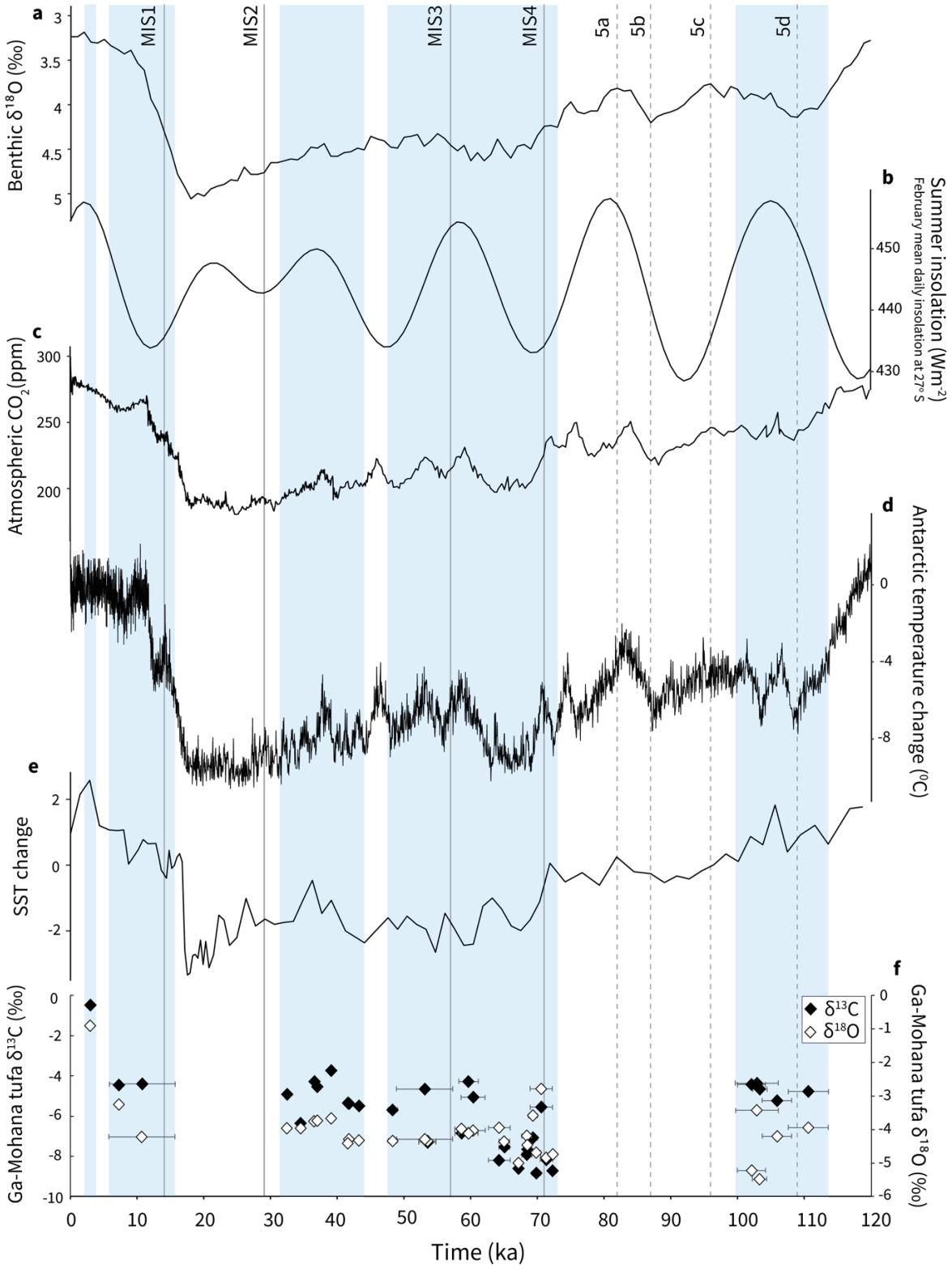

Figure 8.1 Composite plot of global and regional climate parameters (references in text) and Ga-Mohana tufa formation intervals (blue bars). The Ga-Mohana tufa $\delta^{18}O$ and $\delta^{13}C$ values (f; white and black diamonds, respectively) are plotted against time. Grey lines indicate MIS boundaries, dotted lines indicate substages of MIS 5 (Lisiecki and Raymo, 2005).

The U-Th age data indicate that tufa formation at Ga-Mohana Hill ocurred during MIS 5d, almost consistently across MIS 4, over two intervals during MIS 3, and in the early and late stages of the Holocene (Figure 8.1, blue bars). Comparison between this timing and the LR04 plot (Figure 8.1a; Lisiecki and Raymo, 2005) indicates that tufa formation appears to favour mild glacial periods. This adds to growing evidence that the wet/dry, interglacial/glacial dichotomy through which much of southern African (and southern hemisphere) palaeoclimates has traditionally been viewed is overly simplistic (Chase, 2010; Blome et al., 2012; Collins et al., 2014; Burrough, 2016; Kaboth-Bahr et al., 2021; Weij et al., 2024).

Whereas tufas have typically been associated with warm and humid interglacial climate conditions (Soligo et al., 2002; Martín-Algarra et al., 2003; Ordóñez et al., 2005), several other studies also report tufa occurrences during both glacial and interglacial periods (Auler and Smart, 2001; Domínguez-Villar et al., 2011; Doran et al., 2015; Sancho et al., 2015; Ricketts et al., 2019). This highlights that tufa formation is a complex interplay of multiple variables that operate on a local, regional and global scale, and that it cannot be ascribed to simplified climatic conditions. In addition, it is evident that across the globe, regional climates respond variably to boundary conditions. This echoes the conclusion of previous studies that tufa formation is not restricted to interglacial periods, nor is it a simple product of changing global climate states. This study also supports the growing evidence that southern hemisphere mid- and low-latitude regions experienced greater moisture availability during glacial stages, contrary to the prevailing narrative of cold and dry glacial climatic conditions in these regions (Weij et al., 2024).

The limiting factor for tufa formation in semi-arid, low latitude regions is water availability (Cremaschi et al., 2010; Kele et al., 2021). The moisture source for rainfall in the SRZ in South Africa originates primarily from the southwestern Indian Ocean (Reason, 2001a), but the spatial and temporal variability of rainfall in this southern Kalahari region is poorly constrained. Rainfall may be modulated by summer insolation, with increased precipitation corresponding to insolation maxima (Partridge et al., 1997). However, no simple correlation between the mean summer insolation curve for 27°S

and Ga-Mohana tufa formation is evident (Figure 8.1b; Laskar et al., 2004). Tufa formation during the 114-100 ka and 44-32 ka intervals coincide with increasing summer insolation, whereas insolation is variable during tufa formation between 73-48 ka, and at a minimum during the 15-6 ka episode. The most recent tufa formation at ~3 ka coincides with an insolation maximum (Figure 8.1).

Kele et al. (2021) find a similarly poor correlation between the timing of tufa formation in the Kurkur-Dungal area (southern Egypt) and northern hemisphere insolation, which is thought to modulate the position of the ITCZ, i.e., high summer insolation is expected to correspond to increased precipitation. However, the southern Egypt tufa deposits do not align with high summer insolation, even when a delay in aquifer recharge is taken into account (Kele et al., 2021). They proposed that the mechanisms driving rainfall in the region are complex and cannot be attributed to a single forcing factor, e.g. the precession-controlled motion of the ITCZ, and instead conclude that variable forcing mechanisms are likely at play during interglacial vs. glacial periods.

A potential explanation for the lack of correlation between our Ga-Mohana tufa record and high austral summer insolation is that direct insolation forcing has played a lesser role over the last ~50 ka due to lower amplitude changes related to declining eccentricity (Singarayer and Burrough, 2015), and that after ~70 ka, high latitude changes may have had a greater influence on southern African hydroclimate (Chase et al., 2021). This could mean that the first and last intervals of tufa formation (~114-100 ka and ~3 ka), may have been driven by low latitude mechanisms, i.e. high austral summer insolation, whereas favourable conditions for tufa formation across MIS 4 and MIS 3, which occurred across variable insolation, may have been a response to high latitude mechanisms, i.e. an increase in the global ice volume.

Atmospheric CO_2 may play a role in creating conditions conducive to tufa formation, i.e. a large difference between pCO_2 of the emergent groundwater and pCO_2 of the ambient atmosphere encourages diffusion of CO_2 across the air-water interface through degassing (Chen et al., 2004). Carbon dioxide levels also impact several other factors, specifically temperature, and plant, soil, and biological productivity, which in turn plays

a role in creating favourable conditions for tufa precipitation. However, in comparing the timing of tufa formation at Ga-Mohana Hill to the reconstructed curve of atmospheric CO_2 (Figure 8.1c; Bereiter et al., 2015), the concentration of CO_2 in the atmosphere during each of the tufa forming episodes varies considerably and there is no clear relationship between atmospheric CO_2 and tufa formation intervals. There is an overall decrease in atmospheric CO_2 concentration from MIS 5 to MIS 2, and this is followed by a rapid increase leading to MIS 1 (the Holocene). Nevertheless, tufa formation occurs at punctuated intervals over this period, and is maintained for significant lengths of time, despite major fluctuations in atmospheric pCO_2, e.g. during MIS 4 tufa precipitation persists while CO_2 levels plunge from approximately 250-235ppm to a minimum of around 200ppm before steadily returning to 235ppm. MIS 2 includes the Last Glacial Maximum (LGM) and is characterised by the lowest levels of atmospheric CO_2 over the period of interest. The absence of tufa during this time is likely related to a combination of factors, including low atmospheric CO_2 levels and low temperatures, which would have inhibited plant and soil productivity. Even if there was sufficient moisture during this time, it is possible that percolating waters did not become sufficiently enriched in CO_2 to allow for dissolution of the dolomitic bedrock and calcium carbonate saturation. The last two phases of tufa formation are recorded between ~15-6 ka and ~4 to 2 ka. These are coincident with the highest atmospheric CO_2 concentrations (~260-280 ppm) over the last ~114 ka. Based on the Ga-Mohana tufa record, there is no apparent atmospheric CO_2 concentration that favours calcite precipitation, and this dispels the notion of a CO_2 'window' i.e. CO_2 levels between 270-250ppm as being optimum for tufa precipitation, as suggested by Griffiths and Pedley (1995). Evidently, a combination of factors affects tufa formation, making it difficult to single out particular mechanisms.

Warm temperatures are considered favourable for tufa precipitation and are closely linked to atmospheric CO_2 concentrations. An increase in temperature has a multi-pronged effect on the tufa system, affecting several factors involved in tufa precipitation: warmer temperatures encourage greater biological activity and soil respiration, resulting in higher CO_2 in the soil environment, and this leads to a greater capacity for the fluid to dissolve carbonate bedrock. Carbon dioxide is soluble in cold temperatures,

and so higher temperatures encourage degassing of CO_2, which in turn increases the CO_3 saturation of the waters. Solubility of calcite also decreases with increasing temperature, and so higher temperatures mean a greater likelihood of calcite precipitation. However, warmer temperatures can also result in increased evaporation, which restricts aquifer recharge. Variation in the tufa $\delta^{18}O$ values are interpreted to indicate changes in the $\delta^{18}O$ value of the groundwaters that form the tufa, driven by variable $\delta^{18}O$ values of rainfall, plus/minus evaporation effects prior to recharge, as well as variable ambient temperatures during tufa formation. Low $\delta^{18}O$ values are interpreted to represent lower temperatures, and higher $\delta^{18}O$ values represent warmer temperatures (Chapter 7). Comparison between the reconstructed temperature curve from Antarctica (Figure 8.1d; Jouzel et al., 2007), and the Ga-Mohana tufa intervals, it appears that tufa formation predominantly occurred during periods associated with Antarctic temperatures that were ~ 4°C to 8°C lower compared to present. However, the absence of tufa during MIS 2 and the LGM may suggest that temperatures during this period were too low for tufa formation. The last two tufa intervals coincide with temperatures similar to present (Figure 8.1d). The most recent tufa has a high $\delta^{18}O$ value that is interpreted to have been impacted by evaporation (Chapter 7). Evidently, warmer temperatures do not preclude the formation of tufa, although the relatively fewer ages during MIS 1 may indicate a diminishment of the tufa system.

Warmer sea surface temperatures (SSTs) in the southwest Indian Ocean generate increased moisture and correlate with periods of greater rainfall in southeastern Africa today (Reason, 2001b; Reason, 2002; Chevalier and Chase, 2015). However, tufa formation at Ga-Mohana Hill appears to have occurred across a range of SW Indian Ocean SSTs over the last 120 ka (Figure 8.2; Caley et al., 2018), and no clear pattern between SST change and tufa formation can be identified. This observation supports the conclusions made by Caley et al. (2018) that SST anomalies in the SW Indian Ocean are not solely responsible for driving increased precipitation in the summer rainfall region of South Africa. Instead, Caley et al. (2018) argue that the temperature contrast between land and sea, related to increased summer insolation, generates an increase in easterly moisture transport into southern Africa. In addition to this, the Indian Ocean

dipole effect is considered a driver of climate variability in South Africa, i.e., opposing SSTs between the SW and SE Indian Ocean create a dipole effect which influences circulation patterns and may also contribute to increased precipitation in the SRZ of South Africa (Reason, 2002).

The Ga-Mohana tufas form from emergent groundwaters. Recharge of the below surface aquifers is driven by either increased rainfall, less seasonal / more prolonged rainfall, reduced effects of evaporation, or most likely a combination of all three, in response to the interaction of multiple forcing factors. Little is known about the karst dynamics at this site, and so potential lags between rainfall events, aquifer recharge, residence times, and tufa formation are as yet unconstrained. However, Markowska et al. (2016) showed that cooler temperatures and reduced rates of evaporation create favourable conditions for karst recharge in semi-arid regions. As such, the tufa deposits at Ga-Mohana Hill are not simply indicators of 'wet' conditions but rather indicate a positive moisture balance caused by an interplay of local and regional climatic and environmental parameters. The time intervals presented here are thus interpreted to indicate activation of the perched spring system and conditions conducive to tufa formation over the last ~114 ka. The conditions that supported tufa formation may have varied during each of the tufa forming intervals, and this is explored further in the next section.

With an ever-growing body of palaeo-proxy data generated for sites across southern Africa, it is increasingly acknowledged that broad theoretical models evoking a primary driving mechanism do not capture the homogeneity of rainfall across the region, which has experienced a spatially complex pattern of past hydroclimate variability (Thomas and Burrough, 2012; Singarayer and Burrough, 2015). Through HadCM3 climate model simulations, Singarayer and Burrough (2015) show that correlations between SSTs and rainfall varies spatially and temporally over southern Africa depending on the interplay of different mechanisms. This illustrates that rainfall across the region is driven by the interaction of a range of drivers that wax and wane in prominence, and suggests that the governing mechanism of rainfall variability for any particular region has likely varied over time (Singarayer and Burrough, 2015).

It seems clear that tufa formation cannot be simply related to changes in global climate, as these deposits occur in a variety of settings and form in response to variable climatic conditions. However, tufa remains a valuable tool for assessing rainfall regime shifts, karst recharge processes, and changes in environmental parameters, as documented for several deposits world-wide (e.g. Wang et al., 2004; Moeyersons et al., 2006; Capezzuoli et al., 2010; Cremaschi et al., 2010; Domínguez-Villar et al., 2011; Luzón et al., 2011; Alexandrowicz, 2012; Kele et al., 2021), and can be complimentary archives to other proxies such as lake sediments and speleothem deposits (Wang et al., 2004; Andrews, 2006; Pedley et al., 2009). In the following section, I compare the tufa formation intervals at Ga-Mohana Hill with other local and regional palaeoenvironmental records.

8.2 Ga-Mohana tufa related to local and regional palaeoclimate and archaeological records

A compilation of the Ga-Mohana tufa ages and selected records of local and regional climate proxies are presented in Figure 8.2 and discussed within the MIS framework to provide a synthesis of palaeoenvironmental change in the southern Kalahari region over the last ~120 ka. Palaeoclimate proxies from sites that are relatively distant from Ga-Mohana Hill are included in this discussion to provide additional context, but it is noted that the SRZ of South Africa did not experience uniform climatic conditions during this time, as highlighted in previous studies (Chevalier and Chase, 2015, Singarayer and Burrough, 2015). Additionally, I compare the timing of tufa formation and human occupation at Ga-Mohana Hill to records from the nearby sites of Kathu Pan and Wonderwerk Cave, which occur within ~60 km of each other (Figure 8.3). This close proximity means that all three sites likely experienced comparable shifts in local hydroclimate, and it is possible that they were utilized by the same groups of mobile hunter-gatherers, and provides an opportunity to consider the relationship between water availability and human occupation in this southern Kalahari region.

8.2.1 MIS 5 (~130 - 71 ka)

Marine Isotope Stage 5 incorporates the last interglacial and is divided into five substages. The first substage, MIS 5e, is characterised by typical interglacial conditions with high global temperatures (Shackleton, 1969). In contrast, substage, MIS 5d, is characterised by colder conditions, with evidence for ice sheet expansion in the northern hemisphere (Sirocko et al., 2007). In the southern hemisphere, reduced temperatures during this time are evident from Antarctic ice core records, and these are accompanied by a decrease in Indian Ocean SSTs (Figure 8.1). In parts of South Africa, the MIS 5 interglacial is associated with increased regional aridity (Urrego et al., 2015), punctuated with wetter phases during the warmer sub-stages, i.e. MIS 5c and 5a (Knight and Fitchett, 2021).

Tufa formation at Ga-Mohana Hill is dated ~114 - 100 ka, indicating a positive moisture balance during MIS 5d. These Ga-Mohana tufa ages come from two ex-situ cascade samples, 18-16 and 18-17, which may indicate that tufa formed during this period has undergone dismantling and erosion, such that only limited evidence of tufa formation from this time is preserved. The $\delta^{18}O$ and $\delta^{13}C$ values from these samples fall within isotope group 2, i.e. intermediate $\delta^{18}O$ (~-5‰) and $\delta^{13}C$ (~-4 to -5‰) values. The $\delta^{13}C$ values are consistent during this period and indicate a mixed contribution of soil-zone and dolomitic bedrock carbon, and/or mixed C3 and C4 vegetation. This suggests relatively warm and dry conditions (although it was wet enough for tufa formation). The $\delta^{18}O$ values decrease during this interval, which may suggest a gradual increase in the rainfall amount, and / or decreasing temperatures. Altogether, the presence of the large cascade tufa points to sufficient water availability for tufa formation, coupled with moderate temperatures. These conditions may have occurred with a decrease in temperature following the peak temperatures of the last interglacial, leading to lower rates of evaporation and aquifer recharge. It is unclear whether this period of tufa formation represents perennial water availability and extensive development of the tufa system, or episodes of ephemeral flow. The variation in $\delta^{18}O$ values may point to variable temperatures during tufa formation, driven, for example, by seasonal variability. However, this cannot be resolved with the current dataset.

Deposition of tufa at Ga-Mohana Hill during this time coincides with MSA artefacts hosted in the lowermost sediment horizon, DBSR, in the excavation at Ga-Mohana Hill as determined through OSL ages: 109.8 ± 5.7 ka, 103.0 ± 6.5 ka, and 99.2 ± 7.7 ka (Figure 8.2; Wilkins et al., 2020). This indicates contemporaneous human activity and water availability at Ga-Mohana Hill during this time (Wilkins et al., 2021). At Kathu Pan, between ~125 to ~70 ka, palygorskite-coated, water-associated sediments that indicate intermediate conditions and moderate water availability alternate with organic-rich sediments that represent wet and marshy conditions between ~101 and 80 ka (Figure 8.2; Lukich et al., 2019). Evidence of human activity at the pan is coincident with these wetter conditions (Figure 8.3; Lukich et al., 2019; Lukich et al., 2020). At Rooidam, another pan associated with archaeological material southeast of Ga-Mohana Hill, Butzer (1974) reports a U-Th age of 115 ± 10 ka associated with wet conditions. Altogether, this indicates the occurrence of water availability and human occupation in this area (Figure 8.2 and Figure 8.3). These conditions coincide with relatively warm SSTs, linked to moisture sourced from the southwest Indian Ocean (Figure 8.2a), but an overall decrease in rainfall at Tswaing Crater (Figure 8.2b). Pollen assemblages associated with sediments dated to ~90 ka at Mwulu's Cave indicate swampy conditions and water availability east of these sites but also in the SRZ (Esteban et al., 2020a). This points to a persistence of moisture availability in the region.

Other South African palaeoclimate records from this period are mostly focussed along the south coast of South Africa, with relatively few records from the interior region. Microfaunal assemblages at Klassies River Mouth, a MSA site on the southern Cape coast, indicate that the palaeoenvironment during early MIS 5 was characterised by moderate climate and seasonal rainfall concentrated in the summer months, similar to that of today. Morrissey et al. (2020) describe aeolianite deposits at Nahoon Point on the south-eastern coast from MIS 5e/d associated with human activity, and evidence from the archaeological site of Pinnacle Point on the southwest coast, suggests palaeoclimate conditions favourable for human occupation and activity (Braun et al., 2019, Esteban et al., 2020b).

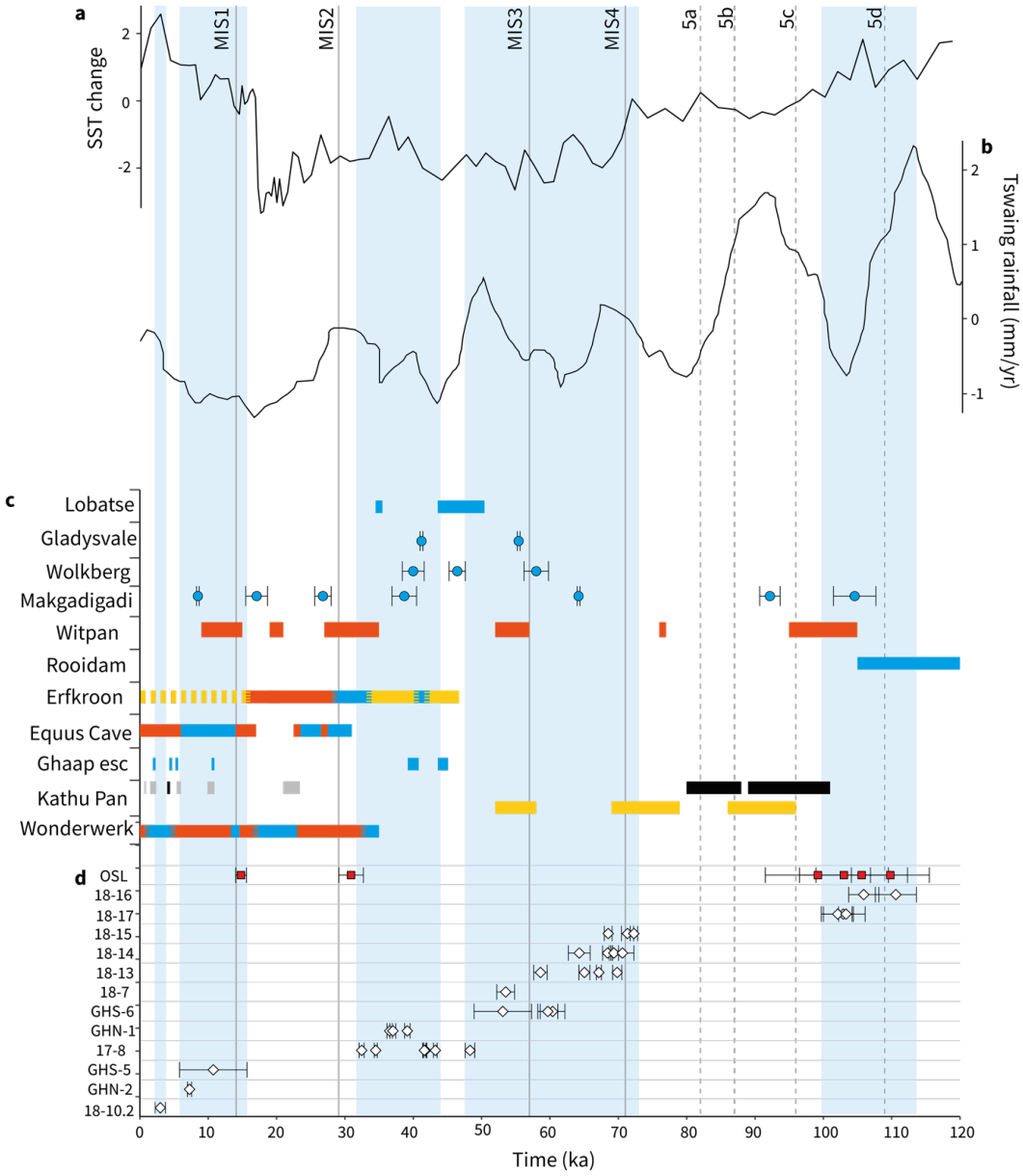

Figure 8.2 Compilation of selected South African palaeoclimate records: a) sea surface temperature variation for the north-east coast of South Africa (Caley et al., 2018); b) reconstructed rainfall record from the Tswaing Meteorite Crater (Partridge et al., 1997); c) selection of palaeoclimate proxy records from sites located in the northern and eastern interior of South Africa (referred to and referenced in text). Horizontal blue bars = wet periods, red bars = dry periods, grey bars = semi-arid conditions, yellow bars = intermediate conditions, black bars = marshy conditions; d) Ga-Mohana Hill OSL-dated archaeological occupation horizons (red squares) and U-Th dated tufa (white diamonds). The vertical blue bars highlight water availability based on Ga-Mohana tufa formation intervals, and the vertical grey lines indicate Marine Isotope Stage (MIS) boundaries, dotted lines indicate substages of MIS 5 (Lisiecki and Raymo, 2005).

On a regional scale, a mega-lake high-stand at 104.6 ± 3.1 ka is recorded for the Makgadikgadi palaeolake in the mid-Kalahari (Figure 8.2; Burrough et al., 2009a), evidence for greater regional water availability during this time. Sediments from the Witpan dune field indicate dune activation and accumulation between ~95-105 ka (Figure 8.2; Telfer and Thomas, 2007). These are not necessarily an indication of aridity, and instead may have been facilitated by a combination of factors, including reduced vegetation and an increase in windiness. These proxies highlight the difficulty in disentangling proxy-climate relationships. Nevertheless, the Ga-Mohana tufa data, together with other local proxy evidence, indicates that favourable conditions that supported human activity were not restricted to coastal sites during this period, and instead extended into the northern interior.

8.2.2 MIS 4 (~71 - 57 ka)

The general assumption has been that MIS 4 was a global glacial period, with climate conditions in southern Africa being cold and dry (van Zinderen Bakker Sr, 1983). This conceptual model is changing as growing evidence from southern African terrestrial and marine proxy records instead indicate that cool and moist conditions prevailed across the sub-continent during this time (Chase, 2010; Scott, 2016). Consistent with this, the tufa record at Ga-Mohana Hill indicates water availability spanning the entire MIS 4 period (Figure 8.2). Most of the tufa samples dated to this time are cascades, along with several rim pool samples. The persistence of tufa over this time, and the presence of the pool tufas may indicate that this period was characterised by perennial, low energy water flow that allowed for the development of slack-water environments. Most of the tufa samples during this period fall into isotope group 1, i.e., the lowest $\delta^{13}C$ values (< -6.5‰) and moderate $\delta^{18}O$ values (> -5‰ and < -3.5‰) (Figure 8.1). These low $\delta^{13}C$ values suggest greater input of soil-zone carbon and / or a higher proportion of C3 vegetation. This may be due to prolonged moisture availability (and reduced groundwater residence times), and conditions favourable for C3 vegetation expansion. The overall increase in $\delta^{18}O$ values may indicate gradually increasing temperatures, and / or decreasing rainfall amounts toward the end of MIS 4 (Figure 8.2b).

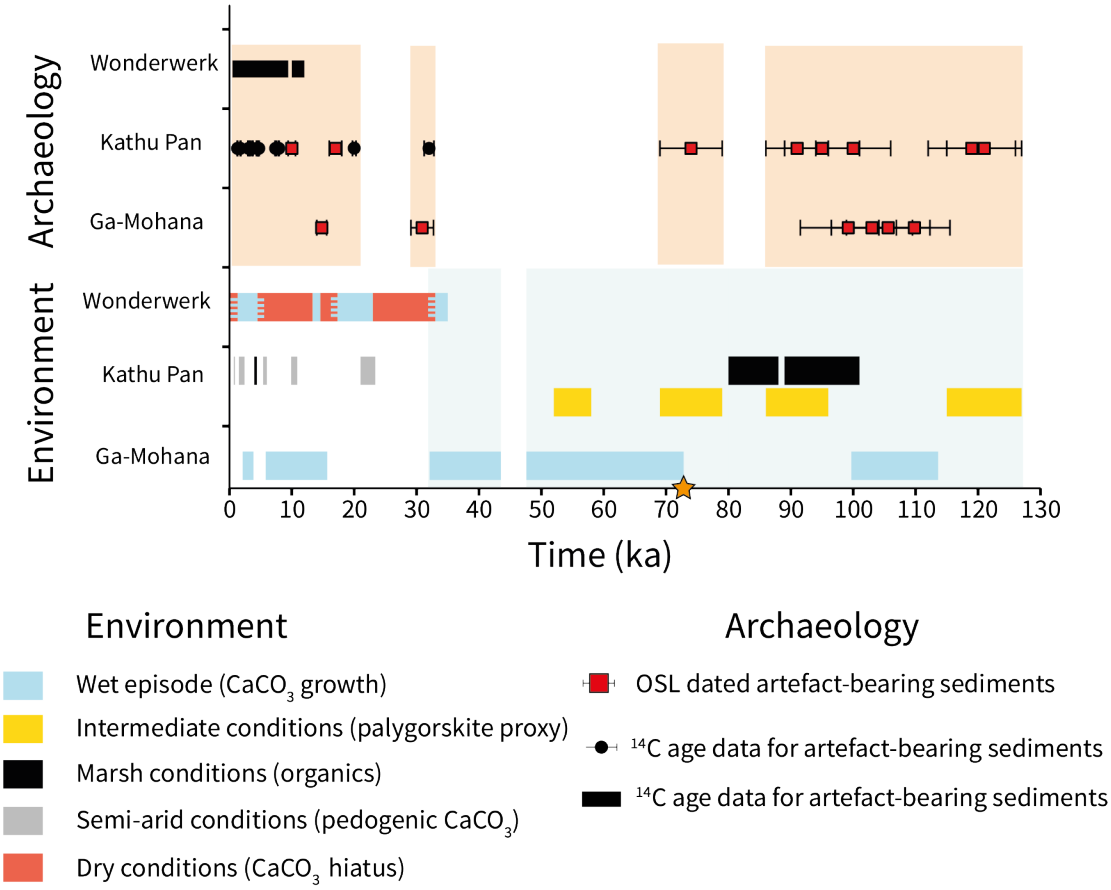

Figure 8.3 Comparison of palaeoenvironmental and archaeological records from Ga-Mohana Hill, Kathu Pan, and Wonderwerk Cave. Archaeological occupation ages for Ga-Mohana Hill (Wilkins et al., 2020; Wilkins et al., 2021), Kathu Pan (Beaumont and Morris, 1990; Porat et al., 2010; Lukich et al., 2019; Lukich et al., 2020), and Wonderwerk Cave (Chazan et al., 2012; Ecker et al., 2018; Chazan et al., 2020). Pale orange bars highlight periods of occupation. Palaeoenvironment proxy data from Ga-Mohana Hill (this study), Kathu Pan (Lukich et al., 2020) and Wonderwerk Cave (Brook et al., 2010; Chazan et al., 2020). Pale blue bars highlight wet periods across the sites. Orange star marks the point at ~71 ka, before which human occupation of the region appears to have been associated with the availability of water.

Water availability during this time is supported by other palaeoenvironmental records nearby, such as at Kathu Pan. The palygorskite-coated sands at Kathu Pan indicate the presence of fluctuating water levels through much of MIS 4 (Lukich et al., 2020). There are multiple other sites in the SRZ of South Africa for which proxy records also indicate moisture availability during this stage (Chase, 2010). Based on the micromammalian

record at Boomplaas Cave, Thackeray and Fitchett (2016) propose a year-round rainfall regime from ~75 ka. Pollen from the Tswaing crater records shifting conditions between ~70-60 ka, with the presence of *Podocarpus* and grass pollen indicating cool and wet conditions between ~72-68 ka, followed by a brief warm and relatively dry period between ~63-60 ka, and then a return to cool and moist conditions from ~60 ka indicated by pollen from grass, forest and fynbos (Scott, 2016). Speleothem growth at Wolkberg cave is dated to ~57.9 ka (Holzkämper et al., 2009), and a flowstone from Gladysvale Cave is dated to 56.77 ± 0.35 ka (Pickering et al., 2007), both suggesting moisture availability in the north-eastern region of South Africa toward the end of MIS 4. Evidence from other dated archaeological sites in eastern South Africa, such as Rose Cottage Cave and Sibudu (Figure 2.10), indicate cool and humid conditions during MIS 4, coeval with human activity at these sites (Butzer, 1984; Herries, 2011; Wadley, 2013).

Based on speleothem records at Pinnacle Point on the south coast (Figure 2.10), Bar-Matthews et al. (2010) suggested that a shift from predominantly winter rainfall to summer rainfall occurred at around 72 ka, i.e. the start of MIS 4. This is further evidence that the summer rainfall regime was greatly enhanced at this time. In addition, a Makgadikgadi mega-lake high-stand dated to 64.2 ± 0.2 ka indicates substantial regional water availability during the middle of MIS 4 (Burrough et al., 2009a), and the absence of southern Kalahari dune accumulation at Witpan dunes during this time suggests a lack of dry and windy conditions favourable for dune accumulation (Figure 8.2; Telfer and Thomas, 2007).

As of yet, there is no record of human activity at Ga-Mohana Hill, Kathu Pan or Wonderwerk Cave during MIS 4 (Figure 8.3). There are Middle Stone Age deposits at Wonderwerk Cave that have not yet been securely dated that could potentially represent this period (Beaumont and Vogel, 2006), but this remains unknown at this point. So while there may have been sufficient moisture in the region, this alone was perhaps insufficient to draw people to these sites. Cooler conditions, along with reduced atmospheric CO_2, may have impacted plant and animal populations, making the area less attractive for humans (Faltein et al., 2020).

8.2.3 MIS 3 (~57 - 29 ka)

MIS 3 is somewhat of an anomalous period in that it is not an interglacial, and instead was characterised by high amplitude, millennial-scale climate oscillations. Southern African proxy records point to an unstable climate with alternating wet and dry episodes (Knight and Fitchett, 2019). Late MIS 3 coincides with the southern hemisphere insolation maximum (~32 ± 1 ka), and the early onset of glacial temperatures (Petherick et al., 2022).

Two episodes of Ga-Mohana tufa formation occurred during MIS 3. The first episode overlaps the MIS 4/3 boundary, with tufa formation between ~57 to 48 ka. The second episode occurs between ~44 to 32 ka. Tufa dated to MIS 3 are only represented by rim pool and terrace breccia samples. This may reflect particular conditions that led to preferential preservation of particular morphologies, e.g., extreme events such as flash floods that would have generated high energy water flow, causing erosion, and the transport and cementation of weathered material down-slope. The $\delta^{18}O$ and $\delta^{13}C$ values are generally higher than those measured in tufas from MIS 4. This may be due to a shift towards warmer conditions and a decrease in the amount of rainfall, but may also point to the greater distance the waters travelled from the point of resurgence, and higher turbulence and degassing of the waters, due to the increase in flow energy.

Other sites near Ga-Mohana Hill also record evidence for wet conditions during this time. Tufa deposits from Groot Kloof, along the Ghaap escarpment, are dated to ~44 and 40 ka (Figure 8.2; Doran et al., 2015), and a stalagmite near the entrance of Wonderwerk Cave is dated to between ~35-33 ka (Figure 8.2; Brook et al., 2010). Human occupation at Ga-Mohana Hill and Kathu Pan is evident during late MIS 3 with sediment layers dated to 31 ± 1.8 ka (Wilkins et al., 2020) and 32 ± 0.78 ka (Porat et al., 2010), respectively. However, sediments at Kathu Pan record progressively drier conditions from ~32 ka (Lukich et al., 2019; Lukich et al., 2020).

The Tswaing crater pollen record indicates cool and moist conditions from ~60-45 ka, with the sediment moisture index indicating the highest precipitation between 55 – 50

ka. The palaeosol record from Erfkroon indicates warm conditions and moderate, seasonal rainfall, estimated to be around 200-400 mm/year between 46-28 ka, with a marked increase in rainfall, up to 600mm/year, identified at ~42 ka (Figure 8.2; Lyons et al., 2014). Flowstone growth at Gladysvale Cave occurred at ~42 ka (Pickering et al., 2007), speleothem formation at Wolkberg cave is recorded from 46.3 ka and ~40 ka, and at Lobatse Cave between ~51-43 ka, and at ~35 ka (Holzkämper et al., 2009). The Tswaing and Wonderkrater pollen records both indicate warm and dry grassy savanna conditions between ~45-41 ka, and an increase in C4 vegetation is reported from Lobatse Cave between ~45-40 ka. Between ~41-32 ka, a return to cool and wet conditions is indicated from grass and forest pollen at the Tswaing crater, and a shift from C4 dominated vegetation to more C3 grasses is interpreted from the Sudwala speleothem record (Green et al., 2015). An intensification and equatorward shift in the westerlies is suggested to have occurred around 32 ka and persisted into MIS 2, producing a winter rainfall dominated regime. Altogether these proxy records point to a mosaic of moisture availability and climate conditions in the region during this time.

Evidence of dune activity at the start of MIS 3 (57-52 ka) from the Witpan dune field suggests reduced moisture conditions, or increased windiness and evaporation (Figure 8.2; Telfer and Thomas, 2007). The re-establishment of the Makgadikgadi mega-lake high-stand by 38.7 ± 1.8 ka (Figure 8.2; Burrough et al., 2009b) supports a period of greater regional water availability during the latter part of MIS 3, coinciding with the second episode of Ga-Mohana tufa formation. The Witpan dune record suggests increasing aridity following the mega-lake high-stand, from late MIS 3 and across the boundary into MIS 2.

Evidently, during MIS 3, the southern Kalahari experienced oscillating conditions with alternating periods of warm and dry, and cool and moist conditions. Nevertheless, conditions at Ga-Mohana Hill supported the formation of tufa during much of this time. Evidence of human occupation at Ga-Mohana Hill and Kathu Pan occurs toward the end of this period, and this may suggest that human occupation at these sites overlapped with a period of decreasing water availability, but the error ranges on the age estimates make it challenging to confidently assert this (Figure 8.3).

8.2.4 MIS 2 (~29 – 14 ka)

Marine Isotope Stage 2 incorporates the Last Glacial Maximum (LGM), a period of maximum ice volume in the northern hemisphere, and minimum temperatures in the southern hemisphere (Figure 8.1d) (Petherick et al., 2022). The timing and duration of the LGM in southern Africa is debated, but is generally thought to have occurred between ~23 – 19 ka (Mix et al., 2001). The Cold Air Cave speleothem record indicates temperatures ~6°C lower than present during the LGM (Holmgren et al., 2003). Multiple proxy records from the SRZ in South Africa indicate dry conditions during this period (Scott, 1989; Metcalfe, 1993; Partridge et al., 1993), although evidence for small-scale glaciation in Lesotho and the Drakensberg mountains indicate an increase in moisture, associated with a northward shift in the Westerlies (Mills et al., 2012).

There is little to no evidence for tufa formation at Ga-Mohana Hill during MIS 2, and it is likely that reduced rainfall (Figure 8.2b), coupled with colder temperatures and decreased atmospheric CO_2 (Figure 8.1) impeded the Ga-Mohana tufa system during this time. Erosion and dismantling of the tufa deposits may have occurred during this episode of quiescence. A carbonate hardpan layer at Kathu Pan, dated to 22.2 ± 1.2 ka (Figure 8.2) indicates pan-wide drying and evidence of arid conditions throughout MIS 2, until 10.4 ka (Lukich et al., 2019). A single Ga-Mohana tufa sample, dated to 10.74 ± 4.93 ka, has a large error of nearly 50%, which overlaps with the MIS 2 / Holocene boundary. Stable isotope data from ostrich eggshells at Equus Cave indicate temperature and rainfall minimums between ~17 to 14 ka, and increasing rainfall after ~ 14 ka (Johnson et al., 1997). At Erfkroon, a shift to colder and drier conditions between ~28-15.5 ka is also recorded, with a return to seasonal moisture availability at the end of MIS 2 (Figure 8.2; Lyons et al., 2014). This evidence seems to indicate that the interior region was dry during the LGM, with a return to humid conditions from ~14 ka. However, contradictory evidence from a portion of the Wonderwerk Cave stalagmite, dated to ~23-17 ka, is interpreted to indicate cool and wet conditions during the LGM, followed by a period of aridity at the MIS 2 / Holocene transition (Figure 8.2; Brook et al., 2010). Two mega-lake high-stand phases occurred during early and late MIS 2, alternating with the existence of dune fields at Witpan (Figure 8.2). As such,

palaeoenvironmental conditions in the northern interior region during MIS 2 remain unresolved.

Evidence for human activity at Ga-Mohana Hill is also lacking, except towards the end of MIS 2. Evidence for human activity at Ga-Mohana Hill around 14.8 ± 0.8 ka comes from the upper layer of excavation sediments, DBGS, which include LSA-type lithic artefacts, such as bladelets, and ostrich eggshell beads (Wilkins et al., 2020; Hatton et al., 2022). This timing falls within the error margin of the tufa sample dated to 10.74 ± 4.93 ka, and coincides with other regional evidence for increasing moisture availability (Figure 8.2). Records from other nearby sites indicate human activity in the area despite evidence for aridity during this time (Figure 8.3). At Kathu Pan, artefact-bearing sediments indicate human occupation during the LGM associated with evidence for relatively drier conditions (Figure 8.3; Beaumont and Morris, 1990; Porat et al., 2010). Late glacial deposits at Wonderwerk Cave also indicate an association of dry conditions and human occupation (Figure 8.3; Chazan et al., 2012). Thus, MIS 2 provides very little coherence with respect to the relationship between water availability and human occupation.

8.2.5 Holocene (~14 ka - present)

The Holocene, or MIS 1, is the present interglacial period, which is characterised by a decrease in global ice volume and an increase in global temperatures following deglaciation after the LGM (Figure 8.1). Despite this general warming trend, significant climatic fluctuations within this period have been identified, predominantly from northern hemisphere records, e.g. cold periods such as the Younger Dryas (~13 to 11.5 ka), the 8.2 ka event, and the Little Ice Age (~1.85 – 1.3 ka). These events were driven by melt-water pulses in the northern hemisphere, and evidence of a response to these cool events in southern Africa has been documented in several proxies (e.g. Holmgren et al., 2003; Thackeray and Scott, 2006; Chase et al., 2015; Fitchett et al., 2016). Overall, Holocene conditions in southern Africa are characterised by warm and dry conditions, punctuated with seasonal moisture availability (Chase and Meadows, 2007; Lyons et al., 2014; Fitchett, 2019; Scott et al., 2022).

Evidence of two phases of tufa formation at Ga-Mohana Hill during the Holocene come from three samples; two cascades that date to the early to mid-Holocene, with ages of 10.74 ± 4.93 ka and 7.27 ± 0.31 ka, and one dome sample dated to the late Holocene with an age of 3 ± 0.91 ka. There is a marked increase in $\delta^{18}O$ values between the two cascade samples in the early Holocene, and this may reflect the increasing temperatures following the deglaciation. In contrast, the $\delta^{13}C$ values from these samples are constant, and indicate mixed C3 and C4 vegetation and carbon input from the dolomitic bedrock, i.e. warmer temperatures and prolonged groundwater residence times. The last episode of tufa formation is associated with the highest $\delta^{18}O$ and $\delta^{13}C$ values, and this suggests the dominance of kinetic fractionation in the formation of this tufa, likely driven by rapid degassing via the drip-and-splash process, and / or evaporation of the tufa-forming water. It is likely that during the Holocene, tufa formation occurred during episodes of ephemeral flow.

The first tufa-forming episode at Ga-Mohana Hill is defined by two tufas dated to 10.74 ± 4.93 ka and 7.27 ± 0.31 ka. A tufa from Groot Kloof is also dated to 10.7 ± 0.23 ka, indicating concurrent tufa formation at both Ga-Mohana Hill and along the Ghaap escarpment at the start of the Holocene. In addition, ostrich eggshell isotope records from Equus Cave are interpreted as evidence for increasing rainfall between ~14 to 6 ka (Johnson et al., 1997). These records are evidence for water availability in the southern Kalahari at this time. Intermittent layers of pedogenic $CaCO_3$ at Kathu Pan during the Holocene suggests episodes of aridity, with some alternating organics suggestive of marsh conditions (Lukich et al., 2019). At Wonderwerk Cave, a hiatus in the stalagmite between ~13 to 4 ka is interpreted to indicate drier conditions for much of the Holocene (Brook et al., 2010; Brook et al., 2015), whereas evidence for wetter conditions coincide with the last episode of Ga-Mohana tufa formation. The first phase of Ga-Mohana tufa formation overlaps with dune activity at Witpan, which is followed by a last mega-lake high-stand in the Makgadikgadi basin (Figure 8.2; Telfer and Thomas, 2007; Burrough et al., 2009b). Despite these fluctuating climatic and environmental conditions, there is persistent evidence for human occupation in this southern Kalahari region during the Holocene (Porat et al., 2010; Ecker et al., 2017; Lukich et al., 2020).

8.2.6 Concluding remarks and future work

The tufas at Ga-Mohana Hill indicate that MIS 5d, much of MIS 4 and 3, and parts of the Holocene, were characterised by moisture availability and conditions conducive to tufa precipitation. It is apparent that periods of tufa formation at Ga-Mohana Hill coincide with cooler conditions (e.g. MIS 5d and MIS 4). This is in contrast to the common perception that tufa formation occurs during 'warm and wet' periods. The fact that temperatures were relatively cool during these times of tufa formation suggests that reduced evaporation was important in creating favourable conditions for tufa formation in the southern Kalahari.

In comparing the three sites of Ga-Mohana Hill, Kathu Pan and Wonderwerk Cave, it is apparent that before ~71 ka, human occupation of the southern Kalahari region appears to have been associated with the availability of water, whereas after ~71 ka, the timing of human occupation and wet periods do not coincide (Figure 8.3). Particularly after ~32 ka and during the Holocene, human occupation of the region appears to coincide with fluctuating and drier conditions, which may point to the development of arid-adaptive behaviours. This apparent decoupling of human occupation and water availability needs to be further explored to determine whether the absence of archaeological evidence during MIS4 and the early stages of MIS3 is evidence of absence, or whether issues with site formation, site visibility and/or dating challenges explain why no archaeological deposits dating to this time have yet been identified. Further exploration of cultural developments, beyond the dichotomy of occupation / no occupation, may also aid in understanding changing human behaviours.

A limit in this thesis is the number and nature of dated samples. The stages of tufa formation presented here are based on twelve disparate samples from across the hillside. More dated tufa from Ga-Mohana would provide additional data to test whether tufa formation is indeed restricted to these stages. Specifically, single tufa samples that can provide a continuous / semi-continuous chronology, linked with higher resolution stable isotope sampling would provide more insight into changing environmental conditions at this site, beyond evidence for activation of the tufa system

and water availability. This continuous, high resolution data could be linked with the high resolution LA-ICP-MS trace element data, and relationships between the trace element and stable isotope data investigated. Further investigation of micro-morphological features, specifically using SEM, would provide complementary high resolution mineralogical data that may also provide additional palaeoenvironmental insights.

8.3 Conclusion

My aim was to investigate the depositional setting, chronology, and palaeoenvironment that the Ga-Mohana Hill tufa deposits represent, and to relate these findings to existing palaeoclimate information and archaeological records of Late Pleistocene and Holocene human occupation in the region. Here, I outline how I accomplished this and summarise my main findings.

Through field observations and petrographic analysis of the Ga-Mohana tufa deposits, I characterised the depositional environment as a perched springline tufa system that produced shallow streams, cascading waterfalls, and pools of standing water (Chapter 4). Tufa formation likely followed a similar three phase model of deposition to that described by Viles et al. (2007) based on the Brandfontein River system in the Naukluft mountains of Namibia. That is, 1) a phase of perennial, low energy water flow that allowed for the development of mosses in continuous flow areas, and the development of slack-water environments, e.g. stage 2 tufa formation, 2) a phase of high flow producing episodic and patchy erosion, e.g. stage 3 tufa formation, and 3) a phase of ephemeral flow, e.g. stage 4 and 5 tufa formation.

I established that calcite is the main crystalline phase, with minor quartz and dolomite present in some samples. High resolution LA-ICP-MS data indicates elevated Mg contents in the Ga-Mohana tufas. This is likely to be in part a consequence of the inclusion of dolomite in the tufas, and may also indicate periods of low recharge due to prolonged contact between groundwater and the dolomitic aquifer. I observed that Mg and U contents tend to co-vary. While more in-depth analysis of the U concentrations was beyond the scope of this study, more detailed investigation of these elements, coupled with analysis of the soils, may provide further insights into the palaeohydrology at this site, e.g. Maher et al. (2014).

Analysis of tufa using LA-ICP-MS proved useful for imaging the U and Th concentrations in the tufa prior to sampling for U-Th dating, and I showed that U-Th

dating of tufas, buoyed by LA-ICP-MS screening to avoid sections of tufa with elevated PCB elements, can produce precise ages. As such, LA-ICP-MS can be a valuable tool for evaluating optimal areas for U-Th dating, particularly in difficult samples. However, LA-ICP-MS is a costly and time-consuming exercise, and it is not clear that these costs justify the benefits. The value in this method is the ability to image spatial relationships between elements at a very high resolution. As such, it is best paired with other high-resolution data and sampling methods, e.g. sub-annual/seasonally resolved chronology, continuous micro-milled isotope data, and supported with more present-day monitoring data, e.g. Carlson et al. (2018).

Trace elements measured via solution are comparable to those measured using laser ablation, given the coarse resolution and with the effect of sample digestion on various elements taken into account. Thorium was below the detection limit of the solution method, and as such this method cannot be used to 'screen' samples for Th content, but other PCB elements, such as Al and Pb, can be used as a proxy for Th since these elements tend to be elevated in conjunction with elevated Th. The solution method is thus adequate for addressing questions related to conditions of tufa formation based on broad element patterns in tufa samples, complimentary to U-Th ages such as those presented in this study. Trace element analyses were less well suited for palaeoclimate interpretation in this study, however this could be an interesting avenue of future research targeting suitable portions of samples that satisfy the right criteria.

The U-Th age results I obtained span the last interglacial cycle, indicating tufa formation, i.e. spring activity, over the last ~114 ka. I identified five intervals of tufa formation at Ga-Mohana Hill, defined by distinct groups of overlapping ages and their associated 2σ uncertainties. These intervals, which represent episodes of increased moisture availability, occurred at approximately 114-100 ka, 73-48 ka, 44-32 ka, 15-6 ka, and ~3 ka. The 2σ uncertainties associated with the ages are small; most samples are associated with errors of <3 ka (on average approximately 1 ka) except for two samples, GHS-5 and GHS-6.3, which have an uncertainty of 4.9 ka (49%) and 4.2 ka (7.9%) respectively. These larger errors are due to a high detrital Th component.

While the presence of tufa deposits is evidence of water availability, the oxygen and carbon isotope values of these deposits provides a more nuanced picture of environmental conditions, beyond the interpretation of wet vs dry. The intermediate $\delta^{13}C$ values of tufa samples dated to MIS 5d, 3, and the early Holocene, indicates a mixed contribution of carbon from the soil-zone and dolomitic bedrock, and/or a predominance of C4 vegetation. These conditions point to relatively drier conditions (although there would have been sufficient moisture available for aquifer recharge and spring activity), either due to seasonal rainfall, and/or higher rates of evaporation linked to moderate to warm temperatures. On the other hand, samples from tufa stage 2 (MIS 4 / / early MIS 3) suggest a higher contribution of carbon from the soil zone compared to input from the bedrock, and a greater proportion of C3 vegetation during this period (~70 ka to ~53 ka). This was likely supported by prolonged, year-round rainfall and reduced rates of evaporation due to cooler temperatures. The overall increase in $\delta^{13}C$ and $\delta^{18}O$ values from the end of tufa stage 2 (late MIS 4 / early MIS 3) into tufa stage 3 (late MIS 3) and the Holocene, indicates a gradual shift in conditions to a higher proportion of C4 grasses, indicating an overall trend towards aridity.

In this southern Kalahari region, with limited, seasonal rainfall and no evidence of actively precipitating tufa, the relict tufa deposits at Ga-Mohana Hill represent past periods of water availability and associated productivity on the landscape. I have shown that Ga-Mohana Hill was characterised by shallow streams, cascading waterfalls and pools of standing water during five intervals over the last ~114 ka. In addition, I showed that these intervals were not restricted to interglacial periods, and in fact, intermediate periods, i.e. cooler temperatures, favour tufa formation as mild temperatures balance effective moisture and evaporation. These results challenge global generalisations of past climate change and highlight the necessity for regionally specific models, in accordance with other recent studies (Chevalier and Chase, 2015; Ecker et al., 2018; Lukich and Ecker, 2021; Weij et al., 2024).

Early human population distributions in the southern Kalahari appear to have been modulated by water availability before ~71 ka. After ~71 ka, the picture is much less clear. Despite evidence for wetter conditions, archaeological deposits dating to MIS 4 and the

early part of MIS 3 have not yet been identified in the punctuated record of human occupation at Ga-Mohana Hill, nor at nearby Kathu Pan or Wonderwerk Cave. This result poses a new dilemma, in that wet conditions in this region of the southern Kalahari should have theoretically made it attractive for human occupation, but as of yet, no archaeological deposits date to this time. The time interval corresponding to MIS 2 provides little coherence with respect to the relationship between water availability and human occupation. The three records considered here do not agree on whether conditions were wetter or drier during the LGM and humans appeared to have occupied the region through both the LGM and late glacial. Others have highlighted that the palaeoenvironmental record for MIS 2 across the Kalahari Basin and surrounding regions is complex, documenting a high degree of spatial and temporal variability (Lukich and Ecker, 2021). This lack of coherence may be in part due to the variable responses of palaeoenvironmental proxies to temperature and water availability changes, and potentially lags in responses. A shift in seasonality may also play a role, with some proxies responding to seasonality changes for precipitation, as evidenced at Kathu Pan (Lukich et al., 2020), as opposed to mean annual precipitation.

Identifying the timing and nature of human occupation in the Kalahari Desert is critical for understanding the emergence of our ability to adapt to new and extreme environments (Roberts and Stewart, 2018). For a long time, the Kalahari Desert has been considered too arid for early human populations to persist, and evidence for occupation was assumed to represent wetter periods. Until now, a rarity of integrated palaeoenvironmental and archaeological records has largely prevented adequate testing of these assumptions. The results presented here provide evidence for prolonged periods of water availability in the southern Kalahari Basin through much of the Late Pleistocene. There is a positive association with wet conditions and human occupation before ~71 ka. However, by the LGM, water availability alone did not mediate human occupation in the southern Kalahari Desert. This result challenges the traditional view that links wet periods to human occupation, and the decoupling of human occupation and wet phases in the Late Pleistocene could reflect new social and technological adaptations that helped hunter-gatherers cope more effectively with diverse environmental conditions.

REFERENCES

Alexandrowicz, W. P. 2012. Assemblages of molluscs from Sulisławice (Małopolska Upland, southern Poland) and their significance for interpretation of depositional conditions of calcareous tufas in small water bodies. *Annales Societatis Geologorum Poloniae*, 82(2), 161-176.

Altermann, W. & Wotherspoon, J. M. 1995. The carbonates of the Transvaal and Griqualand West sequences of the Kaapvaal craton, with special reference to the Lime Acres limestone deposit. *Mineralium Deposita,* 30, 124-134.

Ambrose, S. H. & Lorenz, K. G. 1990. Social and ecological models for the Middle Stone Age in southern Africa. *In:* Mellars, P. (Ed). *The Emergence of Modern Humans: an Archaeological Perspective* Edinburgh: Edinburgh University Press, 3-33.

Andrews, J. E. 2006. Palaeoclimatic records from stable isotopes in riverine tufas: synthesis and review. *Earth-Science Reviews,* 75**,** 85-104.

Andrews, J., Riding, R. & Dennis, P. 1993. Stable isotopic compositions of recent freshwater cyanobacterial carbonates from the British Isles: local and regional environmental controls. *Sedimentology,* 40**,** 303-314.

Andrews, J. E., Riding, R. & Dennis, P. F. 1997. The stable isotope record of environmental and climatic signals in modern terrestrial microbial carbonates from Europe. *Palaeogeography, Palaeoclimatology, Palaeoecology,* 129**,** 171-189.

Andrews, J. E., Pedley, M. & Dennis, P. F. 2000. Palaeoenvironmental records in Holocene Spanish tufas: a stable isotope approach in search of reliable climatic archives. *Sedimentology,* 47**,** 961-978.

Andrews, J. E. & Brasier, A. T. 2005. Seasonal records of climatic change in annually laminated tufas: short review and future prospects. *Journal of Quaternary Science: Published for the Quaternary Research Association,* 20(5)**,** 411-421.

Archer, D., Winguth, A., Lea, D. & Mahowald, N. 2000. What caused the glacial/interglacial atmospheric pCO_2 cycles? *Reviews of Geophysics,* 38**,** 159-189.

Arenas, C., Gutiérrez, F., Osácar, C. & Sancho, C. 2000. Sedimentology and geochemistry of fluvio-lacustrine tufa deposits controlled by evaporite solution subsidence in the central Ebro Depression, NE Spain. *Sedimentology,* 47**,** 883-909.

Arenas, C., Cabrera, L. & Ramos, E. 2007. Sedimentology of tufa facies and continental microbialites from the Palaeogene of Mallorca Island (Spain). *Sedimentary Geology,* 197**,** 1-27.

Arenas-Abad, C., Vázquez-Urbez, M., Pardo-Tirapu, G. & Sancho-Marcén, C. 2010. Fluvial and associated carbonate deposits. In *Carbonates in Continental Settings: Facies, Environments, and Processes.* Alonso-Zarza, A.M. & Tanner, L.H. (Eds.) *Developments in Sedimentology,* 61**,** 133-175.

Arenas, C. & Jones, B. 2017. Temporal and environmental significance of microbial lamination: insights from recent fluvial stromatolites in the River Piedra, Spain. *Sedimentology,* 64**,** 1597-1629.

Arenas, C., Osácar, M. C., Auqué, L. & Sancho, C. 2019. Coupling textural and stable-isotope variations in fluvial stromatolites: comparison of Pleistocene and recent records in NE Spain. *Journal of Palaeogeography,* 8, 1-20.

Arp, G., Bissett, A., Brinkmann, N., Cousin, S., De Beer, D., Friedl, T., Mohr, K. I., Neu, T. R., Reimer, A., Shiraishi, F., Stackebrandt, E. & Zippel, B. 2010. Tufa-forming biofilms of German karstwater streams: microorganisms, exopolymers, hydrochemistry and calcification. *Geological Society, London, Special Publications,* 336**,** 83-118.

Arp, G., Wedemeyer, N. & Reitner, J. 2001. Fluvival tufa formation in a hard-water creek (Deinschwanger Bach, Franconian Alb, Germany). *Facies,* 44**,** 1-22.

Auler, A. S. & Smart, P. L. 2001. Late Quaternary paleoclimate in semiarid northeastern Brazil from U-series dating of travertine and water-table speleothems. *Quaternary Research,* 55**,** 159-167.

Ayalon, A., Bar-Matthews, M. & Kaufman, A. 1999. Petrography, strontium, barium and uranium concentrations, and strontium and uranium isotope ratios in speleothems as palaeoclimatic proxies: Soreq Cave, Israel. *The Holocene,* 9**,** 715-722.

Backwell, L. R., Mccarthy, T. S., Wadley, L., Henderson, Z., Steininger, C. M., Bonita, D., Barré, M., Lamothe, M., Chase, B. M., Woodborne, S., Susino, G. J., Bamford, M. K., Sievers, C., Brink, J. S., Rossouw, L., Pollarolo, L., Trower, G., Scott, L. & D'errico, F. 2014. Multiproxy record of late Quaternary climate change and Middle Stone Age human occupation at Wonderkrater, South Africa. *Quaternary Science Reviews,* 99**,** 42-59.

Bailey, T., Mcarthur, J., Prince, H. & Thirlwall, M. 2000. Dissolution methods for strontium isotope stratigraphy: whole rock analysis. *Chemical Geology,* 167**,** 313-319.

Baker, A. J., Mattey, D. P. & Baldini, J. U. 2014. Reconstructing modern stalagmite growth from cave monitoring, local meteorology, and experimental measurements of dripwater films. *Earth and Planetary Science Letters,* 392**,** 239-249.

Bamford, M. K. 2015. Macrobotanical remains from Wonderwerk Cave (Excavation 1), Oldowan to Late Pleistocene (2 Ma to 14 ka bp), South Africa. *African Archaeological Review,* 32**,** 813-838.

Ban, F., Baker, A., Marjo, C. E., Duan, W., Li, X., Han, J., Coleborn, K., Akter, R., Tan, M. & Nagra, G. 2018. An optimized chronology for a stalagmite using seasonal trace element cycles from Shihua Cave, Beijing, North China. *Scientific reports,* 8**,** 4551.

Banks, V. J., Jones, P. F., Lowe, D. J., Lee, J. R., Rushton, J. & Ellis, M. A. 2012. Review of tufa deposition and palaeohydrological conditions in the White Peak, Derbyshire, UK: implications for Quaternary landscape evolution. *Proceedings of the Geologists' Association,* 123**,** 117-129.

Bar-Matthews, M., Ayalon, A., Matthews, A., Sass, E. & Halicz, L. 1996. Carbon and oxygen isotope study of the active water-carbonate system in a karstic

Mediterranean cave: Implications for paleoclimate research in semiarid regions. *Geochimica et Cosmochimica Acta,* 60**,** 337-347.

Bar-Matthews, M., Ayalon, A. & Kaufman, A. 1997. Late Quaternary paleoclimate in the eastern Mediterranean region from stable isotope analysis of speleothems at Soreq Cave, Israel. *Quaternary Research,* 47**,** 155-168.

Bar-Matthews, M., Marean, C. W., Jacobs, Z., Karkanas, P., Fisher, E. C., Herries, A. I. R., Brown, K., Williams, H. M., Bernatchez, J., Ayalon, A. & Nilssen, P. J. 2010. A high resolution and continuous isotopic speleothem record of paleoclimate and paleoenvironment from 90 to 53 ka from Pinnacle Point on the south coast of South Africa. *Quaternary Science Reviews,* 29**,** 2131-2145.

Barham, L. & Mitchell, P. 2008. *The first Africans: African archaeology from the earliest tool makers to most recent foragers*. Cambridge: Cambridge University Press

Barnes, J., Lang, E. & Potratz, H. 1956. Ratio of ionium to uranium in coral limestone. *Science,* 124**,** 175-176.

Barnes, I. & O'Neil, J. R. 1969. The relationship between fluids in some fresh alpine-type ultramafics and possible modern serpentinization, western United States. *Geological Society of America Bulletin,* 80**,** 1947-1060.

Barnes, I. & O'Neil, J. R. 1971. Calcium-magnesium carbonate solid solutions from Holocene conglomerate cements and travertines in the Coast Range of California. *Geochimica et Cosmochimica Acta,* 35**,** 699-718.

Bean, J. A. 2003. *A criticial review of recharge estimation methods used in southern Africa.* PhD thesis. University of the Free State.

Beaumont, P. B. 1990. Kathu Pan. In *Guide to archaeological sites in the Northern Cape.* Beaumont, P. B. & Morris, D. (Eds.) Kimberley: McGregor Museum, 75-100

Beaumont, P. B. & Vogel, J. C. 1993. What turned the young tufas on at Gorrokop? *South African Journal of Science,* 89**,** 196-198.

Beaumont, P. B. 2004. Kathu Pan and Kathu Townlands/Uitkoms. In *Archaeology in the Northern Cape; some key sites.* Beaumont, P. B. & Morris, D. (Eds.) Kimberley: McGregor Museum, 50-52

Beaumont, P. B. & Vogel, J. C. 2006. On a timescale for the past million years of human history in central South Africa. *South African Journal of Science,* 102, 217-228

Belli, R., Borsato, A., Frisia, S., Drysdale, R., Maas, R. & Greig, A. 2017. Investigating the hydrological significance of stalagmite geochemistry (Mg, Sr) using Sr isotope and particulate element records across the Late Glacial-to-Holocene transition. *Geochimica et Cosmochimica Acta,* 199**,** 247-263.

Bereiter, B., Eggleston, S., Schmitt, J., Nehrbass-Ahles, C., Stocker, T. F., Fischer, H., Kipfstuhl, S. & Chappellaz, J. 2015. Revision of the EPICA Dome C CO_2 record from 800 to 600 kyr before present. *Geophysical Research Letters,* 42**,** 542-549.

Berger, A. & Loutre, M.-F. 1991. Insolation values for the climate of the last 10 million years. *Quaternary science reviews,* 10**,** 297-317.

Berna, F., Goldberg, P., Horwitz, L. K., Brink, J., Holt, S., Bamford, M. & Chazan, M. 2012. Microstratigraphic evidence of *in situ* fire in the Acheulean strata of Wonderwerk Cave, Northern Cape province, South Africa. *Proceedings of the National Academy of Sciences,* 109**,** E1215-E1220.

Beukes, N. J. 1987. Facies relations, depositional environments and diagenesis in a major early Proterozoic stromatolitic carbonate platform to basinal sequence, Campbellrand Subgroup, Transvaal Supergroup, Southern Africa. *Sedimentary Geology,* 54**,** 1-46.

Bischoff, J. L. & Fitzpatrick, J. A. 1991. U-series dating of impure carbonates: an isochron technique using total-sample dissolution. *Geochimica et Cosmochimica Acta,* 55, 543-554.

Blome, M. W., Cohen, A. S., Tryon, C. A., Brooks, A. S. & Russell, J. 2012. The environmental context for the origins of modern human diversity: a synthesis of regional variability in African climate 150,000-30,000 years ago. *Journal of Human Evolution,* 62**,** 563-92.

Borsato, A., Frisia, S., Fairchild, I. J., Somogyi, A. & Susini, J. 2007. Trace element distribution in annual stalagmite laminae mapped by micrometer-resolution X-ray fluorescence: implications for incorporation of environmentally significant species. *Geochimica et Cosmochimica Acta,* 71**,** 1494-1512.

Borsato, A., Johnston, V. E., Frisia, S., Miorandi, R. & Corradini, F. 2016. Temperature and altitudinal influence on karst dripwater chemistry: Implications for regional-scale palaeoclimate reconstructions from speleothems. *Geochimica et Cosmochimica Acta,* 177**,** 275-297.

Bourdon, B., Turner, S., Henderson, G. M. & Lundstrom, C. 2003. Introduction to U-series geochemistry. *Reviews in Mineralogy and Geochemistry,* 52**,** 1-21.

Bowen, G. J. & Revenaugh, J. 2003. Interpolating the isotopic composition of modern meteoric precipitation. *Water Resources Research,* 39(10), 1299.

Brasier, A. T., Andrews, J. E., Marca-Bell, A. D. & Dennis, P. F. 2010. Depositional continuity of seasonally laminated tufas: implications for $\delta^{18}O$ based palaeotemperatures. *Global and Planetary Change,* 71**,** 160-167.

Braun, K., Bar-Matthews, M., Matthews, A., Ayalon, A., Cowling, R. M., Karkanas, P., Fisher, E. C., Dyez, K., Zilberman, T. & Marean, C. W. 2019. Late Pleistocene records of speleothem stable isotopic compositions from Pinnacle Point on the South African south coast. *Quaternary Research,* 91**,** 265-288.

Braun, K., Bar-Matthews, M., Matthews, A., Ayalon, A., Zilberman, T., Cowling, R. M., Fisher, E. C., Herries, A. I. R., Brink, J. S. & Marean, C. W. 2020. Comparison of climate and environment on the edge of the Palaeo-Agulhas Plain to the Little Karoo (South Africa) in Marine Isotope Stages 5–3 as indicated by speleothems. *Quaternary Science Reviews,* 235, 105803.

Bredenkamp, D. & Vogel, J. 1970. Study of a dolomitic aquifer with carbon-14 and tritium. *Symposium on isotope hydrology, IAEA*. 9-13 March 1970. Vienna, Austria.

Bredenkamp, D., Schutte, J. & Du Toit, G. 1974. Recharge of a dolomitic aquifer as determined from tritium profiles. *Symposium on isotope techniques in groundwater hydrology, IAEA*. 11-15 March 1974. Vienna, Austria.

Brink, J. S. 1997. Direct dating of the Florisbad fossil hominid. *Culna,* 1997**,** 52, 7-9.

Broecker, W. S., Peteet, D. M. & Rind, D. 1985. Does the ocean–atmosphere system have more than one stable mode of operation? *Nature,* 315**,** 21-26.

Brook, G. A., Railsback, L. B., Scott, L., Voarintsoa, N. R. G. & Liang, F. 2015. Late Holocene stalagmite and tufa climate records for Wonderwerk Cave: relationships between archaeology and climate in southern Africa. *African Archaeological Review,* 32**,** 669-700.

Brook, G. A., Scott, L., Railsback, L. B. & Goddard, E. A. 2010. A 35 ka pollen and isotope record of environmental change along the southern margin of the Kalahari from a stalagmite and animal dung deposits in Wonderwerk Cave, South Africa. *Journal of Arid Environments,* 74**,** 870-884.

Bruch, A. A., Sievers, C. & Wadley, L. 2012. Quantification of climate and vegetation from southern African Middle Stone Age sites – an application using Late Pleistocene plant material from Sibudu, South Africa. *Quaternary Science Reviews,* 45**,** 7-17.

Buccino, G., D'argenio, B., Ferreri, V., Brancaccio, L., Ferreri, M., Panichi, C. & Stanzione, D. 1978. I travertini della Bassa Valle del Tanagro (Campania); studio geomorfologico, sedimentologico e geochimico. *Bollettino della Societa Geologica Italiana,* 97**,** 617-646.

Burdanowitz, N., Dupont, L., Zabel, M. & Schefus, E. 2018. Holocene hydrologic and vegetation developments in the Orange River catchment (South Africa) and their controls. *The Holocene,* 28**,** 1288-1300.

Burrough, S. L. 2016. Late Quaternary environmental change and human occupation of the southern African interior. In *Africa from MIS 6-2: Population dynamics and Palaeoenvironments.* Jones, S.C. & Stewart, B.A. (Eds.) *Vertebrate Palaeobiology and Palaeoanthropology.* Dordrecht: Springer, 161-174.

Burrough, S. L., Thomas, D. S. G., Shaw, P. A. & Bailey, R. M. 2007. Multiphase Quaternary highstands at Lake Ngami, Kalahari, northern Botswana. *Palaeogeography, Palaeoclimatology, Palaeoecology,* 253**,** 280-299.

Burrough, S. L., Thomas, D. S. G. & Bailey, R. M. 2009a. Mega-Lake in the Kalahari: a Late Pleistocene record of the Palaeolake Makgadikgadi system. *Quaternary Science Reviews,* 28**,** 1392-1411.

Burrough, S. L., Thomas, D. S. G. & Singarayer, J. S. 2009b. Late Quaternary hydrological dynamics in the Middle Kalahari: forcing and feedbacks. *Earth-Science Reviews,* 96**,** 313-326.

Burrough, S. L. & Thomas, D. S. G. 2013. Central southern Africa at the time of the African Humid Period: a new analysis of Holocene palaeoenvironmental and palaeoclimate data. *Quaternary Science Reviews,* 80, 29-46.

Butzer, K. W. 1974. Geo-archeological interpretation of Acheulian calc-pan sites at Doornlaagte and Rooidam (Kimberley, South Africa). *Journal of Archaeological Science,* 1, 1-25.

Butzer, K. W., Stuckenrath, R., Bruzewicz, A. & Helgren, D. 1978. Late Cenozoic paleoclimates of the Gaap Escarpment, Kalahari margin, South Africa. *Quaternary Research,* 10, 310-339.

Butzer, K. W. 1984. Late quaternary environments in South Africa. *Late Cainozic palaeoclimates of the Southern Hemisphere. International symposium held by the South African Society for Quaternary Research*. 29 August 1983. Swaziland. 235-264.

Caley, T., Extier, T., Collins, J. A., Schefuss, E., Dupont, L., Malaize, B., Rossignol, L., Souron, A., Mcclymont, E. L., Jimenez-Espejo, F. J., Garcia-Comas, C., Eynaud, F., Martinez, P., Roche, D. M., Jorry, S. J., Charlier, K., Wary, M., Gourves, P. Y., Billy, I. & Giraudeau, J. 2018. A two-million-year-long hydroclimatic context for hominin evolution in southeastern Africa. *Nature,* 560, 76-79.

Capezzuoli, E., Gandin, A. & Sandrelli, F. 2010. Calcareous tufa as indicators of climatic variability: a case study from southern Tuscany (Italy). *Geological Society, London, Special Publications,* 336, 263-281.

Capezzuoli, E., Gandin, A. & Pedley, M. 2014. Decoding tufa and travertine (fresh water carbonates) in the sedimentary record: the state of the art. *Sedimentology,* 61, 1-21.

Carlson, P. E., Miller, N. R., Banner, J. L., Breecker, D. O. & Casteel, R. C. 2018. The potential of near-entrance stalagmites as high-resolution terrestrial paleoclimate proxies: application of isotope and trace-element geochemistry to seasonally-resolved chronology. *Geochimica et Cosmochimica Acta,* 235, 55-75.

Carthew, K. D., Taylor, M. P. & Drysdale, R. N. 2003. Are current models of tufa sedimentary environments applicable to tropical systems? A case study from the Gregory River. *Sedimentary Geology,* 162, 199-218.

Carthew, K. D., Taylor, M. P. & Drysdale, R. N. 2006. An environmental model of fluvial tufas in the monsoonal tropics, Barkly karst, northern Australia. *Geomorphology,* 73, 78-100.

Cerling, T. E. 1984. The stable isotopic composition of modern soil carbonate and its relationship to climate. *Earth and Planetary Science Letters,* 71, 229-240.

Cerling, T. E., Solomon, D. K., Quade, J. & Bowman, J. R. 1991. On the isotopic composition of carbon in soil carbon dioxide. *Geochimica et Cosmochimica Acta,* 55, 3403-3405.

Cerling, T. E. & Quade, J. 1993. Stable carbon and oxygen isotopes in soil carbonates. *Geophysical Monograph Series,* 78, 217-231.

Chafetz, H. S. & Folk, R. L. 1984. Travertines: depositional morphology and the bacterially constructed constituents. *Journal of Sedimentary Research,* 54**,** 289-316.

Chafetz, H., Rush, P. F. & Utech, N. M. 1991. Microenvironmental controls on mineralogy and habit of $CaCO_3$ precipitates: an example from an active travertine system. *Sedimentology,* 38**,** 107-126.

Chafetz, H. S. & Lawrence, J. R. 1994. Stable isotopic variability within modern travertines. *Géographie physique et Quaternaire,* 48**,** 257-273.

Chase, B. M. 2010. South African palaeoenvironments during marine oxygen isotope stage 4: a context for the Howiesons Poort and Still Bay industries. *Journal of Archaeological Science,* 37**,** 1359-1366.

Chase, B. M. & Meadows, M. E. 2007. Late Quaternary dynamics of southern Africa's winter rainfall zone. *Earth-Science Reviews,* 84**,** 103-138.

Chase, B. M., Meadows, M. E., Carr, A. S. & Reimer, P. J. 2010. Evidence for progressive Holocene aridification in southern Africa recorded in Namibian hyrax middens: Implications for African Monsoon dynamics and the "African Humid Period". *Quaternary Research,* 74**,** 36-45.

Chase, B. M., Boom, A., Carr, A. S., Carré, M., Chevalier, M., Meadows, M. E., Pedro, J. B., Stager, J. C. & Reimer, P. J. 2015. Evolving southwest African response to abrupt deglacial North Atlantic climate change events. *Quaternary Science Reviews,* 121**,** 132-136.

Chase, B., Harris, C., De Wit, M. J., Kramers, J., Doel, S. & Stankiewicz, J. 2021. South African speleothems reveal influence of high- and low-latitude forcing over the past 113.5 ky. *Geology*. 49(11), 1353-1357.

Chazan, M., Avery, D. M., Bamford, M. K., Berna, F., Brink, J., Fernandez-Jalvo, Y., Goldberg, P., Holt, S., Matmon, A., Porat, N., Ron, H., Rossouw, L., Scott, L. & Horwitz, L. K. 2012. The Oldowan horizon in Wonderwerk Cave (South Africa): archaeological, geological, paleontological and paleoclimatic evidence. *Journal of Human Evolution,* 63**,** 859-66.

Chazan, M., Berna, F., Brink, J., Ecker, M., Holt, S., Porat, N., Thorp, J. L. & Horwitz, L. K. 2020. Archeology, Environment, and Chronology of the Early Middle Stone Age Component of Wonderwerk Cave. *Journal of Paleolithic Archaeology,* 3**,** 302-335.

Chellat, S. 2021. Some problems of the application of the U–Th series and radiocarbon absolute dating techniques to Quaternary fluviolacustrine deposits in the Morsott commune of Algeria. *Archaeological and Anthropological Sciences,* 13, 76.

Chen, J., Zhang, D. D., Wang, S., Xiao, T. & Huang, R. 2004. Factors controlling tufa deposition in natural waters at waterfall sites. *Sedimentary Geology,* 166**,** 353-366.

Cheng, H., Lawrence Edwards, R., Shen, C.-C., Polyak, V. J., Asmerom, Y., Woodhead, J., Hellstrom, J., Wang, Y., Kong, X., Spötl, C., Wang, X. & Calvin Alexander, E.

2013. Improvements in ^{230}Th dating, ^{230}Th and ^{234}U half-life values, and U–Th isotopic measurements by multi-collector inductively coupled plasma mass spectrometry. *Earth and Planetary Science Letters,* 371-372**,** 82-91.

Cherdyntsev, V., Chalov, P. & Khaidarov, G. 1955. Uranium series disequilibrium dating. *Transactions of the 3rd Session of the Commission for determining the absolute age of geological formations: Izd. Akad. Nauk., Moscú, URSS***,** 175-182.

Chevalier, M. & Chase, B. M. 2015. Southeast African records reveal a coherent shift from high- to low-latitude forcing mechanisms along the east African margin across last glacial–interglacial transition. *Quaternary Science Reviews,* 125**,** 117-130.

Claes, H., Marques Erthal, M., Soete, J., Özkul, M. & Swennen, R. 2017. Shrub and pore type classification: petrography of travertine shrubs from the Ballık-Belevi area (Denizli, SW Turkey). *Quaternary International,* 437**,** 147-163.

Clark, I. D. & Fritz, P. 1997. *Environmental Isotopes in Hydrogeology*. Boca Raton, Florida: CRC press.

Cockcroft, M., Wilkinson, M. & Tyson, P. 1987. The application of a present-day climatic model to the late Quaternary in southern Africa. *Climatic Change,* 10**,** 161-181.

Collatz, G.J., Berry, J.A. & Clark, J.S. 1998. Effects of climate and atmospheric CO_2 partial pressure on the global distribution of C4 grasses: present, past, and future. *Oecologia*, 114, 441-454.

Collins, J. A., Schefus, E., Govin, A., Mulitza, S. & Tiedemann, R. 2014. Insolation and glacial–interglacial control on southwestern African hydroclimate over the past 140 000 years. *Earth and Planetary Science Letters,* 398**,** 1-10.

Compton, J. S. 2016. *Human Origins*. Cape Town: Earthspun Books.

Copeland, S. R., Cawthra, H. C., Fisher, E. C., Lee-Thorp, J. A., Cowling, R. M., Le Roux, P. J., Hodgkins, J. & Marean, C. W. 2016. Strontium isotope investigation of ungulate movement patterns on the Pleistocene Paleo-Agulhas plain of the Greater Cape floristic region, South Africa. *Quaternary Science Reviews,* 141**,** 65-84.

Coplen, T.B., Kendall, C. and Hopple, J., 1983. Comparison of stabe isotope reference samples. *Nature*, 302, 236-238.

Coplen, T. B. 2007. Calibration of the calcite–water oxygen-isotope geothermometer at Devils Hole, Nevada, a natural laboratory. *Geochimica et Cosmochimica Acta,* 71**,** 3948-3957.

Craig, H. 1953. The geochemistry of the stable carbon isotopes. *Geochimica et Cosmochimica Acta,* 3**,** 53-92.

Craig, H. 1961. Isotopic variations in meteoric waters. *Science,* 133**,** 1702-1703.

Craig, H. 1965. The measurement of oxygen isotope paleotemperatures. *Stable isotopes in oceanographic studies and paleotemperatures: Consiglio Nazionale delle Richerche***,** 161-182.

Craig, H., Gordon, L. & Horibe, Y. 1963. Isotopic Exchange Eeffects in the Evaporation of Water: Low-Temperature Experimental Results. *Journal of Geophysical Research,* 68(17), 5079-5087.

Cremaschi, M., Zerboni, A., Spötl, C. & Felletti, F. 2010. The calcareous tufa in the Tadrart Acacus Mt. (SW Fezzan, Libya). *Palaeogeography, Palaeoclimatology, Palaeoecology,* 287, 81-94.

Cronin, T.M., 2010. *Paleoclimates: Understanding Climate Change Past and Present*. New York: Columbia University Press.

Curnoe, D., Herries, A., Brink, J., Hopley, P., Van Reyneveld, K., Henderson, Z. & Morris, D. 2006. Discovery of Middle Pleistocene fossil and stone tool-bearing deposits at Groot Kloof, Ghaap escarpment, Northern Cape province: news & views. *South African Journal of Science,* 102, 180-184.

Da Silva, J. F. & Williams, J. 1991. *The biological chemistry of the elements: the inorganic chemistry of life.* Oxford: Oxford University Press.

Dabkowski, J., Limondin-Lozouet, N., Antoine, P., Andrews, J., Marca-Bell, A. & Robert, V. 2012. Climatic variations in MIS 11 recorded by stable isotopes and trace elements in a French tufa (La Celle, Seine Valley). *Journal of Quaternary Science,* 27, 790-799.

Dabkowski, J., Royle, S. H., Antoine, P., Marca-Bell, A. & Andrews, J. E. 2015. High-resolution $\delta^{18}O$ seasonality record in a French Eemian tufa stromatolite (Caours, Somme Basin). *Palaeogeography, Palaeoclimatology, Palaeoecology,* 438, 277-284.

Daëron, M., Drysdale, R. N., Peral, M., Huyghe, D., Blamart, D., Coplen, T. B., Lartaud, F. & Zanchetta, G. 2019. Most Earth-surface calcites precipitate out of isotopic equilibrium. *Nature Communications,* 10, 429.

Dansgaard, W. 1964. Stable isotopes in precipitation. *Tellus,* 16, 436-468.

Dansgaard, W., Johnsen, S. J., Clausen, H. B., Dahl-Jensen, D., Gundestrup, N. S., Hammer, C. U., Hvidberg, C. S., Steffensen, J. P., Sveinbjörnsdottir, A. & Jouzel, J. 1993. Evidence for general instability of past climate from a 250-kyr ice-core record. *Nature,* 364, 218-220.

Dart, R. A. 1925. *Australopithecus africanus*: the man-ape of South Africa. *Nature,* 115, 195-199.

De Wet, R. F., West, A. G. & Harris, C. 2020. Seasonal variation in tap water $\delta^{2}H$ and $\delta^{18}O$ isotopes reveals two tap water worlds. *Scientific Reports,* 10, 13544.

Deacon, H. 1976. *Where Hunters Gathered: a study of Holocene Stone Age people in the Eastern Cape*. Claremont, South Africa: South African Archaeological Society Monograph Series.

Deacon, J. & Lancaster, N. 1988. *Late Quaternary palaeoenvironments of southern Africa*. Oxford: Oxford University Press.

Degen, T., Sadki, M., Bron, E., König, U. & Nénert, G. 2014. The highscore suite. *Powder Diffraction,* 29, S13-S18.

Deines, P. 1980. The isotopic composition of reduced organic carbon. In *Handbook of Environmental Isotope Geochemistry.* Fritz, P. (Ed.) Amsterdam: Elsevier, 326-406.

Demenocal, P. B. 2004. African climate change and faunal evolution during the Pliocene–Pleistocene. *Earth and Planetary Science Letters,* 220**,** 3-24.

Demenocal, P., Ortiz, J., Guilderson, T., Adkins, J., Sarnthein, M., Baker, L. & Yarusinsky, M. 2000. Abrupt onset and termination of the African Humid Period: rapid climate responses to gradual insolation forcing. *Quaternary science reviews,* 19**,** 347-361.

Desmarchelier, J. M., Hellstrom, J. C. & Mcculloch, M. T. 2006. Rapid trace element analysis of speleothems by ELA-ICP-MS. *Chemical Geology,* 231**,** 102-117.

Diniz, J. L., Tognoli, F. M. W., Claes, H., De Miranda, T. S., Neumann, V. H. D. M. L., Sial, A. N., Inocencio, L. C. & De Souza, L. V. 2022. Tufa associated with karst features in a fracture-system fed by meteoric water, Araripe basin, NE Brazil. *Journal of South American Earth Sciences,* 115**,** 103772.

Domínguez-Villar, D., Vázquez-Navarro, J. A., Cheng, H. & Edwards, R. L. 2011. Freshwater tufa record from Spain supports evidence for the past interglacial being wetter than the Holocene in the Mediterranean region. *Global and Planetary Change,* 77**,** 129-141.

Domínguez-Villar, D., Vázquez-Navarro, J. A. & Carrasco, R. M. 2012. Mid-Holocene erosive episodes in tufa deposits from Trabaque Canyon, central Spain, as a result of abrupt arid climate transitions. *Geomorphology,* 161**,** 15-25.

Dorale, J. A., Edwards, R. L., Ito, E. & Gonzalez, L. A. 1998. Climate and vegetation history of the midcontinent from 75 to 25 ka: a speleothem record from Crevice Cave, Missouri, USA. *Science,* 282**,** 1871-1874.

Doran, T. L., Herries, A. I., Hopley, P. J., Sombroek, H., Hellstrom, J., Hodge, E. & Kuhn, B. F. 2015. Assessing the paleoenvironmental potential of Pliocene to Holocene tufa deposits along the Ghaap Plateau escarpment (South Africa) using stable isotopes. *Quaternary Research,* 84**,** 133-143.

Drysdale, R. N. 2001. Factors controlling the hydrochemistry of Louie Creek, a travertine-depositing stream in the seasonally wet tropics of northern Australia. *Marine and Freshwater Research,* 52**,** 793-804.

Drysdale, R. N., Paul, B. T., Hellstrom, J. C., Couchoud, I., Greig, A., Bajo, P., Zanchetta, G., Isola, I., Spötl, C., Baneschi, I., Regattieri, E. & Woodhead, J. D. 2012. Precise microsampling of poorly laminated speleothems for U-series dating. *Quaternary Geochronology,* 14**,** 38-47.

Dupont, L. M., Caley, T., Kim, J.-H., Castañeda, I., Malaizé, B. & Giraudeau, J. 2011. Glacial-interglacial vegetation dynamics in South Eastern Africa coupled to sea surface temperature variations in the Western Indian Ocean. *Climate of the Past,* 7**,** 1209-1224.

Ecker, M., Brink, J., Chazan, M., Horwitz, L. K. & Lee-Thorp, J. A. 2017. Radiocarbon dates constrain the timing of environmental and cultural shifts in the Holocene strata of Wonderwerk Cave, South Africa. *Radiocarbon,* 59**,** 1067-1086.

Ecker, M., Brink, J. S., Rossouw, L., Chazan, M., Horwitz, L. K. & Lee-Thorp, J. A. 2018. The palaeoecological context of the Oldowan–Acheulean in southern Africa. *Nature Ecology & Evolution,* 2**,** 1080-1086.

Eikenberg, J., Vezzu, G., Zumsteg, I., Bajo, S., Ruethi, M. & Wyssling, G. 2001. Precise two chronometer dating of Pleistocene travertine: the $^{230}Th/^{234}U$ and $^{226}Ra_{ex}/^{226}Ra(0)$ approach. *Quaternary Science Reviews,* 20**,** 1935-1953.

Elderfield, H., Ferretti, P., Greaves, M., Crowhurst, S., Mccave, I. N., Hodell, D. & Piotrowski, A. M. 2012. Evolution of ocean temperature and ice volume through the mid-Pleistocene climate transition. *Science,* 337**,** 704-709.

Ehleringer, J.R. & Monson, R.K. 1993. Evolutionary and ecological aspects of photosynthetic pathway variation. *Annual Review of Ecology and Systematics*, 411-439.

Ehleringer, J.R. and Cerling, T.E., 2001. Photosynthetic pathways and climate. In *Global Biogeochemical Cycles in the Climate System*. Schulze, E.D., Heimann, M., Harrison, S., Holland, E., Lloyd, J., Prentice, I.C. & Schimel, D.S. (Eds). Academic Press, 267-277.

Emiliani, C. 1955. Pleistocene temperatures. *The Journal of Geology,* 63**,** 538-578.

Emiliani, C. 1966. Paleotemperature analysis of Caribbean cores P6304-8 and P6304-9 and a generalized temperature curve for the past 425,000 years. *The Journal of Geology,* 74**,** 109-124.

Emiliani, C. & Shackleton, N. J. 1974. The Brunhes epoch: isotopic paleotemperatures and geochronology. *Science,* 183**,** 511-514.

Epstein, S., Buchsbaum, R., Lowenstam, H. & Urey, H. C. 1951. Carbonate-water isotopic temperature scale. *Geological Society of America Bulletin,* 62**,** 417-426.

Epstein, S., Buchsbaum, R., Lowenstam, H. A. & Urey, H. C. 1953. Revised carbonate-water isotopic temperature scale. *Geological Society of America Bulletin,* 64**,** 1315-1326.

Epstein, S., Sharp, R. P. & Gow, A. J. 1965. Six-year record of oxygen and hydrogen isotope variations in South Pole firn. *Journal of Geophysical Research,* 70**,** 1809-1814.

Eriksson, P. G. & Altermann, W. 1998. An overview of the geology of the Transvaal Supergroup dolomites (South Africa). *Environmental Geology,* 36**,** 179-188.

Esteban, I., Fitchett, J. M. & De La Peña, P. 2020a. Plant taphonomy, flora exploitation and palaeoenvironments at the Middle Stone Age site of Mwulu's Cave (Limpopo, South Africa): an archaeobotanical and mineralogical approach. *Archaeological and Anthropological Sciences,* 12**,** 226.

Esteban, I., Marean, C. W., Cowling, R. M., Fisher, E. C., Cabanes, D. & Albert, R. M. 2020b. Palaeoenvironments and plant availability during MIS 6 to MIS 3 on the

edge of the Palaeo-Agulhas Plain (south coast, South Africa) as indicated by phytolith analysis at Pinnacle Point. *Quaternary Science Reviews,* 235**,** 105667.

Fairchild, I. J., Borsato, A., Tooth, A. F., Frisia, S., Hawkesworth, C. J., Huang, Y., Mcdermott, F. & Spiro, B. 2000. Controls on trace element (Sr–Mg) compositions of carbonate cave waters: implications for speleothem climatic records. *Chemical geology,* 166**,** 255-269.

Fairchild, I. J., Baker, A., Borsato, A., Frisia, S., Hinton, R. W., Mcdermott, F. & Tooth, A. F. 2001. Annual to sub-annual resolution of multiple trace-element trends in speleothems. *Journal of the Geological Society,* 158**,** 831-841.

Fairchild, I. J. & Treble, P. C. 2009. Trace elements in speleothems as recorders of environmental change. *Quaternary Science Reviews,* 28**,** 449-468.

Fairchild, I. J. & Hartland, A. 2010. Trace element variations in stalagmites: controls by climate and by karst system processes. In *Ion Partitioning in Ambient-temperature aqueous systems.* Prieto, M. & Stoll, H. (Eds.) London: European Mineralogical Union and the Mineralogical Society of Great Britain & Ireland. 259-283.

Faltein, Z., Esler, K., Midgley, G. & Ripley, B. 2020. Atmospheric CO_2 concentrations restrict the growth of *Oxalis pes-caprae* bulbs used by human inhabitants of the Paleo-Agulhas plain during the Pleistocene glacials. *Quaternary Science Reviews,* 235**,** 105731.

Fick, S.E. and Hijmans, R.J., 2017. WorldClim 2: new 1-km spatial resolution climate surfaces for global land areas. *International Journal of Climatology*, *37*, 4302-4315.

Finch, J. M. & Meadows, M. E. 2019. South African biomes and their changes over time. In *The Geography of South Africa: Contemporary Changes and New Directions***.** Knight, J. & Rogerson, C.M. (Eds.) World Regional Geography Book Series. Springer, 57-69.

Fisher, E. C., Bar-Matthews, M., Jerardino, A. & Marean, C. W. 2010. Middle and Late Pleistocene paleoscape modeling along the southern coast of South Africa. *Quaternary Science Reviews,* 29**,** 1382-1389.

Fitchett, J. M., Grab, S. W., Bamford, M. K. & Mackay, A. W. 2016. A multi-proxy analysis of late Quaternary palaeoenvironments, Sekhokong Range, eastern Lesotho. *Journal of Quaternary Science,* 31**,** 788-798.

Fitchett, J. M. 2019. The Holocene climates of South Africa. In *The Geography of South Africa: Contemporary Changes and New Directions***.** Knight, J. & Rogerson, C.M. (Eds.) World Regional Geography Book Series. Springer, 47-55.

Folk, R. L. 1994. Interaction between bacteria, nannobacteria, and mineral precipitation in hot springs of central Italy. *Géographie physique et Quaternaire,* 48**,** 233-246.

Ford, D. & Williams, P. D. 2007. *Karst Hydrogeology and Geomorphology*. West Sussex, England: John Wiley & Sons Ltd.

Ford, T. & Pedley, H. 1996. A review of tufa and travertine deposits of the world. *Earth-Science Reviews,* 41**,** 117-175.

Frančišković-Bilinski, S., Bilinski, H., Barišić, D., Horvatinčić, N. & Daoxian, Y. 2003. Analysis of Karst Tufa from Guangxi, China. *Acta Geologica Sinica-English Edition,* 77, 267-275.

Frančišković-Bilinski, S., Barišić, D., Vertačnik, A., Bilinski, H. & Prohić, E. 2004. Characterization of tufa from the Dinaric Karst of Croatia: mineralogy, geochemistry and discussion of climate conditions. *Facies,* 50, 183-193.

Frisia, S., Borsato, A., Drysdale, R., Paul, B., Greig, A. & Cotte, M. 2012. A re-evaluation of the palaeoclimatic significance of phosphorus variability in speleothems revealed by high-resolution synchrotron micro XRF mapping. *Climate of the Past,* 8, 2039-2051.

Fritz, P. 1965. Composizione isotopica dell'ossigeno e del carbonio nei travertini della Toscana. *Boll. Geofis. Teor. Applic,* 7, 25-30.

Gandin, A., Wright, D. T. & Melezhik, V. 2005. Vanished evaporites and carbonate formation in the Neoarchaean Kogelbeen and Gamohaan formations of the Campbellrand Subgroup, South Africa. *Journal of African Earth Sciences,* 41, 1-23.

Garnett, E. R., Andrews, J. E., Preece, R. C. & Dennis, P. F. 2004a. Climatic change recorded by stable isotopes and trace elements in a British Holocene tufa. *Journal of Quaternary Science,* 19, 251-262.

Garnett, E. R., Gilmour, M. A., Rowe, P. J., Andrews, J. E. & Preece, R. C. 2004b. $^{230}Th/^{234}U$ dating of Holocene tufas: possibilities and problems. *Quaternary Science Reviews,* 23, 947-958.

Gascoyne, M. 1983. Trace-element partition coefficients in the calcite-water system and their paleoclimatic significance in cave studies. *Journal of Hydrology,* 61, 213-222.

Gasse, F., Chalié, F., Vincens, A., Williams, M.A. & Williamson, D. 2008. Climatic patterns in equatorial and southern Africa from 30,000 to 10,000 years ago reconstructed from terrestrial and near-shore proxy data. *Quaternary Science Reviews*, *27*, 2316-2340.

Gat, J. R. 1971. Comments on the stable isotope method in regional groundwater investigations. *Water Resources Research,* 7, 980-993.

Gat, J. R. 1996. Oxygen and hydrogen isotopes in the hydrologic cycle. *Annual Review of Earth and Planetary Sciences,* 24, 225-262.

Gat, J. R. & Dansgaard, W. 1972. Stable isotope survey of the fresh water occurrences in Israel and the northern Jordan Rift Valley. *Journal of Hydrology,* 16, 177-211.

Gates-Rector, S. & Blanton, T. 2019. The powder diffraction file: a quality materials characterization database. *Powder Diffraction,* 34, 352-360.

Gedda, B., Lemdahl, G. & Gaillard, M. J. 1999. Lateglacial and Early Holocene environments inferred from a tufa deposit at Fyledalen, S. Sweden. *GFF,* 121, 33-41.

Goldstein, S. J. & Stirling, C. H. 2003. Techniques for measuring uranium-series nuclides: 1992–2002. *Reviews in Mineralogy and Geochemistry,* 52, 23-57.

Golubić, S. 1969. Cyclic and noncyclic mechanisms in the formation of travertine. *Internationale Vereinigung für Theoretische und Angewandte Limnologie: Verhandlungen,* 17(2), 956-961.

Golubić, S. 1973. The relationship between blue-green algae and carbonate deposits. In *The biology of blue-green algae.* Carr, N. G. & Whitton, B. A. (Eds.) Oxford: Blackwell Scientific Publictions.

Golubić, S., Violante, C., Plenković-Moraj, A. & Grgasović, T. 2008. Travertines and calcareous tufa deposits: an insight into diagenesis. *Geologia Croatica,* 61, 363-378.

Gonfiantini, R., Panichi, C. & Tongiorgi, E. 1968. Isotopic disequilibrium in travertine deposition. *Earth and Planetary Science Letters,* 5, 55-58.

Gradziński, M., Bella, P. & Holúbek, P. 2018. Constructional caves in freshwater limestone: a review of their origin, classification, significance and global occurrence. *Earth-Science Reviews,* 185, 179-201.

Green, H., Pickering, R., Drysdale, R., Johnson, B. C., Hellstrom, J. & Wallace, M. 2015. Evidence for global teleconnections in a late Pleistocene speleothem record of water balance and vegetation change at Sudwala Cave, South Africa. *Quaternary Science Reviews,* 110, 114-130.

Griffiths, H. I. & Pedley, H. M. 1995. Did changes in late Last Glacial and early Holocene atmospheric CO_2 concentrations control rates of tufa precipitation? *The Holocene,* 5, 238-242.

Grootes, P. M., Stuiver, M., White, J., Johnsen, S. & Jouzel, J. 1993. Comparison of oxygen isotope records from the GISP2 and GRIP Greenland ice cores. *Nature,* 366, 552-554.

Grün, R., Brink, J. S., Spooner, N. A., Taylor, L., Stringer, C. B., Franciscus, R. G. & Murray, A. S. 1996. Direct dating of Florisbad hominid. *Nature,* 382, 500-501.

Guo, L. & Riding, R. 1992. Aragonite laminae in hot water travertine crusts, Rapolano Terme, Italy. *Sedimentology,* 39, 1067-1079.

Guo, X., Chafetz, H. S. & Gandin, A. 2013. Trends in $\delta^{18}O$ and $\delta^{13}C$ values in lacustrine tufa mounds: palaeohydrology of Searles Lake, California. *Sedimentology,* 61, 221-237.

Harmon, R. S., Głazek, J. & Nowak, K. 1980. $^{230}Th/^{234}U$ dating of travertine from the Bilzingsleben archaeological site. *Nature,* 284, 132-135.

Harris, C. 2023. O-and H-isotope record of Cape Town rainfall from 1996 to 2022: the effect of increasing temperature, and the 'water crisis' of 2015 to 2018. *South African Journal of Geology,* 126, 515-528.

Hartland, A., Fairchild, I. J., Lead, J. R., Borsato, A., Baker, A., Frisia, S. & Baalousha, M. 2012. From soil to cave: transport of trace metals by natural organic matter in karst dripwaters. *Chemical Geology,* 304, 68-82.

Hatton, A., Collins, B., Schoville, B. J. & Wilkins, J. 2022. Ostrich eggshell beads from Ga-Mohana Hill North Rockshelter, southern Kalahari, and the implications for

understanding social networks during Marine Isotope Stage 2. *Plos One,* 17, e0268943.

Hays, J. D., Imbrie, J. & Shackleton, N. J. 1976. Variations in the Earth's Orbit: Pacemaker of the Ice Ages: For 500,000 years, major climatic changes have followed variations in obliquity and precession. *Science,* 194, 1121-1132.

Hays, P. D. & Grossman, E. L. 1991. Oxygen isotopes in meteoric calcite cements as indicators of continental paleoclimate. *Geology,* 19, 441-444.

Hellstrom, J. 2003. Rapid and accurate U/Th dating using parallel ion-counting multi-collector ICP-MS. *Journal of Analytical Atomic Spectrometry,* 18, 1346-1351.

Hellstrom, J. 2006. U–Th dating of speleothems with high initial ^{230}Th using stratigraphical constraint. *Quaternary Geochronology,* 1, 289-295.

Hellstrom, J. & Mcculloch, M. 2000. Multi-proxy constraints on the climatic significance of trace element records from a New Zealand speleothem. *Earth and Planetary Science Letters,* 179, 287-297.

Hellstrom, J. & Pickering, R. 2015. Recent advances and future prospects of the U–Th and U–Pb chronometers applicable to archaeology. *Journal of Archaeological Science,* 56, 32-40.

Hendy, C. H. 1969. Isotopic Geochemistry of Speleothems and Its Application to the Study of Past Climates. PhD thesis. Victoria University of Wellington, NZ.

Hendy, C. H. 1971. The isotopic geochemistry of speleothems—I. The calculation of the effects of different modes of formation on the isotopic composition of speleothems and their applicability as palaeoclimatic indicators. *Geochimica et Cosmochimica Acta,* 35, 801-824.

Hendy, C. H. & Wilson, A. 1968. Palaeoclimatic data from speleothems. *Nature,* 219, 48-51.

Hennig, G., Grün, R. & Brunnacker, K. 1983. Speleothems, travertines, and paleoclimates. *Quaternary Research,* 20, 1-29.

Henshilwood, C.S., d'Errico, F., Yates, R., Jacobs, Z., Tribolo, C., Duller, G.A., Mercier, N., Sealy, J.C., Valladas, H., Watts, I. & Wintle, A.G. 2002. Emergence of modern human behavior: Middle Stone Age engravings from South Africa. *Science*, *295*, 1278-1280.

Henshilwood, C., D'errico, F., Vanhaeren, M., Van Niekerk, K. & Jacobs, Z. 2004. Middle stone age shell beads from South Africa. *Science,* 304, 404.

Henshilwood, C. S., D'errico, F. & Watts, I. 2009. Engraved ochres from the Middle Stone Age levels at Blombos Cave, South Africa. *Journal of Human Evolution,* 57, 27-47.

Henshilwood, C. S., D'errico, F., Van Niekerk, K. L., Dayet, L., Queffelec, A. & Pollarolo, L. 2018. An abstract drawing from the 73,000-year-old levels at Blombos Cave, South Africa. *Nature,* 562, 115-118.

Herries, A. I. 2011. A chronological perspective on the Acheulian and its transition to the Middle Stone Age in southern Africa: the question of the Fauresmith. *International Journal of Evolutionary Biology,* 1, 961401.

Hesse, P. P., Magee, J. W. & Van Der Kaars, S. 2004. Late Quaternary climates of the Australian arid zone: a review. *Quaternary International,* 118**,** 87-102.

Hijmans, R.J., Cameron, S.E., Parra, J.L., Jones, P.G. & Jarvis, A. 2005. Very high resolution interpolated climate surfaces for global land areas. *International Journal of Climatology: A Journal of the Royal Meteorological Society*, *25*, 1965-1978.

Holmgren, K., Lee-Thorp, J. A., Cooper, G. R. J., Lundblad, K., Partridge, T. C., Scott, L., Sithaldeen, R., Siep Talma, A. & Tyson, P. D. 2003. Persistent millennial-scale climatic variability over the past 25,000 years in Southern Africa. *Quaternary Science Reviews,* 22**,** 2311-2326.

Holzkämper, S., Holmgren, K., Lee-Thorp, J., Talma, S., Mangini, A. & Partridge, T. 2009. Late Pleistocene stalagmite growth in Wolkberg Cave, South Africa. *Earth and Planetary Science Letters,* 282**,** 212-221.

Hopley, P. J., Herries, A. I., Baker, S. E., Kuhn, B. F. & Menter, C. G. 2013. Brief communication: beyond the South African cave paradigm – *Australopithecus africanus* from Plio-Pleistocene paleosol deposits at Taung. *American Journal of Physical Anthropology,* 151**,** 316-324.

Horvatinčić, N., Čalić, R. & Geyh, M. A. 2000. Interglacial growth of tufa in Croatia. *Quaternary Research,* 53**,** 185-195.

Horvatinčić, N., Krajcar Bronić, I. & Obelić, B. 2003. Differences in the ^{14}C age, $\delta^{13}C$ and $\delta^{18}O$ of Holocene tufa and speleothem in the Dinaric Karst. *Palaeogeography, Palaeoclimatology, Palaeoecology,* 193**,** 139-157.

Horwitz, L. K. & Chazan, M. 2015. Past and present at Wonderwerk Cave (Northern Cape Province, South Africa). *African Archaeological Review*, 32, 595-612.

Huang, Y. & Fairchild, I. J. 2001. Partitioning of Sr^{2+} and Mg^{2+} into calcite under karst-analogue experimental conditions. *Geochimica et Cosmochimica Acta,* 65**,** 47-62.

Humphreys, A. J. & Thackeray, A. I. 1983. *Ghaap and Gariep: Later Stone Age studies in the Northern Cape.* Cape Town: South African Archaeological Society.

IAEA/WMO, 2015. Global Network of Isotopes in Precipitation. The GNIP Database. Accessible at https://nucleus.iaea.org/wiser.

Ibarra, Y., Corsetti, F. A., Feakins, S. J., Rhodes, E. J. & Kirby, M. E. 2015. Fluvial tufa evidence of Late Pleistocene wet intervals from Santa Barbara, California, U.S.A. *Palaeogeography, Palaeoclimatology, Palaeoecology,* 422**,** 36-45.

Ihlenfeld, C., Norman, M. D., Gagan, M. K., Drysdale, R. N., Maas, R. & Webb, J. 2003. Climatic significance of seasonal trace element and stable isotope variations in a modern freshwater tufa. *Geochimica et Cosmochimica Acta,* 67**,** 2341-2357.

Imbrie, J., Hays, J. D., Martinson, D. G., Mcintyre, A., Mix, A. C., Morley, J. J., Pisias, N. G., Prell, W. L. & Shackleton, N. J. 1984. The orbital theory of Pleistocene climate:

support from a revised chronology of the marine d^{18}O record. In *Milankovitch and Climate: Understanding the Response to Astronomical Forcing.* Berger, A., Imbrie, J., Hays, J., Kukla, G. & Saltzman, B. (Eds.) Dordrecht, Netherland: D. Reidel Publishing Company, 269-305.

Irion, G. & Mueller, G. 1968. Mineralogy, petrology and chemical composition of some calcareous tufa from the Schwäbische Alb, Germany. In *Recent Developments in Carbonate Sedimentology in Central Europe*. Müller, G. & Friedman, G.M. (Eds.) Springer, Berlin, Heidelberg, 157-171.

Ivanovich, M. & Harmon, R. S. 1992. *Uranium-Series Disequilibrium: Applications to Earth, Marine, and Environmental Sciences.* 2nd edition. United Kingdom: Clarendon Press.

Jacobs, N. 1996. The flowing eye: water management in the Upper Kuruman Valley, South Africa, c. 1800–1962. *The Journal of African History,* 37**,** 237-260.

Jacobs, Z., Roberts, R.G., Galbraith, R.F., Deacon, H.J., Grun, R., Mackay, A., Mitchell, P., Vogelsang, R. & Wadley, L. 2008. Ages for the Middle Stone Age of southern Africa: implications for human behavior and dispersal. *Science*, *322*, 733-735.

Jacobson, R. L. & Usdowski, E. 1975. Geochemical controls on a calcite precipitating spring. *Contributions to Mineralogy and Petrology,* 51**,** 65-74.

Jaffey, A., Flynn, K., Glendenin, L., Bentley, W. T. & Essling, A. 1971. Precision measurement of half-lives and specific activities of ^{235}U and ^{238}U. *Physical Review C,* 4**,** 1889.

Janssen, A. & Swennen, R. 1997. Petrography and geochemistry of the travertine deposit at Treignes (S-Belgium). *Bulletin de la Société belge de Géologie***,** 97-115.

Johnsen, S. J., Dansgaard, W., Clausen, H. & Langway, C. 1972. Oxygen isotope profiles through the Antarctic and Greenland ice sheets. *Nature,* 235**,** 429-434.

Johnson, B. J., Miller, G. H., Fogel, M. L. & Beaumont, P. B. 1997. The determination of late Quaternary paleoenvironments at Equus Cave, South Africa, using stable isotopes and amino acid racemization in ostrich eggshell. *Palaeogeography, Palaeoclimatology, Palaeoecology,* 136**,** 121-137.

Johnson, C. R., Ashley, G. M., De Wet, C. B., Dvoretsky, R., Park, L., Hover, V. C., Bernhart Owen, R. & Mcbrearty, S. 2009. Tufa as a record of perennial fresh water in a semi-arid rift basin, Kapthurin Formation, Kenya. *Sedimentology,* 56**,** 1115-1137.

Johnson, K. R., Hu, C., Belshaw, N. S. & Henderson, G. M. 2006. Seasonal trace-element and stable-isotope variations in a Chinese speleothem: the potential for high-resolution paleomonsoon reconstruction. *Earth and Planetary Science Letters,* 244**,** 394-407.

Jones, B. & Renaut, R. W. 1995. Noncrystallographic calcite dendrites from hot-spring deposits at Lake Bogoria, Kenya. *Journal of Sedimentary Research,* 65**,** 154-169.

Jones, B. & Renaut, R. W. 2010. Calcareous spring deposits in continental settings. *Developments in Sedimentology,* 61**,** 177-224.

Jouzel, J., Lorius, C., Petit, J.-R., Genthon, C., Barkov, N. I., Kotlyakov, V. M. & Petrov, V. M. 1987. Vostok ice core: a continuous isotope temperature record over the last climatic cycle (160,000 years). *Nature,* 329**,** 403-408.

Jouzel, J., Masson-Delmotte, V., Cattani, O., Dreyfus, G., Falourd, S., Hoffmann, G., Minster, B., Nouet, J., Barnola, J.-M. & Chappellaz, J. 2007. Orbital and millennial Antarctic climate variability over the past 800,000 years. *Science,* 317**,** 793-796.

Julia, R. 1983. Travertines. In *Carbonate Depositional Environments.* Scholle, P.A., Bebout, D.G. & Moore, C.H. (Eds). Tulsa, Oklahoma: The American Association of Petroleum Geologists, 64-72.

Kaboth-Bahr, S., Gosling, W. D., Vogelsang, R., Bahr, A., Scerri, E. M., Asrat, A., Cohen, A. S., Düsing, W., Foerster, V. & Lamb, H. F. 2021. Paleo-ENSO influence on African environments and early modern humans. *Proceedings of the National Academy of Sciences,* 118, e2018277118.

Kano, A. & Fujii, H. 2000. Origin of the gross morphology and internal texture of tufas of Shirokawa Town, Ehime Prefecture, southwest Japan. *Journal of Geological Society of Japan,* 106**,** 397-412.

Kano, A., Matsuoka, J., Kojo, T. & Fujii, H. 2003. Origin of annual laminations in tufa deposits, southwest Japan. *Palaeogeography, Palaeoclimatology, Palaeoecology,* 191**,** 243-262.

Kano, A., Hagiwara, R., Kawai, T., Hori, M. & Matsuoka, J. 2007. Climatic conditions and hydrological change recorded in a high-resolution stable-isotope profile of a recent laminated tufa on a subtropical island, southern Japan. *Journal of Sedimentary Research,* 77**,** 59-67.

Kaufman, A. 1993. An evaluation of several methods for determining ^{230}ThU ages in impure carbonates. *Geochimica et Cosmochimica Acta,* 57**,** 2303-2317.

Kaufman, A. & Broecker, W. 1965. Comparison of ^{230}Th and ^{14}C ages for carbonate materials from Lakes Lahontan and Bonneville. *Journal of Geophysical Research,* 70**,** 4039-4054.

Keeling, C. D. 1958. The concentration and isotopic abundances of atmospheric carbon dioxide in rural areas. *Geochimica et Cosmochimica Acta,* 13**,** 322-334.

Kele, S., Sallam, E. S., Capezzuoli, E., Rogerson, M., Wanas, H., Shen, C.-C., Lone, M. A., Yu, T.-L., Schauer, A. & Huntington, K. W. 2021. Were springline carbonates in the Kurkur–Dungul area (southern Egypt) deposited during glacial periods? *Journal of the Geological Society,* 178**,** jgs2020-147.

Kelts, K. & Hsü, K. 1978. Freshwater Carbonate Sedimentation. In *Lakes: Chemistry, Geology, Physics.* Lerman, A. (Ed). New York: Springer.

Keppel, M.N., Clarke, J.D., Halihan, T., Love, A.J. & Werner, A.D. 2011. Mound springs in the arid Lake Eyre South region of South Australia: a new depositional tufa model and its controls. *Sedimentary Geology*, 240, 55-70.

Kim, S. T. & O'Neil, J. R. 1997. Equilibrium and nonequilibrium oxygen isotope effects in synthetic carbonates. *Geochimica et Cosmochimica Acta,* 61**,** 3461-3475.

Kitano, Y. 1962. The behavior of various inorganic ions in the separation of calcium carbonate from a bicarbonate solution. *Bulletin of the Chemical Society of Japan,* 35, 1973-1980.

Kitano, Y. & Kawasaki, N. 1958. Behaviour of strontium in the progress of calcium carbonate separation from a bicarbonate solution. *Journal of Earth Science,* 6, 43-74.

Klein, R. G., Cruz-Uribe, K. & Beaumont, P. B. 1991. Environmental, ecological, and paleoanthropological implications of the late Pleistocene mammalian fauna from Equus Cave, Northern Cape Province, South Africa. *Quaternary Research,* 36, 94-119.

Knight, J. & Fitchett, J. M. 2019. Climate change during the late Quaternary in South Africa. In *The Geography of South Africa: Contemporary Changes and New Directions*. Knight, J. & Rogerson, C.M. (Eds.) World Regional Geography Book Series. Springer, 47-55.

Knight, J. & Fitchett, J. 2021. A proposed chronostratigraphic framework for the late Quaternary of southern Africa. *South African Journal of Geology,* 124, 843-862.

Kölbel, L., Kölbel, T., Maier, U., Sauter, M., Schäfer, T. & Wiegand, B. 2020. Water–rock interactions in the Bruchsal geothermal system by U–Th series radionuclides. *Geothermal Energy,* 8, 1-33.

Koltai, G., Kele, S. & Bárány-Kevei, I. 2012. Preliminary studies of freshwater tufa deposits in Mecsek Mts., Hungary. *Acta Climatologica et Chorologica, Universitatis Szegediensis,* 46, 143-151.

Kristen, I., Fuhrmann, A., Thorpe, J., Rohl, U., Wilkes, H. & Oberhansli, H. 2007. Hydrological changes in southern Africa over the last 200 ka as recorded in lake sediments from the Tswaing impact crater. *South African Journal of Geology,* 110, 311-326.

Kronfeld, J. 1988. $^{230}Th/^{234}U$ dating of the quaternary spring travertines in the Arava Rift Valley of Israel and paleoclimatic implications. IAEA-R-4531-F. International Atomic Energy Agency (IAEA).

Ku, T.-L. & Liang, Z.-C. 1984. The dating of impure carbonates with decay-series isotopes. *Nuclear Instruments and Methods in Physics Research,* 223, 563-571.

Kuhn, B. F., Herries, A. I., Pickering, R., Price, G., Baker, S., Hopley, P. J., Menter, C. & Caruana, M. 2016. Renewed investigations at Taung; 90 years after *Australopithecus africanus*. *Palaeontologia Africana,* 51, 10-26.

Kulongoski, J. T., Hilton, D. R. & Selaolo, E. T. 2004. Climate variability in the Botswana Kalahari from the late Pleistocene to the present day. *Geophysical Research Letters,* 31 (10).

Kuman, K. & Clarke, R. 1986. Florisbad new investigations at a Middle Stone Age hominid site in South Africa. *Geoarchaeology,* 1, 103-125.

Lachniet, M. S. 2009. Climatic and environmental controls on speleothem oxygen-isotope values. *Quaternary Science Reviews,* 28, 412-432.

Laskar, J., Robutel, P., Joutel, F., Gastineau, M., Correia, A. & Levrard, B. 2004. A long-term numerical solution for the insolation quantities of the Earth. *Astronomy & Astrophysics,* 428**,** 261-285.

Latham, A. G. 2001. Uranium-series dating. In *Handbook of Archaeological Sciences***.** Brothwell, D. R. & Pollard, A. M. (Eds). Chichester: Wiley, 63-72.

Lee-Thorp, J. A. & Beaumont, P. B. 1995. Vegetation and seasonality shifts during the late Quaternary deduced from $^{13}C/^{12}C$ ratios of grazers at Equus Cave, South Africa. *Quaternary Research,* 43**,** 426-432.

Lee-Thorp, J. A. & Ecker, M. 2015. Holocene environmental change at Wonderwerk Cave, South Africa: insights from stable light isotopes in ostrich eggshell. *African Archaeological Review,* 32**,** 793-811.

Lennard, C. 2019. Multi-scale drivers of the South African weather and climate. In *The Geography of South Africa: Contemporary Changes and New Directions***.** Knight, J. & Rogerson, C.M. (Eds.) World Regional Geography Book Series. Springer, 81-89.

Leybourne, M. I., Betcher, R. N., Mcritchie, W. D., Kaszycki, C. A. & Boyle, D. R. 2009. Geochemistry and stable isotopic composition of tufa waters and precipitates from the Interlake Region, Manitoba, Canada: constraints on groundwater origin, calcitization, and tufa formation. *Chemical Geology,* 260**,** 221-233.

Lisiecki, L. E. & Raymo, M. E. 2005. A Pliocene-Pleistocene stack of 57 globally distributed benthic δ18O records. *Paleoceanography,* 20(1)**,** 1-17.

Lojen, S., Dolenec, T., Vokal, B., Cukrov, N., Mihelčić, G. & Papesch, W. 2004. C and O stable isotope variability in recent freshwater carbonates (River Krka, Croatia). *Sedimentology,* 51**,** 361-375.

Lojen, S., Trkov, A., Ščančar, J., Vázquez-Navarro, J. A. & Cukrov, N. 2009. Continuous 60-year stable isotopic and earth-alkali element records in a modern laminated tufa (Jaruga, river Krka, Croatia): implications for climate reconstruction. *Chemical Geology,* 258**,** 242-250.

Lombard, M. 2012. Thinking through the Middle Stone Age of sub-Saharan Africa. *Quaternary International,* 270**,** 140-155.

Ludwig, K. 2003. Mathematical–statistical treatment of data and errors for $^{230}Th/U$ geochronology. *Reviews in Mineralogy and Geochemistry,* 52**,** 631-656.

Lukich, V., Porat, N., Faershtein, G., Cowling, S. & Chazan, M. 2019. New Chronology and Stratigraphy for Kathu Pan 6, South Africa. *Journal of Paleolithic Archaeology,* 2**,** 235-257.

Lukich, V., Cowling, S. & Chazan, M. 2020. Palaeoenvironmental reconstruction of Kathu Pan, South Africa, based on sedimentological data. *Quaternary Science Reviews,* 230.

Lukich, V. & Ecker, M. 2021. Pleistocene environments in the southern Kalahari of South Africa. *Quaternary International*, 614, 50-58.

Luo, S. & Ku, T. L. 1991. U-series isochron dating: a generalized method employing total-sample dissolution. *Geochimica et Cosmochimica Acta,* 55**,** 555-564.

Luzón, M., Pérez, A., Borrego, A., Mayayo, M. & Soria, A. 2011. Interrelated continental sedimentary environments in the central Iberian Range (Spain): facies characterization and main palaeoenvironmental changes during the Holocene. *Sedimentary Geology,* 239**,** 87-103.

Lyons, R., Tooth, S. & Duller, G. A. T. 2014. Late Quaternary climatic changes revealed by luminescence dating, mineral magnetism and diffuse reflectance spectroscopy of river terrace palaeosols: a new form of geoproxy data for the southern African interior. *Quaternary Science Reviews,* 95**,** 43-59.

Maape, S. 2021. Drawing creepy places: representing liminal ritual spaces of Kuruman, South Africa. *Dialectic,* 9.

Mackay, A., Stewart, B. A. & Chase, B. M. 2014. Coalescence and fragmentation in the late Pleistocene archaeology of southernmost Africa. *Journal of Human Evolution,* 72**,** 26-51.

Mackay, A., Armitage, S. J., Niespolo, E. M., Sharp, W. D., Stahlschmidt, M. C., Blackwood, A. F., Boyd, K. C., Chase, B. M., Lagle, S. E., Kaplan, C. F. & Low, M. A. 2022. Environmental influences on human innovation and behavioural diversity in southern Africa 92–80 thousand years ago. *Nature Ecology & Evolution,* 6**,** 361-369.

Maher, K., Ibarra, D. E., Oster, J. L., Miller, D. M., Redwine, J. L., Reheis, M. C. & Harden, J. W. 2014. Uranium isotopes in soils as a proxy for past infiltration and precipitation across the western United States. *American Journal of Science,* 314**,** 821-857.

Makhnach, N., Zernitskaja, V., Kolosov, I. & Simakova, G. 2004. Stable oxygen and carbon isotopes in Late Glacial–Holocene freshwater carbonates from Belarus and their palaeoclimatic implications. *Palaeogeography, Palaeoclimatology, Palaeoecology,* 209**,** 73-101.

Mallick, R. & Frank, N. 2002. A new technique for precise uranium-series dating of travertine micro-samples. *Geochimica et Cosmochimica Acta,* 66**,** 4261-4272.

Marean, C. W. 2010. Pinnacle Point Cave 13B (Western Cape Province, South Africa) in context: the Cape Floral kingdom, shellfish, and modern human origins. *Journal of Human Evolution,* 59**,** 425-43.

Marean, C. W. 2014. The origins and significance of coastal resource use in Africa and Western Eurasia. *Journal of Human Evolution,* 77**,** 17-40.

Marean, C. W. 2015. An evolutionary anthropological perspective on modern human origins. *Annual Review of Anthropology,* 44**,** 533-556.

Marean, C. W., Bar-Matthews, M., Bernatchez, J., Fisher, E., Goldberg, P., Herries, A. I., Jacobs, Z., Jerardino, A., Karkanas, P., Minichillo, T., Nilssen, P. J., Thompson, E., Watts, I. & Williams, H. M. 2007. Early human use of marine resources and pigment in South Africa during the Middle Pleistocene. *Nature,* 449**,** 905-8.

Marker, M. E. 1974. Dating Quaternary climatic oscillations using cave and tufa deposits. *South African Archaeological Bulletin, Goodwin Series*, 2, 13-19.

Marker, M. E. 1975. On Taung Revisited. *Current Anthropology*, 16, 295.

Marker, M. 1988. Tufa deposits of southern Africa: a review. In *Palaeoecology of Africa and the surrounding islands*. Heine, K. (Ed). Balkema, Rotterdam, 19, 377-389.

Markowska, M., Baker, A., Andersen, M. S., Jex, C. N., Cuthbert, M. O., Rau, G. C., Graham, P. W., Rutlidge, H., Mariethoz, G. & Marjo, C. E. 2016. Semi-arid zone caves: evaporation and hydrological controls on $\delta^{18}O$ drip water composition and implications for speleothem paleoclimate reconstructions. *Quaternary Science Reviews,* 131, 285-301.

Martín-Algarra, A. N., Martín-Martín, M., Andreo, B., Julià, R. & González-Gómez, C. 2003. Sedimentary patterns in perched spring travertines near Granada (Spain) as indicators of the paleohydrological and paleoclimatological evolution of a karst massif. *Sedimentary Geology,* 161, 217-228.

Maslin, M. A., Brierley, C. M., Milner, A. M., Shultz, S., Trauth, M. H. & Wilson, K. E. 2014. East African climate pulses and early human evolution. *Quaternary Science Reviews,* 101, 1-17.

Matmon, A., Hidy, A. J., Vainer, S., Crouvi, O., Fink, D., Erel, Y., Team, A., Arnold, M., Aumaître, G., Bourlès, D., Keddadouche, K., Horwitz, L. K. & Chazan, M. 2015. New chronology for the southern Kalahari Group sediments with implications for sediment-cycle dynamics and early hominin occupation. *Quaternary Research,* 84, 118-132.

Matsuoka, J., Kano, A., Oba, T., Watanabe, T., Sakai, S. & Seto, K. 2001. Seasonal variation of stable isotopic compositions recorded in a laminated tufa, SW Japan. *Earth and Planetary Science Letters,* 192, 31-44.

Mcbrearty, S. & Brooks, A. S. 2000. The revolution that wasn't: a new interpretation of the origin of modern human behavior. *Journal of Human Evolution,* 39, 453-563.

McDermott, F. 2004. Palaeo-climate reconstruction from stable isotope variations in speleothems: a review. *Quaternary Science Reviews,* 23, 901-918.

McDonald, J., Drysdale, R. & Hill, D. 2004. The 2002–2003 El Niño recorded in Australian cave drip waters: implications for reconstructing rainfall histories using stalagmites. *Geophysical Research Letters,* 31(22).

Mckee, J. K. 1993. Formation and geomorphology of caves in calcareous tufas and implications for the study of the Taung fossil deposits. *Transactions of the Royal Society of South Africa,* 48, 307-322.

Mckee, J. K. & Kuykendall, K. L. 2016. The Dart deposits of the Buxton Limeworks, Taung, South Africa, and the context of the Taung *Australopithecus* fossil. *Journal of Vertebrate Paleontology,* 36(2), e1054937.

Mclean, B. & Scott, L. 1999. Phytoliths in sediments of the Pretoria Saltpan (Tswaing Crater). In *Tswaing, investigations into the origin, age and palaeoenvironments of*

the Pretoria Saltpan. Partridge, T. C. (Ed). Pretoria: Council of Geoscience, 167-171

Mekiso, F., Ochieng, G. & Snyman, J. 2015. Isotope hydrology in the middle Mohlapitsi catchment, South Africa. *International Journal of Engineering Research and Development,* 11**,** 1-7.

Mendelsohn, J., Jarvis, A., Roberts, C. & Robertson, T. 2002. *Atlas of Namibia: a Portrait of the Land and its People.* Cape Town: David Philip Publishers.

Mercedes-Martín, R., Rogerson, M., Prior, T. J., Brasier, A. T., Reijmer, J. J., Billing, I., Matthews, A., Love, T., Lepley, S. & Pedley, M. 2021. Towards a morphology diagram for terrestrial carbonates: evaluating the impact of carbonate supersaturation and alginic acid in calcite precipitate morphology. *Geochimica et Cosmochimica Acta,* 306**,** 340-361.

Merz-Preiz, M. & Riding, R. E. 1999. Cyanobacterial tufa calcification in two freshwater streams: ambient environment, chemical thresholds and biological processes. *Sedimentary Geology,* 126**,** 103-124.

Metcalfe, S. E. Evolution of the Pretoria Saltpan – a diatom record spanning a full glacial-interglacial cycle. *Proceedings of the Twelfth International Diatom Symposium*. 30 August 1992. Renesse, Netherlands: Springer, 159-166.

Meyer, H. 1984. The influence of impurities on the growth rate of calcite. *Journal of Crystal Growth,* 66**,** 639-646.

Midgley, J. & Scott, D. 1994. The use of stable isotopes of water (D and ^{18}O) in hydrological studies in the Jonkershoek Valley. *Water SA,* 17**,** 151-154.

Milankovitch, M. 1941. Canon of insolation and the iceage problem. *Koniglich Serbische Akademice Beograd Special Publication,* 132.

Millard, A. R. & Hedges, R. E. 1996. A diffusion-adsorption model of uranium uptake by archaeological bone. *Geochimica et Cosmochimica Acta,* 60**,** 2139-2152.

Mills, S. C., Grab, S. W., Rea, B. R., Carr, S. J. & Farrow, A. 2012. Shifting westerlies and precipitation patterns during the Late Pleistocene in southern Africa determined using glacier reconstruction and mass balance modelling. *Quaternary Science Reviews,* 55**,** 145-159.

Mix, A. C., Bard, E. & Schneider, R. 2001. Environmental processes of the ice age: land, oceans, glaciers (EPILOG). *Quaternary Science Reviews,* 20**,** 627-657.

Moeyersons, J., Nyssen, J., Poesen, J., Deckers, J. & Haile, M. 2006. Age and backfill/overfill stratigraphy of two tufa dams, Tigray Highlands, Ethiopia: evidence for Late Pleistocene and Holocene wet conditions. *Palaeogeography, Palaeoclimatology, Palaeoecology,* 230**,** 165-181.

Morrissey, P., Knight, J. & Stratford, D. J. 2020. Early Marine Isotope Stage 5 sea levels, coastal dune palaeoenvironments, and human occupation on the southeast coast of South Africa. *Quaternary Science Reviews,* 245**,** 106504.

Mucina, L. & Rutherford, M. C. 2006. *The vegetation of South Africa, Lesotho and Swaziland*. Strelitzia 19. South African National Biodiversity Institute (SANBI), Pretoria.

Müller, G., Irion, G. & Förstner, U. 1972. Formation and diagenesis of inorganic Ca-Mg carbonates. *Naturwissenschaften,* 59**,** 158-164.

Nagra, G., Treble, P. C., Andersen, M. S., Bajo, P., Hellstrom, J. & Baker, A. 2017. Dating stalagmites in mediterranean climates using annual trace element cycles. *Scientific Reports,* 7**,** 621.

Nash, D. J. & Mclaren, S. J. 2003. Kalahari valley calcretes: their nature, origins, and environmental significance. *Quaternary International,* 111**,** 3-22.

Netterberg, F. 1969. Ages of calcretes in southern Africa. *The South African Archaeological Bulletin***,** 88-92.

O'Brien, G. R., Kaufman, D. S., Sharp, W. D., Atudorei, V., Parnell, R. A. & Crossey, L. J. 2006. Oxygen isotope composition of annually banded modern and mid-Holocene travertine and evidence of paleomonsoon floods, Grand Canyon, Arizona, USA. *Quaternary Research,* 65**,** 366-379.

O'Neil, J. R., Clayton, R. N. & Mayeda, T. K. 1969. Oxygen isotope fractionation in divalent metal carbonates. *The Journal of Chemical Physics,* 51**,** 5547-5558.

Ordóñez, S. & García Del Cura, M. 1983. Recent and Tertiary fluvial carbonates in Central Spain. *Modern and ancient fluvial systems***,** 485-497.

Ordóñez, S., González Martín, J. A., García Del Cura, M. A. & Pedley, H. M. 2005. Temperate and semi-arid tufas in the Pleistocene to Recent fluvial barrage system in the Mediterranean area: The Ruidera Lakes Natural Park (Central Spain). *Geomorphology,* 69**,** 332-350.

Orland, I. J., Burstyn, Y., Bar-Matthews, M., Kozdon, R., Ayalon, A., Matthews, A. & Valley, J. W. 2014. Seasonal climate signals (1990–2008) in a modern Soreq Cave stalagmite as revealed by high-resolution geochemical analysis. *Chemical Geology,* 363**,** 322-333.

Ortega, R., Maire, R., Devès, G. & Quinif, Y. 2005. High-resolution mapping of uranium and other trace elements in recrystallized aragonite–calcite speleothems from caves in the Pyrenees (France): implication for U-series dating. *Earth and Planetary Science Letters,* 237**,** 911-923.

Ortiz, J., Torres, T., Delgado, A., Reyes, E. & Díaz-Bautista, A. 2009. A review of the Tagus river tufa deposits (central Spain): age and palaeoenvironmental record. *Quaternary Science Reviews,* 28**,** 947-963.

Osácar, M. C., Arenas, C., Auqué, L., Sancho, C., Pardo, G. & Vázquez-Urbez, M. 2016. Discerning the interactions between environmental parameters reflected in $\delta^{13}C$ and $\delta^{18}O$ of recent fluvial tufas: Lessons from a Mediterranean climate region. *Sedimentary Geology,* 345**,** 126-144.

Parkington, J. 2010. Coastal diet, encephalization, and innovative behaviors in the late Middle Stone Age of southern Africa. *Human brain evolution: The influence of freshwater and marine food resources*, 189-202.

Partridge, T. C. 2000. Hominin-bearing cave and tufa deposits. In *The Cenozoic of Southern Africa.* Partridge, T. C. & Maud, R. R. (Eds). New York: Oxford University Press.

Partridge, T., Kerr, S., Metcalfe, S., Scott, L., Talma, A. & Vogel, J. 1993. The Pretoria Saltpan: a 200,000 year southern African lacustrine sequence. *Palaeogeography, Palaeoclimatology, Palaeoecology,* 101, 317-337.

Partridge, T. C., deMenocal, P. B., Lorentz, S. A., Paiker, M. J. & Vogel, J.C. 1997. Orbital forcing of climate over South Africa: a 200,000-year rainfall record from the Pretoria Saltpan. *Quaternary Science Reviews*, *16*, 1125-1133.

Paton, C., Hellstrom, J., Paul, B., Woodhead, J. & Hergt, J. 2011. Iolite: Freeware for the visualisation and processing of mass spectrometric data. *Journal of Analytical Atomic Spectrometry,* 26, 2508-2518.

Paul, B., Paton, C., Norris, A., Woodhead, J., Hellstrom, J., Hergt, J. & Greig, A. 2012. Cellspace: A Module For Creating Spatially Registered Laser Ablation Images Within The Iolite Freeware Environment. *Journal Of Analytical Atomic Spectrometry,* 27, 700-706.

Pazdur, A., Pazdur, M. F., Starkel, L. & Szulc, J. 1988a. Stable isotopes of Holocene calcareous tufa in southern Poland as paleoclimatic indicators. *Quaternary Research,* 30, 177-189.

Pazdur, A., Pazdur, M. F. & Szulc, J. 1988b. Radiocarbon dating of Holocene calcareous tufa in southern Poland. *Radiocarbon,* 30, 133-152.

Peabody, F. E. 1954. Travertines and cave deposits of the Kaap Escarpment of South Africa, and the type locality of *Australopithecus africanus* Dart. *Geological Society of America Bulletin,* 65, 671-706.

Pedley, M. 1990. Classifiction and environmental models of cool freshwater tufas. *Sedimentary Geology,* 68, 143-154.

Pedley, M. 1992. Freshwater (phytoherm) reefs: the role of biofilms and their bearing on marine reef cementation. *Sedimentary Geology,* 79, 255-274.

Pedley, H. M. 2000. Ambient temperature freshwater microbial tufas. In *Microbial Sediments.* Riding, R. E. & Awramik, S. M. (Eds.) Springer Berlin Heidelberg.

Pedley, M. 2009. Tufas and travertines of the Mediterranean region: a testing ground for freshwater carbonate concepts and developments. *Sedimentology,* 56, 221-246.

Pedley, M., Andrews, J., Ordonez, S., Del Cura, M. A. G., Martin, J. A. G. & Taylor, D. 1996. Does climate control the morphological fabric of freshwater carbonates? A comparative study of Holocene barrage tufas from Spain and Britain. *Palaeogeography, Palaeoclimatology, Palaeoecology,* 121, 239-257.

Pedley, H. M., González Martín, J. A., Ordóñez, S. & García Del Cura, M. A. 2003. Sedimentology of Quaternary perched springline and paludal tufas: criteria for recognition, with examples from Guadalajara Province, Spain. *Sedimentology,* 50, 23-44.

Pedley, M., Rogerson, M. & Middleton, R. 2009. Freshwater calcite precipitates from *in vitro* mesocosm flume experiments: a case for biomediation of tufas. *Sedimentology,* 56, 511-527.

Pedley, H. M. & Rogerson, M. 2010. *In vitro* investigations of the impact of different temperature and flow velocity conditions on tufa microfabric. *Geological Society, London, Special Publications,* 336, 193-210.

Pentecost, A. 1993. British travertines: a review. *Proceedings of the Geologists' Association,* 104, 23-39.

Pentecost, A. 1995. The Quaternary travertine deposits of Europe and Asia Minor. *Quaternary Science Reviews,* 14, 1005-1028.

Pentecost, A. 2005. *Travertine*. Netherlands: Springer-Verlag Berlin Heidleberg.

Pentecost, A. & Lord, T. C. 1988. Postglacial tufas and travertines from the Craven district of Yorkshire. *Cave Science,* 15, 15-19.

Pentecost, A. & Spiro, B. 1990. Stable carbon and oxygen isotope composition of calcites associated with modern freshwater cyanobacteria and algae. *Geomicrobiology Journal,* 8, 17-26.

Pentecost, A. & Viles, H. 1994. A review and reassessment of travertine classification. *Géographie physique et Quaternaire,* 48, 305-314.

Perri, E., Manzo, E. & Tucker, M. E. 2012. Multi-scale study of the role of the biofilm in the formation of minerals and fabrics in calcareous tufa. *Sedimentary Geology,* 263, 16-29.

Petherick, L. M., Knight, J., Shulmeister, J., Bostock, H., Lorrey, A., Fitchett, J., Eaves, S., Vandergoes, M. J., Barrows, T. T. & Barrell, D. J. 2022. An extended Last Glacial Maximum in the Southern Hemisphere: a contribution to the SHeMax project. *Earth-Science Reviews,* 231, 104090.

Pickering, R. 2015. U–Pb dating small buried stalagmites from Wonderwerk Cave, South Africa: a new chronometer for Earlier Stone Age cave deposits. *African Archaeological Review,* 32, 645-668.

Pickering, R. 2017. U-Series dating. In *Encyclopedia of Geoarchaeology*. Gilbert, A. S. (Ed.) Dordrecht: Springer.

Pickering, R., Hancox, P. J., Lee-Thorp, J. A., Grun, R., Mortimer, G. E., Mcculloch, M. & Berger, L. R. 2007. Stratigraphy, U-Th chronology, and paleoenvironments at Gladysvale Cave: insights into the climatic control of South African hominin-bearing cave deposits. *Journal of Human Evolution,* 53, 602-19.

Pike, A. W. G. & Hedges, R. E. M. 2002. U-series dating of bone using the diffusion-adsorption model. *Geochimica et Cosmochimica Acta,* 66, 4273-4286.

Pla-Pueyo, S., Viseras, C., Henares, S., Yeste, L. M. & Candy, I. 2017. Facies architecture, geochemistry and palaeoenvironmental reconstruction of a barrage tufa reservoir analog (Betic Cordillera, S. Spain). *Quaternary International,* 437, 15-36.

Popp, B. N. & Wilkinson, B. H. 1983. Holocene lacustrine ooids from Pyramid lake, Nevada. In *Coated Grains.* Peryt, T. (Ed). Springer-Verlag Berlin Heidelberg, 142-153.

Porat, N., Chazan, M., Grün, R., Aubert, M., Eisenmann, V. & Horwitz, L. K. 2010. New radiometric ages for the Fauresmith industry from Kathu Pan, southern Africa: implications for the Earlier to Middle Stone Age transition. *Journal of Archaeological Science,* 37, 269-283.

Quade, J., Cerling, T. E. & Bowman, J. R. 1989. Systematic variations in the carbon and oxygen isotopic composition of pedogenic carbonate along elevation transects in the southern Great Basin, United States. *Geological Society of America Bulletin,* 101, 464-475.

R Core Team (2022). R: A language and environment for statistical computing. *R Foundation for Statistical Computing, Vienna, Austria.* URL https://www.R-project.org/.

Raynaud, D., Jouzel, J., Barnola, J. M., Chappellaz, J., Delmas, R. J. & Lorius, C. 1993. The ice record of greenhouse gases. *Science,* 259, 926-934.

Reason, C.J.C 2001a. Evidence for the influence of the Agulhas Current on regional atmospheric circulation patterns. *Journal of Climate,* 14, 2769-2778.

Reason, C.J.C 2001b. Subtropical Indian Ocean SST dipole events and southern African rainfall. *Geophysical Research Letters,* 28, 2225-2227.

Reason, C.J.C. 2002. Sensitivity of the southern African circulation to dipole sea-surface temperature patterns in the south Indian Ocean. *International Journal of Climatology,* 22, 377-393.

Reason, C.J.C. & Mulenga, H. 1999. Relationships between South African rainfall and SST anomalies in the southwest Indian Ocean. *International Journal of Climatology: A Journal of the Royal Meteorological Society,* 19, 1651-1673.

Reiners, P. W., Carlson, R. W., Renne, P. R., Cooper, K. M., Granger, D. E., Mclean, N. M. & Schoene, B. 2017. *Geochronology and Thermochronology*. Oxford: John Wiley & Sons.

Ricci, M., Bertini, A., Capezzuoli, E., Horvatinčić, N., Andrews, J. E., Fauquette, S. & Fedi, M. 2015. Palynological investigation of a Late Quaternary calcareous tufa and travertine deposit: the case study of Bagnoli in the Valdelsa Basin (Tuscany, central Italy). *Review of Palaeobotany and Palynology,* 218, 184-197.

Richards, D. A. & Dorale, J. A. 2003. Uranium-series chronology and environmental applications of speleothems. *Reviews in Mineralogy and Geochemistry,* 52, 407-460.

Ricketts, J. W., Ma, L., Wagler, A. E. & Garcia, V. H. 2019. Global travertine deposition modulated by oscillations in climate. *Journal of Quaternary Science,* 34, 558-568.

Riding, R. E. 2000. Microbial carbonates: the geological record of calcified bacterial-algal mats and biofilms. *Sedimentology,* 47**,** 179-214.

Ritter, S. M., Schröter, M. I., Schröder-Ritzrau, A., Scholz, C. & Frank, N. 2017. Geochemical insights into an active calcareous tufa depositing system in southern Germany. *Procedia Earth and Planetary Science,* 17**,** 328-331.

Ritter, S. M., Isenbeck-Schröter, M., Schröder-Ritzrau, A., Scholz, C., Rheinberger, S., Höfle, B. & Frank, N. 2018. Trace element partitioning in fluvial tufa reveals variable portions of biologically influenced calcite precipitation. *Geochimica et Cosmochimica Acta,* 225**,** 176-191.

Roberts, P. & Stewart, B. A. 2018. Defining the 'generalist specialist' niche for Pleistocene *Homo sapiens*. *Nature Human Behaviour,* 2**,** 542-550.

Robbins, L.H. & Murphy, M.L. 2011. An overview of the Later and Middle Stone Age at Tsodilo Hills. *Botswana Notes and Records*, *43*, 130-139.

Roffe, S.J., Fitchett, J.M. & Curtis, C.J. 2021. Quantifying rainfall seasonality across South Africa on the basis of the relationship between rainfall and temperature. *Climate Dynamics*, *56*, 2431-2450.

Rogerson, M., Pedley, H. M., Wadhawan, J. D. & Middleton, R. 2008. New insights into biological influence on the geochemistry of freshwater carbonate deposits. *Geochimica et Cosmochimica Acta,* 72**,** 4976-4987.

Rogerson, M., Pedley, H. M. & Middleton, R. 2010. Microbial influence on macroenvironment chemical conditions in alkaline (tufa) streams: perspectives from *in vitro* experiments. *Geological Society, London, Special Publications,* 336**,** 65-81.

Rogerson, M., Pedley, H. M., Greenway, G. & Wadhawan, J. D. 2022. Interaction of temperature, salinity and extracellular polymeric substances controls trace element incorporation into tufa calcite. *The Depositional Record,* 8**,** 210-219.

Rosenbaum, J. & Sheppard, S. M. F. 1986. An isotopic study of siderites, dolomites and ankerites at high temperatures. *Geochimica et Cosmochimica Acta,* 50**,** 1147-1150.

Rosewarne, P. 2006. Groundwater resource assessment: dolomite aquifer. *Department of Water Affairs and Forestry, Pretoria*.

Rossouw, L. 2016. An early Pleistocene phytolith record from Wonderwerk cave, Northern Cape, South Africa. *African Archaeological Review,* 33**,** 251-263.

Rozanski, K., Araguás-Araguás, L. & Gonfiantini, R. 1993. Isotopic patterns in modern global precipitation. *Climate change in continental isotopic records,* 78**,** 1-36.

Rutlidge, H., Baker, A., Marjo, C. E., Andersen, M. S., Graham, P. W., Cuthbert, M. O., Rau, G. C., Roshan, H., Markowska, M. & Mariethoz, G. 2014. Dripwater organic matter and trace element geochemistry in a semi-arid karst environment: implications for speleothem paleoclimatology. *Geochimica et Cosmochimica Acta,* 135**,** 217-230.

South African National Biodiversity Institute (SANBI). 2021. *Ecosystem Guidelines for the Savanna Biome*. South African National Biodiversity Institute, an entity of the Department of Forestry, Fisheries and the Environment, Pretoria.

Sancho, C., Arenas, C., Vázquez-Urbez, M., Pardo, G., Lozano, M. V., Peña-Monné, J. L., Hellstrom, J., Ortiz, J. E., Osácar, M. C., Auqué, L. & Torres, T. 2015. Climatic implications of the Quaternary fluvial tufa record in the NE Iberian Peninsula over the last 500 ka. *Quaternary Research,* 84, 398-414.

Saunders, P., Rogerson, M., Wadhawan, J., Greenway, G. & Pedley, H. 2014. Mg/Ca ratios in freshwater microbial carbonates: thermodynamic, kinetic and vital effects. *Geochimica et Cosmochimica Acta,* 147, 107-118.

Scholz, D. & Hoffmann, D. 2008. ^{230}Th/U-dating of fossil corals and speleothems. *E&G Quaternary Science Journal,* 57, 52-76.

Schwarcz, H. P. 1992. Uranium-series dating and the origin of modern man. *Philosophical Transactions of the Royal Society of London. Series B: Biological Sciences,* 337, 131-137.

Schwarcz, H. & Latham, A. 1989. Dirty calcites 1. Uranium-series dating of contaminated calcite using leachates alone. *Chemical Geology: Isotope Geoscience section,* 80, 35-43.

Scott, L. 1987. Pollen analysis of hyena coprolites and sediments from Equus Cave, Taung, southern Kalahari (South Africa). *Quaternary research,* 28, 144-156.

Scott, L. 1989. Climatic conditions in southern Africa since the Last Glacial Maximum, inferred from pollen analysis. *Palaeogeography, Palaeoclimatology, Palaeoecology,* 70, 345-353.

Scott, L. 1999. Vegetation history and climate in the Savanna Biome South Africa since 190,000 ka: a comparison of pollen data from the Tswaing Crater (the Pretoria Saltpan) and Wonderkrater. *Quaternary International,* 57, 215-223.

Scott, L. 2016. Fluctuations of vegetation and climate over the last 75 000 years in the Savanna Biome, South Africa: Tswaing Crater and Wonderkrater pollen sequences reviewed. *Quaternary Science Reviews,* 145, 117-133.

Scott, L., Steenkamp, M. & Beaumont, P. 1995. Palaeoenvironmental conditions in South Africa at the Pleistocene-Holocene transition. *Quaternary Science Reviews,* 14, 937-947.

Scott, L. & Nyakale, M. 2002. Pollen indications of Holocene palaeoenvironments at Florisbad spring in the central Free State, South Africa. *The Holocene,* 12, 497-503.

Scott, L. & Thackeray, J. F. 2015. Palynology of Holocene deposits in excavation 1 at Wonderwerk cave, Northern Cape (South Africa). *African Archaeological Review,* 32, 839-855.

Scott, L. & Neumann, F. H. 2018. Pollen-interpreted palaeoenvironments associated with the Middle and Late Pleistocene peopling of Southern Africa. *Quaternary International,* 495, 169-184.

Scott, L., Van Aardt, A. C., Brink, J. S., Toffolo, M. B., Ochando, J. & Carrión, J. S. 2019. Palynology of Middle Stone Age spring deposits in grassland at the Florisbad hominin site, South Africa. *Review of Palaeobotany and Palynology,* 265**,** 13-26.

Scott, L., Sobol, M., Neumann, F., Romera, G. G., Fernández-Jalvo, Y., Bousman, C., Horwitz, L. & Van Aardt, A. 2022. Late Quaternary palaeoenvironments in the central semi-arid region of South Africa from pollen in cave, pan, spring, stream and dung deposits. *Quaternary International,* 614**,** 84-97.

Shackleton, N. J. 1969. The last interglacial in the marine and terrestrial records. *Proceedings of the Royal Society of London. Series B. Biological Sciences,* 174**,** 135-154.

Shackleton, N. J., Berger, A. & Peltier, W. R. 1990. An alternative astronomical calibration of the lower Pleistocene timescale based on ODP Site 677. *Earth and Environmental Science Transactions of the Royal Society of Edinburgh,* 81**,** 251-261.

Sharp, Z. 2007. *Principles of Stable Isotope Geochemistry*. Pearson/Prentice Hall.

Siegenthaler, U., Stocker, T. F., Monnin, E., Luthi, D., Schwander, J., Stauffer, B., Raynaud, D., Barnola, J. M., Fischer, H., Masson-Delmotte, V. & Jouzel, J. 2005. Stable carbon cycle climate relationship during the Late Pleistocene. *Science,* 310**,** 1313-1317.

Sierralta, M., Kele, S., Melcher, F., Hambach, U., Reinders, J., Van Geldern, R. & Frechen, M. 2010. Uranium-series dating of travertine from Süttő: implications for reconstruction of environmental change in Hungary. *Quaternary International,* 222**,** 178-193.

Singarayer, J. S. & Burrough, S. L. 2015. Interhemispheric dynamics of the African rainbelt during the late Quaternary. *Quaternary Science Reviews,* 124**,** 48-67.

Sirocko, F., Claussen, M., Litt, T., Goñi, M. F. S., Berger, A., Boettger, T., Diehl, M., Desprat, S., Delmonte, B. & Degering, D. 2007. Chronology and climate forcing of the last four interglacials. In *The Climate of Past Interglacials*. Sirocko, F., Claussen, M., Goñi, M. F. S. & Litt, T. (Eds). *Developments in Quaternary Sciences,* 7, 597-614.

Smart, P.L. 1991. Uranium series dating. In *Dating Methods in Quaternary Studies – a Users Guide*. Smart, P.L. & Francis, P.D. (Eds). United Kingdom: Quaternary Research Association.

Smit, P. 1978. Groundwater recharge in the dolomite of the Ghaap Plateau near Kuruman in the Northern Cape, Republic of South Africa. *Water SA,* 4**,** 81-92.

Smith, B. N. & Epstein, S. 1971. Two categories of $^{13}C/^{12}C$ ratios for higher plants. *Plant Physiology,* 47**,** 380-384.

Smith, C. L., Fairchild, I. J., Spötl, C., Frisia, S., Borsato, A., Moreton, S. G. & Wynn, P. M. 2009. Chronology building using objective identification of annual signals in trace element profiles of stalagmites. *Quaternary Geochronology,* 4**,** 11-21.

Smith, E. I., Jacobs, Z., Johnsen, R., Ren, M., Fisher, E. C., Oestmo, S., Wilkins, J., Harris, J. A., Karkanas, P., Fitch, S., Ciravolo, A., Keenan, D., Cleghorn, N., Lane, C. S.,

Matthews, T. & Marean, C. W. 2018. Humans thrived in South Africa through the Toba eruption about 74,000 years ago. *Nature,* 555**,** 511-515.

Smith, J. R., Giegengack, R., Schwarcz, H. P., Mcdonald, M. M. A., Kleindienst, M. R., Hawkins, A. L. & Churcher, C. S. 2004. A reconstruction of Quaternary pluvial environments and human occupations using stratigraphy and geochronology of fossil-spring tufas, Kharga Oasis, Egypt. *Geoarchaeology,* 19**,** 407-439.

Soligo, M., Tuccimei, P., Barberi, R., Delitala, M., Miccadei, E. & Taddeucci, A. 2002. U/Th dating of freshwater travertine from Middle Velino Valley (Central Italy): paleoclimatic and geological implications. *Palaeogeography, Palaeoclimatology, Palaeoecology,* 184**,** 147-161.

Spangenberg, J. E. & Vennemann, T. W. 2008. The stable hydrogen and oxygen isotope variation of water stored in polyethylene terephthalate (PET) bottles. *Rapid Communications in Mass Spectrometry,* 22**,** 672-676.

Speer, J. A. 1983. Crystal chemistry and phase relations of orthorhombic carbonates. *Reviews in Mineralogy and Geochemistry,* 11**,** 145-190.

Spiro, B. & Pentecost, A. 1991. One day in the life of a stream – a diurnal inorganic carbon mass balance for a travertine-depositing stream (Waterfall Beck, Yorkshire). *Geomicrobiology Journal,* 9**,** 1-11.

Spötl, C. & Vennemann, T. W. 2003. Continuous-flow isotope ratio mass spectrometric analysis of carbonate minerals. *Rapid communications in mass spectrometry,* 17**,** 1004-1006.

Stewart, B. A., Dewar, G. I., Morley, M. W., Inglis, R. H., Wheeler, M., Jacobs, Z. & Roberts, R. G. 2012. Afromontane foragers of the Late Pleistocene: site formation, chronology and occupational pulsing at Melikane Rockshelter, Lesotho. *Quaternary International,* 270**,** 40-60.

Stirn, A. 1964. *Kalktuffvorkommen und Kalktufftypen der Schwäbischen Alb.* Verband d. Dt. Höhlen-und Karstforscher.

Stone, A. E. C., Viles, H. A., Thomas, L. & Van Calsteren, P. 2010. Can ^{234}U-^{230}Th dating be used to date large semi-arid tufas? Challenges from a study in the Naukluft Mountains, Namibia. *Journal of Quaternary Science,* 25**,** 1360-1372.

Stone, A., Inglis, R., Barfod, D., Ickert, R., Hughes, L., Waters, J., Jourdan, A. L. & Alsharekh, A. M. 2022. Hydroclimatic and geochemical palaeoenvironmental records within tufa: a cool-water fluvio-lacustrine tufa system in the Wadi Dabsa volcanic setting, western Saudi Arabia. *Sedimentary Geology,* 437, 106181.

Stowe, M. J., Harris, C., Hedding, D., Eckardt, F. & Nel, W. 2018. Hydrogen and oxygen isotope composition of precipitation and stream water on sub-Antarctic Marion Island. *Antarctic Science*, 30**,** 83-92.

Sumner, D. Y. 1997. Late Archean calcite-microbe interactions: two morphologically distinct microbial communities that affected calcite nucleation differently. *Palaios,* 12**,** 302-318.

Tan, L., Orland, I. & Cheng, H. 2014. Annually laminated speleothems in paleoclimate studies. *Pages Magazine,* 22**,** 22-23.

Telfer, M. W. & Thomas, D. S. G. 2007. Late Quaternary linear dune accumulation and chronostratigraphy of the southwestern Kalahari: implications for aeolian palaeoclimatic reconstructions and predictions of future dynamics. *Quaternary Science Reviews,* 26**,** 2617-2630.

Telfer, M. W., Thomas, D. S. G., Parker, A. G., Walkington, H. & Finch, A. 2009. Optically Stimulated Luminescence (OSL) dating and palaeoenvironmental studies of pan (playa) sediment from Witpan, South Africa. *Palaeogeography, Palaeoclimatology, Palaeoecology,* 273**,** 50-60.

Terzer-Wassmuth, S., Wassenaar, L. I., Welker, J. M. & Araguás-Araguás, L. J. 2021. Improved high-resolution global and regionalized isoscapes of $\delta^{18}O$, $\delta^{2}H$ and d-excess in precipitation. *Hydrological Processes,* 35**,** e14254.

Thackeray, A. I., Thackeray, J. F., Beaumont, P. B. & Vogel, J. C. 1981. Dated rock engravings from Wonderwerk Cave, South Africa. *Science,* 214**,** 64-67.

Thackeray, J. F. & Scott, L. 2006. The Younger Dryas in the Wonderkrater sequence, South Africa? *Annals of the Transvaal Museum,* 43**,** 111-112.

Thackeray, J. F. & Fitchett, J. M. 2016. Rainfall seasonality captured in micromammalian fauna in Late Quaternary contexts, South Africa. *Palaeontologia africana*, 51, 1-9.

Thomas, D. S. G. 2013. Reconstructing paleoenvironments and palaeoclimates in drylands: what can landform analysis contribute? *Earth Surface Processes and Landforms,* 38**,** 3-16.

Thomas, D. & Shaw, P. A. 1991. *The Kalahari Environment*. New York: Cambridge University Press.

Thomas, D. S. G. & Burrough, S. L. 2012. Interpreting geoproxies of late Quaternary climate change in African drylands: implications for understanding environmental change and early human behaviour. *Quaternary International,* 253**,** 5-17.

Toffolo, M. B., Brink, J. S., Van Huyssteen, C. & Berna, F. 2017. A microstratigraphic re-evaluation of the Florisbad spring site, Free State Province, South Africa: formation processes and paleoenvironment. *Geoarchaeology,* 32**,** 456-478.

Tooth, A. F. & Fairchild, I. J. 2003. Soil and karst aquifer hydrological controls on the geochemical evolution of speleothem-forming drip waters, Crag Cave, southwest Ireland. *Journal of Hydrology,* 273**,** 51-68.

Tostevin, R., Shields, G. A., Tarbuck, G. M., He, T., Clarkson, M. O. & Wood, R. A. 2016. Effective use of cerium anomalies as a redox proxy in carbonate-dominated marine settings. *Chemical Geology,* 438**,** 146-162.

Trauth, M. H., Larrasoaña, J. C. & Mudelsee, M. 2009. Trends, rhythms and events in Plio-Pleistocene African climate. *Quaternary Science Reviews,* 28**,** 399-411.

Treble, P., Shelley, J. & Chappell, J. 2003. Comparison of high resolution sub-annual records of trace elements in a modern (1911–1992) speleothem with instrumental

climate data from southwest Australia. *Earth and Planetary Science Letters,* 216, 141-153.

Treble, P., Chappell, J., Gagan, M. K., Mckeegan, K. D. & Harrison, T. M. 2005. *In situ* measurement of seasonal $\delta^{18}O$ variations and analysis of isotopic trends in a modern speleothem from southwest Australia. *Earth and Planetary Science Letters,* 233, 17-32.

Treble, P. C., Fairchild, I. J., Griffiths, A., Baker, A., Meredith, K. T., Wood, A. & Mcguire, E. 2015. Impacts of cave air ventilation and in-cave prior calcite precipitation on Golgotha Cave dripwater chemistry, southwest Australia. *Quaternary Science Reviews,* 127, 61-72.

Truc, L., Chevalier, M., Favier, C., Cheddadi, R., Meadows, M. E., Scott, L., Carr, A. S., Smith, G. F. & Chase, B. M. 2013. Quantification of climate change for the last 20,000 years from Wonderkrater, South Africa: implications for the long-term dynamics of the Intertropical Convergence Zone. *Palaeogeography, Palaeoclimatology, Palaeoecology,* 386, 575-587.

Turi, B. 1986. Stable isotope geochemistry of travertines. In *Handbook of Environmental Isotope Geochemistry.* Fritz, P. & Fontes, J. C. (Eds). Amsterdam: Elsevier, 207-238.

Turner, J. V. 1982. Kinetic fractionation of carbon-13 during calcium carbonate precipitation. *Geochimica et Cosmochimica Acta,* 46, 1183-1191.

Tyson, P. D. & Preston-Whyte, R. A. 2000. The *Weather and Climate of southern Africa*. Cape Town: Oxford University Press.

Tzedakis, P. C., Crucifix, M., Mitsui, T. & Wolff, E. W. 2017. A simple rule to determine which insolation cycles lead to interglacials. *Nature,* 542, 427-432.

Ukey, M. S. & Pardeshi, R. G. 2019. Micromorphology and textural variations in the Ane Ghat Waterfall tufa deposits from Upland Deccan Traps and their genesis. *Journal of the Geological Society of India,* 94, 86-92.

Urey, H. C. 1947. The thermodynamic properties of isotopic substances. *Journal of the Chemical Society*, 562-581.

Urey, H. C., Lowenstam, H. A., Epstein, S. & Mckinney, C. R. 1951. Measurement of paleotemperatures and temperatures of the Upper Cretaceous of England, Denmark, and the southeastern United States. *Geological Society of America Bulletin,* 62, 399-416.

Urrego, D. H., Sánchez Goñi, M., Daniau, A.-L., Lechevrel, S. & Hanquiez, V. 2015. Increased aridity in southwestern Africa during the warmest periods of the last interglacial. *Climate of the Past,* 11, 1417-1431.

Usdowski, E., Hoefs, J. & Menschel, G. 1979. Relationship between ^{13}C and ^{18}O fractionation and changes in major element composition in a recent calcite-depositing spring: a model of chemical variations with inorganic $CaCO_3$ precipitation. *Earth and Planetary Science Letters,* 42, 267-276.

Van Zinderen Bakker, E. M. 1983. The late Quaternary history of climate and vegetation in East and southern Africa. *Bothalia,* 14**,** 369-375.

Van Zinderen Bakker, E. M. 1989. Middle Stone Age palaeoenvironments at Florisbad (South Africa). In *Palaeoecology of Africa and the surrounding islands.* Heine, K. (Ed). Balkema, Rotterdam, 20**,** 133-154.

Vasconcelos, C., Mckenzie, J. A., Warthmann, R. & Bernasconi, S. M. 2005. Calibration of the $\delta^{18}O$ paleothermometer for dolomite precipitated in microbial cultures and natural environments. *Geology,* 33**,** 317-320.

Vázquez-Urbez, M., Pardo, G., Arenas, C. & Sancho, C. 2011. Fluvial diffluence episodes reflected in the Pleistocene tufa deposits of the River Piedra (Iberian Range, NE Spain). *Geomorphology,* 125**,** 1-10.

Veizer, J. 1983. Trace elements and isotopes in sedimentary carbonates. *Reviews in Mineralogy,* 11**,** 265-300.

Verhagen, B. T., Smith, P., McGeorge, I. & Dziembowski, Z. 1979. Tritium profiles in Kalahari sands as a measure of rain-water recharge. *International symposium on isotope hydrology, IAEA.* 19-23 June 1978. Neuherberg, Germany.

Viles, H. A. & Goudie, A. 1990. Tufas, travertines and allied carbonate deposits. *Progress in Physical Geography,* 14**,** 19-41.

Viles, H. A., Taylor, M. P., Nicoll, K. & Neumann, S. 2007. Facies evidence of hydroclimatic regime shifts in tufa depositional sequences from the arid Naukluft Mountains, Namibia. *Sedimentary Geology,* 195**,** 39-53.

Violante, C., Ferreri, V., Argenio, B. D. & Golubic, S. 1994. Quaternary Travertines at Rocchetta a Volturno (Isernia, Centrai Italy): Facies Analysis and Sedimentary Model of an Organogenic Carbonate System. *IAS 15th Regional Meeting - Ischia, Italy, 5-22.*

Vogel, J. C. 1993. Variability of carbon isotope fractionation during photosynthesis. In *Stable Isotopes and Plant Carbon-Water Relations.* Ehleringer, J. R., Hall, A. E. & Farquhar, G.D. (Eds). Academic Press, 29-46.

Von Der Meden, J., Pickering, R., Schoville, B. J., Green, H., Weij, R., Hellstrom, J., Greig, A., Woodhead, J., Khumalo, W. & Wilkins, J. 2022. Tufas indicate prolonged periods of water availability linked to human occupation in the southern Kalahari. *Plos One,* 17**,** e0270104.

Wadley, L. 2013. MIS 4 and MIS 3 occupations in Sibudu, KwaZulu-Natal, South Africa. *The South African Archaeological Bulletin***,** 41-51.

Wadley, L. 2015. Those marvellous millennia: the Middle Stone Age of Southern Africa. *Azania: Archaeological Research in Africa,* 50**,** 155-226.

Wadley, L., Sievers, C., Bamford, M., Goldberg, P., Berna, F. & Miller, C. 2011. Middle Stone Age bedding construction and settlement patterns at Sibudu, South Africa. *Science*, *334*, 1388-1391.

Walker, M. 2005. *Quaternary dating methods*. England: John Wiley & Sons.

Wanas, H. & Armenteros, I. 2019. Microbially-induced fluvial tufa in Gunna hills, Farafra Oasis, Egypt: facies analysis and stable isotopes. *Journal of African Earth Sciences,* 158**,** 103515.

Wang, X., Auler, A. S., Edwards, R. L., Cheng, H., Cristalli, P. S., Smart, P. L., Richards, D. A. & Shen, C. C. 2004. Wet periods in northeastern Brazil over the past 210 kyr linked to distant climate anomalies. *Nature,* 432**,** 740-743.

Wassenaar, L. I., Van Wilgenburg, S. L., Larson, K. & Hobson, K. A. 2009. A groundwater isoscape (δD, $\delta^{18}O$) for Mexico. *Journal of Geochemical Exploration,* 102**,** 123-136.

Wasson, K., Woolfolk, A. & Fresquez, C. 2013. Ecotones as indicators of changing environmental conditions: rapid migration of salt marsh–upland boundaries. *Estuaries and Coasts,* 36**,** 654-664.

Watts, I., Chazan, M. & Wilkins, J. 2016. Early Evidence for Brilliant Ritualized Display: Specularite Use in the Northern Cape (South Africa) between ~500 and ~300 ka. *Current Anthropology,* 57**,** 287-310.

Weaver, J. M. C., Talma, A. & Cavé, L. 1999. Geochemistry and isotopes for resource evaluation in the fractured rock aquifers of the Table Mountain Group. Water Research Commission, South Africa. WRC Report No. 481/1/99.

Weaver, J. & Talma, A. 2005. Cumulative rainfall collectors: a tool for assessing groundwater recharge. *Water SA,* 31**,** 283-290.

Weij, R., Sniderman, J. M. K., Woodhead, J. D., Hellstrom, J. C., Brown, J. R., Drysdale, R. N., Reed, E., Bourne, S. & Gordon, J. 2024. Elevated Southern Hemisphere moisture availability during glacial periods. *Nature,* 626**,** 319-326.

West, A. G., February, E. & Bowen, G. J. 2014. Spatial analysis of hydrogen and oxygen stable isotopes ("isoscapes") in ground water and tap water across South Africa. *Journal of Geochemical Exploration,* 145**,** 213-222.

Wickham, H., Averick, M., Bryan, J., Chang, W., McGowan, L.D.A., François, R., Grolemund, G., Hayes, A., Henry, L., Hester, J. & Kuhn, M. 2019. Welcome to the Tidyverse. *Journal of Open Source Software*, 4(43), 1686.

Wilkins, J. 2017. Middle Pleistocene lithic raw material foraging strategies at Kathu Pan 1, Northern Cape, South Africa. *Journal of Archaeological Science: Reports,* 11**,** 169-188.

Wilkins, J. 2021. *Homo sapiens* origins and evolution in the Kalahari Basin, southern Africa. *Evolutionary Anthropology: Issues, News, and Reviews,* 30**,** 327-344.

Wilkins, J. & Chazan, M. 2012. Blade production ~500 thousand years ago at Kathu Pan 1, South Africa: support for a multiple origins hypothesis for early Middle Pleistocene blade technologies. *Journal of Archaeological Science,* 39**,** 1883-1900.

Wilkins, J., Schoville, B. J., Brown, K. S., Gliganic, L., Meyer, M. C., Loftus, E., Pickering, R., Collins, B., Blackwood, A. F., Makalima, S., Hatton, A. & Maape, S. 2020. Fabric analysis and chronology at Ga-Mohana Hill North Rockshelter, southern Kalahari Basin: evidence for *in situ*, stratified Middle and Later Stone Age deposits. *Journal of Paleolithic Archaeology,* 3**,** 336-361.

Wilkins, J., Schoville, B. J., Pickering, R., Gliganic, L., Collins, B., Brown, K. S., Von Der Meden, J., Khumalo, W., Meyer, M. C., Maape, S., Blackwood, A. F. & Hatton, A. 2021. Innovative *Homo sapiens* behaviours 105,000 years ago in a wetter Kalahari. *Nature,* 592**,** 248-252.

Wilkins, J. & Schoville, B. J. 2024. Did climate change make *Homo sapiens* innovative, and if yes, how? Debated perspectives on the African Pleistocene record. *Quaternary Science Advances,* 14, 100179.

Will, M., Kandel, A. W., Kyriacou, K. & Conard, N. J. 2016. An evolutionary perspective on coastal adaptations by modern humans during the Middle Stone Age of Africa. *Quaternary International,* 404**,** 68-86.

Willimas, P. W. 2008. The role of the epikarst in karst and cave hydrogeology: a review. *International Journal of Speleology*, 37(1), 1-10.

Woodhead, J. & Pickering, R. 2012. Beyond 500 ka: progress and prospects in the U Pb chronology of speleothems, and their application to studies in palaeoclimate, human evolution, biodiversity and tectonics. *Chemical Geology,* 322**,** 290-299.

Woodhead, J. D., Hellstrom, J., Hergt, J. M., Greig, A. & Maas, R. 2007. Isotopic and elemental imaging of geological materials by laser ablation inductively coupled plasma-mass spectrometry. *Geostandards and Geoanalytical Research,* 31**,** 331-343.

Wurz, S. 2013. Technological trends in the Middle Stone Age of South Africa between MIS 7 and MIS 3. *Current Anthropology,* 54**,** S305-S319.

Xiao, L., Xu, Y. & Talma, A. S. 2019. Hydrochemical and isotopic approach to dynamic recharge of a dolomite aquifer in South Africa. *Hydrogeology Journal,* 27**,** 945-964.

Zavadlav, S., Rožič, B., Dolenec, M. & Lojen, S. 2017. Stable isotopic and elemental characteristics of recent tufa from a karstic Krka River (south-east Slovenia): useful environmental proxies? *Sedimentology,* 64**,** 808-831.

Zhang, K., Zhu, X.-K. & Yan, B. 2015. A refined dissolution method for rare earth element studies of bulk carbonate rocks. *Chemical Geology,* 412**,** 82-91.

Zhao, J.-X., Xia, Q. & Collerson, K. D. 2001. Timing and duration of the Last Interglacial inferred from high resolution U-series chronology of stalagmite growth in Southern Hemisphere. *Earth and Planetary Science Letters,* 184**,** 635-644.

Ziegler, M., Simon, M. H., Hall, I. R., Barker, S., Stringer, C. & Zahn, R. 2013. Development of Middle Stone Age innovation linked to rapid climate change. *Nature Communications,* 4**,** 1905.

APPENDICES

The following appendices can be accessed online via this link.

Appendix I

Some of the results presented in Chapter 4 and Chapter 6 are included in the following peer-reviewed articles. The pdf versions are available in the folder Appendix 1 online.

1) von der Meden., J., Pickering, R., Schoville, B. J., Green, H., Weij, R., Hellstrom, J., Greig, A., Woodhead, J., Khumalo, W., Wilkins, J. (2022). Tufas indicate prolonged periods of water availability linked to human occupation in the southern Kalahari. *PLOS ONE*, 17(7). https://doi.org/10.1371/journal.pone.0270104
2) Wilkins, J., Schoville, B. J., Pickering, R., Gliganic, L., Collins, B., Brown, K. S., von der Meden, J., Khumalo, W., Meyer, M.C., Maape, S., Blackwood, A.F., Hatton, A. (2021). Innovative Homo sapiens behaviours 105,000 years ago in a wetter Kalahari. *Nature*, *592*(7853), 248–252. https://doi.org/10.1038/s41586-021-03419-0

Appendix II

Supplementary raw data files for XRD, LA-ICP-MS and solution ICP-MS results presented in Chapter 5 are available in the folder Appendix 2 online.

Appendix III

Supplementary data files for the U-Th results presented in Chapter 6 are available in the folder Appendix 3 online.

Appendix IV

Supplementary data files for the stable isotope results presented in Chapter 7 are available in the folder Appendix 4 online.